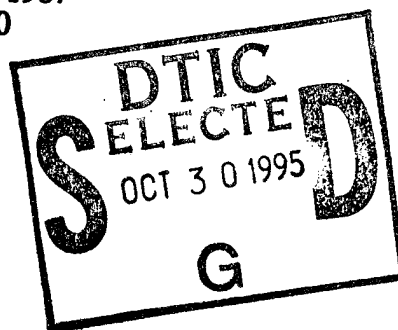


**DIRECT NUMERICAL SIMULATIONS OF
SEPARATED AND SEPARATED-REATTACHING FLOWS
ON MASSIVELY PARALLEL PROCESSING COMPUTERS**

BY

FADY MICHEL NAJJAR

**B. E., American University of Beirut, 1987
M.S., University of Illinois, 1990**



THESIS

**Submitted in partial fulfillment of the requirements
for the degree of Doctor of Philosophy in Mechanical Engineering
in the Graduate College of the
University of Illinois at Urbana-Champaign, 1994**

Urbana, Illinois

19951027 050

DTIC QUALITY INSPECTED 1

DISTRIBUTION STATEMENT A

**Approved for public release;
Distribution Unlimited**

UNIVERSITY OF ILLINOIS AT URBANA-CHAMPAIGN

THE GRADUATE COLLEGE

APRIL, 1994

WE HEREBY RECOMMEND THAT THE THESIS BY

FADY MICHEL NAJJAR

ENTITLED DIRECT NUMERICAL SIMULATIONS OF SEPARATED AND
SEPARATED-REATTACHING FLOWS
ON MASSIVELY PARALLEL PROCESSING COMPUTERS

BE ACCEPTED IN PARTIAL FULFILLMENT OF THE REQUIREMENTS FOR
THE DEGREE OF DOCTOR OF PHILOSOPHY

S. Vanha

Director of Thesis Research

A. R. Addy

Head of Department

Committee on Final Examination†

S. Vanha

Chairperson

J. Craig Dutton

John Walbran

S. Balakrishna

† Required for doctor's degree but not for master's.

O-517

Accession For	
NTIS	CRA&I <input checked="" type="checkbox"/>
DTIC	TAB <input type="checkbox"/>
Unannounced <input type="checkbox"/>	
Justification _____	
By _____	
Distribution / _____	
Availability Codes	
Dist	Avail and/or Special
A-1	

DISTRIBUTION STATEMENT A

Approved for public release;
Distribution Unlimited

ABSTRACT

Direct numerical simulations of separated-reattaching and separated flows have been performed on massively parallel processing computers. Two basic geometrical configurations have been studied: the separated-reattaching flow past a normal flat plate with an attached downstream splitter plate and the separated flow past a flat plate held normal to a uniform stream. A high-order finite-difference formulation on collocated grids has been developed to perform unsteady fluid flow simulations in rectangular geometries. The numerical procedure is based on a fifth-order upwind-biased scheme for the convective terms and a fourth-order accurate stencil for the diffusive terms. A direct solver based on eigenvalue decomposition has been developed for the pressure-Poisson equation. A mixed Fourier-spectral/finite-difference formulation is used for the spanwise discretization, and a data-parallel algorithm has been developed for the CM-5. The performance of the algorithm has been evaluated on various grid sizes in model flow problems and for different partition sizes.

The characteristics of the separated-reattaching flow have been investigated through two-dimensional simulations in the steady and unsteady regimes. The shedding mechanism is characterized by two major modes at $Re = 250$ and a single mode at $Re = 375$ and 500 . Further, the instability of the separated shear layer is found to be consistent with inviscid theory. For the two-dimensional study of the separated flow past a normal flat plate, the time-mean flow quantities are observed to be over-estimated compared to the experiments. The time-mean drag coefficient is also over-predicted by a factor of up to 2. This is attributed to the high coherence of the vortices predicted by the two-dimensional simulations. Two interaction regions have been identified in the far wake for $Re = 500$ and 1000 and are observed to occur pseudo-periodically.

Large-scale computations of the three-dimensional separated flow have also been carried out. The flow is seen to break down into small-scale structures and the spanwise development of these structures has been studied. Streamwise ribs and spanwise rolls are identified in the near wake through visualization techniques. The presence of these coherent structures corroborates the experimental observations and numerical calculations for mixing layers and wakes of circular cylinders. The time-mean velocities and Reynolds stresses are found to agree well with the experiments conducted at higher Reynolds numbers.

*A Michel, Aida, Amal et Mira
pour votre Amour*

A Mi Jenecsis.

To the loving memory of my grand-parents and Katia Sarkis

ACKNOWLEDGMENTS

I would like to thank Professor S. Pratap Vanka for his guidance and support throughout this stimulating study. Working with Professor Vanka has been a challenging and instructive experience and provided me with valuable knowledge.

The work reported in this dissertation was supported by the Office of Naval Research under grants N-00014-92-J-1334 and N-00014-92-J-1640. The calculations were performed on the CRAY-YMP and the Connection Machine Model 5 (CM-5) at the National Center for Supercomputing Applications (NCSA), University of Illinois, Urbana-Champaign. The work was initially supported by the Experimental Research Branch, AFWAL/POPT, at Wright-Patterson Air Force Base. The support of these organizations and the program technical monitors, Drs. D. Fyfe, J. Fein, A.S. Nejad, and S. Ramberg, are gratefully acknowledged.

My thanks are extended to the members of my thesis committee, Professors S. Balachandar, J. Craig Dutton, and John S. Walker. Acknowledgments are also due to my colleagues in the Computational Fluid Dynamics Laboratory - Wm. Kevin Cope, Dr. Ravi K. Madabhushi, Joseph H. Robichaux, and Dr. Mingyu Wang - for their help and interesting discussions. I also would like to thank Dr. Danesh Tafti for his comments on issues related to this work.

Appreciation is due to Tarun Mathur, Nada Khattar, and Jalal Wehbeh, for their friendships. I would like to thank my many friends whose companionship I enjoyed thoroughly. Acknowledgments are due to my teachers whose dedication has constantly motivated me.

I am most grateful to Dr. Jenechs R. Castro (M.D., i.e.) whose love, belief, and devotion have been a constant source of encouragement and motivation.

Finally, I am most thankful to my parents, Michel and Aida Najjar, and my sisters, Amal Najjar-Khlat and Mira Najjar. Their love, support and encouragement throughout my life have been responsible for my achievements.

TABLE OF CONTENTS

	Page
LIST OF TABLES.....	ix
LIST OF FIGURES.....	x
1. INTRODUCTION.....	1
1.1 Problem Considered.....	1
1.2 Technical Approach.....	3
1.3 Present Contributions.....	5
1.4 Outline of the Thesis.....	6
2. LITERATURE REVIEW.....	7
2.1 Separated-Reattaching Flows.....	7
2.2 Separated Flows.....	12
3. NUMERICAL PROCEDURE FOR TWO- DIMENSIONAL SIMULATIONS.....	19
3.1 Governing Equations and the Fractional-Step Method.....	19
3.2 Spatial Discretization Scheme.....	21
3.3 Formulation of the Pressure-Poisson Equation.....	23
3.3.1 Inconsistent Finite-Difference Method.....	24
3.3.2 Consistent Finite-Difference Method.....	25
3.3.3 Consistent Finite-Volume Method.....	27
3.3.4 Satisfaction of Compatibility and Integrability Conditions.....	29
3.4 Direct Solver Algorithm for the Pressure-Poisson Equation.....	33
3.5 Stability Analysis of the Numerical Scheme.....	35
3.6 Capacitance Matrix Technique.....	36
3.7 Validation of the Numerical Scheme.....	37
3.7.1 Vortex-Decay Problem.....	38
3.7.2 Driven-Cavity Flow.....	40
3.7.3 Kovasznay Flow.....	43
3.8 Evaluation of Outlet Boundary Conditions for Flows in Unbounded Domains.....	43

4. NUMERICAL PROCEDURE FOR THREE-DIMENSIONAL SIMULATIONS.....	47
4.1 Fourier-Spectral Representation.....	47
4.2 Spectral Formulation of the Pressure-Poisson Equation.....	48
4.3 Numerical Stability.....	51
4.4 Validation of the Numerical Scheme.....	52
5. DESCRIPTION OF THE DATA-PARALLEL ALGORITHM.....	54
5.1 Details of the CM-5 Architecture.....	54
5.2 Data-Parallel Algorithm for Two-Dimensional Simulations.....	56
5.2.1 Performance of Basic Linear Algebra and Communication Routines.....	57
5.2.2 Implementation.....	59
5.2.3 Timings and Performance.....	61
5.3 Data-Parallel Algorithm for Three-Dimensional Simulations.....	63
5.3.1 Performance of Basic Linear Algebra and Communication Routines.....	63
5.3.2 Implementation.....	65
5.3.3 Timings and Performance.....	67
6. TWO-DIMENSIONAL SIMULATIONS.....	70
6.1 Calculations of Separated-Reattaching Flow Past a Normal Flat Plate with an Attached Downstream Splitter Plate.....	70
6.1.1 Computational Details.....	70
6.1.2 Boundary Conditions.....	71
6.1.3 Steady Regime.....	72
6.1.4 Unsteady Regime.....	74
6.1.4.1 Time-Mean Flow Variables.....	74
6.1.4.2 Description of the Large-Scale Structures.....	78
6.1.4.3 Shedding Frequency, Convective Velocities, and Linear Stability Analysis.....	81
6.2 Calculations of Separated Flow past a Normal Flat Plate.....	85
6.2.1 Computational Details.....	85
6.2.2 Time-Mean Flow Variables.....	87
6.2.3 Description of the Large-Scale Structures.....	90
6.2.4 Drag Signature, Shedding Frequency, Convective Velocity, and Linear Stability Analysis.....	93

7. THREE-DIMENSIONAL SIMULATION OF SEPARATED FLOW PAST A NORMAL FLAT PLATE.....	95
7.1 Computational Details.....	95
7.2 Time-Mean Flow Characteristics.....	96
7.3 Instantaneous Flow Characteristics.....	99
7.4 Eduction of Coherent Structures.....	101
8. CONCLUSIONS AND RECOMMENDATIONS.....	105
8.1 Conclusions.....	105
8.2 Recommendations for Future Research.....	107
TABLES.....	109
FIGURES.....	120
BIBLIOGRAPHY.....	262
APPENDICES.....	273
A Spatial Discretization for Rectilinear Non-Uniform Grids.....	274
B Formulation of Pressure Discretization Schemes.....	278
C Second-Order Finite-Difference Matrices.....	288
D Modifications of the Spatial Derivatives for Interior Obstacles.....	290
E Capacitance Matrix Technique.....	297
VITA.....	299

LIST OF TABLES

		Page
Table 2.1.1	Experimental investigations of separated-reattaching flows.....	110
Table 3.7.1	Summary of different formulations used in the present study (Entries represent order of accuracy of stencil).....	111
Table 3.7.1.2	Error reduction for decay of a vortex at $t = 0.1$ (Grids = 17×17 , 33×33 , 65×65).....	111
Table 3.7.2.1	Results for driven-cavity flow at $Re = 100$ on 65×65 uniform mesh.....	112
Table 3.7.2.2	Results for driven-cavity flow at $Re = 400$ on 65×65 uniform mesh.....	112
Table 3.7.2.3	Results for driven-cavity flow at $Re = 1000$ on 65×65 uniform mesh.....	112
Table 3.7.2.4	Characteristics of pressure formulations.....	113
Table 5.2.1.1	Performance in GFLOPS of basic linear algebra routines for two- dimensional arrays on 256-processor CM-5 partition in scalar mode.....	114
Table 5.2.1.2	Performance in GFLOPS of basic linear algebra routines for two- dimensional arrays on 256-processor CM-5 partition in vector mode.....	114
Table 5.2.3.1	CPU timings and performance in GFLOPS of the two-dimensional algorithm on 512-processor CM-5 partition in vector mode.....	115
Table 5.3.3.1	CPU timings and performance in GFLOPS of the three-dimensional algorithm on 512-processor CM-5 partition in vector mode.....	116
Table 6.1.4.2.1	Characteristics of the shed vortices at $Re = 250$	117
Table 6.1.4.3.1	Modified non-dimensional frequency, ω^* (Equation 6.1.4.3.6) for the separated-reattaching flow.....	117
Table 6.2.1.1	Summary of grid resolution and computational domain.....	118
Table 6.2.4.1	Modified non-dimensional frequency, ω^* , for the separated flow.....	118
Table 7.2.1	Summary of drag coefficient compiled from experiments and numerical simulations.....	119

LIST OF FIGURES

	Page
Figure 3.2.1 Schematic of collocated grid arrangement. (o) collocated variables (x) cell-face variables.....	121
Figure 3.7.1.1 Distribution of L_u^∞ norm with grid size at $t = 0.35$ for the vortex-decay problem ($Re = 1$). (a) CFVM2 ($\lambda = 1.83$), (b) CFVM1 ($\lambda = 1.82$), (c) CFDM3 ($\lambda = 3.69$), (d) CFVM3 ($\lambda = 2.88$), (e) IFDM ($\lambda = 2.61$), (f) CFDM2 ($\lambda = 4.51$) (g) CFDM1 ($\lambda = 4.37$), (•) Le & Moin (1991) ($\lambda = 2.53$).....	122
Figure 3.7.1.2 Maximum divergence in the collocated velocities for the vortex- decay problem ($Re = 1$) as calculated by the various methods. (a) CFVM1, (b) CFVM2, (c) CFVM3, (d) IFDM, (e) CFDM1-3.....	123
Figure 3.7.1.3 Distribution of the error norms with the Reynolds number for the vortex-decay problem using CFVM2. Grid size = 65×65 , $\Delta t = 10^{-4}$, $t = 0.5$	124
Figure 3.7.2.1 Velocity profile along the vertical centerline ($x = 0.5$) for the driven-cavity problem at $Re = 100$. Grid size = 65×65	125
Figure 3.7.2.2 Velocity profile along the vertical centerline ($x = 0.5$) for the driven-cavity problem at $Re = 1000$. Grid size = 65×65	125
Figure 3.7.2.3 Integrated mass based on the cell fluxes for the driven- cavity problem at $Re = 1000$. Grid size = 65×65	126
Figure 3.7.2.4 Integrated mass based on the collocated velocities for the driven- cavity problem at $Re = 1000$. Grid size = 65×65	126
Figure 3.7.2.5 Profile of the pressure along horizontal centerline ($y = 0.5$) for the driven-cavity problem at $Re = 1000$. (a) overall distribution, (b) close-up view. Grid size = 65×65	127
Figure 3.7.3.1 Streamlines for the Kovasznay flow at $Re = 40$	128
Figure 3.7.3.2 Distribution of the error norms based on (a) the streamwise velocity and (b) the pressure with grid resolution for the Kovasznay flow at $Re = 40$	129
Figure 3.8.1 Velocity difference and spanwise vorticity for a convecting vortex using boundary condition (3.8.1a) (a) $t = 0$, (b) $t = 1$, (c) $t = 2$, (d) $t = 3$	130

Figure 3.8.2	Velocity difference and spanwise vorticity for a convecting vortex using boundary condition (3.8.1b) (a) $t = 1$, (b) $t = 2$, (c) $t = 3$	132
Figure 3.8.3	Velocity difference and spanwise vorticity for a convecting vortex using boundary condition (3.8.1c) (a) $t = 1$, (b) $t = 2$, (c) $t = 3$	133
Figure 3.8.4	Velocity difference and spanwise vorticity for a convecting vortex using boundary condition (3.8.1d) (a) $t = 1$, (b) $t = 2$, (c) $t = 3$	134
Figure 3.8.5	Time variation of the maximum streamwise velocity difference, $[(u-u_0)/u_0]_{\max}$, for a convecting vortex. Comparison of various outlet boundary conditions.....	135
Figure 3.8.6	Time variation of the maximum spanwise vorticity, $(\omega_z)_{\max}$, for a convecting vortex. Comparison of various outlet boundary conditions.....	135
Figure 4.4.1	Distribution of the spanwise velocity component in the x-direction at $y = 0$ for the fully-developed laminar flow through a square duct at $Re = 10$ and 30	136
Figure 4.4.2	Temporal evolution of (a) \hat{u}_{kz} and (b) \hat{w}_{kz} at $x = y = -0.5625$ for the decay of a 3-D perturbation in a laminar flow through a square duct at $Re = 10$ and $\epsilon = 0.05$	137
Figure 4.4.3	Temporal variation of the maximum divergence for the decay of a 3-D perturbation in a laminar flow through a square duct at $Re = 10$ and $\epsilon = 0.05$	138
Figure 4.4.4	Temporal evolution of (a) \hat{u}_{kz} and (b) \hat{w}_{kz} at $x = y = -0.5625$ for the decay of a 3-D perturbation in a laminar flow through a square duct at $Re = 30$ and $\epsilon = 0.3$	139
Figure 5.2.1.1	Performance of a triad operation, $A = A + B*C$, in scalar mode for various CM-5 partitions.....	140
Figure 5.2.1.2	Performance of the matrix-matrix multiplication using CMSSL routine, <code>gen_matrix_mult</code> , in scalar mode for various CM-5 partitions.....	140
Figure 5.2.1.3	Performance of a triad operation, $A = A + B*C$, in vector mode for various CM-5 partitions.....	141

Figure 5.2.1.4	Performance of the matrix-matrix multiplication using CMSSL routine, <code>gen_matrix_mult</code> , in vector mode for various CM-5 partitions.....	141
Figure 5.2.1.5	CPU run times for the communication functionalities on 32-processor partition.....	142
Figure 5.2.3.1	Performance of the two-dimensional data-parallel algorithm on various CM-5 partitions.....	143
Figure 5.2.3.2	Speed-up factors of the two-dimensional data-parallel algorithm for various processor ratios.....	143
Figure 5.3.1.1	Performance of a triad operation, $A = A + B * C$, for various CM-5 partitions. Array axes have a (NEWS) layout.....	144
Figure 5.3.1.2	Performance of the matrix-matrix multiplication using CMSSL routine, <code>gen_matrix_mult</code> , for various CM-5 partitions. Array axes have a (NEWS) layout.....	144
Figure 5.3.1.3	Performance of triad operation, $A = A + B * C$, for three-dimensional arrays with $N_z = 128$ on a 32-processor partition.....	145
Figure 5.3.1.4	Performance of matrix-matrix multiplication using CMSSL routine, <code>gen_matrix_mult</code> , for various layouts of the three-dimensional arrays on a 32-processor partition ($N_z = 128$).....	145
Figure 5.3.1.5	Performance of triad operation, $A = A + B * C$, for three-dimensional arrays with various N_z on a 32-processor partition. Array axes have a (BLOCK/PROCS) layout.....	146
Figure 5.3.1.6	Performance of the matrix-matrix multiplication using CMSSL routine, <code>gen_matrix_mult</code> , for three-dimensional arrays on a 32-processor partition. Array axes have a (BLOCK/PROCS) layout.....	147
Figure 5.3.3.1	Performance of the three-dimensional data-parallel algorithm on various CM-5 partition sizes.....	148
Figure 5.3.3.2	Speed-up factors of the three-dimensional data-parallel algorithm for various processor ratios.....	148
Figure 6.1.1	Schematic of the geometrical configuration and the computational domain for the separated-reattaching flow.....	149
Figure 6.1.1.1	Distribution of the mesh size in (a) x-direction, and (b) y-direction.....	150
Figure 6.1.1.2	Distribution of the metrics in (a) x-direction, and (b) y-direction.....	151

Figure 6.1.2.1	Contours of spanwise vorticity, ω_z , near the outlet boundary for (a) Equation (3.8.1c), (b) Equation (3.8.1d), (c) Equation (3.8.1e) (ω_{zmin} , ω_{zmax} , $\Delta\omega_z$) = (-2.05, -0.05, 0.2).....	152
Figure 6.1.3.1	Temporal evolution of the pressure signals at $x = 15.25$, $y = 1.5$ for the steady regime.....	153
Figure 6.1.3.2	Streamlines in the steady regime: (a) $Re = 50$, (b) $Re = 100$, (c) $Re = 150$	154
Figure 6.1.3.3	Variation of the reattachment length, x_R , with free-stream Reynolds number compiled from experiments and calculations.....	155
Figure 6.1.3.4	Streamwise distribution of the surface pressure coefficient, $\overline{C_{p_s}}$, in the steady regime.....	156
Figure 6.1.3.5	Streamwise distribution of the skin-friction factor, $\overline{C_f}$, in the steady regime.....	156
Figure 6.1.3.6	Distribution of the surface pressure coefficient, $\overline{C_{p_s}}$, on the front and rear faces of the plate for $Re = 100$	157
Figure 6.1.3.7	Variation of the time-mean drag coefficient, $\overline{C_D}$, with free-stream Reynolds numbers.....	157
Figure 6.1.4.1.1	Time-mean streamlines in the unsteady regime. (a) $Re = 250$, (b) $Re = 375$, (c) $Re = 500$	158
Figure 6.1.4.1.2	Loci of zero streamfunction ($\overline{\psi} = 0$) for Reynolds number in the unsteady regime.....	159
Figure 6.1.4.1.3	Profiles of the time-mean streamwise velocity, \overline{u} , at (a) $x/x_R = 0.38$, (b) $x/x_R = 0.67$, (c) $x/x_R = 0.93$, (d) $x/x_R = 1.25$ (\square) $Re = 250$, (\square) $Re = 500$ (\blacksquare) Ruderich & Fernholz (1986), (\circ) Castro and Haque (1987)....	160
Figure 6.1.4.1.4	Profiles of the time-mean streamwise velocity, \overline{u} , at (a) $x/x_R = 0.20$, (b) $x/x_R = 0.56$, (c) $x/x_R = 1.09$, (d) $x/x_R = 1.45$ (\square) $Re = 250$, (\square) $Re = 500$ (\blacktriangle) Jaroach & Fernholz (1986).....	162
Figure 6.1.4.1.5	Streamwise distribution of the time-mean skin-friction factor, $\overline{C_f}$, in the unsteady regime.....	164

Figure 6.1.4.1.6	Streamwise distribution of the modified surface pressure coefficient, \tilde{C}_{p_s} , in the unsteady regime.....	164
Figure 6.1.4.1.7	Distribution of the surface pressure coefficient, \overline{C}_{p_s} , on the front and rear faces of the plate in the unsteady regime compared with the experimental measurements.....	165
Figure 6.1.4.1.8	Streamwise distribution of the time-mean velocity difference, $\Delta \bar{u}$	166
Figure 6.1.4.1.9	Streamwise distribution of the vorticity thickness, δ_w/x_R	166
Figure 6.1.4.1.10	Variation of the shear layer center, y_c , with x/x_R	167
Figure 6.1.4.1.11	Loci of zero streamwise velocity for Reynolds numbers in the unsteady regime.....	167
Figure 6.1.4.1.12	Loci of maximum streamwise velocity for Reynolds numbers in the unsteady regime.....	168
Figure 6.1.4.1.13	Flow direction along lines of $\eta = 0$ and $\psi = 0$ compared with Castro and Haque (1987).....	168
Figure 6.1.4.2.1	Instantaneous snapshot of unsteady flow at $Re = 250$. (a) Streamlines. $(\psi_{min}, \psi_{max}, \Delta\psi) = (-1, 0, 0.05)$ (b) Spanwise Vorticity. $(\omega_{zmin}, \omega_{zmax}, \Delta\omega_z) = (-4.05, -0.05, 0.25)$ (c) Skin-friction factor, $C_f \times 10$ (—) and Surface pressure coefficient, C_{p_s} (—).....	169
Figure 6.1.4.2.2	Time signal of the fluctuating surface pressure, p'_s , at $x/x_R = 0.8$ for $Re = 250$. Modes I and II are identified at selected time intervals.....	170
Figure 6.1.4.2.3	Time development of the spanwise vorticity for vortex shedding mode I at $Re = 250$. (a) $t = 380$, (b) $t = 385$, (c) $t = 390$, (d) $t = 395$	171
Figure 6.1.4.2.4	Path of propagating vortex A (refer to Figure 6.1.4.2.3). Core location is shown at intervals of five time units.	173
Figure 6.1.4.2.5	Time evolution of the spanwise vorticity for vortex shedding mode II at $Re = 250$. (a) $t = 740$, (b) $t = 745$, (c) $t = 750$, (d) $t = 755$, (e) $t = 760$	174

Figure 6.1.4.2.6	Time signal of the fluctuating streamwise velocity, u' , at $x = 12.5$, $y = 1$ for (a) $Re = 375$, (b) $Re = 500$	175
Figure 6.1.4.2.7	Representative time frames of the spanwise vorticity at $Re = 375$. (a) $t = 315.6$, (b) $t = 318.8$, (c) $t = 325$, (d) $t = 328.1$, (e) $t = 331.2$	176
Figure 6.1.4.2.8	Representative time frames of the spanwise vorticity at $Re = 500$. (a) $t = 175$, (b) $t = 177.5$, (c) $t = 180$, (d) $t = 185$, (e) $t = 190$	178
Figure 6.1.4.2.9	Streamwise distribution of the minimum instantaneous ω_z in the unsteady regime (arbitrary time unit).....	180
Figure 6.1.4.2.10	Temporal evolution of the drag coefficient for (a) $Re = 250$, (b) $Re = 375$, (c) $Re = 500$	181
Figure 6.1.4.3.1	Autocorrelation coefficient of the fluctuating pressure, Ap' , at $x = 12.5$, $y = 2$ for Reynolds numbers in the unsteady regime.....	183
Figure 6.1.4.3.2	Autocorrelation coefficient of the fluctuating pressure, Ap' , at $x = 1$, $y = 2$ for $Re = 250$ and 500	183
Figure 6.1.4.3.3	Power spectrum of the drag coefficient at $Re = 375$ and 500	184
Figure 6.1.4.3.4	Development of the integral timescale Λ_u^t , U_∞/x_R against x/x_R	185
Figure 6.1.4.3.5	Development of the integral timescale Λ_p^t , U_∞/x_R against x/x_R	185
Figure 6.1.4.3.6	Space-time correlation coefficient of the fluctuating surface pressure, Sp'_s for $Re = 375$	186
Figure 6.1.4.3.7	Streamwise variation of the convective velocity based on the fluctuating pressure, U_c^p/U_∞ , at the surface and at the center of the shear layer for $Re = 375$	187
Figure 6.1.4.3.8	Streamwise variation of the convective velocity based on the fluctuating skin-friction coefficient and the fluctuating streamwise velocity for $Re = 375$	187
Figure 6.2.1	Schematic of the geometrical configuration and the computational domain for the separated flow past a normal flat plate.....	188
Figure 6.2.1.1	Distribution of mesh spacings in (a) x-direction, and (b) y-direction for various grid configurations.....	189
Figure 6.2.1.2	Temporal variation of the drag coefficient for various grid configurations at $Re = 100$	190

Figure 6.2.1.3	Temporal variation of the drag coefficient for grids B and D at $Re = 250$	190
Figure 6.2.1.4	Distribution of mesh spacings in the x-direction for various upstream distances, x_u . Grid Resolution = 513×257	191
Figure 6.2.1.5	Temporal variation of the drag coefficient for various upstream distances, x_u , at $Re = 100$. Grid Resolution = 513×257	191
Figure 6.2.1.6	Temporal variation of the drag coefficient for various downstream distances, x_d , at $Re = 100$. Grid Resolution = 513×257 , $x_u = -10$	192
Figure 6.2.1.7	Distribution of mesh spacings for grid F. Grid Resolution = 513×257	192
Figure 6.2.1.8	Distribution of the metrics in the (a) x-direction, and (b) y-direction. Grid Resolution = 513×257 , $x_u = -10$, $x_d = 25$ (Grid F).....	193
Figure 6.2.2.1	Time-mean streamlines for (a) $Re = 100$, (b) $Re = 500$, (c) $Re = 1000$	194
Figure 6.2.2.2	Profiles of the time-mean streamwise velocity along the centerline ($y = 0$) for the three Reynolds numbers.....	195
Figure 6.2.2.3	Profiles of the time-mean wake-defect velocity at different streamwise locations for (a) $Re = 100$, (b) $Re = 500$, (c) $Re = 1000$	196
Figure 6.2.2.4	Loci of $y(\bar{u} = 0.99)$ for various Reynolds numbers. (—) $Re = 100$, (----) $Re = 500$, (— . —) $Re = 1000$	198
Figure 6.2.2.5	Contours of time-mean spanwise vorticity for (a) $Re = 100$, (b) $Re = 500$, (c) $Re = 1000$. Dashed Lines : $(\omega_{zmin}, \omega_{zmax}, \Delta\omega_z) = (-6.5, -0.5, 0.25)$ Solid Lines : $(\omega_{zmin}, \omega_{zmax}, \Delta\omega_z) = (0.5, 6.5, 0.25)$	199
Figure 6.2.2.6	Variation of the shear-layer center, y_c , for various Reynolds numbers. (—) $Re = 100$, (----) $Re = 500$, (— . —) $Re = 1000$	200
Figure 6.2.2.7	Streamwise distribution of the vorticity thickness, δ_w , for various Reynolds numbers. (—) $Re = 100$, (----) $Re = 500$, (— . —) $Re = 1000$	200
Figure 6.2.2.8	Distribution of the time-mean surface pressure coefficient, $\overline{C_p}$, on the front and rear faces of the flat plate.....	201
Figure 6.2.2.9	Variation of the time-mean drag coefficient with free-stream Reynolds number.....	201

Figure 6.2.3.1	Instantaneous snapshot of the unsteady flow for $Re = 100$. (a) Spanwise Vorticity. Dashed Lines: $(\omega_{zmin}, \omega_{zmax}, \Delta\omega_z) = (-4.5, -0.5, 0.25)$ Solid Lines: $(\omega_{zmin}, \omega_{zmax}, \Delta\omega_z) = (0.5, 4.5, 0.25)$ (b) Streamlines. $(\psi_{min}, \psi_{max}, \Delta\psi) = (-1.5, 1.5, 0.1)$ (c) Pressure. Dashed Lines: $(p_{min}, p_{max}, \Delta p) = (-0.5, -0.025, 0.025)$. Solid Lines: $(p_{min}, p_{max}, \Delta p) = (0.025, 0.5, 0.025)$	202
Figure 6.2.3.2	Location of the vortex cores for $Re = 100$ corresponding to Figure 6.2.3.1. Values in brackets represent $[\omega_z, \Gamma]$, the spanwise vorticity in the core and the total vortex circulation.....	203
Figure 6.2.3.3	(a) Time trace of the streamwise velocity component and (b) u-v phase portrait for $Re = 100$ in the near-wake region ($x = 2, y = 1$).....	204
Figure 6.2.3.4	(a) Time trace of the streamwise velocity component and (b) u-v phase portrait for $Re = 100$ in the far-wake region ($x = 20, y = 2$).....	205
Figure 6.2.3.5	Spanwise vorticity contours for a representative shedding cycle for $Re = 100$. (a) $t = 91$, (b) $t = 92.5$, (c) $t = 94$, (d) $t = 95.5$, (e) $t = 97$. Dashed Lines: $(\omega_{zmin}, \omega_{zmax}, \Delta\omega_z) = (-4.5, -0.5, 0.1)$ Solid Lines: $(\omega_{zmin}, \omega_{zmax}, \Delta\omega_z) = (0.5, 4.5, 0.1)$	206
Figure 6.2.3.6	Instantaneous snapshot of the unsteady flow at $t = 120$ for $Re = 500$. (a) Spanwise Vorticity. Dashed Lines: $(\omega_{zmin}, \omega_{zmax}, \Delta\omega_z) = (-6.5, -0.5, 0.1)$ Solid Lines: $(\omega_{zmin}, \omega_{zmax}, \Delta\omega_z) = (0.5, 6.5, 0.1)$ (b) Streamlines. $(\psi_{min}, \psi_{max}, \Delta\psi) = (-1.5, 1.5, 0.1)$	208
Figure 6.2.3.7	Location of the vortex cores for $Re = 500$ corresponding to Figure 6.2.3.6. Value in brackets represents $[\omega_z]$, the spanwise vorticity in the core. $\Gamma = 6.6$	209
Figure 6.2.3.8	Spanwise vorticity contours for a representative shedding cycle for $Re = 500$. (a) $t = 71$, (b) $t = 74$, (c) $t = 77$, (d) $t = 78.5$. Dashed Lines: $(\omega_{zmin}, \omega_{zmax}, \Delta\omega_z) = (-6.5, -0.5, 0.1)$ Solid Lines: $(\omega_{zmin}, \omega_{zmax}, \Delta\omega_z) = (0.5, 6.5, 0.1)$	210
Figure 6.2.3.9	u-v phase portraits for $Re = 500$ in (a) the near-wake ($x = 2, y = 1$), and (b) the far-wake ($x = 20, y = 2$) regions.....	211

Figure 6.2.3.10	Time trace of the streamwise velocity component at a far-wake point ($x = 16, y = 0$) for $Re = 500$. Far-wake vortex interaction regions I and II are identified.....	212
Figure 6.2.3.11	Spanwise vorticity contours for a representative far-wake vortex interaction region II at $Re = 500$. (a) $t = 82.5$, (b) $t = 85.5$, (c) $t = 88.5$, (d) $t = 91$, (e) $t = 94$, (f) $t = 97$. Dashed Lines : ($\omega_{zmin}, \omega_{zmax}, \Delta\omega_z$) = (-6.5,-0.5,0.1) Solid Lines : ($\omega_{zmin}, \omega_{zmax}, \Delta\omega_z$) = (0.5,6.5,0.1).....	213
Figure 6.2.3.12	Spanwise vorticity contours for $Re = 500$ at $t = 150$. The pairing process in the lower half of the computational domain is shown. Dashed Lines : ($\omega_{zmin}, \omega_{zmax}, \Delta\omega_z$) = (-6.5,-0.5,0.1) Solid Lines : ($\omega_{zmin}, \omega_{zmax}, \Delta\omega_z$) = (0.5,6.5,0.1).....	215
Figure 6.2.3.13	Instantaneous snapshot of the unsteady flow at $t = 230$ for $Re = 1000$. (a) Spanwise Vorticity. Dashed Lines : ($\omega_{zmin}, \omega_{zmax}, \Delta\omega_z$) = (-8.5,-0.5,0.1) Solid Lines : ($\omega_{zmin}, \omega_{zmax}, \Delta\omega_z$) = (0.5,8.5,0.1) (b) Streamlines. ($\psi_{min}, \psi_{max}, \Delta\psi$) = (-1.5,1.5,0.1).....	216
Figure 6.2.3.14	Location of the vortex cores for $Re = 1000$ corresponding to Figure 6.2.3.13. Value in brackets represents the spanwise vorticity in the core, $[\omega_z]$. $\Gamma = 6.6$	217
Figure 6.2.3.15	Time traces of the streamwise velocity for $Re = 1000$ in (a) the near wake ($x = 2, y = 1$), and (b) the far wake ($x = 16, y = 0$). Far -wake interaction regions I and II are identified.....	218
Figure 6.2.3.16	u-v phase portraits for $Re = 1000$ in (a) the near wake ($x = 2, y = 1$), and (b) the far wake ($x = 20, y = 2$).....	219
Figure 6.2.3.17	Spanwise vorticity contours for a representative far-wake vortex interaction region II at $Re = 1000$. (a) $t = 111$, (b) $t = 112.5$, (c) $t = 114$, (d) $t = 115.5$, (e) $t = 117$, (f) $t = 118.5$	220
Figure 6.2.4.1	Temporal variation of the drag coefficient for (a) $Re = 100$ and 500 , (b) $Re = 1000$	222
Figure 6.2.4.2	Power spectrum in the near wake ($x = 2, y = 1$) for (a) $Re = 100$, (b) $Re = 500$, (c) $Re = 1000$	223
Figure 6.2.4.3	Streamwise variation of the convective velocity at $y = 0.5$ and 1 for $Re = 100$	225

Figure 7.1.1	Grid Distribution in (a) the x-direction, and (b) the y-direction.....	226
Figure 7.2.1	Contours of the time and span-averaged (a) streamlines, and (b) ω_z	227
Figure 7.2.2	Streamwise variation of the \overline{u} -velocity component along the centerline.....	228
Figure 7.2.3	Profiles of the time-mean streamwise velocity component at $x = 8$	228
Figure 7.2.4	Distributions of the normal stresses: (a) $\overline{u'^2}$, (b) $\overline{v'^2}$, (c) $\overline{w'^2}$	229
Figure 7.2.5	Distribution of the Reynolds shear stress, $\overline{u'v'}$	230
Figure 7.2.6	Streamwise variation of the rms stresses along the centerline.....	231
Figure 7.2.7	Profiles of (a) the streamwise stresses, $\overline{u'^2}$, (b) the cross-stream stress, $\overline{v'^2}$, (c) the spanwise stress, $\overline{w'^2}$, (d) the Reynolds stress, $\overline{u'v'}$, at $x = 8$. (____) Current Simulation, (-----) Joshi et al. (1994), (o) Kiya and Matsumura (1988).....	232
Figure 7.2.8	Streamwise variation of the time-mean pressure coefficient, C_p , along the centerline.....	234
Figure 7.2.9	Distribution of the time-mean surface pressure coefficient, C_p , on the front and rear sides of the flat plate.....	234
Figure 7.2.10	Distribution of $\overline{p'^2}$	235
Figure 7.3.1	Velocity vectors in (a) $z = \pi$ and (b) $y = 0$ planes for $t = 45$	236
Figure 7.3.2	Particle trajectories at $t = 45$. (a) Injection Line ($x = 0, y = 0.5$) (b) Injection Line ($x = -0.5, y = 0$).....	237
Figure 7.3.3	Contours of spanwise velocity for $t = 45$ in (a) $y = 0$, and (b) $x = 2$ planes. Dashed Lines ($w_{min}, w_{max}, \Delta w$) = (-0.1, -1.0, 0.1) Solid Lines ($w_{min}, w_{max}, \Delta w$) = (0.1, 1.0, 0.1).....	238

Figure 7.3.4	Spanwise variation of the instantaneous streamwise and spanwise velocity components. (a) upstream of the plate ($x = -0.5, y = 0$) (b) in the near wake ($x = 2, y = 0.5$) (c) at point ($x = 8, y = 0.5$) (d) in the far wake ($x = 16, y = 0.5$).....	239
Figure 7.3.5	Contours of span-averaged streamlines, $\langle \psi \rangle_z$, at $t = 45$. (a) stationary frame of reference Contour levels : $(\psi_{\min}, \psi_{\max}, \Delta\psi) = (-2.0, 2.0, 0.2)$ (b) frame of reference moving at a convective velocity of $0.6U_\infty$ Contour levels : $(\psi_{\min}, \psi_{\max}, \Delta\psi) = (-1.0, 1.0, 0.1)$	241
Figure 7.3.6	Contours of span-averaged spanwise vorticity, $\langle \omega_z \rangle_z$, at $t = 45$. Solid Lines : $(\omega_{z\min}, \omega_{z\max}) = (0.4, 40)$ Dashed Lines : $(\omega_{z\min}, \omega_{z\max}) = (-40, -0.4)$	242
Figure 7.3.7	Contours of instantaneous spanwise vorticity, ω_z , at $t = 45$. (a) $z = 0$, (b) $z = \frac{\pi}{4}$, (c) $z = \frac{\pi}{2}$, (d) $z = \frac{3\pi}{4}$ (e) $z = \pi$, (f) $z = \frac{5\pi}{4}$, (g) $z = \frac{3\pi}{2}$, (h) $z = \frac{7\pi}{4}$ Solid Lines : $(\omega_{z\min}, \omega_{z\max}) = (0.4, 40)$ Dashed Lines : $(\omega_{z\min}, \omega_{z\max}) = (-40, -0.4)$	243
Figure 7.3.8	Contours of spanwise vorticity, ω_z , for a representative shedding cycle : (a) $t = 42$, (b) $t = 44$, (c) $t = 46$, (d) $t = 48$. Solid Lines : $(\omega_{z\min}, \omega_{z\max}) = (0.4, 40)$ Dashed Lines : $(\omega_{z\min}, \omega_{z\max}) = (-40, -0.4)$	246
Figure 7.3.9	Time trace of the instantaneous streamwise and spanwise velocity components. (a) in the near-wake region ($x = 2, y = 0.5, z = 0$) and (b) at point $x = 8, y = 0$ and $z = \pi/2$	247
Figure 7.3.10	Time trace of the instantaneous drag coefficient at $Re = 1000$ predicted by (a) 2-D and (b) 3-D simulations.....	248
Figure 7.4.1	Surface of three-dimensional spanwise vorticity at $t = 45$. Surface Levels : Red = -2, Cyan = +2. Tic increments along x and z directions = 1 Tic increments along y direction = 0.5 Origin of axis at (0,-3,0). Flat Plate is shown as black shaded surface.....	249

Figure 7.4.2	Contours of spanwise vorticity at $t = 45$ in x - z planes : (a) $y = -0.5$, (b) $y = 0$, (c) $y = +0.5$ Solid Lines : $(\omega_{zmin}, \omega_{zmax}, \Delta \omega_z) = (0.5, 7.5, 0.5)$ Dashed Lines : $(\omega_{zmin}, \omega_{zmax}, \Delta \omega_z) = (-7.5, -0.5, 0.5)$ Arrows indicate spanwise rollers.	250
Figure 7.4.3	Surface of three-dimensional streamwise vorticity at $t = 45$. Surface Levels : Magenta = -2, Cyan = +2. Tic increments along x and z directions = 1 Tic increments along y direction = 0.5 Origin at $(0, -3, 0)$	252
Figure 7.4.4	Close-up view of the streamwise ribs. Surface Level : Magenta = -2. Tic increments along x and z directions = 1 Tic increments along y direction = 0.5 Origin at $(0, -3, 0)$	253
Figure 7.4.5	Spanwise variation of the streamwise vorticity for $t = 45$. (a) $z = 0$, (b) $z = \frac{\pi}{4}$, (c) $z = \frac{\pi}{2}$	254
Figure 7.4.6	Surface of three-dimensional cross-stream vorticity, ω_y , at $t = 45$. Surface Levels : Green = -2, Yellow = +2. Tic increments along x and z directions = 1 Tic increments along y direction = 0.5 Origin at $(0, -3, 0)$	255
Figure 7.4.7	Surface of three-dimensional (a) strain rate magnitude, D and (b) enstrophy, Q , at $t = 45$. Surface Levels : Red = 5, Cyan = 10. Tic increments along x and z directions = 1 Tic increments along y direction = 0.5 Origin at $(0, -3, 0)$	256
Figure 7.4.8	Contours of spanwise vorticity at $t = 45$ in : (a) the first core plane (CP): $x = 2$, (b) the mid-braid plane (MBP) : $x = 3.6$, and (c) the second core plane (CP) : $x = 5.5$. $(\omega_{zmin}, \omega_{zmax}, \Delta \omega_z) = (-7.5, -0.5, 0.5)$ Arrows indicate cusp regions.....	257
Figure 7.4.9	Contours of streamwise vorticity at $t = 45$ in : (a) the first core plane (CP): $x = 2$, (b) the mid-braid plane (MBP) : $x = 3.6$, and (c) the second core plane (CP) : $x = 5.5$. $(\omega_{xmin}, \omega_{xmax}, \Delta \omega_x) = (-7.5, -0.5, 0.5)$ Arrows indicate cusp regions.....	258

Figure 7.4.10	Contours of (a) ω_z , (b) ω_x in the rib plane (RP) at $z = \frac{3\pi}{16}$ and (c) ω_z , (d) ω_x in the between-rib plane (BRP) at $z = \frac{\pi}{4}$. (ω_{imin} , ω_{imax} , $\Delta \omega_i$) = (-7.5, -0.5, 0.5); $i = x$ or z Arrow indicates cusp region.....	259
Figure 7.4.11	Contours of streamwise vorticity at $t = 55$. Surface Level : Magenta = -2, Cyan = +2.....	261

1. INTRODUCTION

1.1 Problem Considered

Separated flows have been described by Morkovin (1964) as a 'kaleidoscope of challenging fluid dynamic phenomena'. Flow separation can be induced by several means. An attached boundary layer on a surface can separate if an adverse pressure gradient or a centrifugal force directed away from the wall is applied. Separated flows are also generated when a bluff body is placed normal to the flow. At low Reynolds number, a steady wake region is formed downstream of the body. Above a critical Reynolds number, the separated shear layer becomes unstable resulting in the shedding of Karman vortices. The study of wake instability dates back to the Renaissance when Leonardo daVinci sketched the flow patterns of circular cylinder wakes based on visual observations. However, the major work did not progress until the end of the nineteenth century with the studies of Strouhal (1878) and the theoretical analyses of von Karman (1912).

The study of wake instability past bluff bodies provides a rich and challenging environment from fundamental fluid dynamics to basic engineering applications. During the past five decades, separated flows have been extensively studied because of their relevance to drag on vehicles, flow over ship hulls, and submarines. Studies of vehicle propulsion are aimed on drag reduction and shape optimization. The wake signatures of ships and submarines are also of importance for defense surveillance and detection purposes. Bluff bodies such as plates, discs, circular and rectangular cylinders, and V-shaped prisms, are used in combustors to enhance the scalar mixing process and provide a flame-stabilizing region. Other considered applications have been offshore platforms, buildings, skyscrapers and bridges. Several basic geometrical configurations including circular and rectangular cylinders, flat plates, and airfoils have been experimentally and numerically investigated to understand the fundamental aspects of flow separation and wake instability. Further, the responses of the Karman vortices to perturbations in the freestream have been analyzed. Such perturbations are relevant to flow-induced vibrations of bluff bodies. A 'lock-on' mechanism is induced in a certain frequency range; as a result, the forced frequency of the perturbation becomes dominant and hinders the natural shedding frequency. The forces exerted on the bluff body increase significantly from the value for an unperturbed flow. These aspects are of interest to the study of flow-induced oscillations of buildings, marine structures and offshore platforms.

Wake-control mechanisms and their effects on the far-wake dynamics have also been proposed and include base mass injection, splitter plates, and immersion of small structures in the vicinity of the bluff body. These mechanisms have been observed as either enhancing the shear layer instability or eliminating the vortex shedding.

Flows with separation and reattachment, confining regions referred to as 'separation bubbles', are also of much interest in the design of heat exchangers, diffusers, combustors and flow meters. Separated regions cause excessive pressure losses and are also associated with high rates of heat transfer and scalar mixing. For the study of shear-layer instability from sharp-edged corners, several configurations have evolved as basic test cases: the backward-facing step, the blunt plate, and the normal plate with a long attached downstream splitter plate. At low Reynolds numbers, the shear layer separation is steady for steady upstream conditions. As the Reynolds number is increased, the separated shear layer becomes unstable and begins rolling into vortices. These vortices start growing by entraining mass from the uniform stream, coalesce half way from the time mean reattachment point, and finally are shed pseudo-periodically from the reattachment line. Rapid growth of the vortical structures develops in the first quarter of the time mean reattachment length and reaches a plateau downstream of the reattachment line. Much of the literature concerning unsteady separated flows has been in the turbulent flow regime.

The objectives of the present research are to study the fundamental aspects inherent in wake instability and separated-reattaching flows. To this end, two basic geometrical configurations have been considered. For the wake instability study, the flow past a flat plate held normal to a freestream is investigated. For such a configuration, the flow separates from the two fixed edges of the plate, and, unlike the circular cylinder, the separation point is independent of Reynolds number. For the separated-reattaching flow, the flow past the the normal plate with a long attached downstream splitter plate is studied. For this configuration, the flow separates from a fixed edge and subsequently reattaches on the splitter plate surface. The formation, evolution and propagation of the unsteady vortical structures are interesting fundamental fluid dynamic phenomena, and, to our knowledge, few studies have documented the characteristics of these flows in the low Reynolds number regime.

1.2 Technical Approach

Computational fluid dynamic studies are based on the solution of a non-linear system of equations, the Navier-Stokes equations, and complement experiments in understanding and predicting fundamental fluid dynamic mechanisms. These studies can be categorized under two principal types. The first approach referred to as Direct Numerical Simulation (DNS) integrates the time-dependent Navier-Stokes equations with resolution of all the temporal and spatial scales. In the laminar unsteady regime, the spatial scales can be resolved with modest sized grids. However, in the turbulent regime, very fine spatial resolution, up to the Kolmogorov scales, is required, thus mandating a corresponding fine temporal resolution. The grid requirements in a DNS vary as $Re^{9/4}$ where Re is the Reynolds number. Hence, these simulations are performed at low Reynolds numbers and are not in the range of practical interest. The computational complexity of such direct numerical simulations is enormous and high-speed vector supercomputers have been used over the past decade.

A second promising approach is the Large-Eddy Simulation (LES) concept, in which only the large anisotropic scales are resolved and the small scales are modeled. Since the computational resources required by large-eddy simulation are not as demanding as for direct numerical simulations, calculations can be performed in a more practical range of Reynolds numbers. Models for the small scales have been suggested to relate the effect of small scales on the large scales. Recent research in turbulence modeling has concentrated on this aspect. In the large-eddy simulation concept, the resolved scales are separated from the subgrid scales by applying a spatial filter to a continuous function in space and time (the velocity vector field, for example). The filtered Navier-Stokes equations represent the transport of the resolved-scale velocity field and include the contributions of the unresolved scales through a subgrid stress. The subgrid stresses quantify the interaction between the resolved scales and the unresolved scales, and the filtered equations require a turbulence model for closure. Although the LES concept has not been used in the current research study, we believe that it is a viable approach to investigate flows in a practical range of Reynolds number.

Since DNS and LES calculations resolve the temporal and spatial flow characteristics, accurate computational methods are needed in order to minimize the numerical errors. Direct numerical simulations of fluid flows have been primarily performed using spectral methods (Canuto et al., 1984). These methods have been

successfully applied to study turbulent flow in a straight channel (Moin and Kim, 1980), turbulent flow through a square duct (Madabhushi et al., 1993), etc. However, one shortcoming of the spectral schemes is the difficulty of their extension to complex geometries. Although spectral domain decomposition and spectral-element methods have been successfully used to study some complex flows (Macaraeg and Streett, 1986; Patera, 1984; Karniadakis, 1989; Karniadakis and Triantafyllou, 1992), such schemes are computationally more expensive and complicated to program. In comparison, finite-difference methods are simple and efficient for the simulation of flows within complex boundaries. In recent years, high-order accurate finite-difference schemes have been successfully applied to perform direct numerical simulations of unsteady incompressible fluid flows (Clarkson and McMurtry, 1990; Rai and Moin, 1991; Najjar and Vanka, 1993). Both staggered and non-staggered (i.e., collocated) grid arrangements have been used to discretize the governing equations. In the collocated-grid arrangement, all dependent variables (i.e., velocities and pressure) are located at the same physical location in contrast to the staggered arrangement where velocities are centered with the pressure locations. In general, the collocated arrangement of velocities and pressure reduces the amount of interpolation required when compared with discretization on a staggered mesh. Further, the collocated arrangement is more convenient for the use of high-order discretizations as well as general curvilinear coordinate systems. Recently, second-order accurate collocated schemes have successfully calculated several model flows with good accuracy (Strikwerda, 1984; Abdallah, 1987a,b; Birigen and Cook, 1988; Sotiropoulos and Abdallah, 1991; Armfield, 1991).

The computational requirements to perform direct numerical simulations are intensive even with vector supercomputer technology such as CRAY Y-MP and CRAY C-90. Several hundred hours on a CRAY Y-MP are required to perform simulations at low Reynolds numbers and these requirements considerably increase as higher Reynolds numbers are attempted. The advent of high-performance, scalable, massively parallel computers permits one to efficiently perform large-scale fluid flow computations. DNS of separated flows are ideally suited to scalable massively parallel processing (MPP) architectures such as the Thinking Machine CM-5, the Intel Paragon, and the CRAY T-3D platforms. The need for high spatial and temporal resolution in direct numerical simulations makes it an ideal application for the development of efficient parallel processing algorithms. Novel numerical algorithms are currently being devised to exploit the improved speeds of computation and the availability of larger memories on parallel machines. Several parallel processing architectures have been developed including the

Single-Instruction, Multiple-Data (SIMD) concept, and the Multiple-Instruction, Multiple-Data (MIMD) concept with shared and distributed memories (Ortega, 1989). With the advent of massively parallel processors, the computational fluid dynamics (CFD) field has been radically revised. Recent finely-resolved CFD simulations of compressible flows (Agrawal, 1989; Long et al., 1989; Wake and Egolf, 1989; Jespersen and Levit, 1989; Olsson and Johnsson, 1990; Oran et al., 1990; Saati et al., 1990), compressible reacting flows (Planche and Reynolds, 1992; Oran et al., 1992) and incompressible flows (Robichaux et al., 1992; Perot, 1992) have shown that parallel supercomputers such as the hypercubes IPSC/860 and CM-2 can attain speed-up factors of 5 over the CRAY vector supercomputers. In the present research effort, a data parallel CFD code on the Connection Machine 5 (CM-5) has been developed to perform large-scale computations of separated and separated-reattaching flows.

1.3 Present Contributions

The main contributions of the present research effort may be summarized as follows :

- (i) A high-order accurate finite-difference procedure has been developed to integrate the time-dependent Navier-Stokes equations. The governing equations are integrated by the fractional step method and discretized with a fully-explicit, Adams-Bashforth, high-order, finite-difference scheme on collocated grids. The convective terms are formulated using a fifth-order upwind biased scheme and the diffusive terms are discretized with fourth-order central-difference stencils. The discrete pressure-Poisson equation has a finite-volume formulation and is solved using matrix diagonalization. Further, the numerical procedure is extended to simulate three-dimensional flows. Fourier-spectral discretization is applied in the homogeneous spanwise direction.
- (ii) A scalable computational fluid dynamics computer program has been developed for use on massively parallel processing platforms. The data-parallel algorithm is based on a SIMD computing mode and is designed in a structured modular manner with emphasis on easy portability to various MPP machines. Most recent compile directives as well as library routines have been used to construct an algorithm with high parallel efficiency. The modular and general code structure will permit the calculations of a variety of fluid dynamics problems.

- (iii) The separated-reattaching flow past a normal flat plate with an attached downstream splitter plate has been investigated through two-dimensional simulations. Finely-resolved calculations have been performed at several Reynolds numbers. The characteristics of the flow in the steady and unsteady regimes are studied.
- (iv) Two-dimensional simulations of the separated flow past a normal flat plate have also been carried out. A systematic grid refinement study is performed to obtain accurate numerical results. Several interesting pairing processes of the Karman vortices have been identified.
- (v) Finally, a three-dimensional direct numerical simulation of the flow past a normal flat plate has been performed. Time-mean statistics are obtained and are seen to agree satisfactorily with the experiments conducted at higher Reynolds numbers. The temporal evolution of the coherent structures and their spanwise development have been studied.

1.4 Outline of the Thesis

The next six chapters present the various aspects of this dissertation. A review of previous work is summarized in Chapter 2. In Chapters 3 and 4, the governing equations and details of the numerical methods are presented. The data-parallel algorithm as well as the performance and representative timings are described in Chapter 5. Chapter 6 presents the results from the two-dimensional simulations for separated-reattaching and separated flows. The results from the three-dimensional calculation are discussed in Chapter 7. A summary of the present research effort and recommendations for future work are given in Chapter 8.

2. LITERATURE REVIEW

2.1 Separated-Reattaching Flows

Much of the literature concerning unsteady separated-reattaching flow past a normal flat plate with an attached splitter plate has been in the turbulent flow regime. Early experimental work dates back to Arie and Rouse (1956) who used Pitot tubes to characterize the time-mean velocities and turbulence intensities in the separation bubble. The Reynolds number (based on half of the plate height) range was from 7×10^3 to 3.5×10^4 . They determined the streamline profile with an analytical model based on a sink-source formulation. Their measurements characterized the time-mean velocities and turbulence intensities in the separation bubble. Further, the force exerted on the plate was measured and the mean drag coefficient was found to be 1.4. Roshko and Lau (1965) used Preston tubes to measure the time-mean pressure distributions on the splitter plate for various body configurations. The Reynolds number was varied from 1.4×10^3 to 5.3×10^3 . Based on their extensive measurements, a renormalized pressure coefficient was defined and used to characterize the pressure recovery profile for a wide range of separated-reattaching flows. Smits (1982) measured the velocity and pressure field within the separation bubble using a square edged circular Pitot tube and a disc static probe with a rounded edge. The measurements included the reattachment length, the distribution of the pressure coefficient along the splitter plate, the spanwise variation of the wall friction factor, and the streamwise velocity profile. Further, Smits (1982) investigated the effect of tunnel blockage ratio and reported a decrease in the reattachment length and an increase in the bubble height with increase in blockage ratio.

Recently, advances in experimental techniques, such as pulsed-wire anemometry, laser-Doppler velocimetry (LDV), and the split-film method, permitted detailed measurements of velocity, Reynolds stresses, energy spectra, pressure coefficient and skin-friction factor in the separation bubble. Experiments have been conducted by Ruderich and Fernholz (1986), Castro and Haque (1987, 1988), and Jaroach and Fernholz (1989). The Reynolds numbers of these studies were in the range of 1×10^4 - 2×10^4 where the flow is quite turbulent. Depending on the freestream conditions, a large recirculation length in the range of 16-30 h_F (where h_F is the height of the plate above the splitter plate) was measured. The concentrated efforts in these recent experiments were aimed at characterizing the large-scale vortical structures that are shed from the shear layer. Measurements were made of the shedding frequency, power spectra, space-time and auto

correlations, integral length-scales and the coherence of the structures. The turbulence in the freestream, the model aspect ratio, and the tunnel blockage were observed to significantly affect the length and height of the separation bubble as well as its two-dimensionality in the spanwise direction.

Ruderich and Fernholz (1986) have performed experimental measurements using hot-wire and pulsed-wire anemometers in the Reynolds number range of 9×10^3 - 1.4×10^4 . They described the topological development of the time-mean flow through oil-flow visualizations and revealed the formation of three-dimensional 'near-corner' vortices and the presence of a reattachment region near the plate ($x = 2.3h_F$). The streamwise distribution of the modified time-mean and root-mean square pressure coefficient and skin-friction factor as well as the reverse-flow parameter were discussed. Spanwise variations of the wall shear stress, the time-mean velocity and the Reynolds stresses emphasized the three-dimensionality of the time-mean flow. Profiles of the time-mean velocity and Reynolds shear and normal stresses were measured in the streamwise direction and showed the fast recovery of the time-mean flow to a boundary-layer-like distribution. Near-wall measurements of the streamwise velocity did not show the existence of a logarithmic profile. Loci of the maximum streamwise velocity and Reynolds stresses were also determined. Time-mean quantities such as the streamwise velocity and the Reynolds stresses revealed a self-similar behavior upstream of reattachment. Jaroch (1987) conducted oil-flow visualization to quantify the three-dimensional characteristics in the near-corner regions.

Castro and Haque (1987) undertook detailed measurements of the mean velocity, and the Reynolds stresses using pulsed-wire anemometry. The Reynolds number was 1.1×10^4 . The streamwise distributions of the pressure coefficient, skin-friction factor, vorticity growth thickness, and the velocity difference were presented. The loci of the center of the shear layer, the zero and maximum streamwise velocity were also determined. The spatial variation of the separated shear layer was further quantified through measurements of the time-mean velocity field and the Reynolds stresses. They emphasized that the current flow development did not follow the concepts derived for mixing layers. The large-scale structures shed from the separated shear layer were characterized through measurements of the auto-correlations and integral time-scales. A dominant frequency of $0.12 U_\infty / x_R$ was identified as a low-frequency motion of the separated shear layer. Castro and Haque (1988) further extended their previous study to analyze the effect of freestream turbulence on the flow structure. To this end, they

installed a square mesh upstream of the plate to generate small-scale turbulence in the freestream flow. It was observed that the increase of freestream turbulence intensity enhances the mixing and results in a decrease in the reattachment length. Significant differences were obtained from their measurements with freestream turbulence compared to those from their earlier study without freestream turbulence. It was concluded that freestream turbulence enhances shear-layer entrainment rates, reduces the reattachment length, and modifies the low-frequency flapping of the shear layer.

Jaroch and Fernholz (1989) applied pulsed-wire anemometry to quantify the three-dimensional aspects of the separated-reattaching flow. The Reynolds number in the experiments was 1.4×10^4 with a very low freestream turbulence level of 0.08%. Their experimental set-up was based on a large aspect ratio of 26 and a small blockage ratio of 2.75% while the model aspect ratio (W/h_F where W is the spanwise model width) was 64. Due to the high aspect ratio, no end plates were used in these experiments. Measurements of mean velocities and Reynolds stresses quantified the large spanwise variations present in the flow. Time-mean measurements revealed higher turbulence intensities than previous studies (Ruderich and Fernholz, 1986; Castro and Haque, 1987).

The maximum streamwise turbulent stress, $\overline{u'^2}$, was measured to be 0.22 compared to 0.13 and 0.09 reported by Ruderich and Fernholz (1986), and Castro and Haque (1987), respectively. The streamwise development of the integral length-scales showed a rapid growth of the large-scale structure up to the reattachment point followed by a plateau. Detailed measurements of the power spectra did not reveal any dominant frequency in the separated shear layer. It was concluded from their study that the current flow configuration cannot be characterized as nominally two-dimensional as the three-dimensional aspects are very strong.

Subsequently, McCluskey et al. (1991) quantified the three-dimensional topology of the separation bubble using flow visualization techniques and conducted measurements of the mean velocities and Reynolds stresses using a 'small' pulsed-wire probe. The experiments have been performed with model aspect ratios of 153 and 174 at a Reynolds number of 1.6×10^3 . Significant three-dimensional effects were observed even at these large aspect ratios. Measurements of the streamwise and spanwise velocity components as well as the Reynolds turbulent stresses were discussed. Further, McCluskey et al. (1991) noted that the results of Jaroch and Fernholz (1989) are affected significantly by three-dimensional effects due to the wind tunnel side walls. Recently,

Hancock and Castro (1993) performed experiments with model aspect ratios varying from 20 to 80 and blockage ratios ranging from 1% to 3.4% for a Reynolds number of 1.8×10^3 . Their measurements of the maximum streamwise turbulent stresses, $\overline{u^2}$, at $x/x_R = 0.5$ (where x_R is the reattachment length) agree more closely with the data of Ruderich and Fernholz (1986), Castro and Haque (1987) and Dengel and Hancock (1992) but were half the values presented by Jaroch and Fernholz (1989). The maximum streamwise Reynolds stresses near the reattachment point were found to be nearly invariant with model aspect ratio. They concluded that a model aspect ratio of 20 to 40 was sufficient to minimize the effects of the side walls; however, they were unable to explain the differences in the observed Reynolds stress at the reattachment point between their experiments and previous results.

In related configurations, Nakamura and Nakashima (1986) conducted experiments on a variety of prisms with H and I— shaped cross-sections. The hydrogen-bubble method was used to visualize the temporal evolution of the flow. Measurements with hot-wire probes were undertaken to determine the shedding frequency. The variation of the Strouhal number for various configurations was presented. Further, Govinda Ram and Arakeri (1990) have investigated the pressure distribution on a variety of bluff bodies with an attached splitter plate. Measurements of the surface time-mean and fluctuating pressure coefficients were presented for nose model shapes ranging from triangular (including flat plate), blunt edge, semicircular to elliptical geometries. It was observed that for most of the bluff bodies considered the maximum rms pressure coefficient in the shear layer is nearly equal to the maximum surface rms pressure coefficient.

Compared to the experimental studies, only a limited number of calculations has been performed for this configuration. Castro et al. (1982) performed numerical simulations in the steady laminar regime ($10 \leq Re \leq 100$) using finite-difference and finite-element (FE) techniques. Several upwinding schemes including the hybrid-difference scheme (HDS) and vector-differencing scheme (VDS) have been investigated to determine their effects on the solution field. The computational domain extended from -20 to 47 fence heights in the streamwise direction with a cross-stream height of 5 fence heights. Three non-uniform grid distributions with resolutions of 40×40 and 50×40 were used in this study. The minimum and maximum mesh sizes were 0.06 and 4.0 fence heights in the streamwise direction and 0.014 and 0.5 fence heights in the cross-stream

direction. The HDS method revealed a high numerical diffusion leading to poor predictions of the flow, particularly the reattachment length, while the VDS method resulted in more accurate predictions. The results of the finite-element method were found to have the least numerical diffusion. Jaroch and Graham (1988) performed a numerical study using the discrete vortex method. Their calculated time-mean velocity profiles were in satisfactory agreement with the experimental data, but the turbulence moments were over-predicted considerably.

Studies of related configurations, mainly the backward-facing step and the flat blunt plate, have also provided much information on the dynamics of separation and reattachment. Chandrsuda and Bradshaw (1981), and Driver and Seegmiller (1985) have reported measurements for the backward-facing step, while Adams and Johnston (1988) and Devenport and Sutton (1991) investigated the near-wall behavior. An extensive review of this flow configuration until 1981 is given by Eaton and Johnston (1981). For a blunt plate placed in a freestream, the flow separates from the leading edge of the plate and reattaches on the downstream section. Similar to the flat plate, experimental work has been concentrated in the turbulent regime in the Reynolds number range of 2×10^4 - 6×10^4 . Ota and coworkers (1974, 1976, 1978, 1983) conducted experiments using hot-wire anemometry techniques. The Reynolds number was varied from 2.1×10^4 to 6.6×10^4 . Detailed measurements of the time-mean velocity and surface pressure coefficient, the turbulent kinetic energy and the spatial correlations were reported. The reattachment length was found to be nearly invariant of the Reynolds number with a value of 4-5 plate thicknesses. Lane and Loehrke (1980) reported measurements of the reattachment length in the laminar regime ($100 \leq Re \leq 325$) using dye injection techniques while Ota et al. (1981) used aluminum powder to measure the reattachment length for $75 \leq Re \leq 270$. In both studies, the steady reattachment length was seen to increase linearly with the Reynolds number. The experiments agreed with the trends of the numerical simulations of Ghia and Davis (1974). Hillier and Cherry (1981), Kiya and Sasaki (1983a-b, 1985) and Cherry et al. (1983, 1984) have provided detailed measurements in the turbulent region. A low-frequency flapping of the separated shear layer with a magnitude of $0.12-0.20U_\infty/x_R$ was observed in the experiments of Cherry et al. (1984). Kiya et al. (1982) performed unsteady two-dimensional calculations using the discrete-vortex method. Dijlali et al. (1990) studied the two-dimensional steady-state flow and compared their results with experimental values. However, this work is of limited use since the unsteady flow characteristics are not captured. Recently, Tafti and Vanka (1991a,b) carried out detailed two and three-dimensional time-dependent

numerical studies of the flow over a blunt plate at low Reynolds numbers. Satisfactory comparisons with experimental data were obtained, especially when three-dimensional spanwise variations were included. Recent review papers of separated-reattaching flows have been presented by Kiya (1989) for the blunt plate, and Castro (1990) for the flat plate with an attached splitter plate. Experimental investigations of separated-reattaching flows, spanning a period of four decades, are compiled and summarized in Table 2.1.1.

2.2 Separated Flows

Various geometrical configurations including circular and rectangular cylinders, flat plates, and airfoils have been experimentally and numerically investigated to understand the fundamental aspects of wake instability. The flow past a flat plate is characterized by a fixed separation point, namely the edge of the plate, while the separation point for a circular cylinder moves along the cylinder surface as the Reynolds number is varied. Early theoretical analyses to characterize the mean flow past a normal flat plate were performed by Kirchhoff (1869) and extended by Rayleigh (1876) to include the case of plates at angles of attack to the freestream. The drag force was found to be solely based on the dynamic pressure on the front face of the plate and was formulated as follows (Lamb, 1932) :

$$C_D = \frac{2\pi \sin \alpha}{4 + \pi \sin \alpha} \quad (2.2.1)$$

where α is the angle of attack. Based on the above relation, the mean drag coefficient was evaluated to be 0.88 for $\alpha = 90^\circ$. However, the experimental studies of Stanton (1903) and Fage and Johansen (1927) measured a significantly higher drag coefficient. Fage and Johansen (1927) conducted extensive measurements for the flow over a plate held at different angles of attack. Pressure taps built in the plate were used to measure the pressures on the front and rear faces of the plate. They determined the time-mean drag coefficient to be approximately 2.0. The underestimation of the drag coefficient calculated by the Kirchhoff-Rayleigh theory was attributed to several limiting assumptions. First, the base pressure at the rear face of the plate was set to be equal to the freestream pressure which implies a zero pressure coefficient. Second, the velocity at the separation point was set equal to the free-stream velocity. However, in reality, the pressure at the rear face of the plate is lower than in the free stream and the velocity in the separated shear layer is higher than the free-stream velocity. Based on the measurements

of Fage and Johansen (1927), the Strouhal number was observed to be approximately constant and equal to 0.148 for a range of α between 30° and 90° .

Subsequently, Roshko (1954a, 1955) improved the classical free-streamline Kirchhoff-Rayleigh theory by modifying the base pressure coefficient, C_{ps} , as follows :

$$C_{ps} = 1 - k^2 \quad (2.2.2)$$

where k is the base pressure parameter given by $k = U_s/U_\infty$, and U_s is the velocity on the free streamline at separation. The time-mean drag coefficient based on the modified base pressure in Equation (2.2.2) was found to agree well with the experiments of Fage and Johansen (1927) for a value of $k = 1.54$. Roshko (1954b) reported a drag coefficient of 1.74 and a Strouhal number of 0.135 for the flow past a normal flat plate. Fail et al. (1957) studied wakes of normal plates for different aspect ratios ranging from 1 to 20. The drag coefficient was observed to increase with aspect ratio while the length of the time-mean wake region was observed to decrease. Abernathy (1962) performed experiments in the Reynolds number range of 3.6×10^4 to 1.4×10^5 and found a time-mean drag coefficient of 2.15 and a Strouhal number of 0.15. Hoerner (1967) reported the drag coefficients as well as the Strouhal numbers for a wide variety of bluff bodies including the flat plate.

Castro (1971) investigated wakes behind perforated plates in the Reynolds number range of 2.5×10^4 to 9.0×10^4 for a porosity factor varying from 0 to 0.645. The measurements were carried out using pulsed-wire anemometry. For zero porosity, the drag coefficient and the Strouhal number were measured to be 1.87 and 0.14, respectively. Two distinct regimes were observed depending on the plate porosity. For a porosity factor below 0.2, the vortex street dominated the wake; while, for a porosity factor above 0.2, the drag coefficient decreased suddenly as a result of the disappearance of the vortex street. Bradbury and Moss (1975) measured the turbulence statistics in the wake of a normal flat plate in uniform and shear flows using the pulsed-wire technique. Their measurements, conducted for Reynolds numbers in the range of 1.5×10^4 to 4.5×10^4 , showed that the streamwise and spanwise normal stress components were nearly equal while the cross-stream normal stresses were found to be significantly larger. The Strouhal number was calculated to be nearly constant (0.14) in the range considered. Sarpkaya and Kline (1982) used force transducers to measure the instantaneous lift and drag forces and moments on circular and D-shaped cylinders as well as flat plates. The

Reynolds number was 2.1×10^4 and two angles of attack ($\alpha = 60^\circ$ and 90°) were considered. The drag coefficient was found to reach a constant value of 2.2 for $\alpha = 90^\circ$ and had an oscillatory behavior for $\alpha = 60^\circ$.

Perry and Steiner (1987), and Steiner and Perry (1987) performed a detailed experimental study for normal and inclined plates at $Re = 2 \times 10^4$ using flying hot-wire probes. The Strouhal number was found to vary from 0.161 to 0.248. The velocity field and phase-averaged streamline contours were identified for sixteen phases of the vortex shedding cycle. The phase-averaged spanwise vorticity and Reynolds stresses were found to be similar to those observed by Cantwell and Coles (1983) for the wake of a circular cylinder. Using the triple decomposition scheme, the phase-averaged contributions to the turbulent stresses were found to be 25% for u^2 , 45% for v^2 and 50% for $u'v'$. Kiya and Matsumura (1988) applied the triple decomposition method (Reynolds and Hussain, 1972) to study the turbulent wake flow past a normal flat plate at $Re = 2.3 \times 10^4$. Based on the triple decomposition method, an instantaneous flow variable (ϕ) is decomposed as follows :

$$\phi = \bar{\phi} + \tilde{\phi} + \phi' \quad (2.2.3)$$

where $\bar{\phi}$ represents the time-mean component, $\tilde{\phi}$ is the phase-averaged or coherent component, and ϕ' is the random or incoherent component. The measurements of the time-mean streamwise velocity and Reynolds stresses were made using hot-wire anemometry in a normal plane eight plate heights downstream of the plate. The contribution of the incoherent components was found to be negligible for the streamwise and spanwise stresses, but significant (up to 50%) for the cross-stream stress. The primary Strouhal number was computed to be 0.146 and the convective velocity of the structures was calculated to be 0.85 of the freestream velocity in the far-wake region. Frequency analyses were carried out to identify the dominant frequencies contributing to incoherent turbulent fluctuations. The distributions of the incoherent energy and shear stress were also presented. Arrangements of the ribs and rollers structures were postulated.

Chua et al. (1990) investigated the flow past non-oscillating and oscillating normal flat plates using tow-tank experiments. The Reynolds number was in the range of

5×10^3 to 1×10^4 at angles of attack varying from 85° to 95° . After an initial transient stage during which the drag coefficient had a peak value of 4, the drag coefficient for the non-oscillating case was found to have a steady state value of 2.05 ± 0.05 . The Strouhal number was measured to be 0.133. For the oscillating case, the drag coefficient was found to be slightly higher (by 0.2 to 0.5) than the non-oscillating case; the shedding frequency locked on to the forcing frequency. Leder (1991) performed measurements at $Re = 2.8 \times 10^4$ using Laser-Doppler anemometry and extracted six phases of the vortex shedding cycle. A wake length of 2.5 plate heights was measured. The Strouhal number of 0.14 was found to be nearly constant over a range of Reynolds number from 10^3 to 10^5 . Further, phase-averaged normal and shear stress fields were presented for the six phases. Recently, Lisoski (1993) extended the work of Chua (1990) in the tow-tank facility. The Reynolds number was varied from 1×10^3 to 1.25×10^4 at angles of attack of 87.5° and 90° . A force balance method was used to measure the instantaneous lift and drag coefficients. A visualization technique based on Laser Induced Fluorescence (LIF) captured the vortical structures in the wake of the plate. The drag coefficient was found to be 2.1 and a Strouhal number of 0.149 was measured. LIF visualizations of the wake flow were also performed in a stratified tank.

Experiments (Taneda and Honji, 1971) and calculations (Yoshida and Nomura, 1985) have also been reported on impulsively started flow past a flat plate. The initial transient stage has been discussed extensively and the temporal development of the wake length was measured. Further, studies in related geometries have included rectangular and triangular prisms. Sarpkaya and Ihrig (1986) performed measurements similar to those of Sarpkaya and Kline (1982) for impulsively started flow past rectangular cylinders. Nakagawa (1989) investigated the wakes of triangular prisms using a Mach-Zehnder interferometer for flow visualization and observed two distinct regimes depending on the orientation of the prism. Several extensive reviews (e.g. Morkovin, 1964; Oertel, 1990; Coutanceau and Defaye, 1991; Sarpkaya, 1992) have surveyed the research work on flow separation over bluff bodies, specifically circular and rectangular cylinders.

Compared to the experimental work, numerical studies have been primarily concentrated on two-dimensional simulations of the flow past a normal flat plate. Kuwahara (1973) applied the vortex-element method and has found the drag coefficient to vary from 2.0 to 4.0. Subsequently, Sarpkaya (1975) simulated the flow past a plate at an angle of attack of 80° and calculated a drag coefficient of 2.4 as well as a Strouhal

number of 0.154. Kiya and Arie (1980) made use of the discrete-vortex method to simulate the unsteady flow. The mean drag coefficient was over-estimated by a factor of 20% to 40% over the value measured by Fage and Johansen (1927) and the base pressure at the rear face of the plate was found to be 26% in error. The convection velocity of the vortices was observed to increase in the streamwise direction from $0.4U_\infty$ to $0.75U_\infty$. As the profiles of the time-mean velocity and the rms fluctuations did not agree with the experiments, a vortex aging scheme was devised with an optimum circulation decay parameter, λ , of 0.8. This improved the predictions of the model, in particular one plate height downstream of the plate. The profiles of the time-mean velocities and the Reynolds shear stress agreed well with the experiments in the far-wake region.

Castro and Jones (1987) performed two-dimensional steady-state numerical simulations for $100 \leq Re \leq 800$ using finite-difference and finite-element (FE) techniques. Several upwinding methods including the hybrid-difference (HYDS), vector-differencing (VDS), and higher-order differencing (HODS) (based on the QUICK procedure) schemes have been investigated to determine their effects on the solution field. Non-uniform grid distributions with resolutions of 40×40 , 60×40 and 70×40 were used in this study. The HYDS method was observed to have high numerical diffusion errors leading to poor predictions; while the HODS and FE methods resulted in better predictions. However, as a result of the steady-state assumption, the wake lengths were overpredicted significantly (e.g. 63 plate heights for $Re = 800$). Chein and Chung (1988) investigated numerically the flow past flat plates at angles of attack of 60° and 90° using the vortex-blob method (Chorin, 1973) and the vortex aging scheme proposed by Kiya and Arie (1980). The Strouhal numbers were calculated to be 0.17 and 0.14 for $\alpha = 60^\circ$ and 90° , respectively, and the corresponding drag coefficients were determined to be 2.0 and 2.8. Further, the time-mean profiles and turbulent statistics were found to agree well with the numerical results of Kiya and Arie (1980) and the experimental data of Bradbury (1976).

Raghavan et al. (1990) performed two-dimensional simulations using ARC2D, a computer program based on an Eulerian finite-difference method for solving the Navier-Stokes equations. Although the computed Strouhal number of 0.14 agreed well with the experiments, the time-mean drag coefficient was calculated to be 2.8, 40% higher than the experimental value. Ingham et al. (1990) investigated experimentally and numerically the flow past a row of flat plates. The experiments were carried out in a tow tank with water and ethylene glycol and the flow was visualized by illuminating the flow seeded with polyester spheres. The numerical procedure was based on a vorticity-

streamfunction formulation, and the simulations were performed for $0 \leq Re \leq 500$ and a solidity ratio of 50%. The calculations were in excellent agreement with the experiments for $Re \leq 25$. The wake length, L , was found to correlate with the Reynolds number through the relation, $L \approx 0.21 Re$. Further, the drag coefficient was predicted fairly well in the Reynolds number range.

Chua et al. (1990) applied the vortex blob/panel method to simulate the transient startup of the flow past non-oscillating and oscillating plates. The numerical study complemented their experimental work discussed earlier. The Reynolds number, estimated from the modeled boundary layer at separation, was 1×10^4 . The calculated drag coefficient and Strouhal number were 3.6 and 0.11, respectively. Lisoski (1993) further improved the numerical model of Chua et al. (1990). These numerical simulations resulted in a time-mean drag coefficient of 3.2 and a Strouhal number of 0.121. Numerical flow visualizations were further used to characterize the unsteady shedding cycle. Recently, Joshi (1993) performed two and three-dimensional simulations using a second-order accurate finite-volume (Harlow-Welch) time-splitting scheme. The Reynolds number was varied from 40 to 10^3 for the two-dimensional simulations. The time-mean drag coefficient was found to increase with Reynolds number from 2.4 to 4.65. The effects of base mass injection on the wake instability were also investigated. It was observed that above a certain injection velocity the vortex shedding mechanism was inhibited. Three-dimensional large-eddy simulations were performed for Re of 60 and 1000. The flow was observed to remain two-dimensional at $Re = 60$ and the three-dimensional perturbations did not grow temporally. However, the velocity field became three-dimensional at $Re = 1000$ and the drag coefficient was seen to decrease significantly to a mean value of 2.4. The main contributions of this study have been summarized in Joshi et al. (1994). Further, two- and three-dimensional calculations of the heat transfer from the plate with a uniform surface temperature were carried out. Recently, Tamaddon-Jahromi et al. (1994) performed two-dimensional simulation using the Taylor-Galerkin/pressure-correction time-stepping scheme for Re of 126, 250 and 500. The initial transient startup process was seen to agree well with the experiments of Taneda and Honji (1971). The temporal flow development was described through instantaneous streamlines. The values of the Strouhal number were computed as 0.173, 0.165 and 0.115 for $Re = 126, 250$ and 500, respectively.

To summarize, although extensive measurements and simulations are available in the literature, their objectives have been limited to the properties of the time-mean flow

field. The values of the drag coefficient and the Strouhal number are seen to vary significantly among the various studies. While the experiments have been in the turbulent regime, the simulations were performed with the assumption of two-dimensional flow and have been limited to the low-Re regime. Further, the effects of the spanwise variations have not been quantified in the experiments as well as in the computations. Detailed descriptions of the three-dimensional flow field have not been attempted so far, even after a considerable period of research in this area of separated flows. Characterizing the inherent structures in the wake of a flat plate represents one of the objectives of the current research effort.

3. NUMERICAL PROCEDURE FOR TWO-DIMENSIONAL SIMULATIONS

The governing equations and the numerical method used in the current research effort for 2-D simulations are discussed in this chapter. The numerical procedure extended for 3-D simulations is presented in Chapter 4. Section 3.1 outlines the governing equations and the fractional-step method. Section 3.2 presents the discretization of the spatial derivatives. Section 3.3 describes three principal formulations of the pressure-Poisson equation on collocated grids and analyzes the satisfaction of the compatibility and integrability conditions for these formulations. Details of the direct solver algorithm for the pressure-Poisson equation are reported in Section 3.4. The stability requirements of the current scheme are discussed in Section 3.5. Section 3.6 describes the Capacitance Matrix Technique for the pressure-Poisson equation. The validation of the current numerical scheme is presented in Section 3.7 for several model problems including the vortex-decay problem, the driven-cavity problem, and the Kovasznay flow. Section 3.8 evaluates appropriate boundary conditions for simulating flows in unbounded domains.

3.1 Governing Equations and the Fractional-Step Method

The current numerical procedure solves the nonconservative form of the two-dimensional time-dependent Navier-Stokes equations governing the motion of an incompressible fluid. The non-dimensionalized mass and momentum equations, written in tensor form, are:

$$\nabla \cdot \mathbf{u} = 0 \quad (3.1.1)$$

$$\frac{\partial \mathbf{u}}{\partial t} + (\mathbf{u} \cdot \nabla) \mathbf{u} = -\nabla p + \frac{1}{Re} \nabla^2 \mathbf{u} \quad (3.1.2)$$

The equations are non-dimensionalized by appropriate length (l) and velocity (U) scales. The Reynolds number is defined as $Re = l U / \nu$. In the above equations, $\mathbf{u} = \{u, v\}$ is the instantaneous velocity field, p represents the instantaneous pressure, and t is the non-dimensional time.

The governing equations are discretized in time using a second-order accurate, time-splitting procedure. In the current solution algorithm, the convective and diffusive

terms are discretized using a fully-explicit second-order time-accurate Adams-Bashforth scheme. Application of the temporal discretization to the momentum equations gives :

$$\frac{u^{n+1} - u^n}{\Delta t} = \frac{3}{2} \left(H^n + \frac{1}{Re} L^n \right) - \frac{1}{2} \left(H^{n-1} + \frac{1}{Re} L^{n-1} \right) - (\nabla p)^{n+1} \quad (3.1.3)$$

where $H = - (u \cdot \nabla) u$ and $L = \nabla^2 u$ are the advection and diffusion terms, respectively.

Equations (3.1.1) and (3.1.3) are solved in a decoupled manner with the fractional-step method (Chorin, 1967, 1968; Temam, 1979; Goda, 1979; Kim and Moin, 1985). In the first step, an intermediate velocity field, \tilde{u} , is calculated from the momentum equations without the contribution of the pressure gradient. The governing equations of the intermediate velocity field are written as :

$$\frac{\tilde{u} - u^n}{\Delta t} = \frac{3}{2} \left(H^n + \frac{1}{Re} L^n \right) - \frac{1}{2} \left(H^{n-1} + \frac{1}{Re} L^{n-1} \right) \quad (3.1.4)$$

In the next step, the intermediate velocity field is corrected to satisfy the continuity equation by solving for the pressure field at time $(n+1)$. The velocity field at the $(n+1)$ time step, u^{n+1} , should satisfy the continuity equation :

$$\nabla \cdot u^{n+1} = 0 \quad (3.1.5)$$

Subtracting Equation (3.1.3) from Equation (3.1.4) results :

$$\frac{u^{n+1} - \tilde{u}}{\Delta t} = - (\nabla p)^{n+1} \quad (3.1.6)$$

Applying the divergence operator to Equation (3.1.6) and using the continuity equation, Equation (3.1.5), the Poisson equation for the pressure field is derived to be:

$$\nabla \cdot (\nabla p^{n+1}) = \frac{1}{\Delta t} (\nabla \cdot \tilde{u}) \quad (3.1.7)$$

After solving Equation (3.1.7), the divergence-free velocity at the $(n+1)$ time step is determined from Equation (3.1.6). The explicit representation of the viscous terms results in a stringent restriction on the time-step size at low Reynolds number; however,

the viscous stability restriction is eased at high Reynolds numbers. This outlines the overall numerical procedure.

3.2 Spatial Discretization Scheme

The spatial derivatives in Equations (3.1.4-3.1.7) are discretized with a high-order accurate collocated finite-difference stencil. In the collocated-grid arrangement, all variables (i.e., velocities and pressure) are located at the same physical location in contrast to the staggered arrangement where velocities are centered with pressure locations (Figure 3.2.1). The discretized variable on a cell (i,j) is denoted by $\phi_{i,j}$. N_x and N_y denote the number of grid nodes in the x and y directions, respectively; Δx and Δy are the corresponding grid sizes.

The convective terms, H , are discretized using a fifth-order upwind-biased difference scheme (Rai and Moin, 1991). As an illustrative example, the term $\left(u \frac{\partial u}{\partial x}\right)$ in the x -momentum equation is evaluated as follows :

• if $u > 0$

$$\begin{aligned} \left(u \frac{\partial u}{\partial x}\right)_{i,j} &= u_{i,j} \left(\frac{1}{120 \Delta x} \right) \\ &\quad (-6 u_{i+2,j} + 60 u_{i+1,j} + 40 u_{i,j} \\ &\quad - 120 u_{i-1,j} + 30 u_{i-2,j} - 4 u_{i-3,j}) \end{aligned} \quad (3.2.1a)$$

• if $u < 0$

$$\begin{aligned} \left(u \frac{\partial u}{\partial x}\right)_{i,j} &= u_{i,j} \left(\frac{1}{120 \Delta x} \right) \\ &\quad (4 u_{i+3,j} - 30 u_{i+2,j} + 120 u_{i+1,j} \\ &\quad - 40 u_{i,j} - 60 u_{i-1,j} + 6 u_{i-2,j}) \end{aligned} \quad (3.2.1b)$$

Fourth-order accuracy is maintained for the near-boundary grid points by using unsymmetric finite-difference formulations (Collatz, 1960). The near-boundary formulations of the streamwise derivatives are given by :

$$\left(\frac{\partial \phi}{\partial x}\right)_{2,j} = \frac{1}{12 \Delta x} (-3 \phi_{1,j} - 10 \phi_{2,j} + 18 \phi_{3,j} - 6 \phi_{4,j} + \phi_{5,j}) \quad (3.2.2)$$

$$\left(\frac{\partial \phi}{\partial x}\right)_{3,j} = \frac{1}{12 \Delta x} (\phi_{1,j} - 8 \phi_{2,j} + 8 \phi_{4,j} - \phi_{5,j}) \quad (3.2.3)$$

$$\left(\frac{\partial \phi}{\partial x}\right)_{Nx-2,j} = \frac{1}{12\Delta x} (\phi_{Nx-4,j} - 8\phi_{Nx-3,j} + 8\phi_{Nx-1,j} - \phi_{Nx,j}) \quad (3.2.4)$$

$$\begin{aligned} \left(\frac{\partial \phi}{\partial x}\right)_{Nx-1,j} = \frac{1}{12\Delta x} (3\phi_{Nx,j} + 10\phi_{Nx-1,j} - 18\phi_{Nx-2,j} \\ + 6\phi_{Nx-3,j} - \phi_{Nx-4,j}) \end{aligned} \quad (3.2.5)$$

In the above equations, ϕ denotes either the streamwise velocity (u) or the transverse velocity (v).

The diffusive terms, L , are evaluated using a fourth-order accurate central difference scheme. For example, the term $\left(\frac{\partial^2 u}{\partial x^2}\right)$ is discretized as :

$$\left(\frac{\partial^2 u}{\partial x^2}\right)_{i,j} = \frac{1}{12\Delta x^2} (-u_{i-2,j} + 16u_{i-1,j} - 30u_{i,j} + 16u_{i+1,j} - u_{i+2,j}) \quad (3.2.6)$$

The near-boundary second-order derivatives (i.e., $i = 2$ and $Nx-1$) are expanded using a fourth-order unsymmetric finite-difference stencil :

$$\left(\frac{\partial^2 \phi}{\partial x^2}\right)_{2,j} = \frac{1}{12\Delta x^2} (11\phi_{1,j} - 20\phi_{2,j} + 6\phi_{3,j} + 4\phi_{4,j} - \phi_{5,j}) \quad (3.2.7)$$

$$\begin{aligned} \left(\frac{\partial^2 \phi}{\partial x^2}\right)_{Nx-1,j} = \frac{1}{12\Delta x^2} (11\phi_{Nx,j} - 20\phi_{Nx-1,j} + 6\phi_{Nx-2,j} \\ + 4\phi_{Nx-3,j} - \phi_{Nx-4,j}) \end{aligned} \quad (3.2.8)$$

The convective and diffusive terms in the transverse (y) direction are formulated in a similar manner. These formulations calculate the intermediate velocity field, \tilde{u} , to fourth-order accuracy.

The pressure gradient, $(\nabla p)^{n+1}$, is expanded using a fourth-order central finite-difference scheme. The streamwise pressure derivative, $\frac{\partial p}{\partial x}$, is evaluated as:

$$\left(\frac{\partial p}{\partial x}\right)_{i,j} = \frac{1}{12\Delta x} (p_{i-2,j} - 8p_{i-1,j} + 8p_{i+1,j} - p_{i+2,j}) \quad (3.2.9)$$

for interior nodes ($i = 3$ to $Nx-2$), and the near-boundary derivatives are formulated as:

$$\left(\frac{\partial p}{\partial x}\right)_{2,j} = \frac{1}{12\Delta x} (-3p_{1,j} - 10p_{2,j} + 18p_{3,j} - 6p_{4,j} + p_{5,j}) \quad (3.2.10)$$

$$\begin{aligned} \left(\frac{\partial p}{\partial x}\right)_{Nx-1,j} = \frac{1}{12\Delta x} (3p_{Nx,j} + 10p_{Nx-1,j} - 18p_{Nx-2,j} \\ + 6p_{Nx-3,j} - p_{Nx-4,j}) \end{aligned} \quad (3.2.11)$$

The equations presented in this section are applied for uniform grids. Appendix A presents the formulation of the high-order finite-difference stencils on non-uniform grids.

3.3 Formulation of the Pressure-Poisson Equation

High-order accurate finite-difference schemes have been successfully applied to perform direct numerical simulations of unsteady incompressible fluid flows (Rai and Moin, 1991; Clarksean and McMurtry, 1990; Najjar and Vanka, 1993). Both staggered and non-staggered (i.e., collocated) grid arrangements have been used to discretize the governing equations. In the collocated-grid arrangement, all dependent variables (i.e., velocities and pressure) are located at the same physical location in contrast to the staggered arrangement where velocities are centered between the pressure locations. In general, the collocated arrangement of velocities and pressure has reduced the amount of interpolation when compared with discretization on staggered meshes. Further, the collocated arrangement is more convenient for the use of high-order discretizations as well as general curvilinear coordinate systems. Several second-order accurate collocated schemes have been reported in the literature, for example, Chorin (1967), Strikwerda (1984), Abdallah (1987a,b), Biringen and Cook (1988), Sotiropoulos and Abdallah (1991), and Armfield (1991). These schemes have successfully calculated several model flows with good accuracy.

A major issue in numerical schemes employing a collocated arrangement is the satisfaction of the divergence-free condition for the velocity field. For example, Armfield (1991) discusses the loss in the ellipticity of the pressure-Poisson equation giving rise to a checkerboard pressure split in collocated schemes applied to the SIMPLE algorithm

(Patankar, 1980). Biringen and Cook (1988) solve the unsteady pressure-Poisson equation and suggest a perturbation to the right-hand side of the pressure equation in order to satisfy the compatibility condition. Abdallah (1987a,b) and Sotiropoulos and Abdallah (1991) discuss the inability of the collocated schemes to satisfy the divergence-free condition of the velocity field without a loss in ellipticity of the pressure equation. Sotiropoulos and Abdallah (1991) analyze two different formulations of the pressure equation and conclude that not obtaining a divergence-free velocity field is more tolerable than an oscillatory pressure field.

In this section, we describe various formulations for discretizing the pressure-Poisson equation (Equation 3.1.7) on collocated grids. We will also study the implications of the high-order evaluation of the operators on satisfying the divergence-free condition. The formulations vary in the accuracy of the stencil as well as in the manner of representing the operators. Three main representations of the operators are considered. These schemes are referred to as the Inconsistent Finite-Difference Method (IFDM), Consistent Finite-Difference Method (CFDM), and Consistent Finite-Volume Method (CFVM). The satisfaction of the compatibility and integrability conditions has also been investigated for the various schemes. The validation of these formulations is given in Sections 3.7.1 and 3.7.2.

3.3.1 Inconsistent Finite-Difference Method

In this method, the divergence ($\nabla \cdot$) and gradient (∇) operators are combined into a Laplacian operator (∇^2) and the pressure-Poisson equation (Equation 3.1.7) is written as:

$$\nabla^2 p^{n+1} = \frac{1}{\Delta t} (\nabla \cdot \tilde{u}) \quad (3.3.1.1)$$

The operators $\nabla^2 p$ and $(\nabla \cdot \tilde{u})$ are then discretized individually on the collocated grid points with fourth-order accurate stencils. As the discrete divergence ($\nabla \cdot$) and gradient (∇) operators do not commute with the discrete Laplacian operator (∇^2), the method is labeled as inconsistent (see Appendix B).

The Laplacian operator is formulated with a fourth-order accurate stencil :

$$(\nabla^2 p)_{i,j} = \frac{1}{12\Delta x^2} (-p_{i-2,j} + 16p_{i-1,j} - 30p_{i,j} + 16p_{i+1,j} - p_{i+2,j}) \\ + \frac{1}{12\Delta y^2} (-p_{i,j-2} + 16p_{i,j-1} - 30p_{i,j} + 16p_{i,j+1} - p_{i,j+2}) \quad (3.3.1.2)$$

The discrete divergence operator of the velocity field $(\nabla \cdot \tilde{u})$, denoted by $D_{i,j}$, is evaluated with a fourth-order accurate scheme :

$$D_{i,j} = \frac{1}{12\Delta x} (\tilde{u}_{i-2,j} - 8\tilde{u}_{i-1,j} + 8\tilde{u}_{i+1,j} - \tilde{u}_{i+2,j}) \\ + \frac{1}{12\Delta y} (\tilde{v}_{i,j-2} - 8\tilde{v}_{i,j-1} + 8\tilde{v}_{i,j+1} - \tilde{v}_{i,j+2}) \quad (3.3.1.3)$$

Adjacent to the boundaries, second-order accurate stencils are used. Neumann conditions are imposed on the pressure field along the boundaries of the computational domain and are discretized with a third-order one-sided finite-difference scheme (Fornberg, 1988) :

$$\left(\frac{\partial p}{\partial x}\right)_{1,j} = \frac{1}{\Delta x} \left(-\frac{11}{6}p_{1,j} + 3p_{2,j} - \frac{3}{2}p_{3,j} + \frac{1}{3}p_{4,j}\right) \quad (3.3.1.4)$$

This relation is then used to evaluate the boundary pressure ($p_{1,j}$, say) in terms of the boundary gradient and the interior nodal values. Finally, the pressure gradient in the update procedure (Equation 3.1.6) is formulated with fourth-order central difference stencils. At the final step of the solution procedure, the collocated velocities are not divergence-free due to the inconsistency in applying the Laplace operator instead of the divergence of the gradient operator. Details are given in Appendix B.

3.3.2 Consistent Finite-Difference Method

In this method, the same discrete operator is used for the divergence on the two sides of Equation (3.1.7). This method is consistent in the formulation of the operators and will be referred to as the Consistent Finite-Difference Method (CFDM).

Both second and fourth-order formulations are considered. The second-order formulations of the divergence and gradient operators are :

$$D_{i,j} = \frac{1}{2\Delta x} (\tilde{u}_{i+1,j} - \tilde{u}_{i-1,j}) + \frac{1}{2\Delta y} (\tilde{v}_{i,j+1} - \tilde{v}_{i,j-1}) \quad (3.3.2.1)$$

$$\left(\frac{\partial p}{\partial x}\right)_{i,j} = \frac{1}{2\Delta x} (p_{i+1,j} - p_{i-1,j}) \quad (3.3.2.2)$$

$$\left(\frac{\partial p}{\partial y}\right)_{i,j} = \frac{1}{2\Delta y} (p_{i,j+1} - p_{i,j-1}) \quad (3.3.2.3)$$

In the fourth-order representation, the following relations are applied :

$$D_{i,j} = \frac{1}{12\Delta x} (\tilde{u}_{i-2,j} - 8\tilde{u}_{i-1,j} + 8\tilde{u}_{i+1,j} - \tilde{u}_{i+2,j}) + \frac{1}{12\Delta y} (\tilde{v}_{i,j-2} - 8\tilde{v}_{i,j-1} + 8\tilde{v}_{i,j+1} - \tilde{v}_{i,j+2}) \quad (3.3.2.4)$$

$$\left(\frac{\partial p}{\partial x}\right)_{i,j} = \frac{1}{12\Delta x} (p_{i-2,j} - 8p_{i-1,j} + 8p_{i+1,j} - p_{i+2,j}) \quad (3.3.2.5)$$

$$\left(\frac{\partial p}{\partial y}\right)_{i,j} = \frac{1}{12\Delta y} (p_{i,j-2} - 8p_{i,j-1} + 8p_{i,j+1} - p_{i,j+2}) \quad (3.3.2.6)$$

The second-order (Equation 3.3.2.1) or fourth-order (Equation 3.3.2.4) discrete divergence operator is in turn applied on $\partial p/\partial x$ and $\partial p/\partial y$ to derive the pressure-Poisson equation. As an illustrative example, the second-order formulation for the divergence and gradient operators results in the following pressure equation :

$$\frac{1}{4\Delta x^2} (p_{i+2,j} - 2p_{i,j} + p_{i-2,j}) + \frac{1}{4\Delta y^2} (p_{i,j+2} - 2p_{i,j} + p_{i,j-2}) = \frac{1}{2\Delta x \Delta t} (\tilde{u}_{i+1,j} - \tilde{u}_{i-1,j}) + \frac{1}{2\Delta y \Delta t} (\tilde{v}_{i,j+1} - \tilde{v}_{i,j-1}) \quad (3.3.2.7)$$

Equation (3.3.2.7) will give rise to a checkerboard split in the pressure. Other discrete operators (Equations 3.3.2.1-3.3.2.6) can also be derived through various combinations of the divergence and gradient stencils (see Appendix B for detail).

Adjacent to the boundaries, second-order stencils (Equations (3.3.2.1-3.3.2.3)) for the divergence and gradient operators are used. Finally, the pressure gradient in the update procedure (Equation (3.1.6)) is consistent with the formulation implemented in deriving the pressure-Poisson equation. At the final step of the solution procedure, the collocated velocities are divergence-free.

3.3.3 Consistent Finite-Volume Method

In this method, the continuity equation is written in terms of the velocities at half points surrounding the grid nodes (or cell fluxes) using a finite-volume formulation (see Figure 3.2.1). Hence, the approach is referred to as the Consistent Finite-Volume Method. This method requires that the cell fluxes, \tilde{c} , be related to the collocated velocity, \tilde{u} , and then corrected to give :

$$\nabla \cdot \mathbf{c}^{n+1} = 0 \quad (3.3.3.1)$$

The pressure-Poisson equation is written as :

$$\nabla \cdot (\nabla p^{n+1}) = \frac{1}{\Delta t} \nabla \cdot \tilde{\mathbf{c}} \quad (3.3.3.2)$$

The velocities at the grid nodes are no longer required to satisfy the divergence-free condition. The velocities at half points, $\tilde{\mathbf{c}}$, are computed from the collocated velocity field, $\tilde{\mathbf{u}}$, using either a second-order interpolation function :

$$(\tilde{c}_x)_{i-1/2,j} = \frac{1}{2} (\tilde{u}_{i-1,j} + \tilde{u}_{i,j}) \quad (3.3.3.3a)$$

$$(\tilde{c}_y)_{i,j-1/2} = \frac{1}{2} (\tilde{v}_{i,j-1} + \tilde{v}_{i,j}) \quad (3.3.3.3b)$$

or a fourth-order interpolation function :

$$(\tilde{c}_x)_{i-1/2,j} = \frac{1}{16} (-\tilde{u}_{i-2,j} + 9\tilde{u}_{i-1,j} + 9\tilde{u}_{i,j} - \tilde{u}_{i+1,j}) \quad (3.3.3.3c)$$

$$(\tilde{c}_y)_{i,j-1/2} = \frac{1}{16} (-\tilde{v}_{i,j-2} + 9\tilde{v}_{i,j-1} + 9\tilde{v}_{i,j} - \tilde{v}_{i,j+1}) \quad (3.3.3.3d)$$

The divergence operator is formulated in terms of these cell face velocities as :

$$D_{i,j} = \frac{1}{\Delta x_c} ((\tilde{c}_x)_{i+1/2,j} - (\tilde{c}_x)_{i-1/2,j}) + \frac{1}{\Delta y_c} ((\tilde{c}_y)_{i,j+1/2} - (\tilde{c}_y)_{i,j-1/2}) \quad (3.3.3.4)$$

for second-order accuracy and as :

$$D_{i,j} = \frac{1}{24 \Delta x_c} (\tilde{c}_x)_{i-3/2,j} - 27(\tilde{c}_x)_{i-1/2,j} + 27(\tilde{c}_x)_{i+1/2,j} - (\tilde{c}_x)_{i+3/2,j}$$

$$+ \frac{1}{24 \Delta y_c} ((\tilde{c}_y)_{i,j-3/2} - 27 (\tilde{c}_y)_{i,j-1/2} + 27 (\tilde{c}_y)_{i,j+1/2} - (\tilde{c}_y)_{i,j+3/2}) \quad (3.3.3.5)$$

for fourth-order accuracy. In Equations (3.3.3.4-3.3.3.5), Δx_c and Δy_c represent the cell sizes in the x and y directions, respectively. Equation (3.3.3.4) corresponds to the second-order finite-volume formulation of Harlow and Welch (1965) for the staggered mesh arrangement (see also Kim and Moin (1985)). The pressure gradient is similarly discretized at the cell faces by a second-order stencil :

$$\left(\frac{\partial p}{\partial x} \right)_{i-1/2,j} = \frac{1}{\Delta x} (p_{i,j} - p_{i-1,j}) \quad (3.3.3.6a)$$

$$\left(\frac{\partial p}{\partial y} \right)_{i,j-1/2} = \frac{1}{\Delta y} (p_{i,j} - p_{i,j-1}) \quad (3.3.3.6b)$$

or by a fourth-order stencil :

$$\left(\frac{\partial p}{\partial x} \right)_{i-1/2,j} = \frac{1}{24 \Delta x} (-p_{i-2,j} + 27 p_{i-1,j} - 27 p_{i,j} + p_{i+1,j}) \quad (3.3.3.7a)$$

$$\left(\frac{\partial p}{\partial y} \right)_{i,j-1/2} = \frac{1}{24 \Delta y} (-p_{i,j-2} + 27 p_{i,j-1} - 27 p_{i,j} + p_{i,j+1}) \quad (3.3.3.7b)$$

The second-order (Equation 3.3.3.4) or fourth-order (Equation 3.3.3.5) discrete divergence operator is then applied on the pressure gradient to derive the pressure-Poisson equation. Similar to the Consistent Finite-Difference Method, other discrete pressure equations can be derived through various combinations of the discrete operators and are summarized in Appendix B. Near the boundaries, a lower-order accurate formulation is again applied. It is to be noted that no *ad hoc* boundary pressure condition is required for this formulation (Kim and Moin, 1985).

The cell fluxes at the $(n+1)$ time step are corrected with the pressure gradient as follows :

$$(c_x^{n+1})_{i-1/2,j} = (\tilde{c}_x)_{i-1/2,j} - \Delta t \left(\frac{\partial p}{\partial x} \right)_{i-1/2,j} \quad (3.3.3.8a)$$

$$(c_y^{n+1})_{i,j-1/2} = (\tilde{c}_y)_{i,j-1/2} - \Delta t \left(\frac{\partial p}{\partial y} \right)_{i,j-1/2} \quad (3.3.3.8b)$$

In Equations (3.3.3.8a-b), the discrete pressure gradients are consistent with the formulation of the pressure-Poisson equation. The collocated velocities are also updated with the collocated pressure gradients using central finite-difference schemes (see Section 3.3.2). Since the pressure-Poisson equation is derived by satisfying the continuity equation (Equation (3.3.3.1)) on the cell velocities instead of the collocated velocity, the cell face values satisfy the divergence-free condition, but the velocities at the grid nodes are not divergence-free.

3.3.4 Satisfaction of Compatibility and Integrability Conditions

The solution of the Poisson equation for pressure with all Neumann boundary conditions requires that the compatibility condition be satisfied. Integrating Equation (3.1.7) over the computational domain results in the compatibility condition :

$$\iint_{\Omega} \nabla \cdot (\nabla p) dA = \frac{1}{\Delta t} \iint_{\Omega} \left(\frac{\partial \tilde{u}}{\partial x} + \frac{\partial \tilde{v}}{\partial y} \right) dA \quad (3.3.4.1)$$

where Ω is the computational domain and dA is a differential area. Applying Green's theorem, the integrability conditions are given by :

$$\iint_{\Omega} \nabla \cdot (\nabla p) dA = \int_{\partial\Omega} \frac{\partial p}{\partial n} \cdot \mathbf{n} dS \quad (3.3.4.2)$$

and

$$\iint_{\Omega} \left(\frac{\partial \tilde{u}}{\partial x} + \frac{\partial \tilde{v}}{\partial y} \right) dA = \int_{\partial\Omega} u^{n+1} \cdot \mathbf{n} dS \quad (3.3.4.3)$$

where $\partial\Omega$ represents the boundary of the computational domain, dS is a differential length, and \mathbf{n} is the unit vector normal to the boundary. In this section, we will analyze the satisfaction of these conditions in the context of the formulations discussed in Sections 3.3.1-3.3.3.

The discrete form of the compatibility condition, Equation (3.3.4.1), is written :

$$\sum_i \sum_j (\nabla \cdot (\nabla p))_{ij} \Delta x \Delta y = \frac{1}{\Delta t} \sum_i \sum_j D_{ij} \Delta x \Delta y \quad (3.3.4.4)$$

Further, the discrete integrability conditions are:

$$\sum_i \sum_j (\nabla \cdot (\nabla p))_{ij} \Delta x \Delta y = \sum_B \left(\frac{\partial p}{\partial n} \right)_B \Delta s \quad (3.3.4.5)$$

and

$$\sum_i \sum_j D_{ij} \Delta x \Delta y = \sum_B u_B^{n+1} \Delta s \quad (3.3.4.6)$$

where B represents the boundary of the computational domain, Δs corresponds to the grid size along the boundary, u_B^{n+1} is the boundary normal velocity and $\left(\frac{\partial p}{\partial n} \right)_B$ is the boundary normal pressure gradient.

The second-order finite-volume discretization of Harlow and Welch (1965) satisfies the compatibility and integrability conditions (Miyakoda, 1962; Briley, 1974; Roache, 1976; Peyret and Taylor, 1983; Armfield, 1991). Amongst the procedures considered in this study, the Inconsistent Finite-Difference Method (IFDM) violates both the compatibility (Equation 3.3.4.4) and the integrability conditions (Equations 3.3.4.5-6). Briley (1974), and Biringen and Cook (1988) suggest the addition of a perturbation such that the compatibility condition is satisfied. The modified discretized pressure-Poisson equation is written as :

$$(\nabla^2 p^{n+1})_{i,j} = \frac{1}{\Delta t} [D_{ij} - (\delta_R)_{ij}] \quad (3.3.4.7)$$

$$\text{where } (\delta_R)_{i,j} = \frac{1}{Nx-2} \frac{1}{Ny-2} \sum_{i=2}^{Nx-1} \sum_{j=2}^{Ny-1} D_{ij} \quad (3.3.4.8)$$

However, even with the perturbation, the first integrability condition (Equation (3.3.4.5)) is not satisfied due to the inconsistency in applying the Laplacian instead of the divergence of the gradient operator. Further, the second integrability condition (Equation (3.3.4.6)) is violated since the stencil size decreases near the boundary. As a result, the final velocity field is not divergence-free.

The Consistent Finite Difference Method satisfies the compatibility condition, but violates the integrability conditions. The compatibility condition holds since the pressure-Poisson equation is derived with a consistent formulation. The violation of the integrability condition can be proved by summing the discrete equations over the computational domain. As an illustrative example, the sum of the fourth-order discrete divergence operator (or the RHS of Equation (3.1.7)) is :

$$\begin{aligned}
& \sum_{j=2}^{Ny-1} \sum_{i=2}^{Nx-1} \left(\frac{\partial \tilde{u}}{\partial x} + \frac{\partial \tilde{v}}{\partial y} \right) \\
&= \sum_{j=2}^{Ny-1} \frac{1}{12\Delta x} \left(-5 u_{1,j}^{n+1} - 7 \tilde{u}_{2,j} - \tilde{u}_{3,j} + \tilde{u}_{4,j} \right. \\
&\quad \left. + 5 u_{Nx,j}^{n+1} + 7 \tilde{u}_{Nx-1,j} + \tilde{u}_{Nx-2,j} - \tilde{u}_{Nx-3,j} \right) \\
&+ \sum_{i=2}^{Nx-1} \frac{1}{12\Delta y} \left(-5 v_{1,i}^{n+1} - 7 \tilde{v}_{i,2} - \tilde{v}_{i,3} + \tilde{v}_{i,4} \right. \\
&\quad \left. + 5 v_{i,Ny}^{n+1} + 7 \tilde{v}_{i,Ny-1} + \tilde{v}_{i,Ny-2} - \tilde{v}_{i,Ny-3} \right) \quad (3.3.4.9)
\end{aligned}$$

The sum of the discrete pressure gradients (or the LHS of Equation (3.1.7)) is :

$$\begin{aligned}
& \sum_{j=2}^{Ny-1} \sum_{i=2}^{Nx-1} \frac{\partial}{\partial x} \left(\frac{\partial p}{\partial x} \right) + \frac{\partial}{\partial y} \left(\frac{\partial p}{\partial y} \right) \\
&= \sum_{j=2}^{Ny-1} \frac{1}{12\Delta x} \left(-7 \left(\frac{\partial p}{\partial x} \right)_{2,j} - \left(\frac{\partial p}{\partial x} \right)_{3,j} + \left(\frac{\partial p}{\partial x} \right)_{4,j} \right. \\
&\quad \left. + 7 \left(\frac{\partial p}{\partial x} \right)_{Nx-1,j} + \left(\frac{\partial p}{\partial x} \right)_{Nx-2,j} - \left(\frac{\partial p}{\partial x} \right)_{Nx-3,j} \right) \\
&+ \sum_{i=2}^{Nx-1} \frac{1}{12\Delta y} \left(-7 \left(\frac{\partial p}{\partial y} \right)_{i,2} - \left(\frac{\partial p}{\partial y} \right)_{i,3} + \left(\frac{\partial p}{\partial y} \right)_{i,4} \right. \\
&\quad \left. + 7 \left(\frac{\partial p}{\partial y} \right)_{i,Ny-1} + \left(\frac{\partial p}{\partial y} \right)_{i,Ny-2} - \left(\frac{\partial p}{\partial y} \right)_{i,Ny-3} \right) \quad (3.3.4.10)
\end{aligned}$$

Clearly, the interior intermediate collocated velocities (\tilde{u} and \tilde{v}) and the interior pressure gradients ($\partial p/\partial x$ and $\partial p/\partial y$) do not cancel out in the summation, thus violating relations (3.3.4.5) and (3.3.4.6). Hence, the collocated velocities are locally divergence-free but the global balance over the computational domain is not satisfied.

The Consistent Finite-Volume Method with the second-order discretization of the divergence operator and any order of accuracy of the gradient operator satisfies Equations (3.3.4.4), (3.3.4.5) and (3.3.4.6). However, a fourth-order (or higher) representation of the divergence operator in the CFVM will violate the integrability condition as seen by summing the discrete equations over the computational domain. The sum of the divergence of the discrete fluxes is :

$$\begin{aligned}
& \sum_{j=2}^{Ny-1} \sum_{i=2}^{Nx-1} \left(\frac{\partial \tilde{c}_x}{\partial x} + \frac{\partial \tilde{c}_y}{\partial y} \right) \\
&= \sum_{j=2}^{Ny-1} \frac{1}{\Delta x_c} \left(- (c_x^{n+1})_{1,j} + \frac{1}{24} (\tilde{c}_x)_{5/2,j} - \frac{2}{24} (\tilde{c}_x)_{7/2,j} + \frac{1}{24} (\tilde{c}_x)_{9/2,j} \right. \\
&\quad \left. + (c_x^{n+1})_{Nx,j} - \frac{1}{24} (\tilde{c}_x)_{Nx-3/2,j} + \frac{2}{24} (\tilde{c}_x)_{Nx-5/2,j} - \frac{1}{24} (\tilde{c}_x)_{Nx-7/2,j} \right) \\
&\quad + \sum_{i=2}^{Nx-1} \frac{1}{\Delta y_c} \left(- (c_y^{n+1})_{i,1} + \frac{1}{24} (\tilde{c}_y)_{i,5/2} - \frac{2}{24} (\tilde{c}_y)_{i,7/2} + \frac{1}{24} (\tilde{c}_y)_{i,9/2} \right. \\
&\quad \left. + (c_y^{n+1})_{i,Ny} - \frac{1}{24} (\tilde{c}_y)_{i,Ny-3/2} + \frac{2}{24} (\tilde{c}_y)_{i,Ny-5/2} - \frac{1}{24} (\tilde{c}_y)_{i,Ny-7/2} \right) \quad (3.3.4.11)
\end{aligned}$$

The sum of the discrete pressure gradients (or the LHS of Equation 3.1.5) is :

$$\begin{aligned}
& \sum_{j=2}^{Ny-1} \sum_{i=2}^{Nx-1} \frac{\partial}{\partial x} \left(\frac{\partial p}{\partial x} \right) + \frac{\partial}{\partial y} \left(\frac{\partial p}{\partial y} \right) \\
&= \sum_{j=2}^{Ny-1} \frac{1}{24 \Delta x_c} \left(\left(\frac{\partial p}{\partial x} \right)_{5/2,j} - 2 \left(\frac{\partial p}{\partial x} \right)_{7/2,j} + \left(\frac{\partial p}{\partial x} \right)_{9/2,j} \right. \\
&\quad \left. - \left(\frac{\partial p}{\partial x} \right)_{Nx-3/2,j} + 2 \left(\frac{\partial p}{\partial x} \right)_{Nx-5/2,j} - \left(\frac{\partial p}{\partial x} \right)_{Nx-7/2,j} \right) \\
&\quad + \sum_{i=2}^{Nx-1} \frac{1}{24 \Delta y_c} \left(\left(\frac{\partial p}{\partial y} \right)_{i,5/2} - 2 \left(\frac{\partial p}{\partial y} \right)_{i,7/2} + \left(\frac{\partial p}{\partial y} \right)_{i,9/2} \right. \\
&\quad \left. - \left(\frac{\partial p}{\partial y} \right)_{i,Ny-3/2} + 2 \left(\frac{\partial p}{\partial y} \right)_{i,Ny-5/2} - \left(\frac{\partial p}{\partial y} \right)_{i,Ny-7/2} \right) \quad (3.3.4.12)
\end{aligned}$$

The interior cell fluxes (\tilde{c}_x and \tilde{c}_y) and the interior pressure gradients ($\partial p / \partial x$ and $\partial p / \partial y$) do not cancel out in the summation, thus violating relations (3.3.4.5) and (3.3.4.6). Hence, the cell fluxes are locally divergence-free but the global balance over the computational domain is not satisfied.

As a result of the analysis, the following conclusions hold :

- (i) the Inconsistent Finite-Difference Method violates the compatibility and integrability conditions,
- (ii) the Consistent Finite-Difference Method will not satisfy the integrability conditions, and
- (iii) the Consistent Finite-Volume Method will not satisfy the integrability conditions for a high-order formulation of the divergence operator.

The divergence-free condition is satisfied locally at the collocated grid nodes for CFDM or at the cell faces for CFVM. The integrated divergence over the computational domain for CFDM and CFVM with a high-order discretization of the ($\nabla \cdot$) operator results in artificial mass sinks and sources due to the violation of the integrability conditions. It does not seem possible to satisfy the divergence-free condition as well as the discrete mass balance inside the computational domain at the nodes of the collocated grid. It may be noted that CFDM and CFVM will satisfy the integrability conditions for computational domains with periodic boundary conditions. Therefore, although a scheme may satisfy the divergence-free condition locally, it is not implied that global mass balance is achieved. Only a second-order finite-volume discretization for the divergence operator will satisfy all of the desired criteria.

3.4 Direct Solver Algorithm for the Pressure-Poisson Equation

The discretized pressure-Poisson equation is solved directly using an efficient procedure based on the matrix diagonalization technique (Haidvogel and Zang, 1979; Canuto et al., 1988). The linear system of equations is obtained and can be written in matrix form as follows (Ku et al., 1987; Madabhushi et al., 1993) :

$$D_{F2x} \cdot P + P \cdot D_{F2y}^T = f \quad (3.4.1)$$

where P is the pressure matrix of size $(N_x-2) \times (N_y-2)$.

D_{F2x} is the reduced finite-difference second derivative matrix in the x -direction of dimension $(N_x-2) \times (N_x-2)$.

D_{F2y} is the reduced finite-difference second derivative matrix in the y -direction

of dimension $(N_y-2) \times (N_y-2)$.

D_{F2y}^T is the transpose of D_{F2y} .

f is the modified right hand side matrix of size $(N_x-2) \times (N_y-2)$.

The modified matrix includes the contributions from the boundary values.

Appendix C presents the finite-difference second derivative matrices whose coefficients are determined using CFVM. In the next step of the algorithm, D_{F2x} and D_{F2y}^T are decomposed into their respective eigenvalue $(\lambda_x I$ and $\lambda_y I)$ and eigenvector $(E_x$ and $E_y)$ matrices as follows:

$$D_{F2x} = E_x \lambda_x I E_x^{-1} \quad (3.4.2a)$$

$$D_{F2y}^T = E_y \lambda_y I E_y^{-1} \quad (3.4.2b)$$

The matrix decomposition is performed using the EISPACK library routines, SGECO and SGEDI. Substituting Equations (3.4.2a-b) into Equation (3.4.1) results in :

$$E_x \lambda_x I E_x^{-1} P + P E_y \lambda_y I E_y^{-1} = f \quad (3.4.3)$$

Equation (3.4.3) is then pre-multiplied by E_x^{-1} and post-multiplied by E_y . This yields to the following expression :

$$\lambda_x I P' + P' \lambda_y I = f' \quad (3.4.4)$$

where $P' = E_x^{-1} P E_y$ and $f' = E_x^{-1} f E_y$. Equation (3.4.4) is an algebraic relation and P'_{ij} is calculated from :

$$P'_{ij} = \frac{1}{\lambda_{x_i} + \lambda_{y_j}} f'_{ij} \quad (3.4.5)$$

Finally, the pressure matrix, P , is obtained from:

$$P = E_x P' E_y^{-1} \quad (3.4.6)$$

For incompressible flows, the pressure field has an arbitrary level; hence, the formulation of the reduced matrix method is numerically singular. This effect is reflected

in the presence of two null eigenvalues (one for each x and y direction). To overcome the mathematical singularity, the denominator in Equation (3.4.5), $\left(\frac{1}{\lambda_{x_i} + \lambda_{y_j}}\right)$, is replaced by an arbitrary value (say, 1) when the denominator is zero. In the present computations, the threshold value below which the magnitude of the eigenvalue is considered to be 'zero' is set to 1.0×10^{-11} .

The above algorithm involves four matrix-matrix multiplications and solution of $((Nx-2) \times (Ny-2))$ algebraic equations. The overall operation count is $O(Nx^2 \times Ny + Nx \times Ny^2)$. Although the algorithm consists of a flexible solver for the high-order discrete Poisson and Helmholtz equations on non-uniform rectilinear grids, its basic limitation is that the coefficients of the discretization operator matrices, DF_{2x} and DF_{2y} , can vary only in their respective discretization directions. Thus, for computational domains with interior obstacles, the solution algorithm of the pressure-Poisson equation is modified and will be presented in Section 3.6.

3.5 Stability Analysis of the Numerical Scheme

The explicit evaluation of the convective and diffusive terms controls the numerical stability and dictates the time-step size in terms of the appropriate Courant-Friederich-Lewy (CFL) numbers (Anderson et al., 1984). To determine these restrictions, a von Neumann stability analysis has been performed on two model equations, the one-dimensional unsteady diffusion equation and the linear Burgers equation. Based on this analysis, the following stability criteria are derived :

$$r_1 = v \Delta t \max \left[\frac{1}{\Delta x^2} + \frac{1}{\Delta y^2} \right] \leq \frac{3}{16} \quad (3.5.1a)$$

$$r_2 = \Delta t \max \left[\frac{|u|}{\Delta x} + \frac{|v|}{\Delta y} \right] \leq \frac{3}{8} \quad (3.5.1b)$$

It should be noted that the stability requirements for second-order central difference stencils are $r_1 \leq 1/4$ and $r_2 \leq 1/2$ (Anderson et al., 1984). The stability analysis for the Navier-Stokes' equations requires a more elaborate study and has not been attempted. The values of the diffusive and convective CFL numbers in Equation (3.5.1) will provide guidelines on the time-step size limitations for the Navier-Stokes equations.

3.6 Capacitance Matrix Technique

Appendix D describes in detail the modifications of the spatial derivatives for interior obstacles. This section presents the modifications of the solution algorithm for the pressure-Poisson equation. The presence of irregular regions in the computational domain such as obstacles and baffles renders the pressure-Poisson equation non-separable. The Capacitance Matrix Technique (Buzbee et al., 1971; Schumann, 1980) has been incorporated to overcome this difficulty. Briefly described, the objective is to solve the non-separable Poisson equation, called the *A*-problem, satisfying :

$$A \cdot P = f \quad (3.6.1)$$

where *A* is a sparse banded matrix describing the original problem whose non-zero coefficients are computed and stored. A 'separable' *B*-problem is constructed from the *A*-problem, and can be solved using the eigenvalue decomposition algorithm. The *B*-problem does not satisfy Equation (3.6.2.11) but solves :

$$B \cdot P_1 = f \quad (3.6.2)$$

The matrix *B* has the same coefficients as the matrix *A* except at the *M* locations adjacent to the baffle(s).

The Capacitance Matrix Technique (CMT) is an algorithm that solves Equation (3.6.2) using a direct solver while concurrently satisfying Equation (3.6.1). To attain this objective, a capacitance matrix, denoted by *C*, is first constructed by solving (once for the entire problem) *M* number of *B*-problems with sequential unit perturbations to the right hand sides of the equations. The residuals at the *M* positions in the corresponding *A*-problem are computed and become the column elements of *C*. The algorithm to calculate the *C* matrix is symbolically summarized as follows :

$$\begin{aligned} & \text{do } j = 1, M \\ & \quad \delta_j = 1 \\ & \quad B \cdot P_1 = \delta \\ & \quad \text{do } i = 1, M \\ & \quad \quad C = A \cdot P_1 \\ & \quad \text{end do} \\ & \quad \delta = 0 \\ & \text{end do} \end{aligned} \quad (3.6.3)$$

C is a matrix of size $M \times M$. The final stage of the algorithm consists in computing the inverse of the capacitance matrix (C^{-1}). These calculations are performed at the pre-processing stage of the simulation; further, for a prescribed grid configuration, C^{-1} will be stored for subsequent use in the time-stepping procedure. During the time integration procedure, the following solution steps are executed:

- (i) Solve first the B -problem with the original source term using the direct solver algorithm :

$$D_{F2x} \cdot P_1 + P_1 \cdot D_{F2y}^T = f \quad (3.6.4a)$$

- (ii) Compute the residuals (R^A) on the A -problem :

$$R^A = A \cdot P_1 - f \quad (3.6.4b)$$

- (iii) Perturb the source term :

$$f^* = f - C^{-1} R^A \quad (3.6.4c)$$

- (iv) Solve again the B -problem with the perturbed source term, f^* :

$$D_{F2x} \cdot P_2 + P_2 \cdot D_{F2y}^T = f^* \quad (3.6.4d)$$

Steps (i) and (iv) are solved using the algorithm described in Section 3.4. At the end of Step (iv), the pressure field, P_2 , is also the solution field of the original A -problem (Equation 3.6.1) (see Appendix E for proof). The overall operation count of the solution algorithm with the Capacitance Matrix Technique is $O(2Nx^2xNy + 2NxxNy^2)$, i.e. twice as large as the original algorithm discussed in Section 3.4.

3.7 Validation of the Numerical Scheme

A computer code has been developed based on the numerical procedure discussed in the previous sections. The pressure formulation methods described in Section 3.3 are evaluated for two 2-D model problems, the vortex-decay and the driven-cavity, and the results are discussed in Sections 3.7.1 and 3.7.2. Table 3.7.1 summarizes seven schemes considered for the discretization of the pressure-Poisson equation. A detailed description of the stencils is presented in Appendix B. We will study the effect of these formulations on the accuracy of the numerical procedure. Section 3.7.3 presents the results for the Kovasznay flow.

The error norms are used to evaluate the formal accuracy of the numerical discretization for the test problems and are defined as follows :

$$L_1\text{-norm : } L_{\phi}^1 = \frac{\sum_{j=2}^{Ny-1} \sum_{i=2}^{Nx-1} |\phi - \phi^*|}{(Nx-2)(Ny-2)} \quad (3.7.1)$$

$$L_2\text{-norm : } L_{\phi}^2 = \frac{\left(\sum_{j=2}^{Ny-1} \sum_{i=2}^{Nx-1} (\phi - \phi^*)^2 \right)^{1/2}}{(Nx-2)(Ny-2)} \quad (3.7.2)$$

$$L_{\infty}\text{-norm : } L_{\phi}^{\infty} = \max |\phi - \phi^*| \quad (3.7.3)$$

where ϕ represents the discretized variable and ϕ^* is its corresponding analytical value. The order of error reduction, λ_{ϕ} , between two grid levels, Nx_1 and Nx_2 , is defined as :

$$\lambda_{\phi} = \frac{\ln \left(\frac{(L_{\phi}^i)_1}{(L_{\phi}^i)_2} \right)}{\ln \left(\frac{Nx_2}{Nx_1} \right)} \quad (3.7.4)$$

where $i = 1, 2$ or ∞ , $(L_{\phi}^i)_1$ represents one of the error norms on grid Nx_1 and $(L_{\phi}^i)_2$ is one of the error norms on grid Nx_2 .

3.7.1 Vortex-Decay Problem

The code was initially validated for several simple test problems including the scalar convection and scalar diffusion equations, and the linear and non-linear Burger's equations. The error reduction for the numerical scheme is found to be fifth order. In this section, we will study the effects of the pressure formulations in Table 3.7.1 on the numerical solution of the two-dimensional vortex-decay problem. The observed L^1 and L^{∞} error norms as well as the order of error reduction (λ) are discussed below for the various field variables.

The analytical solution of the two-dimensional vortex-decay problem is (Taylor, 1923) :

$$u^*(x,y,t) = -\cos(x) \sin(y) e^{-\sigma t} \quad (3.7.1.1a)$$

$$v^*(x,y,t) = \sin(x) \cos(y) e^{-\sigma t} \quad (3.7.1.1b)$$

$$p^*(x,y,t) = -\frac{1}{4} (\cos(2x) + \cos(2y)) e^{-\sigma t} \quad (3.7.1.1c)$$

where $\sigma = 2/Re$.

The computational domain extends from 0 to π in the x and y directions. The boundary conditions for the velocities are set according to Equations (3.7.1.1a) and (3.7.1.1b). Neumann boundary conditions are imposed for the pressure field. Numerical simulations are performed for Reynolds numbers of 1, 100, and 1000. The time step, Δt , is set to 2.5×10^{-5} so as to minimize the temporal discretization errors.

Figure 3.7.1.1 presents the L_u^∞ error norm at $Re = 1$ as computed by the various methods described in Section 3.3. These errors are determined at $t = 0.35$ at which time the vortex decays to half of its original strength. Also shown are the results of Le and Moin (1991) for the second-order time-split finite-volume method. Results obtained with IFDM are fifth-order accurate ($\lambda_u = 5.11$) between the first two grid sizes (17×17 and 33×33); however, λ_u drops to 0.16 for grid sizes of 33×33 and 65×65 . At this refinement, the local divergence errors are significant and mask the accuracy of the convection and diffusion operators. The overall error reduction is calculated to be 2.6. In the Consistent Finite Difference Methods (CFDM1-3), the error is seen to decrease with the fourth power of grid size. The solution obtained with the Consistent Finite-Volume Method is second-order accurate for CFVM1 and CFVM2 and third-order for CFVM3. It was observed that the solution of the velocity field is sensitive to the near-boundary pressure gradient stencil. A second-order discretization of the near-boundary pressure gradient in CFVM3 resulted in an overall second-order accuracy of the velocity. Consequently, a fourth-order discretization is also implemented at the boundaries. The maximum divergences of the calculated velocity field at $t = 0.35$ obtained from the various formulations are summarized in Figure 3.7.1.2. As expected, for the CFVM procedure, the cell fluxes are divergence free but the cell-centered velocity field is not.

Subsequently, simulations are performed using CFVM2 for Re between 1 and 10^4 . The grid resolution is 65×65 nodes, and the time-step size, Δt , is 10^{-4} . The

calculations are undertaken for 5000 time steps ($t = 0.5$). Figure 3.7.1.3 presents the error norms of the streamwise velocity and pressure. It is observed that the error norms remain bounded with increasing Reynolds numbers. This behavior is a characteristic of the vortex decay problem since the convective terms balance the pressure gradient while the diffusive terms balance the temporal derivative. Hence, at high Reynolds numbers, the accuracy of the scheme will be mainly dictated by the discretization of the pressure gradient term. Table 3.7.1.2 summarizes the orders of reduction, λ_u and λ_p , based on the average errors at $Re = 1, 100$ and 1000 as computed by the various schemes. It is seen that the error reductions decrease with increasing Re for most of the schemes. This aspect quantifies the deterioration in accuracy seen in Figure 3.7.1.3. For the vortex-decay problem, the Consistent Finite Difference Method is seen to result in the highest order of error reduction.

3.7.2 Driven-Cavity Flow

The results for the shear-driven flow in a square cavity with a unit velocity ($u = 1$) applied on the top boundary are presented in this section. The velocity field is started with zero initial conditions. The computational domain extends from 0 to 1 in the x and y directions. The simulations are performed on grid sizes of 17×17 , 33×33 and 65×65 for Reynolds numbers of 100, 400 and 1000. The solutions obtained with a 65×65 grid are discussed and compared with the numerical results of Ghia et al. (1982) and Vanka (1986). The different formulations for the pressure-Poisson equation, summarized in Table 3.7.1, are considered in order to evaluate their relative accuracy in predicting the flow in the driven-cavity problem.

Figure 3.7.2.1 presents the u -velocity profile along the vertical centerline of the cavity at $Re = 100$ as computed by the different pressure formulations. Also shown are the numerical results of Ghia et al. (1982) on a 129×129 grid. The results obtained with CFDM and CFVM are seen to collapse on a single curve; however, the u -velocity calculated by IFDM has a higher value than that of Ghia et al. (1982) and the other formulations of the current study. The minimum x -velocity (u_{min}) along the vertical centerline of the cavity ($x = 0.5$), the minimum and maximum y -velocity (v_{min} and v_{max}) along the horizontal centerline of the cavity ($y = 0.5$), and the minimum stream-function (ψ_{min}) at the center of the primary vortex, are summarized in Table 3.7.2.1 for $Re = 100$ on a mesh resolution of 65×65 nodes. Also shown are the results obtained by Ghia et al. (1982) on a 129×129 grid and Vanka (1986) on a 321×321 grid. It is observed that the

solutions obtained with CFDM1-3 and CFVM2-3 match the results from the calculations of Vanka (1986). The results obtained by the seven schemes are presented in Table 3.7.2.2 for $Re = 400$. It can be seen that the values predicted by CFVM3 compare more satisfactorily with the results obtained by Ghia et al. (1982) while those predicted by IFDM have significant errors.

Figure 3.7.2.2 presents the u -velocity profile along the vertical centerline of the cavity at $Re = 1000$ as computed by the different pressure formulations. Also shown are the numerical results of Ghia et al. (1982). It is seen that the u -velocities computed with CFDM and CFVM compare satisfactorily with the solution obtained by Ghia et al. (1982), but the solution given by IFDM has significant error. Table 3.7.2.3 summarizes u_{min} (along $x = 0.5$), v_{min} (along $y = 0.5$), v_{max} (along $y = 0.5$), and ψ_{min} for $Re = 1000$ obtained by the various pressure formulations and the numerical results from Ghia et al. (1982) on a 129×129 grid and Vanka (1986) on a 321×321 grid. The values obtained with CFVM3 compare more satisfactorily with the data of Ghia et al. (1982) and Vanka (1986) than CFDM3. Further, the calculations performed with IFDM have significant differences; for example, u_{min} is over-predicted by 30%. The solutions obtained with CFVM2 are also in close agreement with the results of Ghia et al. (1982) but the differences are larger than those obtained with CFVM3.

Subsequently, the satisfaction of the global divergence-free condition is evaluated for the various schemes and is used as a measure of the overall accuracy of the numerical formulations. The integrated mass (along the y -direction, say) is defined as :

$$m_{\phi}^y = \sum_{j=2}^{N_y-1} \phi^{n+1} \Delta y \quad (3.7.2.1)$$

where ϕ represents either the collocated velocity (u) or the cell fluxes (c_x). The variation of $m_{c_x}^y$ along the x -direction is presented in Figure 3.7.2.3 for the Consistent Finite Volume Methods. For CFVM1 and CFVM2, the global divergence-free condition is satisfied to machine accuracy (order of 10^{-15}) by the cell face fluxes. However, since CFVM3 does not satisfy the integrability conditions as discussed in Section 3.3.4, it generates artificial mass sources (and sinks) within the computational domain giving rise to errors in the global divergence. It is observed that the global divergence of the cell face fluxes is of the order of approximately 10^{-3} . Figure 3.7.2.4 displays the distribution

of m_u^y along constant x -lines for the various pressure formulations. The magnitudes of these global divergence deficiencies are observed to be of the order of 10^{-3} for IFDM, CFDM1, CFDM2, and CFDM3. These errors arise from the violation of the integrability conditions (Equations 3.3.4.5-6). It is also seen from Figure 3.7.2.4 that the collocated velocity field obtained with CFVM3 has global divergence errors of the same order of magnitude as the cell fluxes ($\sim 10^{-3}$). The behavior of the global divergence for CFVM1 and CFVM2 is high ($\sim 10^{-4}$) near the boundaries, but then drops sharply to 10^{-6} for CFVM1 and 10^{-8} for CFVM2 in the interior of the computational domain. In addition to these errors in global balance, the Consistent Finite Difference Methods (CFDM1-3) also display an oscillatory pressure field. Figure 3.7.2.5 shows the pressure distribution for CFDM1-3 along the horizontal centerline ($y = 0.5$). Severe checkerboard splitting is observed in the pressure variation.

To summarize, several different formulations for representing the pressure-Poisson equation have been examined in numerical schemes employing a collocated arrangement of the velocities and the pressure. The methods consider discretizations of the divergence and gradient operators with different orders of accuracy using finite-difference and finite-volume concepts; their formulations have been discussed in Section 3.3. These representations have been evaluated by computing the decay of a vortex and the steady flow in a driven cavity. It is seen that the Inconsistent Finite-Difference Method leads to significant errors. The Consistent Finite-Difference Approach obtains a divergence-free velocity field but the pressure field is seen to be oscillatory and global divergence is not satisfied. In the Consistent Finite-Volume methods, the divergence-free condition is satisfied by the cell face fluxes and the resulting pressure field is smooth. However, if the divergence operator is discretized with fourth-order (or higher) accuracy, the cell face fluxes do not satisfy the global divergence-free condition. The characteristics of the various pressure formulations discussed in the current study are summarized in Table 3.7.2.4. Based on these observations, we conclude that the Consistent Finite-Volume Approach with second-order discretization of the divergence operator and fourth-order discretization of the pressure gradient provides the best compromise between accuracy and satisfaction of the compatibility and integrability criteria and should be the preferred approach when used in conjunction with collocated grids and high-order differencing of the momentum equations.

3.7.3 Kovaszny Flow

As a final test problem, the laminar flow behind a two-dimensional grid, known as the Kovaszny flow, is investigated. The exact solution derived by Kovaszny (1948) is a function of the Reynolds number of the form :

$$u^*(x,y) = 1 - e^{\lambda x} \cos(2\pi y) \quad (3.7.3.1a)$$

$$v^*(x,y) = \frac{\lambda}{2\pi} e^{\lambda x} \sin(2\pi y) \quad (3.7.3.1b)$$

$$p^*(x,y) = \frac{1}{2} (1 - e^{2\lambda x}) \quad (3.7.3.1c)$$

where $\lambda = \frac{Re}{2} - \left(\frac{Re^2}{4} + 4\pi^2 \right)^{1/2}$.

The boundary conditions are based on the above relations, and the initial flow field is set to zero. The computational domain extends from -0.5 to 2.0 in the x -direction and from -0.5 to 1.5 in the y -direction. The pressure formulation is based on CFVM2. Figure 3.7.3.1 shows the time-mean streamlines for $Re = 40$. Two recirculation regions are formed near the inlet whereas the streamlines become parallel farther downstream. Figure 3.7.3.2a presents the distribution of the error norms in the computed u -velocity field for several grid sizes. The error reductions, λ_u , are calculated to be 2.6, 3.8 and 2.4 for L_u^1 , L_u^2 , and L_u^∞ , respectively. Figure 3.7.3.2b shows the distribution of the error norms in the calculated pressure field for several grid sizes. The error reductions, λ_p , are calculated to be 2.6, 3.6 and 2.1 for L_p^1 , L_p^2 , and L_p^∞ , respectively. It is observed that the error reductions presented for the Kovaszny flow are higher than for the vortex-decay problem.

3.8 Evaluation of Outlet Boundary Conditions for Flows in Unbounded Domains

Prescribing the appropriate outlet boundary conditions for flows in open domains has been an area of intensive research (Lowery and Reynolds, 1986; Pauley et al., 1990; Poinso and Lele, 1992). Although our aim is not to resolve conclusively this issue, several outlet boundary conditions are tested to evaluate their applicability in two types of flow configurations, the separated and the separated-reattaching flows. In separated flows, propagating structures are dominant, while, for separated-reattaching flows,

propagating structures with boundary layer development are of importance. The appropriate outlet boundary condition should result in minimal numerical distortion of these structures. The boundary conditions tested are as follows :

$$\frac{\partial u_k}{\partial x} = 0 \quad (3.8.1a)$$

$$\frac{\partial^2 u_k}{\partial x^2} = 0 \quad (3.8.1b)$$

$$\frac{\partial u_k}{\partial t} = \frac{1}{Re} \left(\frac{\partial^2 u_k}{\partial x^2} \right) \quad (3.8.1c)$$

$$\frac{\partial u_k}{\partial t} + U_c \left(\frac{\partial u_k}{\partial x} \right) = 0 \quad (3.8.1d)$$

$$\frac{\partial u_k}{\partial t} + U_c \left(\frac{\partial u_k}{\partial x} \right) = \frac{1}{Re} \left(\frac{\partial^2 u_k}{\partial x^2} \right) \quad (3.8.1e)$$

where U_c is a representative convection velocity, and the index $k = 1, 2$ represents the x (streamwise) and y (cross-stream) directions, respectively.

These boundary conditions are tested for a convecting vortex superimposed on a uniform flow (Poinsot and Lele, 1992). The computational domain extends in the streamwise (x) direction from -1 to 1 and in the cross-stream (y) direction from -2 to 2 . A uniform grid of 41×81 nodes is used resulting in mesh sizes, Δx and Δy , of 0.05 . The time-step size, Δt , is set to be 2.5×10^{-3} . The initial conditions of the velocity field are based on the streamfunction for an incompressible viscous vortex in cylindrical coordinates :

$$u = u_0 + \frac{\partial \psi}{\partial y} \quad (3.8.2a)$$

$$v = - \frac{\partial \psi}{\partial x} \quad (3.8.2b)$$

$$\text{where } \psi = C \exp \left(- \frac{x^2 + y^2}{2R_c^2} \right) \quad (3.8.2c)$$

In Equation (3.8.2), u_0 represents the uniform inlet velocity, and R_c and C are the radius and strength of the vortex, respectively. The mean flow has a uniform value, $u_0 = 1$, at a Reynolds of 10000 . The vortex is initially located in the center of the domain ($x = y = 0$) and defined by :

$$C = -0.0005; \quad R_c = 0.15 \quad (3.8.3)$$

Uniform velocity ($u = u_0 = 1, v = 0$) is imposed at the inlet ($x = -1$), and freestream conditions ($u = 1, v = 0$) are specified at $y = \pm 2$. The outlet boundary condition ($x = 1$) is based on one of the expressions given by Equations (3.8.1a-e). The convective velocity, U_c , in Equations (3.8.1d-e) is set to $u_0 (= 1)$. Null pressure gradients are imposed along the edges of the computational domain. The simulations are performed for three non-dimensional time units, corresponding to 12000 time-steps.

The streamwise velocity difference is defined as $\left(\frac{u-u_0}{u_0}\right)$ and the spanwise vorticity, ω_z , is computed from :

$$\omega_z = \frac{\partial v}{\partial x} - \frac{\partial u}{\partial y} \quad (3.8.4)$$

Figure 3.8.1a shows contours of the streamwise velocity difference and the spanwise vorticity for the initial field ($t = 0$). The dashed lines represent negative values. The maximum velocity difference induced initially by the vortex is 2.02×10^{-3} with the corresponding maximum spanwise vorticity of 4.2×10^{-2} . The vortex has a counter-clockwise rotation with a central core of negative vorticity surrounded by a ring of positive vorticity. Figures 3.8.1b-d present the results obtained with a zero normal boundary gradient of the velocity field (Equation 3.8.1a) for three time instances. At $t = 1$, the vortex leaves the computational domain as seen in Figure 3.8.1b. The values of the maximum velocity difference and spanwise vorticity are 1.9×10^{-3} and 3.2×10^{-2} , respectively. At $t = 2$ (Figure 3.8.1c), a new elongated structure is present near the center of the computational domain. This structure is formed as a result of the numerical reflection generated by the outlet boundary condition. The maximum vorticity magnitude is computed to be 1×10^{-3} . At $t = 3$ corresponding to 2 time units after the initial vortex left the computational domain (Figure 3.8.1d), the numerical vortex has convected back towards the edge of the computational domain. The maximum vorticity at this instant is calculated to be 8.5×10^{-4} . Figures 3.8.2, 3.8.3, and 3.8.4 present contours of the velocity difference and the spanwise vorticity for the remaining boundary conditions, Equations (3.8.1b-d). The time sequences in the figures are for $t = 1, 2$ and 3. The results obtained with Equation (3.8.1e) are similar to those obtained with Equation (3.8.1d) (see Figure 3.8.4). For the boundary condition corresponding to Equation (3.8.1c), the convecting vortex exiting the computational domain is observed to be subjected to high numerical

distortion (Figure 3.8.3a). Although numerical reflection is present for all of the computed vorticity fields, the magnitudes differ significantly between the various boundary conditions. Based on these time sequences, it is seen that boundary condition (3.8.1d) (as well as (3.8.1e)) has the lowest numerical reflection from the boundary, and, therefore, results in minimal distortion of the vorticity field.

Figures 3.8.5 and 3.8.6 summarize the temporal variations of the maximum velocity difference and spanwise vorticity for the various outlet boundary conditions tested. It is seen that boundary conditions (3.8.1d) and (3.8.1e) result in the lowest values while the values obtained by Equation (3.8.1a) are two orders of magnitude larger than the remaining ones. Thus, of these, boundary conditions (3.8.1d and 3.8.1e) allow the convecting vortex to leave the computational domain with minimal distortion and result in the lowest numerical reflection (see also Lowery and Reynolds, 1986; Pauley et al., 1990).

4. NUMERICAL PROCEDURE FOR THREE-DIMENSIONAL SIMULATIONS

This chapter extends the two-dimensional numerical procedure presented in Chapter 3 to a three-dimensional formulation. A Fourier-spectral representation is used in conjunction with the high-order finite-difference method. Section 4.1 outlines the mixed Fourier-spectral/finite-difference scheme. The algorithm of the pressure-Poisson solver is presented in Section 4.2. The stability requirements of the numerical scheme are reported in Section 4.3. Section 4.4 presents the validation of the numerical scheme.

4.1 Fourier-Spectral Representation

The time-dependent Navier-Stokes equations governing the motion of an incompressible fluid (Equations 3.1.1-3.1.2) are considered with spanwise variation. Since the simulations are performed for homogenous boundary conditions in the z -direction, the instantaneous flow field is assumed to be periodic in the spanwise direction. Hence, the Fourier-spectral scheme is an appropriate representation of the flow variables in the spanwise (z) direction. The finite Fourier series expansion of a field variable, ϕ , is written as :

$$\phi(x, y, z_m, t) = \sum_{k_z=-Nz/2}^{Nz/2-1} \hat{\phi}(x, y, k_z, t) e^{ik_z z_m} ; m = 0, \dots, Nz-1 \quad (4.1.1)$$

where Nz is the number of Fourier modes and k_z is the Fourier wavenumber. The Fourier coefficients, $\hat{\phi}$, are complex with $\hat{\phi} = \hat{\phi}_r + i \hat{\phi}_i$ and $i = \sqrt{-1}$.

In the current numerical procedure, the simulations are performed in physical space and Fourier transforms are applied to evaluate the spanwise derivatives with spectral accuracy. The following procedure outlines the steps undertaken to compute the velocity and pressure fields. For the first step of the time-splitting scheme, the convective and viscous derivatives in the spanwise direction are evaluated using the fifth and fourth-order formulations as described in Section 3.2. A Fourier-spectral representation will be considered in the future. In the second step, the pressure field is decomposed into its Fourier modes and computed in spectral space. Hence, the divergence of the intermediate velocity is evaluated with Fourier representation. As a

result, the Fourier coefficients of \tilde{w} are computed from Equation (4.1.1) and the gradient in the z -direction, $\partial\tilde{w}/\partial z$, is evaluated as follows :

$$\frac{\partial\tilde{w}}{\partial z} = \sum_{k_z=-N_z/2}^{N_z/2-1} \hat{\frac{\partial\tilde{w}}{\partial z}} e^{ik_z z_m} \quad (4.1.2a)$$

$$\hat{\frac{\partial\tilde{w}}{\partial z}} = i k_z \hat{\tilde{w}} \quad (4.1.2b)$$

In the update procedure, the Fourier modes of the z -velocity at the $(n+1)$ time step are then determined from:

$$\hat{w}^{n+1} = \hat{\tilde{w}} - i k_z \hat{p}^{n+1} \Delta t \quad (4.1.3)$$

Finally, the divergence-free z -velocity is determined from its Fourier coefficients through an inverse Fourier transform :

$$w^{n+1} = \sum_{k_z=-N_z/2}^{N_z/2-1} \hat{w}^{n+1} e^{-ik_z z_m} ; m = 0, \dots, N_z-1 \quad (4.1.4)$$

Efficient Conventional Discrete Fourier Transforms (CDFT) or Fast Fourier Transforms (FFT) (Temperton, 1983) are used to transform from physical space to spectral space and vice-versa. The formulation of the pressure-Poisson equation is presented in the section to follow.

4.2 Spectral Formulation of the Pressure-Poisson Equation

For the three-dimensional simulations, the pressure field, p , is decomposed into its complex Fourier modes, \hat{p}_k , in the z -direction as follows :

$$\hat{p}(x, y, k_z, t) = \frac{1}{N_z} \sum_{m=0}^{N_z-1} p(x, y, z_m, t) e^{-ik_z z_m} \quad (4.2.1)$$

where k_z is the Fourier wavenumber ($k_z = -\frac{N_z}{2}, \dots, \frac{N_z}{2} - 1$) and $i = \sqrt{-1}$. Taking the Fourier transforms of Equation (3.1.7), the Fourier coefficients of the pressure field will satisfy the following equation :

$$\left(\frac{\partial}{\partial x} \left(\frac{\partial \hat{p}}{\partial x} \right) \right) + \left(\frac{\partial}{\partial y} \left(\frac{\partial \hat{p}}{\partial y} \right) \right) - k_z^2 \hat{p} = \frac{1}{\Delta r} (\hat{\nabla} \cdot \mathbf{u}) \quad (4.2.2)$$

Equation (4.2.2) is discretized in the x and y -directions based on the Consistent Finite Volume Method (CFVM2). The Fourier modes of divergence of the intermediate velocity are given by :

$$(\hat{\nabla} \cdot \mathbf{u}) = \frac{\partial \hat{c}_x}{\partial x} + \frac{\partial \hat{c}_y}{\partial y} + \frac{\partial \hat{w}}{\partial z} \quad (4.2.3)$$

where

$$\frac{\partial \hat{c}_x}{\partial x} = \frac{1}{N_z} \sum_{m=0}^{N_z-1} \left(\frac{\partial \tilde{c}_x}{\partial x} \right) e^{-ik_z z_m} \quad (4.2.4a)$$

$$\frac{\partial \hat{c}_y}{\partial y} = \frac{1}{N_z} \sum_{m=0}^{N_z-1} \left(\frac{\partial \tilde{c}_y}{\partial y} \right) e^{-ik_z z_m} \quad (4.2.4b)$$

$$\frac{\partial \hat{w}}{\partial z} = i k_z \hat{w} \quad (4.2.4c)$$

Hence, Equation (4.2.2) results in $((N_x-2) \times (N_y-2) \times (N_z))$ number of linear equations. The direct solver described in Section 3.4 can be easily extended to solve for the Fourier coefficients in Equation (4.2.2). The three-dimensional discretized pressure-Poisson equation is written symbolically as :

$$D_{F2x} \cdot \hat{P} + \hat{P} \cdot D_{F2y}^T - k_z^2 I \hat{P} = \hat{f} \quad (4.2.5)$$

where \hat{P} is the complex Fourier coefficient matrix of the pressure of size $((N_x-2) \times (N_y-2) \times N_z)$. $\hat{P} = \hat{P}_r + i \hat{P}_i$

D_{F2x} is the reduced finite-difference second derivative matrix in the x -direction of dimension $((N_x-2) \times (N_x-2) \times N_z)$.

D_{F2y} is the reduced finite-difference second derivative matrix in the y -direction

of dimension $(N_y-2) \times (N_y-2) \times N_z$.

\hat{D}_{F2y}^T is the transpose of D_{F2y} .

\hat{f} is the complex Fourier coefficient matrix for the discretized divergence operator of the intermediate velocity of size $(N_x-2) \times (N_y-2) \times N_z$.

$$\hat{f} = \hat{f}_r + i \hat{f}_i$$

Appendix C presents the finite-difference second-derivative matrices whose coefficients are determined using CFVM2. Decomposing D_{F2x} and \hat{D}_{F2y}^T into their respective eigenvalue ($\lambda_x I$ and $\lambda_y I$) and eigenvector (E_x and E_y) matrices (see Section 3.4) and substituting into Equation (4.2.2) results in :

$$E_x \lambda_x I E_x^{-1} \hat{P} + \hat{P} E_y \lambda_y I E_y^{-1} - k_z^2 I \hat{P} = \hat{f} \quad (4.2.6)$$

Equation (4.2.6) is then pre-multiplied by E_x^{-1} and post-multiplied by E_y . This yields the following expression :

$$\lambda_x I \hat{P}' + \hat{P}' \lambda_y I - k_z^2 I \hat{P}' = \hat{f}' \quad (4.2.7)$$

where $\hat{P}' = E_x^{-1} \hat{P} E_y$ and $\hat{f}' = E_x^{-1} \hat{f} E_y$. Equation (4.2.7) is an algebraic relation and $\hat{P}'_{i,j,k}$ is calculated from :

$$\hat{P}'_{i,j,k} = \frac{\hat{f}'_{i,j,k}}{\lambda_{x_i} + \lambda_{y_j} - k_z^2} \quad (4.2.8)$$

The Fourier coefficients of the pressure matrix, \hat{P} , are then obtained from:

$$\hat{P} = E_x \hat{P}' E_y^{-1} \quad (4.2.9)$$

Equations (4.2.7)-(4.2.9) are solved for the real and imaginary parts of the Fourier coefficients. It is to be noted that, since the pressure field is a real variable, only $(N_z/2+1)$ modes need to be computed and the remaining modes are their complex conjugates. Finally, the pressure field is determined from its Fourier coefficients through an inverse Fourier transform :

$$p(x, y, z, t) = \sum_{k_z=-Nz/2}^{Nz/2-1} \hat{p}(x, y, k_z, t) e^{ik_z z} ; m = 0, \dots, Nz-1 \quad (4.2.10)$$

The formulation of the reduced matrix method is singular for the zeroth wavenumber ($k_z = 0$). This arises from the arbitrariness of the level of the pressure field in incompressible flow and is translated by zero eigenvalues (one for each x and y direction). To overcome the mathematical singularity, the denominator $\left(\frac{1}{\lambda_{x_i} + \lambda_{y_j} - k_z^2} \right)$ at $k_z = 0$ is replaced by an arbitrary value (say, 1) when the denominator is zero. In the present computations, the threshold value below which the magnitude of the eigenvalue is considered to be 'zero' is set to 1.0×10^{-11} . In addition, for the Fourier representation, spurious modes for pressure are present for the highest wavenumber ($k_z = -Nz/2$), and hence its contribution is removed by setting its corresponding Fourier coefficient, $\hat{p}(x, y, -Nz/2, t)$, to zero (Balachandar and Madabhushi, 1992).

In the presence of obstacles and baffles inside the computational domain, the direct solver is used in conjunction with the Capacitance Matrix Technique (Buzbee et al., 1971; Schumann, 1980). Details of the CMT method are discussed in Section 3.6 for the two-dimensional simulations. The spectral representation of the pressure field decouples the discretized linear equations in the z -direction for every Fourier wavenumber. As a result, the size of the capacitance matrix, C , will be reduced from a size of $(M \times (Nz/2+1))^2$ to $(M \times M \times (Nz/2+1))$ where M is the number of nodes to be modified adjacent to the baffle. The capacitance matrix is constructed for the three-dimensional problem in a procedure similar to that described in Equation (3.6.3). The inverse of the capacitance matrix, C^{-1} , of size $(M \times M \times (Nz/2+1))$, is computed at the initial stage of the simulation. For a prescribed grid configuration, C^{-1} is stored for subsequent use in the time-stepping procedure. At every time step, the algorithm described in Section 3.6 is applied for every Fourier mode (see Equations 3.6.5a-d).

4.3 Numerical Stability

Since the viscous terms are treated explicitly through the Adams-Bashforth second-order accurate formulation, the time step size is restricted by the diffusive stability criterion at low Reynolds numbers. The implicit Crank-Nicolson scheme can be applied in the future to override such a limitation. However, for relatively high Reynolds

numbers (say above 100), the stability criterion based on the diffusive terms will not dictate the time-step size. Based on the von Neumann analysis, the stability criteria for the three-dimensional calculations are given by:

$$r_1 = v \Delta t \max \left[\frac{1}{\Delta x^2} + \frac{1}{\Delta y^2} + \frac{1}{\Delta z^2} \right] \leq \frac{3}{16} \quad (4.3.1)$$

$$r_2 = \Delta t \max \left[\frac{|u|}{\Delta x} + \frac{|v|}{\Delta y} + \frac{|w|}{\Delta z} \right] \leq \frac{3}{8} \quad (4.3.2)$$

where Δz is the grid size in the z -direction.

4.4 Validation of the Numerical Scheme

To test the present three-dimensional scheme for a problem with two non-periodic directions and one periodic direction, simulations of fully-developed laminar flow through a square duct are undertaken. The computational domain extends from -1 to 1 in the x and y -directions and from 0 to 2π in the z -direction. No-slip boundary conditions are applied along the edges of the computational domain in the x and y -directions and periodic conditions are imposed in the z -direction. The simulations are conducted for a grid size of $33 \times 33 \times 16$ at $Re = 10$ and 30 . The Reynolds number is based on the friction velocity and the duct half-width. The solutions obtained are compared with the numerical results of Madabhushi (1992) performed using Chebyshev collocation procedure in the x and y -directions and Fourier spectral representation in the z -direction (see Madabhushi et al. (1993)).

Figure 4.4.1 presents the w -velocity distribution along $y = 0$ in the x -direction for a fully-developed laminar flow through a square duct at $Re = 10$ and 30 . Also shown are the numerical results of Madabhushi (1992), based on Method 3 of Madabhushi et al. (1993), obtained on a $16 \times 16 \times 16$ grid. The results are seen to be in excellent agreement with the fully-spectral procedure. A divergence-free 3-D perturbation is then superimposed on the fully-developed laminar flow and has a form similar to that used by Kim and Moin (1980) given by :

$$u'(x,y,z) = -\epsilon [1 + \cos(\pi x)] \sin(\pi y) \sin(z) \quad (4.4.1a)$$

$$v'(x,y,z) = -\epsilon \sin(\pi x) [1 + \cos(\pi y)] \sin(z) \quad (4.4.1b)$$

$$w'(x,y,z) = 2\pi\epsilon \sin(\pi x) \sin(\pi y) \cos(z) \quad (4.4.1c)$$

where ϵ is the amplitude of the perturbation. Calculations are performed for the decay of a 3-D perturbation at $Re = 10$ with $\epsilon = 0.05$. The temporal developments of the zeroth, first and second Fourier modes of the streamwise and spanwise velocities, \hat{u}_{k_z} and \hat{w}_{k_z} for $k_z = 0, 1$ and 2 , are presented in Figure 4.4.2 at $x = y = -0.5625$. Also plotted are the results obtained by Madabhushi (1992) at $x = y = -0.5557$. It is seen that the results obtained with the current formulation agree well with the results obtained with the spectral method. The maximum divergences of the velocity field in the interior and along the boundary of the computational domain are displayed in Figure 4.4.3 for one time unit. It is observed that the errors in the divergence of the velocity generated in the interior of the computational domain are one order of magnitude lower than the errors of the boundary divergence generated by the spectral code; while the divergence of the velocity field near the boundaries are one order of magnitude higher. Simulations are also performed at $Re = 30$ with $\epsilon = 0.30$. Figures 4.4.4 a and b present the temporal evolution of the zeroth, first and second Fourier modes of the streamwise and spanwise velocities, \hat{u}_{k_z} and \hat{w}_{k_z} for $k_z = 0, 1$ and 2 at $x = y = -0.5625$. Comparison with the results obtained by Madabhushi (1992) shows satisfactory agreement. To summarize, the current mixed high-order finite-difference Fourier-spectral method is seen to result in accurate predictions. Subsequently, the study of spatially and temporally evolving flows will be undertaken based on the developed numerical procedure described in Chapters 3 and 4.

5. DESCRIPTION OF THE DATA-PARALLEL ALGORITHM

This chapter presents the implementation of the two and three-dimensional numerical algorithms discussed in Chapters 3 and 4 on the massively parallel processing (MPP) computer, the Connection Machine Model 5 (CM-5). Section 5.1 outlines the CM-5 architecture. In Section 5.2, the two-dimensional data-parallel algorithm is described along with the performance and representative timings. Section 5.3 presents the three-dimensional data-parallel algorithm with its corresponding representative timings and performance.

5.1 Details of the CM-5 Architecture

The Connection Machine Model 5 (CM-5) is a massively parallel processing platform with a 'Universal Architecture' supporting both SIMD (Single-Instruction, Multiple-Data) and MIMD (Multiple-Instruction, Multiple-Data) computing models. It can consist of hundreds or thousands of computational processing nodes, one or more control processors and Input/Output (I/O) units. All these components are integrated into a system by two internal communications networks, the Control Network and the Data Network (Thinking Machines Corp., 1992a). A system including a control processor, a subset of computational processing nodes and a dedicated portion of the communication network is called a 'partition'. Timesharing, batch mode and multi-user environments are supported on individual partitions. Each partition can be viewed as a stand-alone parallel supercomputer.

The control processor element is like a standard high-performance workstation computer. It consists of a SPARC (RISC-based) microprocessor with its hierarchical memory and I/O devices such as local disk and Ethernet connection. It also includes a CM-5 Network Interface providing access to the Control Network and the Data Network. It acts as a partition manager executing system administration tasks and serial user tasks. An enhanced UNIX-based operating system, CMOST, is executed on each control processor and manages the CM-5 parallel-processing resources.

The processing node consists of a SPARC microprocessor, a memory subsystem and a CM-5 Network Interface. The microprocessor has a clock speed of 32 MHz and is capable of 22 MIPS and 5 MFLOPS. These components are connected to a 64-bit bus system. All logical connections to the rest of the system pass through the Network

Interface. The memory subsystem consists of a memory controller, four DRAM memory banks of 8 *MBytes* each, and 64 *KBytes* of cache memory. The memory banks are connected by a 72-bit path (64 data bits plus 8 ECC bits) to the memory controller which, in turn, is attached to the node bus. The Network Interface connects the processing elements to the rest of the system through the Control Network and the Data Network. Optionally, the processing nodes can be configured with the Data-path floating point system, referred to as DASH or Vector Units (VU). These vector units are high-performance arithmetic accelerators. Four vector units replace the memory controller. The vector-unit clock rate is 16 *MHz*. Each vector unit has 32 *MFLOPS* peak 64-bit floating-point performance and a peak memory bandwidth of 128 *MBytes/sec*, and performs all the functions of a memory controller. Attached to each vector unit is an 8 *MByte* memory bank. Together, the vector units provide 512 *MBytes/sec* memory bandwidth and 128 *MFLOPS* peak 64-bit floating-point performance.

Each vector unit is a memory controller and a computational engine controlled by a memory-mapped control register interface. Vector units cannot fetch their own instructions; they merely execute instructions issued by the RISC microprocessor. The vector unit processes both scalar and vector instructions. A scalar-mode instruction is handled as if it were a vector-mode instruction of length 1. Thus, scalar-mode instructions always operate on single registers; while vector-mode instructions operate on a sequence of registers. The vector unit module includes an adder, a multiplier, a memory load/store, an indirect register addressing, an indirect memory addressing, and a population count. The vector-unit instruction can specify at least one arithmetic operation and an independent memory operation.

Communication topologies on the CM-5 are integrated through two internal networks, the Control Network and the Data Network. The Control Network supports communication patterns that may involve all the processors in cooperative operations such as broadcasting and reduction, as well as system management operations such as error signaling. Further, global synchronized communication is managed through the Control Network. The Data Network supports point-to-point data communication with a fat-tree topology. Similar to the 2-D mesh and hypercube topologies, the fat-tree structure can be divided into smaller pieces of the same topology. Hence, each group of processors has its own dedicated portion of the network. Traffic among the processors in one partition does not compete for bandwidth with traffic within another partition. However, unlike the 2-D mesh and the hypercube topologies, traffic between two

partitions does not interfere with traffic internal to a third partition. The CM-5 Data Network is a 4-way fat tree where each node has four children. Scalability, partitionability, non-interference and redundancy constitute its main properties. The fat tree topology of the Data Network guarantees a communication speed of 5 *MBytes/second* per node regardless of destination, and can sustain a delivery rate of 10 *MBytes/second* within a group of 16 processors and 20 *MBytes/second* within a group of 4 processors. The topology of the Control Network is also a binary 'skinny tree' and guarantees a minimum bandwidth of 5 *MBytes/sec*, regardless of destination.

The I/O device is connected to the CM-5 system through the Data Network. Each I/O interface requires a control processor to act as its file server and supervise all I/O operations. The Scalable Disk Array (SDA), a high-performance expandable RAID-3 disk storage system, is a file system environment supporting parallel I/O on the CM-5. The basic Disk Storage Node consists of an I/O control processor (IOCP), a Network Interface, a large disk buffer, four advanced SCSI controllers, and eight 3.5-inch hard disk drives. This I/O subsystem provides 9.2 *GBytes* of storage, a peak bandwidth of over 17 *MBytes/sec* and 25 *MIPS* of processing power. All disks in the SDA act together in conjunction with the operating system to transfer data simultaneously.

The CM-5 at the National Center for Supercomputing Applications (NCSA), University of Illinois, Urbana-Champaign, currently consists of 512 processing nodes with vector units. This platform provides 64 *GFLOPS* peak performance for 64-bit floating-point operations and has 16 *GBytes* of total available memory. It is configured in five partitions of 32, 32, 64, 128 and 256 processing nodes, and the 512-processor CM-5 can also be accessed. The SDA configuration consists of 12 Disk Storage Nodes that provide 100 *GBytes* of storage at I/O bandwidths of up to 132 *MBytes/sec* sustained rate.

5.2 Data-Parallel Algorithm For Two-Dimensional Simulations

This section presents the implementation of the data-parallel algorithm to perform two-dimensional simulations. Section 5.2.1 discusses the performance of basic 'kernels' and communication functionalities. The portability of the high-order finite-difference procedure into a data-parallel structure is summarized in Section 5.2.2 and representative timings are provided in Section 5.2.3. The programming environment is based on CMFORTRAN, a Thinking Machine parallel version of FORTRAN 90, and the data-

parallel algorithm consists of a modular structure that emphasizes ease of portability to various massively parallel processing platforms.

5.2.1 Performance of Basic Linear Algebra and Communication Routines

The performances of the CM-5 hardware and system software for basic communication functionalities and model linear algebra routines are first evaluated. These speeds will provide an estimate of feasible target values on the CM-5 platform. Starting with elemental addition, multiplication and triad operations of matrices, the speeds of matrix-vector multiplications, matrix-matrix multiplications performed by the CMSSL library routines are determined. The operating system (OS) is CSMOST V7.2 prefinal and the code is compiled with CMF2.1 and linked to the CM Scientific Subroutine Library, CMSSL 3.1.

The Connection Machine Scientific Subroutine Library (CMSSL) is a set of numerical routines supporting computational applications while exploiting the massive parallelism of the Connection Machine system. The CMSSL provides data-parallel implementation of numerical routines such as matrix operations, linear equation solvers, eigensystem analysis, Fourier Transform, and statistical analysis among others. The library also includes optimized communication functions such as polyshift, all-to-all broadcast and reduction, gather and scatter, and partitioning. For example, matrix-vector multiplication ($M \times V$), and matrix-matrix ($M \times M$) multiplication use the CMSSL routines, `gen_matrix_vector_mult` and `gen_matrix_mult`, respectively.

All axes of the arrays have a NEWS (North-East-West-South) layout configuration. Such mapping is found to be optimal for two-dimensional arrays. All floating-point operations are performed on 64-bit (double precision) words. Table 5.2.1.1 presents the performance of the basic kernels on a 256-processor partition for different array sizes without using the vector units, referred to as the scalar mode. Table 5.2.1.2 summarizes corresponding speeds with the vector units activated, referred to as the vector mode. It is seen that in the scalar mode, the basic kernels have a moderate performance profile of several hundred MFLOPS. However, in the vector mode, performances greater than 10 GFLOPS are feasible for large matrix sizes. Most explicit computations encountered in Computational Fluid Dynamics (CFD) embed triad operations (see Section 3.2), while matrix-matrix multiplications will be invoked in the pressure-Poisson solver (see Section 3.4). Figures 5.2.1.1 and 5.2.1.2 present the performance of a triad

operation ($A+B*C$) and a matrix-matrix multiplication ($M \times M$) on various CM-5 partition sizes in scalar mode. It is observed that the performance rate increases up to 1.8 MFLOPS/node for a triad operation and 2.5 MFLOPS/node for a matrix-matrix multiplication, then drops off to reach a plateau. Figures 5.2.1.3 and 5.2.1.4 show the performance rates (in MFLOPS per processing node) for the triad and matrix-matrix operations, respectively, in vector mode. The triad operation has a peak performance rate of approximately 22 MFLOPS/node; while the optimized CMSSL routine for matrix-matrix multiplication can sustain rates of up to 70 MFLOPS/node.

Several communication functionalities are provided through CMFORTRAN as well as through CMSSL routines to access an element of an array along a specific axis. The command *CSHIFT*(*ARRAY*,*DIM*,*SHIFT*) performs a circular shift of the elements of *ARRAY*; while the command *EOSHIFT*(*ARRAY*,*DIM*,*SHIFT*,*BOUNDARY*) is appropriate when a boundary value (*BOUNDARY*) is to be imposed. *BOUNDARY* could be either specified as a scalar value or as an array. The rates of these communication functionalities have been evaluated under the following conditions :

$$B = \text{CSHIFT}(A,1,-1) \quad (5.2.1.1a)$$

$$B = \text{CSHIFT}(A,2,-1) \quad (5.2.1.1b)$$

$$B = \text{EOSHIFT}(A,1,-1,\beta) \quad (5.2.1.1c)$$

$$B = \text{EOSHIFT}(A,1,-1,BXM) \quad (5.2.1.1d)$$

where *A* and *B* are two-dimensional arrays with NEWS layout, β is a scalar variable and *BXM* is a one-dimensional array containing the boundary values. Figure 5.2.1.5 illustrates the CPU run times of the functionalities given by Equations (5.2.1.1a-d). The *CSHIFT* commands along *DIM* = 1 and *DIM* = 2 have similar CPU times; hence, there is no preferential direction in computing these functionalities. It is also observed that the ratio of CPU run time for performing *EOSHIFT* over *CSHIFT* is 1.5 when *BOUNDARY* is set as a scalar and can be as high as 8.5 when *BOUNDARY* is chosen as an array. This may be resulting from the specific array layout used by the CM-5 and its communication network. Instead of using *EOSHIFT* commands, shifts with specified boundary values on array elements can also be implemented by performing a *CSHIFT* command and then imposing the correct boundary conditions in a separate statement, as follows:

$$uw = \text{CSHIFT}(u,1,-1) \quad (5.2.1.2a)$$

$$uw(1,:) = u(1,:) \quad (5.2.1.2b)$$

For the current high-order accurate finite-difference procedure, up to 6 array shifts along each array axis are needed to compute the stencil. The fifth-order upwind-biased scheme requires 5 shifts in each direction. It is possible to perform multiple array shifts referred to as 'polyshifts' via the CMSSL routine, *PSHIFT*; however, currently, the *PSHIFT* routine has not been fully optimized for the CM-5. Thus, multiple '*CSHIFT*'s with imposed boundary conditions (Equations 5.2.1.2a-b) are implemented in determining the components of the high-order stencil.

5.2.2 Implementation

The performances of the basic 'kernels' and communication functionalities discussed in the previous section provide general guidelines regarding programming in the data-parallel environment on the CM-5. The key issues in developing computational tools based on data-parallel structure are to maintain load balance and maximum communication efficiency (Olsson and Johnsson, 1990). It is important to subdivide the numerical algorithm into separate components and recognize the basic kernels needed. For the current time-splitting scheme, the code consists of three major separate structures:

- (i) calculating the intermediate velocity field (Equation 3.1.3),
- (ii) solving the pressure-Poisson equation (Equation 3.1.5),
- (iii) updating the intermediate velocity field (Equation 3.1.4).

For the two-dimensional simulations, all field arrays (u , v , p) have the layout of their axes in the *NEWS* (North-East-West-South) configuration. As mentioned earlier, such mapping is found to be optimal for two-dimensional arrays. Communication steps have been separated from computations and reduced to a minimum. In step (i) of the fractional-step procedure (Equation 3.1.3), the convection and diffusion terms are formulated in terms of finite-difference stencils (see Section 3.2). For the current high-order accurate finite-difference procedure, up to 6 array shifts along each array axis are needed to compute the stencil. Communication comprises a major part of this step of the numerical algorithm. In order to optimize inter-processor communication, all communications steps (*CSHIFT*) are performed before undertaking the computations. However, this requires storage of additional temporary arrays within each processor. Once the neighbor values are communicated and stored, the calculations involve

multiplications of the coefficients by their neighbor values. For example, the first-order x-component derivative at point q , $\frac{\partial u}{\partial x}$, is expressed as :

$$\begin{aligned} \left(\frac{\partial u}{\partial x}\right)_q = & [upwndp * fcpim3 + (1 - upwndp) * fcnim3]] * uim3 \\ & + [upwndp * fcpim2 + (1 - upwndp) * fcnim2]] * uim2 \\ & + [upwndp * fcpim1 + (1 - upwndp) * fcnim1]] * uim1 \\ & + [upwndp * fcp i + (1 - upwndp) * fcni m1]] * ui \\ & + [upwndp * fcpip1 + (1 - upwndp) * fcnip1]] * uip1 \\ & + [upwndp * fcpip2 + (1 - upwndp) * fcnip2]] * uip2 \\ & + [upwndp * fcpip3 + (1 - upwndp) * fcnip3]] * uip3 \end{aligned} \quad (5.2.2.1a)$$

$$uim1 = cshift(ui, -1); uim2 = cshift(uim1, -1); uim3 = cshift(uim2, -1) \quad (5.2.2.1b)$$

$$uip1 = cshift(ui, 1); uip2 = cshift(uip1, 1); uip3 = cshift(uip2, 1) \quad (5.2.2.1c)$$

$$upwndp = 1 \text{ for } ui \geq 0 \quad (5.2.2.1d)$$

$fcp i$ and $fcni$ represent the coefficients in the finite-difference stencil of ui for positive and negative upwinding values, respectively (see Equations 3.2.1-5). The remaining coefficients are defined in a similar manner. The boundary conditions are applied as given in Equation (5.2.1.2b). The second-order x-component derivative, $\frac{\partial^2 u}{\partial x^2}$, at point q , is computed from :

$$\begin{aligned} \nabla(\nabla(\frac{\partial^2 u}{\partial x^2}))_q = & fdim2 * uim2 + fdim1 * uim1 + fdi * ui \\ & + fdip1 * uip1 + fdip2 * uip2 \end{aligned} \quad (5.2.2.2)$$

where ui is the velocity at point q , $uim2$, $uim1$, $uip1$, $uip2$ are the velocities at the west-west, west, east and east-east locations computed as shown in Equations (5.2.2.2b-c), and fdi , $fdim2$, $fdim1$, $fdip1$, and $fdip2$ are their corresponding coefficients in the finite-difference stencil whose values are given in Equation (3.2.6-8).

In general, these coefficients may vary over the computational domain and, therefore, are stored as arrays. However, for constant viscosity and uniform grid, they do not vary with spatial location, except near the boundaries. Scalar values for these coefficients may then be used, thus leading to an additional computational step in the

programming algorithm to account for the boundary stencils. The finite-difference stencils in step (iii) are computed in a similar manner to step (i).

The pressure-Poisson solver (step (ii)) is the most computationally intensive algorithm in the fractional-step procedure. The direct solver consists primarily of products of matrices (see Section 3.4) which are performed through the efficient CMSSL routine, `gen_matrix_mult`. The eigenvalues (λ_x and λ_y), and their corresponding eigenvector matrices, (E_x and E_y), as well as their inverses (E_x^{-1} and E_y^{-1}) are calculated *a-priori* using EISPACK routines. The CMSSL matrix-matrix multiplication can attain a speed of 13 GFLOPS on a 256-processor partition for 4096x4096 matrices, as seen in Section 5.2.1. In CFD calculations, typically the grid nodes in any direction may be less than 1024, so the peak speed observed may not be realized in practice. However, increases in speed may be possible through future improvements in the compiler and by programming in lower level languages.

The overall operation count of step (i) is $O(N_x \times N_y)$. The operation count of the direct solver (step (ii)) is $O(N_x^2 \times N_y + N_y^2 \times N_x)$. In simulations with internal obstacles, the Capacitance Matrix Technique requires the pressure equation to be solved twice, thus doubling the operation count. The update procedure (step (iii)) has an operation count of $O(N_x \times N_y)$.

5.2.3 Timings and Performance

Two-dimensional calculations have been carried out for different grid sizes in order to evaluate the scaling of the machine as well as the performance of the algorithm for finer mesh sizes. Table 5.2.3.1 shows the timings and computational speeds in GFLOPS for the momentum equations (Equation 3.1.4), the pressure solver (Equation 3.1.7) and the update procedure (Equation 3.1.6) for various two-dimensional grids on a 512-processor partition. The floating-point operations are performed with 64-bit precision. It is observed that the pressure solver requires 90% of the total CPU run-time compared to the computations of the intermediate velocity and the update procedure. Also presented is the CPU run time ratio of the CRAY-YMP code over the CM-5 code. The simulations on the CRAY-YMP are run on a single processor under UNICOS 6.0 with a peak performance of 300 MFLOPS. It can be seen that for grid sizes smaller than 64x64, the CM-5 is slower than the CRAY Y-MP by up to a factor of 3. However, for a 2048x2048 grid, a speedup factor of 37 over the CRAY Y-MP can be obtained. The

representative timings in Table 5.2.3.1 have been obtained from two-dimensional simulations of the driven-cavity problem; hence, they do not account for the additional time incurred by the Capacitance Matrix Technique (Section 3.6). However, the CPU run times for two-dimensional simulations with obstacles could be estimated by multiplying the values of the third column in Table 5.2.3.1 by a factor of 2.

Figure 5.2.3.1 shows the increase of the performance per processing node with grid size for different CM-5 partition sizes. It can be seen that for a given problem size, the best performance per node is obtained always by the 32-processor partition attaining 34 MFLOPS per processing element for 1024x1024 grid. For 2048x2048 grid, the peak performance of 41 MFLOPS per node is achieved on the 128-processor partition. There are two factors contributing to such behavior: first, the communication costs are relatively small; and second, the vectors lengths are large. It is expected that the processor performance will reach a peak at some grid size. However, before such a limit is reached, the memory required per node by the current computer program exceeded that available in the current machine. Nevertheless, Figure 5.2.3.1 illustrates an important characteristic of the CM-5 that both the vector length as well as the computing-communication ratio play important roles in achieving maximum performance.

The parallel efficiency of the algorithm is evaluated by computing the speed-up factor. The speed-up factor, σ_a , is defined as the ratio of the algorithm performance on a partition of size p over the algorithm performance for a reference partition of size p_r , and is given by :

$$\sigma_a = \frac{(MFLOPS)_p}{(MFLOPS)_{p_r}} \quad (5.2.3.1)$$

The theoretical speed-up factor, σ_t , is the processor ratio $\left(\frac{p}{p_r}\right)$. Figure 5.2.3.2 presents the speed-up factors against processor ratio for various grid sizes with the 64-processor partition taken as reference. Also shown is the theoretical limit. At low processor ratio $\left(\frac{p}{p_r} = 2\right)$, σ_a is close to the theoretical limit of 2 for fine mesh sizes. However, as the number of processors is increased, the processor utilization efficiency decreases because of the increased communication and the loss in vectorization efficiency. For example, σ_a is 4.6 at processor ratio of 8 for a 1024x1024 grid. Hence, the theoretical limit can be attained by considering a large grid size on a small partition size; however, the memory

requirements become the limiting factor. Therefore, the optimum parallel efficiency depends on the grid size and the number of processors and is achieved by minimizing communication and increasing the performance of the vector units within the limits of the available memory.

5.3 Data-Parallel Algorithm For Three-Dimensional Simulations

This section describes the data-parallel algorithm implemented to perform three-dimensional simulations. Section 5.3.1 presents the performance of basic 'kernels' and communication functionalities. The portability of the numerical algorithm described in Chapter 4 into a data-parallel environment is summarized in Section 5.3.2 and representative timings are provided in Section 5.3.3.

5.3.1 Performance of Basic Linear Algebra and Communication Routines

The performance of the CM-5 hardware and system software for basic communication functionalities and model linear algebra routines are further evaluated for the three-dimensional data-parallel algorithms. These speeds provide an estimate of target values that are feasible on the machine. Starting with elemental addition, multiplication and triad operations of matrices, the speeds of matrix-vector multiplications, and matrix-matrix multiplications performed by the CMSSL library routines are determined. Figures 5.3.1.1 and 5.3.1.2 present the performance of a triad operation ($A+B*C$) and a matrix-matrix multiplication ($M \times M$) for different three-dimensional array sizes on various CM-5 partition sizes in vector mode. The axes of the three-dimensional arrays have a (NEWS) layout configuration. It is seen that the triad operation has a peak performance of 6 GFLOPS, and the performance rate of the matrix-matrix operation increases to 2.6 GFLOPS. These values correspond to 22 MFLOPS/node for a triad operation and 9.8 MFLOPS/node for a matrix-matrix multiplication.

Compared to the (NEWS) configuration, a more detailed array layout is available through compile directives and is referred to as (BLOCK/PROCS) layout. As an illustration, the (BLOCK/PROCS) layout of a two-dimensional array, A , of size $M \times N$ is described as follows :

$$A(:,BLOCK=s:PROCS=m,:BLOCK=q:PROCS=n) \quad (5.3.1.1)$$

In Equation (5.3.1.1), $(:BLOCK=s)$ and $(:BLOCK=q)$ represent the subgrid length; while $(:PROCS=m)$ and $(:PROCS=n)$ are the number of processors desired for each axis such that $(s \times m) = M$ and $(q \times n) = N$ (Thinking Machines, 1992b). The 'processors' (m) and (n) are a subset of the CM-5 vector units where $(m \times n)$ is the number of vector units available on the partition. For example, a 256-processor CM-5 partition has 256×4 (1024) vector units. To clarify this concept for three-dimensional arrays, an array, $A(32,128,64)$, can have its axes laid out on a 256-processor CM-5 partition as follows :

$$A(:BLOCK=32:PROCS=1,:BLOCK=8:PROCS=16,:BLOCK=1:PROCS=64) \quad (5.3.1.2)$$

For such a mapping, the first axis is totally local to the vector unit, the 128 elements of the second axis are subdivided equally between 16 vector units while the third axis is laid across 64 vector units, one element in each. It is to be noted that the $(:PROCS)$ entries and their product of every array axis should be a value of power of 2 between p and $4p$ where p is the partition size. This layout directive allows a greater flexibility in array management as compared to the (NEWS) mapping.

Several axis layouts of a three-dimensional array, A , of size $N_x \times N_y \times N_z$ are considered to evaluate the basic kernels :

$$A(:NEWS,:NEWS,:NEWS) \quad (5.3.1.3a)$$

$$A(:BLOCK=N_x:PROCS=1,:BLOCK=N_y:PROCS=1,:BLOCK=1:PROCS=N_z) \quad (5.3.1.3b)$$

$$A(:BLOCK=N_x/2:PROCS=2,:BLOCK=N_y:PROCS=1,:BLOCK=2:PROCS=N_z/2) \quad (5.3.1.3c)$$

$$A(:BLOCK=N_x/2:PROCS=2,:BLOCK=N_y/2:PROCS=2,:BLOCK=4:PROCS=N_z/4) \quad (5.3.1.3d)$$

$$A(:BLOCK=N_x/4:PROCS=4,:BLOCK=N_y/4:PROCS=4,:BLOCK=16:PROCS=N_z/16) \quad (5.3.1.3e)$$

The (NEWS) layout in Equation (5.3.1.3a) is solely controlled by the compiler. For the (BLOCK/PROCS) layout in Equation (5.3.1.3b), two-dimensional arrays of size $(N_x \times N_y)$ are local to each vector unit. The arrays local to the vector units have sizes of $(N_x/2 \times N_y)$, $(N_x/2 \times N_y/2)$, and $(N_x/4 \times N_y/4)$ corresponding to the layouts in Equation (5.3.1.3c), (5.3.1.3d) and (5.3.1.3e), respectively. For this test, the third dimension, N_z , is dictated by the partition size, and is set to be the number of vector units on the specified partition.

In what follows, the computations are undertaken on the 32-processor partition; hence N_z is 128. Figure 5.3.1.3 illustrates the performance of a triad operation ($A+B*C$) with $(N_x \times N_y)$ values. The performance increases rapidly to reach a plateau of 22MFLOPS/node. The curve shown in Figure 5.3.1.3 is representative of the different array layouts in Equations (5.3.1.3a-e); thus, the triad operation has a performance rate nearly independent of the array layout. Figure 5.3.1.4 presents the performance of the matrix-matrix multiplication routine for the various array layouts (Equations (5.3.1.3a-e)). It is seen that near-peak performance of 115 MFLOPS/node is obtained with the layout given in Equation (5.3.1.3b) since the computations are local to the vector units. The performance rate drops significantly to 42 MFLOPS/node for the layout given in Equation (5.3.1.3c) since across-processor communication is initiated, and the performance deteriorates further for the remaining layout configurations. The (NEWS) layout (Equation 5.3.1.3a) shows a performance rate of 15 MFLOPS/node similar to Equation (5.3.1.3e). Therefore, although the (NEWS) layout was found to be optimal for two-dimensional arrays, the (BLOCK/PROCS) layout provides greater flexibility in array management and leads to higher performance rate of matrix-matrix multiplications for three-dimensional arrays.

To evaluate the effect of a varying third dimension, the axes have a (BLOCK/PROCS) layout configuration of the form :

$$A(:,BLOCK=N_x/r:PROCS=r,:BLOCK=N_y/s:PROCS=s,BLOCK=1:PROCS=N_z) \quad (5.3.1.4)$$

such that the product $(N_z \times r \times s)$ is equal to the number of vector units of the partition. Figure 5.3.1.5 presents the performance of a triad operation ($A+B*C$) with a peak performance of 22 MFLOPS/node. The performance rate of the matrix-matrix multiplication operation for varying N_z on a 32-processor partition is illustrated in Figure 5.3.1.6. It is seen that the performance improves rapidly with N_z as the operations become local to the vector units and reaches a peak value of 112 MFLOPS/node for $N_z = 128$ and 256.

5.3.2 Implementation

Based on the experiences with the performance of the basic kernels, the data-parallel implementation of the three-dimensional numerical algorithm becomes more elaborate than the two-dimensional algorithm presented in Section 5.2.2. The arrays

pertaining to the computations of the intermediate velocity field and the update procedure (see steps (i) and (iii) in Section 5.2.2) have an axis layout of the (*NEWS*) mapping. The stencil computation in the x and y directions are carried out in a similar procedure as described in Equations (5.2.1.5a-b), (5.2.2.1) and (5.2.2.2).

For the computations performed in the pressure solver (step (ii)), detailed layout for the array axes is specified using the compiler directive (*BLOCK/PROCS*) discussed in Section 5.3.1. Two distinct array layout configurations are implemented in the solution procedure of the pressure-Poisson equation. In devising the three-dimensional data-parallel algorithm, the strategy was focused on minimizing the communication/computation ratio. To this end, the computations pertaining to the determination of the Fourier coefficients are done with the x -direction across the vector units, while the computations relating to the matrix multiplications are done with the z -direction across the vector units. The various steps of the three-dimensional data-parallel algorithm for the pressure-Poisson solver are summarized as follows :

(a) The right-hand side of the pressure equation represented by array f with (*NEWS*) layout is first copied to an intermediate array $f_yzinprc$. The first axis of $f_yzinprc$ is distributed across the vector units while the second and third axes are local to the vector units as follows :

$$f_yzinprc(:BLOCK=1:PROCS=Nx,:BLOCK=Ny/r:PROCS=r,:BLOCK=Nz/s:PROCS=s) \quad (5.3.2.1)$$

such that the product ($Nx \times r \times s$) is equal to the number of vector units of the partition.

(b) The Fourier coefficients of $f_yzinprc$, $\hat{f_yzinprc}$, are computed using a Conventional Discrete Fourier Transform (CDFT) as follows :

$$\hat{f_yzinprc} = f_yzinprc \cdot D_{Frz} \quad (5.3.2.2a)$$

$$D_{Frz} = \frac{1}{N_z} e^{-ik_z z_m}; \frac{-N_z}{2} \leq k_z \leq \frac{N_z}{2} - 1; 0 \leq m \leq N_z - 1 \quad (5.3.2.2b)$$

The computation in Equation (5.3.2.2a) is performed using CMSSL matrix-matrix multiplications; alternatively, a Fast Fourier Transform (FFT) algorithm may also be incorporated.

(c) The array $\hat{f}_{yzinprc}$ is copied into the array $\hat{f}_{xyinprc}$ which has the following layout:

$$\hat{f}_{xyinprc}(:BLOCK=Nz/r:PROCS=r,:BLOCK=Ny/s:PROCS=s,:BLOCK=1:PROCS=Nz) \quad (5.3.2.3)$$

such that the product $(r \times s \times Nz)$ is equal to the number of vector units of the partition.

(d) Equation (4.2.6) is solved simultaneously for each wavenumber. All arrays in Equation (4.2.6) have layout similar to Equation (5.3.2.3).

(e) The array $\hat{p}_{xyinprc}$ (Equation 5.3.2.3) is copied into the array $\hat{p}_{yzinprc}$ (Equation 5.3.2.1) where \hat{p} are the Fourier coefficients of p and the solutions of Equation (4.2.6).

(f) An inverse CDFT is then performed to extract the physical pressure field, $p_{yzinprc}$, from its Fourier coefficients, $\hat{p}_{yzinprc}$.

$$p_{yzinprc} = \hat{p}_{yzinprc} \cdot D_{Friz} \quad (5.3.2.3a)$$

$$D_{Friz} = e^{ik_z z_m}; -\frac{Nz}{2} \leq k_z \leq \frac{Nz}{2} - 1; 0 \leq m \leq Nz - 1 \quad (5.3.2.3b)$$

(g) Finally, $p_{yzinprc}$ is copied to p where p has the (NEWS) layout.

Steps (a), (c), (e) and (g) represent communication patterns and steps (b), (d), and (f) are in-processor operations.

This data-parallel algorithm efficiently uses the machine resources with the current operating system and the library routines. The operation count of the calculations pertaining to the intermediate velocity is $O(Nx \times Ny \times Nz)$. The operation count of the direct solver is $O(Nx^2 \times Ny \times Nz + Nx \times Ny^2 \times Nz, Nx \times Ny \times Nz^2)$. The update procedure has an operation count of $O(Nx \times Ny \times Nz^2)$.

5.3.3 Timings and Performance

The three-dimensional data-parallel algorithm presented in Section 5.3.2 is programmed in CM FORTRAN. Calculations are carried out on mesh sizes varying from 64^3 to 256^3 for different partition sizes. The performance statistics of the momentum

equations (Equation 3.1.4), the pressure-Poisson solver (Equation 3.1.7) and the update procedure (Equation 3.1.6) are summarized in Table 5.3.3.1 for the 512-processor partition. A peak performance of 10.3 GFLOPS is obtained for the pressure solver step on a 256^3 grid; this results in an overall performance of the algorithm of 9.4 GFLOPS. The CPU requirements of the pressure-Poisson solver, compared to the other steps of the algorithm, account for most of the CPU run-time; thus, the data-parallel algorithm, discussed in Section 5.3.2, is devised to efficiently make use of optimized functionalities and library routines. The representative CPU timings in Table 5.3.3.1 have been obtained from three-dimensional simulations of the driven cavity problem; hence, they do not account for the additional time incurred by the Capacitance Matrix Technique (Section 3.6.2). However, the CPU run-times with the CMT algorithm could be estimated by multiplying the values of the third column in Table 5.3.3.1 by two.

Figure 5.3.3.1 shows the performance rate (per processing node) with grid size for different CM-5 partition sizes. It can be seen that for a given problem size, the best performance per node is obtained always by the 64-processor partition, attaining 16 MFLOPS/node for the 128^3 grid. Further, the computational speed per processor decreases from 16 MFLOPS/node on a 64-processor partition to 9 MFLOPS/node on a 512-processor partition for 128^3 grid points. The main factors contributing to this trend are the communication cost and the vector length. Due to memory limitations, calculations with grids finer than 128^3 could not be performed on the 64-processor partition. A peak performance of 18 MFLOPS/node is achieved for 256^3 grid points on a 512-processor partition. Observations similar to the performance of the two-dimensional algorithm illustrate that both the vector length and the computation-communication ratio play important roles in achieving the maximum performance.

To evaluate the parallel efficiency of the algorithm, the speed-up factor, σ_a , (Equation 5.2.3.1) is presented in Figure 5.3.3.2 against processor ratio for various grid sizes with the 64-processor partition taken as reference. Also shown in Figure 5.3.3.2 is σ_a for $256 \times 256 \times 64$ grid with a 128-processor partition as reference. At low processor ratio ($\frac{p}{p_r} = 2$), σ_a is close to the theoretical limit of 2 at fine meshes. For a processor ratio of 8, σ_a is 4.8 for $128 \times 128 \times 64$ grid points. Thus, as the number of processors is increased, the processor utilization efficiency decreases because of the increased communication and the loss in vectorization efficiency. Further, the loss of performance of the 128^3 grid over the $128 \times 128 \times 64$ grid may be attributed to the high cost in

communication incurred by transposing the matrix axes. Therefore, the optimum parallel efficiency depends on the optimum grid size for a given partition size.

This concludes the description of the data-parallel algorithms to perform two and three-dimensional simulations of unsteady flows. In the following sections, the results obtained from simulations of separated-reattaching and separated flows will be presented.

6. TWO-DIMENSIONAL SIMULATIONS

This chapter describes two-dimensional direct numerical simulations of separated and separated-reattaching flows. Section 6.1 discusses results from calculations performed for the separated-reattaching flow over a normal flat plate with a downstream attached splitter plate. Results from numerical simulations of the separated flow past a normal flat plate are presented in Section 6.2.

6.1 Calculations of Separated-Reattaching Flow Past a Normal Flat Plate with an Attached Downstream Splitter Plate

The present study is concerned with the flow past a normal flat plate with an attached downstream splitter plate as shown in Figure 6.1.1. For this geometrical configuration, the flow separates from a fixed edge and subsequently reattaches on a downstream surface. A steady elongated separation bubble is formed in the region bounding the vertical plate and the horizontal surface. At low Reynolds numbers, the shear layer separation is steady for steady upstream conditions. As the Reynolds number is increased, the separated shear layer becomes unstable and begins to shed vortices. The formation, evolution and propagation of these unsteady vortical structures are interesting fluid dynamic phenomena and, to our knowledge, few studies have documented their characteristics in the low Reynolds number regime.

This section is organized as follows. Section 6.1.1 discusses the computational details of the simulations. The boundary conditions imposed along the edges of the computational domain are summarized in Section 6.1.2. Section 6.1.3 presents the results obtained in the steady regime. The unsteady regime characteristics are discussed in Section 6.1.4.

6.1.1 Computational Details

The governing equations are non-dimensionalized by the fence height, h_F , and the free-stream velocity, U_∞ . The Reynolds number is defined as $Re = h_F U_\infty / \nu$. Calculations are made for several Reynolds numbers, $Re = 25, 50, 75, 100, 150, 250, 375$ and 500 . The computational domain extends in the streamwise (x) direction from $10h_F$ upstream to $45h_F$ downstream of the normal plate and in the cross-stream (y) direction from 0 to $20h_F$. The grid size for these simulations is 513×257 nodes. However, for $Re = 100$ and 150 ,

the computational domain is extended in the streamwise direction to $x = 93$ and the grid size in the x -direction is increased to 1025 nodes in order to accommodate the large separation length. For Reynolds numbers up to 150, a uniform grid is used in both directions. For $Re \geq 250$, a smoothly varying non-uniform grid spacing is used to better resolve the flow features adjacent to the plate. Figures 6.1.1.1a and b present the grid spacings in the x and y directions, respectively. The minimum grid size in the x -direction is 0.025 adjacent to the plate and the maxima are 0.65 upstream of the plate and 0.38 downstream of the plate. In the y -direction, the minimum and maximum grid sizes are 0.025 and 0.34. The distributions of the metrics in the x -direction, $\left(\frac{\partial \xi}{\partial x}\right)$ and $\left(\frac{\partial^2 \xi}{\partial x^2}\right)$, and in the y -direction, $\left(\frac{\partial \eta}{\partial y}\right)$ and $\left(\frac{\partial^2 \eta}{\partial y^2}\right)$, are illustrated in Figures 6.1.1.2a and b, respectively. A smooth variation of these derivatives is maintained in the computational domain.

The time step size, Δt , is set to 2.5×10^{-3} which maintains the convective and diffusive Courant-Friedrichs-Lewy (CFL) numbers under their respective limits (see Section 3.5). The simulations are started either from a uniform flow field or from a solution previously obtained at a different Reynolds number. The computations are performed on a 256-processor CM-5 partition, and require approximately $5.3 \mu s$ per time step per grid node. Approximately 90% of the total CPU time is spent for the solution of the pressure Poisson equation. Numerical simulations are performed for Reynolds numbers of 25, 50, 75, 100, 150, 250, 375 and 500. A steady separation regime is observed for Re up to 150 while the flow is observed to be unsteady for $Re \geq 250$. Computations in the steady regime are continued until the temporal variations of the velocity and pressure signals reach a plateau. The calculation for $Re = 250$ is performed for 895 non-dimensional time units and the time-mean values are obtained by averaging for 770 time units. For $Re = 375$ and 500, the simulations are carried out for 375 and 425 non-dimensional time units, respectively. Time signals of pressure and streamwise velocity at specific locations in the computational domain are also stored every tenth time step. These data are used for calculating the autocorrelations and space-time correlations.

6.1.2 Boundary Conditions

Since the splitter plate eliminates the downstream interaction between the top and bottom edges of the plate, the equations are solved only in the upper half of the domain. Additionally, the following boundary conditions are applied :

(i) At the inlet (left boundary) of the computational domain, a uniform unit streamwise velocity, $u = U_\infty = 1$, and a zero cross-stream velocity are specified. The normal pressure gradient ($\partial p / \partial x$) is set to zero.

(ii) The bottom boundary upstream of the normal plate is considered to be a symmetry line. Thus the normal derivatives of u and p are prescribed to be zero and are represented with third-order one-sided differences. Further, the normal velocity (v) at the symmetry line is set to zero. Downstream of the plate, both velocities and the pressure gradient are prescribed to be zero.

(iii) At the top boundary, free-stream conditions ($u = 1, p = v = 0$) are imposed.

(iv) At the outlet, the outlet boundary conditions discussed in Section 3.8 (Equations 3.8.1a-e) are tested to determine their relative influences on the computed flow field. The effect of the outlet boundary condition is investigated for the present flow configuration at $Re = 250$. A convective velocity (U_c) of 0.75 is chosen *a-priori* from the experiments of flow over a blunt plate (Kiya and Sasaki, 1983a). This is subsequently found to agree well with the value inferred from the current calculations. It is observed that in this flow, boundary conditions (3.8.1a) and (3.8.1b) make the calculation unstable. Figure 6.1.2.1 shows the spanwise vorticity, ω_z , contours at one time instant for the remaining three boundary conditions. Of these, boundary conditions (3.8.1d) allows the propagating structures to leave the computational domain with minimal distortion (see also Lowery and Reynolds, 1986; Pauley et al., 1990). Therefore, condition (3.8.1d) is used in all of the subsequent calculations reported in Sections 6.1.3 and 6.1.4.

6.1.3 Steady Regime

The present flow field is observed to be steady up to a Reynolds number of 150, characterized by a steady separation bubble downstream of the normal plate. For this regime, the simulations are carried in time to reach the asymptotic steady solution. The temporal evolution of the pressure is monitored at several locations. Figure 6.1.3.1 shows the signal at one such location ($x = 15.25$ and $y = 1.5$) for five Reynolds numbers. The integration time required to attain a steady value is seen to increase with the Reynolds number. For $Re = 150$, the transient solution displays some features of unsteady vortex shedding, but eventually the flow becomes steady after further integration. The streamlines

for three representative Reynolds numbers ($Re = 50, 100$ and 150) are illustrated in Figure 6.1.3.2. It is seen that both the streamwise length and the transverse width of the bubble increase with Reynolds number. This trend is consistent with observations in two other separated flows, such as the flow over a blunt plate (Lane and Loehrke, 1980) and flow over a backward-facing step (Armaly et al., 1983). However, for the same Reynolds number, the separation bubble in the present configuration is considerably larger than that in the above two flows.

A representative quantity characterizing the separation bubble is the reattachment length, x_R , defined as the distance between the point of separation and the furthest downstream location on the reattaching wall where the skin friction coefficient becomes zero. Experimental observations (Smits, 1982; Castro and Haque, 1988; Jaroch and Fernholz, 1989) show that the reattachment length is significantly influenced by parameters such as the freestream Reynolds number, the upstream turbulence intensity, the model aspect ratio and the wind-tunnel blockage. However, to our knowledge, no experiments have been conducted in the low Reynolds number range, i.e. $Re < 1000$. Castro et al. (1981) performed numerical simulations in the steady laminar regime ($10 \leq Re \leq 100$) using finite-difference and finite-element techniques. Figure 6.1.3.3 presents the measured and calculated reattachment lengths at different freestream Reynolds numbers. In the steady regime, the reattachment length is seen to grow monotonically from 10.5 to 40 for $25 \leq Re \leq 150$. However, Castro et al. (1981) predict a linear growth from 3.8 to 24.4 for $10 \leq Re \leq 100$. These large differences between the current predictions and those of Castro et al. (1981) may be attributed to the inadequate grid refinement in the simulations of the latter.

The mean surface pressure coefficient ($\overline{C_p}$) and wall skin friction factor ($\overline{C_f}$) are defined as :

$$\overline{C_p} = \frac{\overline{p_s} - p_\infty}{\frac{1}{2} \rho U_\infty^2} \quad (6.1.3.1)$$

$$\text{and } \overline{C_f} = \frac{\overline{\tau_w}}{\frac{1}{2} \rho U_\infty^2} \quad (6.1.3.2)$$

$$\text{where } \overline{\tau_w} = \mu \frac{\partial \overline{u}}{\partial y} \quad (6.1.3.3)$$

The streamwise distributions of $\overline{C_p}$ and $\overline{C_f}$ are shown in Figures 6.1.3.4 and 6.1.3.5, respectively. It is seen that with increasing Reynolds number, the location of the minimum skin friction moves closer to the reattachment point (from $0.22 x_R$ at $Re = 25$ to $0.85 x_R$ for $Re = 150$). The maximum surface pressure coefficient increases from -0.40 to -0.36 . Further, the $\overline{C_p}$ curve upstream of reattachment becomes flatter at higher Re . The pressure recovery, initiated before the reattachment point, becomes steeper with increase in the Reynolds number. This is a consequence of the fact that the center of the bubble moves closer to the reattachment point (Figure 6.1.3.2). Figure 6.1.3.6 shows the distribution of the pressure coefficient on the front and rear faces of the normal plate for $Re = 100$ and compared with numerical results obtained by Castro et al. (1981). On the downstream face of the normal plate, the predictions of Castro et al. (1981) are a factor of 2 larger than the present simulations as a result of inadequate mesh refinement in the near-plate region. The time-mean drag coefficient on the normal plate, $\overline{C_D}$, is defined as:

$$\overline{C_D} = \frac{\int_0^{h_F} (\overline{p_u} - \overline{p_d}) dy}{\frac{1}{2} \rho U_\infty^2} \quad (6.1.3.4)$$

where $\overline{p_u}$ and $\overline{p_d}$ are the mean pressure on the upstream and downstream faces of the normal plate, respectively. Figure 6.1.3.7 presents the computed time-mean drag coefficient at different freestream Reynolds numbers. The drag coefficient is seen to drop monotonically from 2.10 to 1.74 in the steady regime ($Re \leq 150$).

6.1.4 Unsteady Regime

6.1.4.1 Time-Mean Flow Variables

For Reynolds numbers larger than 150, the shear layer becomes unsteady and begins to break down into coherent large scale vortices. At $Re = 200$, the flow is seen to be unsteady, but the shedding of the vortices is erratic and slow. At $Re = 250$, a clear shedding of the vortices from the shear layer is established. The variation of time-mean reattachment length, x_R , with Reynolds number in the unsteady regime is presented in Figure 6.1.3.3. The time-mean reattachment lengths are 12.6 and 6.9 for $Re = 250$ and

500, respectively. The onset of unsteadiness is observed to result in a substantial decrease of the time-mean length of the recirculation bubble (from 40 to 12.6 at $Re = 150$ and 250, respectively). As the Reynolds number increases into the unsteady regime, the separated shear layer begins to entrain the freestream flow initiating the formation and growth of vortical structures. As these structures impinge on the splitter plate, the time-mean reattachment length sharply decreases. This trend is consistent with the experiments on a backward-facing step flow (Armaly et al., 1983). With increasing Reynolds number ($Re = 500$), the instability of the separated shear layer is initiated closer to the normal plate causing a further decrease in the time-mean reattachment length.

Figure 6.1.4.1.1 shows the time-averaged streamlines for $Re = 250, 375$ and 500. It can be seen that the mean reattachment length is considerably smaller (as compared to that at $Re = 150$ (see Figure 6.1.3.2c)). Another unique aspect of the time-mean flow characteristics in the unsteady regime is the appearance of a secondary separation bubble embedded within the primary bubble. This second separation bubble, which is not present at low Reynolds numbers, is a consequence of the counter-clockwise motion induced by the clockwise rotating primary vortices shed from the edge of the shear layer. The calculated length of this secondary separation bubble decreases from 4.6 ($0.36x_R$) to 1.3 ($0.19x_R$) for $Re = 250$ and 500, respectively. A second separation bubble of length 2.3 ($0.13x_R$) was also observed in the oil-film flow visualizations of Ruderich and Fernholz (1986) at $Re = 1.4 \times 10^4$. Figure 6.1.4.1.2 presents the locus of zero streamfunction (ψ) in the unsteady regime. Also shown are the data at higher Re obtained by Ruderich and Fernholz (1986) and Castro and Haque (1987). The shape of the time-averaged separation bubble at $Re = 250$ agrees closely with the experimental measurements with a height of 2.3 and is seen to shrink to a value of 1.9 for $Re = 375$ and 500. In contrast, in the steady flow regime, the bubble height is seen to increase with Reynolds number from 1.6 to 3.0 for Re of 50 and 150, respectively.

The calculated profiles of time-averaged streamwise velocities for $Re = 250$ and 500 at several non-dimensional streamwise distances (x/x_R) are compared with the experimental data of Ruderich and Fernholz (1986) and Castro and Haque (1987) in Figure 6.1.4.1.3 and with the measurements of Jaroch and Fernholz (1989) in Figure 6.1.4.1.4. As a result of the separation bubble, the freestream is accelerated, reaching a maximum velocity of $1.4U_\infty$. Inside the separation bubble, the maximum negative velocity is observed to be as high as $-0.4U_\infty$. Downstream of the time mean reattachment point, the flow begins to recover to a boundary-layer like profile, but is not completely recovered by the end of the

current flow domain. The simulations are seen to agree well qualitatively with all three data sets. However, there are considerable differences between the three experimental data sets themselves. It is not certain if these differences are due to the effects of freestream turbulence, wind tunnel blockage or other experimental conditions. The presents calculations are seen to agree most closely with the data of Ruderich and Fernholz (1986).

The streamwise distributions of the skin-friction coefficient, $\overline{C_f}$, in the unsteady regime are shown in Figure 6.1.4.1.5. The positive skin-friction coefficient immediately behind the plate represents the region of positive near-wall streamwise velocity arising from the counter-clockwise rotating secondary bubble (Figure 6.1.4.1.1). The location at which the skin friction first becomes negative, referred to as the reattachment point (Ruderich and Fernholz, 1986), decreases with increasing Reynolds number. The slight wiggles in the $\overline{C_f}$ profile, downstream of the reattachment point at $Re = 375$ and 500 , are a consequence of the small sample size. The minimum in the skin-friction factor is located at $0.62x_R$, $0.70x_R$ and $0.75x_R$ for $Re = 250, 375$ and 500 , respectively, compared with $0.6x_R$ measured in the experiments of Ruderich and Fernholz (1986), Castro and Haque (1987), and Jaroach and Fernholz (1989). The calculated values of $\overline{C_f}$ in the low-Re range are a factor of 10 higher than the values measured at higher Reynolds numbers.

Roshko and Lau (1965) have defined a modified surface pressure coefficient as :

$$\tilde{C}_{p_s} = \frac{\overline{C_{p_s}} - \overline{C_{p_{smin}}}}{1 - \overline{C_{p_{smin}}}} \quad (6.1.4.1.1)$$

Figure 6.1.4.1.6 shows the streamwise distribution of \tilde{C}_{p_s} compared with the experimental data of Roshko and Lau (1965), Ruderich and Fernholz (1986), Castro and Haque (1987), and Jaroach and Fernholz (1989). In the first half of the separation bubble ($x/x_R < 0.5$), the entrainment of the near-wall fluid by the vortices causes the formation of a strong suction zone as indicated by the minimum in the profile. Downstream of the reattachment point, $1 < x/x_R < 1.25$, the flow recovers some of this pressure loss. \tilde{C}_{p_s} reaches a maximum around the reattachment point, before leveling off further downstream. With increasing Reynolds number, the pressure recovery is initiated at a faster rate for $x/x_R < 0.5$ and levels off at a larger value downstream of the reattachment point. It is also observed that the

minimum of \tilde{C}_p is located closer to the reattachment point. The present numerical simulations are able to capture the correct trend, but some quantitative differences are observed. The current maximum \tilde{C}_p values of 0.42 at $Re = 250$ and 0.47 for $Re = 500$ are higher than the measured ones of 0.4. This stronger recovery of pressure may be due to the lower Reynolds number in the simulations or due to the neglect of spanwise variations. Jaroch and Graham (1988) also have predicted a higher maximum \tilde{C}_p value of 0.57 using a two-dimensional discrete vortex method.

Figure 6.1.4.1.7 presents the distributions of the time-mean pressure coefficient on the front and rear faces of the normal plate in the unsteady regime. These distributions are compared with measurements of Arie and Rouse (1956). Also shown are the data of Fage and Johansen (1927) for the case of a normal plate without the splitter plate. The presence of the splitter plate leads to a lower pressure drop on the downstream face of the fence since the vortices shed from the opposite edges of the plate are not allowed to interact. The present computations predict a constant pressure coefficient on the downstream face of -1.0 and -1.2 at $Re = 250$ and 500, respectively. This compares with a value of -0.57 measured by Arie and Rouse (1956) and -1.36 measured by Fage and Johansen (1927). The calculated time-mean drag coefficient in the unsteady regime is presented in Figure 6.1.3.7. It is seen that $\overline{C_D}$ has a value of 1.72 at $Re = 250$ and levels off at 1.90 for $Re = 375$ and 500. Arie and Rouse (1956) measured a time-mean drag coefficient of 1.38 for $Re = 7 \times 10^3 - 3.5 \times 10^4$; while Fage and Johansen (1927) obtained a value of 1.84 for a normal plate for $Re = 1.5 \times 10^5$. Similar over-predictions of the drag coefficient are also observed for the two-dimensional simulations of separated flows that will be presented in Section 6.2 (see also Joshi et al., 1994).

Two other representative quantities that characterize the present flow are the velocity difference, $\Delta \bar{u}$, and the vorticity thickness, δ_w . $\Delta \bar{u}$ is the difference between the maximum velocity on the high speed side of the shear layer, \bar{u}_{max} , and the minimum velocity on the low speed side, \bar{u}_{min} . Upstream of the reattachment point ($x/x_R < 1$), \bar{u}_{min} reaches $-0.46U_\infty$ in the reverse-flow region and \bar{u}_{max} increases over U_∞ by up to 40% (see Figures 6.1.4.1.3-4). The streamwise variation of $\Delta \bar{u}$ obtained from the calculations and the experiments is plotted in Figure 6.1.4.1.8. The calculated distribution correctly displays the trends of the experiments and agrees better with the data of Ruderich and Fernholz

(1986). The growth of the separated shear layer may be described by the vorticity thickness, δ_w , as defined by Brown and Roshko (1974):

$$\delta_w = \frac{\Delta \bar{u}}{\left(\frac{\partial \bar{u}}{\partial y} \right)_{max}} \quad (6.1.4.1.2)$$

The profile of the vorticity thickness, δ_w , normalized by x_R , is shown in Figure 6.1.4.1.9. The vorticity thickness initially grows almost linearly from separation up to $0.4x_R$ and then the growth rate slows down until reattachment ($x/x_R = 1$). The growth rate is again rapid after reattachment until $x/x_R = 1.5$. These trends are consistent with the experimental results of Ruderich and Fernholz (1986), Castro and Haque (1987) and Jaroach and Fernholz (1989). Owing to the current complex flow characteristics, the growth rate is not expected to vary linearly as in the case of an unforced planar mixing layer.

The time-mean center of the separated shear layer (y_c) is defined, by analogy with the mixing layer, as the transverse location at which the time-mean streamwise velocity has a value of $(0.67\Delta \bar{u} + \bar{u}_{min})$. y_c remains at a constant height of 2.3 as shown in Figure 6.1.4.1.10. The loci of zero ($\bar{u} = 0$) and maximum streamwise (\bar{u}_{max}) velocities are presented in Figures 6.1.4.1.11 and 6.1.4.1.12, respectively, and are found to be in good agreement with the experimental measurements. Figure 6.1.4.1.13 shows the direction of the time-mean flow field as the ratio of the transverse and streamwise velocities along the $\eta = 0$ and $\psi = 0$ lines for $Re = 250$. η is defined as $(y_c - y)/\delta_w$. Up to $x/x_R = 0.7$, the flow follows the same path along these two lines; however, downstream of $0.7x_R$, the flow angles along these two lines become different. After the reattachment point ($x/x_R \geq 1.5$), the flow tries to realign itself parallel to the splitter surface. The present calculations follow closely the measured values of Castro and Haque (1987) up to $0.7x_R$ but deviate somewhat afterwards. It is to be noted that the present flow is not characterized by a single flow direction, as in the case of a planar mixing layer. Similar characteristics have been observed for $Re = 375$ and 500 .

6.1.4.2 Description of the Large-Scale Structures

The temporal evolution of the large-scale structures shed from the separated shear layer is of considerable importance in understanding the characteristics of the current flow. Figures 6.1.4.2.1a and b present an instantaneous snapshot of the flow field through

contours of streamfunction, ψ , and spanwise vorticity, ω_z , for $Re = 250$. A vortex is seen developing at the edge of the shear layer by entraining fluid from the uniform stream while several others are convecting downstream of the reattachment point. The passage of a vortex at any given streamwise location is associated with corresponding changes in the surface pressure and the skin friction factor. Figure 6.1.4.2.1c shows the distributions of the surface pressure coefficient, C_{p_s} , and skin-friction factor, C_f , at one instant ($t = 375$) corresponding to Figure 6.1.4.2.1b. As the vortex passes a given streamwise location, it entrains the near-wall fluid, thus causing a low pressure at the surface. The negative velocity at the wall associated with the clockwise rotating vortex causes a sharp drop in the skin friction. It is observed that the negative peaks in the surface pressure coincide with the centers of the vortices but always lead the valleys in the skin-friction. This indicates that the vortex is tilted and elongated such that the largest negative velocity is not vertically below the vortex center. The positive surface pressure coefficients correspond to the regions between two vortices. In the separation region ($x = 5$), the positive C_{p_s} generates a vertical velocity which tears vortex A from the shear layer. The size and orientation of these convecting vortices can be calculated graphically by using the instantaneous streamlines. Table 6.1.4.2.1 summarizes the inclination of the eddy with the horizontal line (α), the location of the minimum negative ψ (y_{cl}/h_F), and the ratio of the major to minor axes ($\Omega = b/a$) (see Figure 6.1.4.2.1a for definitions). These values averaged over several time frames agree satisfactorily with the experimental data of Kiya and Sasaki (1983a) for the flow over a blunt plate.

The temporal development of the surface fluctuating pressure, p'_s , at $x/x_R = 0.8$ is illustrated in Figure 6.1.4.2.2 over a selected time interval. The valleys in the signal reflect the passage of a vortex above the probe location and are observed to occur pseudo-periodically. Two distinct modes of the vortex interactions (referred to as modes I and II) in the reattachment region could be identified in Figure 6.1.4.2.2. Mode I of the vortex dynamics is predominant during the first 200 time units (one occurrence of mode II is observed at $t = 87.5$). With further integration in time, these two vortex dynamics modes are seen to occur in an alternate sequence. To describe these modes, the spanwise vorticity fields are stored at every fifth time unit, and contours plots are visualized.

Figure 6.1.4.2.3 presents a set of instantaneous plots of the contours of negative spanwise vorticity at several time frames for shedding mode I at $Re = 250$. One representative vortex interaction cycle spans the time period of $t = 375$ to 395 (Figures 6.1.4.2.1b and 6.1.4.2.3a-d). As the separated shear layer becomes unstable, a vortex B

grows at the edge of the shear layer by entraining fluid from the uniform stream while vortex *A*, shed during an earlier time sequence, is convecting in the downstream direction. A complex sequence of vortex mergings (Figures 6.1.4.2.3a-c) occurs before the vortex detaches from the shear layer and rolls up into an independent structure (Figure 6.1.4.2.3d) and is convected by the local flow. The path of the center of vortex *A* is shown in Figure 6.1.4.2.4 over the interval of 375 and 425 time units. The core is defined as the location in the vortex with minimum negative spanwise vorticity, ω_z . Vortex *A* initially rises away from the wall moving from y of 1.9 to 2.65, propagates along a horizontal path between $x = 20$ and 30, and then descends to y of 2.15 before exiting the computational domain. Evidently, the path of the shed vortex follows closely the center of the shear layer shown in Figure 6.1.4.1.10.

Figure 6.1.4.2.5 presents the contours of negative spanwise vorticity at five time instances from $t = 740$ to $t = 760$. At $t = 740$ (Figure 6.1.4.2.5a), we see that there are two vortices (*A* and *B*) joined at the edges and attached to the shear layer. Based on the vortex interaction of mode I, it was expected that vortex *A* will subsequently detach from *B* and vortex *B* will detach from the shear layer thus forming two independent vortices. However, as time progresses, vortex *B* first grows in size and vortex *A* becomes elongated (Figure 6.1.4.2.5b); while a smaller vortex (*C*) begins to develop at the edge of the shear layer. At this time, the three vortices are joined together. With further progress in time, vortices *C* and *B* grow in size, but vortex *A* does not detach from *B*. Instead, vortex *B* engulfs vortex *A* and forms an irregular blob of fluid. At $t = 750$, vortices *B* and *A* are indistinguishable and *C* has grown to a larger size. At $t = 755$, vortices *A*, *B* and *C* are all combined into a single vortex, which is finally shed at $t = 760$ (Figures 6.1.4.2.5d-e). As a result of this new sequence of vortex interactions time period for the shedding cycle is considerably increased. A similar phenomenon was reported in the experiments of Cherry et al. (1984) who refer to this vortex interaction mode as 'necking' of the shear layer.

The two distinct vortex dynamics modes observed at $Re = 250$ are not captured at Reynolds numbers of 375 and 500. Instead, the shedding process has characteristics similar to mode I of $Re = 250$. The temporal development of the fluctuating streamwise velocity, u' , at $x = 12.5$ and $y = 1$ for $Re = 375$ and 500 is presented in Figure 6.1.4.2.6a-b over a selected time interval. The valleys in the signal reflect the passage of a vortex through the probe location and are observed to occur periodically for $Re = 375$ and pseudo-periodically for $Re = 500$. One distinct mode of the vortex shedding downstream of the reattachment region is identified in Figure 6.1.4.2.6a; however, the frequency of the time

signal for $Re = 500$ is observed to change up to 300 time units after which it becomes constant.

Figure 6.1.4.2.7 illustrates a time sequence of negative ω_z -contours for $Re = 375$ in the interval of 315.6 and 331.2 time units. Two vortices have undergone a merging process in Figure 6.1.4.2.7a and then are shed as a single structure from the reattachment point in Figure 6.1.4.2.7b. A vortex is developing at the edge of the separated shear layer in Figure 6.1.4.2.7b-c, merges with another developing vortex in Figure 6.1.4.2.7d and sheds as a coherent structure at $t = 331.2$ as seen in Figure 6.1.4.2.7e. This process is similar to that observed at $Re = 250$ (see Figures 6.1.4.2.3c-d). Similar observations of the shedding mechanism are made at $Re = 500$ and a time sequence of negative ω_z -contours in the interval of 175 and 190 time units is presented in Figure 6.1.4.2.8. Two vortices are undergoing a merging process in Figure 6.1.4.2.8a and then are shed as a single structure from the reattachment point in Figure 6.1.4.2.8b. This shedding mechanism is similar to that observed at $Re = 250$ (see Figures 6.1.4.2.3c-d) and $Re = 375$ (see Figures 6.1.4.2.7d-e). The shear layer emanating from the edge of the normal plate at $Re = 375$ and 500 does not extend further downstream as for $Re = 250$; thus, the entrainment mechanism is initiated at a closer distance to the normal plate. Further, the vortical structures at $Re = 375$ and 500 have higher spanwise vorticity in their cores than at $Re = 250$ and are comparatively more distorted by the freestream flow. The streamwise distribution of the instantaneous minimum spanwise vorticity (at an arbitrary time frame) is presented in Figure 6.1.4.2.9 and shows larger negative values for $Re = 500$ than for $Re = 250$, and the core location of the vortical structure can be identified from the valleys.

Figure 6.1.4.2.10 presents the time trace of the drag coefficient for the Reynolds numbers in the unsteady regime. At $Re = 250$, the instantaneous drag coefficient shows a wide spectrum of frequencies; while, a distinctive pattern in the signal of the drag coefficient is established for $Re = 375$ and 500 after an initial transient as shown in Figure 6.1.4.2.10b and c.

6.1.4.3 Shedding Frequency, Convective Velocities, and Linear Stability Analysis

Autocorrelations of pressure and velocity signals at selected locations are calculated to derive the dominant frequencies of the large-scale structures. The auto-correlation coefficient for a fluctuating variable ϕ' is defined as:

$$A\phi'(\Delta t) = \frac{\overline{\phi'(t,x) \phi'(t+\Delta t,x)}}{\overline{\phi'^2(x)}} \quad (6.1.4.3.1)$$

Figure 6.1.4.3.1 presents the autocorrelation coefficient of the fluctuating pressure, $A\phi'$, at $x = 12.5$ and $y = 2$ for Reynolds numbers in the unsteady regime. The dominant peak in $A\phi'$ occurs first at $\Delta t = 25$ for $Re = 250$ and $\Delta t = 15.25$ for $Re = 375$ and 500 . Thus, the dominant Strouhal number, St_1 ($St = fU_\infty/H$, $H = 2h_F$), of the large-scale vortical structures shedding from the reattachment point is measured as 0.08 for mode I of $Re = 250$ and 0.13 for $Re = 375$ and 500 . These values compare with 0.12 obtained by Kiya and Sasaki (1983a) at $Re = 2.6 \times 10^4$, 0.14 determined by Cherry et al. (1984) at $Re = 3.2 \times 10^4$ and 0.11 calculated by Tafti and Vanka (1991a) for the blunt plate flow at $Re = 1 \times 10^3$. Figure 6.1.4.3.2 shows $A\phi'$ near the edge of the separated shear layer ($x = 1$ and $y = 2$) for $Re = 250$ and 500 . It is seen that the first dominant peak in $A\phi'$ occurs at $\Delta t = 6.6$ and 7.6 for $Re = 250$ and 500 , respectively. Hence, another representative Strouhal number, St_2 , based on the shear layer shedding frequency is calculated as 0.30 and 0.26 . This means that each vortex shed from the reattachment point is formed from the coalescence of several vortices (three for $Re = 250$ and two for $Re = 375$ and 500) inside the separation bubble. This corroborates the sequence of vortex interactions presented in Figures 6.1.4.2.5, 6.1.4.2.7, and 6.1.4.2.8. Figure 6.1.4.3.3 shows the power spectrum of the drag coefficient for $Re = 375$ and 500 . A distinct frequency centered at St_1 of 0.13 is captured with its superharmonics.

The integral timescale evaluated from the autocorrelation coefficient is defined as:

$$\Lambda_{\phi'}^t = \int_0^{\tau} A\phi'(\tau) d\tau \quad (6.1.4.3.2)$$

τ' is the location where $A\phi'(\tau)$ first crosses the axis ($\tau' = \infty$ if there is no crossing). Figures 6.1.4.3.4 and 6.1.4.3.5 present the streamwise development of the integral timescales, Λ_u^t and Λ_p^t , (scaled by U_∞/x_R), at the surface of the splitter plate and the center of the shear layer for $Re = 375$. Also shown are the results obtained by Castro and Haque (1987) and Jaroach and Fernholz (1989). It is observed that the integral timescales reach a peak halfway from the reattachment point ($x/x_R = 0.5$) then drop before leveling off further

downstream. This increase in Λ_u^t and Λ_p^t can be contributed to the coalescence of several vortical structures at $x/x_R \leq 1$ as shown in Figure 6.1.4.2.7. Compared with the experiments, the calculated integral timescales are over-estimated by at least a factor of 2 in the separation region ($x/x_R \leq 1$) and agree more satisfactorily after the reattachment line. This may be attributed to differences in Reynolds numbers between the experiments and the simulations as well as the two-dimensionality assumption of the current calculations.

Space-time correlations have been used to estimate the convective velocities of the large-scale structures at three locations downstream of the reattachment point. The space-time correlation coefficient is defined as:

$$S_{\phi'}(\Delta x, \Delta t) = \frac{\overline{\phi'(x, t) \phi'(x + \Delta x, t + \Delta t)}}{\sqrt{\overline{\phi'^2(x)} \overline{\phi'^2(x + \Delta x)}}} \quad (6.1.4.3.3)$$

Figure 6.1.4.3.6 presents the space-time correlation coefficient of the fluctuating surface pressure between various streamwise locations for $Re = 375$. The time period (Δt_p) at which the first peak in the space-time correlation coefficient occurs represents the time for a large-scale vortical structure to convect from one location to the other. The streamwise convective velocity, $U_c^{\phi'}$, is defined as :

$$\frac{U_c^{\phi'}}{U_{\infty}} = \frac{\Delta x}{x_R} \frac{x_R}{\Delta t_p U_{\infty}} \quad (6.1.4.3.4)$$

Figure 6.1.4.3.7 shows the distribution of the convective velocities ($U_c^{\phi'}$) of the fluctuating pressure (p') at the surface ($y = 0$) and the center of the shear layer ($y = y_c$). These results calculated for $Re = 375$ are typical of the unsteady regime. The convective velocity is seen to rapidly increase up to the reattachment point after which it becomes constant. The low convective velocity between $0.2x_R$ and $0.5x_R$ is a consequence of the coalescence of several vortices in this region as shown in Figure 6.1.4.3.7. The phase velocity varies between 0.5 and 0.8 of the freestream velocity which is in fair agreement with the experimental values (Kiya and Sasaki, 1983a; Cherry et al., 1984) and the numerical simulations of Tafti and Vanka (1991b). The streamwise variations of the convective velocity based on the fluctuating skin-friction coefficient ($U_c^{C_f}$) and the streamwise velocity

(U_c^u) are summarized in Figure 6.1.4.3.8. Trends similar to Figure 6.1.4.3.7 are captured. The average distance between two shed vortices downstream of reattachment, x_{dl} , defined as:

$$\frac{x_{dl}}{x_R} = \frac{U_c^p / U_\infty}{St_I} \quad (6.1.4.3.5)$$

is calculated as 0.6 and 0.9 for $Re = 250$ and 500, respectively. This agrees with the range of 0.7-0.8 measured by Kiya and Sasaki (1983a). The cross-stream phase velocity can also be evaluated by calculating the space-time correlations between two streamwise points separated in the y -direction. The distance of transverse separation is estimated from the time sequence of the spanwise vorticity contours. Two cross-stream convective velocities, V_{c1}^p and V_{c2}^p , corresponding to the upward and downward motions of the propagating vortex, are computed as $0.04U_\infty$ and $-0.07U_\infty$. These values corroborate with the path of the propagating vortex shown in Figure 6.1.4.2.4.

Linear stability theory has been successfully applied in the study of unforced free shear layer flows (Michalke, 1964; Monkewitz and Huerre, 1982). Monkewitz and Huerre (1982) define a non-dimensional frequency, ω^* :

$$\omega^* = \frac{\delta_w}{4} \frac{2\pi f}{\bar{U}} \quad (6.1.4.3.6)$$

where δ_w is the vorticity thickness (Equation 6.1.4.1.2), f is the shedding frequency, and $\bar{U} = \frac{1}{2} (\bar{u}_{max} + \bar{u}_{min})$ is the average velocity across the shear layer. Their analysis has shown that the most amplified frequency, ω_{max}^* , is approximately 0.21. To assess the consistency of the current shedding mechanism with the stability analysis, the values of ω^* at the separation point ($x/x_R \approx 0.0$) and the edge of the shear layer ($x/x_R = 0.125$) are calculated and summarized in Table 6.1.4.3.1. ω^* is approximately 0.06 at the separation point and varies between 0.21 and 0.22 at $x/x_R = 0.125$ for the three Reynolds numbers. Therefore, the current simulations are consistent with the inviscid instability theory. Further, the unsteady separation occurs at the location in the shear layer corresponding with the most amplified mode. Similar results were presented by Pauley et al. (1990) for a boundary layer subject to a transverse pressure gradient.

6.2 Calculations of Separated Flow Past a Normal Flat Plate

In this section, results from two-dimensional simulations of the flow past a normal flat plate (Figure 6.2.1) are presented. For this configuration, the flow separates from the two fixed edges and forms a wake downstream of the plate. At low Reynolds numbers, the flow is steady for steady upstream conditions. However, above a critical Reynolds number, the shear layers become unstable resulting in the initiation of Karman vortices. These vortices grow by entraining fluid from the free stream and are shed from the shear layers in an alternate pattern. The present study is concerned with the understanding of the dynamics of these unsteady vortical structures at low Reynolds numbers. Section 6.2.1 provides the computational details. Section 6.2.2 presents the time-mean results. Sections 6.2.3 and 6.2.4 discuss some important aspects of the vortex dynamics.

6.2.1 Computational Details

For this configuration, the governing equations are non-dimensionalized by the plate height, h_p , and the free-stream velocity, U_∞ . Calculations are made for Reynolds numbers ($Re = h_p U_\infty / \nu$) in the range of 80 to 1000. The following boundary conditions are applied along the edges of the computational domain:

- (i) At the inlet of the computational domain a uniform streamwise velocity (U_∞) of unity, and zero cross-stream velocity (v) are specified. Further, the normal pressure gradient is set to zero.
- (ii) At the top and bottom boundaries, freestream conditions ($u = 1, p = v = 0$) are imposed.
- (iii) At the outlet of the computational domain, the convective boundary condition (Equation 6.1.1d) with a convective velocity (U_c) of 0.8 is applied. The normal pressure gradient is set to zero.

A systematic study of the influences of grid resolution and size of the computational domain upstream and downstream of the plate was performed. Table 6.2.1.1 presents the various grids and the domain sizes considered. Grids A to C use a uniform distribution whereas grids D and E use non-uniform grid spacings. Figure 6.2.1.1 shows the distributions of the grid spacings in the x and y -directions. For all of these grids, the time-

step size, Δt , is set to 2.5×10^{-3} which maintains the convective and diffusive Courant-Friedrichs-Lewy (CFL) numbers under their respective limits (see Section 3.5). Figure 6.2.1.2 shows the variation of the drag coefficient, C_D , defined as

$$C_D = \frac{\int_0^{h_p} (p_u - p_d) dy}{\frac{1}{2} \rho U_\infty^2} \quad (6.2.1.1)$$

for the various grids considered at $Re = 100$. p_u and p_d are the instantaneous pressures on the upstream and downstream faces of the normal plate, respectively. It can be seen that the results have become grid independent at mesh spacings corresponding to grids D and E. For low mesh resolution of 129×129 nodes (grid A), the drag signature has humps in the peaks. However, with increasing grid resolution, these humps disappear and also the drag decreases in magnitude. The average drag coefficient decreases from 3.7 (for grid A) to 2.9 (for grid E). Results obtained for grids D and E are nearly identical. The effect of grid resolution at $Re = 250$ is shown in Figure 6.2.1.3 for grids B and D. Again humps in the drag coefficient are seen when a coarser mesh is used. It is to be noted that grid B gave a smoother variation at $Re = 100$, thus indicating the effect of Reynolds number on the necessary grid resolution.

To examine the influence of the distance of the upstream boundary from the plate, calculations are performed for upstream distances (x_u) varying from 2.5 to 15. In the y-direction, the domain size was -8 to 8 as in grid D. A 513×257 grid size was used for these calculations. The grid distributions in the x-direction for the various upstream distances considered are presented in Figure 6.2.1.4. Figure 6.2.1.5 shows the variation of the drag coefficient from these calculations. It is seen that C_D has a maximum value of 3.8 for an upstream distance of 2.5, decreasing to 3 for an upstream distance of 15. Further, the results for upstream distances of 10 and 15 are nearly indistinguishable. Simulations are also performed for several downstream distances (x_d) between 10 and 25. The influence of the downstream distance on the drag coefficient is seen to be insignificant (Figure 6.2.1.6).

As a result of the above study, the subsequent calculations are performed for a computational domain which extends in the streamwise direction from -10 to 25 and in the cross-stream direction from -8 to 8 with a grid resolution of 513×257 nodes (grid F). A

smoothly varying non-uniform grid spacing is used to better resolve the flow features adjacent to the plate. Figure 6.2.1.7 shows the spacings in the x and y directions for this grid. For this grid, the minimum and maximum grid sizes in the x -direction are 0.02 and 0.68. In the y -direction, the minimum and maximum grid sizes are 0.02 and 0.34. The distributions of the metrics in the x -direction, $\sqrt{(\partial\xi/\partial x)}$ and $\sqrt{(\partial^2\xi/\partial x^2)}$, and in the y -direction, $\frac{\partial\eta}{\partial y}$ and $\frac{\partial^2\eta}{\partial y^2}$, are illustrated in Figures 6.2.1.8a-b. A smooth variation of these derivatives is ensured.

Numerical simulations are carried out for Re of 80, 100, 150, 200, 500 and 1000. However, the results from the calculations for Reynolds numbers of 100, 500, and 1000 will be discussed in detail. The simulations are started either from a uniform flow field or from a solution previously obtained at a lower Reynolds number. The computations are performed on a 256-processor CM-5 partition, and required approximately $5.3 \mu s$ per time step per grid node. Approximately 90% of the total CPU time is spent for the solution of the pressure-Poisson equation. The calculations for $Re = 100$ and 500 are performed for 150 non-dimensional time units and the time-mean values are obtained by averaging for 125 time units. For $Re = 1000$, the simulations are carried out for 250 non-dimensional time units and temporal averaging is performed for 225 time units. Time signals of pressure and streamwise velocity at specific locations in the computational domain are also stored every one-tenth time unit for calculating the power spectra and the space-time correlations.

6.2.2 Time-Mean Flow Variables

The current flow field is observed to be steady up to a Reynolds number of approximately 40, characterized by a steady wake (Hudson and Dennis, 1985; Joshi, 1993). For Reynolds numbers above 40, the shear layer becomes unstable resulting in the initiation of Karman vortices. These vortices are shed periodically from the upper and lower shear layers with a characteristic frequency. In this section, the time-averaged characteristics of this unsteady flow are presented. The unsteady flow characteristics are discussed in Sections 6.2.3 and 6.2.4.

Figure 6.2.2.1 shows the time-mean streamlines for $Re = 100, 500$ and 1000. The time-averaged flow field is characterized by an elongated wake whose length is seen to increase with Reynolds number. The wake-closure length, x_{wc} (defined as the distance

between the point of separation and the furthest downstream location on the centerline where the time-averaged streamwise velocity becomes zero), is calculated to be 1.3 at $Re = 100$, increasing to 14.0 and 14.6 at $Re = 500$ and 1000, respectively. These values may be compared with the results of Castro and Jones (1987) who performed steady two-dimensional simulations in the Reynolds number range of 100 to 800. Their calculations show a wake length of 7 at $Re = 100$, increasing to 63 at $Re = 800$. Since Castro and Jones (1987) solved the steady state equations and not the unsteady equations, they were unable to capture the effects of flow unsteadiness. The unsteady vortex street increases the momentum transfer, lowering the 'effective' Reynolds number (Karniadakis and Triantafyllou, 1989) and changing the time mean wake characteristics. To our knowledge, there are no experiments of this flow in the low Reynolds number regime. However, experimental data are available at much higher Reynolds numbers (Bradbury and Moss (1975) at a Reynolds number of 2.6×10^4 , Leder (1991) at $Re = 2.8 \times 10^4$). At these Reynolds numbers, the measured wake lengths were 1.92 and 2.5, respectively. Comparisons with these data are inappropriate because at these high Reynolds numbers the flow is highly three-dimensional and turbulent. Figure 6.2.2.2 presents the profiles of the time-mean streamwise velocity along the centerline ($y = 0$) for the three Reynolds numbers calculated in this study. It is observed that for Re of 500 and 1000 the streamwise velocity maintains a plateau at $-0.2U_\infty$ for 10 plate heights before the wake closes. Time-averaged values have also been computed for the Reynolds stresses, $\overline{u'^2}$ and $\overline{v'^2}$ at Reynolds number of 1000. It is observed that the magnitudes of these Reynolds stresses are much greater than those measured in the experiments of Bradbury and Moss (1975) and Kiya and Matsumura (1988). As will be shown in section 7.2, the values from the two-dimensional calculations are also much larger than those predicted by a three-dimensional simulation. This is due to the larger coherence of the spanwise vortices resulting from the two-dimensional assumption.

The profiles of the time-averaged wake-defect velocity, defined as $1 - \bar{u}$, at streamwise distances of 1, 2, 4, 8 and 16, are presented in Figures 6.2.2.3a-c for the three Reynolds numbers. Some intriguing characteristics are noticed in these plots. At Reynolds numbers of 500 and 1000, the center-line velocity stays constant for a significant distance and then suddenly increases to a value near 0.40, much above the corresponding value for $Re = 100$. At $x = 16$, all three simulations indicate that a self-similar state has not yet been attained. The maximum streamwise velocity outside the wake ($y \leq -2$ and $y \geq 2$) is seen to be 20% larger than the freestream velocity, U_∞ . Figure 6.2.2.4 show the loci of $y0.99U_\infty$

($y(\bar{u} = 0.99U_\infty)$). The width of the wake, b , defined as the distance separating $y_{0.99U_\infty}$ across the centerline, is seen to grow very slowly after $x = 4$, almost independent of the Reynolds number. This contrasts with a \sqrt{x} growth rate observed for fully-developed wakes (Schlichting, 1975).

Figures 6.2.2.5a-c show the contours of time-mean spanwise vorticity ($\bar{\omega}_z$) which also indicate the position of the time-mean shear layer. The regions of high $\bar{\omega}_z$ that originate at the plate spread in the streamwise direction as narrow bands. The time-mean center of the separated shear layer (y_c) (see Section 6.1.4.1 for definition), shown in Figure 6.2.2.6, remains at a constant height of $1.6hp$, $1.2hp$ and $1.0hp$ for $Re = 100$, 500 and 1000 , respectively. This corroborates with the $\bar{\omega}_z$ -contours presented in Figure 6.2.2.5. The streamwise variation of the vorticity thickness, δ_w (see Equation 6.1.4.1.2), is shown in Figure 6.2.2.7. Below the centerline, the vorticity thickness is assigned a negative value for plotting purposes. The vorticity thickness grows almost linearly from separation up to $y = 2$, tapering off downstream. The profile of δ_w has a similar trend as the loci of $y_{0.99U_\infty}$ and y_c .

Figure 6.2.2.8 presents the distributions of the time-mean pressure coefficient on the upstream and downstream faces of the normal plate for the three Reynolds numbers. Also shown are the measurements of Fage and Johansen (1927) at $Re = 1.5 \times 10^5$. The present computations predict a constant pressure coefficient on the downstream face with values of -2.1 at $Re = 100$ and -3.1 at $Re = 1000$. These compare with a value of -1.36 measured by Fage and Johansen (1927). The variation of the time-mean drag coefficient with the free-stream Reynolds number is displayed in Figure 6.2.2.9 and compared with the two-dimensional simulations of Joshi (1993) and the tow-tank measurements of Lisoski (1993) at $Re = 1000$ and 5000 . The measurements of Fage and Johansen (1927) and Lisoski (1993) indicate a value of \bar{C}_D equal to 1.84 and 2.11 , respectively. The two-dimensional simulations overpredict the mean drag by a factor of up to 2. The value of 3.71 obtained in the current study for $Re = 1000$ compares with 4.65 computed by Joshi (1993), 3.6 by Chua et al. (1990) and 3.26 by Lisoski (1993). The latter two studies were carried out using the discrete-vortex method.

6.2.3 Description of the Large-Scale Structures

The temporal evolution of the large-scale Karman vortical structures shed from the separated shear layer is of considerable importance in understanding the unsteady characteristics of the current flow. Figures 6.2.3.1a and b present a snapshot of the instantaneous flow field through contours of spanwise vorticity, ω_z , and stream-function, ψ , for $Re = 100$ at an instant in time ($t = 90$). This figure illustrates the development and spatial organization of the Karman vortices shed from the two shear layers. The negative (positive) spanwise vorticity corresponds to clockwise (counter-clockwise) rotation of the vortices. The propagating vortices are observed to be circular with a radius of approximately $3 h_p$ up to ten plate heights then stretch into elliptical shapes farther downstream. The stream function (Figure 6.2.3.1b) has a wavy distribution with a wavelength of approximately four plate heights. The pressure field shown in Figure 6.2.3.1c, consists of alternate regions of positive and negative values with their magnitudes dissipating with increasing distance from the plate. Regions of low (or negative) pressure correspond to the vortex cores and positive pressures correspond to the irrotational fluid in between the vortices.

Figure 6.2.3.2 presents the loci of the cores of the propagating vortices at the same time instant ($t = 90$). The vortex core is defined as the position with the maximum magnitude of the spanwise vorticity, $|\omega_z|$. The lines connecting the vortex cores correspond to a typical path followed by the Karman vortices. The vortex cores are initially located closer to the centerline. Subsequently, they diverge away and propagate approximately at $y = \pm 1.5$. The path of the shed vortical structures is observed to closely follow the center of the time mean shear layer (y_c) shown in Figure 6.2.2.6. Also shown in Figure 6.2.3.2 are the values of the spanwise vorticity at the cores and the total vortex circulation, Γ , ($\Gamma = \int \omega_z dA$). As a result of viscous diffusion, the vortex strength (as described by the magnitude of ω_z) is seen to decrease in the streamwise direction. However, the total circulation, Γ , remains fairly constant. The average streamwise spacing of the cores for vortices of identical rotation is seen to be approximately four plate heights, while the average cross-stream distance separating vortices of opposite rotation is three plate heights.

Figure 6.2.3.3a shows the time trace of the streamwise velocity in the near-wake region ($x = 2, y = 1$) over a selected time interval. The velocity is seen to vary between 0.4 and 1.3 of the free-stream velocity. The u - v phase portrait at the same point ($x = 2, y =$

1), is presented in Figure 6.2.3.3b and shows a limit cycle with a distinct harmonic. Figure 6.2.3.4 presents the time trace of the streamwise velocity and the u - v phase portrait at a location in the far wake ($x = 20, y = 2$). The phase portrait displays an initial chaotic behavior; however, a limit cycle is eventually attained. This is consistent with the observations of Karniadakis and Triantafyllou (1989) in the numerical study of the wake of a circular cylinder at the same Reynolds number. Figure 6.2.3.5 presents a set of instantaneous plots of the spanwise vorticity corresponding to a representative vortex shedding cycle at $Re = 100$. The time period of the shedding cycle in Figure 6.2.3.5 spans from $t = 91$ to 97. The initiation, growth, detachment and final propagation of the vortices are clearly characterized in these snapshots. Through extensive graphical visualization, it is seen that the vortex cores follow closely the path shown in Figure 6.2.3.2.

Figure 6.2.3.6 illustrates the instantaneous ω_z and ψ at $t = 120$ for $Re = 500$. Compared to $Re = 100$, the magnitude of the spanwise vorticity is larger at $Re = 500$. Further, as a result of lower viscous diffusion, it is seen that the vortices are more cylindrical and also maintain their shape while they propagate downstream. The wavelength of the vortex street is approximately four plate heights in the near wake region but increases to 6.3 in the far wake. Figure 6.2.3.7 presents the position and vorticity magnitude of the vortex cores at this time instant. The total circulation, Γ , remains constant at a value of 6.6. Further, because of the low diffusion, the vortices are seen to dissipate at a slower rate compared to $Re = 100$. The path of the propagating vortices at $Re = 500$ is seen to differ substantially from that of $Re = 100$. At $Re = 100$, the vortices are seen to propagate parallel to the centerline; however, interestingly, at $Re = 500$, the vortices are seen to converge towards the centerline (Figure 6.2.3.7) before exiting the computational domain at $y = \pm 0.5$. The cross-stream spacing of the vortex cores is 2.4 in the region $5 \leq x \leq 15$ decreasing to 0.9 for $x \geq 20$. A sequence of the ω_z -contours corresponding to a representative shedding cycle at $Re = 500$ is shown in Figure 6.2.3.8 and illustrates the above-mentioned convergence of the vortices towards the centerline.

The u - v phase portraits at $(x = 2, y = 1)$ and $(x = 20, y = 2)$ are shown in Figure 6.2.3.9 and reveal a limit cycle in the near-wake region but a chaotic behavior in the far-wake region. This chaotic behavior is caused by complex vortex interactions that are a result of the high Reynolds number. Figure 6.2.3.10 shows the time trace of the streamwise velocity at $x = 16$ and $y = 0$ over a selected time interval. The time trace reveals a dominant high frequency mode corresponding to the Karman vortices, superimposed on a low frequency oscillation. The valleys of the low frequency oscillation

(region I) are seen to be associated with the vortex propagation described in Figure 6.2.3.8. However, at the peaks of the low frequency oscillation (region II), complex vortex interactions are observed. Figure 6.2.3.11 presents a sequence of ω_z snapshots corresponding to a representative cycle of region II during the time span of 82.5 to 97. At $t = 82.5$ (Figure 6.2.3.11a), vortices A-E are identified at various locations in the computational domain. Vortices A, C and E have a clockwise rotation; while vortices B and D have a counter-clockwise rotation. Based on the mechanism observed in region I (Figure 6.2.3.8), it was expected that these vortices will convect without further interaction. However, it is observed that, vortex A has crossed the centerline and its core is located closer to B than for a typical shedding cycle of region I. As a result, the convection of vortex B is slowed down. At $t = 85.5$ (Figure 6.2.3.11b), B has an upward motion to preserve its momentum and enters the upper-half region of the computational domain, thus interacting with vortex C. Being of opposite spanwise vorticity, B can not merge with C instead, vortex B deforms C as shown in Figure 6.2.3.11c. As a result, the motion of vortices B and C is hindered but vortices D and E continue to move towards the interaction zone. At $t = 91$ (Figure 6.2.3.11d), B and D interact in a manner similar to that described between B and C at $t = 88.5$. At the same time, E propagates towards D. As time progresses to $t = 94$ (Figure 6.2.3.11e), the pairing of C and E is initiated resulting in an irregular blob of fluid and vortex D is further deformed and reduced in size. At the end of the interaction cycle, vortex D is displaced from its normal path exiting the computational domain with its core located at $y = -3$. This far-wake vortex interaction process is also seen to occur around $t = 45$ and around $t = 140$ (see Figure 6.2.3.10). However, at these time spans, the vortices that pair have a counter-clockwise rotation. Figure 6.2.3.12 presents a snapshot of ω_z -contours at $t = 150$ illustrating the mode of pairing in the lower half of the computational domain. It is to be noted that this pairing process is not seen distinctly in the results of the three-dimensional simulation and is, therefore, a result of the highly coherent vortices predicted by the two-dimensional assumption.

Figure 6.2.3.13 presents contours of ω_z and ψ at $t = 230$ for $Re = 1000$. Small-scale vortical structures with positive ω_z are seen merging with the vortex developing from the upper shear layer. This mechanism in the near-plate region is only present at $Re = 1000$ (refer to 6.2.3.1a and 6.2.3.6a for $Re = 100$ and 500 , respectively). The vortex street has a wavelength also of approximately four plate heights as seen in Figure 6.2.3.13b. Figure 6.2.3.14 presents the loci of the core of the propagating vortices. At $Re = 1000$, the exit vorticity is approximately 50% of that observed in the near-plate region. This value compares with 18% and 27% for Reynolds numbers of 100 and 500, respectively. The

total circulation, Γ , remains constant at 6.6. The path of the propagating vortices is seen to be similar to that at $Re = 500$. Figures 6.2.3.15 and 6.2.3.16 show the time traces of velocities and the u - v phase portraits in the near wake and far wake regions. In the near-wake region, a limit cycle with a small irregularity is seen. The far wake shows a behavior similar to that observed at $Re = 500$ characterized by a low frequency oscillation superimposed on the regular vortex shedding frequency. However, we observe that the sequence of vortex interactions shown for $Re = 500$ does not occur at $Re = 1000$. Figure 6.2.3.17 shows snapshots of spanwise vorticity for three time instances near the peak of the low frequency oscillation. It can be seen that at $Re = 1000$, the vortices in the upper half of the domain do not pair but penetrate into the lower half and convect out of the domain. This difference is the effect of lower viscosity and consequent lower diffusion between adjacent vortices.

6.2.4 Drag Signature, Shedding Frequency, Convective Velocity and Linear Stability Analysis

The temporal development of the instantaneous and time-mean drag coefficients is plotted in Figure 6.2.4.1 for the three Reynolds numbers. A distinct frequency with its superharmonics is observed for $Re = 100$ and 500 ; while a wide spectrum of frequencies is seen at $Re = 1000$. The root-mean-square fluctuation of C_D is computed to be 0.140 and 0.238 at $Re = 100$ and 1000 , respectively. These compare with measured values of 0.219 and 0.133 at $Re = 1000$ and 5000 , respectively, and a calculated value of 0.57 for a circulation decay parameter, $\lambda = 1$, and 0.20 for $\lambda = 0.86$ using the discrete-vortex method (Lisoski, 1993).

Figure 6.2.4.2 presents the power spectra for the time traces of streamwise velocity in the near-wake ($x = 2, y = 1$) at the three Reynolds numbers. At $Re = 1000$ a broad spectrum of frequencies is observed. The primary Strouhal numbers are calculated to be 0.166, 0.137 and 0.132 for $Re = 100, 500$, and 1000 , respectively. The value at Re of 1000 compares with the measured values of 0.135 for $Re = 4 \times 10^3 - 10^4$ (Roshko, 1954a) and 0.148 for $Re = 3 \times 10^3 - 9 \times 10^3$ (Lisoski, 1993) and the computed one of 0.121 for $\lambda = 1$ and 0.161 for $\lambda = 0.86$ (Lisoski, 1993). At low Reynolds numbers, comparisons can be made with data for a circular cylinder. The empirical formula suggested by Roshko (1954c) for a circular cylinder given by :

$$St = 0.212 (1 - 21.2/Re), 50 < Re < 150 \quad (6.2.4.1)$$

results in a primary Strouhal number of 0.167 at $Re = 100$. Our computed value differs by 0.6% from the above empirical value for a circular cylinder.

The streamwise distribution of the convective velocities ($U_c^{p'}$) at $y = 0.5$ and 1 is shown in Figure 6.2.4.3. The convective velocity is seen to rapidly increase up to four plate heights after which it becomes constant. The average distance between two propagating vortices, x_{dl} , (Equation 6.1.4.3.5) is calculated as 4.2 . This agrees with the value determined from the visualizations discussed in Section 6.2.3.

In addition to the above aspects, the non-dimensional frequencies, ω^* , (Equation 6.1.4.3.6) have been computed at two locations in the shear layer from the expression given by the linear stability analysis (Monkewitz and Huerre, 1982). The non-dimensional frequencies calculated at the separation point ($x/hp \approx 0.0$) and at the edge of the shear layer ($x/hp \approx 0.25$) are given in Table 6.2.4.1 for the three Reynolds numbers. ω^* is seen to vary between 0.023 - 0.034 at the separation point and between 0.212 and 0.222 at $x/hp = 0.25$. The value of ω^* calculated at the edge of the shear layer corresponds to the most amplified mode and is consistent with the inviscid instability theory.

7. THREE-DIMENSIONAL SIMULATION OF SEPARATED FLOW PAST A NORMAL FLAT PLATE

This chapter presents results obtained from a three-dimensional direct numerical simulation of the separated flow past a normal flat plate. Section 7.1 provides the computational details. The time-mean flow quantities are discussed in Section 7.2. Section 7.3 and 7.4 present the temporal and spatial characteristics of the unsteady three-dimensional flow.

7.1 Computational Details

As in the case of the two-dimensional simulation, the governing equations are non-dimensionalized by the plate height, h_p , and the freestream velocity, U_∞ . The computational domain extends in the streamwise (x) direction from -5 to 20 and in the cross-stream (y) direction from -8 to 8. A spanwise width of 2π is used and is considered to adequately resolve the important spanwise variations. The finite-difference grid contained 256×256 nodes in the x and y directions and 32 nodes in the spanwise direction. A grid with smoothly varying non-uniform spacing is used in the x and y -directions (Figure 7.1.1). This grid distribution was found to accurately resolve the two-dimensional flow at a Reynolds number of 1000. In the spanwise direction, a uniform grid spacing ($\Delta z = \pi/16$) is used.

The following boundary conditions are applied along the edges of the computational domain :

- (i) At the inlet of the computational domain ($x = -5$), a uniform freestream streamwise velocity, $u = U_\infty = 1$, and zero cross-stream and spanwise velocities are specified. The normal pressure gradient ($\partial p / \partial x$) is set to zero.
- (ii) At the top and bottom boundaries ($y = \pm 8$), freestream conditions ($u = 1, p = v = w = 0$) are imposed.
- (iii) At the outlet ($x = 20$), the convective boundary condition (Equation 3.8.1d) is applied with a convective velocity (U_c) of 0.8 for the three velocity components. A zero normal gradient is specified for the pressure.

(iv) Periodic boundary conditions are imposed in the spanwise direction .

The non-dimensional time-step size, Δt , is set to 2.0×10^{-3} which maintained the convective and diffusive Courant-Friedrichs-Lewy (CFL) numbers under their respective limits. The initial flow field was obtained by interpolating a three-dimensional solution field calculated by Joshi et al. (1994). The computations are performed on a 128-processor CM-5 partition, and require approximately $5.7 \mu s$ per time step per grid node. Calculations are conducted at a Reynolds number of 1000 and the numerical simulations are performed for 60 non-dimensional time units corresponding to approximately 10 shedding cycles. The time-mean flow field and the turbulent stresses are obtained by averaging for 35 and 26 time units, respectively. A temporal and spanwise averaging procedure has been performed, resulting in a sample size of 5.6×10^5 and 4.16×10^5 for the time-mean field and the turbulent stresses, respectively. Because of limited computer resources, it was not possible to obtain a large enough statistical sample for these quantities. However, the present simulation still provides valuable information on the spatial and temporal evolution of this three-dimensional flow and its underlying coherent structures.

7.2 Time-Mean Flow Characteristics

Figure 7.2.1a shows the contours of the time and span averaged streamlines ($\bar{\psi}$). The time averaged length of the wake is seen to be three plate heights compared with a value of 14.6 obtained from the two-dimensional simulation (Figure 6.2.2.1c). The measured values for the wake length are 1.9 for $Re = 2.6 \times 10^4$ (Bradbury and Moss, 1975) and 2.5 for $Re = 2.8 \times 10^4$ (Leder, 1991). The differences between the result of the three-dimensional calculation and the experimental values may be attributed to the effect of the Reynolds number as well as to the limited integration time. Further integration of the present simulation may clarify this issue. The LES calculation of Joshi et al. (1994) with a much longer integration time predicted a value of 2.3 at a Reynolds number of 1000. Figure 7.2.1b shows the time and span averaged $\bar{\omega}_z$ field. This distribution also differs considerably from that calculated by the two-dimensional simulation. The elongated trailing edges seen in the two-dimensional simulation (Figure 6.2.2.5c) are not present in the three-dimensional result.

Figure 7.2.2 compares the profile of the time-mean streamwise velocity along the centerline ($y = 0$) with the measurements of Bradbury and Moss (1975) and the LES results

of Joshi et al. (1994). In the wake region, the minimum streamwise velocity has a value of $-0.44U_\infty$. This compares with $-0.46U_\infty$ measured by Bradbury and Moss (1975) and $-0.42U_\infty$ calculated by Joshi et al. (1994). The calculated flow field shows a low-velocity reverse flow region extending up to $x = 0.8$. This low-velocity reverse flow region is not seen in the experiments. We are not sure if this is an effect of the short integration time of the current simulation. As a result of the low-velocity reverse region, the location of the minimum velocity is predicted to be at $x = 1.87$ compared with $x = 1.0$ measured by Bradbury and Moss (1975). The peak reverse velocities in this separated flow are approximately 40% higher than the corresponding ones for wall-bounded separated-reattaching flows. For example, the experiments of Castro and Haque (1987) and Jaroch and Fernholz (1989) have respectively measured minimum streamwise velocities of $-0.32U_\infty$ and $-0.33U_\infty$ upstream of the reattachment point (x_R).

Figure 7.2.3 compares the streamwise velocity at eight plate heights with measurements of Kiya and Matsumura (1988). Also shown are results from the corresponding two-dimensional simulation. The velocity profile obtained from the three-dimensional simulation agrees favorably with the measurements. The calculated minimum streamwise velocity, $0.67U_\infty$, compares well with measured value of $0.69U_\infty$. Further, the time-mean flow calculated at $x = 8$ is fairly one-dimensional with magnitudes of \bar{v} and \bar{w} as $0.03U_\infty$ and $0.02U_\infty$, respectively. These values agree satisfactorily with the measurements of Kiya and Matsumura (1988). However, significant errors are seen in the results obtained by the two-dimensional calculation. The two-dimensional simulation predicts a negative streamwise velocity of $-0.12U_\infty$ at this location.

Contours of the three normal stresses components, $\overline{u'^2}$, $\overline{v'^2}$ and $\overline{w'^2}$, are presented in Figures 7.2.4a-c. These stresses represent the contributions of both the coherent and incoherent components of the fluctuating signals. The maximum streamwise normal stress has a value of $0.26U_\infty^2$ and is located at $x = 2$ in the lower and upper separated shear layers; while $\overline{v'^2}_{max}$ and $\overline{w'^2}_{max}$ have values of $0.48U_\infty^2$ and $0.15U_\infty^2$, respectively, and are located on the symmetry line at $x = 3$. The Reynolds turbulent shear stress, $\overline{u'v'}$, field downstream of the plate, shown in Figure 7.2.5, is symmetrical about the centerline. The maximum magnitude of the shear stress is $0.14U_\infty^2$ located at $x = 3$ inside the separated shear layer. The profiles of the root-mean square (rms) values are plotted along the centerline ($y = 0$) in Figure 7.2.6. Also shown are the measurements of Bradbury and Moss (1975). Although the distributions do not match exactly those of

Bradbury and Moss (1975), the values of the maximum stresses are in fair agreement. Figures 7.2.7a-d present the profiles of $\overline{u'^2}$, $\overline{v'^2}$, $\overline{w'^2}$, and $\overline{u'v'}$ at $x = 8$ along with the measurements of Kiya and Matsumura (1988) at $Re = 2.3 \times 10^4$ and the calculations of Joshi (1993). The maximum normal streamwise stress is predicted to be $0.068U_\infty^2$ compared to $0.054U_\infty^2$ (Joshi, 1993) and $0.034U_\infty^2$ (Kiya and Matsumura, 1988). The maximum normal cross-stream stress is computed to be 0.146 compared to 0.15 (Joshi, 1993) and 0.047 (Kiya and Matsumura, 1988). $(\overline{w'^2})_{max}$ is calculated to be $0.042U_\infty^2$ by the present simulation, $0.029U_\infty^2$ by Joshi (1993) and $0.021U_\infty^2$ by Kiya and Matsumura (1988). $(\overline{u'v'})_{max}$ has a value of $0.016U_\infty^2$ compared to $0.012U_\infty^2$ calculated by Joshi (1993) and $0.007U_\infty^2$ measured by Kiya and Matsumura (1988). The values predicted by the two-dimensional simulation are one order of magnitude higher than the measurements. For example, the maximum normal streamwise and cross-stream stresses have values of $0.64U_\infty^2$ and $0.90U_\infty^2$, respectively.

Figure 7.2.8 displays the streamwise variation of the time-mean pressure coefficient, $\overline{C_p}$, along the centerline ($y = 0$). Also presented are the LES results of Joshi et al. (1994). It is observed that the pressure coefficient distribution is similar to that of the streamwise velocity shown in Figure 7.2.2. The current simulations are seen to predict a higher near-plate pressure coefficient of -1.2 compared to -1.8 by Joshi et al. (1994). Further, the recovery rate of the pressure coefficient is calculated to be faster than that from the LES results. Figure 7.2.9 presents the distributions of the time-mean pressure coefficient on the front and rear faces of the normal plate. Also shown are the measurements of Fage and Johansen (1927) at $Re = 1.5 \times 10^5$ as well as the numerical calculations of Chua et al. (1990), Lisoski (1993), Joshi et al. (1994) and the predictions of the current two-dimensional simulations. The pressure coefficient on the rear face of the plate is predicted to be -1.39 and compares with a value of -1.36 measured by Fage and Johansen (1927). The present two-dimensional simulations as well as the results of the discrete-vortex method of Chua et al. (1990) and Lisoski (1993) are observed to predict a lower pressure coefficient at the rear side of the plate, thus, over-estimating the drag coefficient. Table 7.2.1 summarizes the time-mean drag coefficient compiled from previous experiments and numerical simulations. The current three-dimensional simulation results in a $\overline{C_D}$ of 2.16 which agrees well with the experimental values of 1.84 , 2.10 and 2.11 by Fage and Johansen (1927), Arie and Rouse (1956), and Lisoski (1993), respectively. Contours of p'^2 downstream of the flat plate, shown in Figure 7.2.10, are

seen to have a distribution similar to the distribution of $\overline{u'v'}$. The peak value of $\overline{p^2}$ (0.15) is located in the shear layer at $x = 1.7$.

7.3 Instantaneous Flow Characteristics

Figure 7.3.1a shows a snapshot of the instantaneous velocity field in the x - y plane at $z = \pi$ and Figure 7.3.1b shows a snapshot in the x - z plane at $y = 0$. The flow field, presented in Figure 7.3.1a, is observed to have characteristics similar to the two-dimensional flow. A vortex is seen developing at the edge of the shear layer with its core located at $x = 2$ while several shed large-scales structures are convecting downstream. Figure 7.3.1b illustrates the spanwise variation of the instantaneous flow. The three-dimensional nature of the flow is further depicted in the particle trajectories shown in Figure 7.3.2. These particle trajectories are derived for a velocity field frozen in time and hence are the same as the instantaneous streamlines. Particles released at the top of the plate (at $x = 0$ and $y = 0.5$) are seen to be entrained by the spanwise roller originating from the upper shear layer as shown in Figure 7.3.2a whereas particles released upstream near the center of the plate ($x = -0.5$, $y = 0$) are drawn to the bottom half and are entrained by the vortex under development as shown in Figure 7.3.2b. The particle trajectories are seen to be very complex and three-dimensional.

Contours of the spanwise velocity component in the $y = 0$ and $x = 2$ planes are presented in Figures 7.3.3a and b, respectively, at one time instant ($t = 45$). The spanwise velocity field is observed to be organized as concentrated zones of positive and negative values with maximum magnitudes as high as the freestream velocity. The spanwise velocity is the largest in the near wake region and decreases with distance away from the plate. Figure 7.3.4 shows spanwise variations of the streamwise and spanwise velocities for different locations in the computational domain. Upstream of the plate ($x = -0.5$, $y = 0$), the flow is two-dimensional with a nearly zero spanwise velocity. In the near-wake region ($x = 2$, $y = 0.5$), significant spanwise variations of u and large values of w , characterizing the three-dimensional structure of the flow are observed. These variations become small at $x = 8$ and at $x = 16$ (Figures 7.3.4c-d). The magnitude of the spanwise velocity decreases from 0.8 at $x = 2$ to 0.4 at $x = 16$.

The instantaneous three-dimensional flow field is averaged along the spanwise (z) direction to construct a smooth two-dimensional projection. Figure 7.3.5a presents

contours of the instantaneous spanwise-averaged stream function, $\langle \psi \rangle_z$, at $t = 45$ in a stationary frame of reference. A vortex street with a wavelength of 5-6 plate heights is clearly seen. To better illustrate the wake street, the streamlines in a frame of reference moving at a convective velocity of $0.6U_\infty$, are plotted in Figure 7.3.5b. The structures emanating from both sides of the separated shear layer are more evident in this figure. Contours of the instantaneous spanwise-averaged vorticity field, $\langle \omega \rangle_z$, are illustrated in Figure 7.3.6. In the near-wake region, the roll up of the shear layer into Karman vortices is seen to contain several small scale structures which amalgamate and form a coherent structure. These Karman vortices are very strong and organized at four plate heights. However, by eight plate heights, they lose their coherence and become weaker. At a distance of twelve plate heights, the vortices are dissipated and fragmented into smaller structures. The vorticity distribution in the near wake somewhat resembles that of the two-dimensional simulation. However, significant differences exist farther from the plate.

The three-dimensional instantaneous ω_z field can also be visualized through two-dimensional (x - y) sections at various spanwise positions. Figures 7.3.7a-h present contours of ω_z for 8 spanwise planes ($z = 0, \pi/4, \pi/2, 3\pi/4, \pi, 5\pi/4, 3\pi/2, 7\pi/4$). It is seen that in each spanwise plane there is a significant number of small scale structures superimposed on the larger vortices. The large-scale structures shedding from the shear layer are formed from the amalgamation of these fine-scale structures. Instantaneously, the structure of the flow is significantly different for the various planes presented. When the spanwise distributions are averaged, the small scale variations are mitigated and the large-scale structures are more clearly seen. Figure 7.3.8 presents snapshots of the instantaneous ω_z -contours (at $z = \pi$) for a representative vortex shedding cycle between $t = 42$ and $t = 48$. The temporal evolution, propagation and breakdown of the vortices can be seen in these snapshots. Several small-scale structures are seen to interact throughout the shedding cycle.

The temporal developments of the instantaneous streamwise and spanwise velocity components in the near-wake region ($x = 2, y = 0.5, z = 0$) and at a point further downstream ($x = 8, y = 0.5, z = \pi/2$) are presented in Figure 7.3.9a and b for a selected time interval. The time traces are dominated by high-frequency components superimposed on a low-frequency motion. In contrast to the results of the two-dimensional simulation, no limit cycle is observed in the three-dimensional results. The primary Strouhal number is calculated to be 0.156 at the near-wake point. This compares with a value of 0.149 measured at $Re = 3 \times 10^3 - 9 \times 10^3$ in a tow-tank experiment and 0.121 obtained from a

numerical simulation by Lisoski (1993). This also compares well with results of Joshi (1993) who determined a primary shedding Strouhal number of 0.16. Figure 7.3.10 presents the time variation of the instantaneous drag coefficient. Also shown are the results obtained from the two-dimensional simulations. The breakdown of the flow in the spanwise direction is seen to significantly reduce the magnitude of the drag coefficient (from 3.7 to 2.16). The drag calculated from the three-dimensional simulation does not vary much in time while the two-dimensional result shows a much larger temporal variation. A low frequency modulation similar to the previous observation of Joshi (1993) is also captured by our simulation. Such a low frequency variation has also been previously reported in other geometries: Eaton and Johnston (1981) for the flow over a backward-facing step and Tafti and Vanka (1991b) for the flow over a blunt plate. It is conjectured that a low-frequency flapping of the separated shear layer is caused by the enlargement and reduction of the time-mean wake closure region. Joshi (1993) found the time scale of this mechanism to be approximately 50 time units. Our simulation was carried for only sixty time units and hence we are unable to precisely determine this time period. Further time integration will be required to study more thoroughly this phenomenon.

7.4 Eduction of Coherent Structures

Coherent structures have been observed in several previous experimental and numerical studies of mixing layers (Brown and Roshko, 1974; Jiminez et al., 1985; Bernal and Roshko, 1986; Miyauchi et al., 1991; Bell and Mehta, 1992; Rogers and Moser, 1992, Leep et al., 1993), and wake flows (Hussain and Hayakawa, 1987; Hayakawa and Hussain, 1989; Karniadakis and Triantafyllou, 1992). At low Reynolds number, the unsteady flow is dominated by large, predominantly two-dimensional spanwise vortex structures, commonly referred to as rollers. With increasing Reynolds number, the flow becomes unstable to three-dimensional perturbations, resulting in the formation of streamwise vortices, or rib vortices (following Hussain, 1983). These structures have been observed to enhance the turbulence production and scalar mixing. This section investigates the formation and evolution of such three-dimensional coherent structures in the case of the wake of a normal flat plate.

Figure 7.4.1 presents contour surfaces of the 3-D spanwise vorticity. These surfaces correspond to a vorticity magnitude of 2.5 at a time instant $t = 45$. Distinct spanwise rollers can be identified at several locations downstream of the flat plate. It is to be observed that when the flow separates from the edges of the plate, the developing

spanwise roller is essentially two-dimensional. However, after separating from the shear layer, the roller becomes distorted, and subsequently breaks into smaller structures. The rollers are easily identifiable up to $x = 8$ after which only fragments of the rollers are seen. Sections of this vorticity field in $(x-y)$ planes have been shown earlier in Figure 7.3.7. Figure 7.4.2 presents contours of spanwise vorticity at three sections in the $(x-z)$ plane (at $y = -0.5, 0, 0.5$). These sections pass through the rollers originating from the upper and lower shear layers. Arrows in Figures 7.4.2a-c highlight the positions of the spanwise rollers. At $y = 0$ (Figure 7.4.2.b), two rollers with clockwise rotation (negative ω_z) and one with counter-clockwise rotation (positive ω_z) are observed. At $y = 0.5$ (Figure 7.4.2.c), the regions of negative vorticity correspond to the top two rollers while only a small section of the bottom roller is captured. This indicates that the bottom roller does not penetrate fully up to the upper edge of the plate. At $y = -0.5$ (Figure 7.4.2.a), for this time instant, only the bottom roller is captured as the top roller is not completely formed. The distortions of the spanwise rollers in the near wake region are clearly seen. However, after $x = 7$, only 'blobs' of concentrated vorticity with no clearly identifiable structure are observed.

The distortions of the spanwise rollers are accompanied with the generation of streamwise and cross-stream vorticities, as in the case of the mixing layers and shear layers (Jimenez et al., 1985; Bernal and Roshko, 1986; Lasheras et al., 1986; Bell and Mehta, 1992, Ashurst and Meiburg, 1988; Miyauchi et al., 1991; Rogers and Moser, 1992). Figure 7.4.3 shows the surfaces of streamwise vorticity with values of ± 2.0 . The 'rib'-like structures are also observed here; however, because of the interactions between the top and bottom shear layers, the formation of these ribs is not as clear as observed in mixing layers. At the separation point, the shear layer is distorted, resulting in regions of concentrated streamwise vorticity. When the spanwise roller is shed from the shear layer, the streamwise vorticity becomes organized into elongated structures that attach themselves to the rollers. The region where the ribs are attached to the rollers has been previously termed as the 'braid region'. Two individual rib structures above and below the symmetry plane have been isolated and are shown in Figure 7.4.4. It is observed that the rib in the upper half of the domain ($y \geq 0$) extends from the bottom of the roller at $x = 2$ to the top of the roller at $x = 5.5$, while the rib forming in the lower half of the domain ($y \leq 0$) connects the top of the roller at $x = 3.5$ to the bottom of the roller at $x = 7$. This topology is similar to that conjectured by Hussain and Hayakawa (1987) for the turbulent wake of a circular cylinder. Figure 7.4.5 shows cross sections of the streamwise vorticity field for several spanwise planes ($z = 0, \pi/4$, and $\pi/2$). It can be seen that near the separation point, there

are several small scale structures of streamwise vorticity which then amalgamate into elongated structures. Figure 7.4.6 displays contour surfaces of the cross-stream vorticity field, ω_y , for a magnitude of 2. The evolutions of these surfaces are similar to that of the streamwise vorticity structures discussed in Figure 7.4.3.

The enstrophy field, Q , and the magnitude of the strain rate tensor, D , defined as:

$$Q = \omega_x^2 + \omega_y^2 + \omega_z^2 \quad (7.4.3)$$

$$D = S_{ij} S_{ji} \quad (7.4.4)$$

$$S_{ij} = \frac{1}{2} \left(\frac{\partial u_j}{\partial x_i} + \frac{\partial u_i}{\partial x_j} \right) \quad (7.4.5)$$

are also calculated and are shown in Figures 7.4.7a and b. In the braid region, the primary contribution to the enstrophy is from the streamwise and cross-stream vorticities, while the roller regions have their contribution from the spanwise vorticity.

To further understand the spatial development of the coherent structures, several representative planes are defined (following Rogers and Moser, 1992):

- (i) the core plane (CP) is the (y-z) plane through the core of the spanwise roller,
- (ii) the mid-braid plane (MBP) is the (y-z) plane midway between two spanwise rollers of same direction of rotation,
- (iii) the rib plane (RP) corresponds to the (x-y) plane through the rib structure, and
- (iv) the between-rib plane (BRP) corresponds to the (x-y) plane between two rib structures.

Contours of ω_z in the core plane (CP) at $x = 2$, the mid-braid plane (MBP) at $x = 3.6$ and the second core plane (CP) at $x = 5.5$ are shown in Figure 7.4.8a-c and the corresponding ω_x -contours are presented in Figure 7.4.9a-c. The spanwise rollers are identified in the CP while ω_z is nearly nonexistent in the MBP. The ω_x -field is dominated by small scale structures in the first CP (Figure 7.4.9a) and then organizes into large-scale structures at the MBP and the second CP (Figures 7.4.9 b and c). Further, these rib vortices appear in

pairs of alternating rotational directions at the MBP and the second CP, but are distributed in an irregular pattern in the spanwise direction. Figures 7.4.10a-d present the spanwise and streamwise vorticity fields in the rib plane (RP) and between the rib planes (BRP). The presence of cusp regions (concentrated regions of ω_z) in the roller can be seen in Figures 7.4.8c and 7.4.10c identified by arrows. These cusp regions are similar to those observed in numerical studies of the mixing layer by Miyauchi et al. (1991) and Rogers and Moser (1992) who conjectured that the streamwise ribs connect to the spanwise rollers through these cusp regions. Due to the complex organization of these structures, a clear conclusion as to the mechanism of connection between the ribs and rollers could not be made from the present results.

Finally, these coherent structures are observed to change their size and strength in time as the simulation progressed. No periodic or quasi-periodic pattern was observed. Figure 7.4.11 shows the streamwise vorticity field at $t = 55$, ten time units later than the results presented earlier. Instead of several thin elongated structures, the flow has now organized into a few thick 'cigar shaped' structures. We also observe that around this time period the drag coefficient is on the increase from its low value of the low frequency variation. Thus, the topology of the coherent structures is intricately related to the momentum transfer occurring in the wake region. Further time integration and more sophisticated processing techniques are required to clearly describe the evolution of these structures. Also, a lower Reynolds number is necessary in order to obtain a better spatial organization of the flow.

8. CONCLUSIONS AND RECOMMENDATIONS

8.1 Conclusions

A high-order finite-difference formulation on collocated grids has been developed to perform time-dependent fluid flow simulations in rectangular geometries. The numerical procedure is based on a fifth-order upwind-biased scheme for the convective terms and a fourth-order accurate stencil for the diffusive terms. A direct solver based on eigenvalue decomposition has been developed for the pressure-Poisson equation. Several representations of the Laplace operator with different orders of accuracy have been examined. The finite-difference and finite-volume concepts have been considered in the discretizations of the divergence and gradient operators. Issues pertaining to satisfying the divergence-free condition of the velocity field are studied in detail and validated for several test problems. It is observed that an error reduction of 4 or higher is not always possible due to the low-order formulation of the stencil adjacent to the boundaries. A mixed Fourier-spectral/finite-difference formulation is used in the three-dimensional algorithm. The Capacitance Matrix Technique is applied to solve the pressure-Poisson equation in the presence of obstacles in the computational domain.

Further, a data-parallel algorithm has been implemented on the massively parallel processing computer, CM-5. The performance of the algorithm has been evaluated on various grid sizes in model flow problems and for different partition sizes on the CM-5. Several basic linear algebra routines are also tested to determine the peak performances feasible on the machine. The performance is observed to not only depend on the communication/computing ratio but also on the optimum use of the vector registers. The peak performance attained by the current data-parallel algorithm is approximately *40MFLOPS* per node on a *128*-processor partition. A maximum speed of *14.5GFLOPS* is reached for a problem with *2048x2048* mesh points using a *512*-processor partition. It is anticipated that future improvements in the compiler may provide even higher performance rates.

Having established an accurate numerical procedure and an efficient parallel algorithm, unsteady two-dimensional numerical simulations have been carried out. Two basic yet fundamental geometrical configurations have been investigated: the separated-reattaching flow past a normal flat plate with an attached downstream splitter plate and the separated flow past a flat plate held normal to a uniform stream. The characteristics

of the separated-reattaching flow are studied in the steady and unsteady regimes. The Reynolds number is varied between 25 and 500. Steady separation of the shear layer is predicted for a Reynolds number up to 150. The reattachment length is found to increase monotonically up to $40h_F$. Unsteady separation characterized by vortex formation, coalescence and shedding was observed at a Reynolds number greater than 250. The onset of unsteady separation results in a sudden drop in the time-mean reattachment length. Time-mean properties of the unsteady regime (such as the surface pressure coefficient, the velocity difference, the vorticity thickness, and the shear layer center) have been calculated and compared with the experimental data available at higher Reynolds numbers. The large-scale structures are observed to have specific signatures on the surface pressure and the skin-friction factor. The shedding mechanism is characterized by two major modes at $Re = 250$ and a single mode at $Re = 375$ and 500. Mode II for $Re = 250$ is observed to be closely related to the necking phenomenon in the experiments of Cherry et al. (1984). The shedding frequencies and the phase velocities predicted by the current simulations in the low Reynolds numbers range are calculated to be nearly the same as those measured in the experiments at higher Reynolds numbers. The instability of the separated shear layer is also found to be consistent with the inviscid theory.

For the study of the separated flow past a flat plate held normal to a uniform freestream, two-dimensional unsteady simulations have been performed for Reynolds numbers varying from 100 to 1000. The time-mean wake length is seen to increase from 1.3 for $Re = 100$ to 14.6 for $Re = 1000$. The time-mean flow quantities are observed to be over-estimated compared to the experiments. The time-mean drag coefficients are also over-predicted by a factor of up to 2. This is attributed to the high coherence of the vortices predicted by the two-dimensional simulations. The unsteady characteristics of the separated flow are also discussed. Limit cycles with a distinct frequency are captured for Reynolds numbers below 1000. Interaction regions I and II have been identified in the far wake for $Re = 500$ and 1000 and are observed to occur pseudo-periodically. The signatures of the drag coefficient are seen to differ significantly between Re of 100 and 1000. The calculated shedding frequencies and streamwise convective velocity are seen to agree satisfactorily with the experiments. Further, linear stability analysis shows that the shedding of Karman vortices occurs at the location in the separated shear layer corresponding to the most amplified mode.

Finally, large-scale computations of the three-dimensional separated flow past a normal flat plate have been carried out. The direct numerical simulation shows that the flow at $Re = 1000$ is inherently three-dimensional. The time-mean velocities and Reynolds stresses are found to agree well with the experiments conducted at higher Reynolds numbers. The flow is seen to break down into small-scale structures and the spanwise development of these structures has been studied. Visualization techniques have been applied to capture the spanwise development of the instantaneous flow field. Streamwise ribs and spanwise rollers are identified in the near wake. The presence of these coherent structures corroborates the experimental observations and numerical calculations for mixing layers and wakes of circular cylinders.

Striking differences are seen between the results from the two-dimensional simulations and those from the three-dimensional calculations. Since the flow is found to be inherently three-dimensional for a Reynolds of 1000 , the results obtained from the two-dimensional simulations are significantly in error when compared with the measurements and the three-dimensional simulation. Within the two-dimensional assumption, the large-scale structures maintain their coherence and are not permitted to break in the spanwise direction. The results from the two-dimensional simulations should be compared more appropriately with a two-dimensional experiment such as soap-films (Gharib, 1993). However, since fluid dynamics processes in Nature are inherently three-dimensional, two-dimensional flow simulations for all their computational and conceptual convenience are part of 'a comfortable dream world' (Morkovin, 1964).

8.2 Recommendations for Future Research

Although the present study has attempted to analyze in depth some fundamental aspects concerning separated and separated-reattaching flows, the study is far from being complete and represents the initial stages of continuing research to understand wake-flow instabilities. Several issues to be addressed in the future have emerged from this study.

Concerning the numerical algorithm, the current computations have been restricted by the time step size to maintain numerical stability. As a result, only a few shedding cycles have been simulated due to limited computational resources. It is to be noted that the present three-dimensional study required approximately *170 CPU hours* on the CM-5. However, a large ensemble size is required for the results to become statistically reliable. These statistical quantities, including normal and shear stresses, are

of importance in turbulence modeling. Thus, to simulate a larger number of shedding modes without extensive computational requirements, the limitation on the time-step size should be eased. An implicit formulation for the discretization of the convective and diffusive terms should be considered and iterative methods to solve the non-linear terms should be investigated. Further, three-dimensional simulations at higher Reynolds numbers (say above 10^4) could be attempted to gain insight into the flow characteristics in a practical range of Reynolds number. However, as the computational requirements to perform DNS become overwhelming with increasing Reynolds numbers, large-eddy simulations will provide a more promising approach to tackle these high-Re flows. Filtering procedures and selection of appropriate sub-grid scale models, amongst a myriad of proposed ones, are some of the issues concerning turbulence modeling in separated flows.

Concerning the fluid dynamics issues, a major difficulty that was faced during the research was the lack of appropriate processing tools to probe the three-dimensional flow field. At each time step, the present DNS generates 8.4×10^6 values representing the velocity and pressure fields. Interrogating such large datasets is an overwhelming task. More inquisitive diagnostic methods such as proper-orthogonal decomposition (POD) and stochastic estimation (SE) can be applied to gain insight into the inherent coherent structures. However, their applicability, as well as the extent of information to be gained, is not yet known. Further, enhanced graphical interfaces, such as holographic images and virtual reality, will also help the interrogation procedure.

In addition to the issues studied in this thesis, wake control mechanisms such as base mass injection, splitter plates, and immersion of bodies in the near wake, can also be simulated with the present computational algorithm. Effects of freestream oscillation, freestream turbulence, flow compressibility, and transverse and spanwise shear are other areas that need further research. Three-dimensional calculations in the transition regime (for Reynolds numbers between 150 and 250) may provide clearer insight into the formation and organization of the coherent structures in wake flows.

TABLES

Table 2.1.1 Experimental investigations of separated-reattaching flows

Investigator	Configuration	Method	Re	$T_u(\%)$	$\beta(\%)$	W/h	x_R/h
Arie & Rouse (1956)	Flat Plate w/ Splitter Plate	Pitot Cylinders	7×10^3 - 3.5×10^4	1.5	10	12	16.8
Roshko & Lau (1965)	Model B	Preston Tubes	5.3×10^3	-	10	20	24
	Model C		1.4×10^3	-	5	40	33.6
Smits (1982)	Flat Plate w/ Splitter Plate	Pitot Tube	4.2×10^4 - 2.9×10^5		1.5-10	16-31	16-32
Kiya & Sasaki (1983, 1985)	Blunt Base	Split Film X-wire	2.9×10^4	0.3	5	10	5.0
Cherry et al. (1984)	Blunt Base	Hot wire	3.2×10^4	0.07	3.8	13	4.9
Ruderich & Fernholz (1986)	Flat Plate w/ Splitter Plate	Hot and Pulsed Wires	1.4×10^4	0.66	5.7	23	17.1
			9×10^3	0.66	10		22.6
Castro & Haque (1987)	Flat Plate w/ Splitter Plate	Pulsed Wire	1.1×10^4	0.25	6.5	19	19.2
Castro & Haque (1988)	Flat Plate w/ Splitter Plate	Pulsed Wire	1.1×10^4	0.75	6.5	19	14.8
Jaroch & Fernholz (1989)	Flat Plate w/ Splitter Plate	Pulsed Wire	1.4×10^4	0.08	2.75	63	25.0
Govinda Ram & Arakeri (1990)	Flat Plate at various angles Splitter Plate	Pressure Tappings	5.7×10^3 - 1.3×10^4	0.3	4.9	30-67	26.5
McCluskey et al. (1991)	Flat Plate w/ Splitter Plate	Pressure Tappings	1.6×10^3	0.25	0.8	174	29
Hancock & Castro (1993)	Flat Plate w/ Splitter Plate	Pulsed Wire	1.8×10^3	0.25	1.4	113	26.7

T_u : Turbulence Intensity; β : Blockage Ratio; W : spanwise width

x_R : reattachment length; h : height of plate above splitter plate or height of blunt plate.

Table 3.7.1 Summary of different formulations used in the present study
(Entries represent order of accuracy of stencil).

Scheme	(∇p)	($\nabla \cdot$)	Flux Interpolation
IFDM	4	4 [†]	-
CFDM1	2	2	-
CFDM2	4	2	-
CFDM3	4	4	-
CFVM1	2	2	2
CFVM2	4	2	4
CFVM3	4	4	4

[†] Laplace operator ($\nabla^2 p$) is used instead of Divergence of Gradient operator ($\nabla \cdot (\nabla p)$).

Table 3.7.1.2 Error reduction for decay of a vortex at $t = 0.1$.
(Grids = 17×17 , 33×33 , 65×65)

Scheme	Re = 1		Re = 100		Re = 1000	
	λ_u	λ_p	λ_u	λ_p	λ_u	λ_p
IFDM	2.09	1.82	3.74	3.59	1.99	3.13
CFDM1	3.73	2.12	3.84	2.14	1.77	2.14
CFDM2	3.55	3.52	3.73	3.84	1.56	3.84
CFDM3	3.87	3.02	3.75	4.02	3.74	4.05
CFVM1	1.92	2.61	1.78	2.32	1.77	2.25
CFVM2	1.92	2.12	1.78	1.96	1.78	1.97
CFVM3	3.02	2.09	2.89	2.20	2.88	2.15

Table 3.7.2.1 Results for driven-cavity flow at $Re = 100$ on a 65×65 uniform mesh.

	IFDM	CFDM1	CFDM2	CFDM3	CFVM1	CFVM2	CFVM3	Ghia (1982)	Vanka (1986)
u_{\min}	-0.186	-0.212	-0.212	-0.213	-0.210	-0.211	-0.214	-0.211	-0.213
v_{\min}	-0.223	-0.248	-0.251	-0.252	-0.248	-0.248	-0.252	-0.245	-
v_{\max}	0.161	0.176	0.178	0.178	0.175	0.176	0.178	0.175	-
Ψ_{\min}	-0.091	-0.102	-0.103	-0.103	-0.102	-0.102	-0.103	-0.103	-0.103

Table 3.7.2.2 Results for driven-cavity flow at $Re = 400$ on a 65×65 uniform mesh.

	IFDM	CFDM1	CFDM2	CFDM3	CFVM1	CFVM2	CFVM3	Ghia (1982)	Vanka (1986)
u_{\min}	-0.304	-0.317	-0.318	-0.319	-0.310	-0.313	-0.322	-0.327	-0.327
v_{\min}	-0.417	-0.434	-0.435	-0.437	-0.419	-0.421	-0.442	-0.450	-
v_{\max}	0.276	0.290	0.290	0.292	0.280	0.282	0.296	0.302	-
Ψ_{\min}	-0.108	-0.110	-0.110	-0.111	-0.107	-0.108	-0.112	-0.114	-0.114

Table 3.7.2.3 Results for driven-cavity flow at $Re = 1000$ on a 65×65 uniform mesh.

	IFDM	CFDM1	CFDM2	CFDM3	CFVM1	CFVM2	CFVM3	Ghia (1982)	Vanka (1986)
u_{\min}	-0.266	-0.355	-0.355	-0.357	-0.342	-0.350	-0.364	-0.383	-0.387
v_{\min}	-0.366	-0.474	-0.474	-0.476	-0.455	-0.464	-0.488	-0.516	-
v_{\max}	0.251	0.340	0.341	0.343	0.326	0.335	0.351	0.371	-
Ψ_{\min}	-0.085	-0.109	-0.109	-0.110	-0.105	-0.107	-0.112	-0.118	-0.117

Table 3.7.2.4 Characteristics of pressure formulations.

Approach	Characteristics
IFDM	<ul style="list-style-type: none"> • Local divergence of velocity field is not achieved. • Global divergence is not satisfied. • Perturbation parameter required for solution of Poisson equation.
CFDM	<ul style="list-style-type: none"> • Local divergence is satisfied. • Global divergence is not achieved. • Pressure field is oscillatory.
CFVM1, CFVM2	<ul style="list-style-type: none"> • Local divergence is satisfied for cell fluxes. • Global divergence is satisfied. • Collocated velocity is not divergence-free.
CFVM3	<ul style="list-style-type: none"> • Local divergence is satisfied for cell fluxes. • Global divergence is not satisfied. • Collocated velocity does not satisfy the divergence-free condition.

Table 5.2.1.1 Performance in GFLOPS of basic linear algebra routines for two-dimensional arrays on 256-processor CM-5 partition in scalar mode.

	64 ²	128 ²	256 ²	512 ²	1024 ²	2048 ²
A+B	0.082	0.15	0.24	0.29	0.15	0.098
A*B	0.082	0.15	0.24	0.28	0.14	0.096
A/B	0.068	0.091	0.12	0.13	0.091	0.069
A+B*C	0.16	0.25	0.39	0.44	0.17	0.13
C + α B	0.16	0.27	0.39	0.48	0.26	0.18
(A,B)	0.048	0.13	0.29	0.41	0.23	0.17
MxV [†]	0.0015	0.0059	0.027	0.095	0.26	0.49
MxM ^{††}	0.077	0.26	0.49	0.64	0.65	0.31

[†] CMSSL Routine : gen_matrix_vector_mult

^{††} CMSSL Routine : gen_matrix_mult

Table 5.2.1.2 Performance in GFLOPS of basic linear algebra routines for two-dimensional arrays on 256-processor CM-5 partition in vector mode.

	64 ²	128 ²	256 ²	512 ²	1024 ²	2048 ²	4096 ²	8192 ²	16384 ²
A+B	0.11	0.61	1.73	3.01	3.50	3.50	3.40	3.41	3.42
A*B	0.11	0.61	1.73	2.95	3.50	3.50	3.40	3.41	3.42
A/B	0.10	0.50	1.15	1.58	1.70	1.70	1.66	1.68	1.69
A+B*C	0.21	1.17	3.12	5.14	5.20	5.60	5.63	5.65	5.66
C + α B	0.21	1.06	3.28	5.89	4.19	7.00	6.33	6.83	6.85
(A,B)	0.053	0.21	0.77	2.22	3.89	4.90	5.10	5.15	5.17
MxV [†]	8x10 ⁻⁴	0.02	0.07	0.18	0.70	1.70	3.36	5.97	8.73
MxM ^{††}	0.070	0.35	1.18	2.70	5.20	8.60	13.11	15.84	19.57

[†] CMSSL Routine : gen_matrix_vector_mult

^{††} CMSSL Routine : gen_matrix_mult

Table 5.2.3.1 CPU timings and performance in GFLOPS of the two-dimensional algorithm on 512-processor CM-5 partition in vector mode.

Grid	Momentum (Eq. 3.1.4) CPU sec/ Δt [GFLOPS]	Poisson Solver (Eq. 3.1.7) CPU sec/ Δt [GFLOPS]	Update (Eq. 3.1.6) CPU sec/ Δt [GFLOPS]	<u>CRAY-YMP time</u> CM-5 time
64x64	4.61×10^{-3} [0.210]	3.52×10^{-2} [0.062]	5.48×10^{-3} [0.024]	0.3
128x128	5.59×10^{-3} [0.706]	5.97×10^{-2} [0.286]	6.41×10^{-3} [0.084]	1.1
256x256	8.14×10^{-3} [1.928]	1.03×10^{-1} [1.314]	9.40×10^{-3} [0.206]	4.6
512x512	1.32×10^{-2} [4.727]	2.95×10^{-1} [3.650]	1.60×10^{-2} [0.553]	11.5
1024x1024	3.12×10^{-2} [8.011]	1.09 [7.898]	3.86×10^{-2} [0.920]	19.6 [†]
2048x2048	9.77×10^{-2} [10.226]	4.71 [14.606]	1.21×10^{-1} [1.173]	36.8 [†]

[†] Estimated CPU time on CRAY-YMP.

Table 5.3.3.1 CPU timings and performance in GFLOPS of the three-dimensional algorithm on 512-processor CM-5 partition in vector mode.

Grid	Momentum (Eq. 3.1.4) CPU sec/ Δt [GFLOPS]	Poisson Solver (Eq. 3.1.7) CPU sec/ Δt [GFLOPS]	Update (Eq. 3.1.6) CPU sec/ Δt [GFLOPS]
64x64x64	1.55×10^{-1} [1.155]	3.19×10^{-1} [1.708]	6.57×10^{-2} [1.191]
128x128x64	3.12×10^{-1} [1.249]	9.37×10^{-1} [3.471]	1.51×10^{-1} [2.071]
128x128x128	4.02×10^{-1} [3.550]	1.82 [4.754]	3.60×10^{-1} [3.194]
256x256x64	7.00×10^{-1} [4.070]	3.32 [6.506]	4.08×10^{-1} [3.003]
256x256x128	1.28 [4.451]	6.147 [8.425]	9.44×10^{-1} [4.871]
256x256x256	1.94 [5.874]	13.41 [10.287]	1.69 [10.525]

Table 6.1.4.2.1 Characteristics of the shed vortices at $Re = 250$.

	$\frac{y_{cl}}{h_F}$	α	Ω
$Re = 250$ (Present Calculations)	1.6	35°	0.78
$Re = 26000$ (Kiya and Sasaki, 1983a)	1.8	45°	0.70

Table 6.1.4.3.1 Modified non-dimensional frequency, ω^* (Equation 6.1.4.3.6) for the separated-reattaching flow.

	$Re = 250$	$Re = 375$	$Re = 500$
Separation Point ($x/x_R=0.002$)	0.064	0.059	0.060
Edge of Shear Layer ($x/x_R = 0.125$)	0.221	0.214	0.213

Table 6.2.1.1 Summary of grid resolution and computational domain.

Grid	$N_x \times N_y$	$[x_u, x_d]^\dagger$	$[y_b, y_t]^{\dagger\dagger}$	Distribution
A	129x129	[-5.8, 19.8]	[-6.4, 6.4]	Uniform
B	257x257	[-5.8, 19.8]	[-6.4, 6.4]	Uniform
C	513x513	[-5.8, 19.8]	[-6.4, 6.4]	Uniform
D	257x257	[-5.5, 20]	[-8.0, 8.0]	Non-Uniform
E	513x513	[-5.5, 20]	[-8.0, 8.0]	Non-Uniform
F	513x257	[-10, 25]	[-8.0, 8.0]	Non-Uniform

† x_u and x_d are the upstream and downstream distances, respectively.

†† y_b and y_t are the bottom and top widths, respectively.

Table 6.2.4.1 Modified non-dimensional frequency, ω^* , for the separated flow.

	Re = 100	Re = 500	Re = 1000
Separation Point ($x = 0.01$)	0.034	0.023	0.025
Edge of Shear Layer ($x = 0.25$)	0.216	0.212	0.222

Table 7.2.1 Summary of drag coefficient compiled from experiments and numerical simulations for the flow past a normal flat plate.

Investigator	Method	Re	C _D
Fage & Johansen (1927)	Wind Tunnel	1.5×10^5	1.84
Roshko (1954)	Wind Tunnel	4×10^3 - 10^4	1.74
Arie & Rouse (1956)	Wind Tunnel	7×10^3 - 3.5×10^4	2.10
Castro (1971)	Wind Tunnel	2.5×10^4 - 7×10^4	1.87
Bearman & Trueman (1972)	Wind Tunnel	2×10^4 - 7×10^4	2.05
Kuwahara (1973)	Discrete Vortex	-	2.0-4.0
Courchesne & Laneville (1979)	Wind Tunnel	2×10^4 - 10^5	2.3
Kiya & Arie (1980)	Discrete Vortex	-	2.0-3.5
Sarpkaya & Kline (1982)	Wind Tunnel	2.1×10^4	2.2
Spalart et al. (1983)	Discrete Vortex	10^7	3.5
Igarashi (1986)	Wind Tunnel	1.1×10^4 - 4.4×10^4	2.0
Dutta (1988)	Vortex Element	-	3.39
Chein & Chung (1988)	Discrete Vortex	-	2.8
Raghavan et al. (1990)	ARC2D	200	2.8
Knisely (1990)	Wind Tunnel	720- 8.1×10^4	2.0
Chua et al. (1990)	Tow Tank	5×10^3	2.05
	Discrete-Vortex	-	3.6
Lisoski (1993)	Tow Tank	10^3	2.11
		5×10^3	2.19
	Discrete Vortex	-	3.47
Joshi (1993)	2-D Simulations	40 - 10^3	2.41-4.65
	3-D Simulations	10^3	2.4
Present	2-D Simulations	10^2 - 10^3	2.85-3.70
	3-D Simulations	10^3	2.16

FIGURES

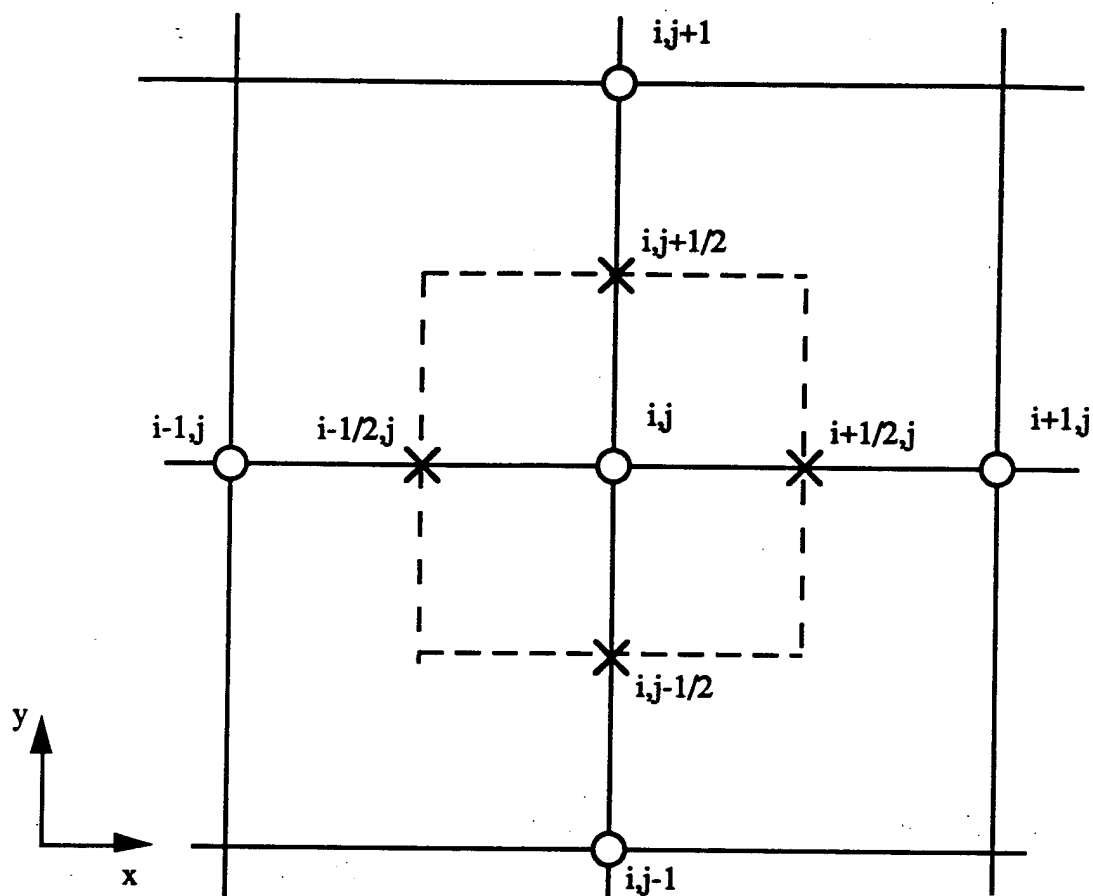


Figure 3.2.1 Schematic of collocated grid arrangement.
 (o) collocated variables
 (x) cell-face variables

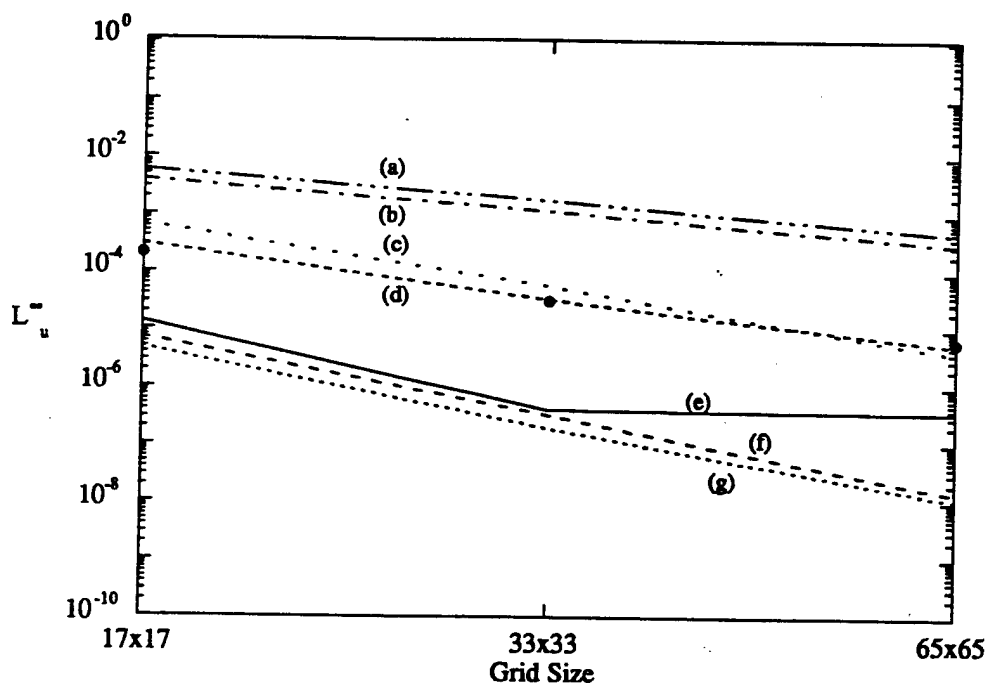


Figure 3.7.1.1 Distribution of L_u^∞ norm with grid size at $t = 0.35$ for the vortex-decay problem ($Re = 1$).

(a) CFVM2 ($\lambda = 1.83$), (b) CFVM1 ($\lambda = 1.82$), (c) CFDM3 ($\lambda = 3.69$),
 (d) CFVM3 ($\lambda = 2.88$), (e) IFDM ($\lambda = 2.61$), (f) CFDM2 ($\lambda = 4.51$)
 (g) CFDM1 ($\lambda = 4.37$), (•) Le & Moin (1991) ($\lambda = 2.53$).

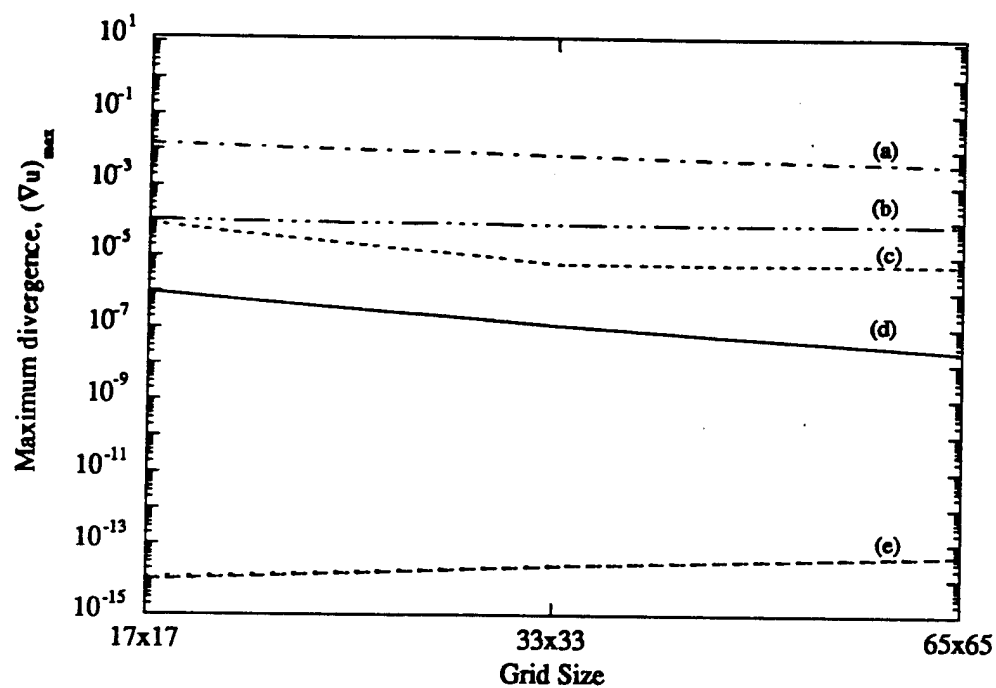


Figure 3.7.1.2 Maximum divergence in the collocated velocities for the vortex-decay problem ($Re = 1$) as calculated by the various methods.
 (a) CFVM1, (b) CFVM2, (c) CFVM3, (d) IFDM, (e) CFDM1-3.

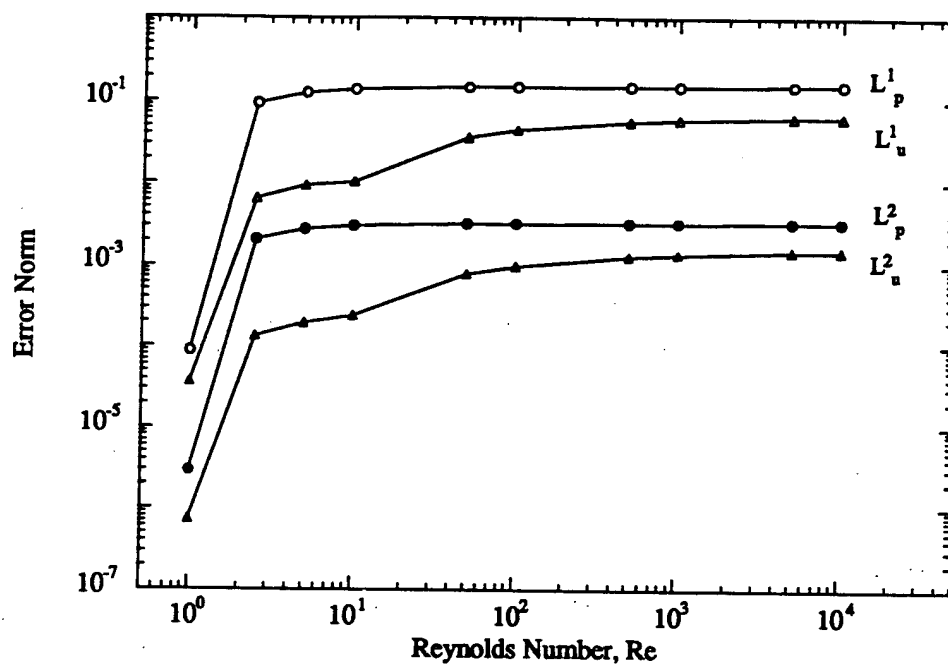


Figure 3.7.1.3 Distribution of the error norms with the Reynolds number for the vortex-decay problem using CFVM2.
Grid size = 65×65 , $\Delta t = 10^{-4}$, $t = 0.5$.

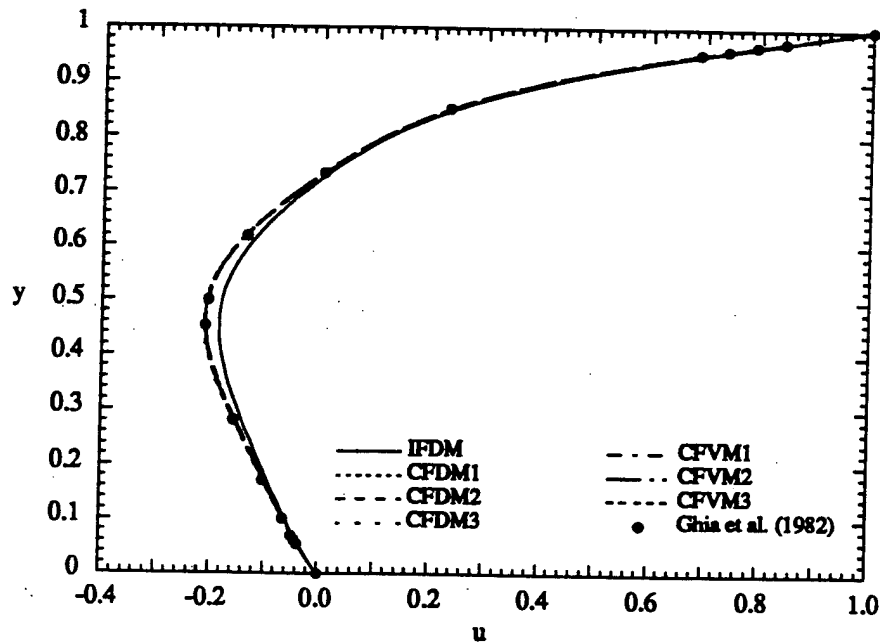


Figure 3.7.2.1 Velocity profile along the vertical centerline ($x = 0.5$) for the driven-cavity problem at $Re = 100$. Grid size = 65×65 .

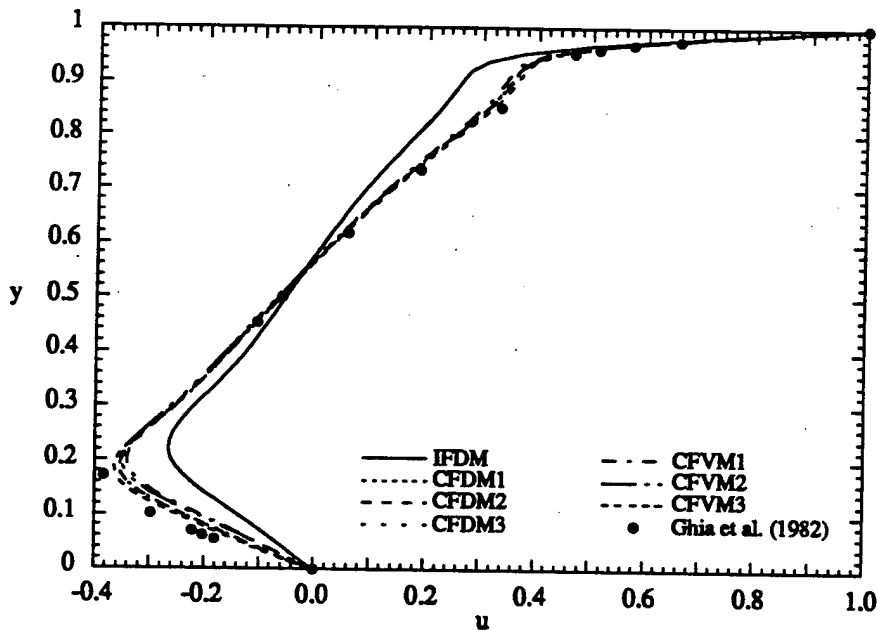


Figure 3.7.2.2 Velocity profile along the vertical centerline ($x = 0.5$) for the driven-cavity problem at $Re = 1000$. Grid size = 65×65 .

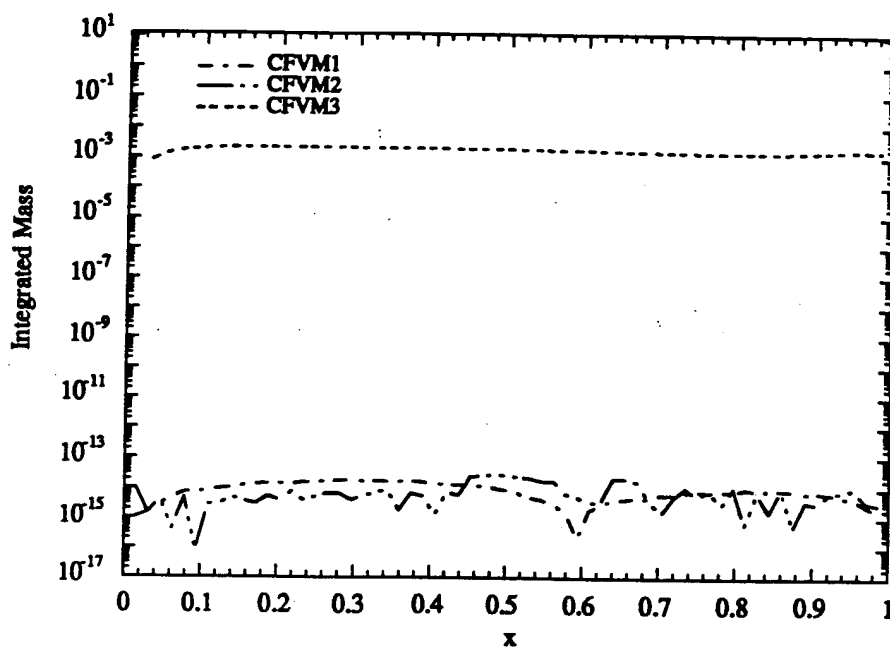


Figure 3.7.2.3 Integrated mass based on the cell fluxes for the driven-cavity problem at $Re = 1000$. Grid size = 65×65 .

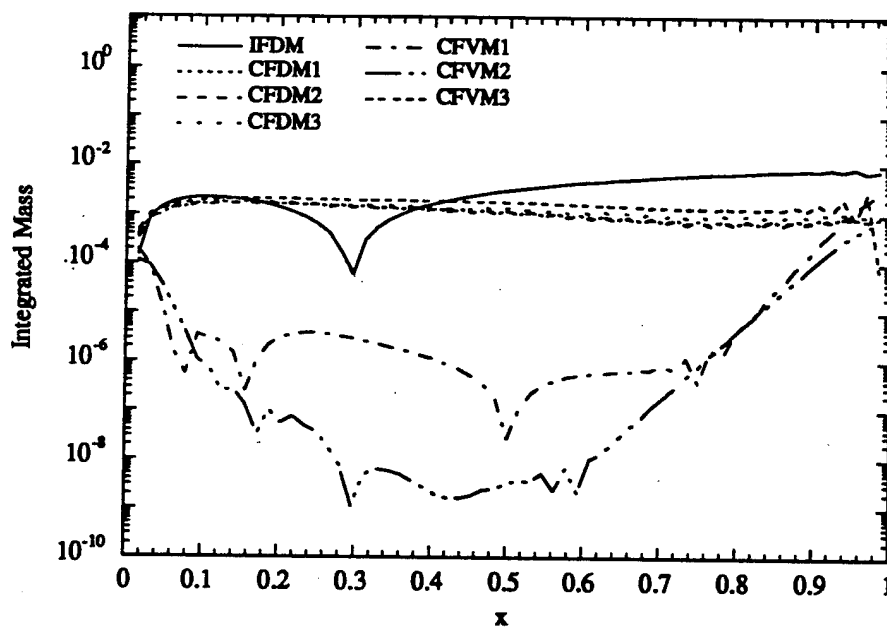


Figure 3.7.2.4 Integrated mass based on the collocated velocities for the driven-cavity problem at $Re = 1000$. Grid size = 65×65 .

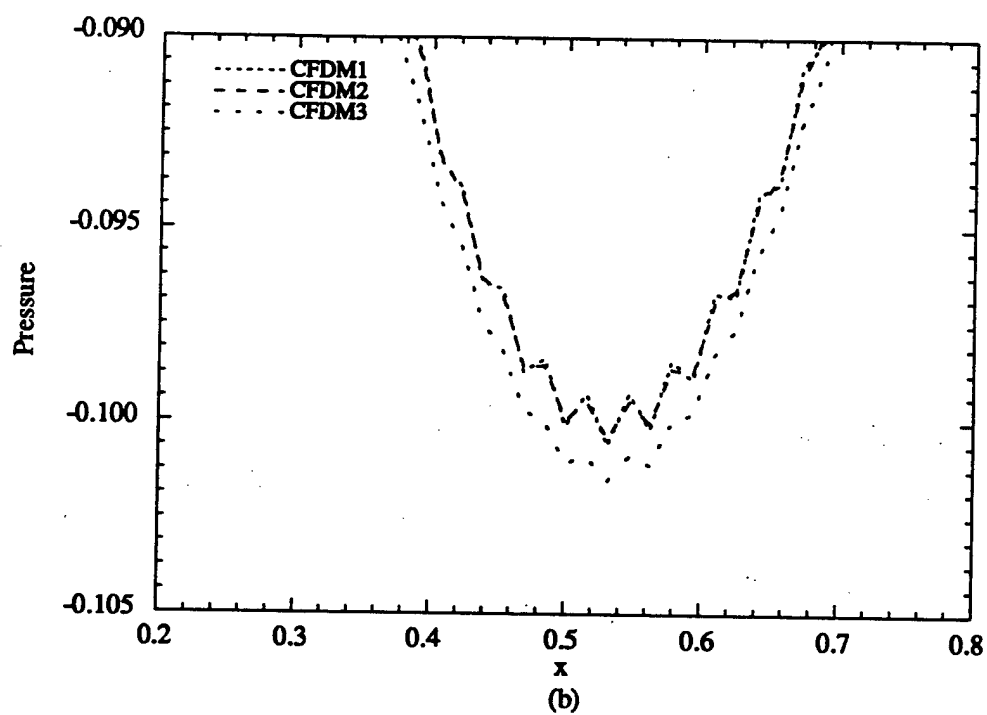
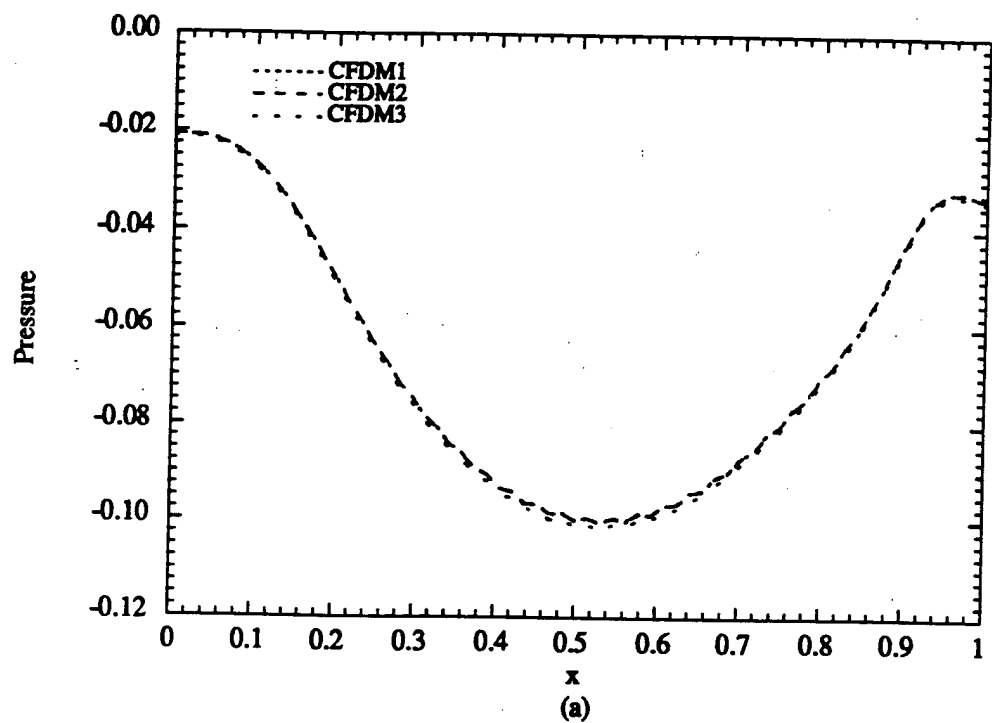


Figure 3.7.2.5 Profile of the pressure along horizontal centerline ($y = 0.5$) for the driven-cavity problem at $Re = 1000$.
(a) overall distribution, (b) close-up view. Grid size = 65×65 .

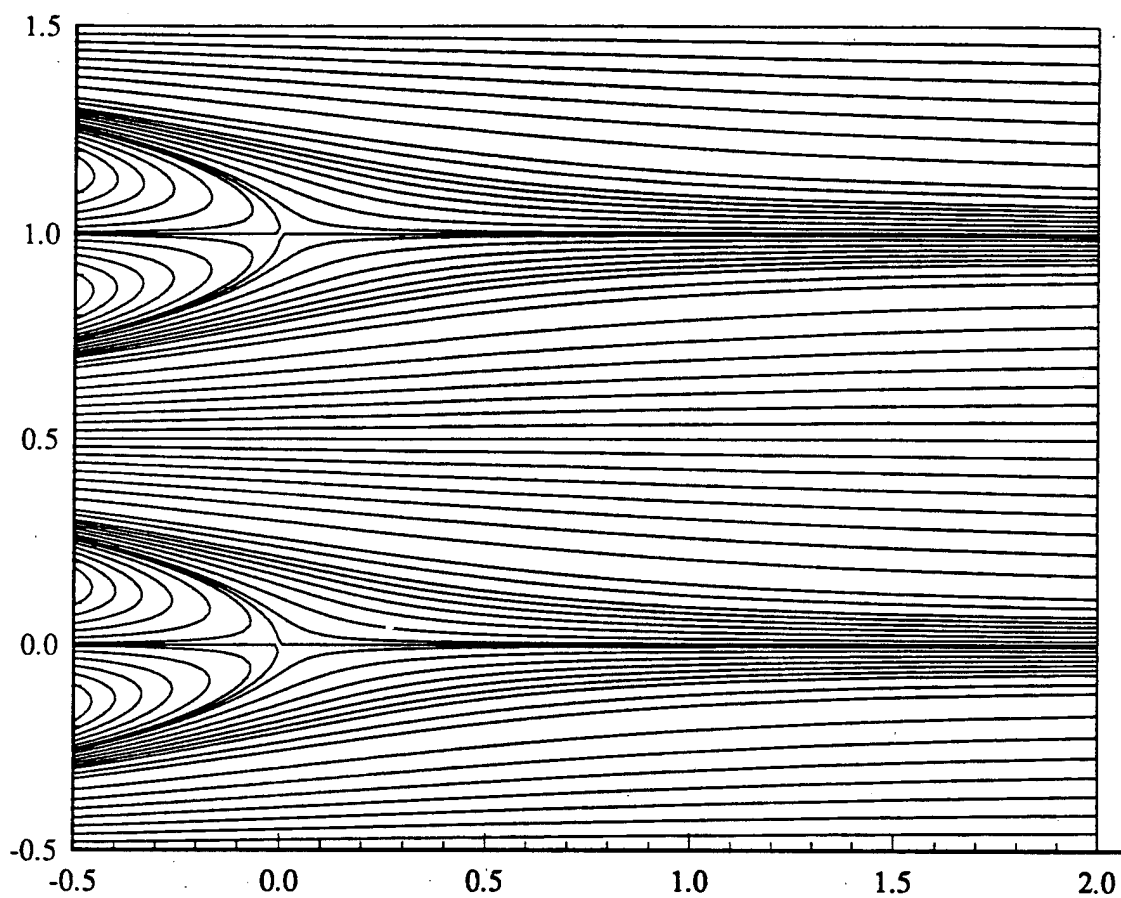
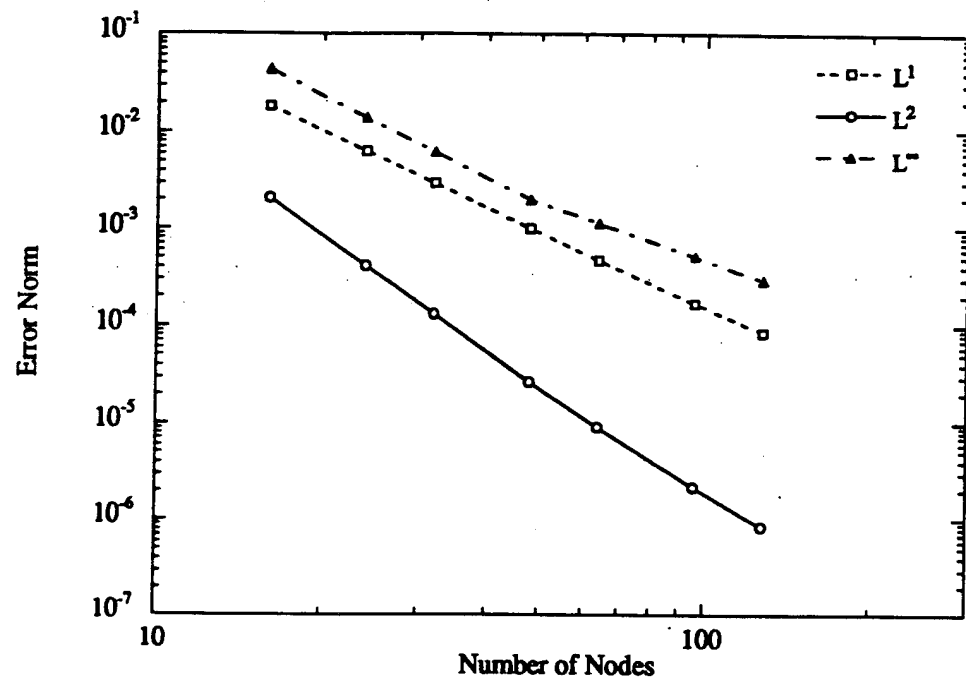
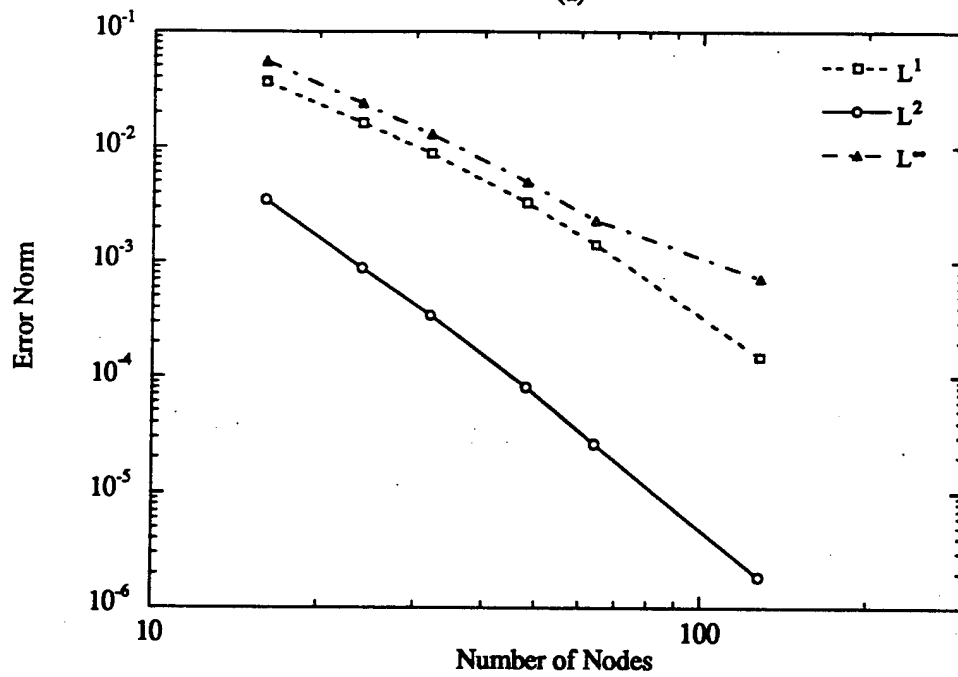


Figure 3.7.3.1 Streamlines for the Kovasznay flow at $Re = 40$.



(a)



(b)

Figure 3.7.3.2 Distribution of the error norms based on (a) the streamwise velocity and (b) the pressure with grid resolution for the Kovasznay flow at $Re = 40$.

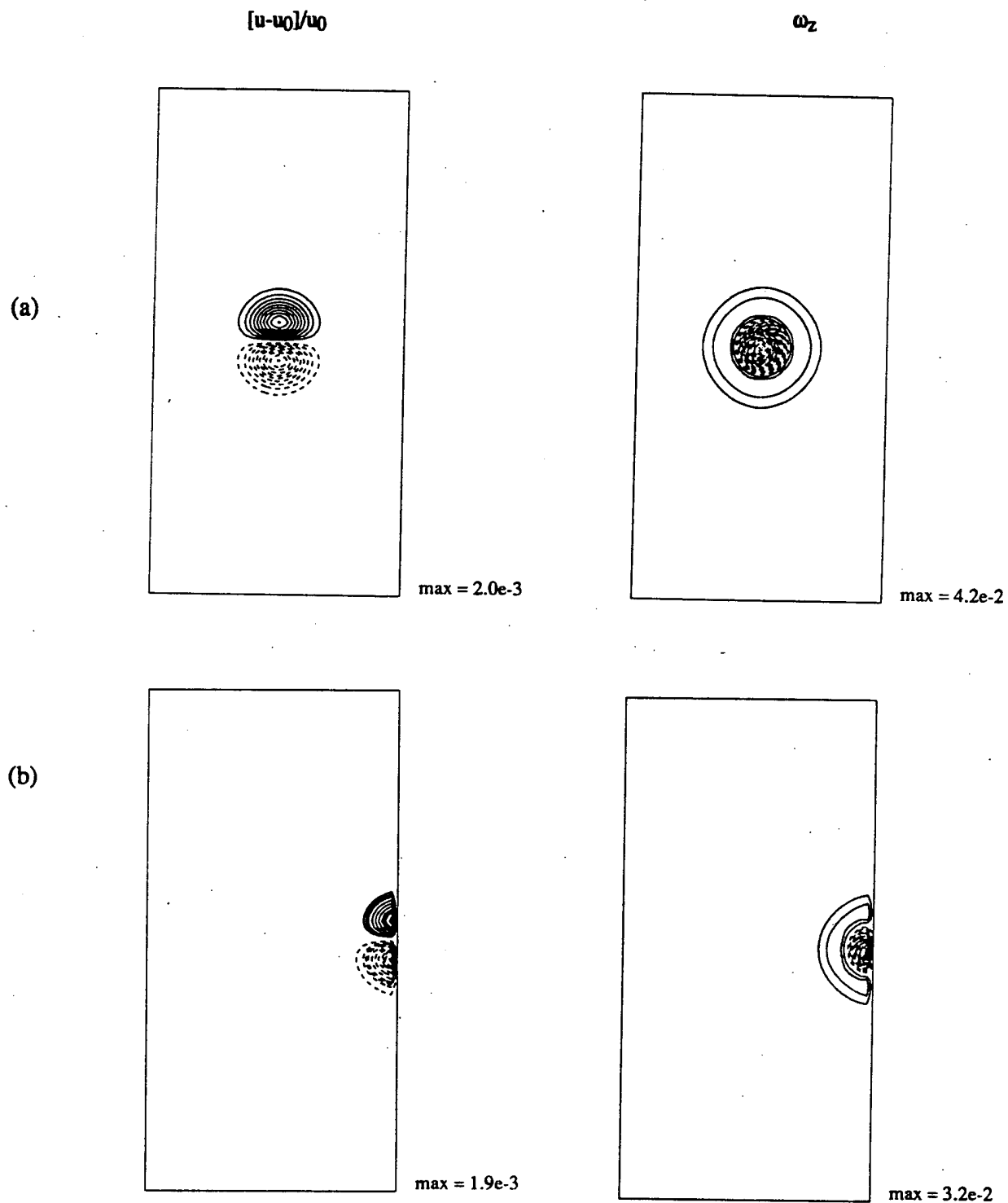


Figure 3.8.1 Velocity difference and spanwise vorticity for a convecting vortex using boundary condition (3.8.1a)
(a) $t = 0$, (b) $t = 1$.

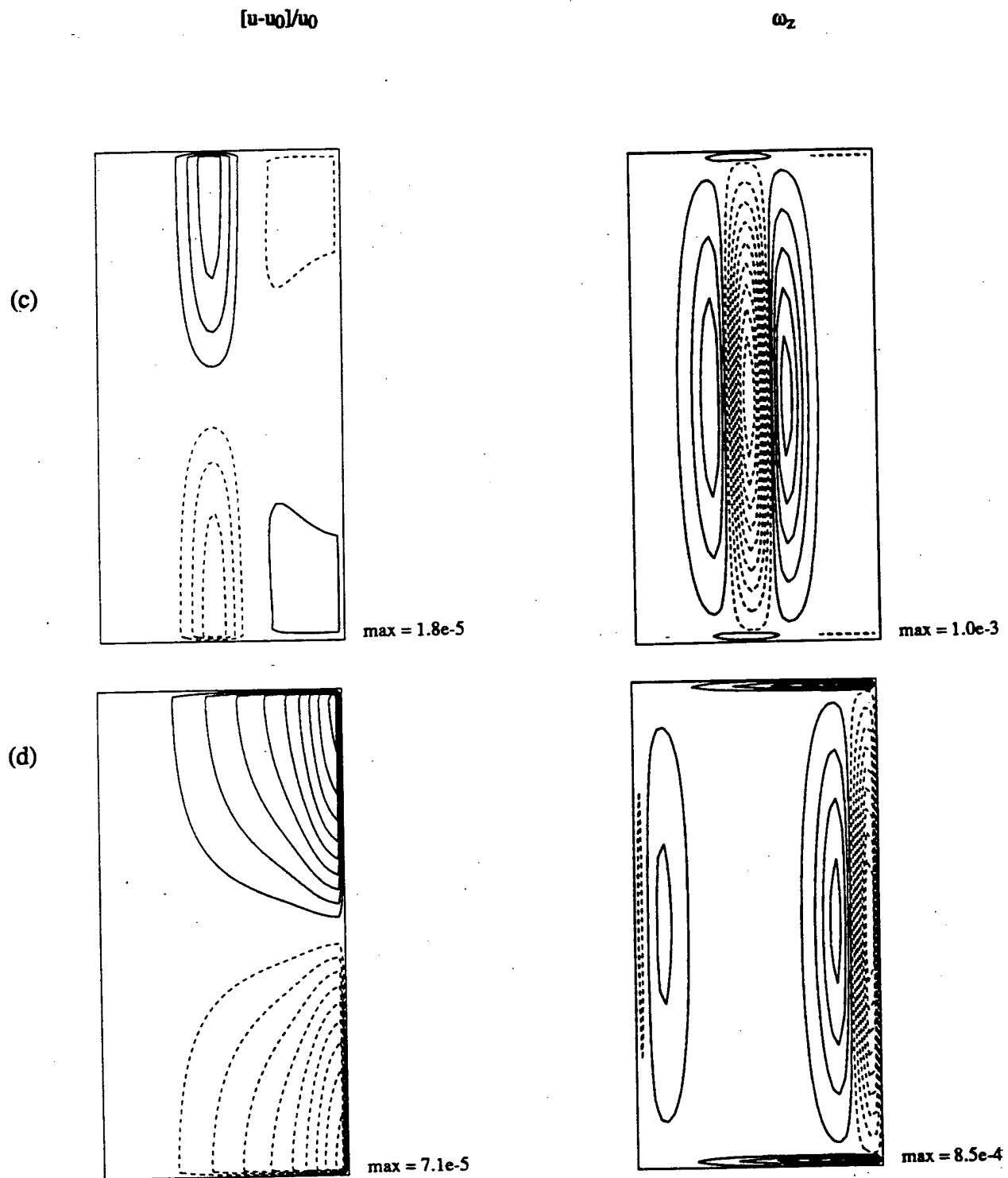


Figure 3.8.1(continued) (c) $t = 2$, (d) $t = 3$.

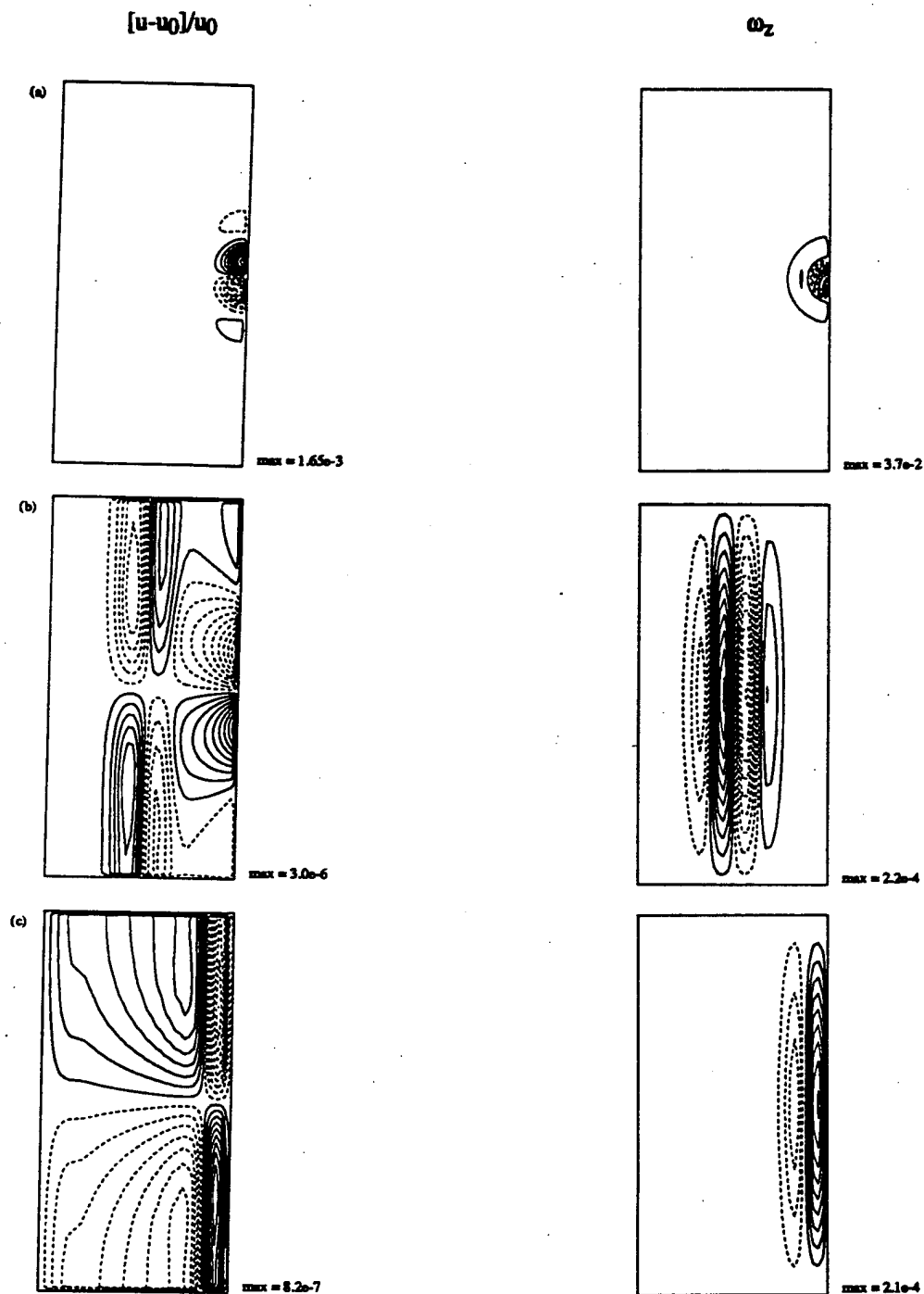


Figure 3.8.2 Velocity difference and spanwise vorticity for a convecting vortex using boundary condition (3.8.1b)
(a) $t = 1$, (b) $t = 2$, (c) $t = 3$.

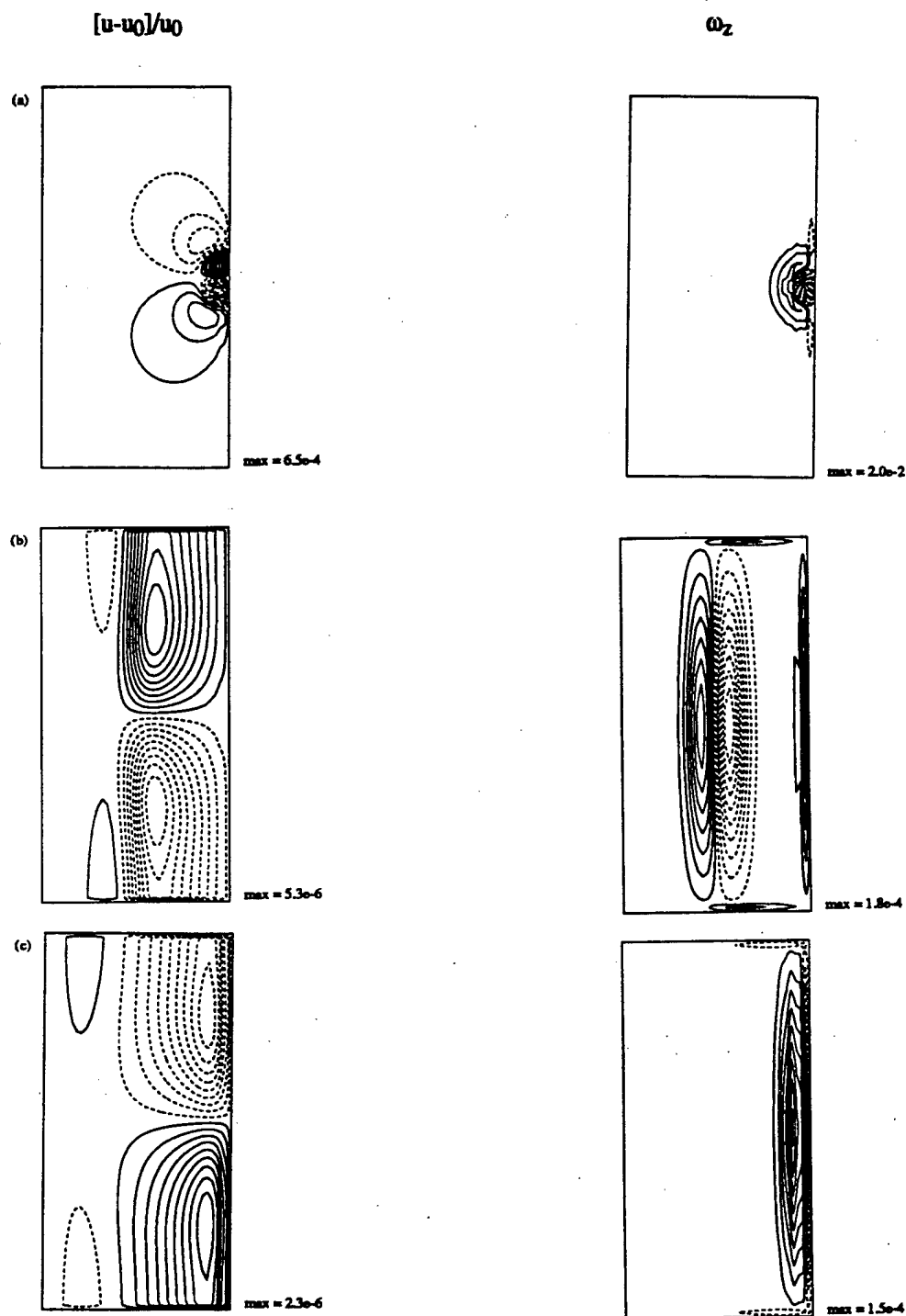


Figure 3.8.3 Velocity difference and spanwise vorticity for a convecting vortex using boundary condition (3.8.1c) (a) $t = 1$, (b) $t = 2$, (c) $t = 3$.

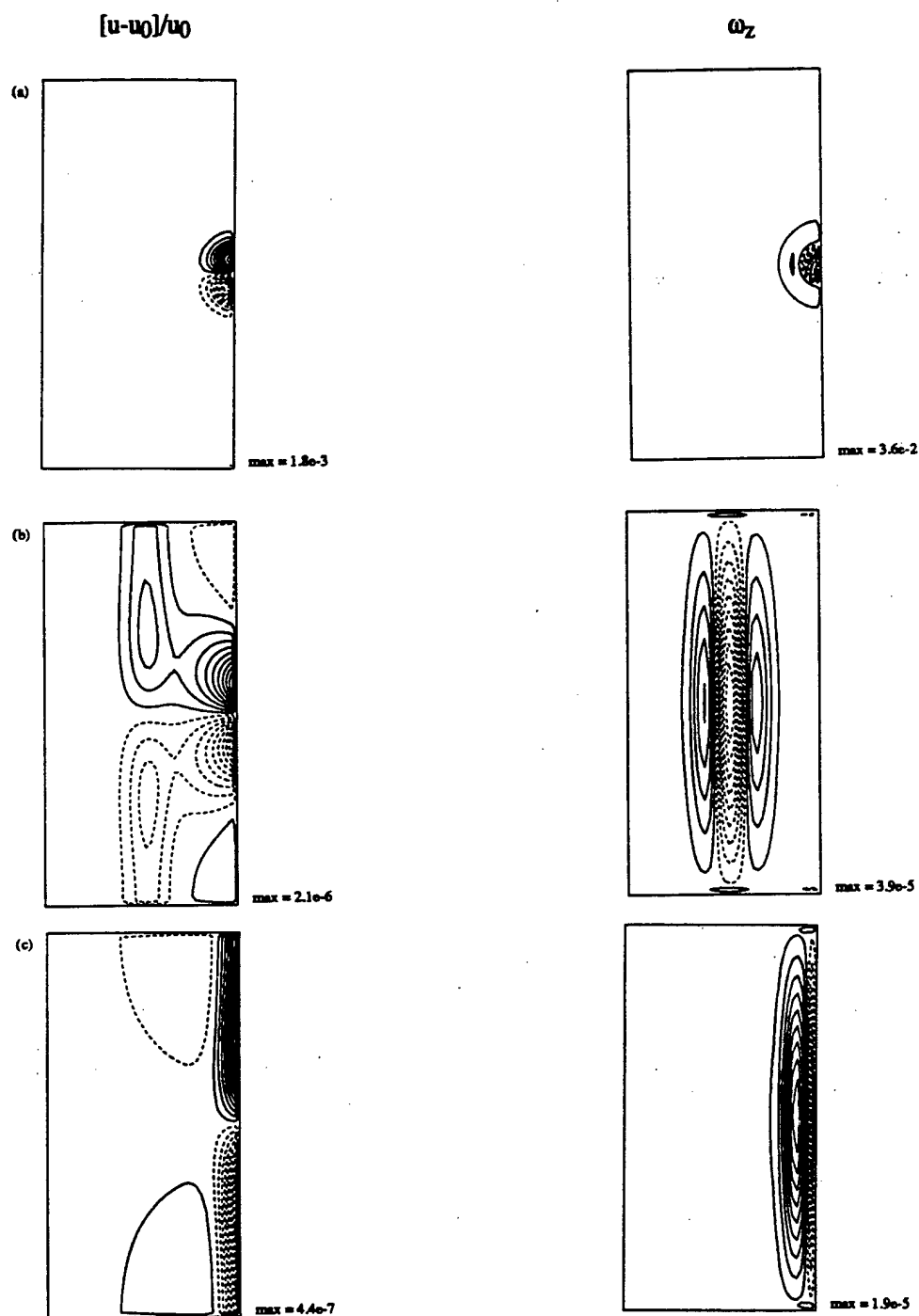


Figure 3.8.4

Velocity difference and spanwise vorticity for a convecting vortex using boundary condition (3.8.1d)
(a) $t = 1$, (b) $t = 2$, (c) $t = 3$.

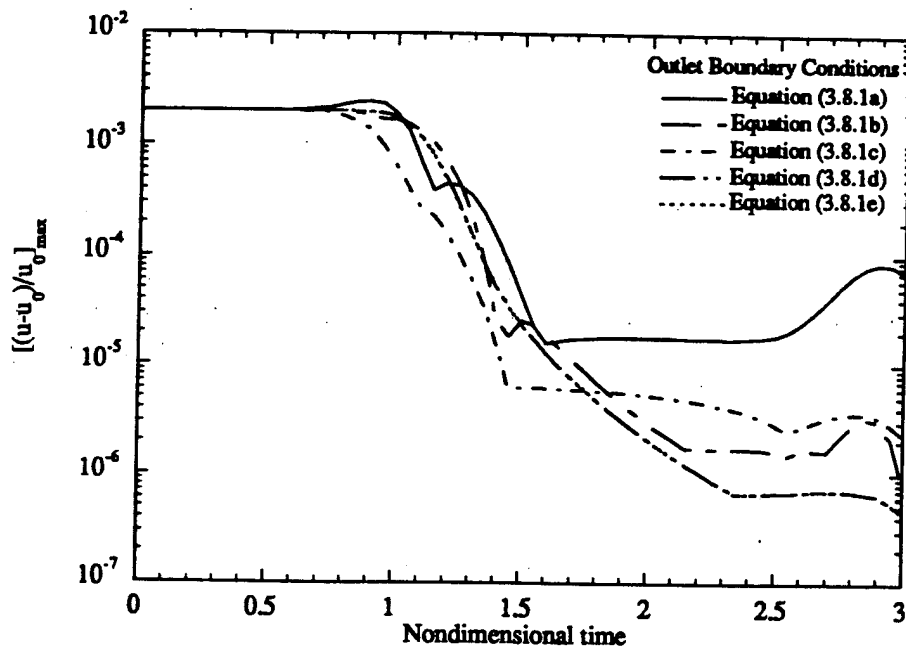


Figure 3.8.5 Time variation of the maximum streamwise velocity difference, $[(u-u_0)/u_0]_{\max}$, for a convecting vortex. Comparison of various outlet boundary conditions.

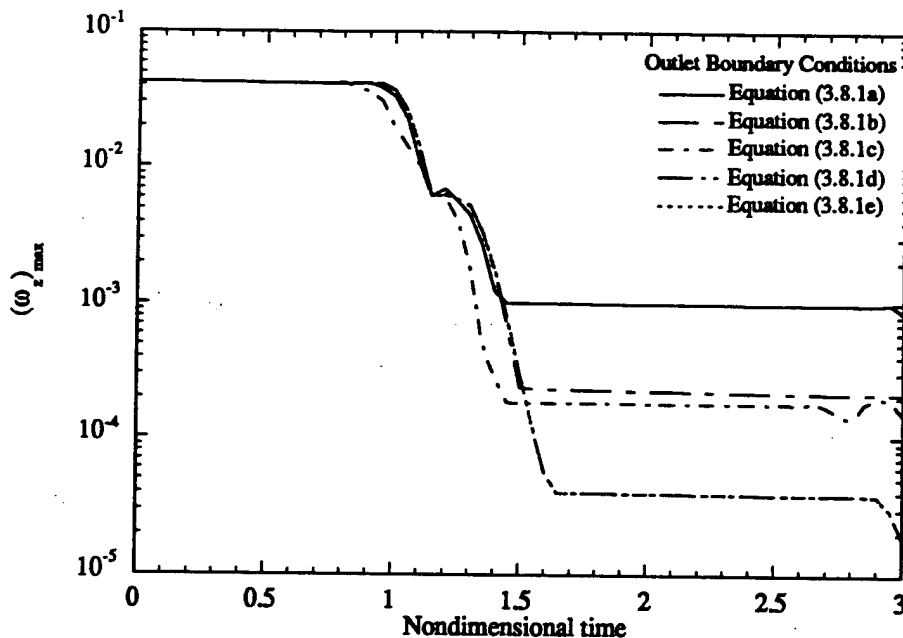


Figure 3.8.6 Time variation of the maximum spanwise vorticity, $(\omega_z)_{\max}$, for a convecting vortex. Comparison of various outlet boundary conditions.

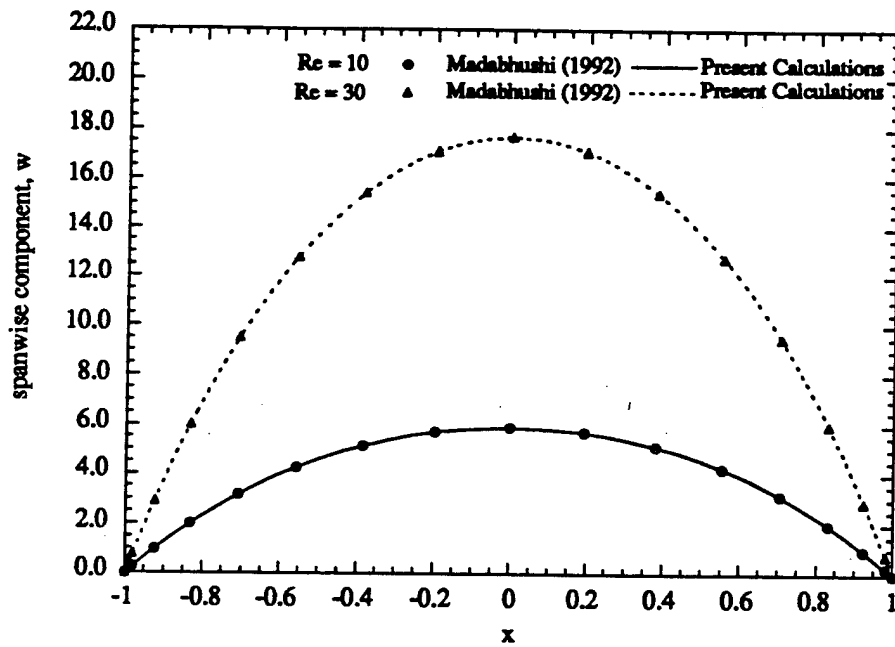


Figure 4.4.1 Distribution of the spanwise velocity component in the x-direction at $y = 0$ for the fully-developed laminar flow through a square duct at $Re = 10$ and 30 .

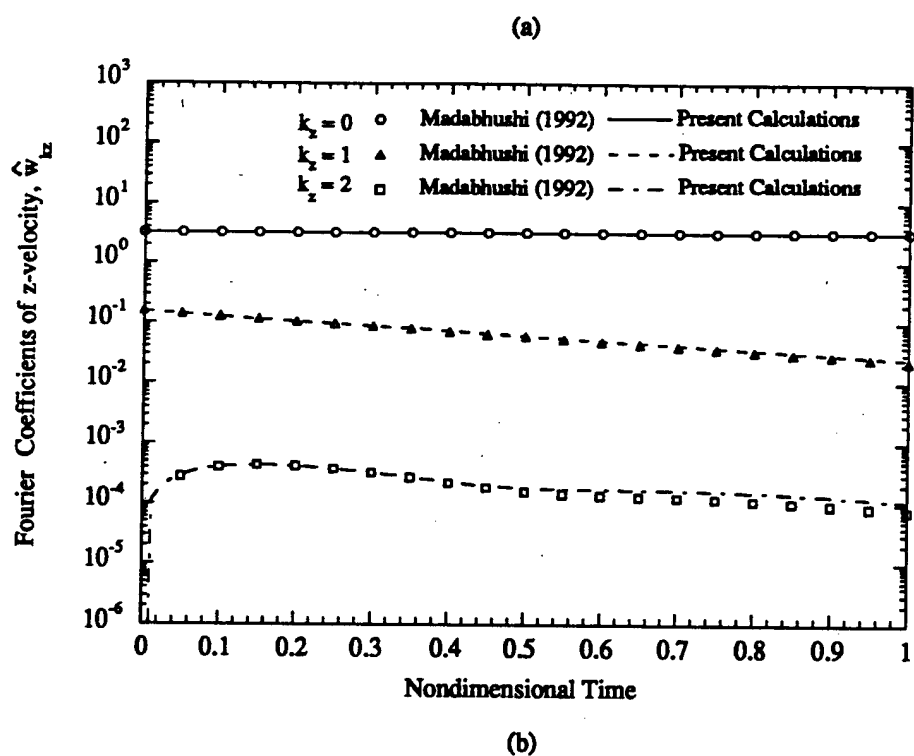
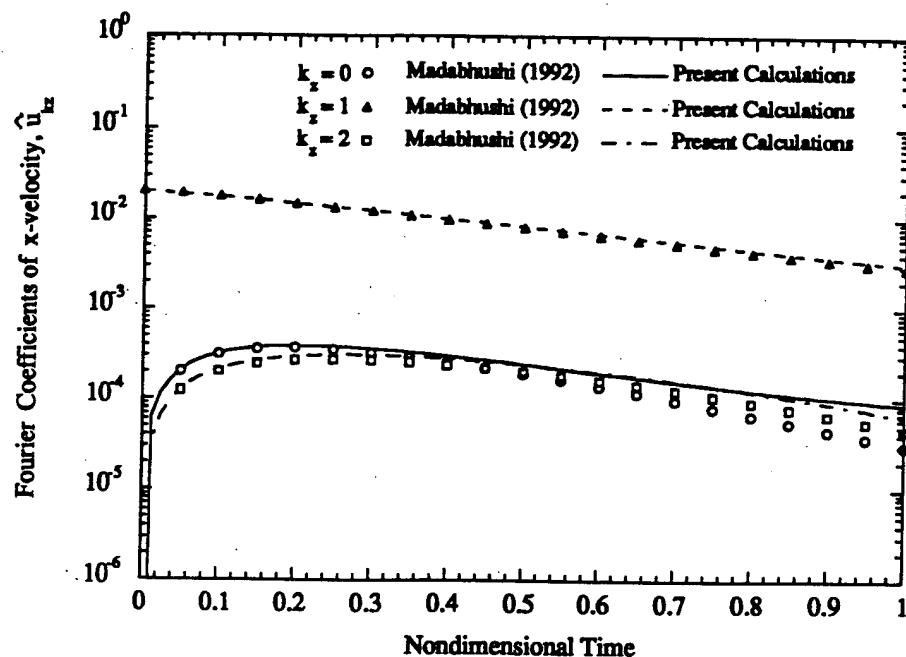


Figure 4.4.2

Temporal evolution of (a) \hat{u}_{kz} and (b) \hat{w}_{kz} at $x = y = -0.5625$ for the decay of a 3-D perturbation in a laminar flow through a square duct at $Re = 10$ and $\epsilon = 0.05$.

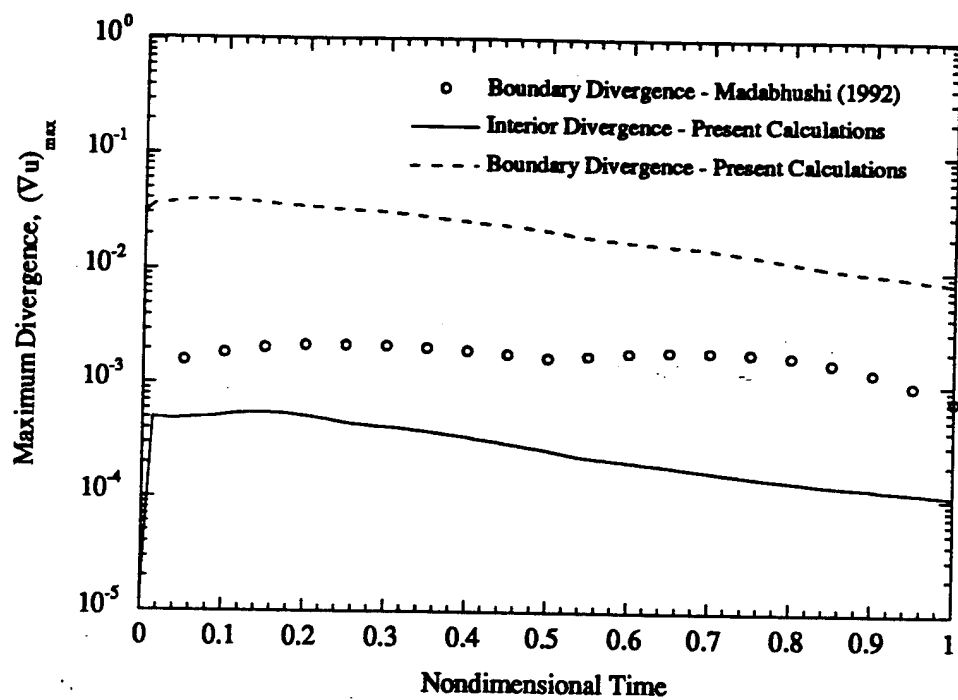


Figure 4.4.3 Temporal variation of the maximum divergence for the decay of a 3-D perturbation in a laminar square duct at $Re = 10$ and $\epsilon = 0.05$.

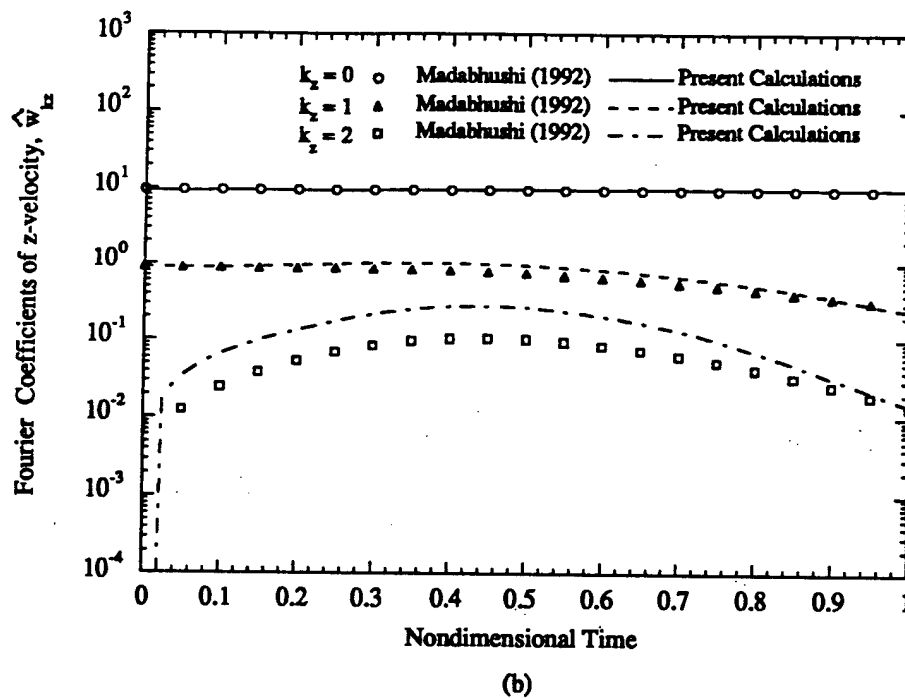
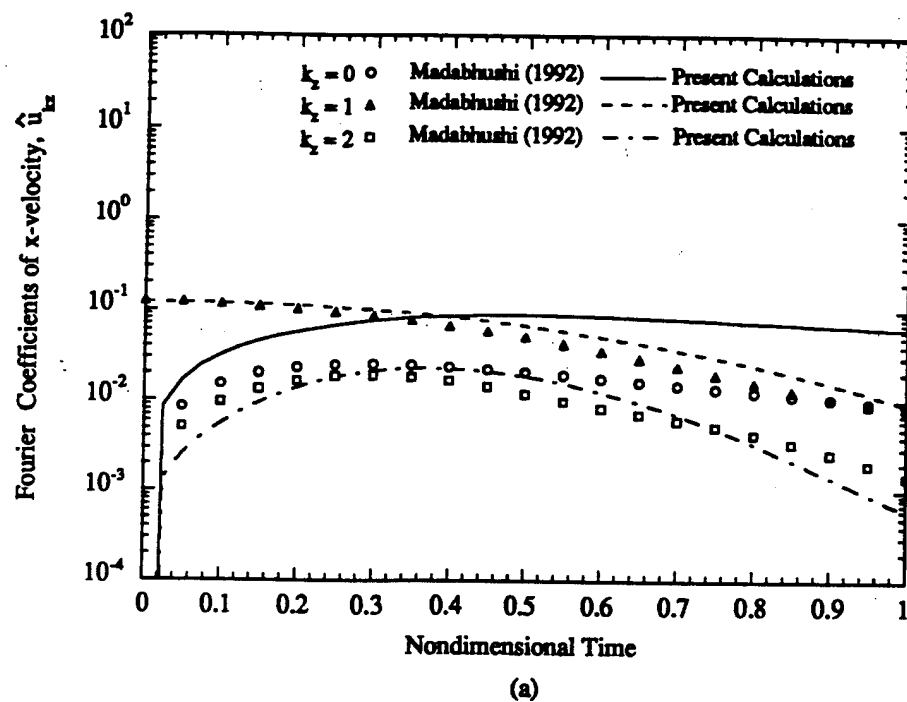


Figure 4.4.4 Temporal evolution of (a) \hat{u}_{kz} and (b) \hat{w}_{kz} at $x = y = -0.5625$ for the decay of a 3-D perturbation in a laminar flow through a square duct at $Re = 30$ and $\epsilon = 0.3$.

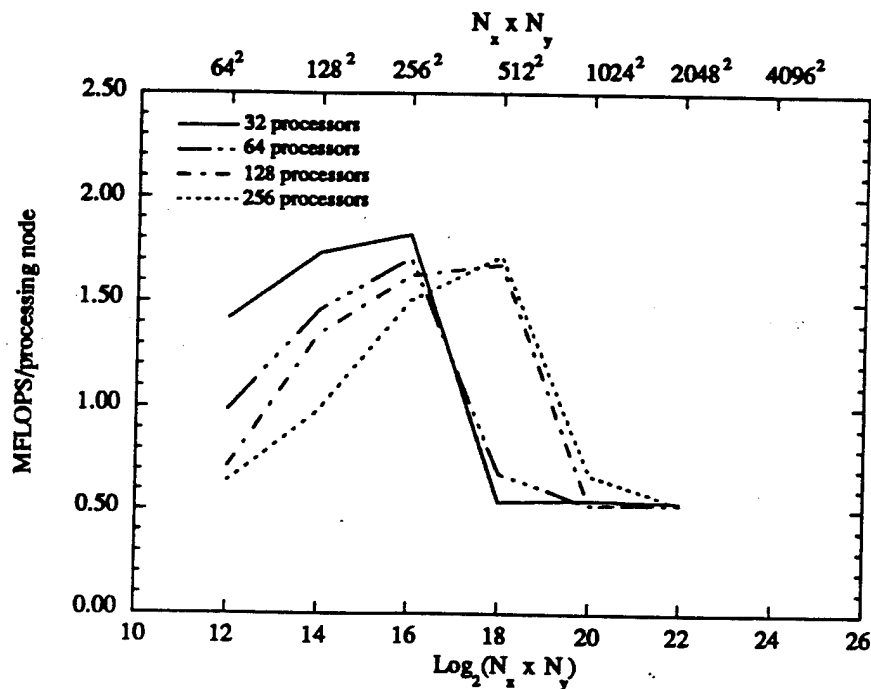


Figure 5.2.1.1 Performance of a triad operation, $A = A + B \cdot C$, in scalar mode for various CM-5 partitions.

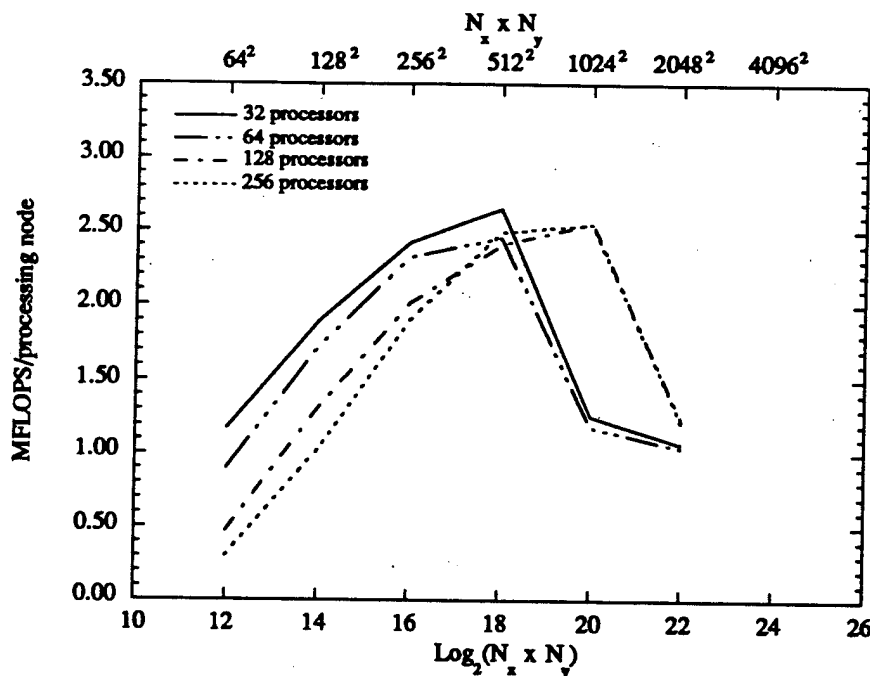


Figure 5.2.1.2 Performance of the matrix-matrix multiplication using CMSSL routine, `gen_matrix_mult`, in scalar mode for various CM-5 partitions.

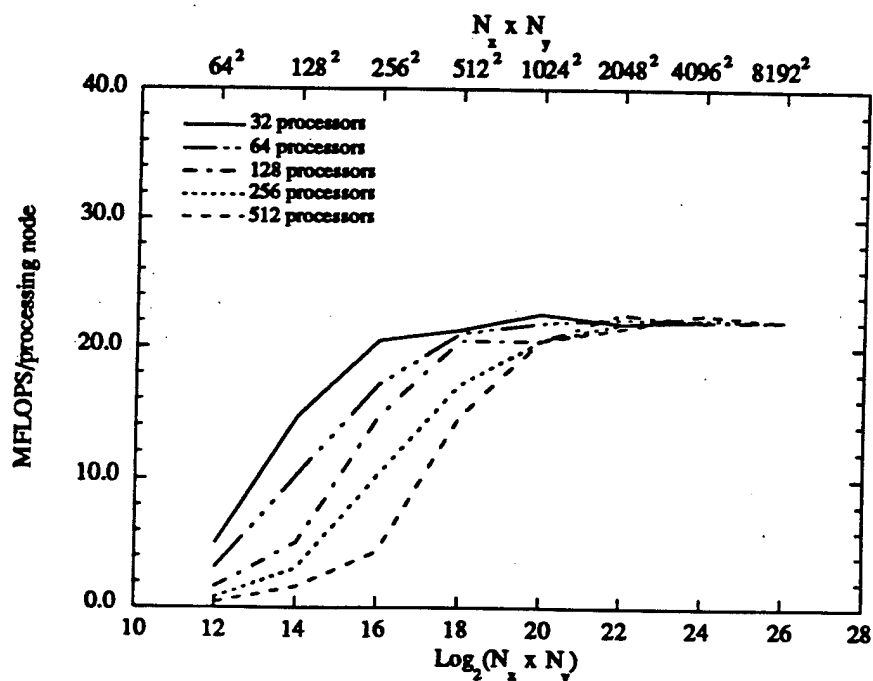


Figure 5.2.1.3 Performance of a triad operation, $A = A + B \cdot C$, in vector mode for various CM-5 partitions.

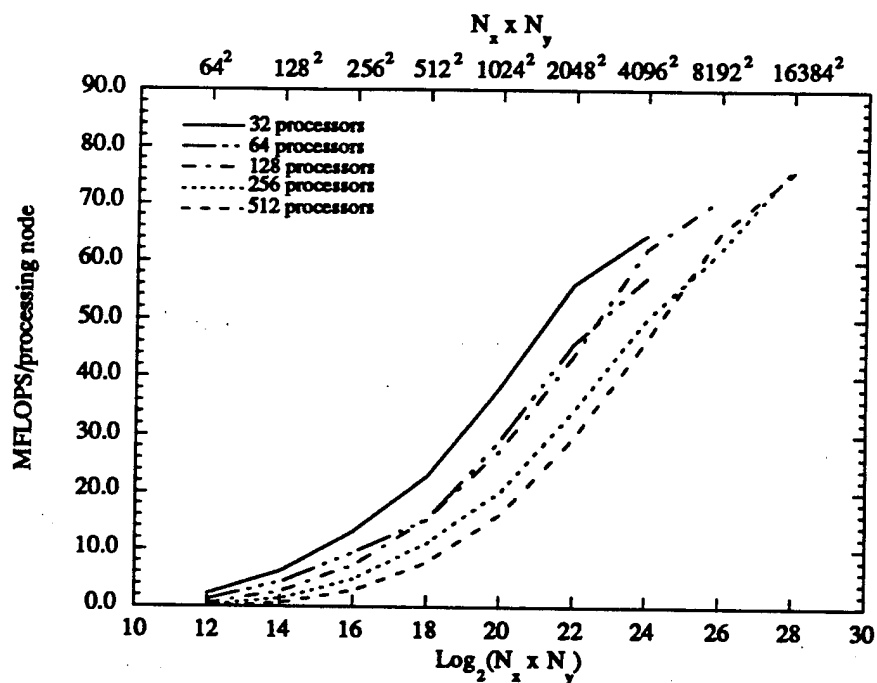


Figure 5.2.1.4 Performance of the matrix-matrix multiplication using CMSSL routine, `gen_matrix_mult`, in vector mode for various CM-5 partitions.

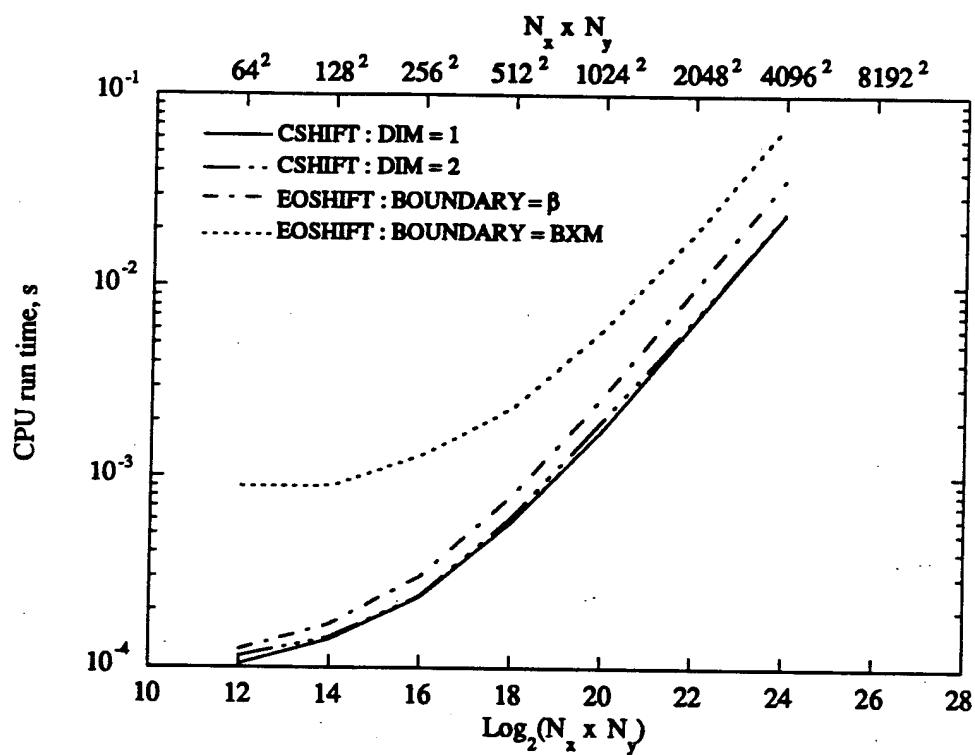


Figure 5.2.1.5 CPU run times for the communication functionalities on 32-processor partition.

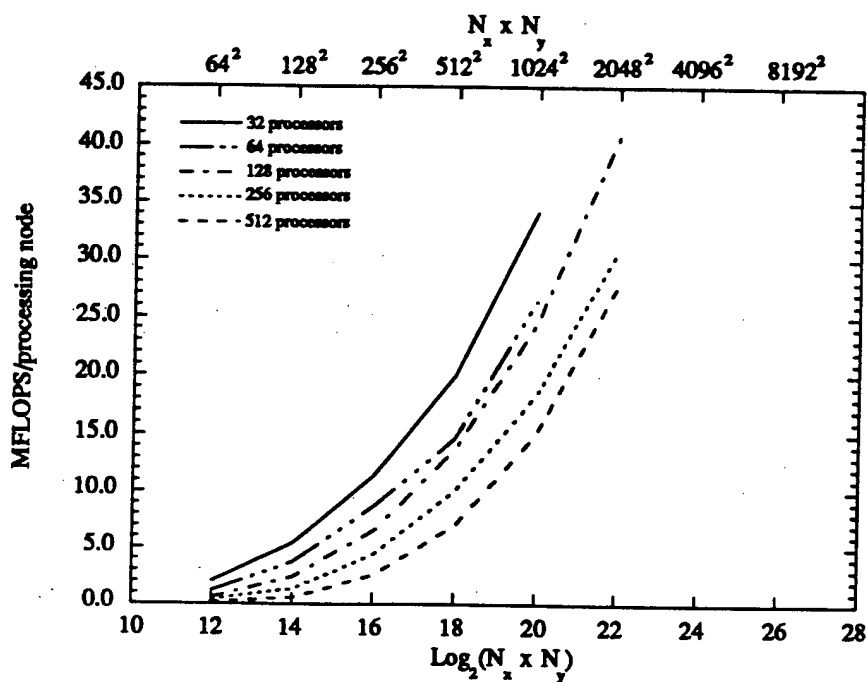


Figure 5.2.3.1 Performance of the two-dimensional data-parallel algorithm on various CM-5 partitions.

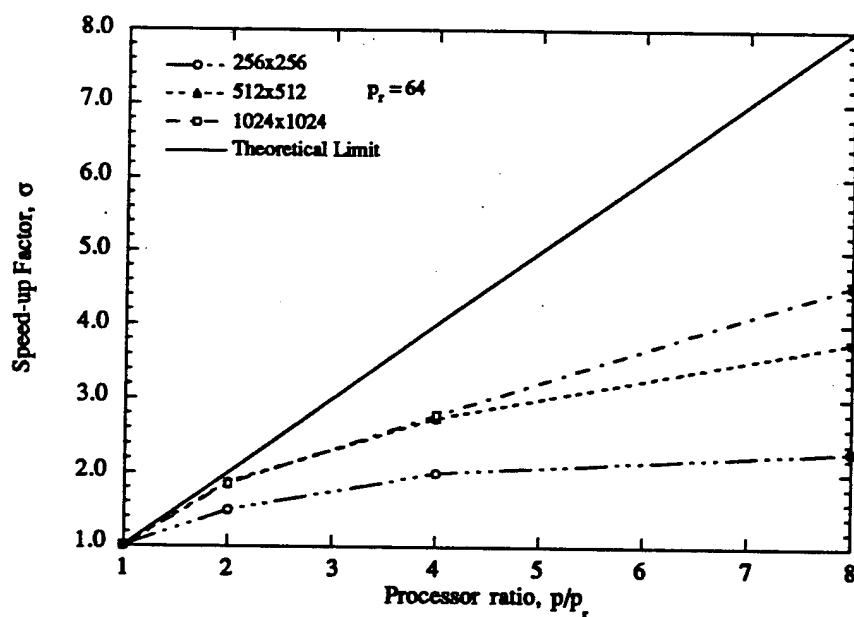


Figure 5.2.3.2 Speed-up factors of the two-dimensional data-parallel algorithm for various processor ratios

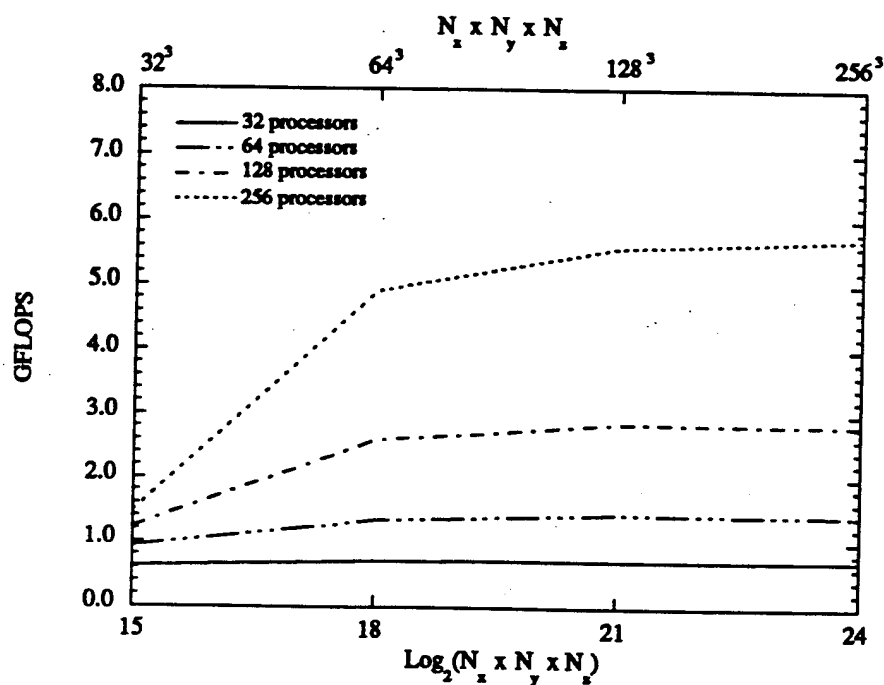


Figure 5.3.1.1 Performance of a triad operation, $A = A + B * C$, for various CM-5 partitions. Array axes have a (NEWS) layout.

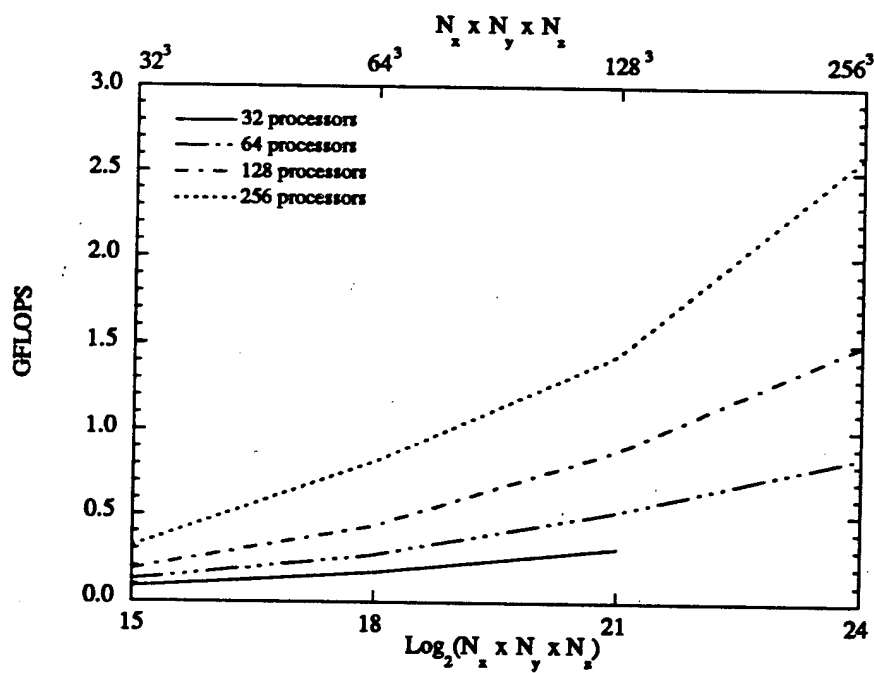


Figure 5.3.1.2 Performance of the matrix-matrix multiplication using CMSSL routine, gen_matrix_mult , for various CM-5 partitions. Array axes have a (NEWS) layout.

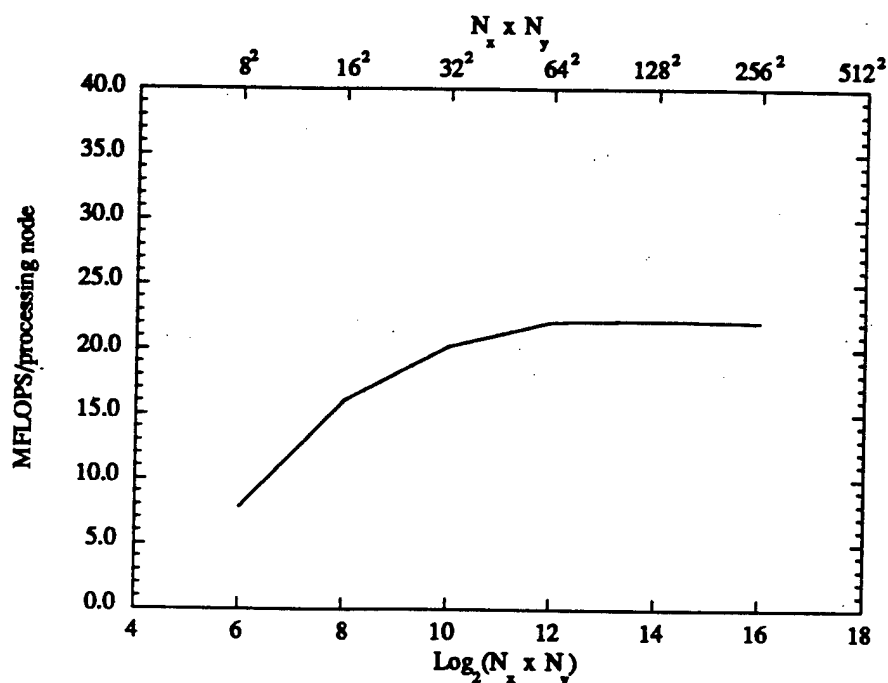


Figure 5.3.1.3 Performance of triad operation, $A = A + B \cdot C$, for three-dimensional arrays with $N_z = 128$ on a 32-processor partition.

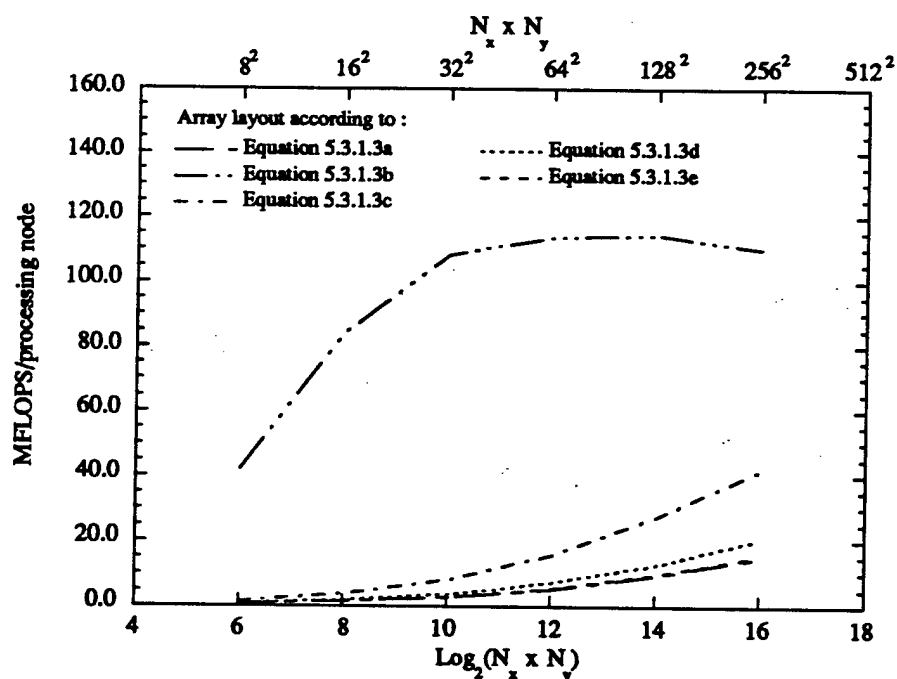


Figure 5.3.1.4 Performance of matrix-matrix multiplication using CMSSL routine, `gen_matrix_mult`, for various layouts of the three-dimensional arrays on a 32-processor partition ($N_z = 128$).

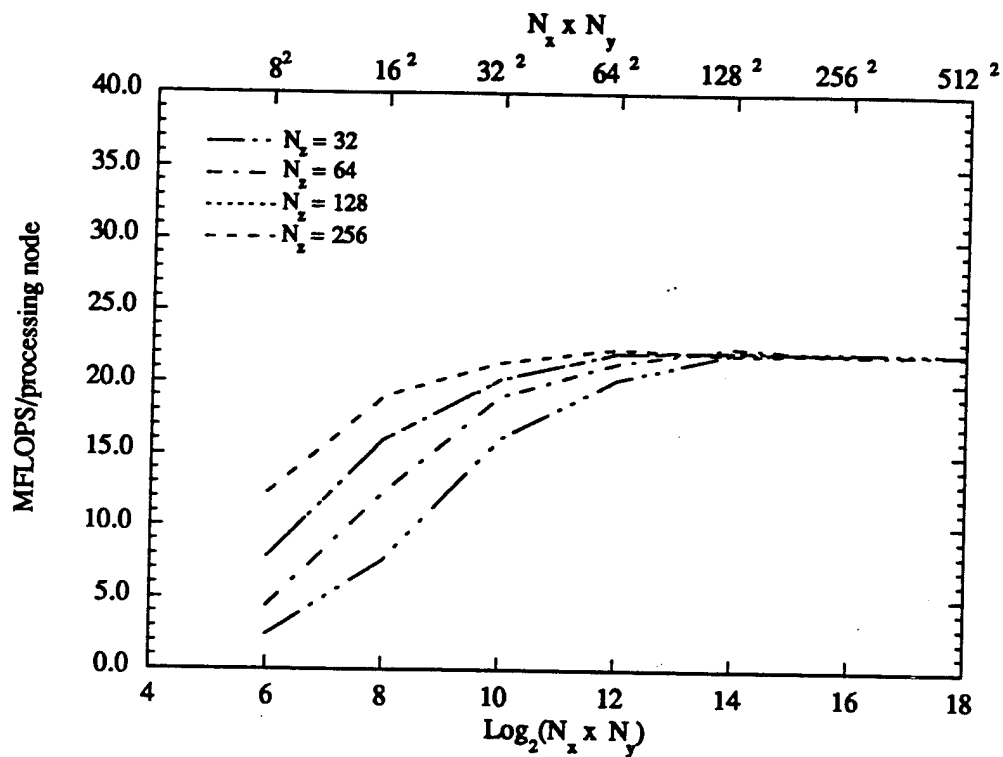


Figure 5.3.1.5 Performance of triad operation, $A = A + B \cdot C$, for three-dimensional arrays with various N_z on a 32-processor partition. Array axes have a (BLOCK/PROCS) layout.

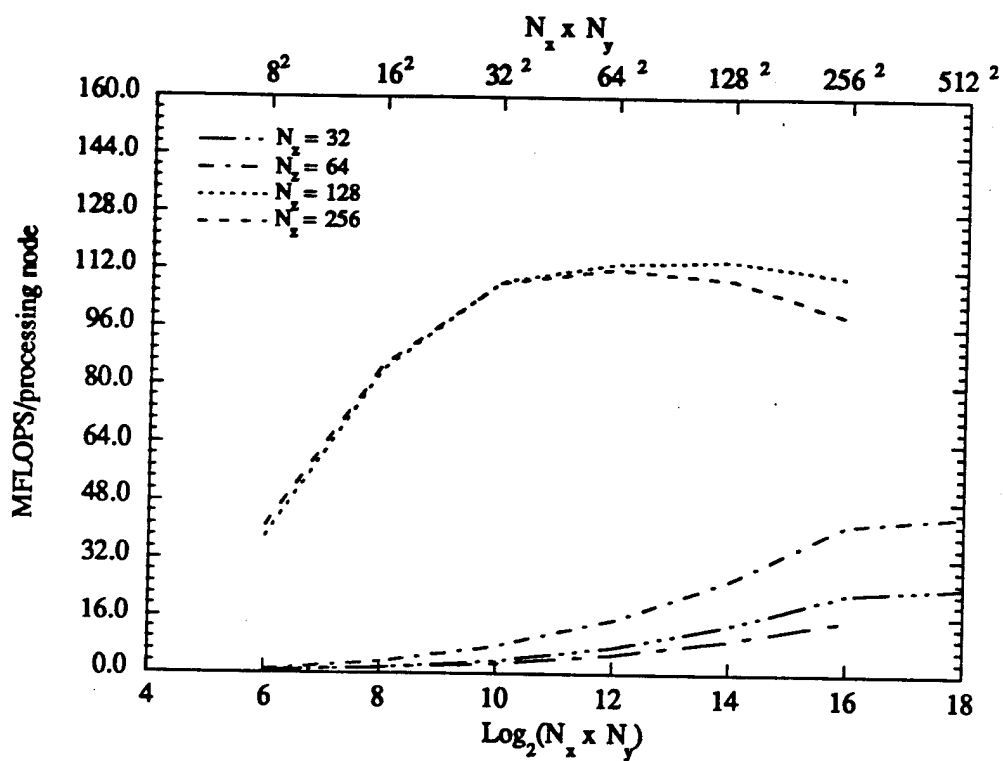


Figure 5.3.1.6 Performance of the matrix-matrix multiplication using CMSSL routine, `gen_matrix_mult`, for three-dimensional arrays on a 32-processor partition. Array axes have a (BLOCK/PROCS) layout.

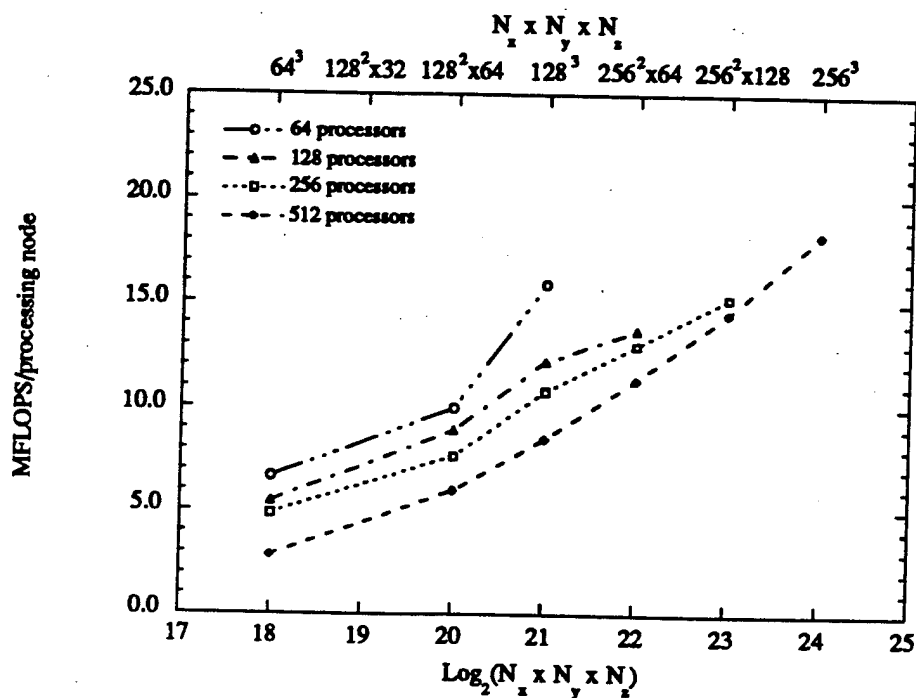


Figure 5.3.3.1 Performance of the three-dimensional data-parallel algorithm on various CM-5 partition sizes.

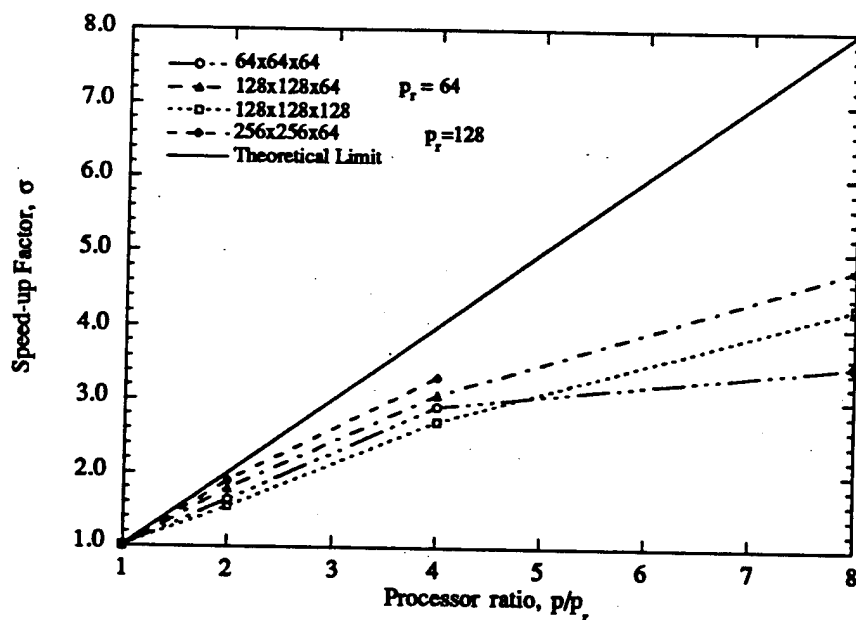


Figure 5.3.3.2 Speed-up factors of the three-dimensional data-parallel algorithm for various processor ratios.

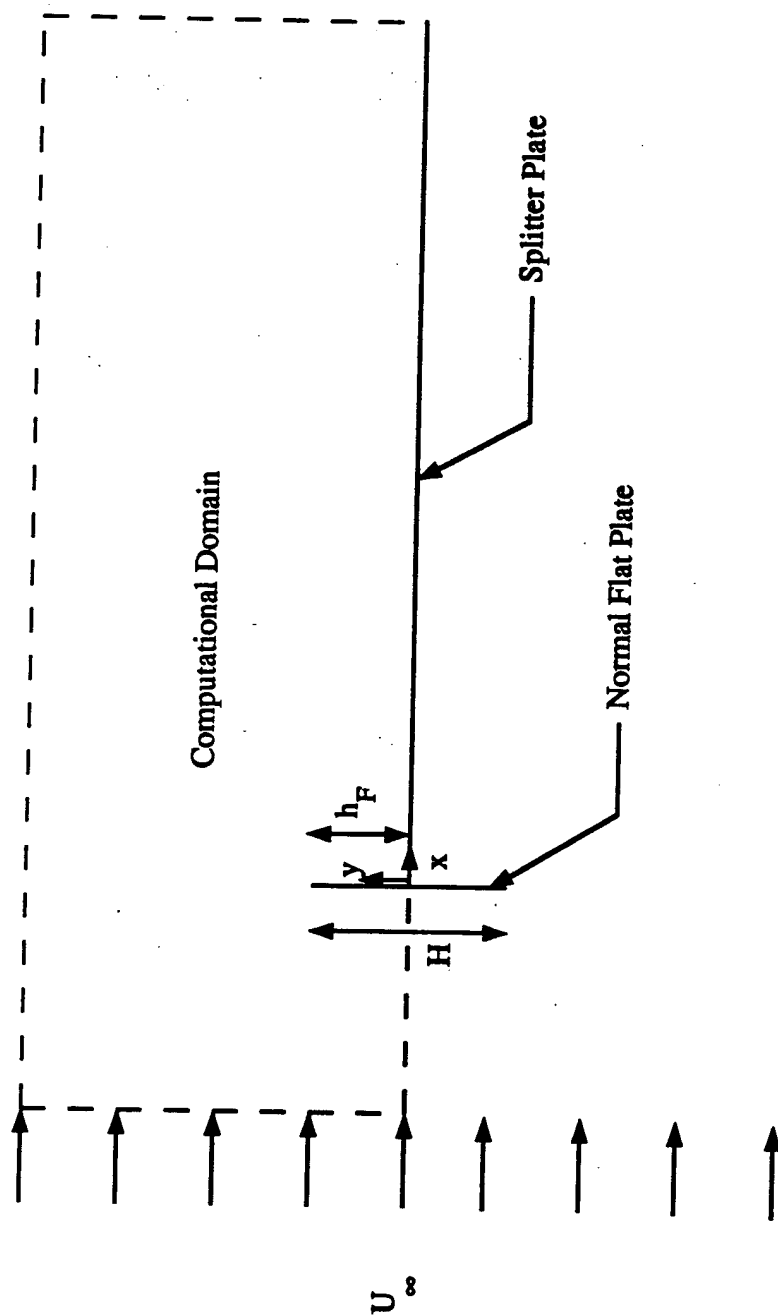


Figure 6.1.1 Schematic of the geometrical configuration and the computational domain for the separated-reattaching flow.

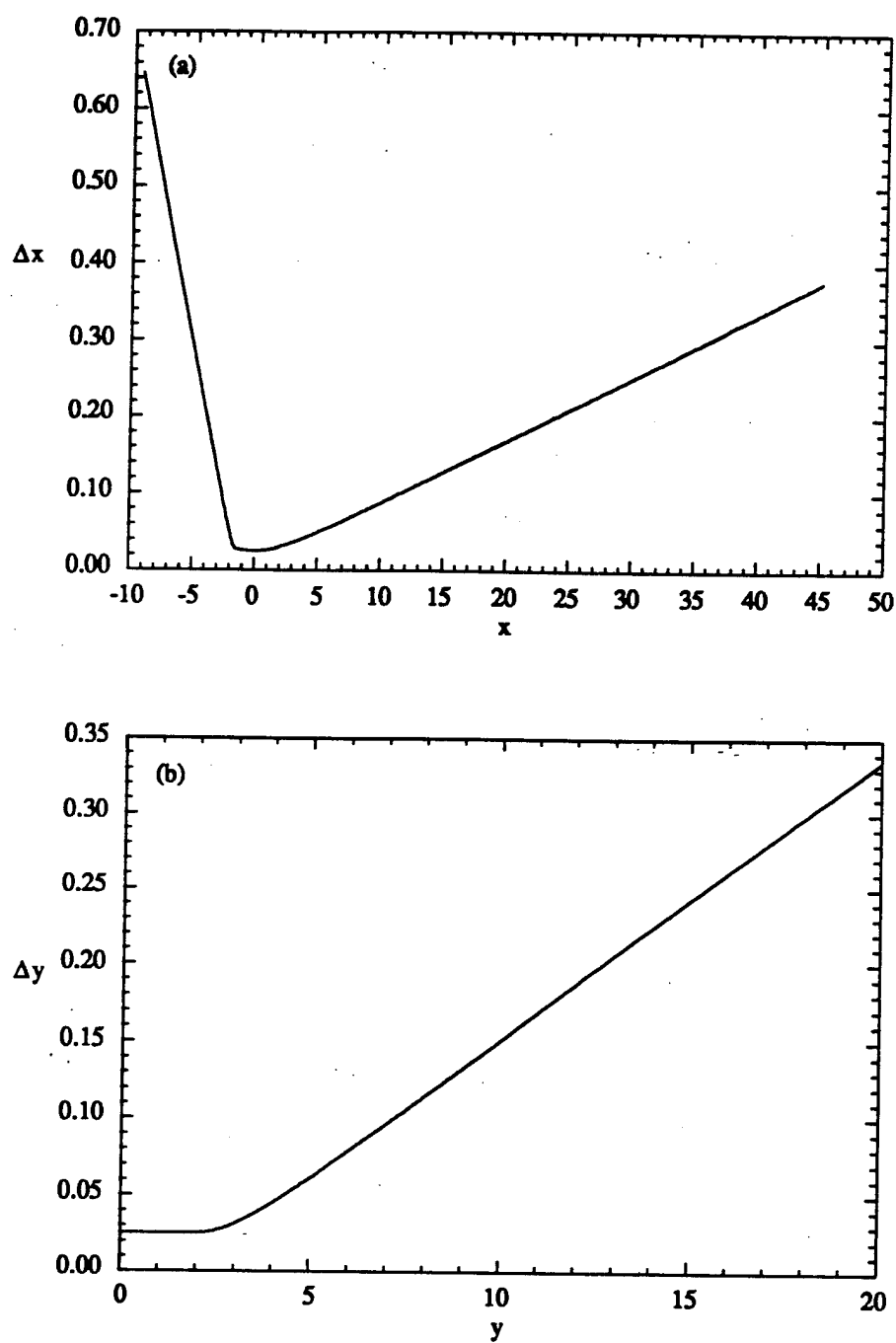


Figure 6.1.1.1 Distribution of the mesh size in (a) x-direction, and (b) y-direction.

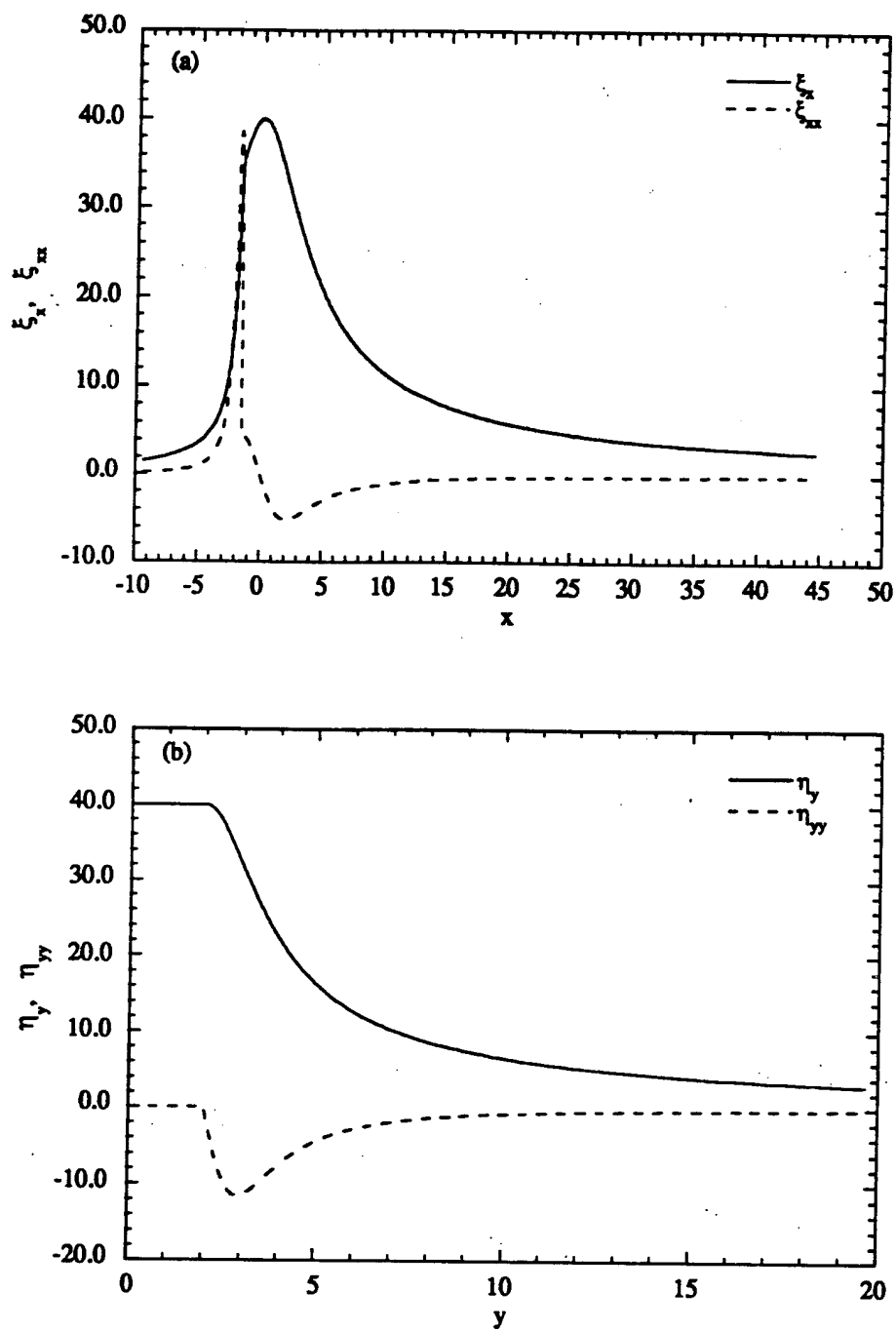


Figure 6.1.1.2 Distribution of the metrics in (a) x-direction, and (b) y-direction.

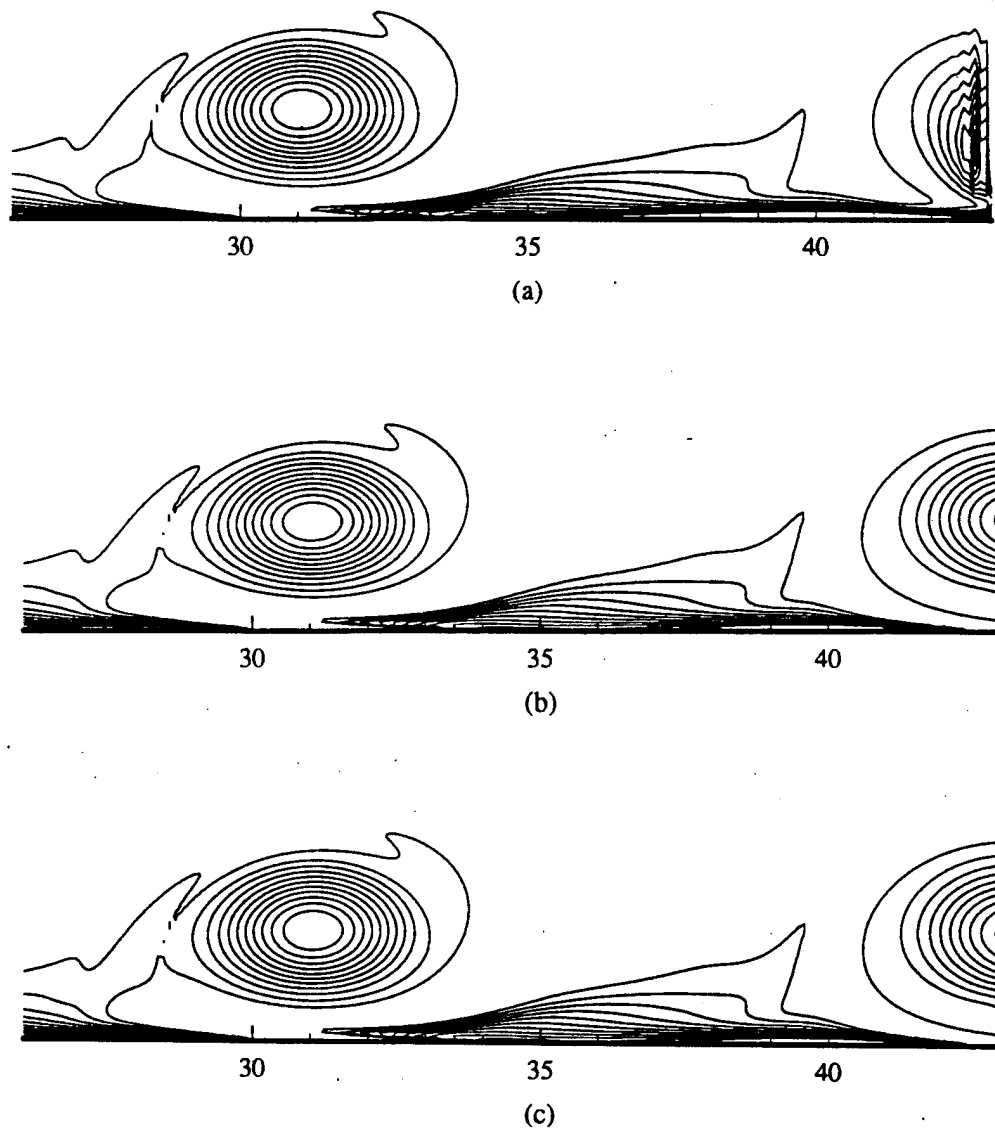


Figure 6.1.2.1 Contours of spanwise vorticity, ω_z , near the outlet boundary for (a) Equation (3.8.1c), (b) Equation (3.8.1d), (c) Equation (3.8.1e) ($\omega_{zmin}, \omega_{zmax}, \Delta\omega_z = (-2.05, -0.05, 0.2)$)

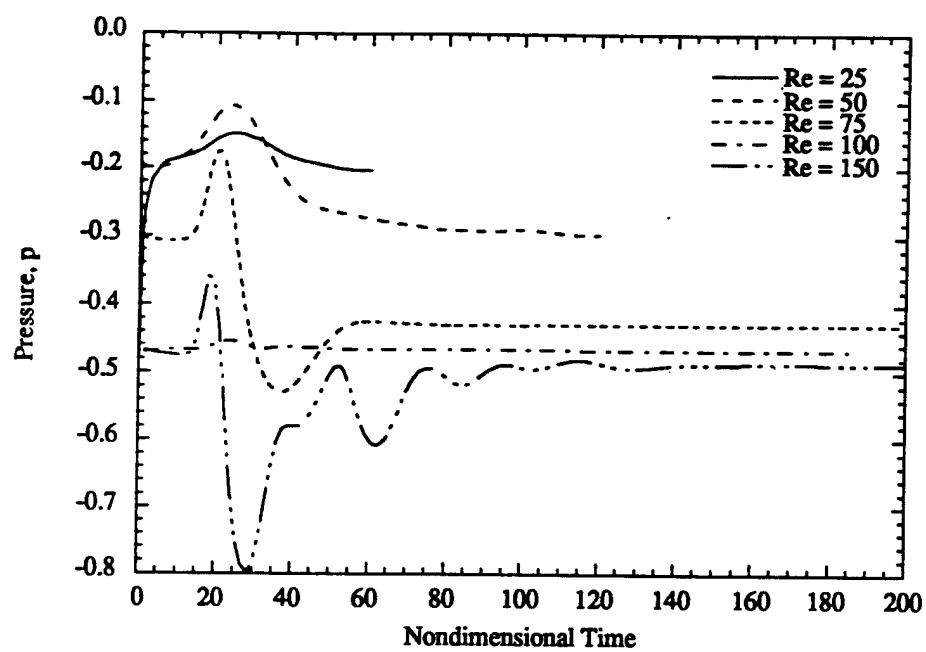


Figure 6.1.3.1 Temporal evolution of the pressure signals at $x = 15.25$, $y = 1.5$ for the steady regime.

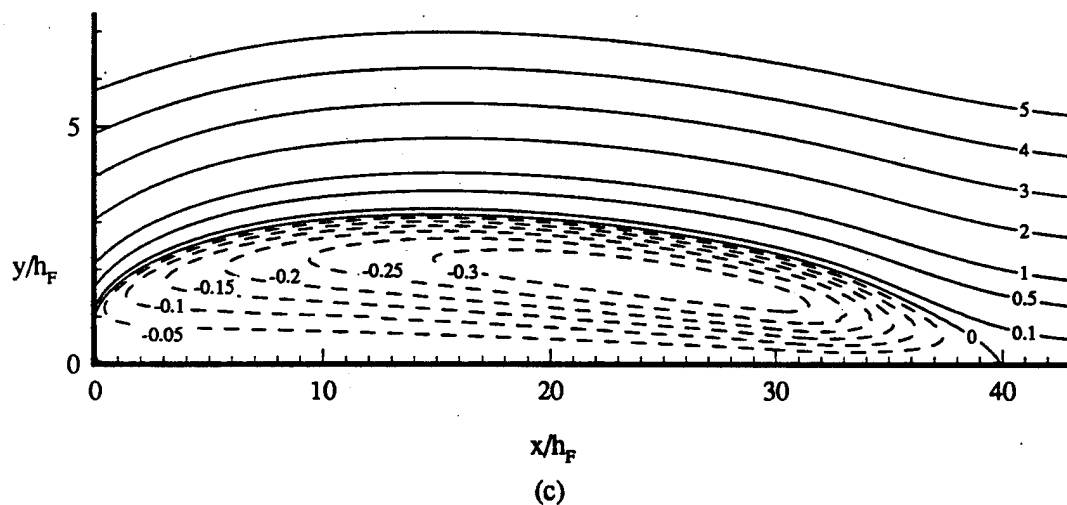
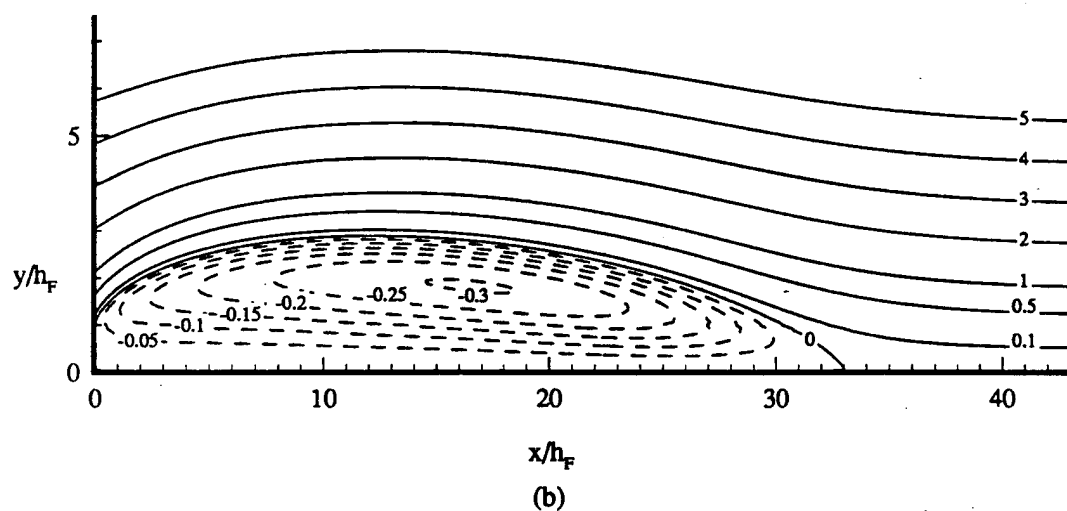
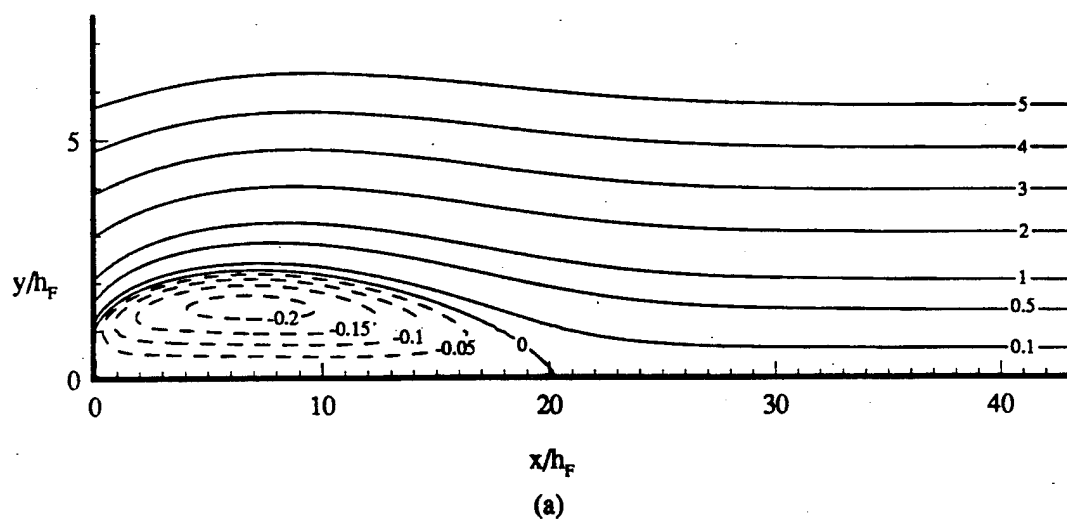


Figure 6.1.3.2 Streamlines in the steady regime: (a) $Re = 50$, (b) $Re = 100$, (c) $Re = 150$.

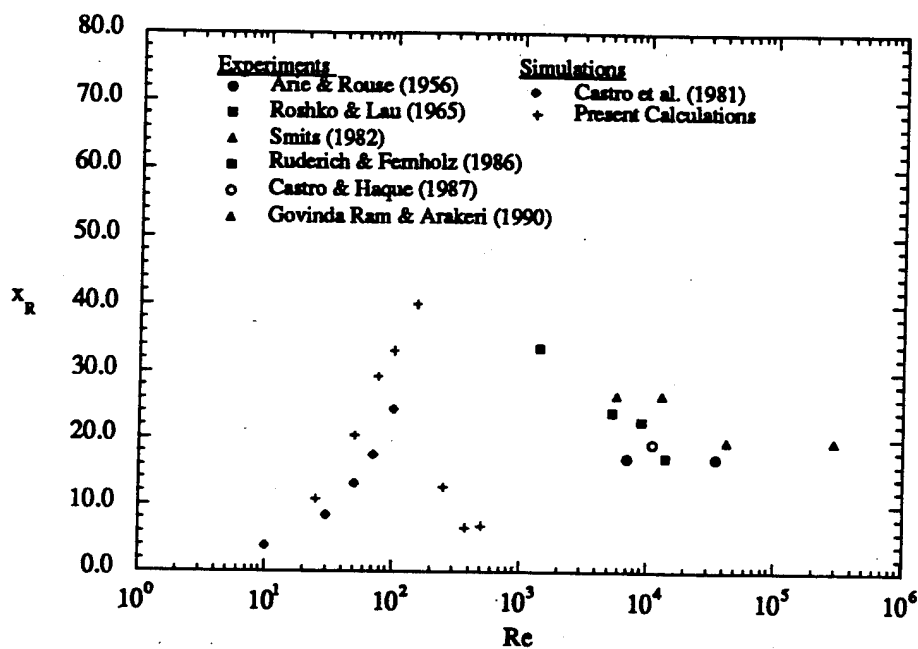


Figure 6.1.3.3 Variation of the reattachment length, x_R , with free-stream Reynolds number compiled from experiments and calculations.

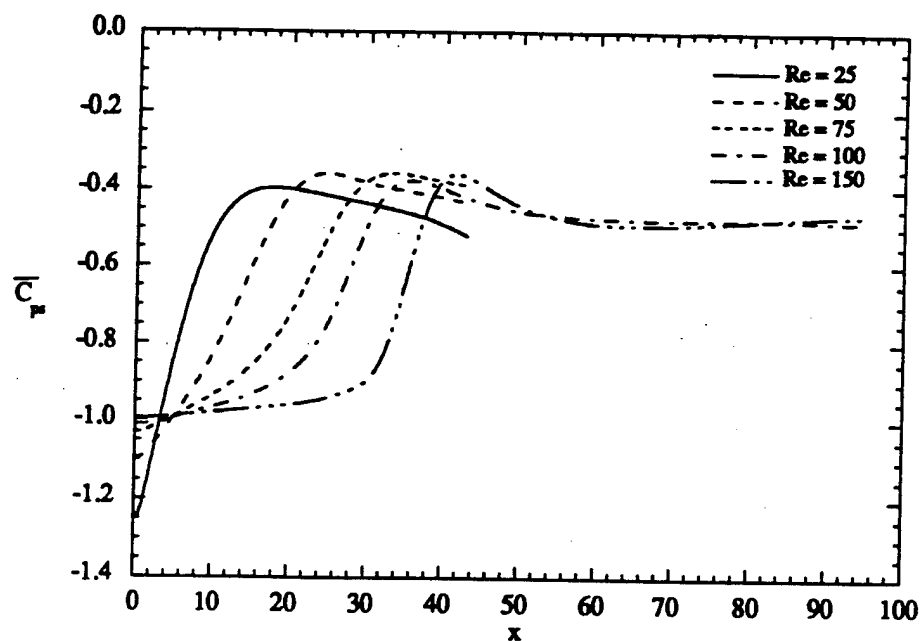


Figure 6.1.3.4 Streamwise distribution of the surface pressure coefficient, \overline{C}_{p_s} , in the steady regime.

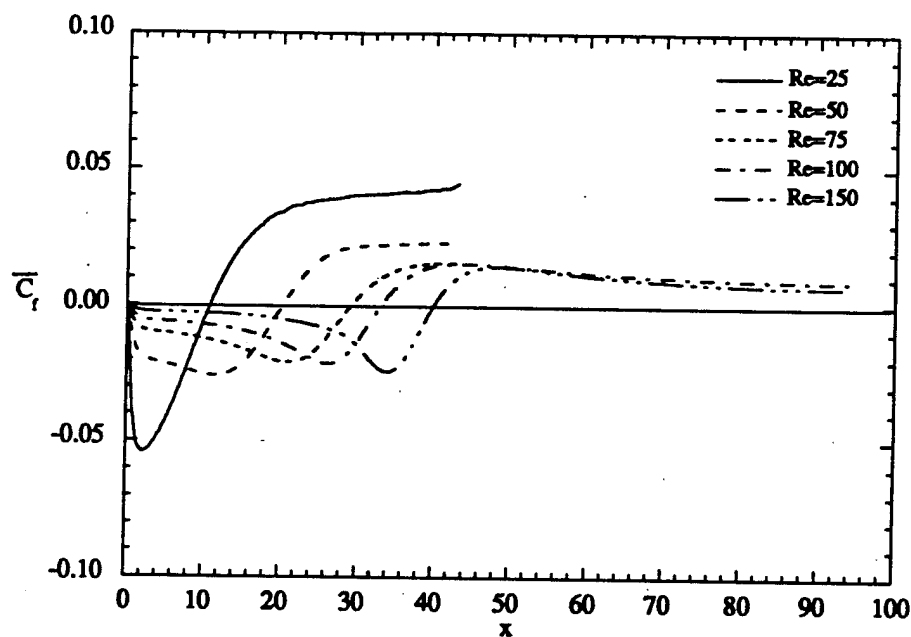


Figure 6.1.3.5 Streamwise distribution of the skin-friction factor, \overline{C}_f , in the steady regime.

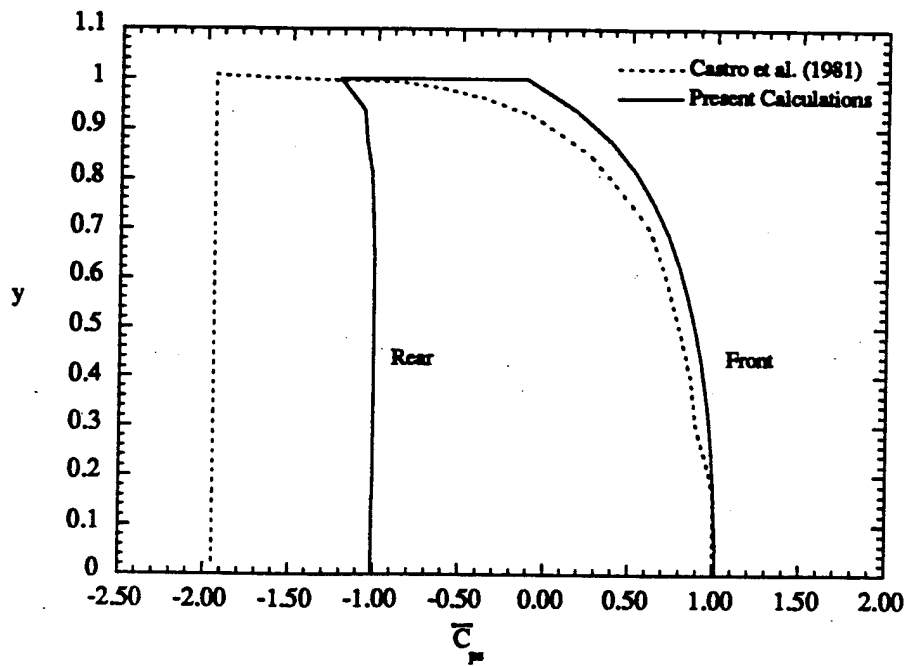


Figure 6.1.3.6 Distribution of the surface pressure coefficient, \overline{C}_p , on the front and rear faces of the plate for $Re = 100$.

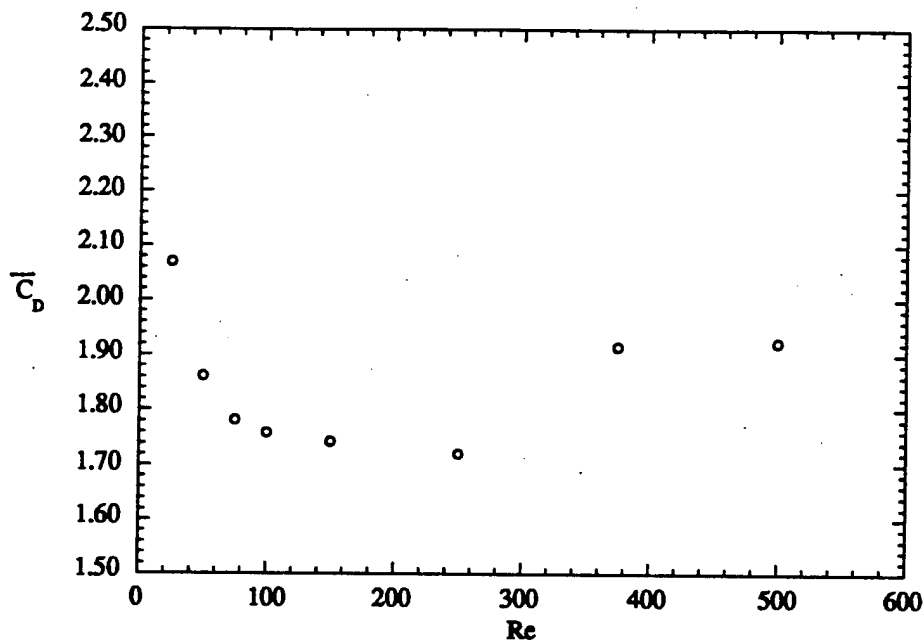


Figure 6.1.3.7 Variation of the time-mean drag coefficient, \overline{C}_D , with free-stream Reynolds numbers.

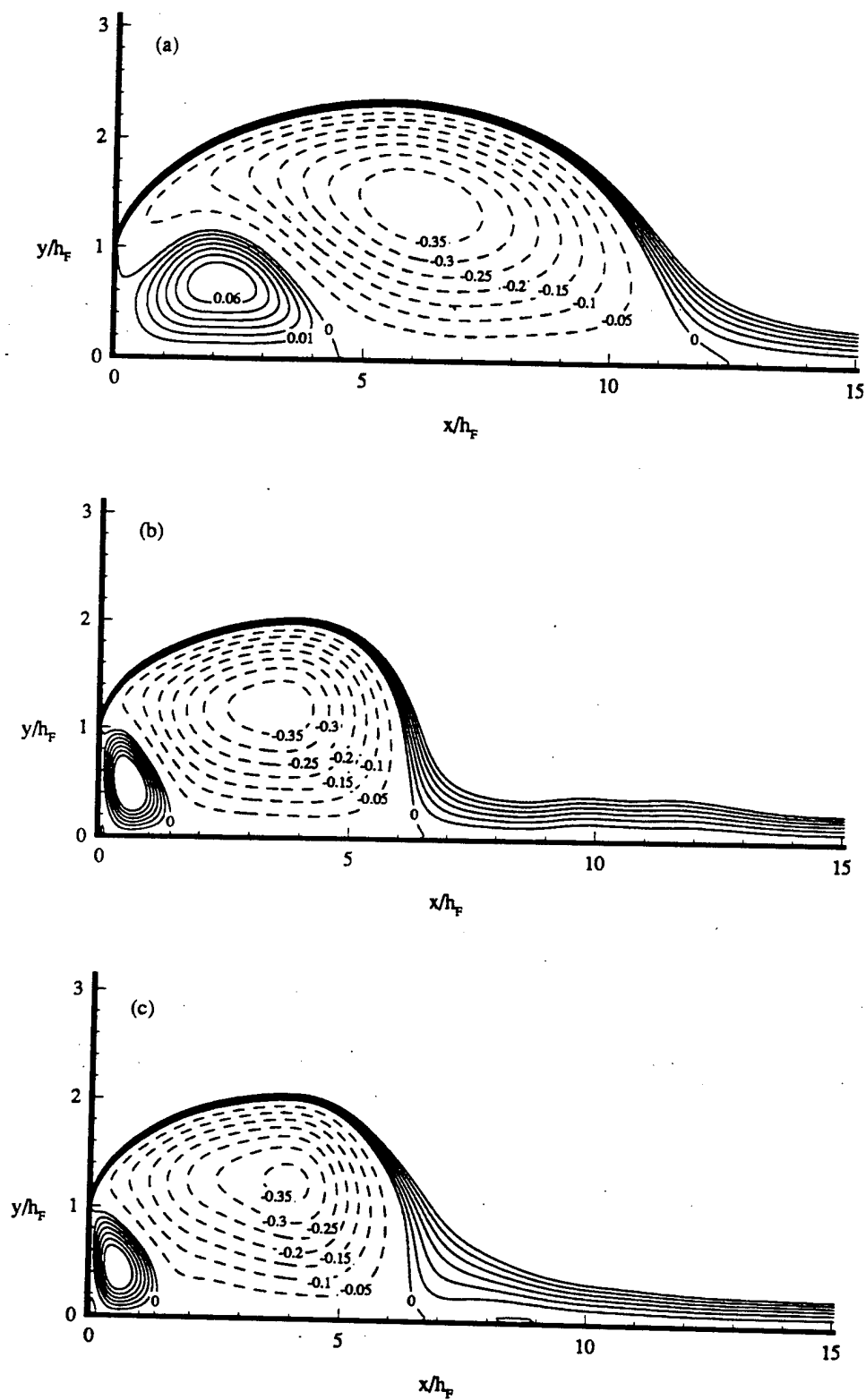


Figure 6.1.4.1.1 Time-mean streamlines in the unsteady regime.
 (a) $Re = 250$, (b) $Re = 375$, (c) $Re = 500$.

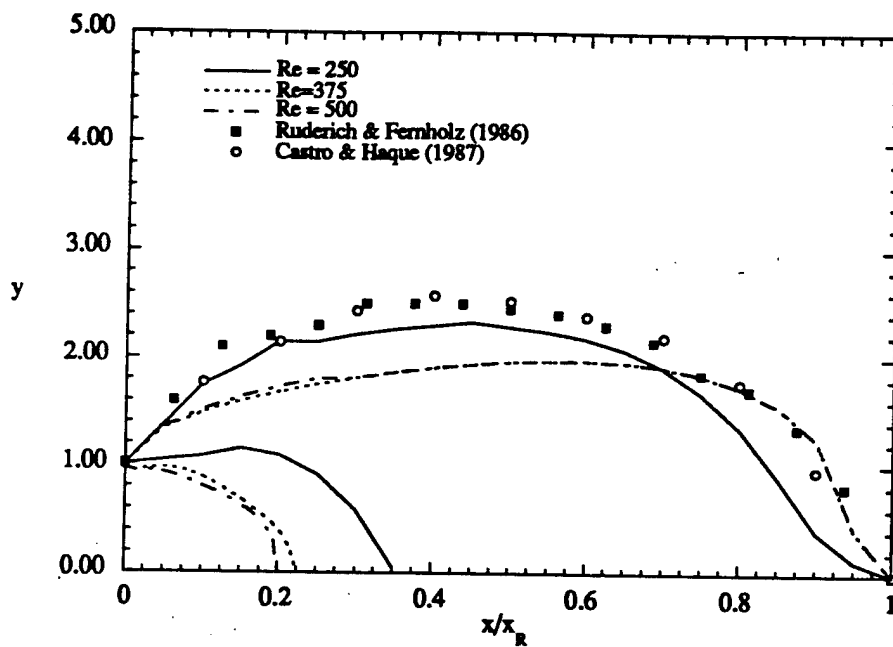


Figure 6.1.4.1.2 Loci of zero streamfunction ($\psi = 0$) for Reynolds number in the unsteady regime.

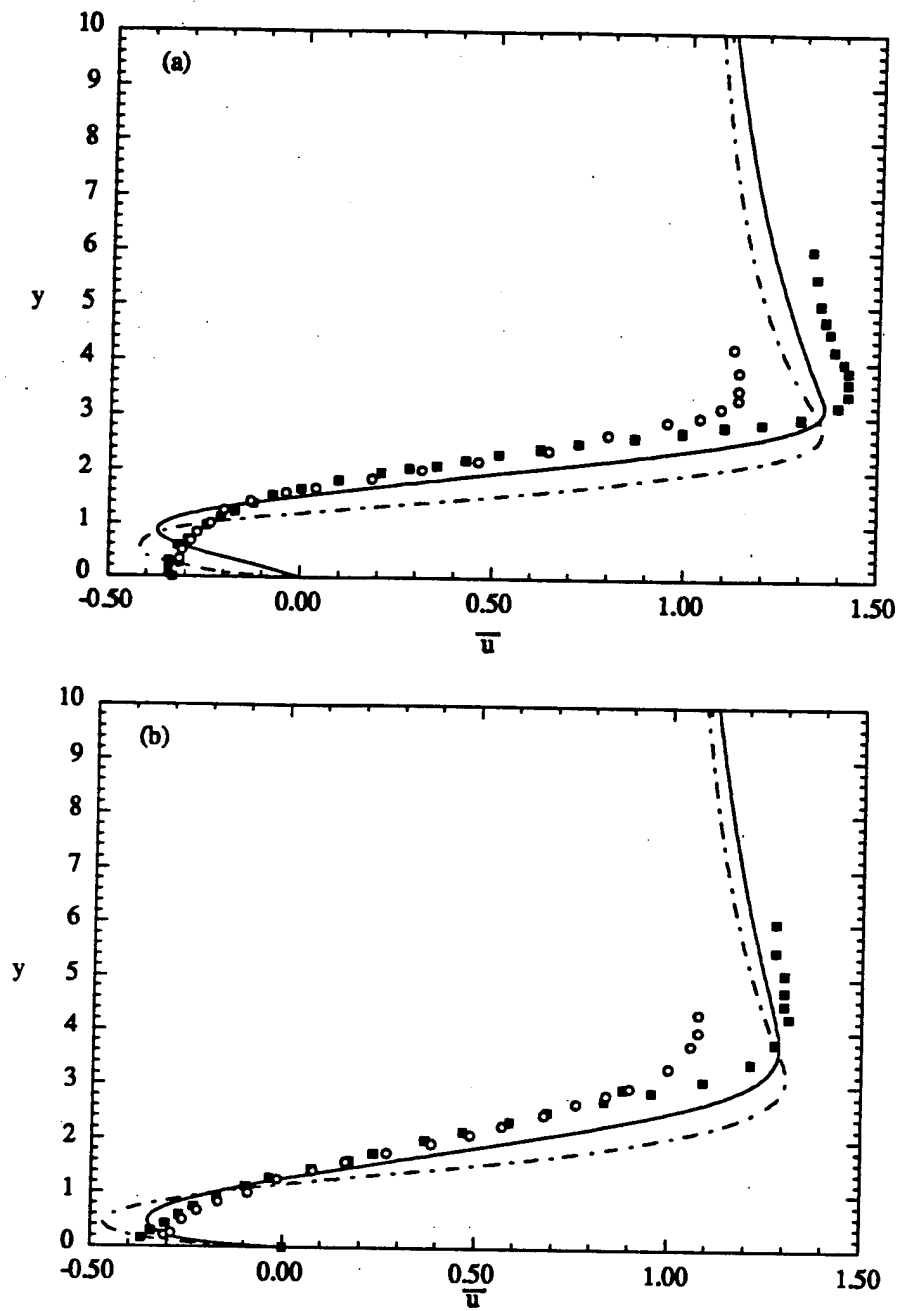


Figure 6.1.4.1.3 Profiles of the time-mean streamwise velocity, \bar{u} , at
 (a) $x/x_R = 0.38$, (b) $x/x_R = 0.67$.
 (—) $Re = 250$, (---) $Re = 500$
 (\blacksquare) Ruderich & Fernholz (1986), (\circ) Castro and Haque (1987).

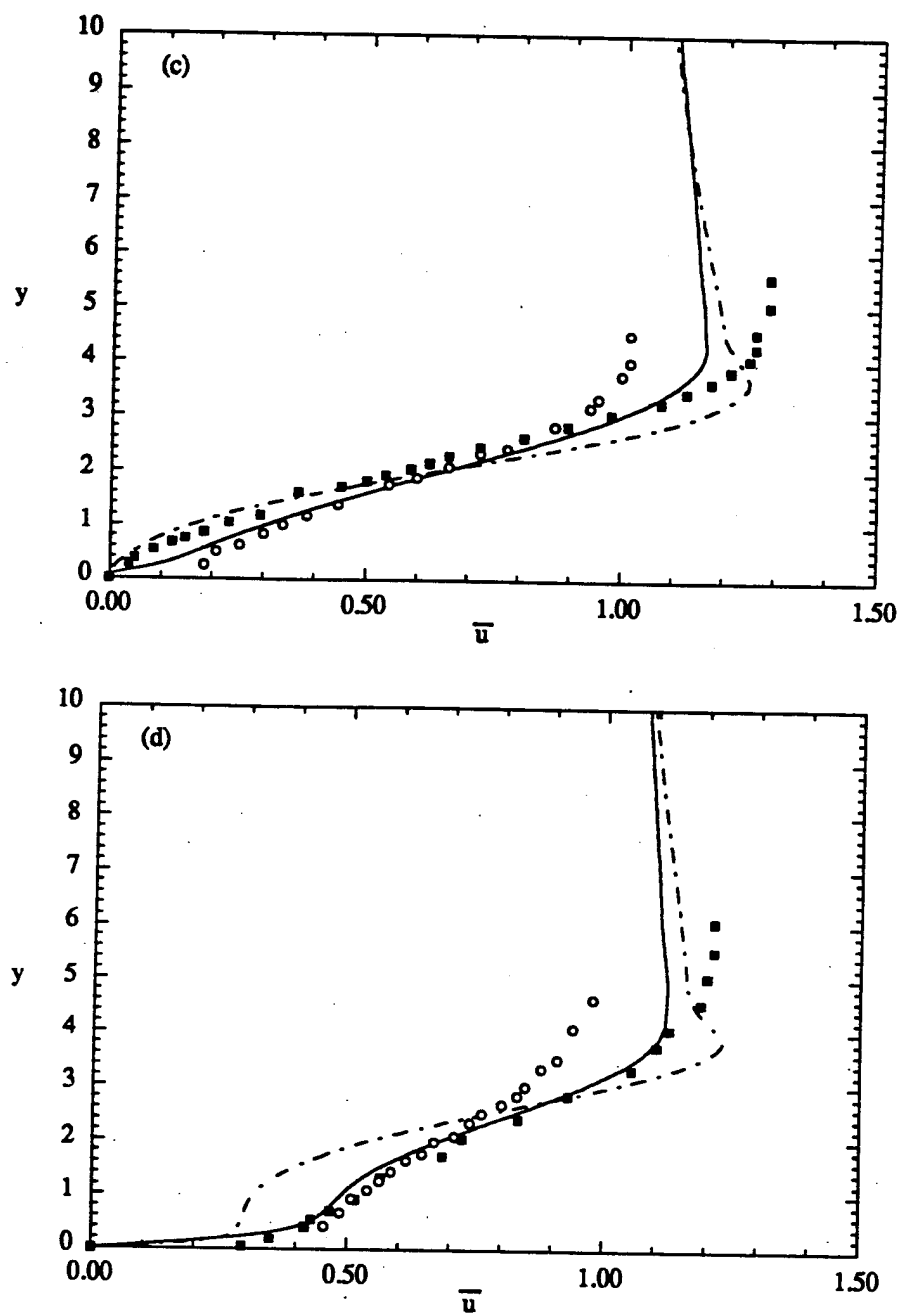


Figure 6.1.4.1.3(continued) (c) $x/x_R = 0.93$, (d) $x/x_R = 1.25$.

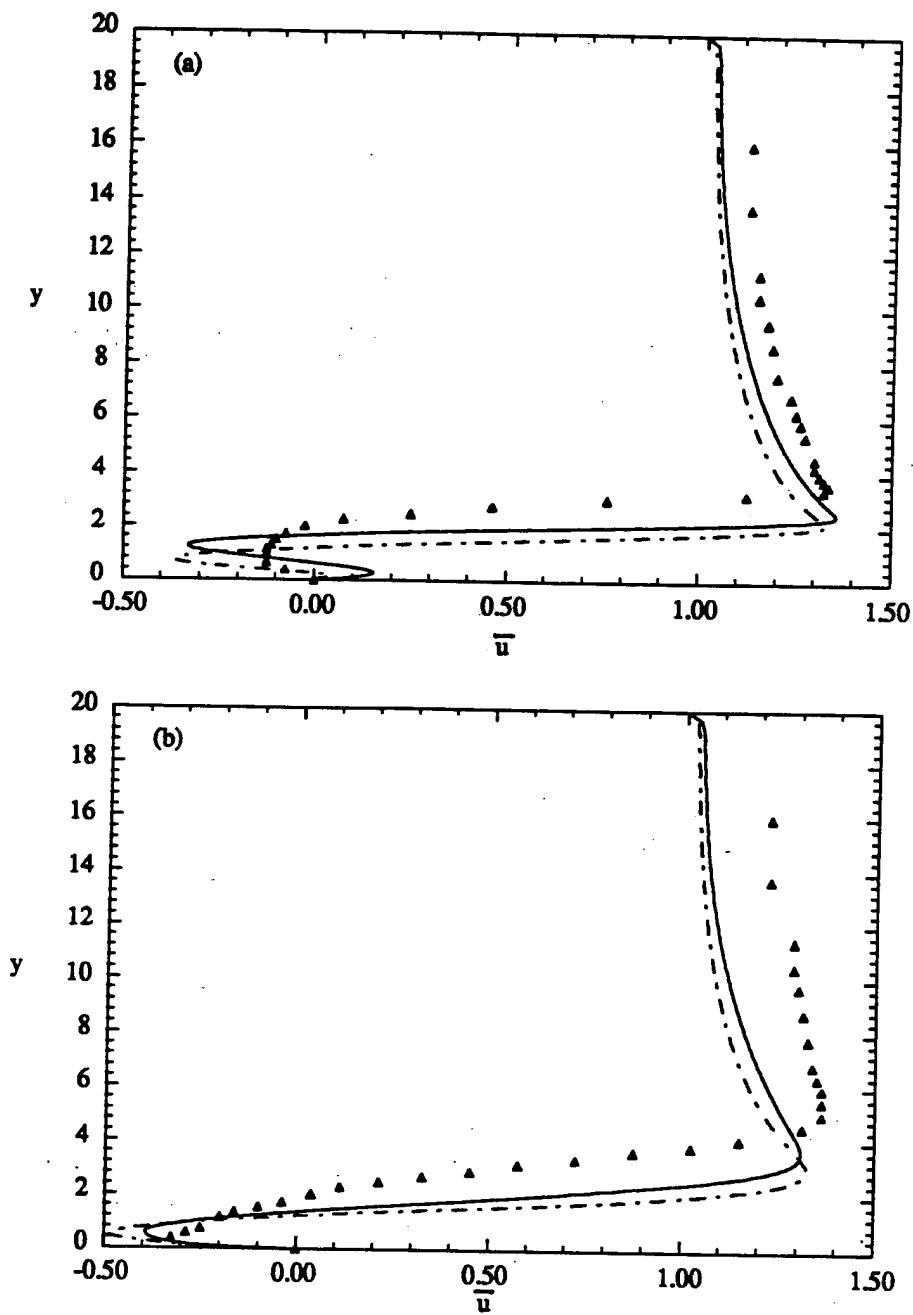


Figure 6.1.4.1.4 Profiles of the time-mean streamwise velocity, \bar{u} , at
 (a) $x/x_R = 0.20$, (b) $x/x_R = 0.56$.
 (—) $Re = 250$, (---) $Re = 500$
 (\blacktriangle) Jaroach & Fernholz (1986).

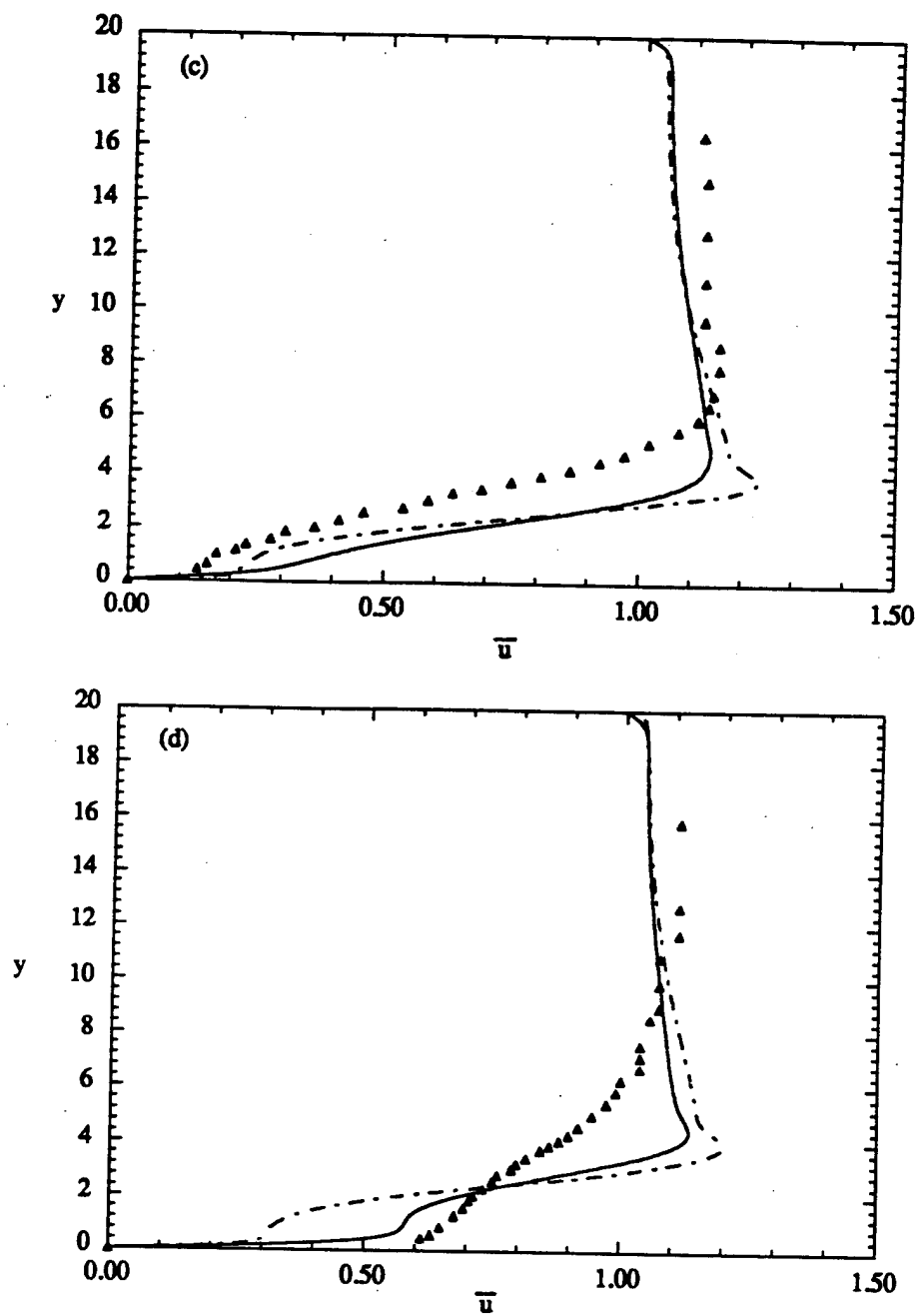


Figure 6.1.4.1.4(continued) (c) $x/x_R = 1.09$, (d) $x/x_R = 1.45$.

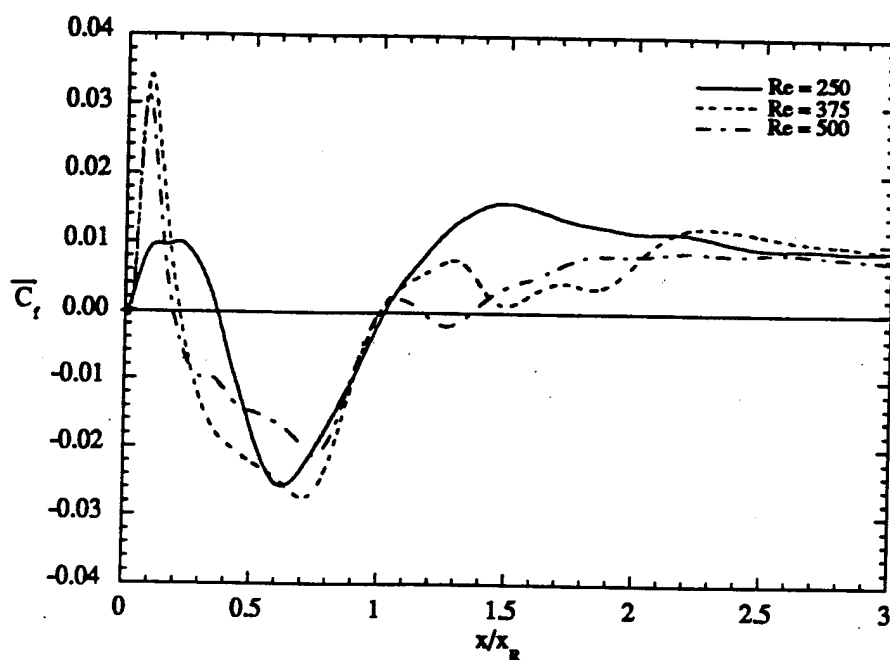


Figure 6.1.4.1.5 Streamwise distribution of the time-mean skin-friction factor, $\overline{C_f}$, in the unsteady regime.

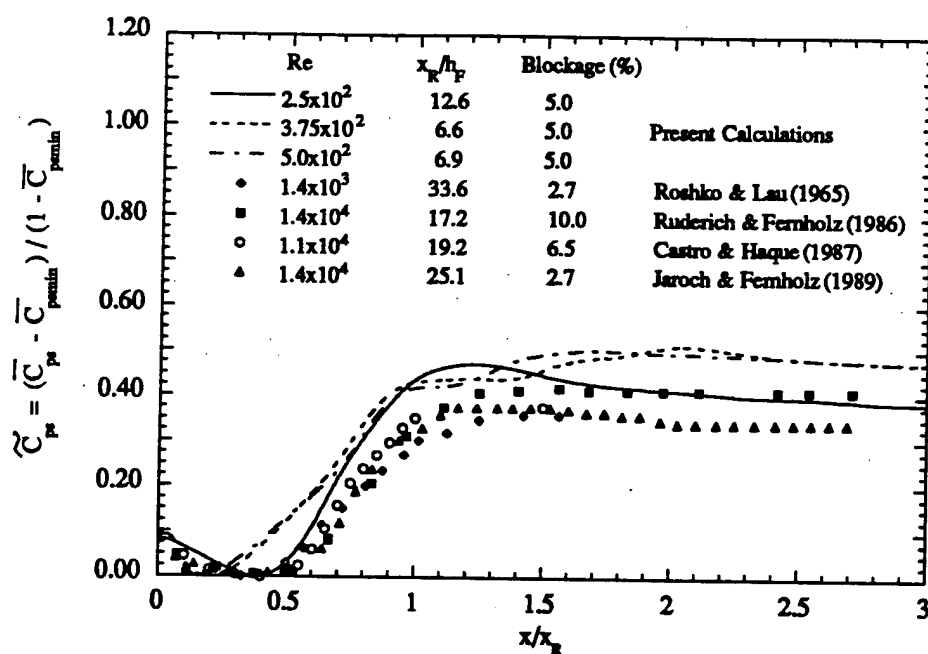


Figure 6.1.4.1.6 Streamwise distribution of the modified surface pressure coefficient, \tilde{C}_{p_s} , in the unsteady regime.

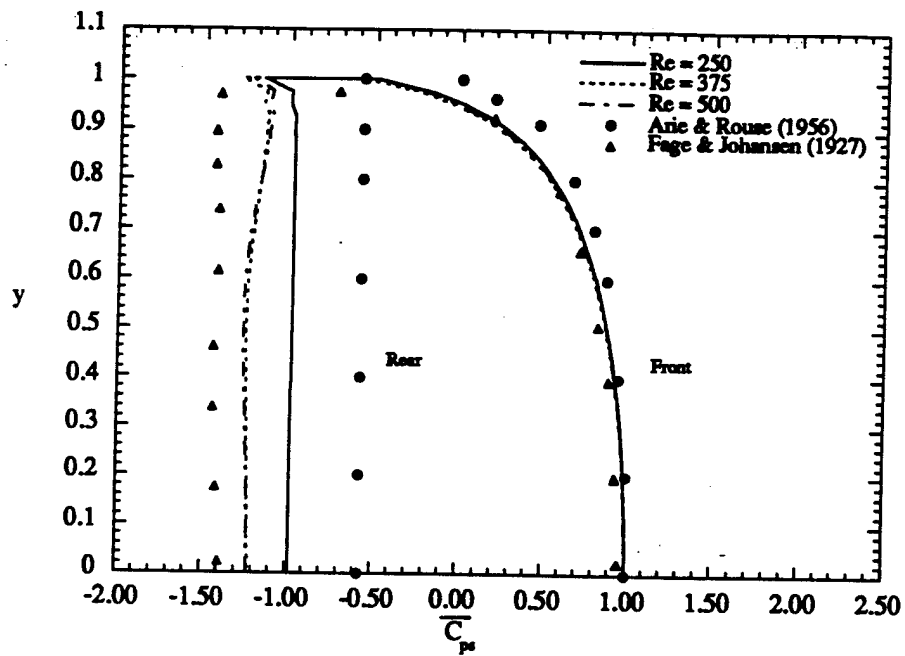


Figure 6.1.4.1.7 Distribution of the surface pressure coefficient, $\overline{C_p}$, on the front and rear faces of the plate in the unsteady regime compared with the experimental measurements.

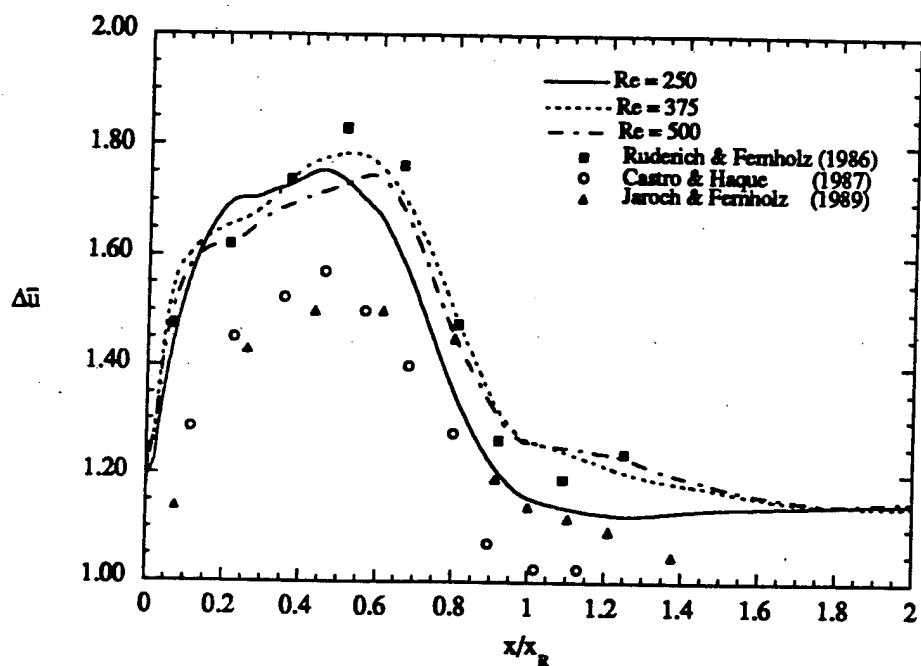


Figure 6.1.4.1.8 Streamwise distribution of the time-mean velocity difference, $\Delta\bar{u}$.

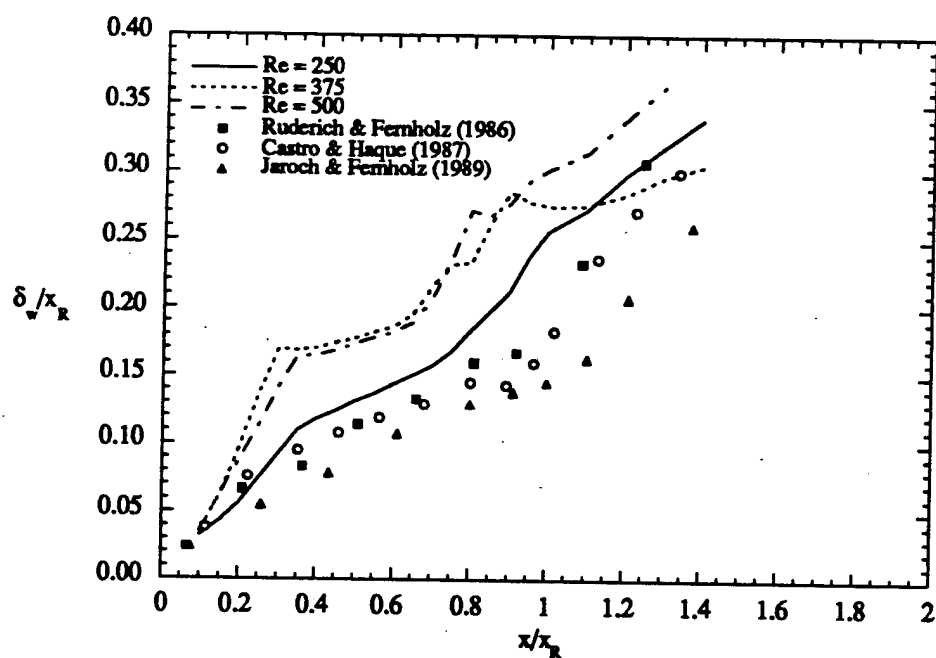


Figure 6.1.4.1.9 Streamwise distribution of the vorticity thickness, δ_w/x_R .

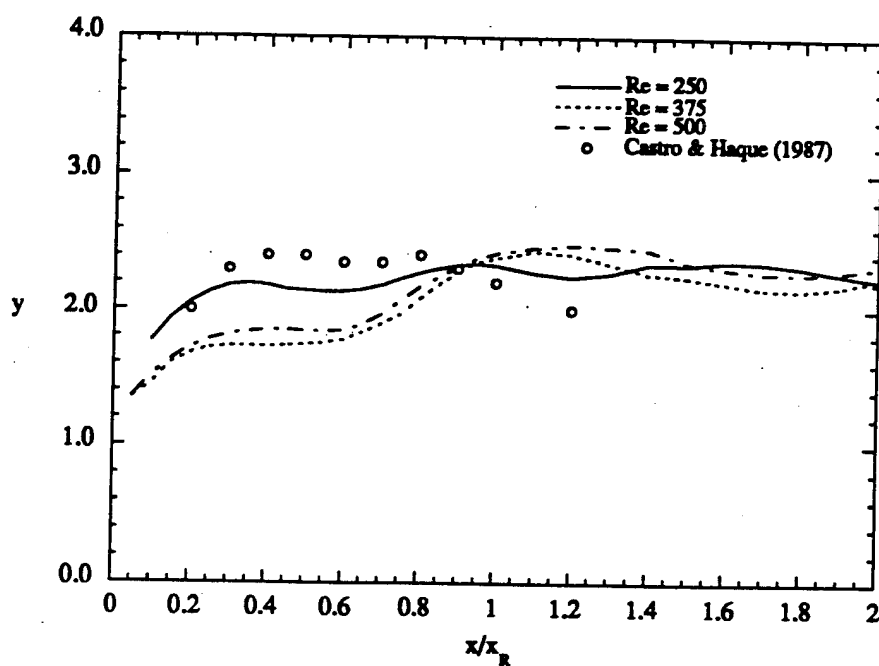


Figure 6.1.4.1.10 Variation of the shear layer center, y_c , with x/x_R .

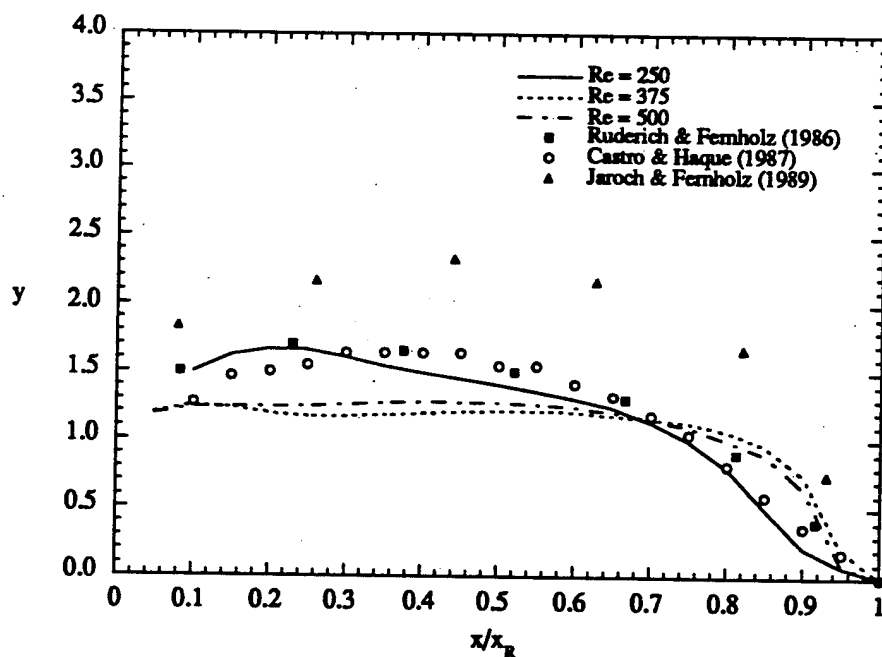


Figure 6.1.4.1.11 Loci of zero streamwise velocity for Reynolds numbers in the unsteady regime.

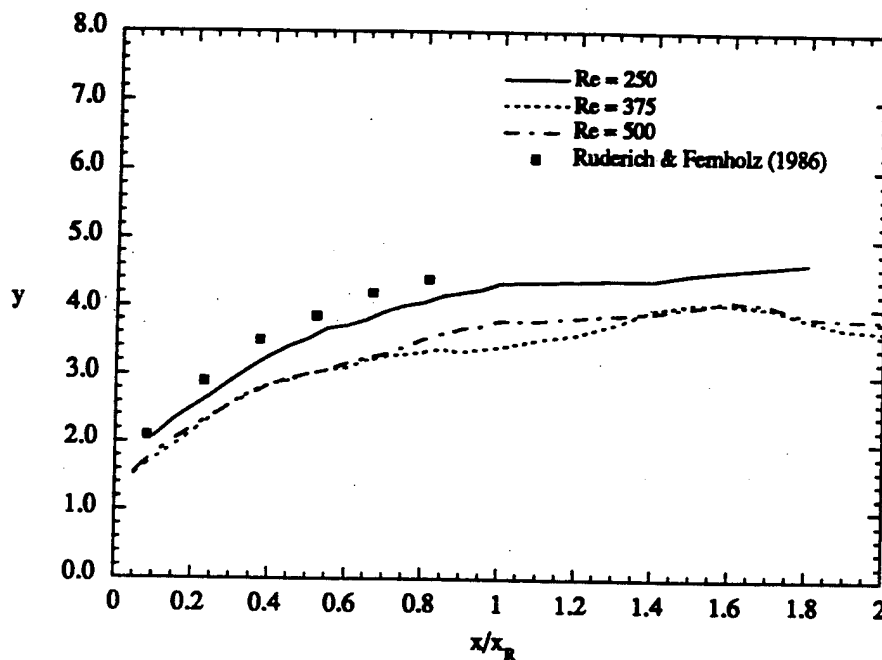


Figure 6.1.4.1.12 Loci of maximum streamwise velocity for Reynolds numbers in the unsteady regime.

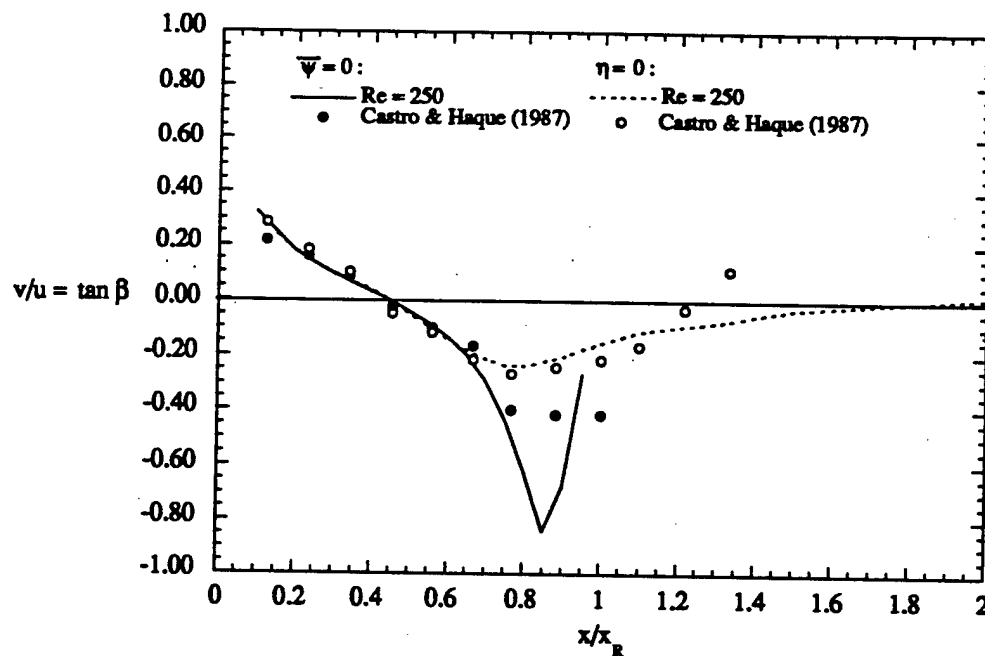


Figure 6.1.4.1.13 Flow direction along lines of $\eta = 0$ and $\bar{\psi} = 0$ compared with Castro and Haque (1987).

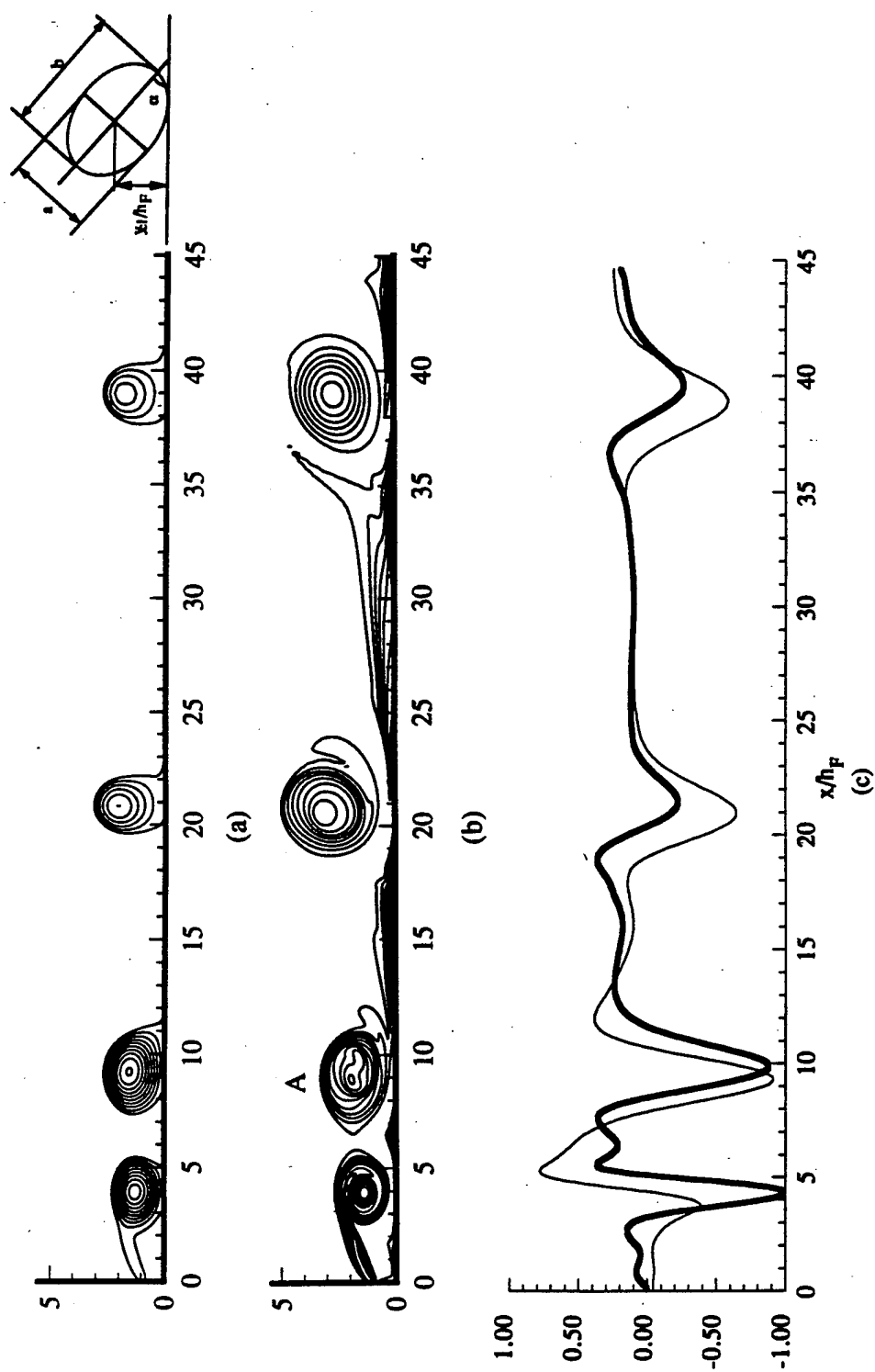


Figure 6.1.4.2.1 Instantaneous snapshot of the unsteady flow at $Re = 250$. (a) Streamlines ($\psi_{min}, \psi_{max}, \Delta\psi = (-1, 0, 0.05)$) (b) Spanwise Vorticity ($\omega_{zmin}, \omega_{zmax}, \Delta\omega_z = (-4.05, -0.05, 0.25)$), (c) Skin-friction factor, $C_f \times 10$ (—) and Surface pressure coefficient, C_{p_s} (---).

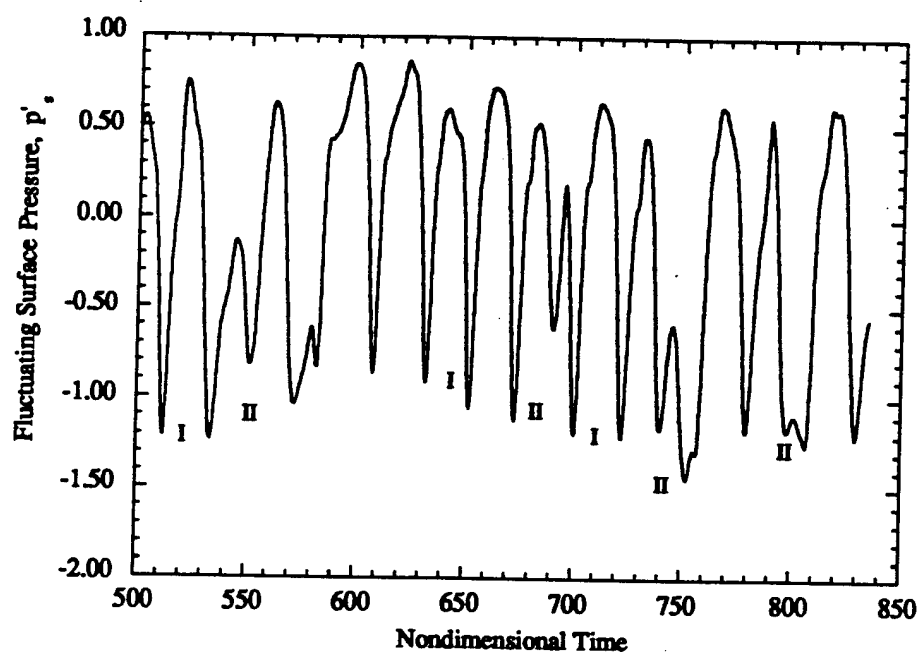


Figure 6.1.4.2.2 Time signal of the fluctuating surface pressure, p'_s , at $x/x_R = 0.8$ for $Re = 250$. Modes I and II are identified at selected time intervals.

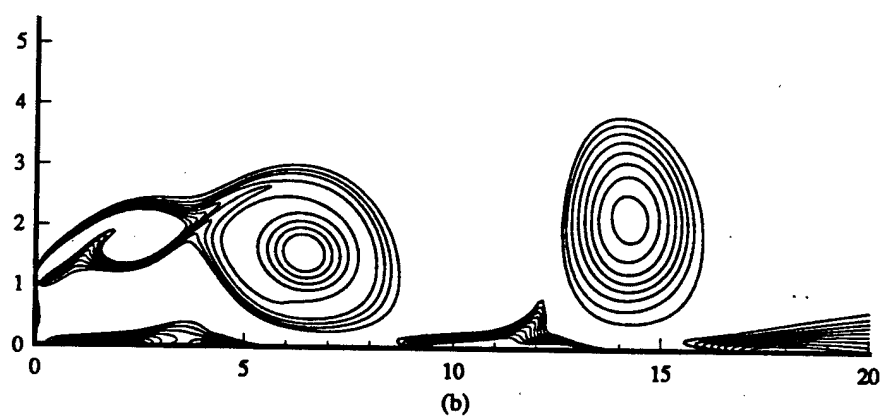
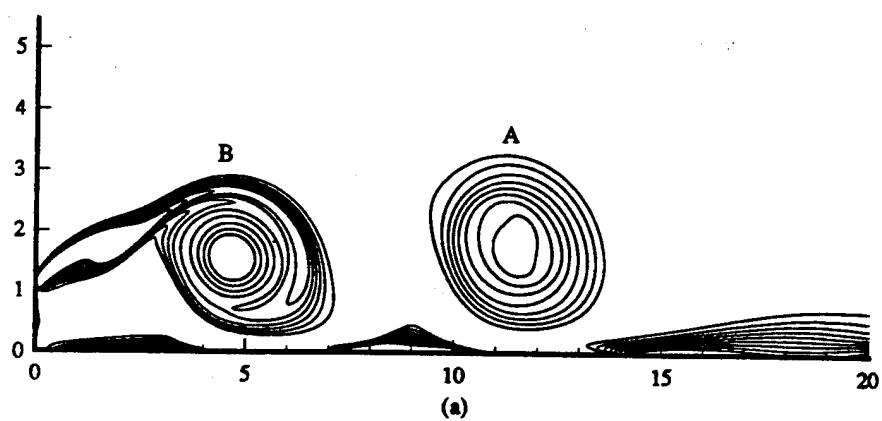


Figure 6.1.4.2.3 Time development of the spanwise vorticity for vortex shedding mode I at $Re = 250$.
(a) $t = 380$, (b) $t = 385$.

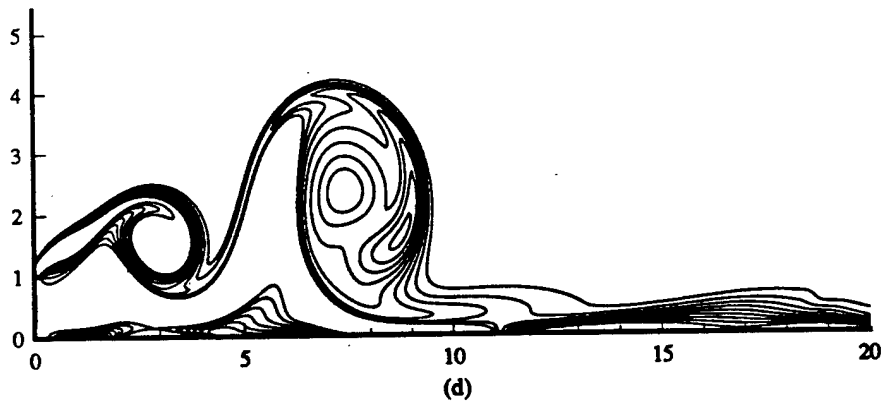
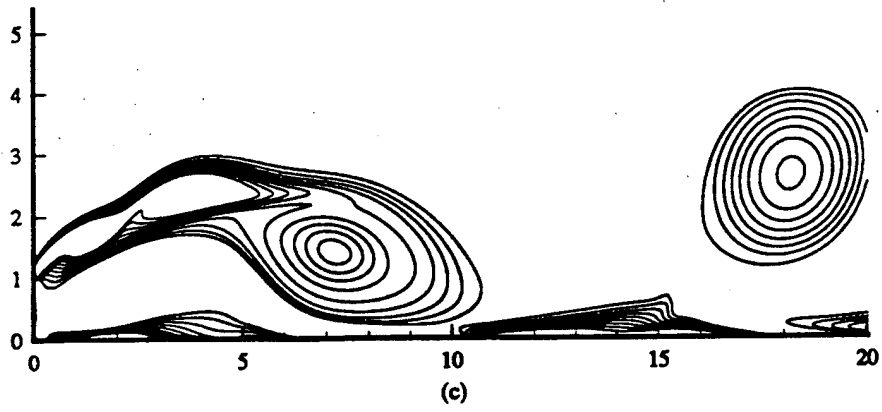


Figure 6.1.4.2.3(continued) (c) $t = 390$, (d) $t = 395$.

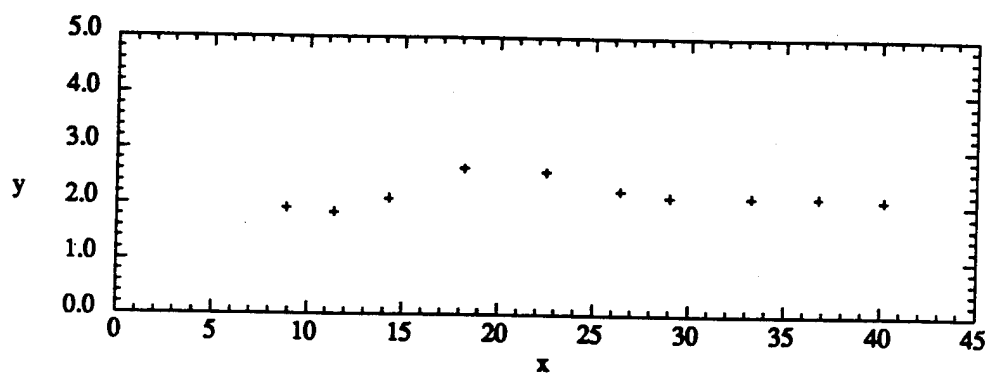


Figure 6.1.4.2.4 Path of propagating vortex A (refer to Figure 6.1.4.2.3).
Core location is shown at intervals of five time units.

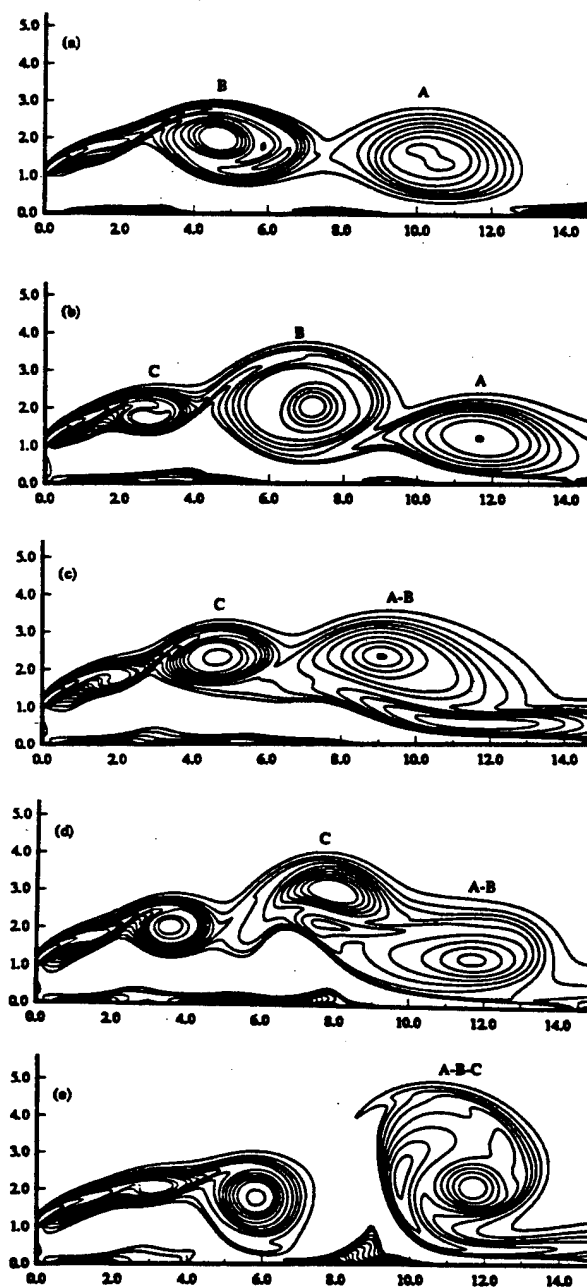


Figure 6.1.4.2.5 Time evolution of the spanwise vorticity for vortex shedding mode II at $Re = 250$.
(a) $t = 740$, (b) $t = 745$, (c) $t = 750$, (d) $t = 755$, (e) $t = 760$.

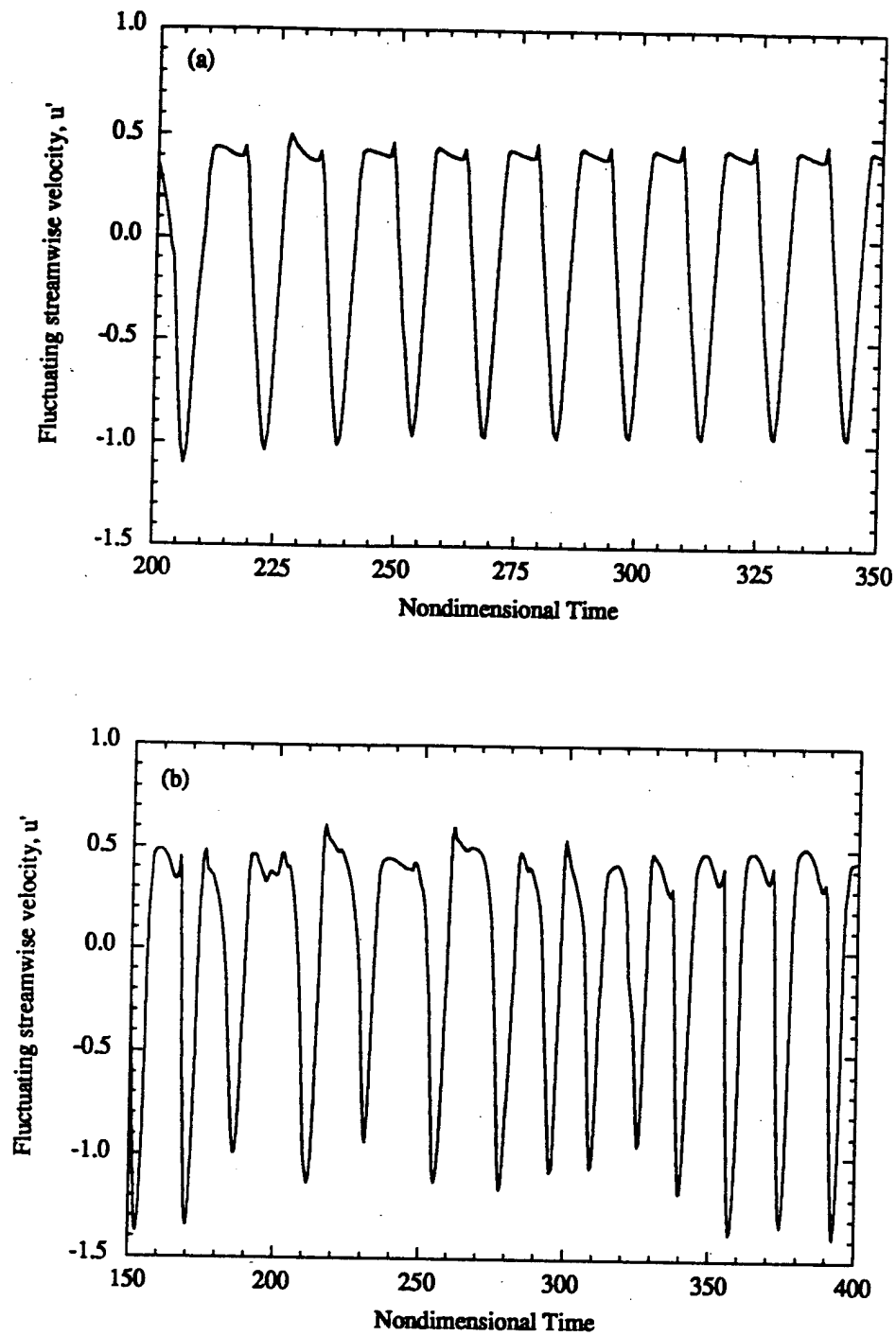


Figure 6.1.4.2.6 Time signal of the fluctuating streamwise velocity, u' , at $x = 12.5$, $y = 1$ for (a) $Re = 375$, (b) $Re = 500$.

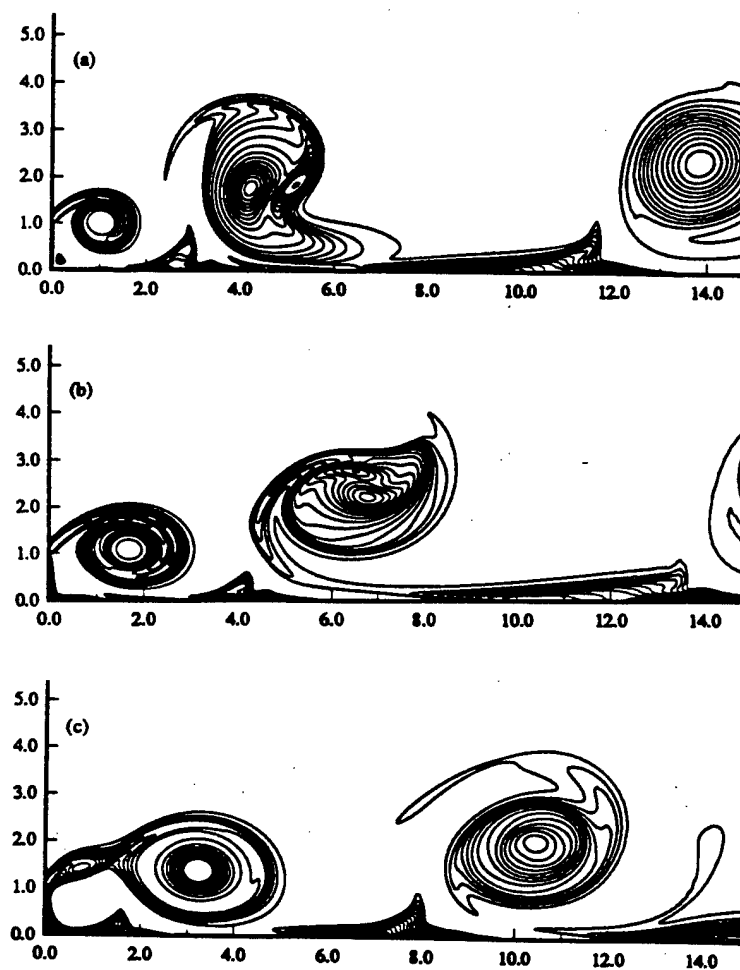


Figure 6.1.4.2.7 Representative time frames of the spanwise vorticity at $Re = 375$.
 (a) $t = 315.6$, (b) $t = 318.8$, (c) $t = 325$.

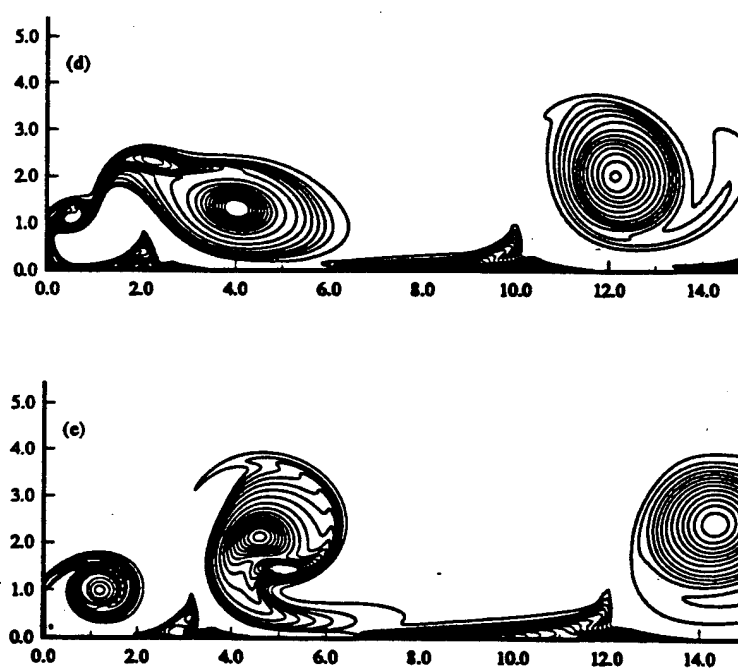


Figure 6.1.4.2.7(continued) (d) $t = 328.1$, (e) $t = 331.2$.

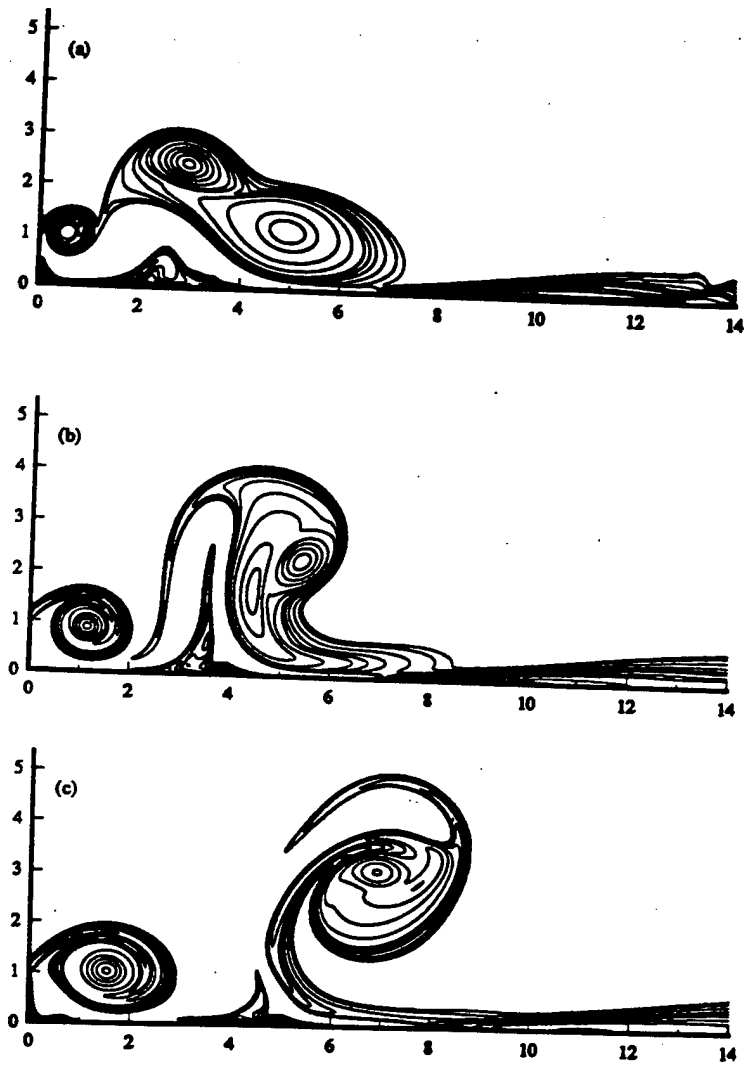


Figure 6.1.4.2.8 Representative time frames of the spanwise vorticity at $Re = 500$.
 (a) $t = 175$, (b) $t = 177.5$, (c) $t = 180$.

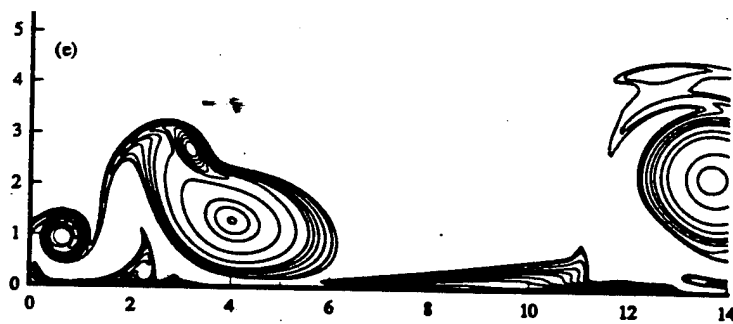
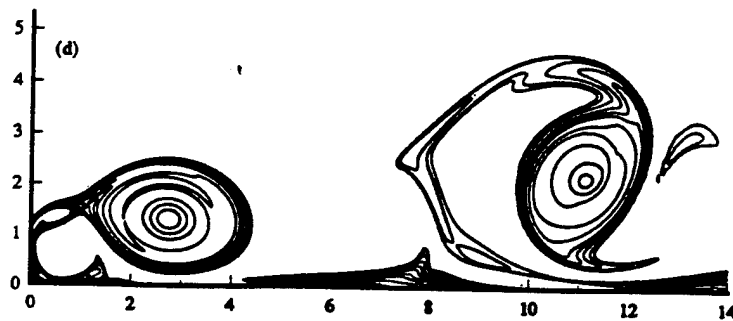


Figure 6.1.4.2.8(continued) (d) $t = 185$, (e) $t = 190$.

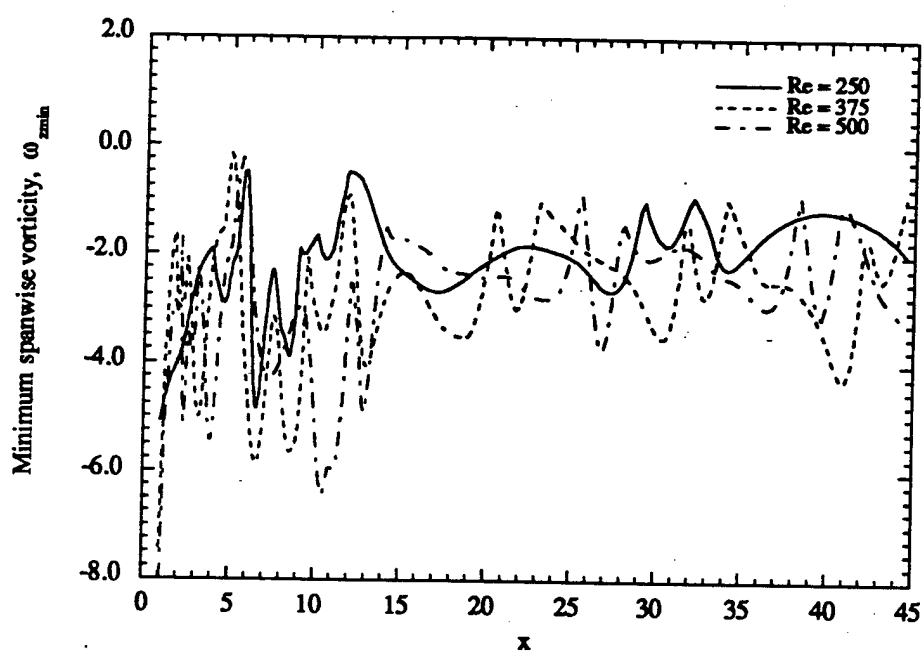


Figure 6.1.4.2.9 Streamwise distribution of the minimum instantaneous ω_z in the unsteady regime (arbitrary time unit).

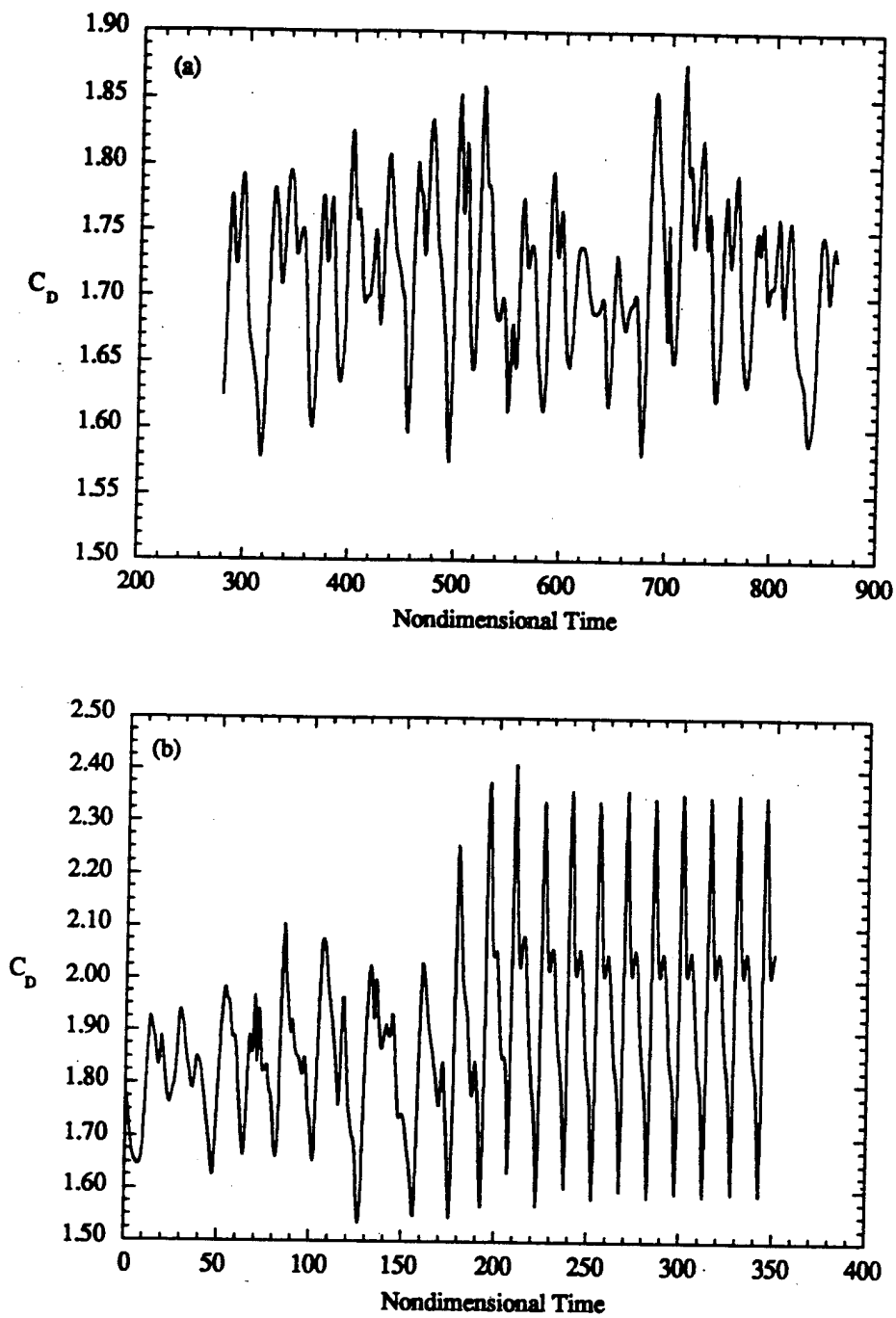


Figure 6.1.4.2.10 Temporal evolution of the drag coefficient for
(a) $Re = 250$, (b) $Re = 375$.

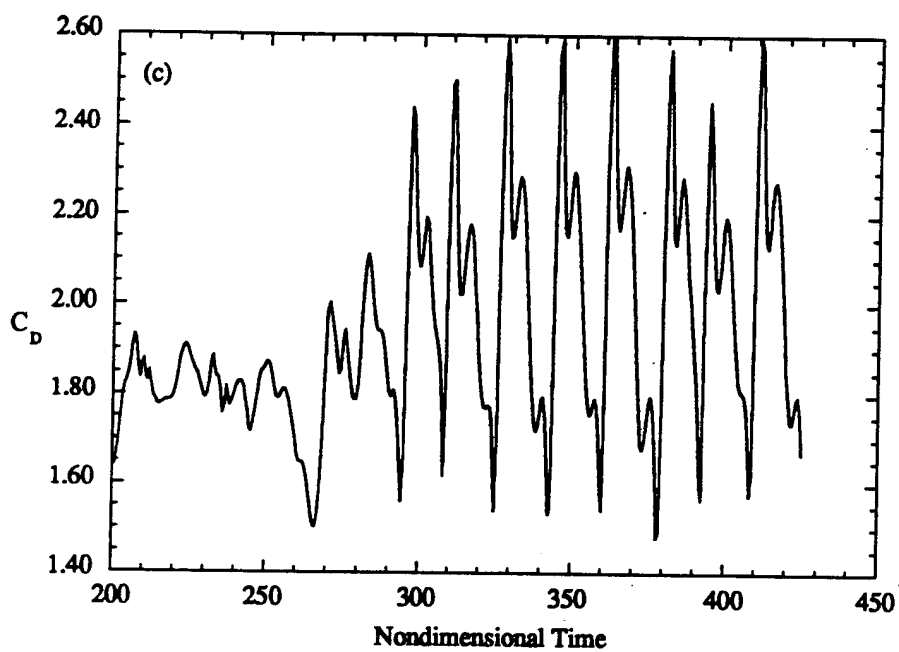


Figure 6.1.4.2.10 (continued) (c) $Re = 500$.

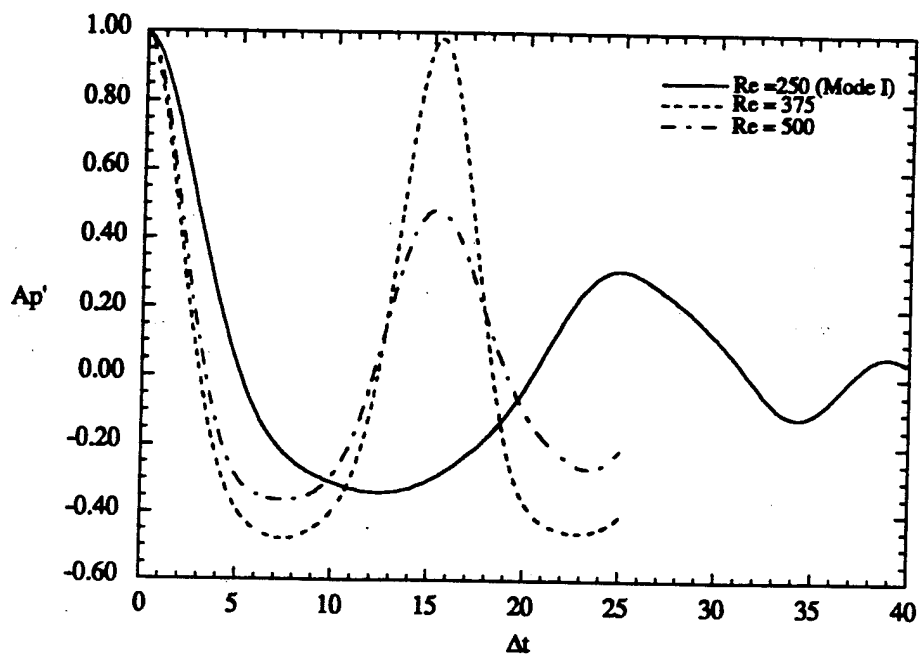


Figure 6.1.4.3.1 Autocorrelation coefficient of the fluctuating pressure, Ap' , at $x = 12.5, y = 2$ for Reynolds numbers in the unsteady regime.

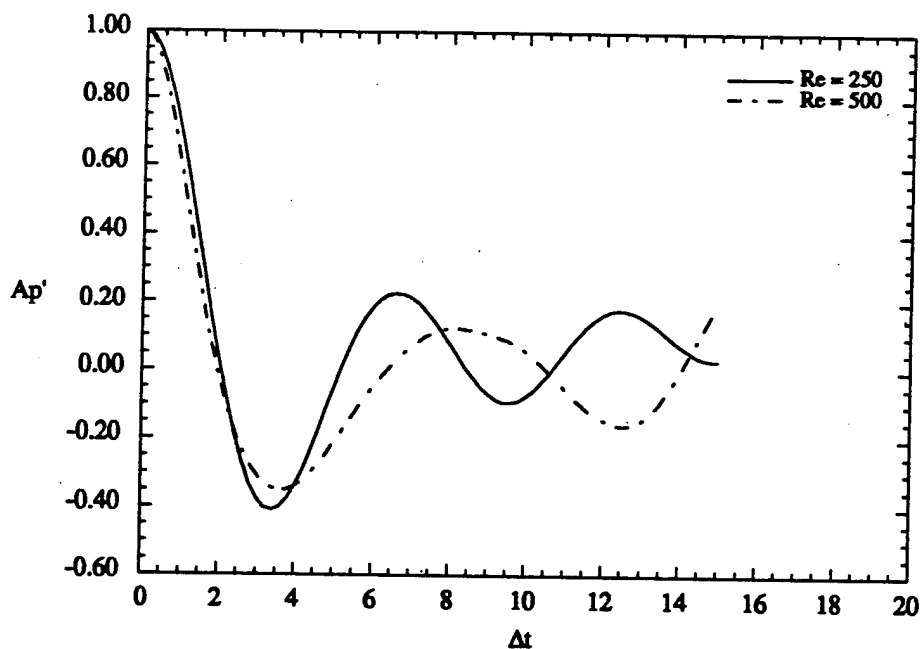


Figure 6.1.4.3.2 Autocorrelation coefficient of the fluctuating pressure, Ap' , at $x = 1, y = 2$ for $Re = 250$ and 500 .

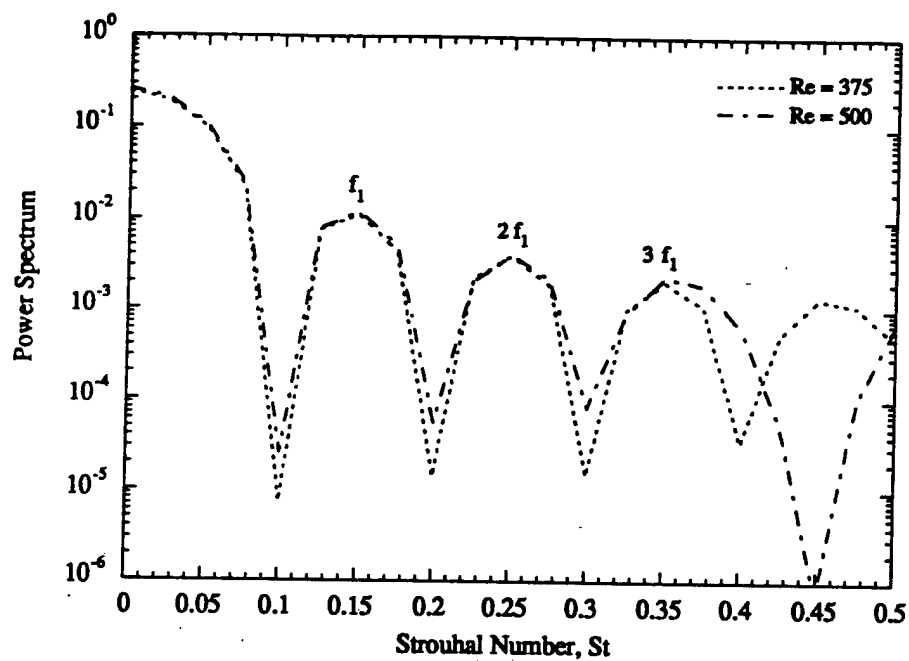


Figure 6.1.4.3.3 Power spectrum of the drag coefficient at $Re = 375$ and 500 .

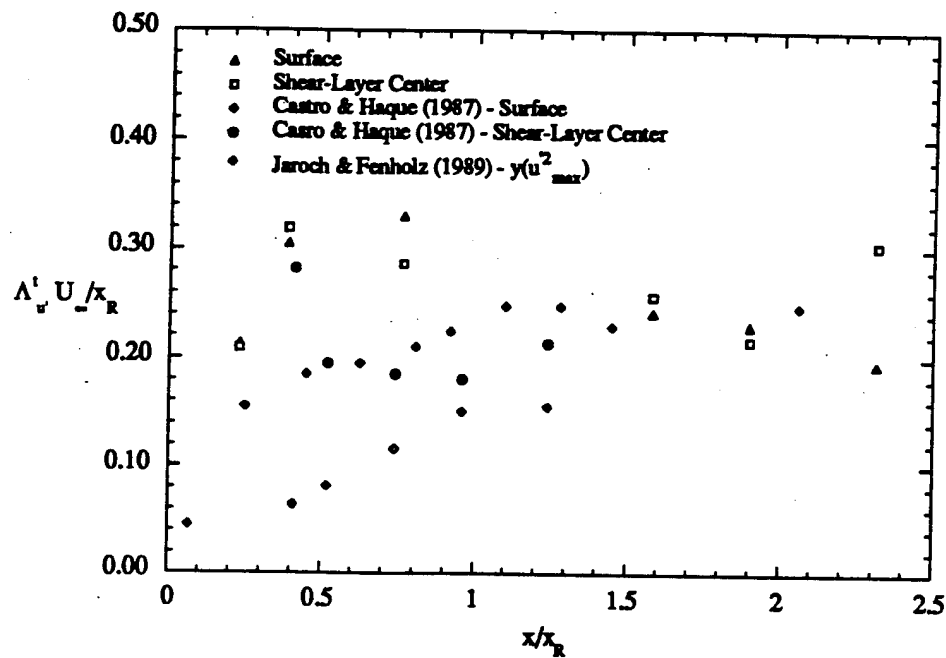


Figure 6.1.4.3.4 Development of the integral timescale $\Lambda_v^t U_\infty / x_R$ for x/x_R .

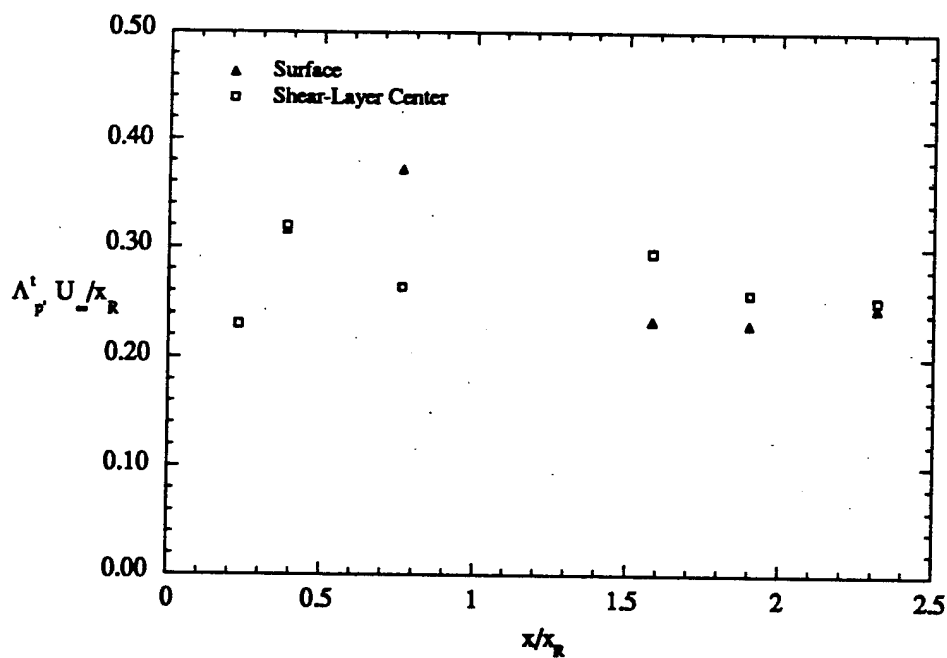


Figure 6.1.4.3.5 Development of the integral timescale $\Lambda_p^t U_\infty / x_R$ for x/x_R .

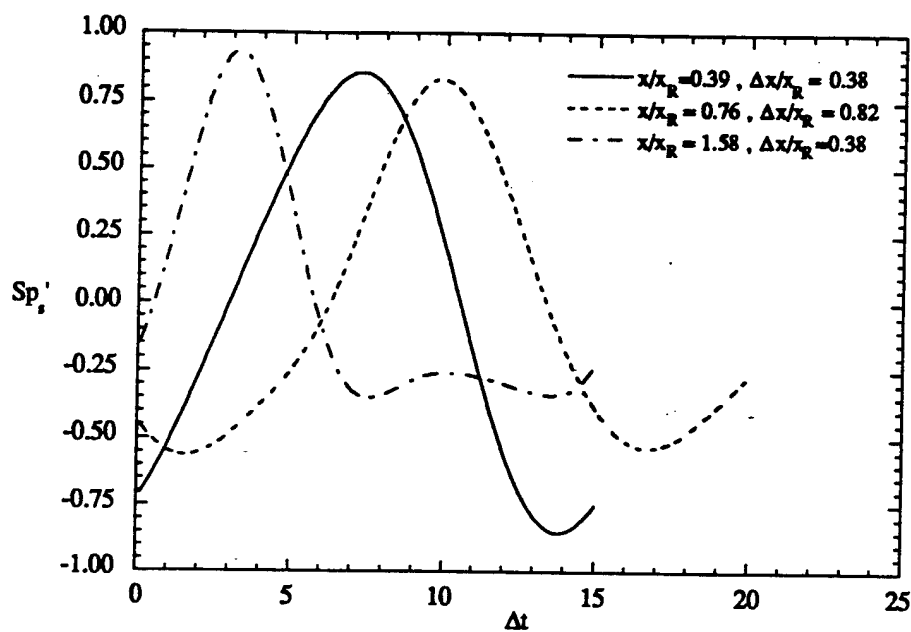


Figure 6.1.4.3.6 Space-time correlation coefficient of the fluctuating surface pressure, Sp'_s , for $Re = 375$.

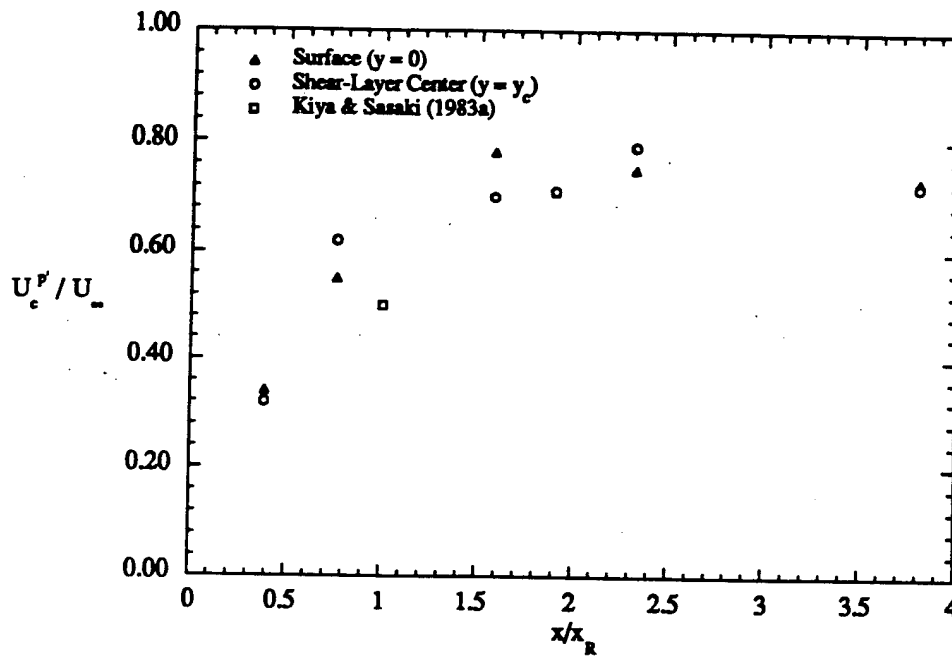


Figure 6.1.4.3.7 Streamwise variation of the convective velocity based on the fluctuating pressure at the surface and at the center of the shear layer for $Re = 375$.

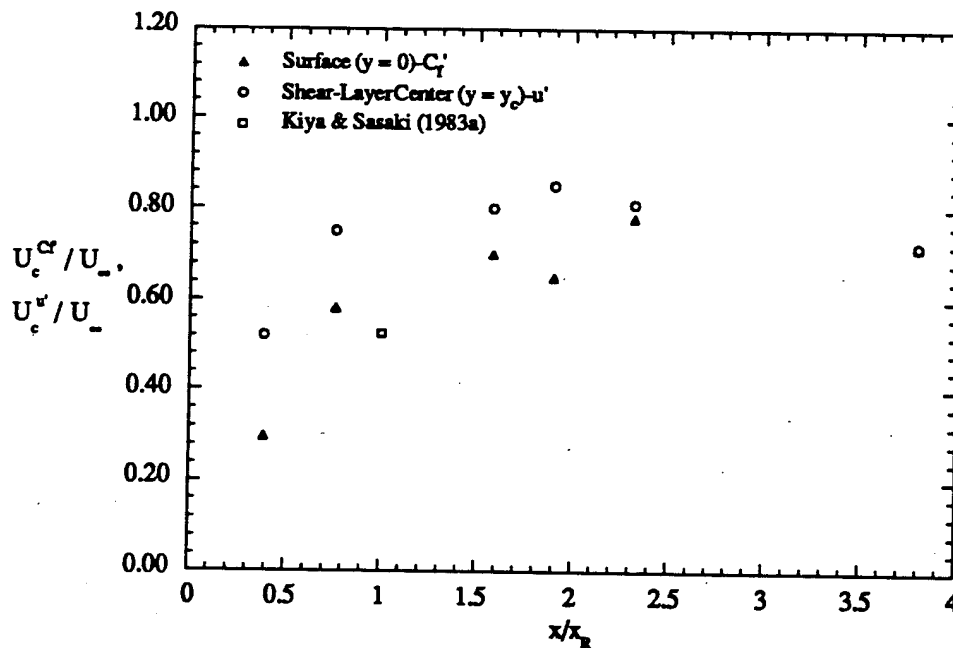


Figure 6.1.4.3.8 Streamwise variation of the convective velocity based on the fluctuating skin-friction coefficient and the fluctuating streamwise velocity for $Re = 375$.

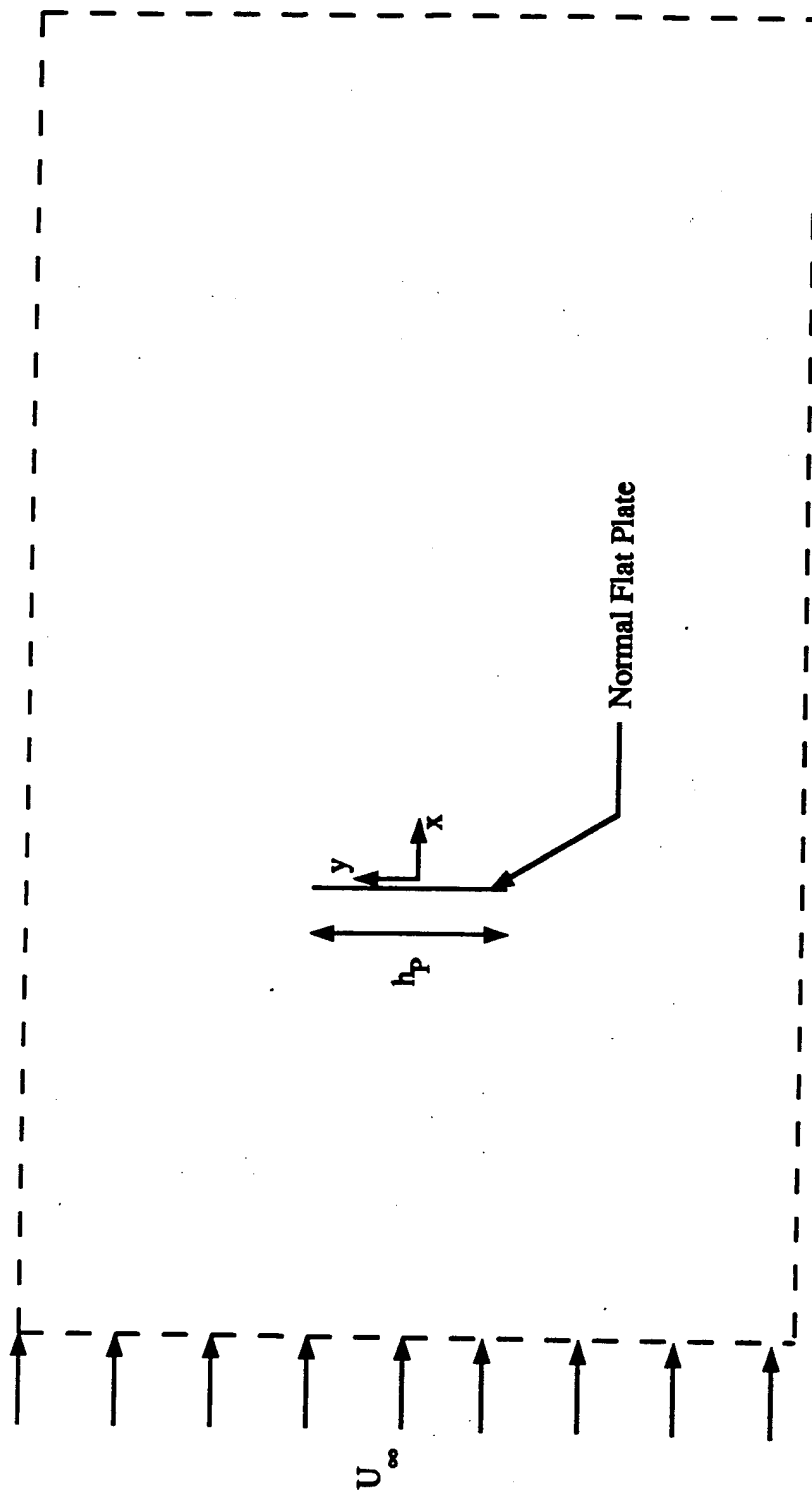
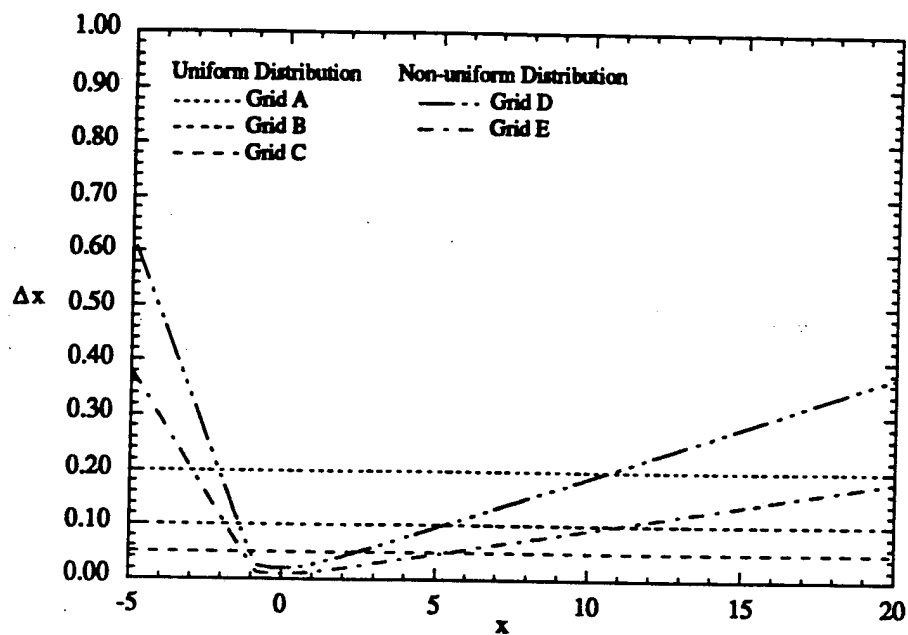
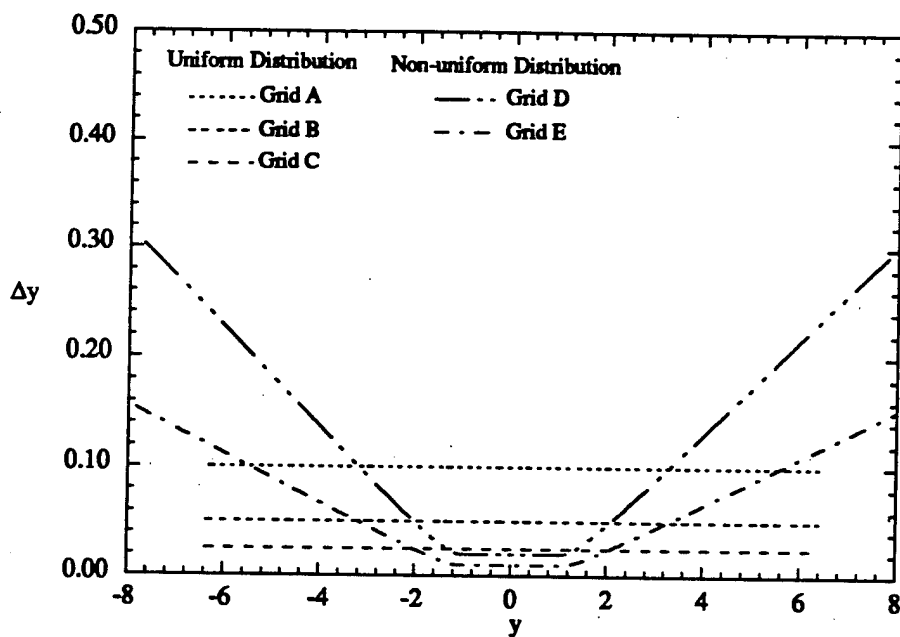


Figure 6.2.1 Schematic of the geometrical configuration and the computational domain for the separated flow past a normal flat plate.



(a)



(b)

Figure 6.2.1.1 Distribution of mesh spacings in (a) x-direction, and (b) y-direction for various grid configurations.

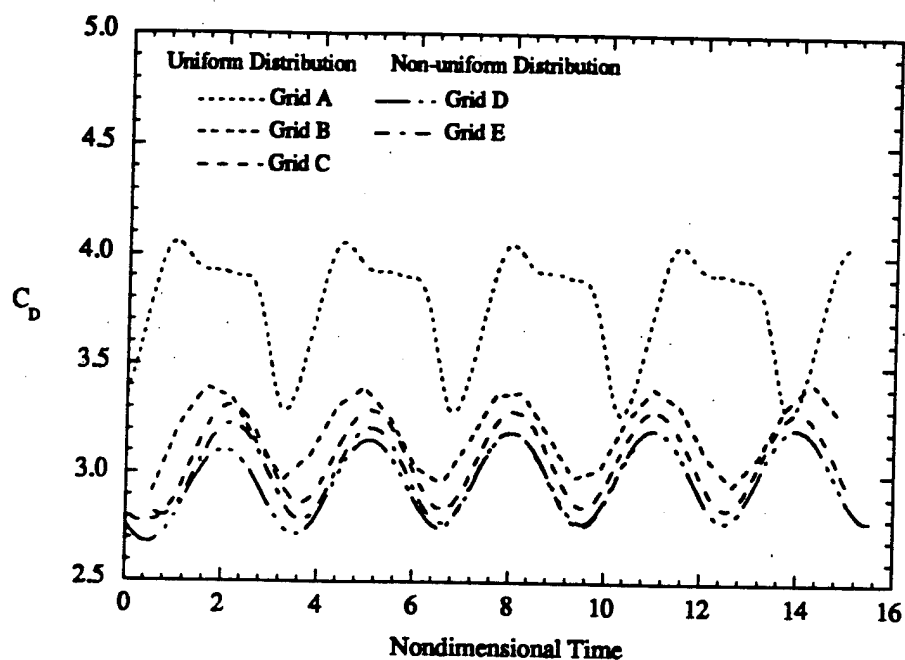


Figure 6.2.1.2 Temporal variation of the drag coefficient for various grid configurations at $Re = 100$.

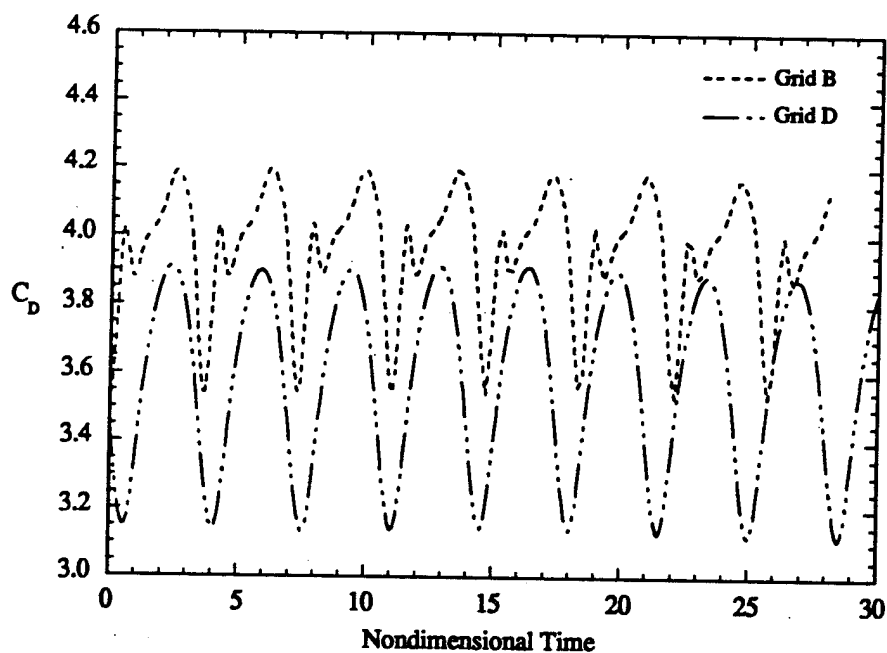


Figure 6.2.1.3 Temporal variation of the drag coefficient for grids B and D at $Re = 250$.

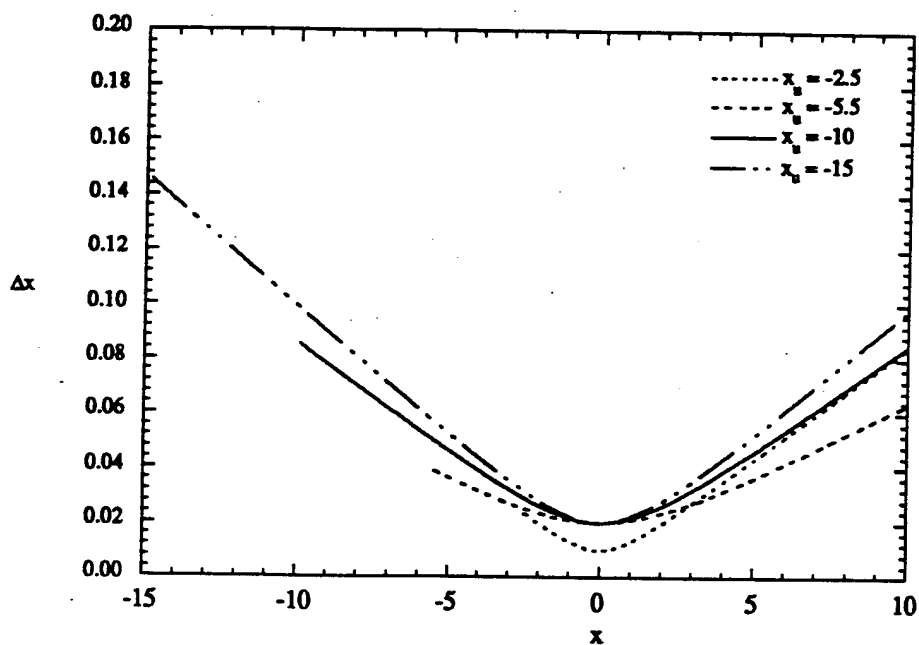


Figure 6.2.1.4 Distribution of mesh spacings in the x -direction for various upstream distances, x_u . Grid Resolution = 513×257 .

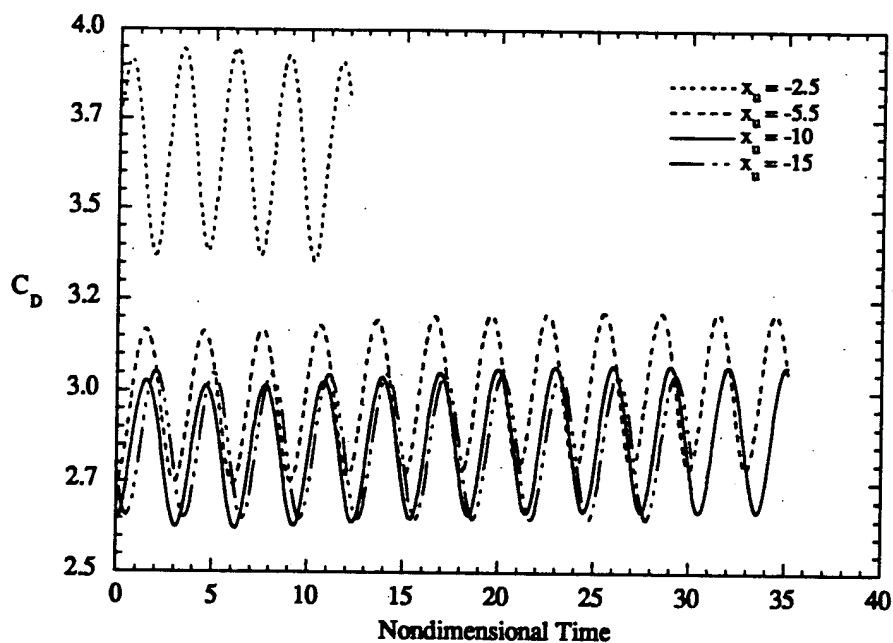


Figure 6.2.1.5 Temporal variation of the drag coefficient for various upstream distances, x_u , at $Re = 100$. Grid Resolution = 513×257 .

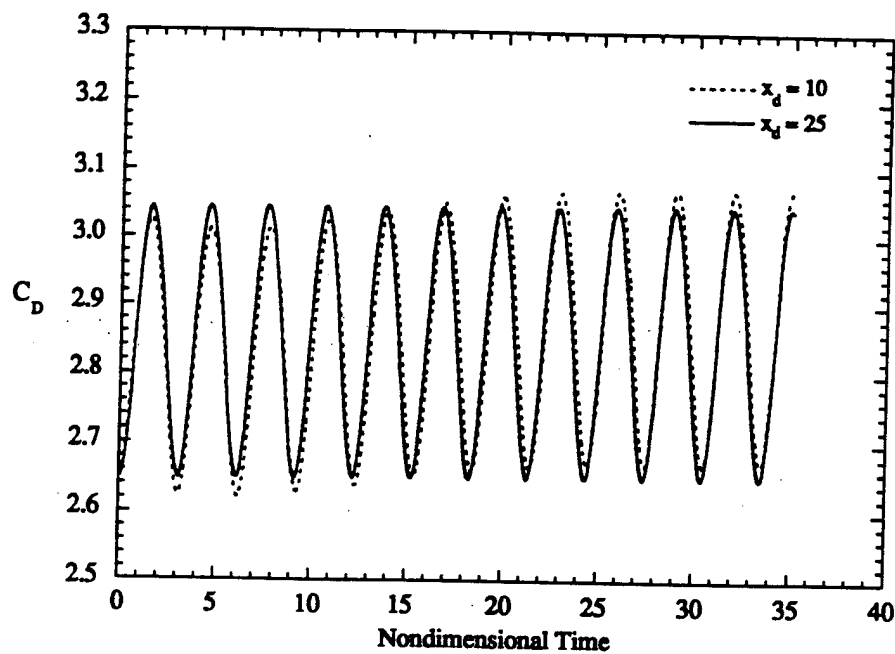


Figure 6.2.1.6 Temporal variation of the drag coefficient for various downstream distances, x_d , at $Re = 100$. Grid Resolution = 513×257 , $x_u = -10$.

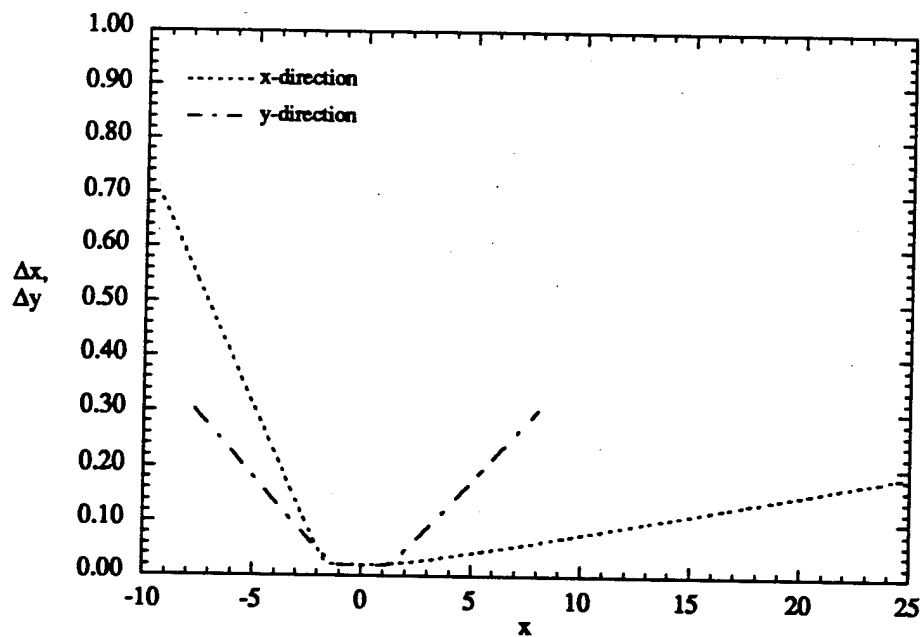


Figure 6.2.1.7 Distribution of mesh spacings for grid F. Grid Resolution = 513×257 .

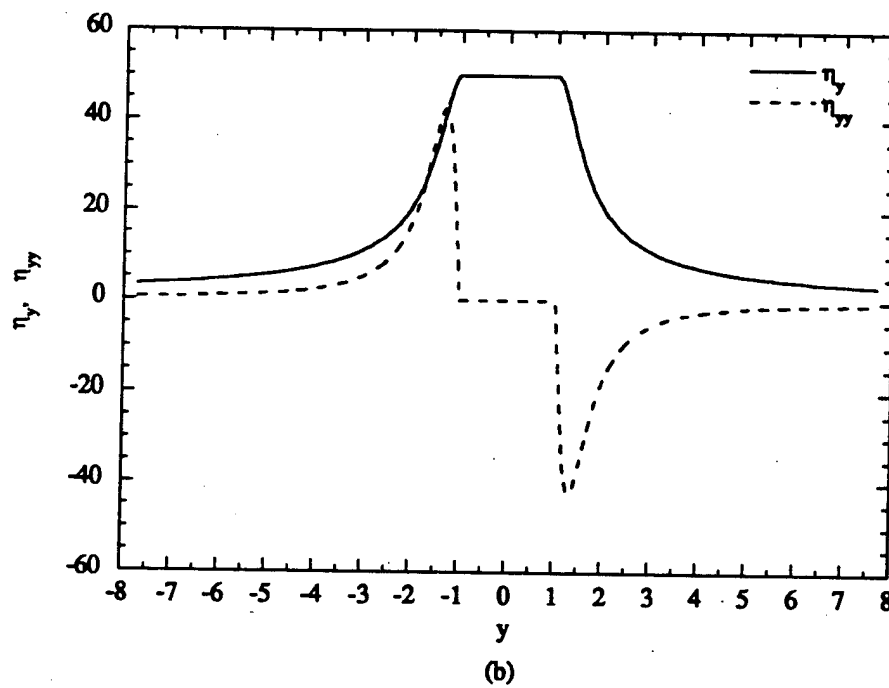
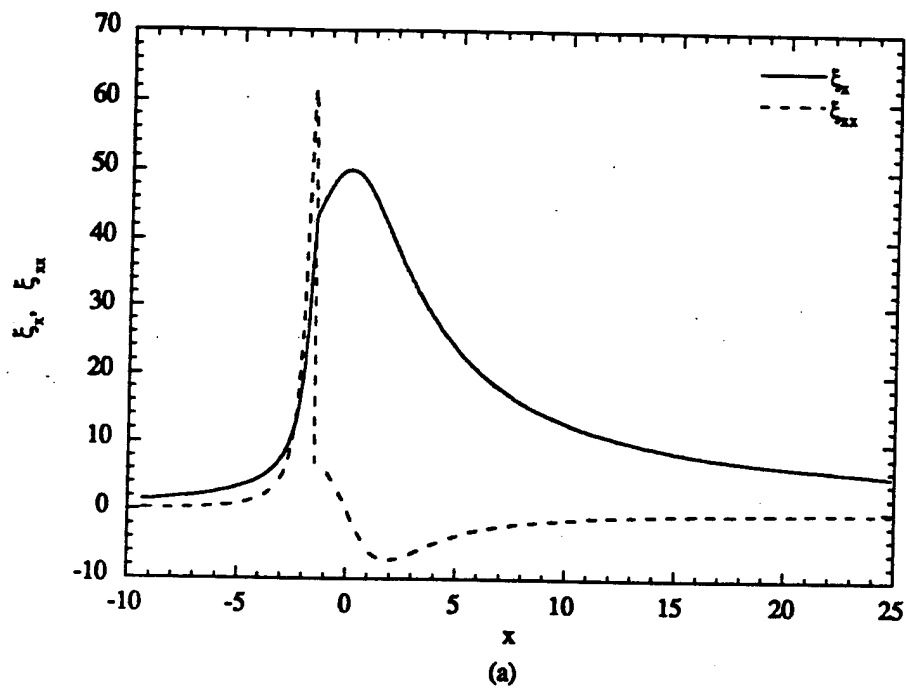


Figure 6.2.1.8 Distribution of the metrics in the (a) x-direction, and (b) y-direction. Grid Resolution = 513x257, $x_u = -10$, $x_d = 25$ (Grid F).

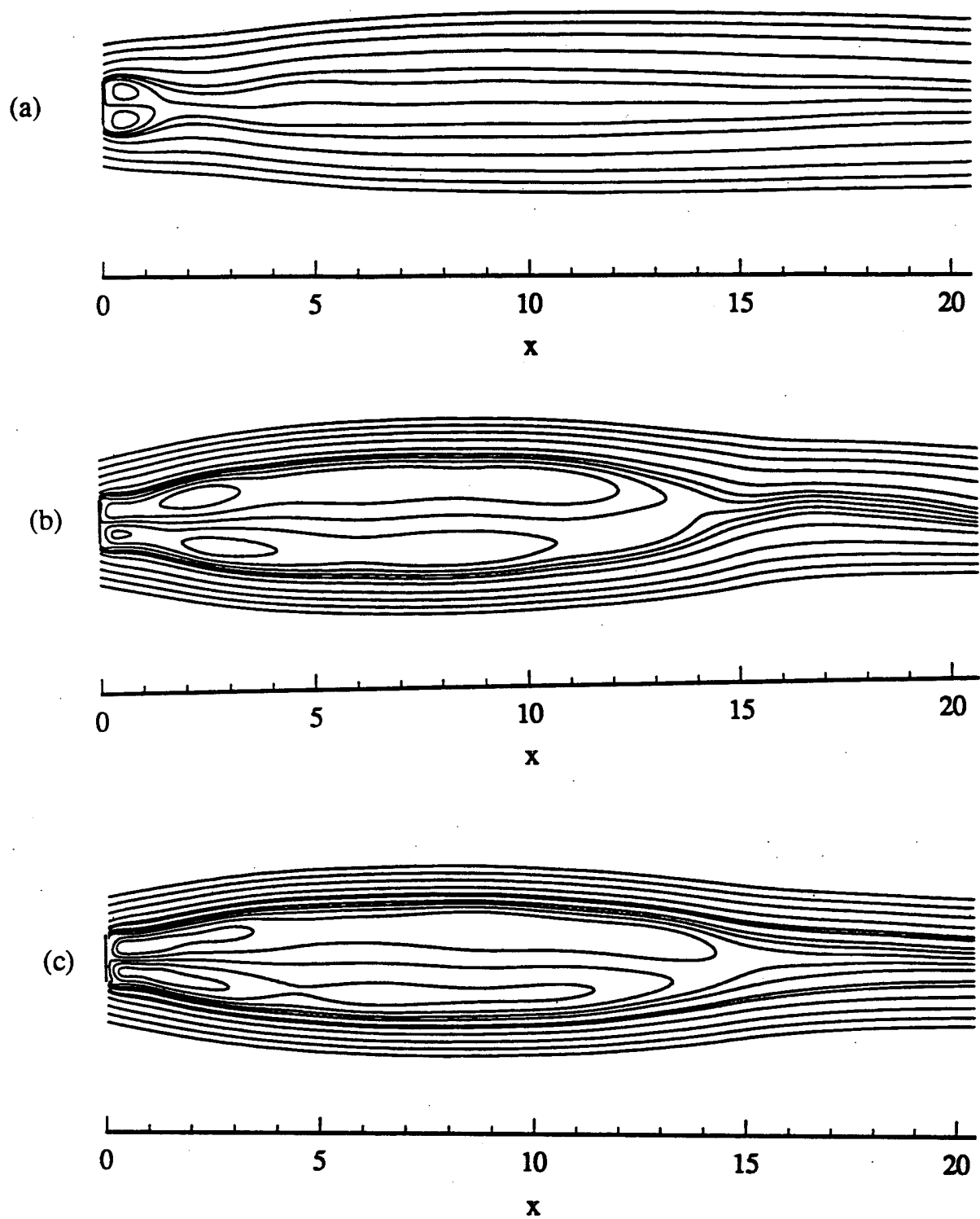


Figure 6.2.2.1 Time-mean streamlines for (a) $Re = 100$, (b) $Re = 500$, (c) $Re = 1000$.

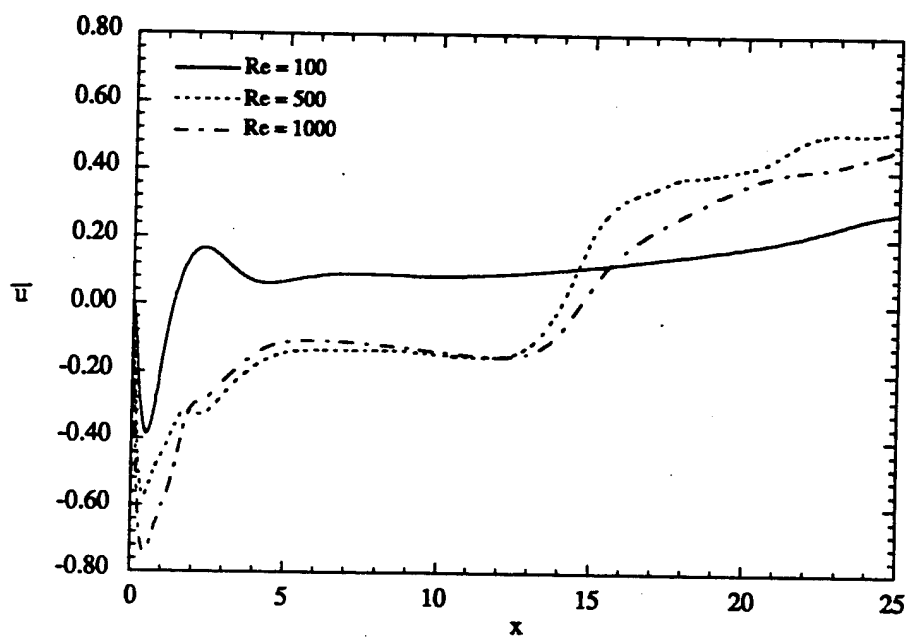


Figure 6.2.2.2 Profiles of the time-mean streamwise velocity along the centerline ($y = 0$) for the three Reynolds numbers.

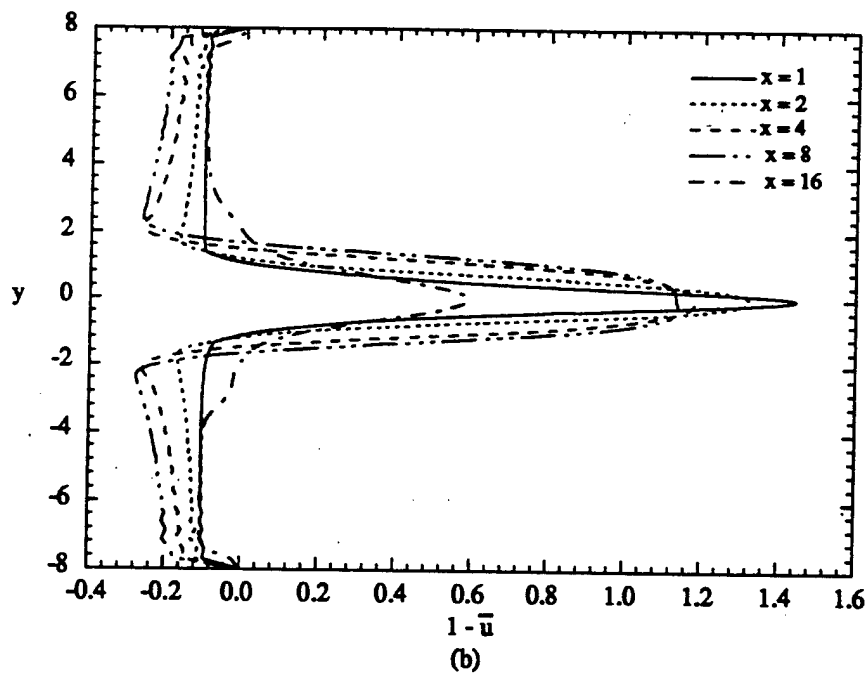
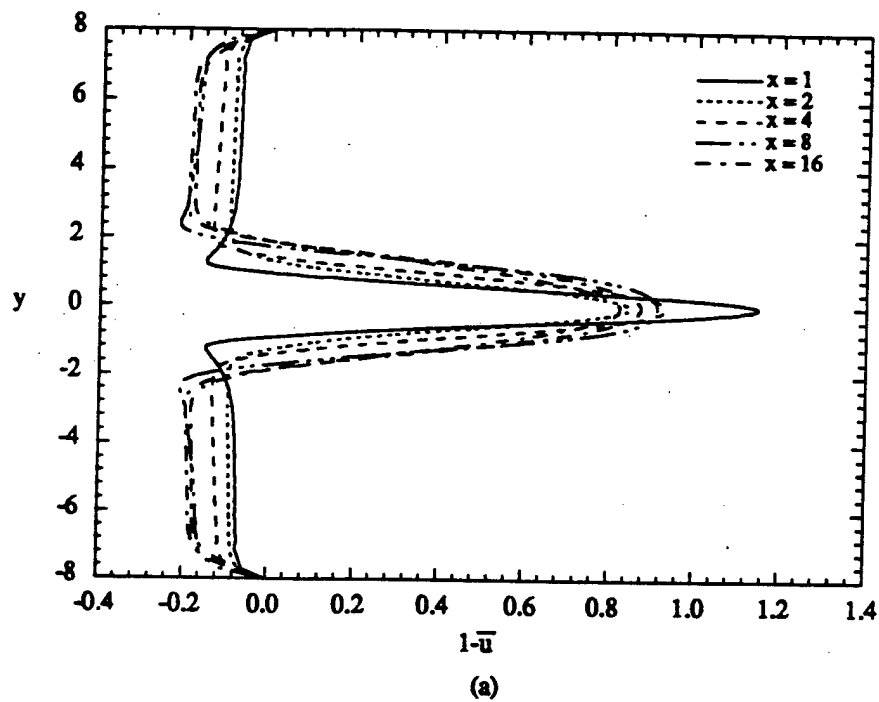


Figure 6.2.2.3 Profiles of the time-mean wake-defect velocity at different streamwise locations for (a) $Re = 100$, (b) $Re = 500$.

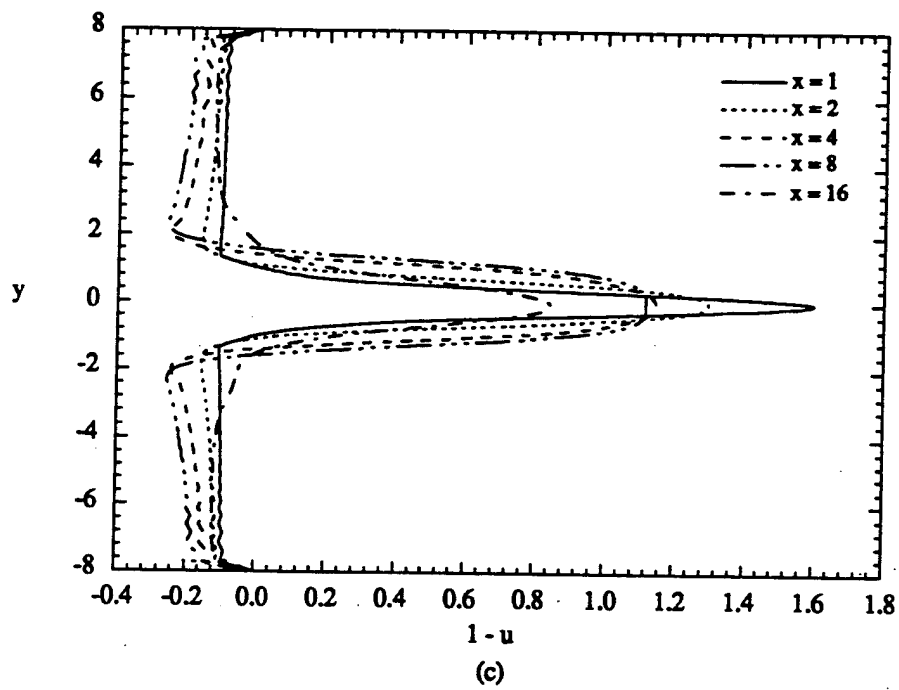


Figure 6.2.2.3(continued) (c) $Re = 1000$.

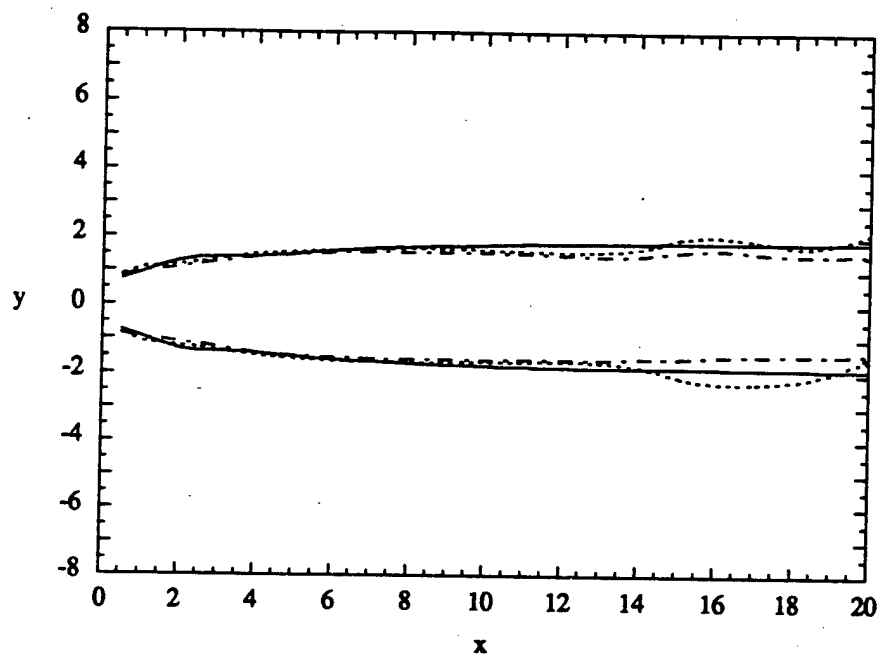


Figure 6.2.2.4 Loci of $y(\bar{u} = 0.99)$ for various Reynolds numbers.
 (—) $Re = 100$, (----) $Re = 500$, (— · —) $Re = 1000$.

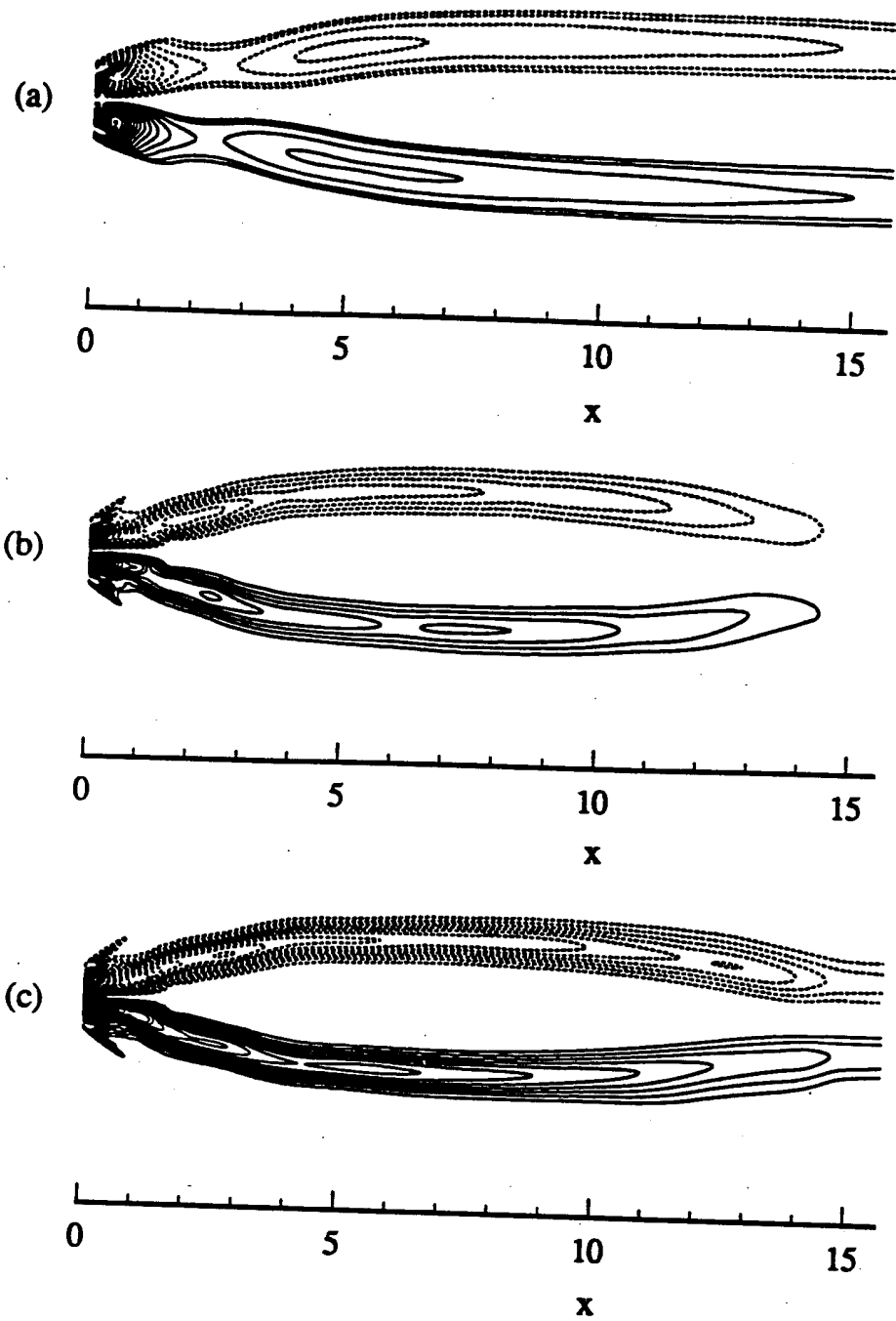


Figure 6.2.2.5 Contours of time-mean spanwise vorticity for
 (a) $Re = 100$, (b) $Re = 500$, (c) $Re = 1000$.
 Dashed Lines : $(\omega_{zmin}, \omega_{zmax}, \Delta\omega_z) = (-6.5, -0.5, 0.25)$
 Solid Lines : $(\omega_{zmin}, \omega_{zmax}, \Delta\omega_z) = (0.5, 6.5, 0.25)$

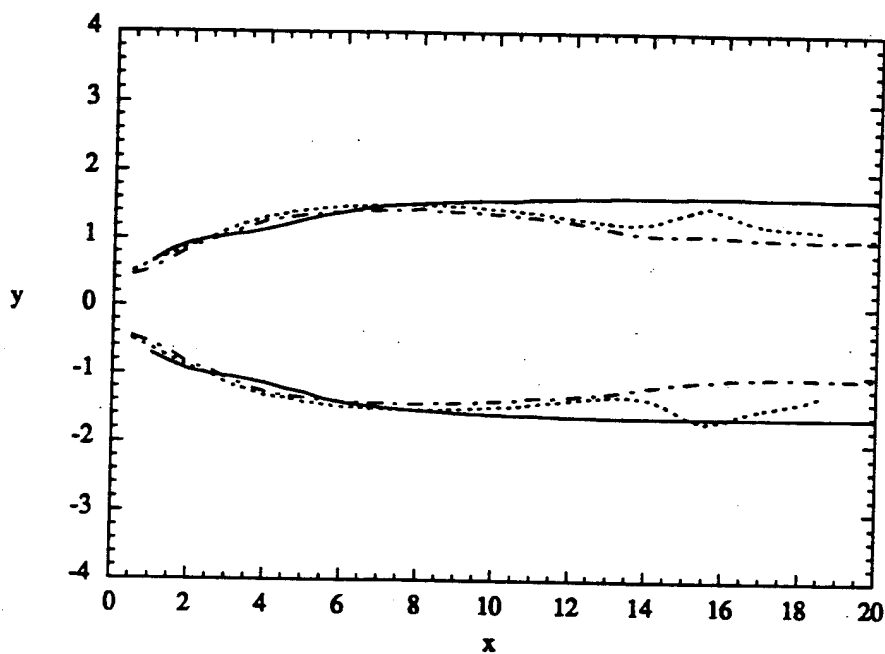


Figure 6.2.2.6 Variation of the shear-layer center, y_c , for various Reynolds numbers. (—) $Re = 100$, (----) $Re = 500$, (— · —) $Re = 1000$.

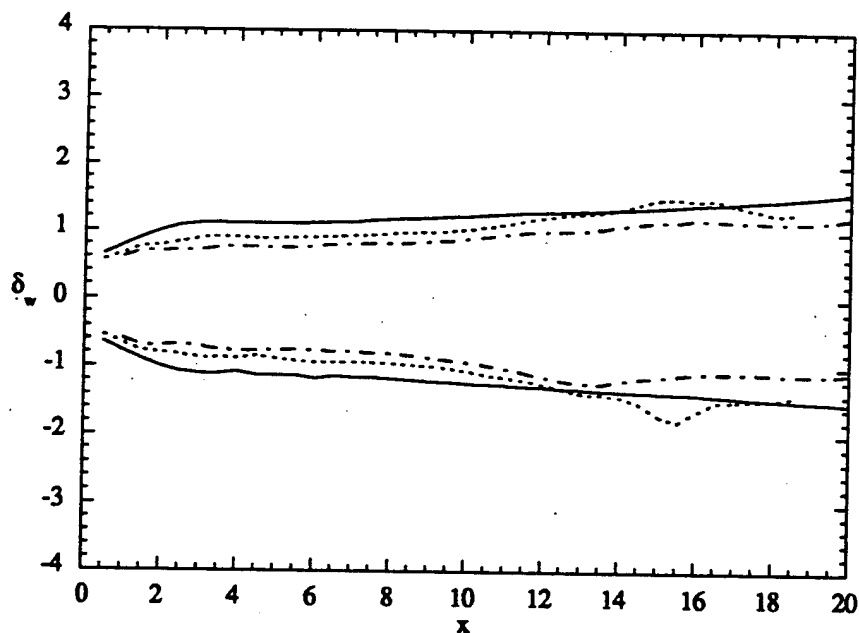


Figure 6.2.2.7 Streamwise distribution of the vorticity thickness, δ_w , for various Reynolds numbers. (—) $Re = 100$, (----) $Re = 500$, (— · —) $Re = 1000$.

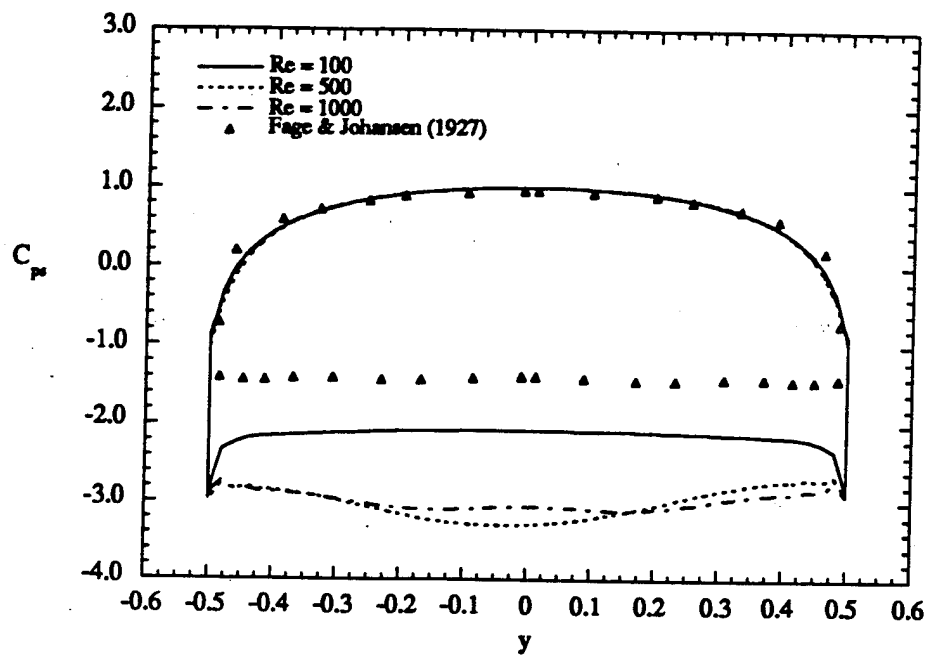


Figure 6.2.2.8 Distribution of the time-mean surface pressure coefficient, \overline{C}_{ps} , on the front and rear faces of the plate.

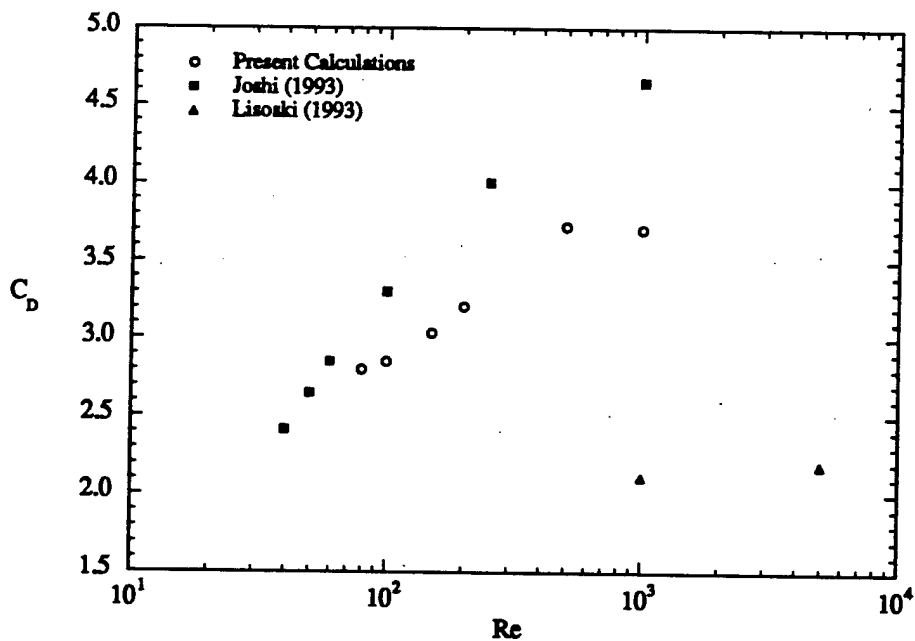
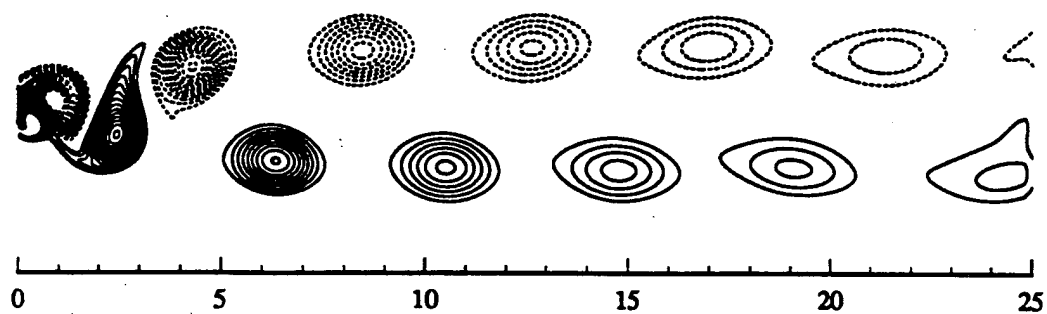
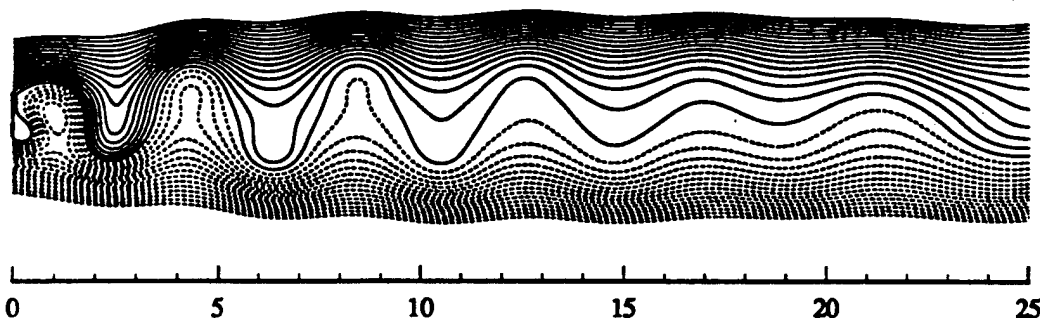


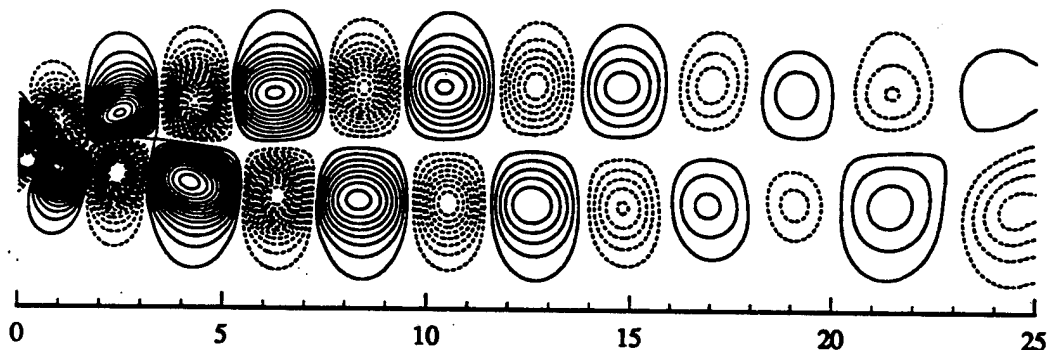
Figure 6.2.2.9 Variation of the time-mean drag coefficient with free-stream Reynolds number.



(a)



(b)



(c)

Figure 6.2.3.1 Instantaneous snapshot of the unsteady flow for $Re = 100$.

(a) Spanwise Vorticity.

Dashed Lines: $(\omega_{zmin}, \omega_{zmax}, \Delta\omega_z) = (-4.5, -0.5, 0.25)$

Solid Lines: $(\omega_{zmin}, \omega_{zmax}, \Delta\omega_z) = (0.5, 4.5, 0.25)$

(b) Streamlines. $(\psi_{min}, \psi_{max}, \Delta\psi) = (-1.5, 1.5, 0.1)$

(c) Pressure.

Dashed Lines: $(p_{min}, p_{max}, \Delta p) = (-0.5, -0.025, 0.025)$.

Solid Lines: $(p_{min}, p_{max}, \Delta p) = (0.025, 0.5, 0.025)$.

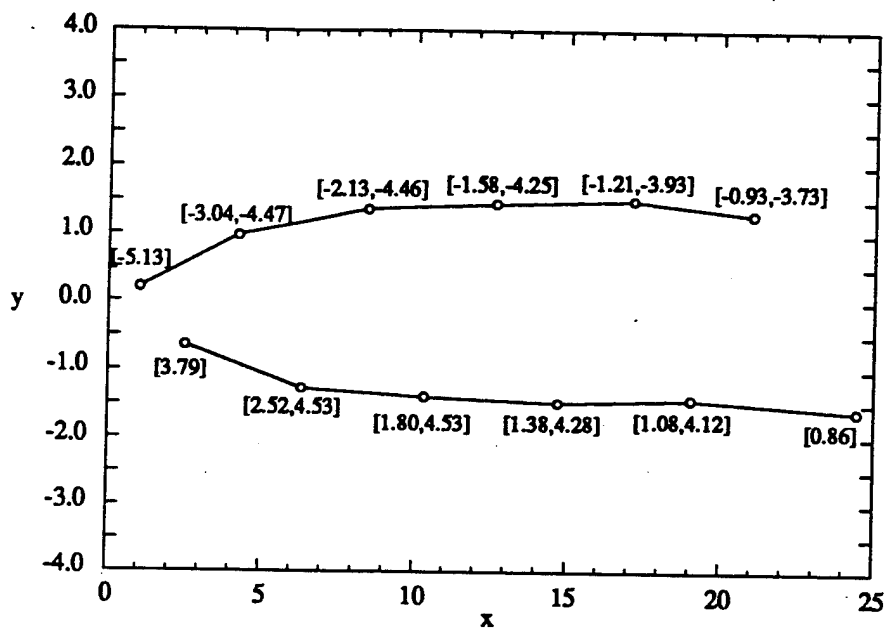


Figure 6.2.3.2 Location of the vortex cores for $Re = 100$ corresponding to Figure 6.2.3.1. Values in brackets represent $[\omega_z, \Gamma]$, the spanwise vorticity in the core and the total vortex circulation.

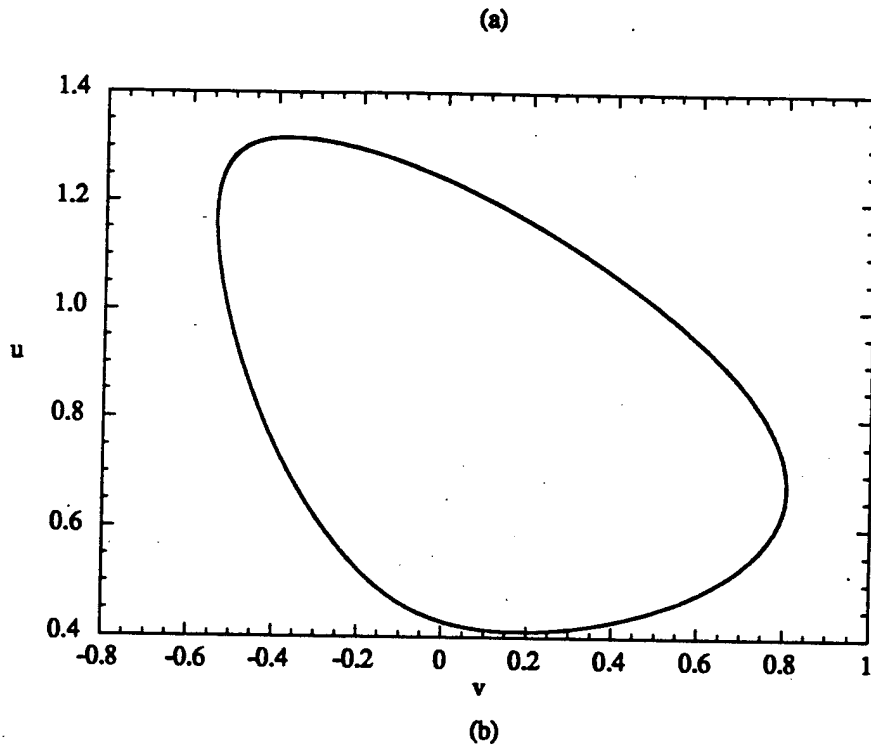
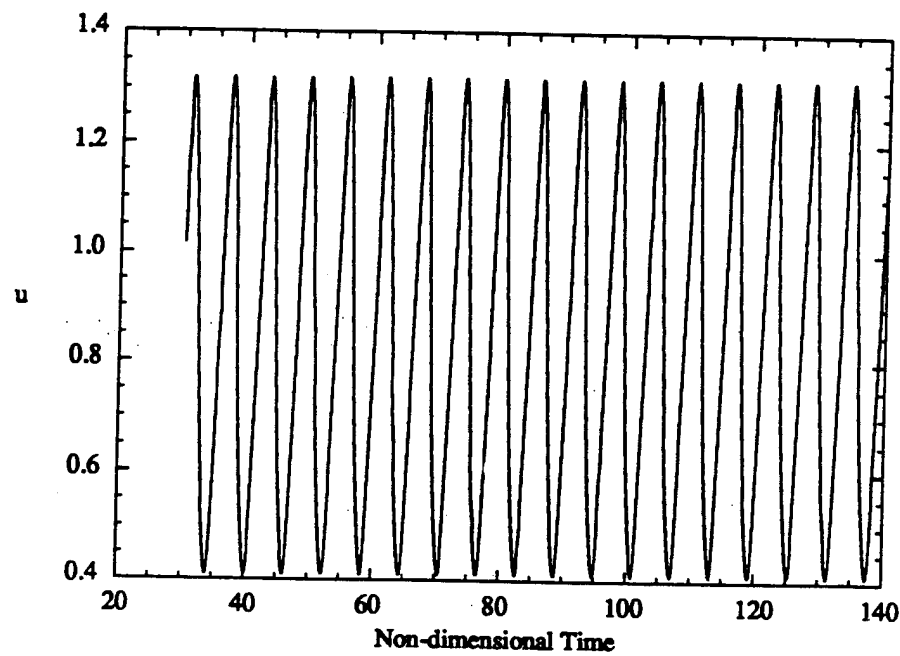
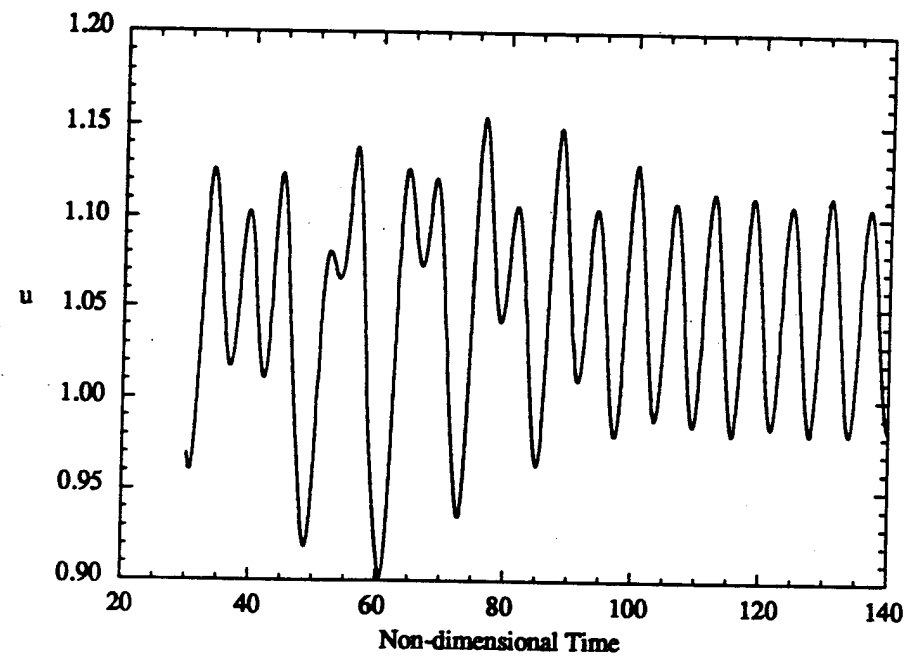
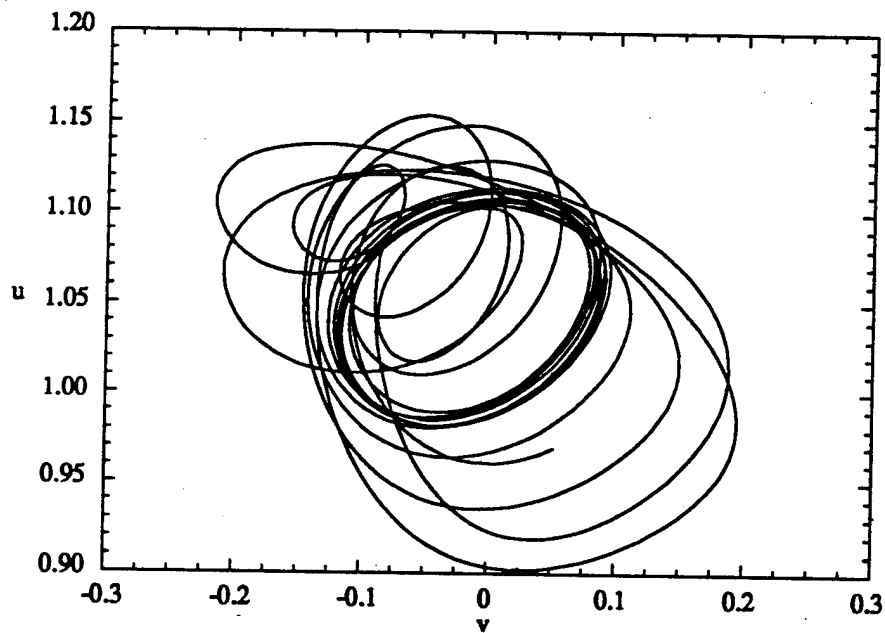


Figure 6.2.3.3 (a) Time trace of the streamwise velocity component and (b) u - v phase portrait for $Re = 100$ in the near-wake region ($x = 2$, $y = 1$).



(a)



(b)

Figure 6.2.3.4 (a) Time trace of the streamwise velocity component and (b) u - v phase portrait for $Re = 100$ in the far-wake region ($x = 20$, $y = 2$).

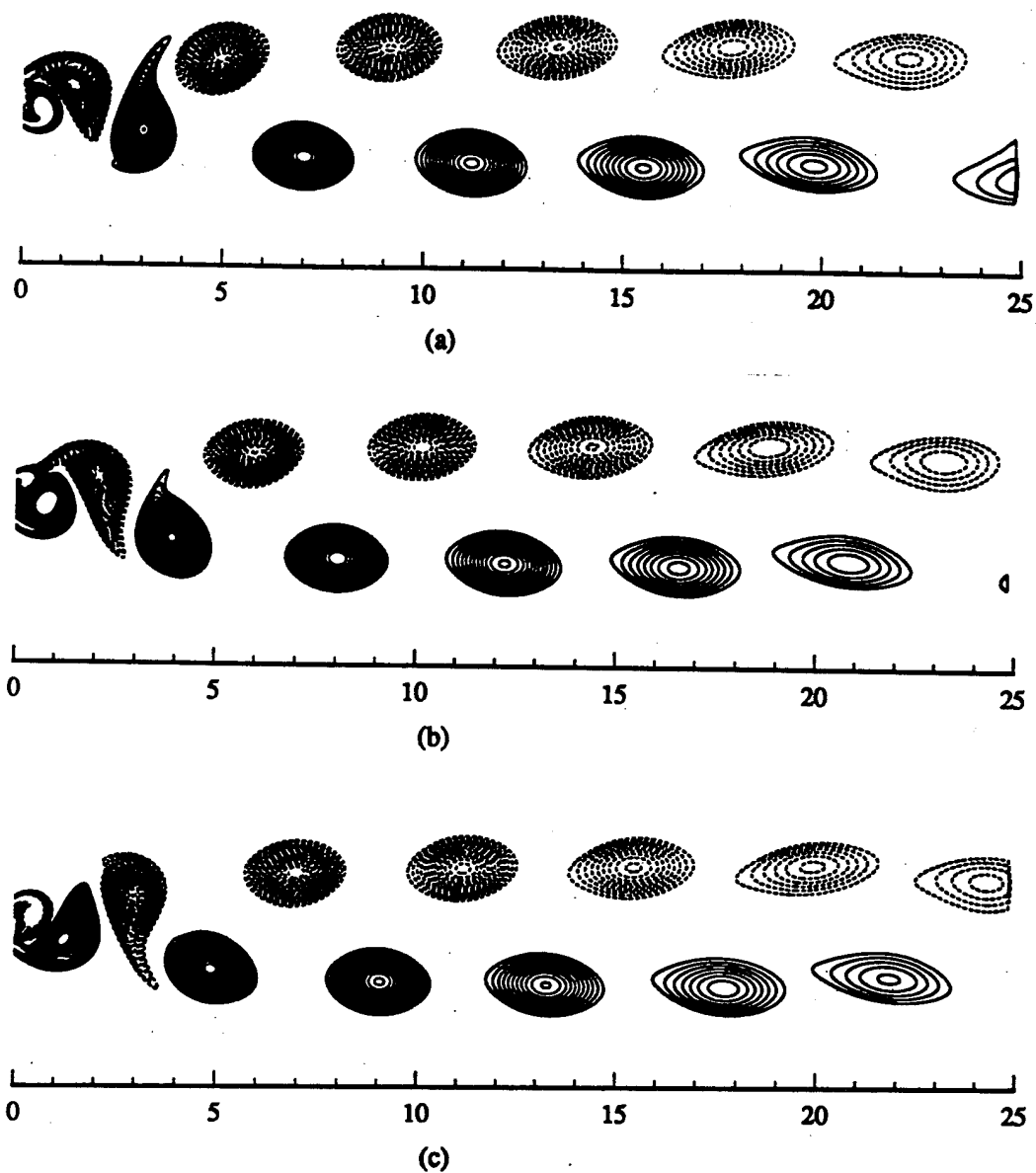


Figure 6.2.3.5 Spanwise vorticity contours for a representative shedding cycle for $Re = 100$. (a) $t = 91$, (b) $t = 92.5$, (c) $t = 94$.

Dashed Lines: $(\omega_{zmin}, \omega_{zmax}, \Delta\omega_z) = (-4.5, -0.5, 0.1)$

Solid Lines: $(\omega_{zmin}, \omega_{zmax}, \Delta\omega_z) = (0.5, 4.5, 0.1)$

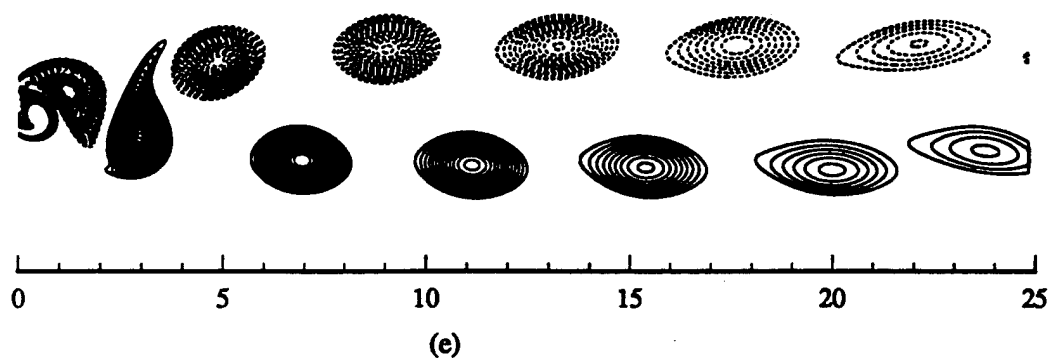
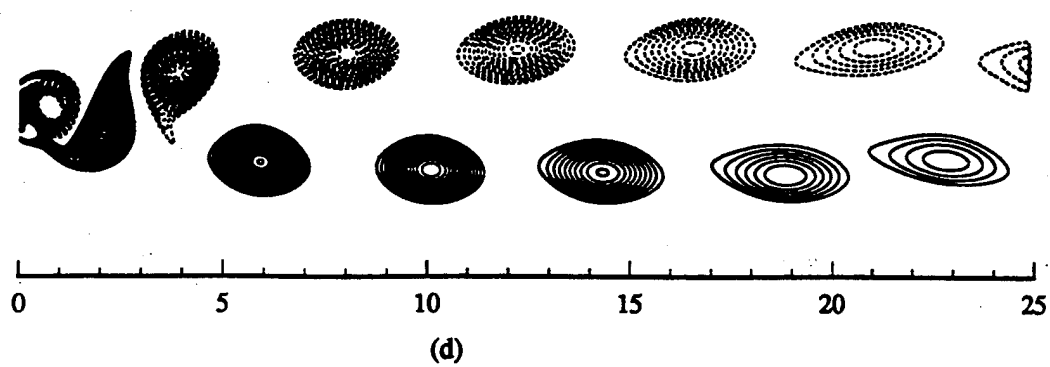


Figure 6.2.3.5(continued) (d) $t = 95.5$, (e) $t = 97$.

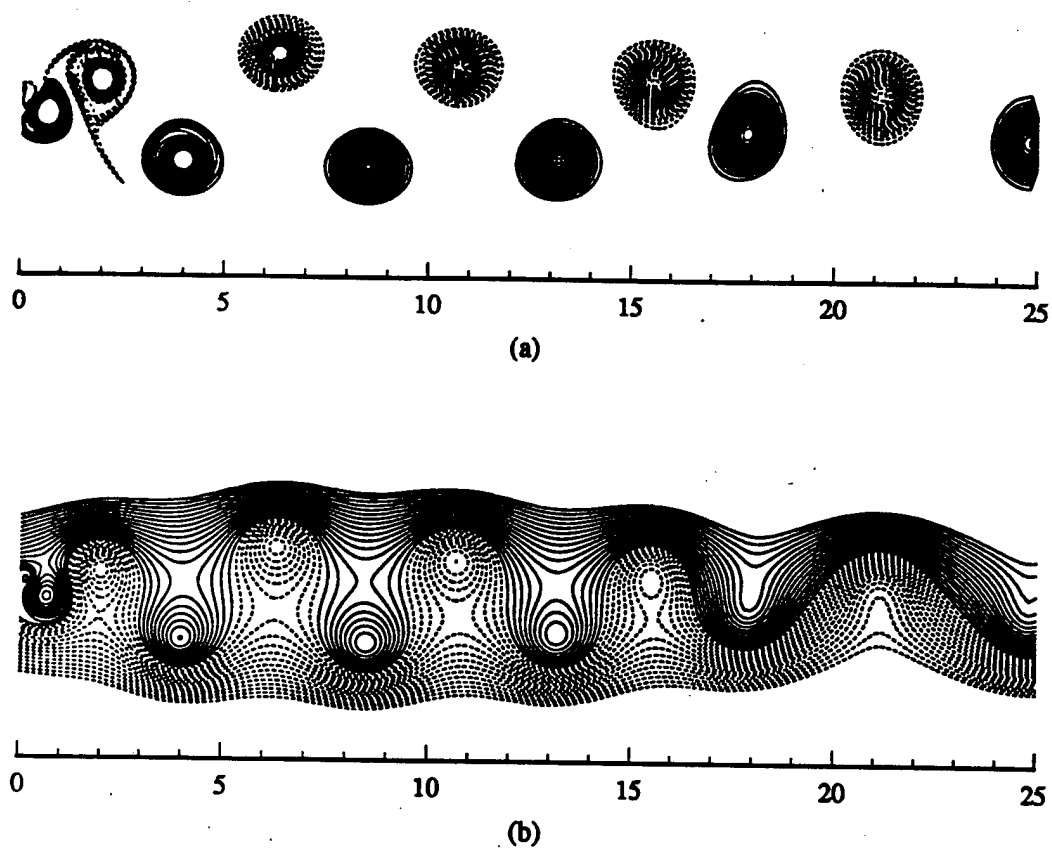


Figure 6.2.3.6 Instantaneous snapshot of the unsteady flow at $t = 120$ for $Re = 500$.
 (a) Spanwise Vorticity.
 Dashed Lines : $(\omega_{zmin}, \omega_{zmax}, \Delta\omega_z) = (-6.5, -0.5, 0.1)$
 Solid Lines : $(\omega_{zmin}, \omega_{zmax}, \Delta\omega_z) = (0.5, 6.5, 0.1)$
 (b) Streamlines. $(\psi_{min}, \psi_{max}, \Delta\psi) = (-1.5, 1.5, 0.1)$

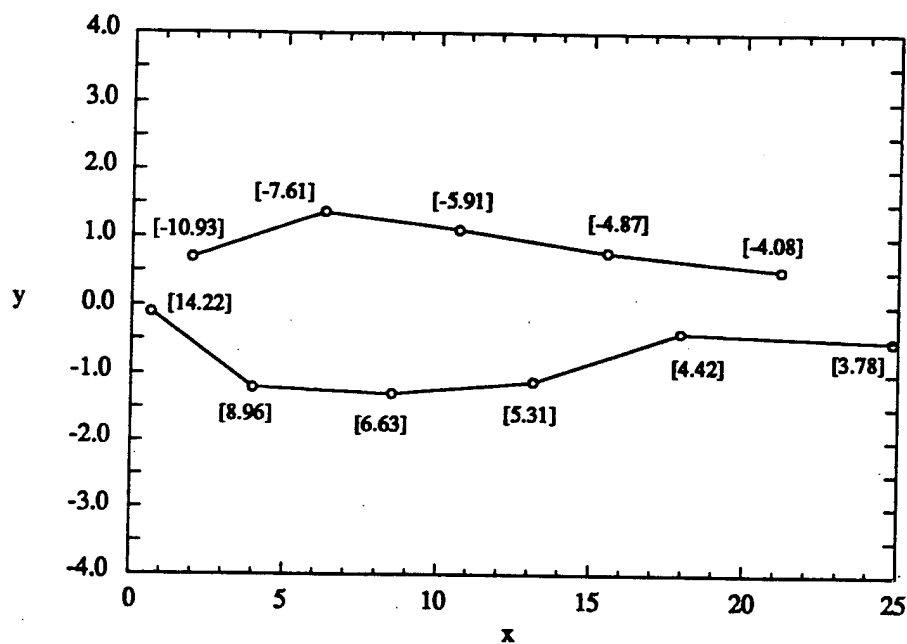


Figure 6.2.3.7 Location of the vortex cores for $Re = 500$ corresponding to Figure 6.2.3.6. Value in brackets represents $[\omega_z]$, the spanwise vorticity in the core. $\Gamma = 6.6$.

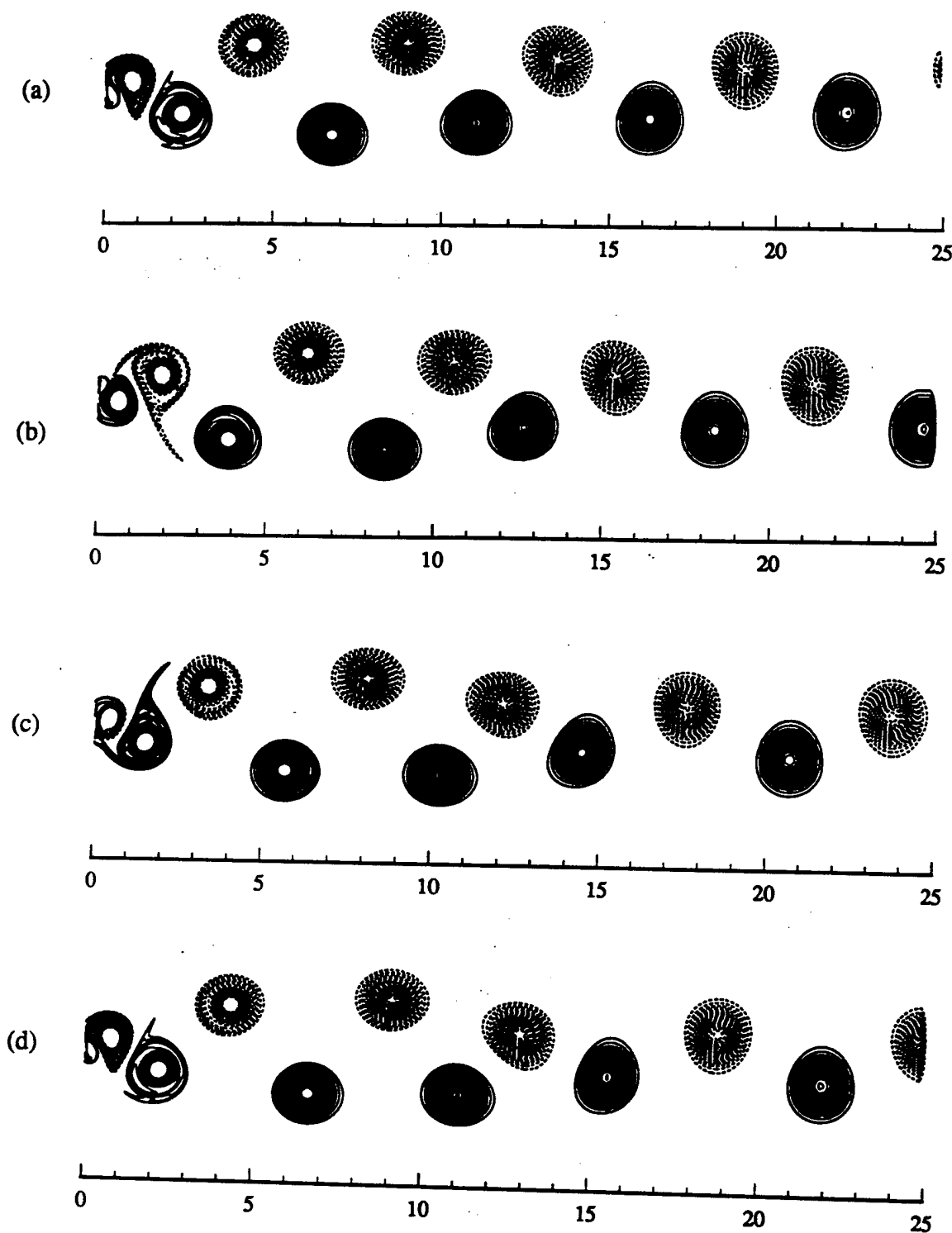


Figure 6.2.3.8 Spanwise vorticity contours for a representative shedding cycle for $Re = 500$. (a) $t = 71$, (b) $t = 74$, (c) $t = 77$, (d) $t = 78.5$.

Dashed Lines : $(\omega_{zmin}, \omega_{zmax}, \Delta\omega_z) = (-6.5, -0.5, 0.1)$

Solid Lines : $(\omega_{zmin}, \omega_{zmax}, \Delta\omega_z) = (0.5, 6.5, 0.1)$

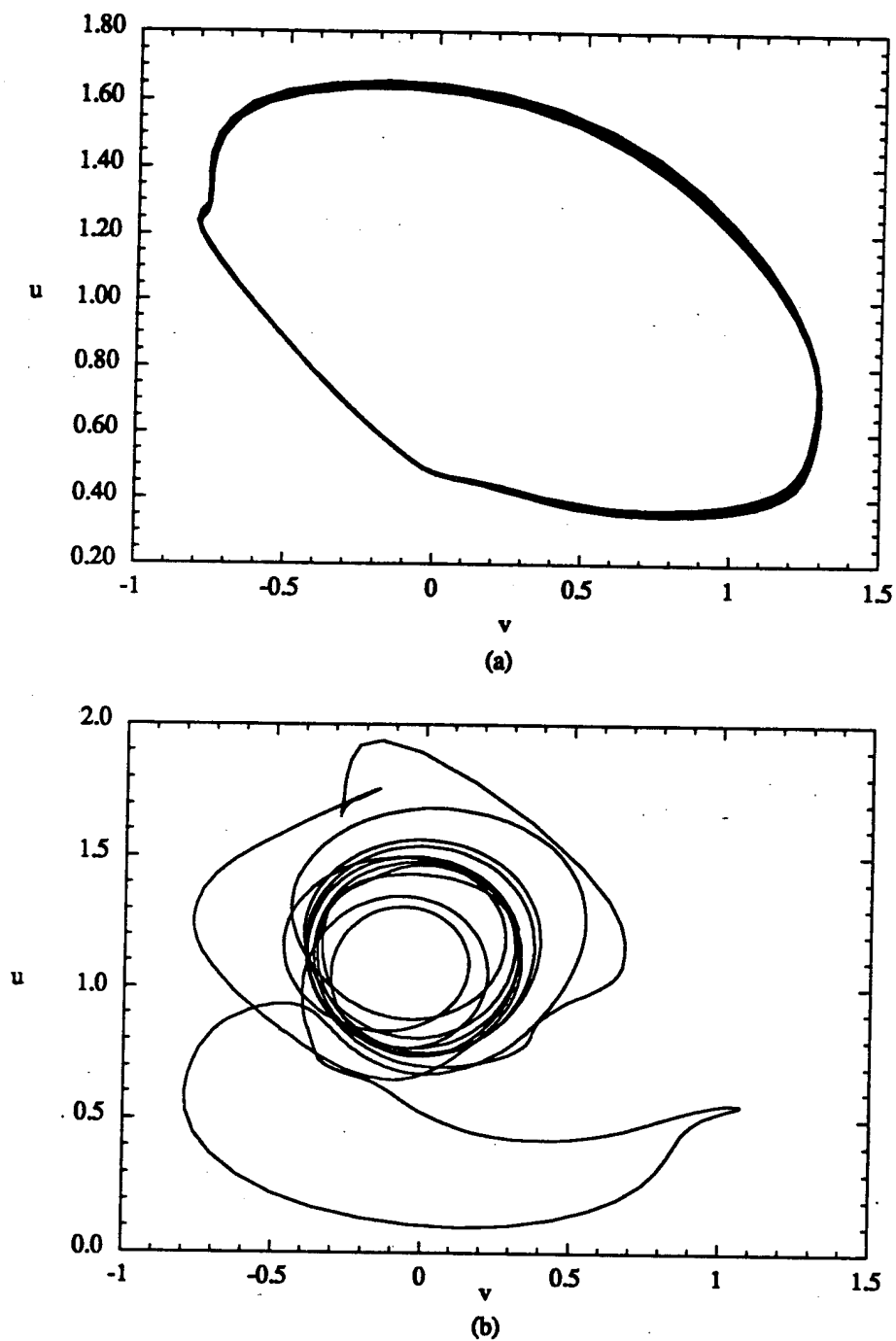


Figure 6.2.3.9 u - v phase portraits for $Re = 500$ in (a) the near-wake ($x = 2, y = 1$), and (b) the far-wake ($x = 20, y = 2$) regions.

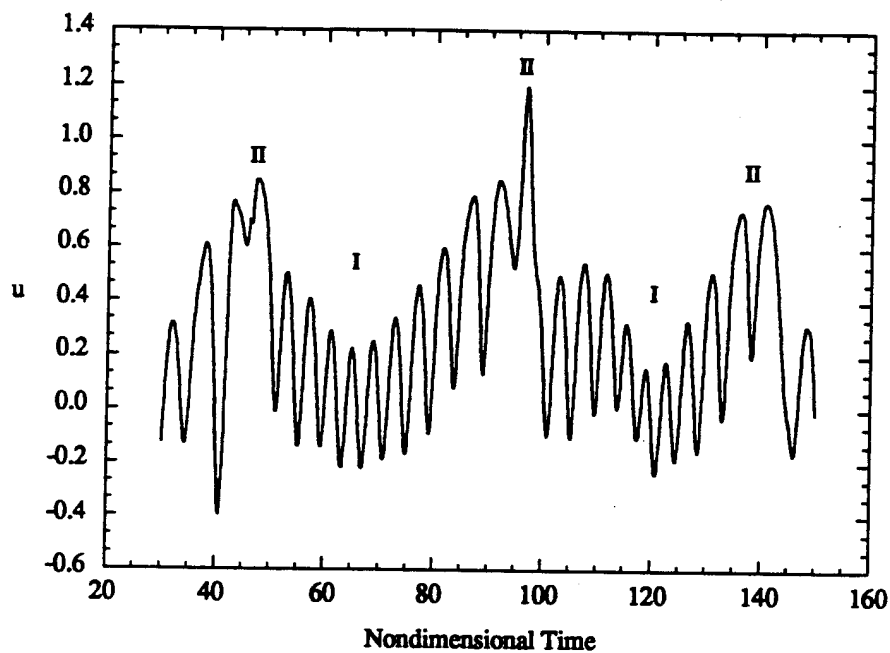


Figure 6.2.3.10 Time trace of the streamwise velocity component at a far-wake point ($x = 16$, $y = 0$) for $Re = 500$. Far-wake vortex interaction regions I and II are identified.

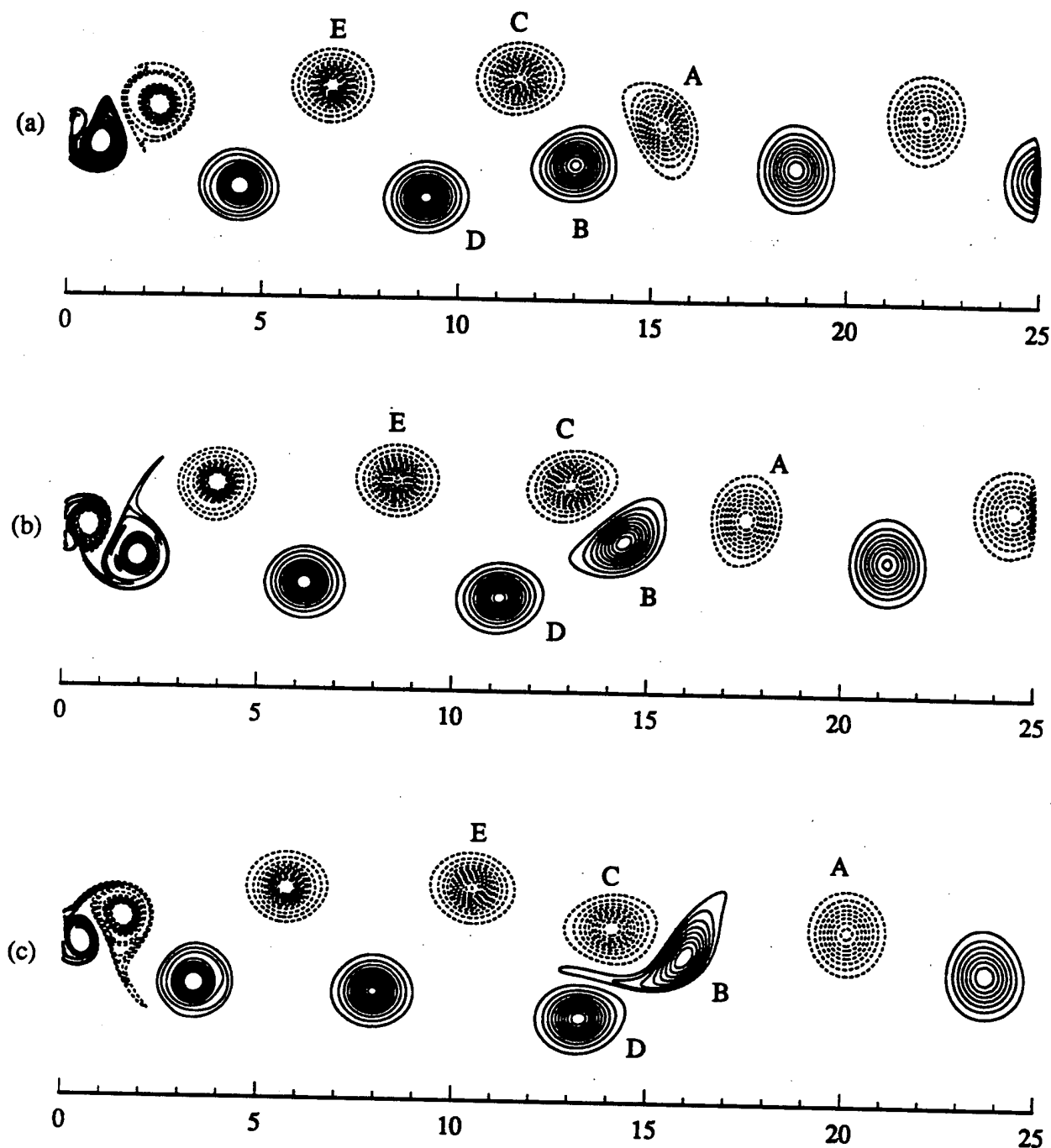


Figure 6.2.3.11 Spanwise vorticity contours for a representative far-wake vortex interaction region II at $Re = 500$.
 (a) $t = 82.5$, (b) $t = 85.5$, (c) $t = 88.5$.
 Dashed Lines : $(\omega_{zmin}, \omega_{zmax}, \Delta\omega_z) = (-6.5, -0.5, 0.1)$
 Solid Lines : $(\omega_{zmin}, \omega_{zmax}, \Delta\omega_z) = (0.5, 6.5, 0.1)$

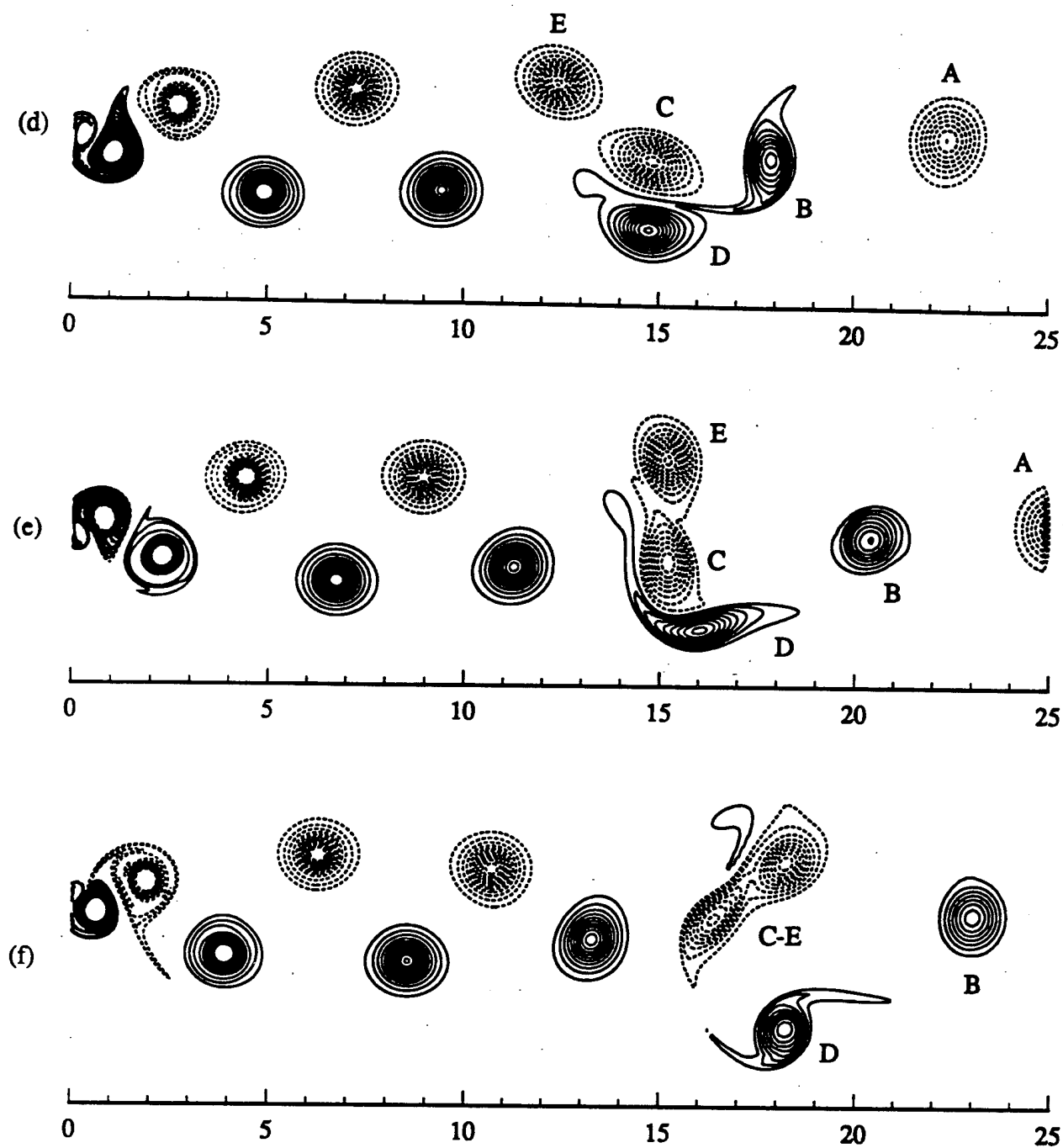


Figure 6.2.3.11(continued) (d) $t = 91$, (e) $t = 94$, (f) $t = 97$.

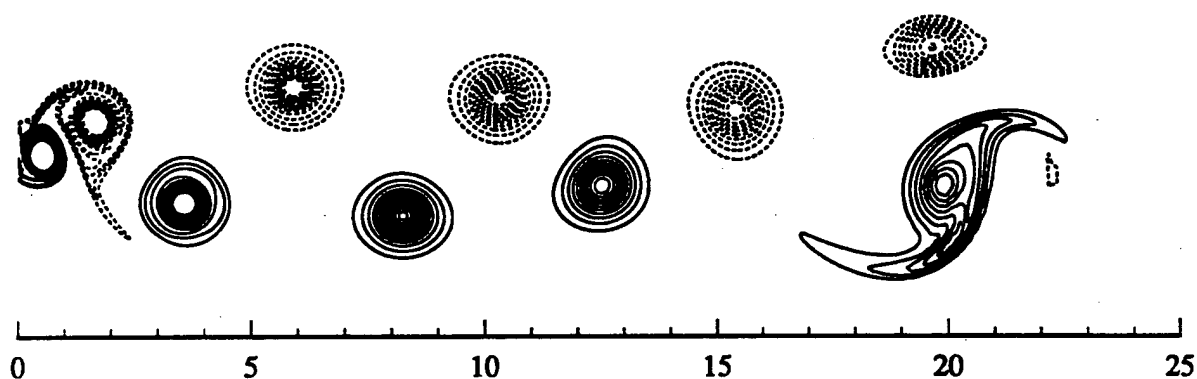


Figure 6.2.3.12 Spanwise vorticity contours for $Re = 500$ at $t = 150$. The pairing process in the lower half of the computational domain is shown.

Dashed Lines : $(\omega_{zmin}, \omega_{zmax}, \Delta\omega_z) = (-6.5, -0.5, 0.1)$

Solid Lines : $(\omega_{zmin}, \omega_{zmax}, \Delta\omega_z) = (0.5, 6.5, 0.1)$

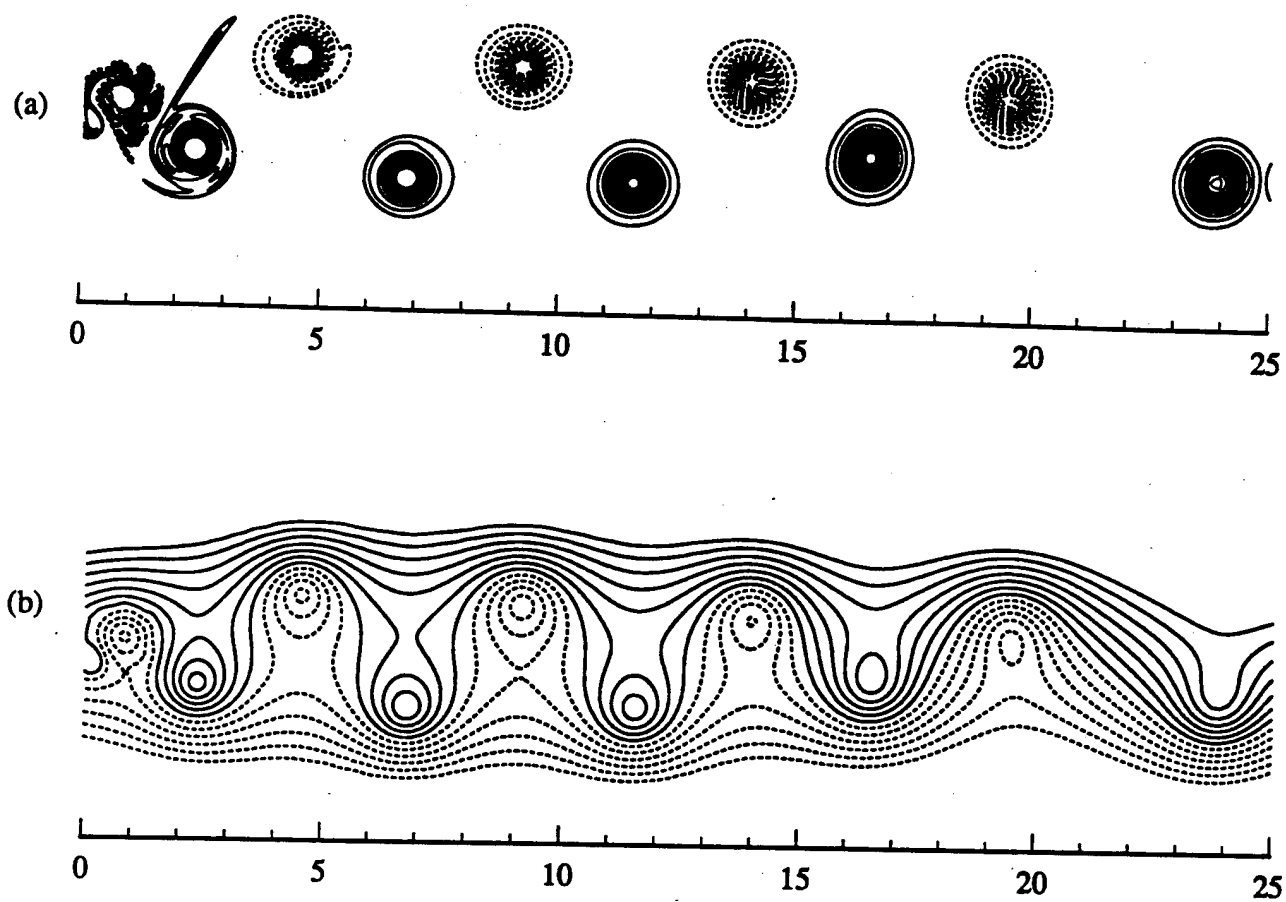


Figure 6.2.3.13 Instantaneous snapshot of the unsteady flow at $t = 230$ for $Re = 1000$.
 (a) Spanwise Vorticity.
 Dashed Lines : $(\omega_{zmin}, \omega_{zmax}, \Delta\omega_z) = (-8.5, -0.5, 0.1)$
 Solid Lines : $(\omega_{zmin}, \omega_{zmax}, \Delta\omega_z) = (0.5, 8.5, 0.1)$
 (b) Streamlines. $(\psi_{min}, \psi_{max}, \Delta\psi) = (-1.5, 1.5, 0.1)$

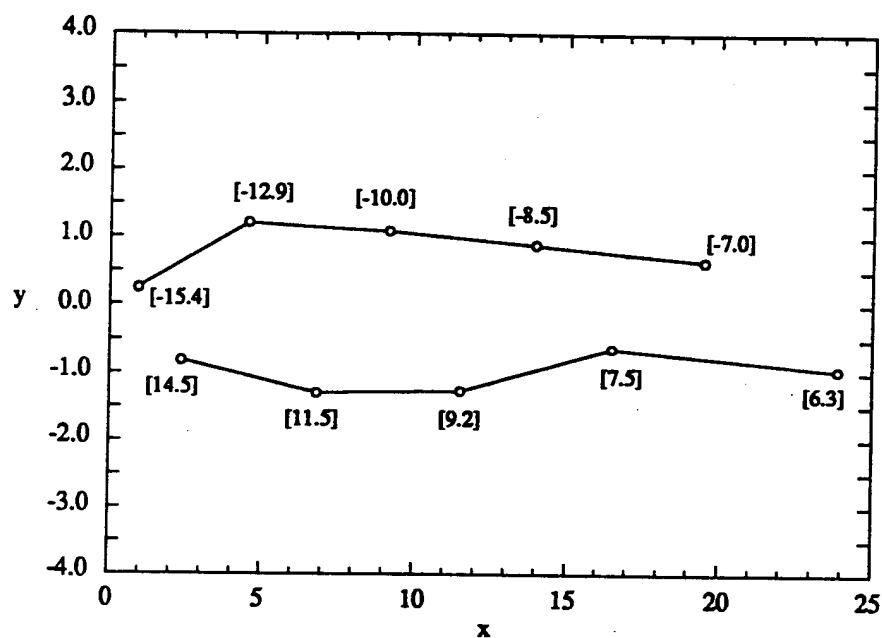
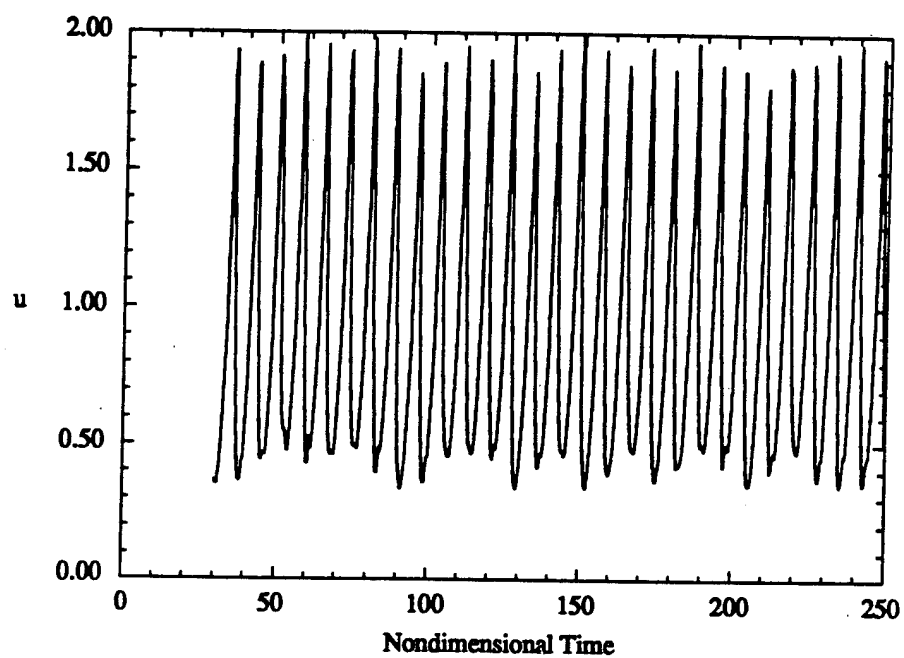
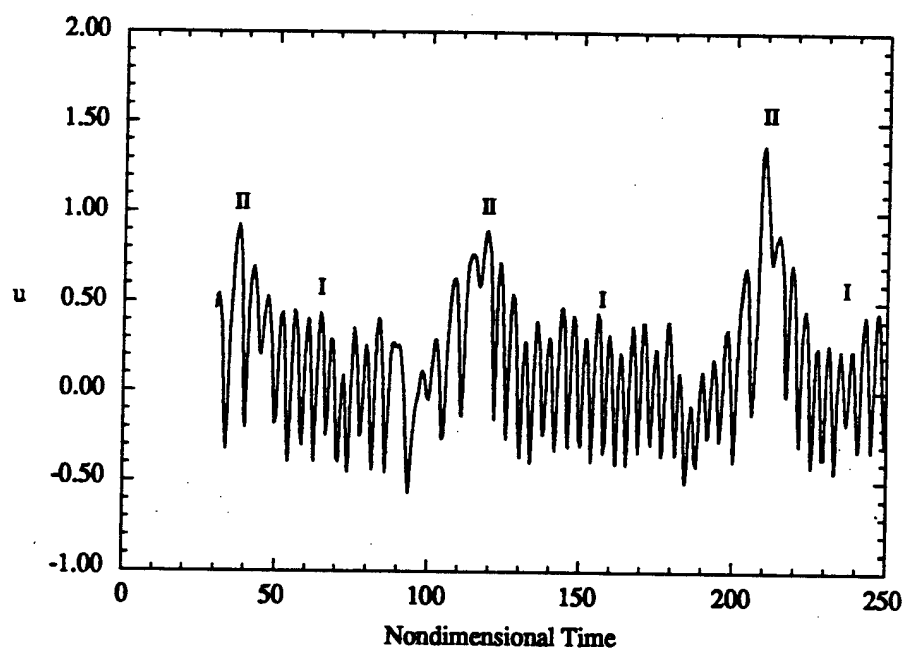


Figure 6.2.3.14 Location of the vortex cores for $Re = 1000$ corresponding to Figure 6.2.3.13. Value in brackets represents the spanwise vorticity in the core, $[\omega_z]$. $\Gamma = 6.6$.



(a)



(b)

Figure 6.2.3.15 Time traces of the streamwise velocity for $Re = 1000$ in (a) the near wake ($x = 2, y = 1$), and (b) the far wake ($x = 16, y = 0$). Far-wake interaction regions I and II are identified.

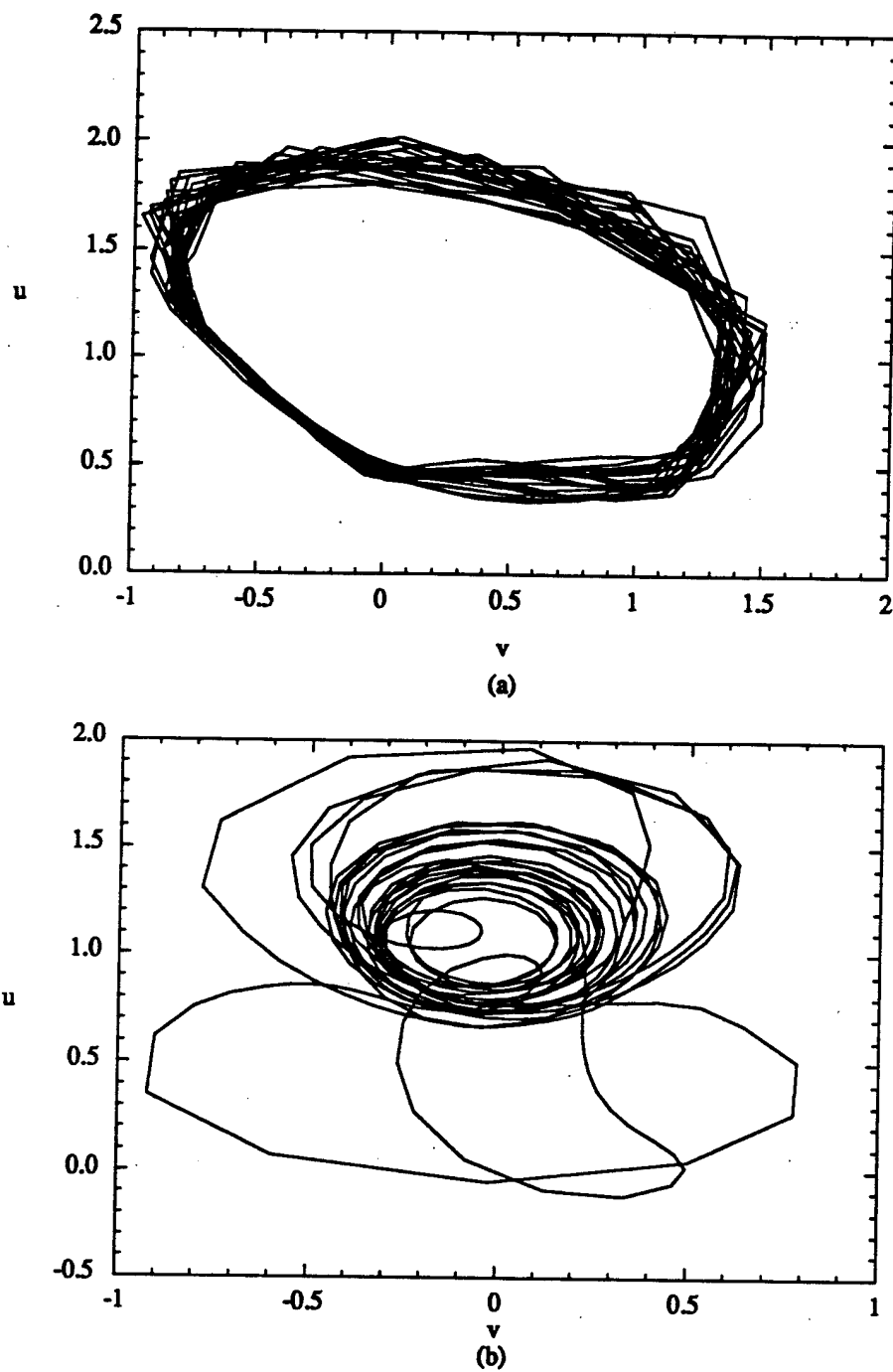


Figure 6.2.3.16 u - v phase portraits for $Re = 1000$ in (a) the near wake ($x = 2, y = 1$), and (b) the far wake ($x = 20, y = 2$).

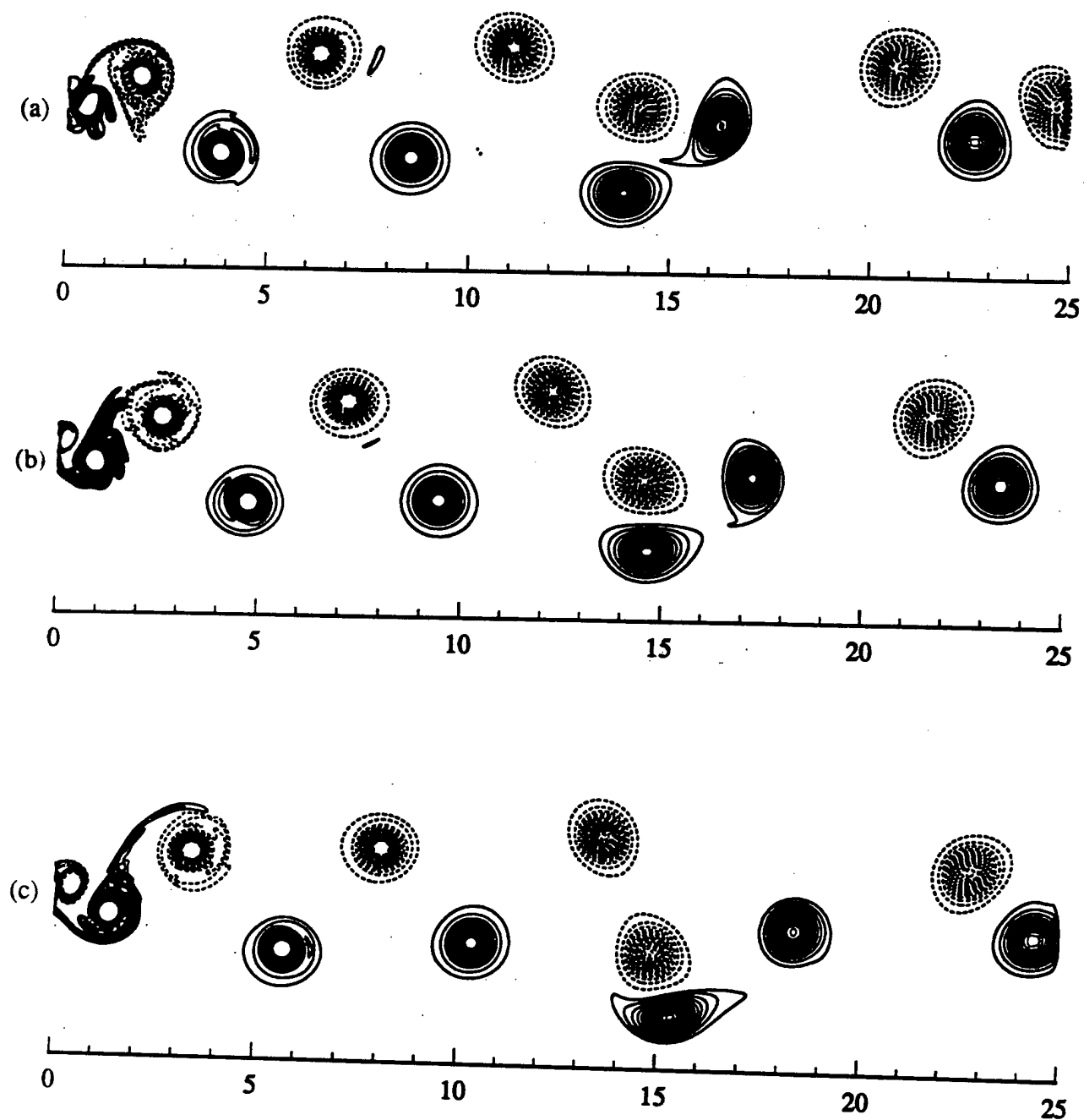


Figure 6.2.3.17 Spanwise vorticity contours for a representative far-wake vortex interaction region II at $Re = 1000$.
 (a) $t = 111$, (b) $t = 112.5$, (c) $t = 114$, (d) $t = 115.5$.

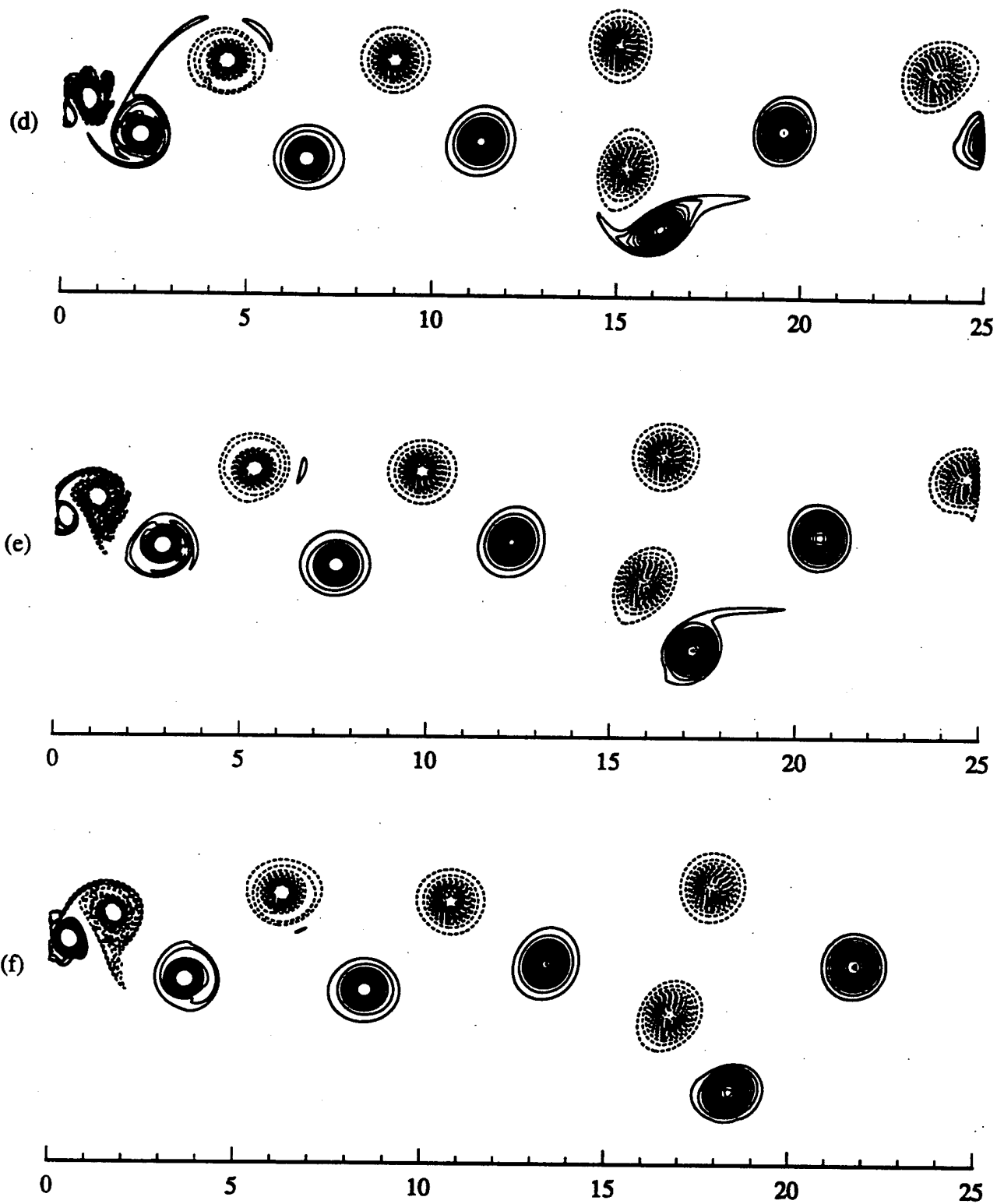


Figure 6.2.3.17(continued)

(d) $t = 115.5$, (e) $t = 117$, (f) $t = 118.5$.

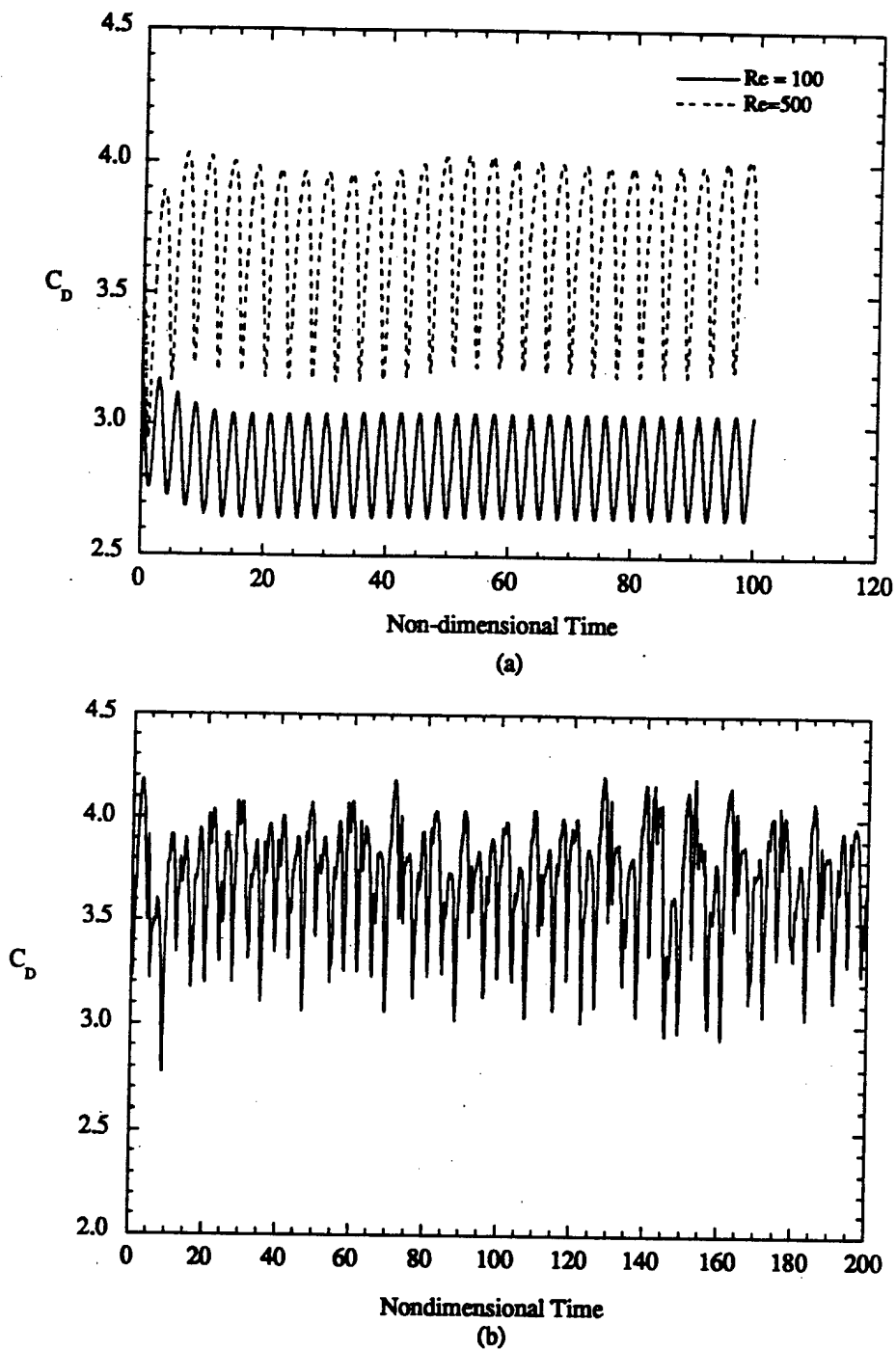


Figure 6.2.4.1 Temporal variation of the drag coefficient for (a) $Re = 100$ and 500, (b) $Re = 1000$.

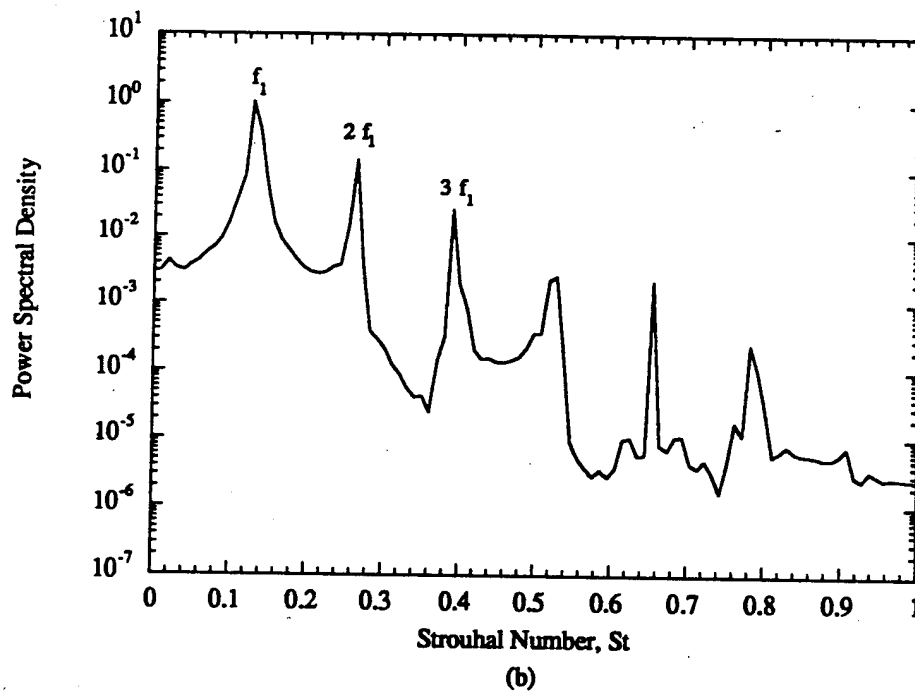
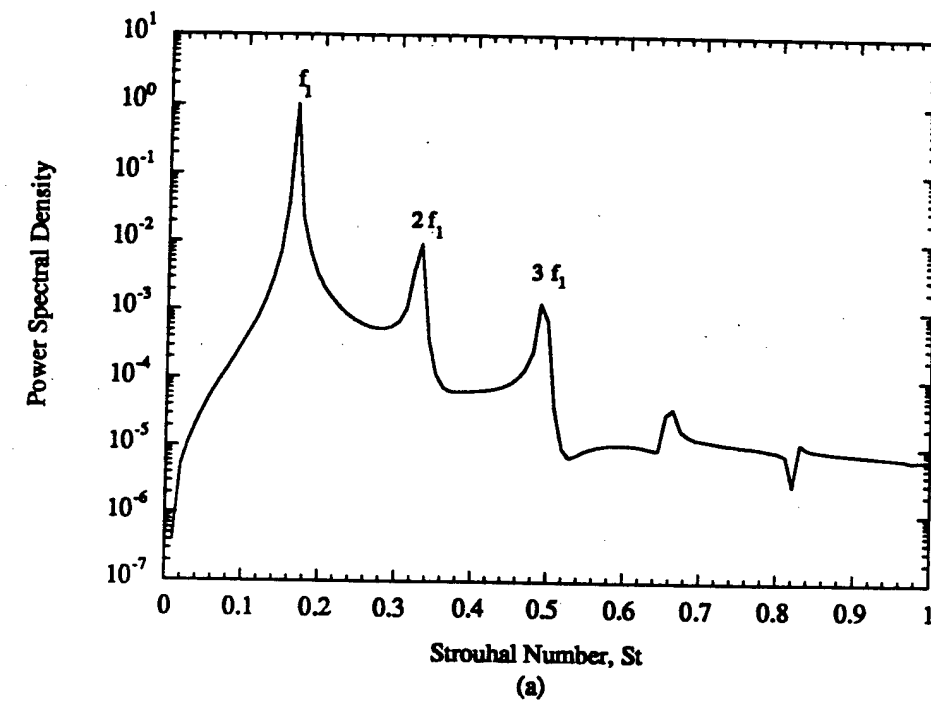


Figure 6.2.4.2 Power spectrum in the near wake ($x = 2$, $y = 1$) for
(a) $Re = 100$, (b) $Re = 500$

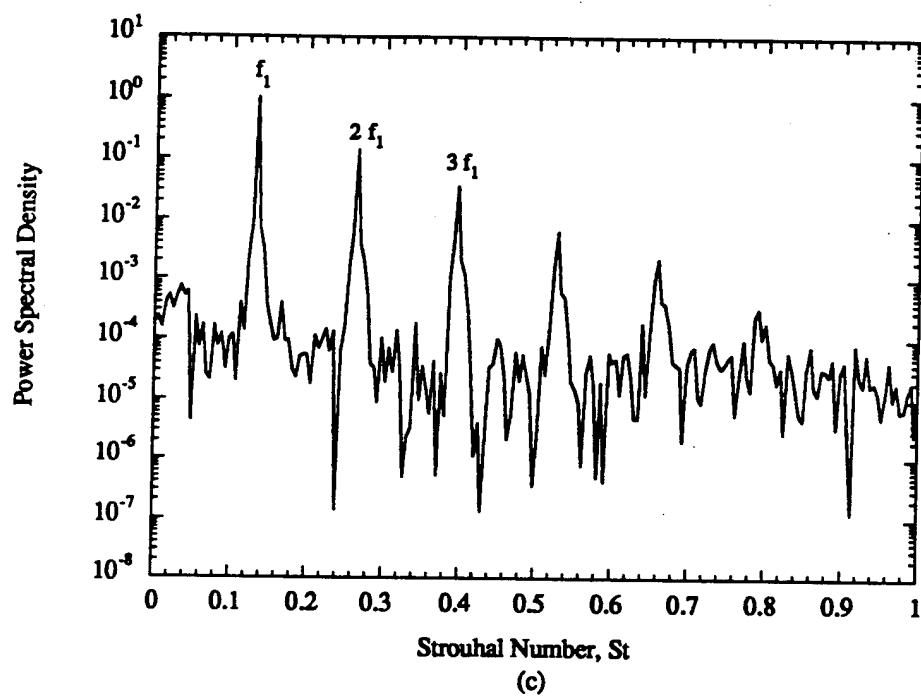


Figure 6.2.4.2(continued) (c) $Re = 1000$.

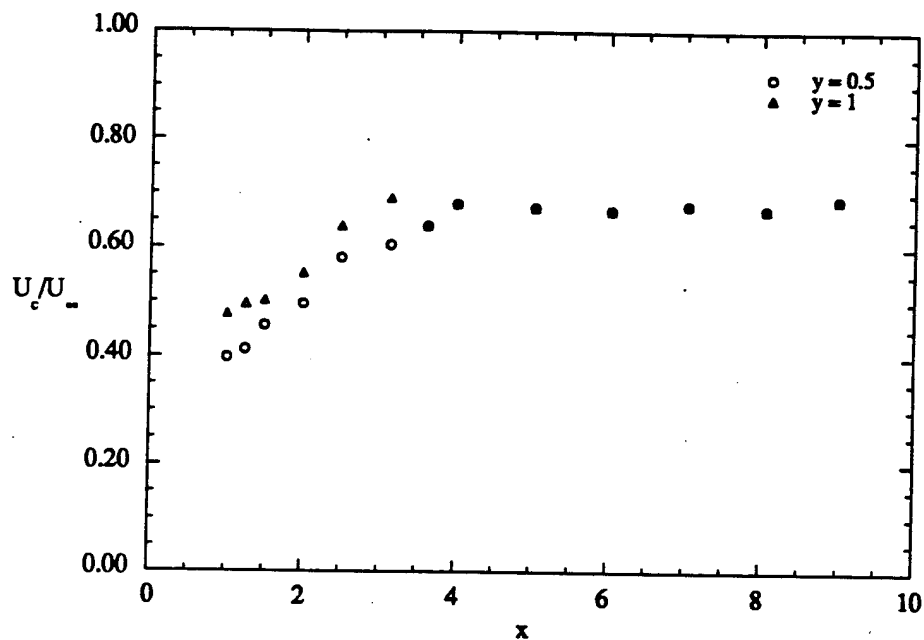


Figure 6.2.4.3 Streamwise variation of the convective velocity at $y = 0.5$ and 1 for $Re = 100$.

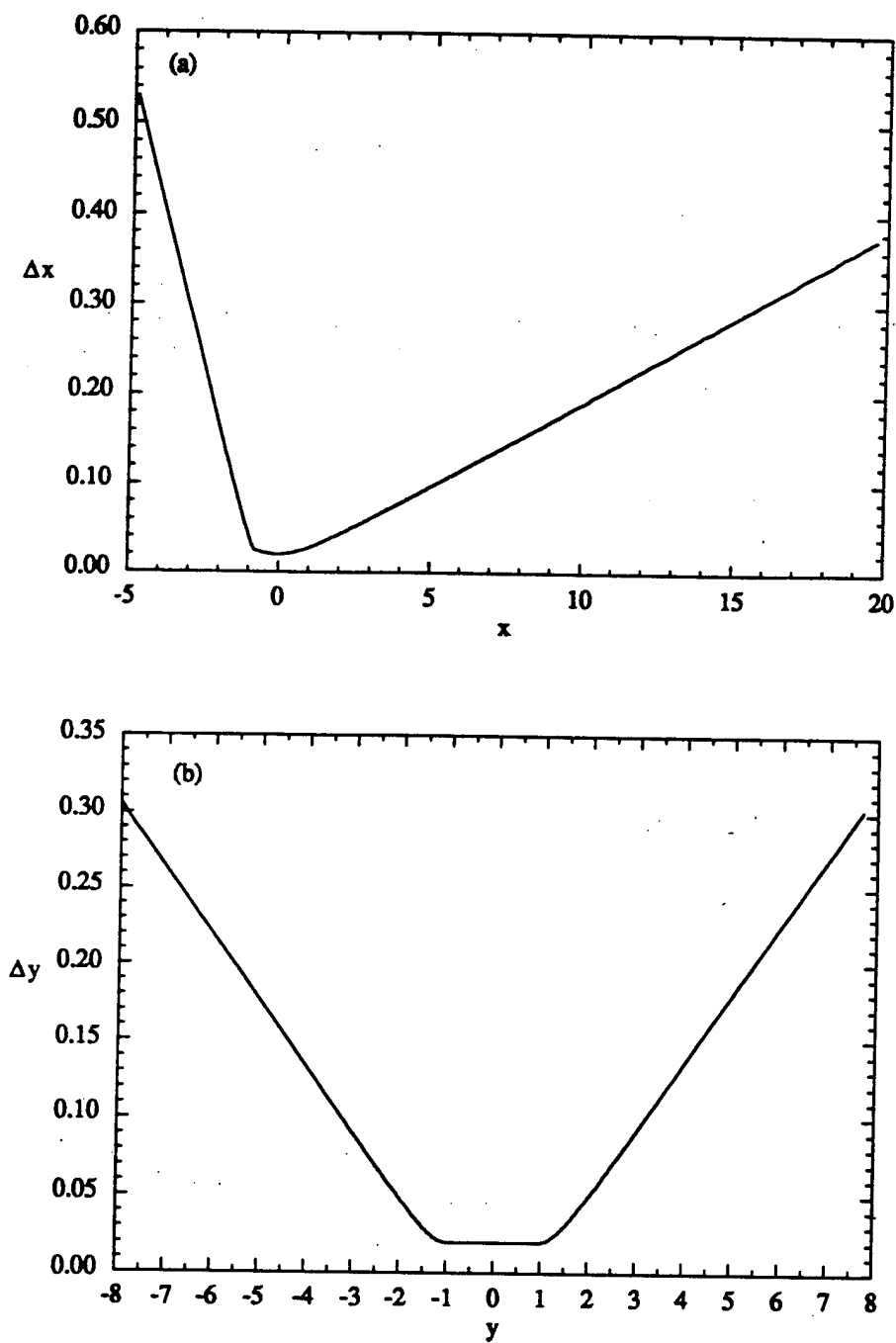


Figure 7.1.1 Grid Distribution in (a) the x-direction, and (b) the y-direction.

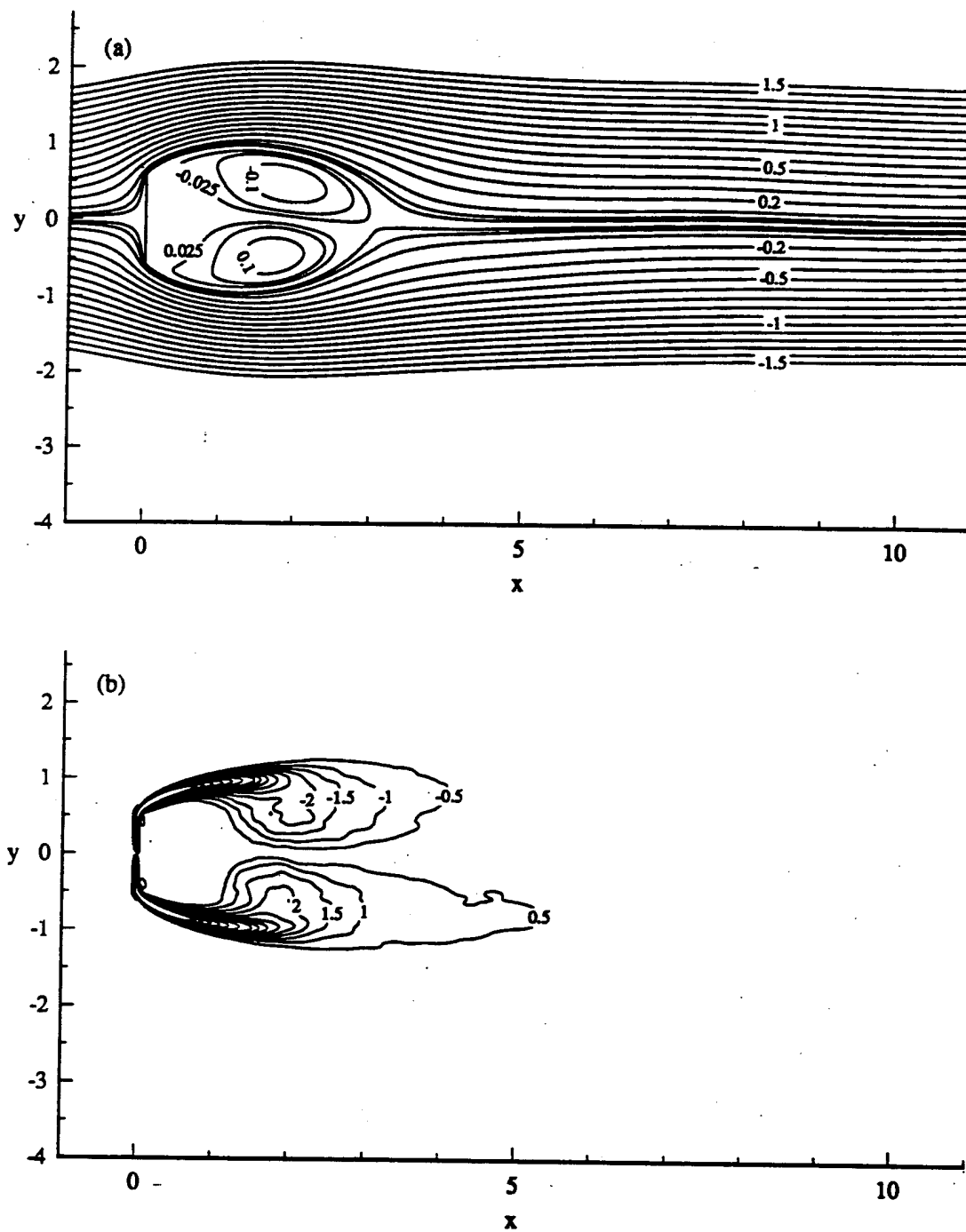


Figure 7.2.1 Contours of the time and span-averaged (a) streamlines, and (b) ω_z .

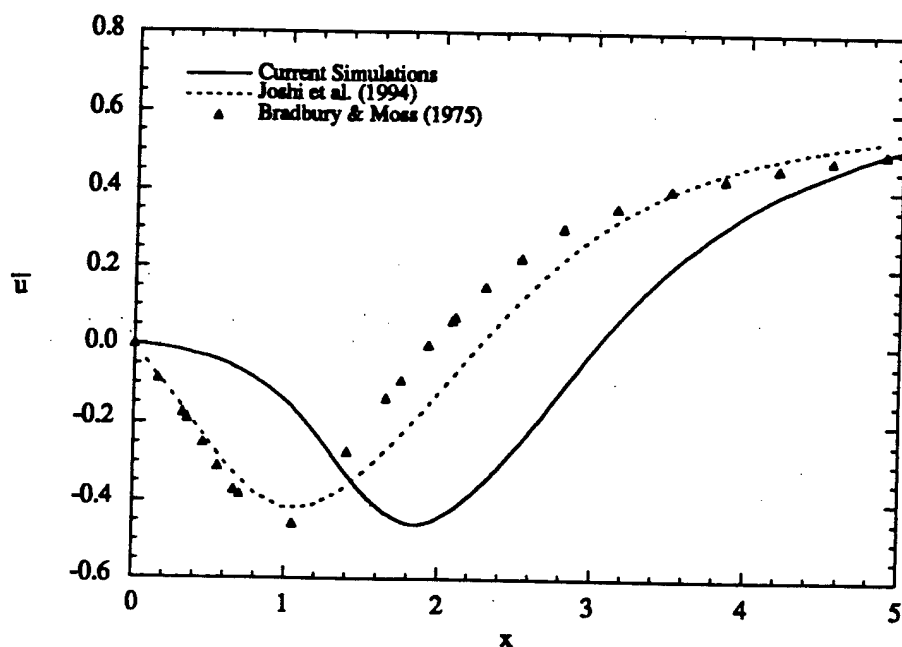


Figure 7.2.2 Streamwise variation of the \bar{u} -velocity component along the centerline.

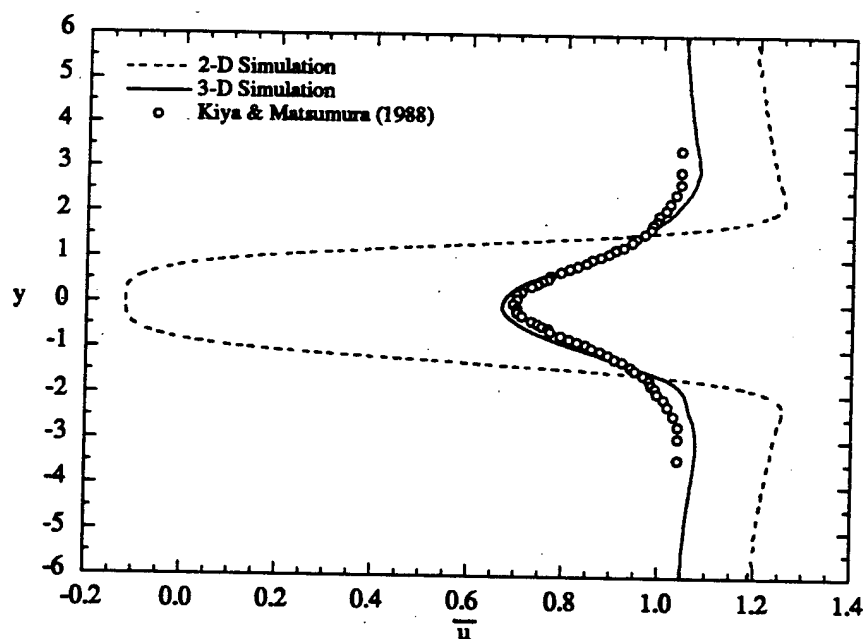


Figure 7.2.3 Profiles of the time-mean streamwise velocity component at $x = 8$.

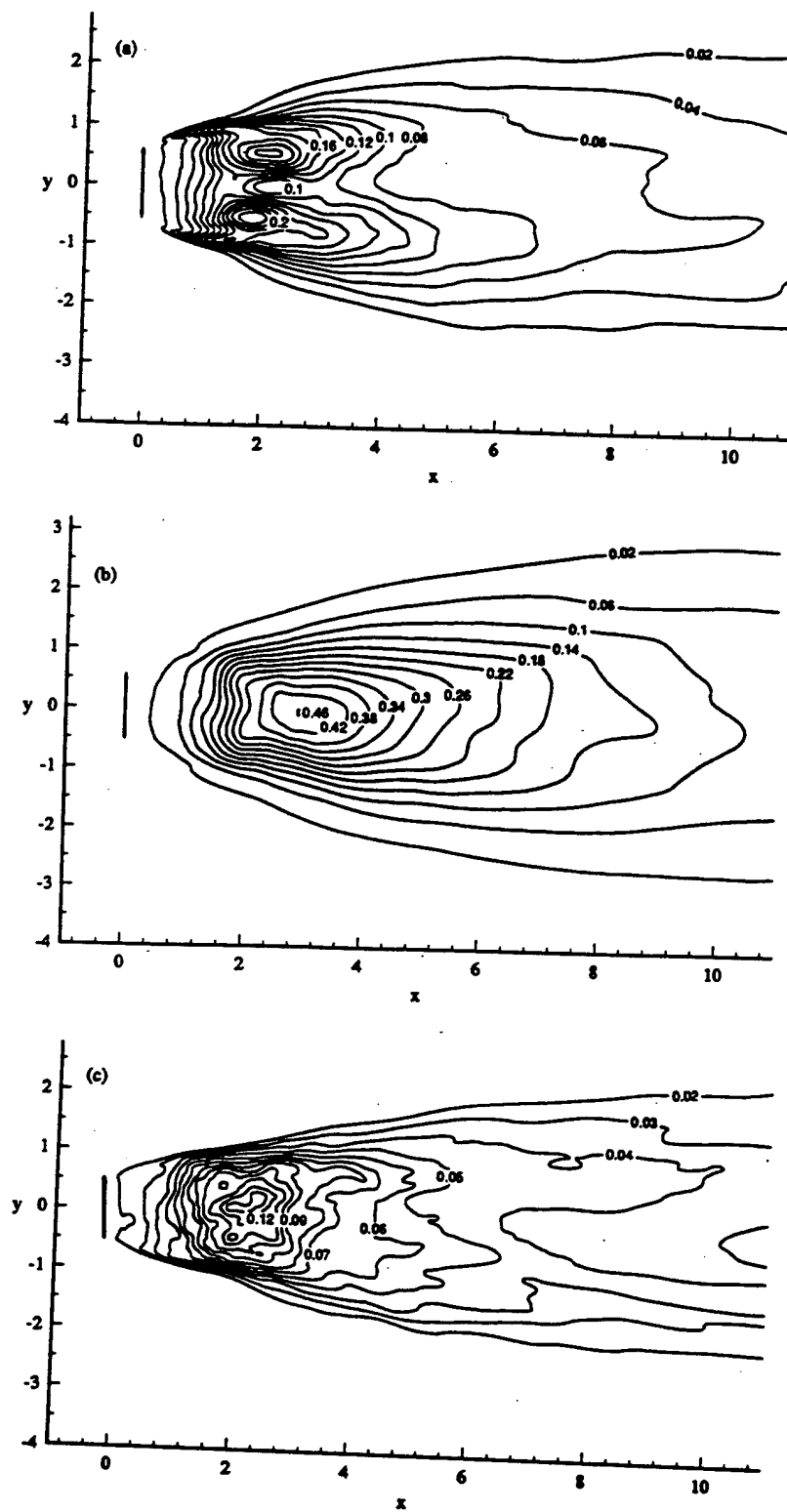


Figure 7.2.4 Distributions of the normal stresses: (a) $\overline{u'^2}$, (b) $\overline{v'^2}$, (c) $\overline{w'^2}$.

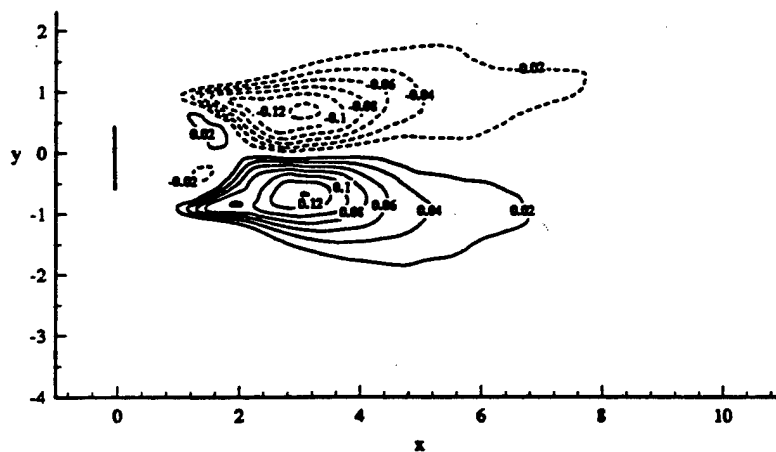


Figure 7.2.5 Distribution of the Reynolds shear stress, $\overline{u'v'}$.

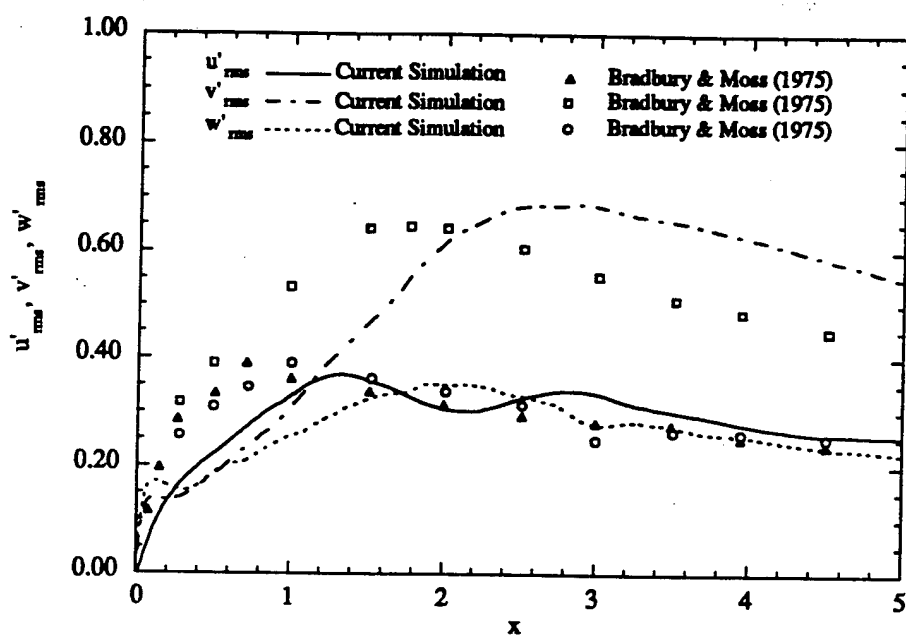


Figure 7.2.6 Streamwise variation of the rms stresses along the centerline.

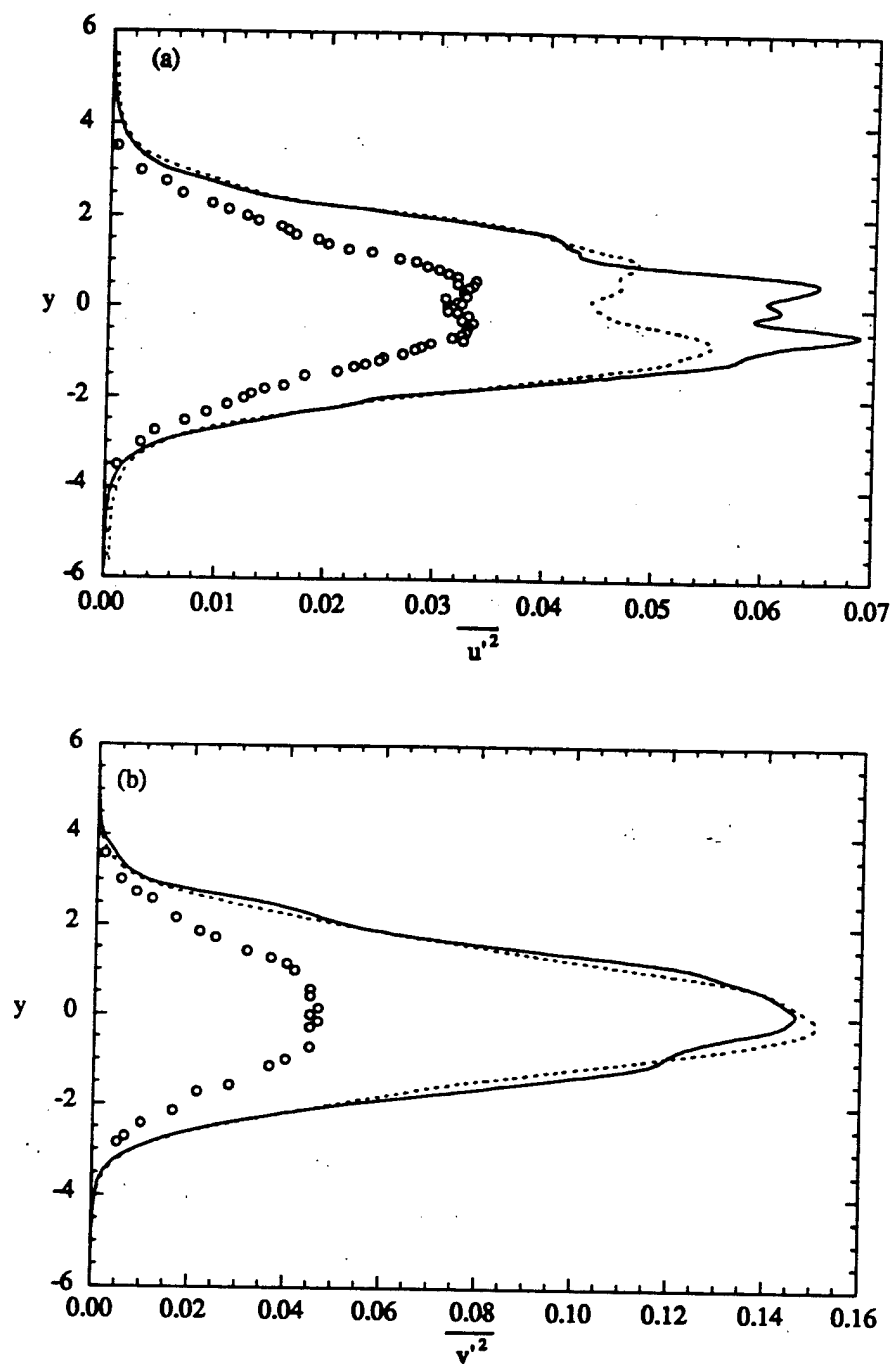


Figure 7.2.7 Profiles of (a) the streamwise stresses, $\overline{u'^2}$,
 (b) the cross-stream stress, $\overline{v'^2}$ at $x = 8$.
 (—) Current Simulation, (-----) Joshi et al. (1994),
 (o) Kiya and Matsumura (1988).

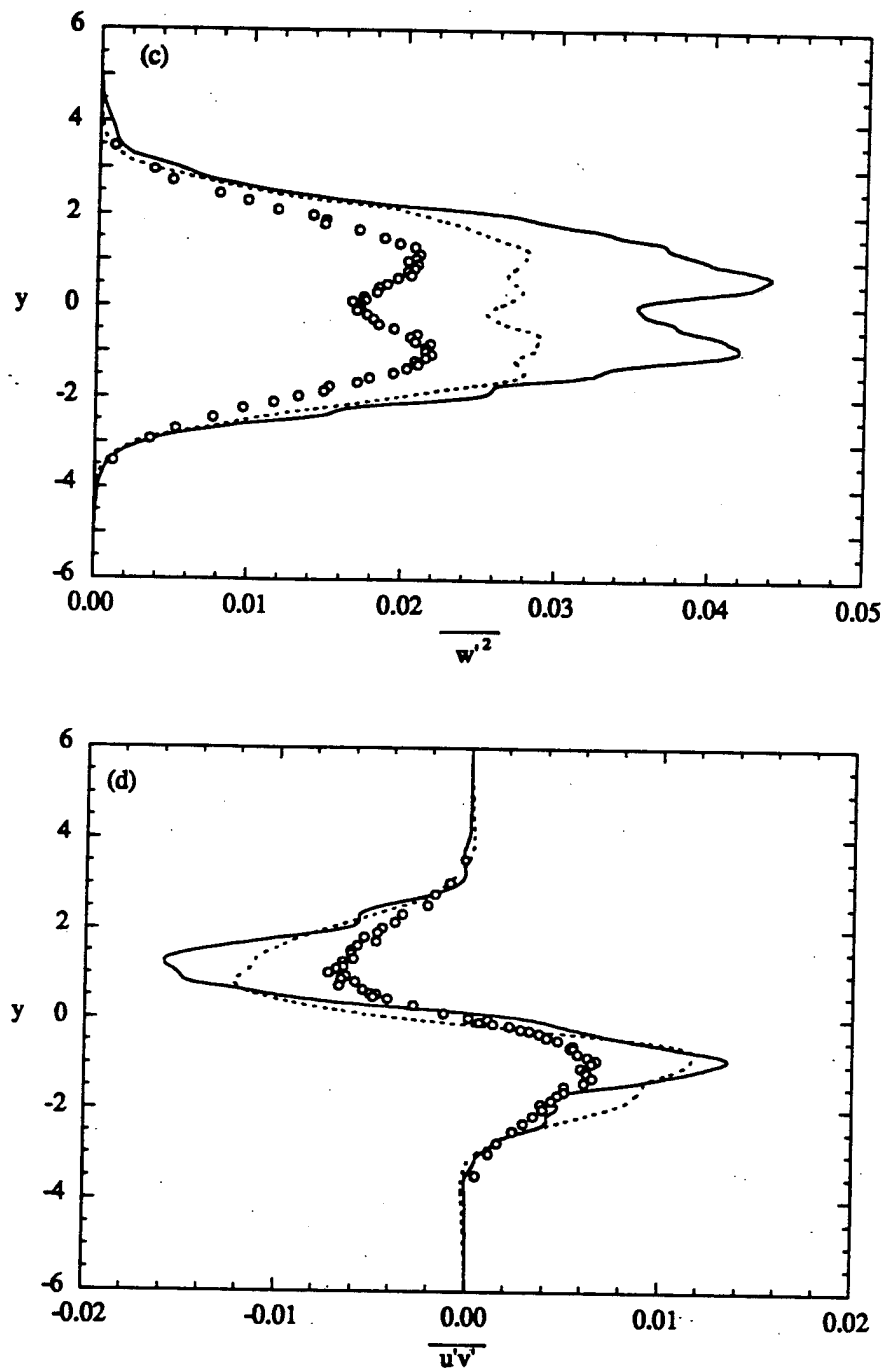


Figure 7.2.7(continued)

(c) the spanwise stress, $\overline{w'^2}$,
 (d) the Reynolds stress, $\overline{u'v'}$.

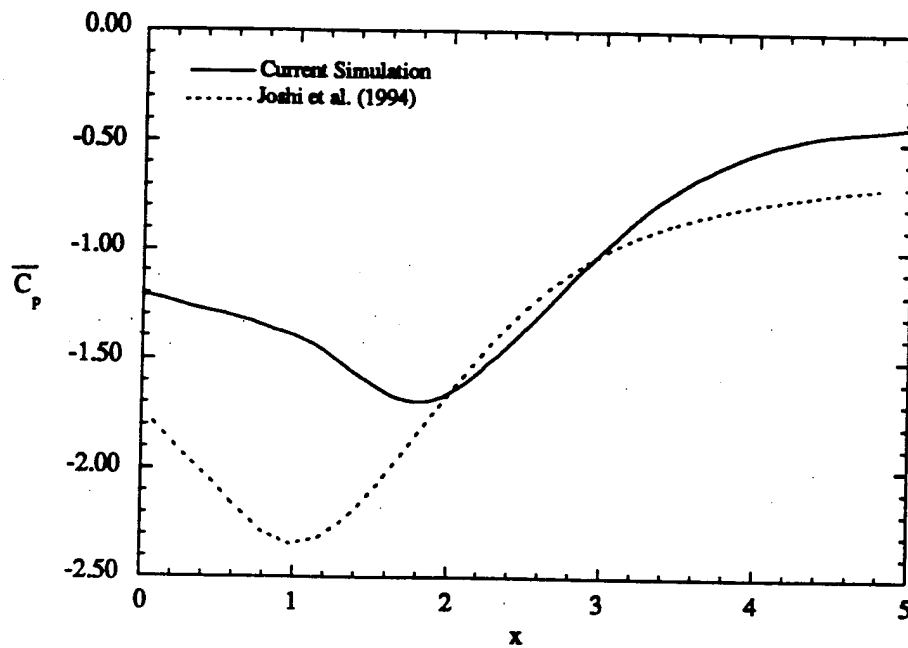


Figure 7.2.8 Streamwise variation of the time-mean pressure coefficient, $\overline{C_p}$, along the centerline.

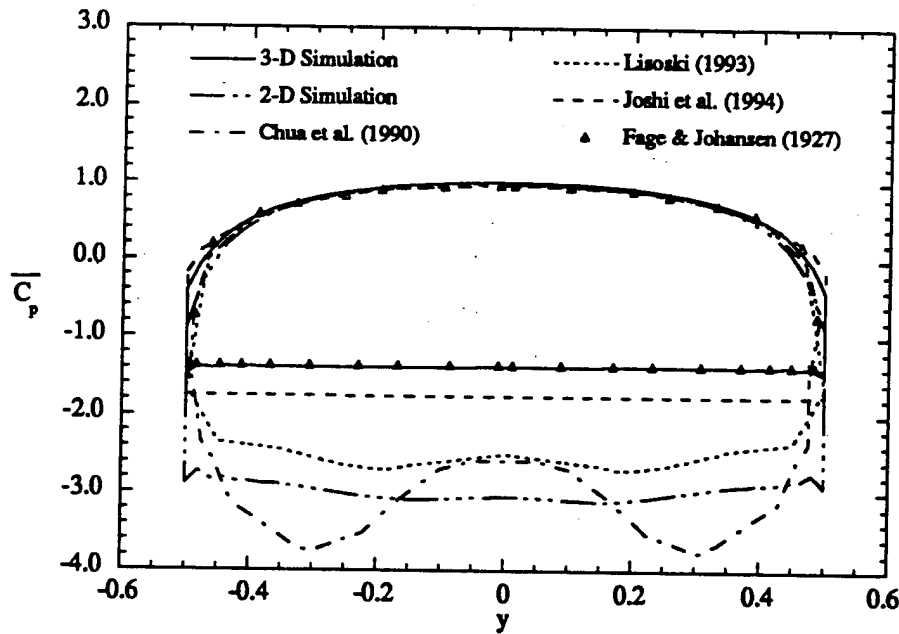


Figure 7.2.9 Distribution of the time-mean surface pressure coefficient, $\overline{C_p}$, on the front and rear sides of the flat plate.

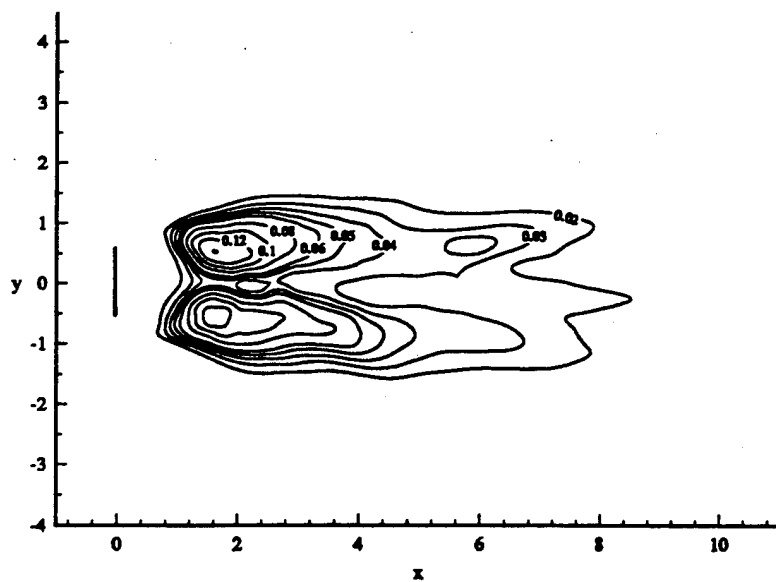


Figure 7.2.10 Distribution of $\overline{p^2}$.

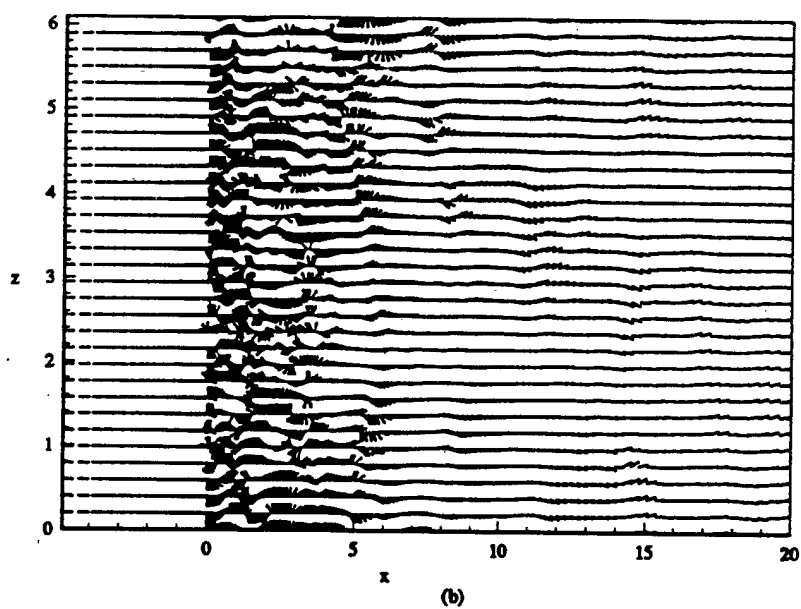
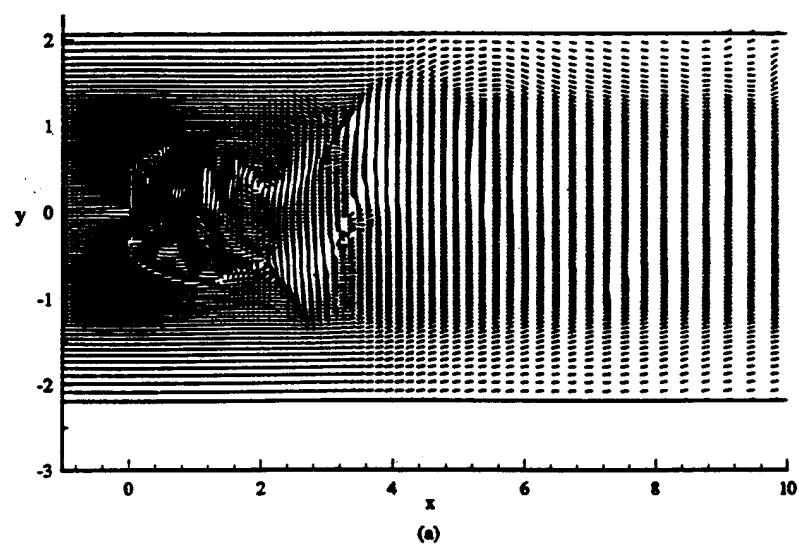


Figure 7.3.1 Velocity vectors in (a) $z = \pi$ and (b) $y = 0$ planes for $t = 45$.

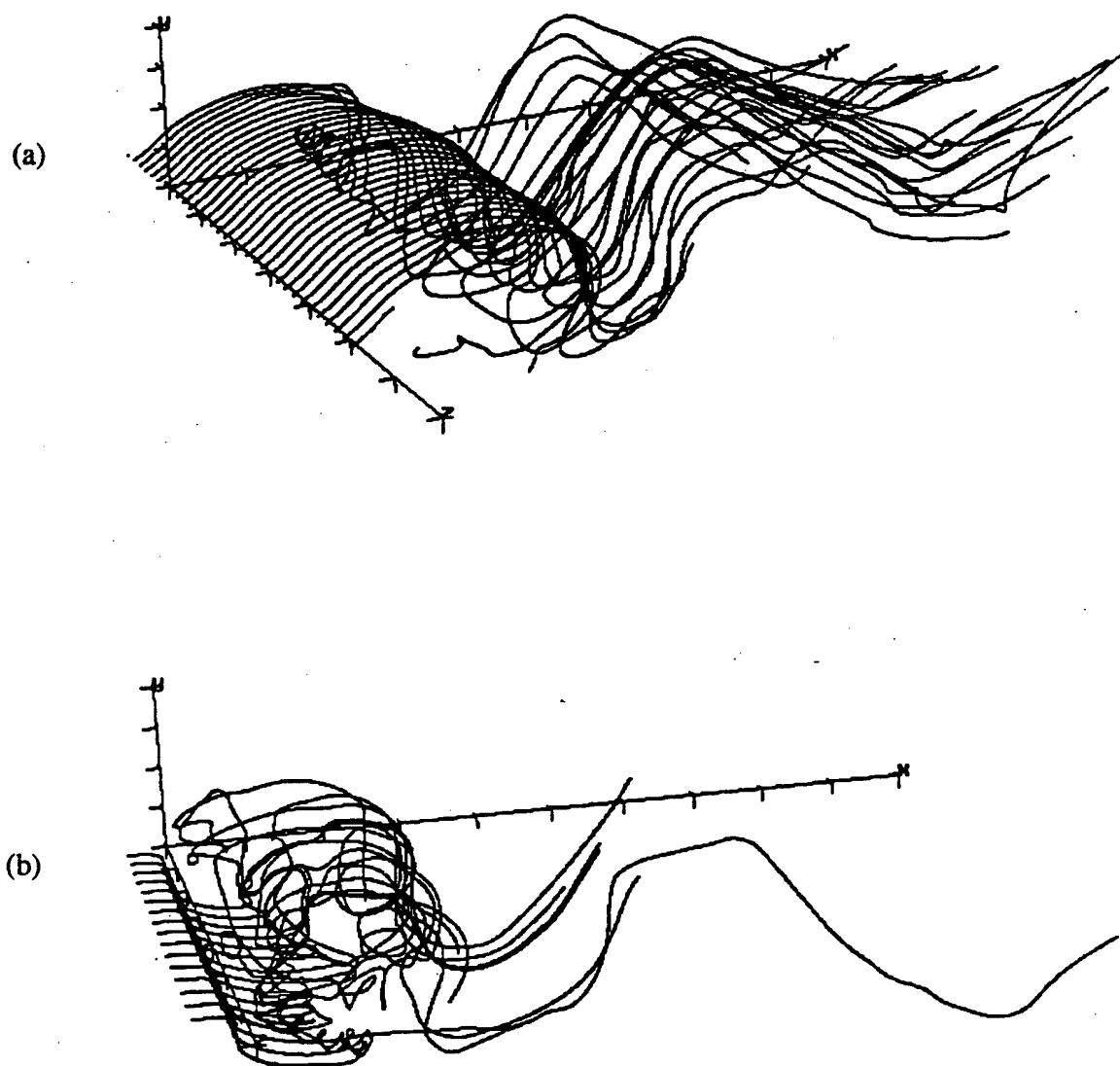


Figure 7.3.2 Particles trajectories at $t = 45$.
(a) Injection Line ($x = 0, y = 0.5$)
(b) Injection Line ($x = -0.5, y = 0$)

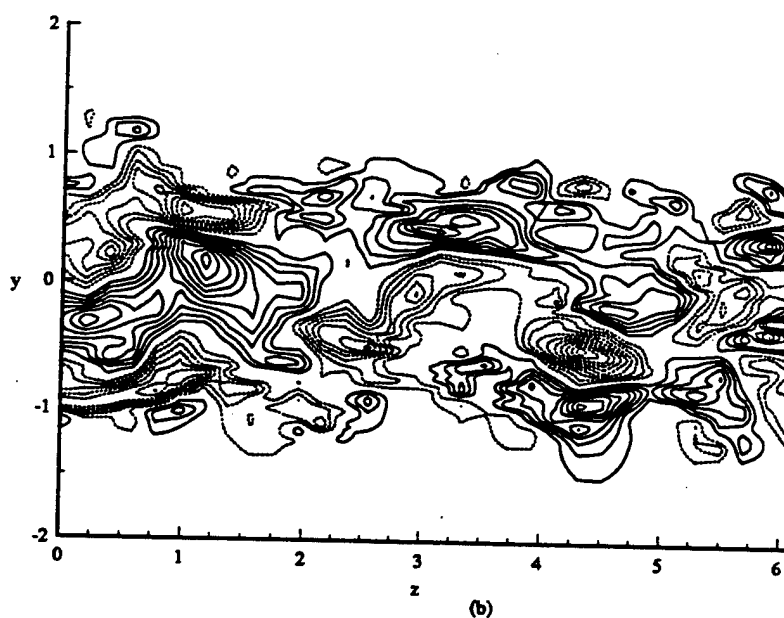
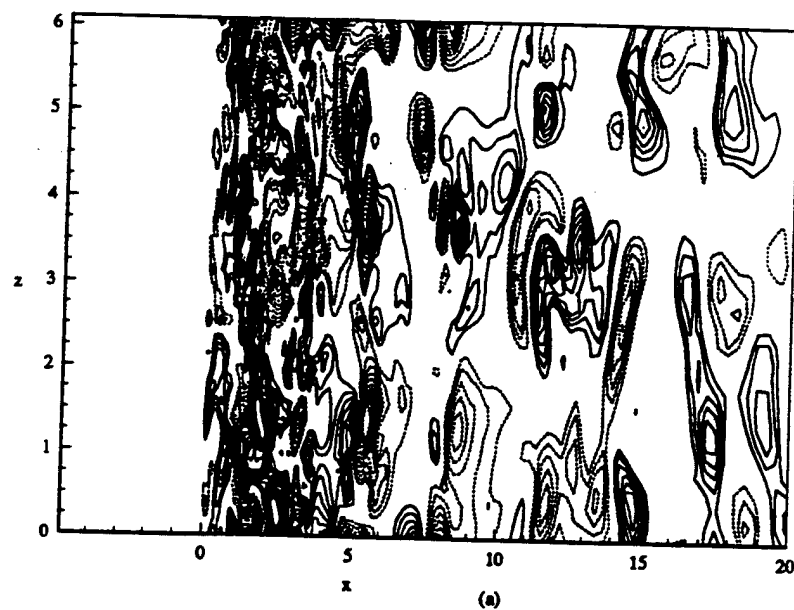


Figure 7.3.3 Contours of spanwise velocity for $t = 45$
 in (a) $y = 0$, and (b) $x = 2$ planes.
 Dashed Lines ($w_{\min}, w_{\max}, \Delta w$) = $(-1.0, -0.1, 0.1)$
 Solid Lines ($w_{\min}, w_{\max}, \Delta w$) = $(0.1, 1.0, 0.1)$

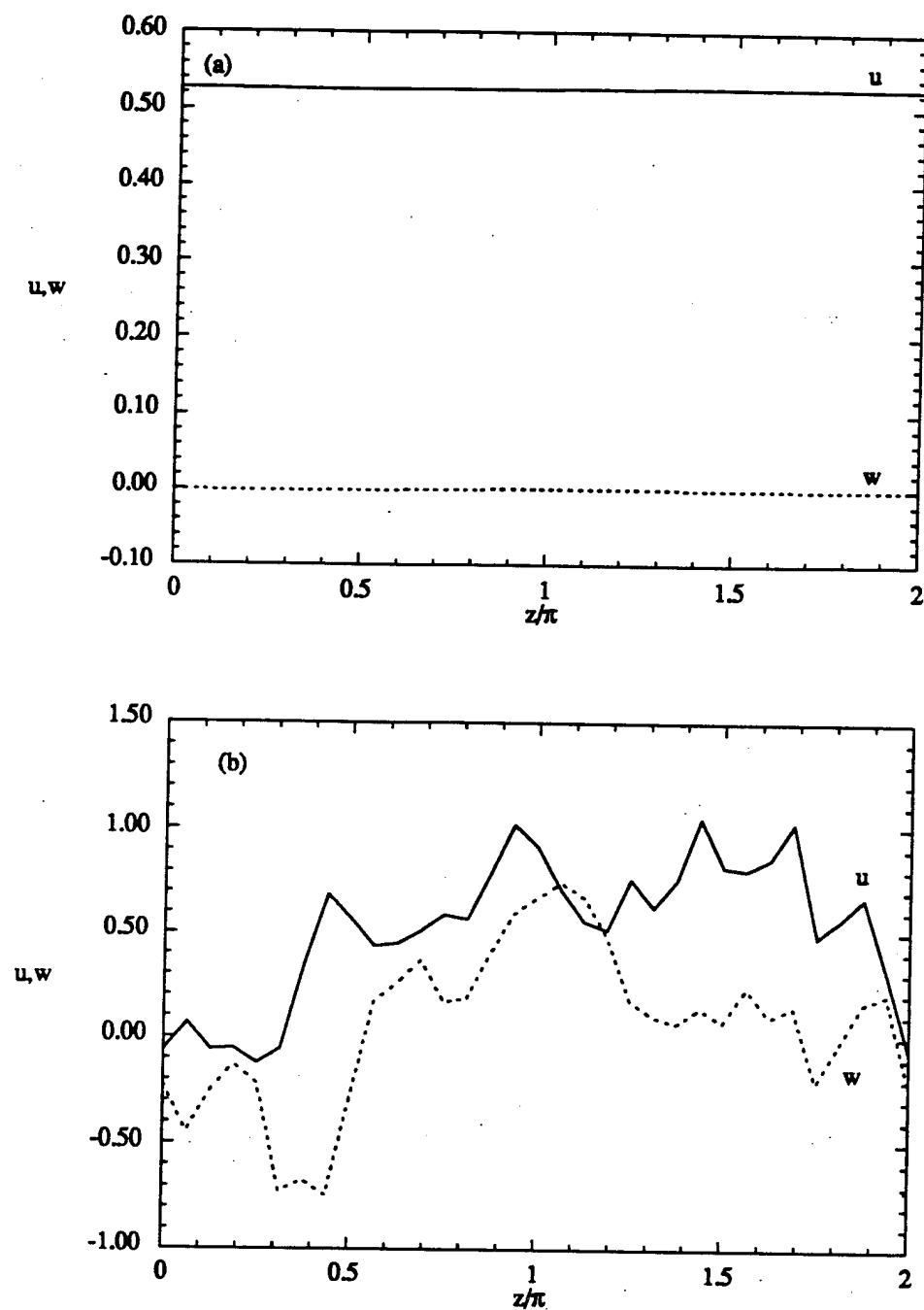


Figure 7.3.4 Spanwise variation of the instantaneous streamwise and spanwise velocity components.
 (a) upstream of the plate ($x = -0.5, y = 0$)
 (b) in the near wake ($x = 2, y = 0.5$).

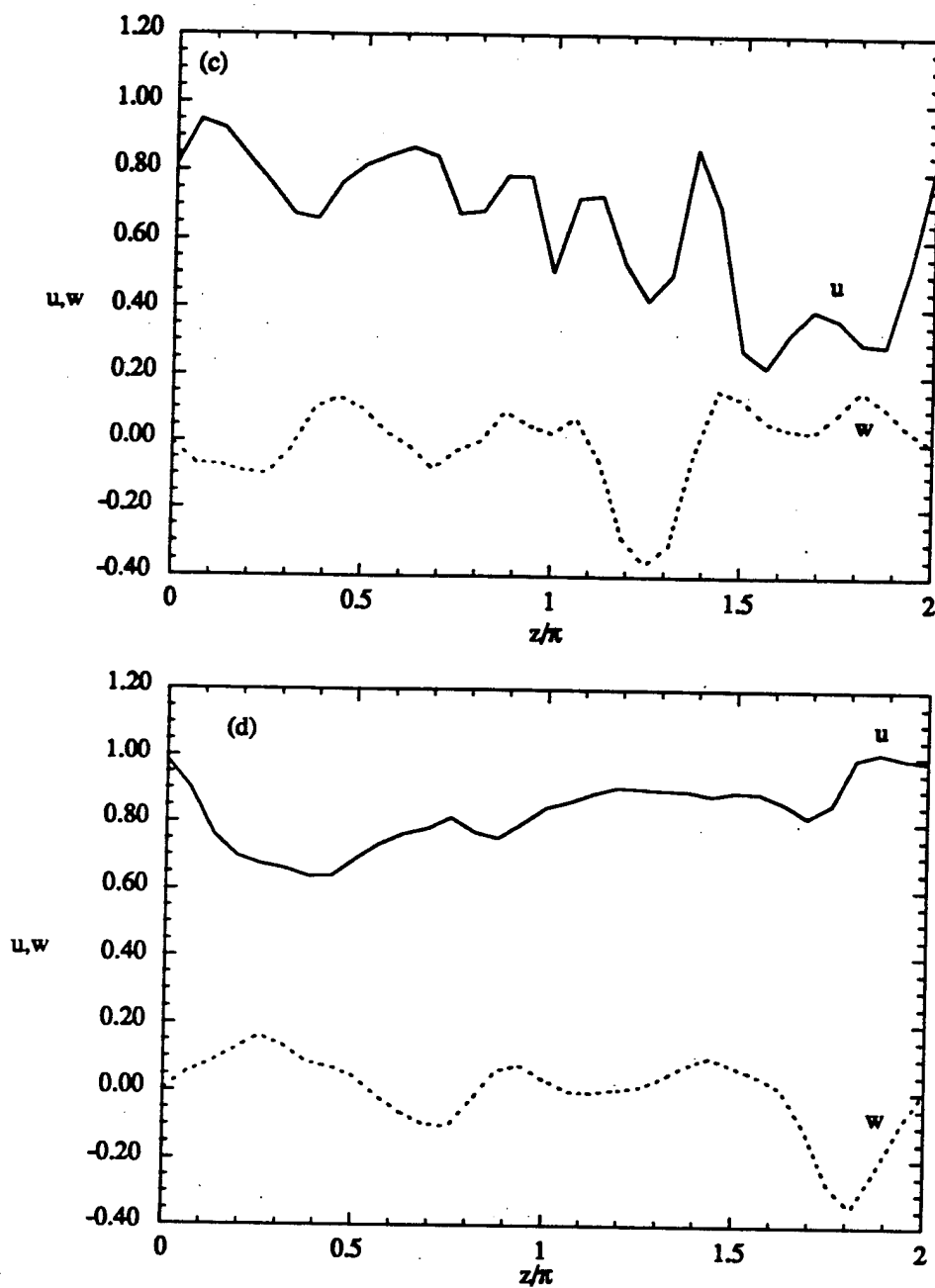


Figure 7.3.4(continued)

(c) at point $(x = 8, y = 0.5)$

(d) in the far wake $(x = 16, y = 0.5)$.

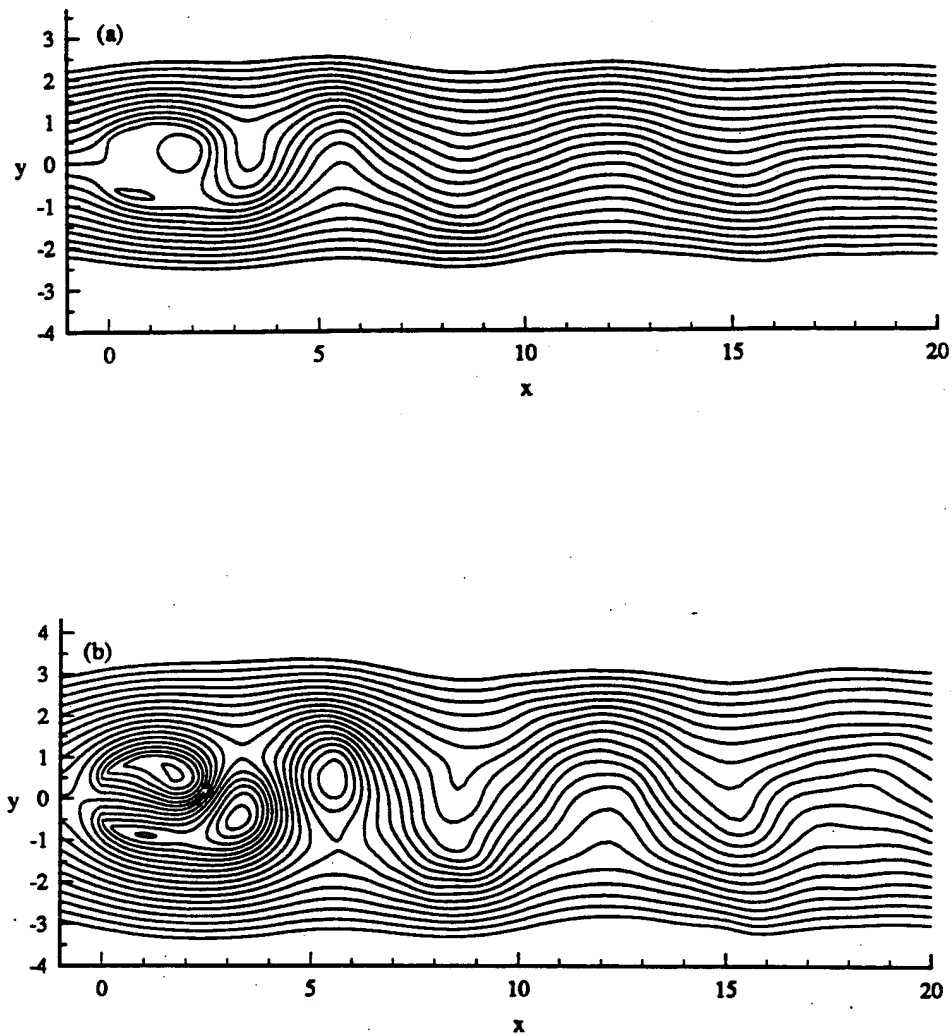


Figure 7.3.5 Contours of span-averaged streamlines, $\langle \psi \rangle_z$, at $t = 45$.
 (a) stationary frame of reference.
 Contour Levels $(\psi_{\min}, \psi_{\max}, \Delta\psi) = (-2.0, 2.0, 0.2)$
 (b) frame of reference moving at a convective velocity of $0.6U_\infty$
 Contour Levels $(\psi_{\min}, \psi_{\max}, \Delta\psi) = (-1.0, 1.0, 0.1)$

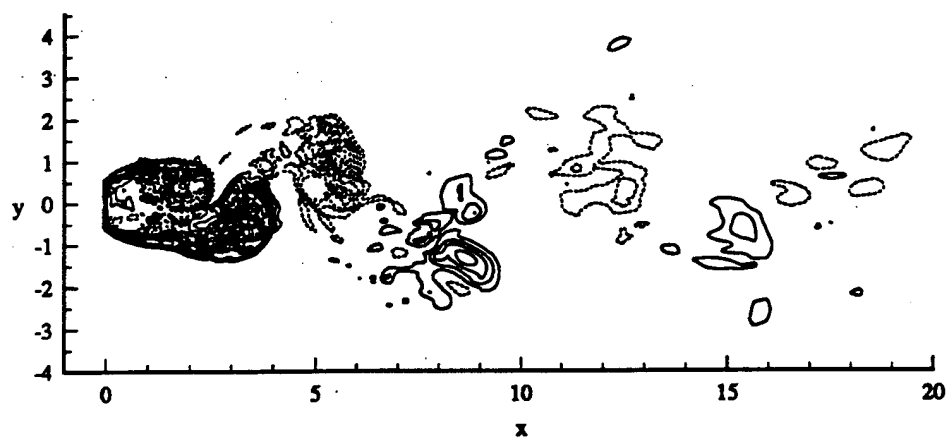


Figure 7.3.6 Contours of span-averaged spanwise vorticity, $\langle \omega_z \rangle_z$, at $t = 45$.
Solid Lines : $(\omega_{zmin}, \omega_{zmax}) = (0.4, 40)$
Dashed Lines : $(\omega_{zmin}, \omega_{zmax}) = (-40.0, -0.4)$

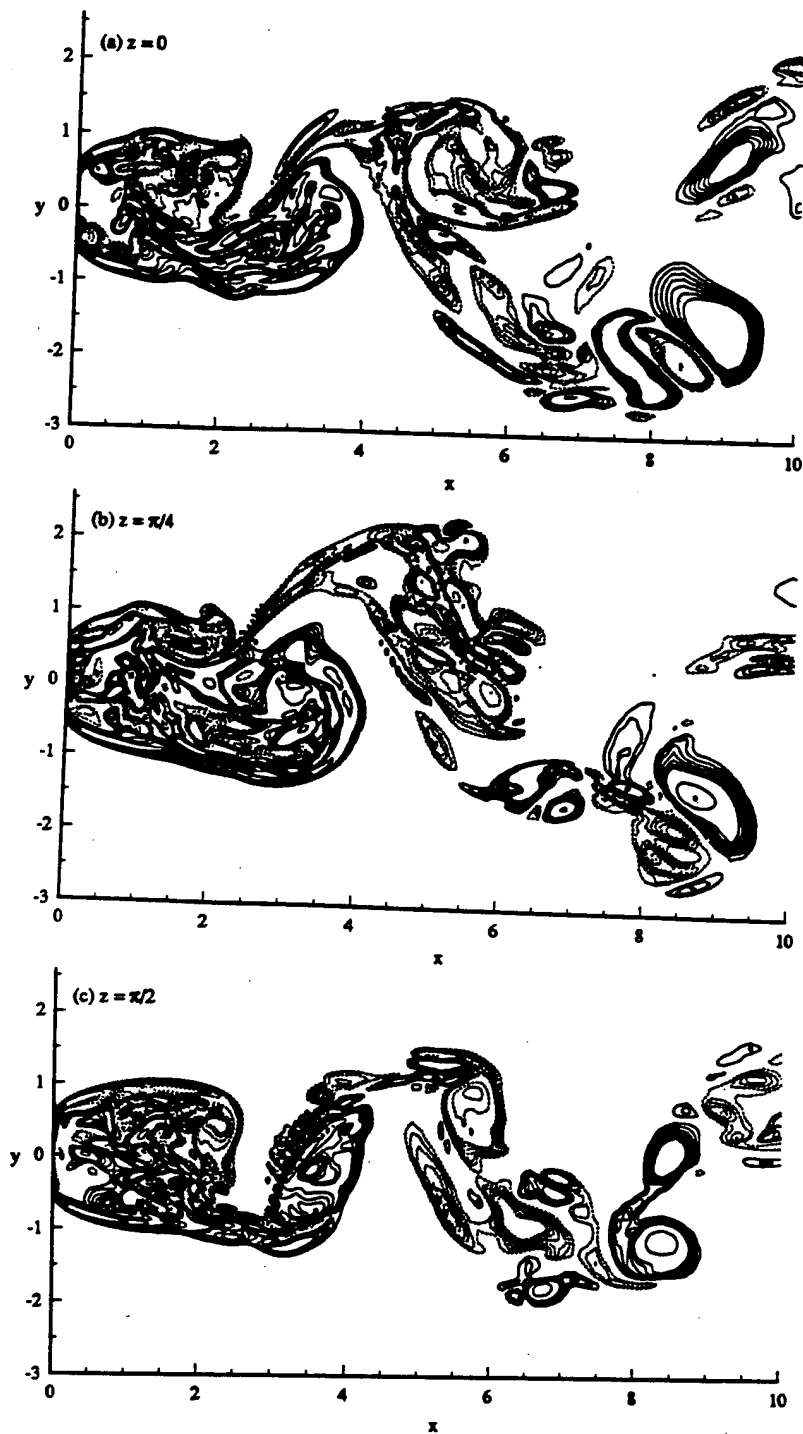


Figure 7.3.7 Contours of instantaneous spanwise vorticity, ω_z , at $t = 45$.

(a) $z = 0$, (b) $z = \frac{\pi}{4}$, (c) $z = \frac{\pi}{2}$

Solid Lines : $(\omega_{zmin}, \omega_{zmax}) = (0.4, 40)$

Dashed Lines : $(\omega_{zmin}, \omega_{zmax}) = (-40, -0.4)$

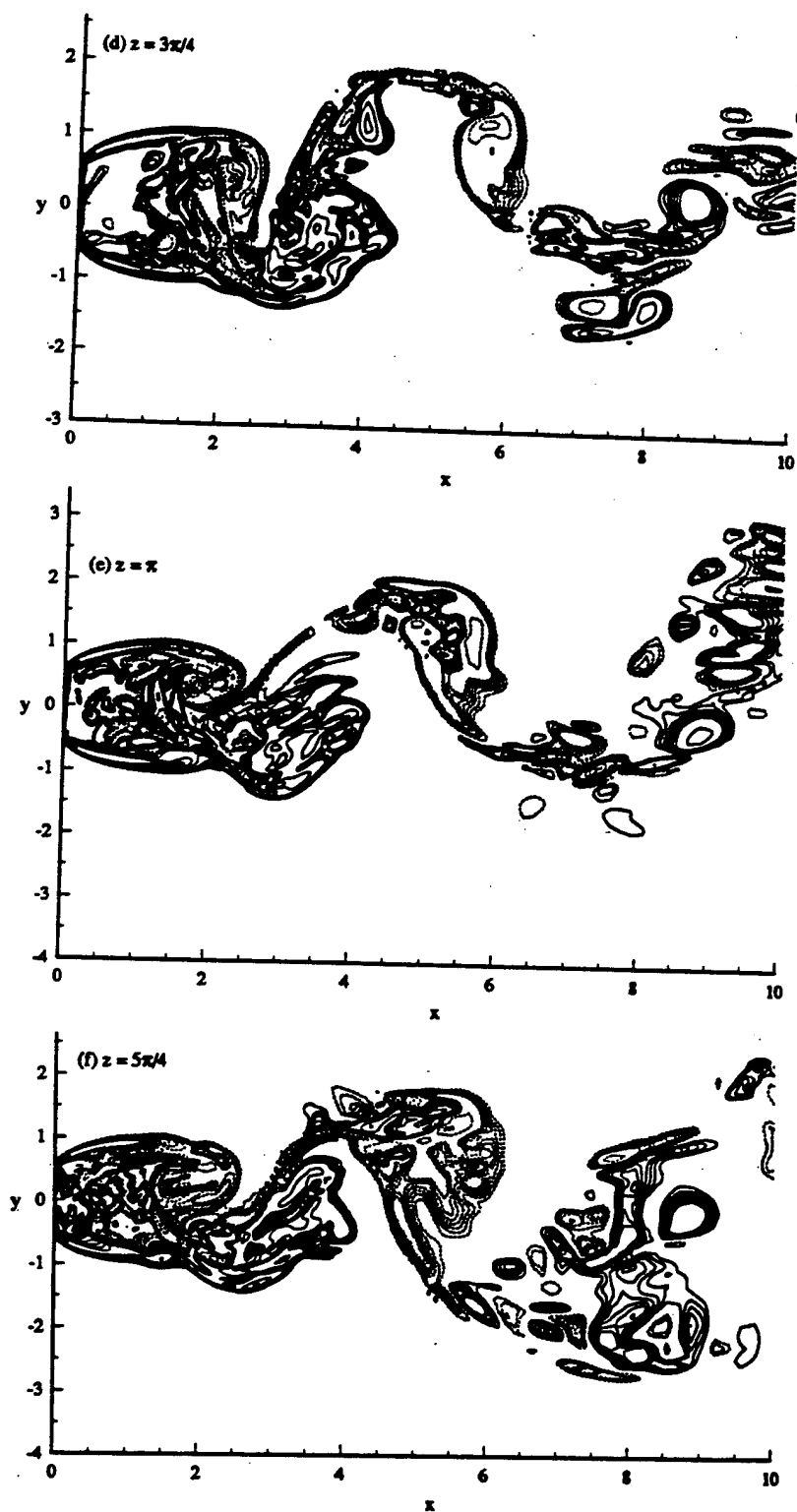


Figure 7.3.7(continued) (d) $z = \frac{3\pi}{4}$, (e) $z = \pi$, (f) $z = \frac{5\pi}{4}$.

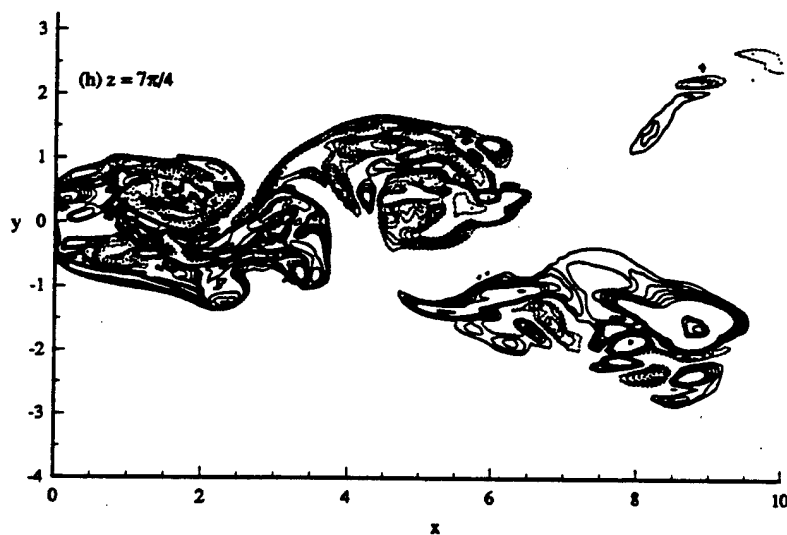
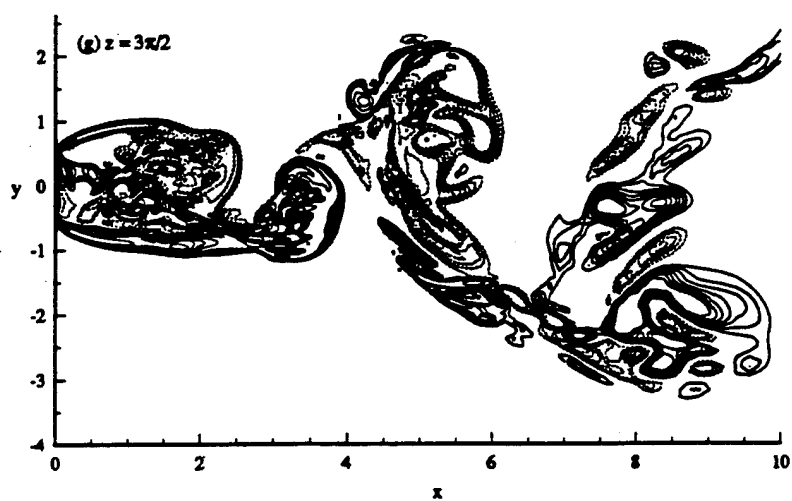


Figure 7.3.7(continued) (g) $z = \frac{3\pi}{2}$, (h) $z = \frac{7\pi}{4}$

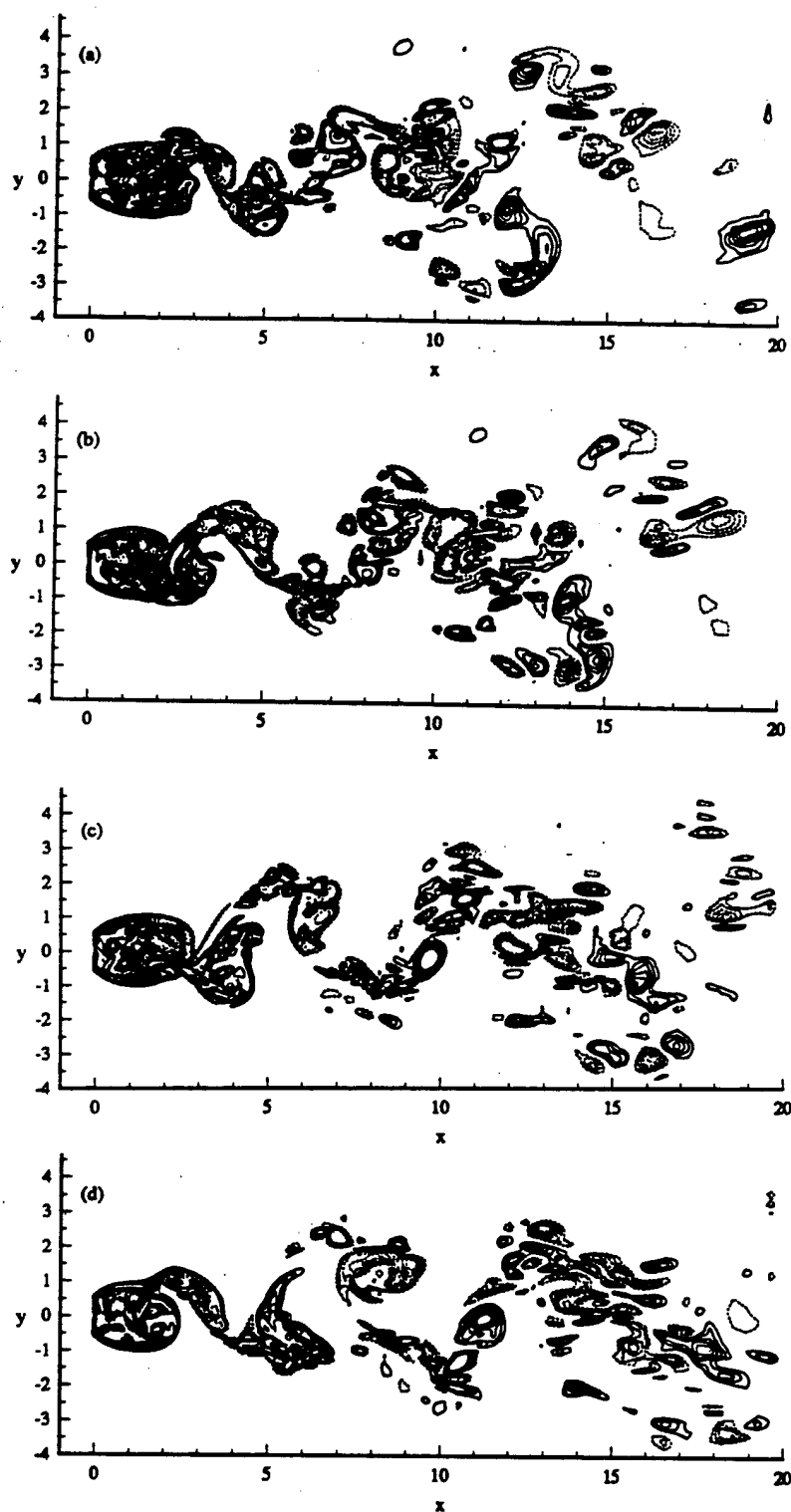


Figure 7.3.8 Contours of spanwise vorticity for a representative shedding cycle:
 (a) $t = 42$, (b) $t = 44$, (c) $t = 46$, (d) $t = 48$.

Solid Lines : $(\omega_{zmin}, \omega_{zmax}) = (0.4, 40)$

Dashed Lines : $(\omega_{zmin}, \omega_{zmax}) = (-40, -0.4)$

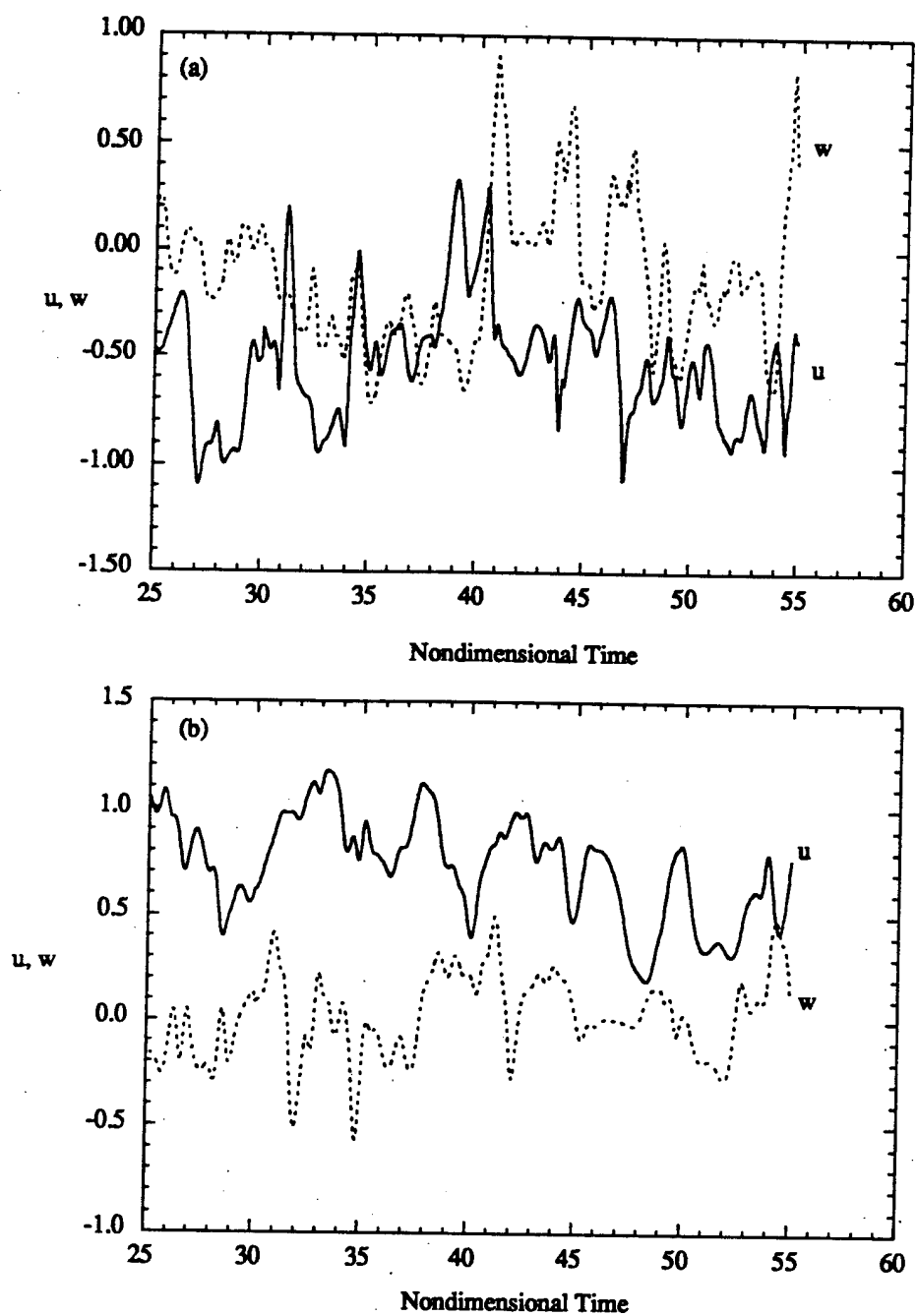


Figure 7.3.9 Time trace of the instantaneous streamwise and spanwise velocity components. (a) in the near-wake region ($x = 2, y = 0.5, z = 0$) and (b) at point $x = 8, y = 0$ and $z = \pi/2$.

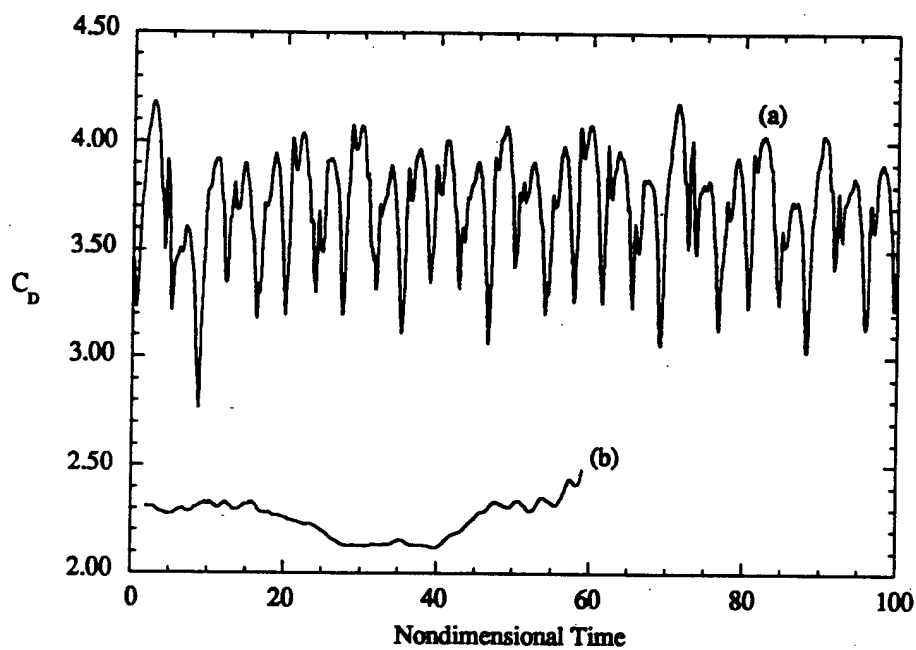


Figure 7.3.10 Time trace of the instantaneous drag coefficient at $Re = 1000$ predicted by (a) 2-D and (b) 3-D simulations.

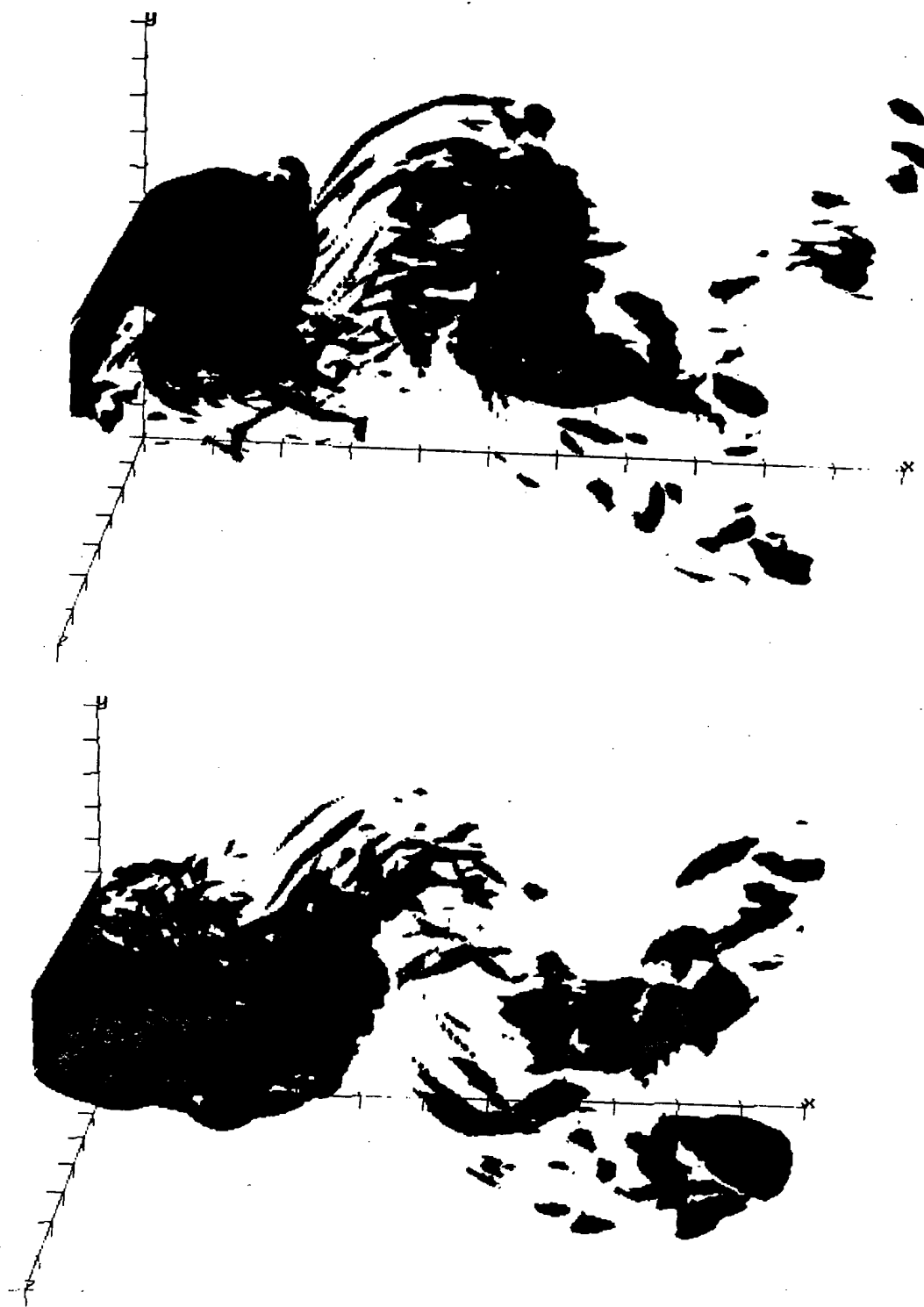


Figure 7.4.1 Surface of three-dimensional spanwise vorticity at $t = 45$.
 Surface Levels : Red = -2, Cyan = +2.
 Tic increments along x and z directions = 1.
 Tic increments along y -direction = 0.5.
 Origin of axis at (0,-3,0). Flat Plate is shown as black shaded surface.

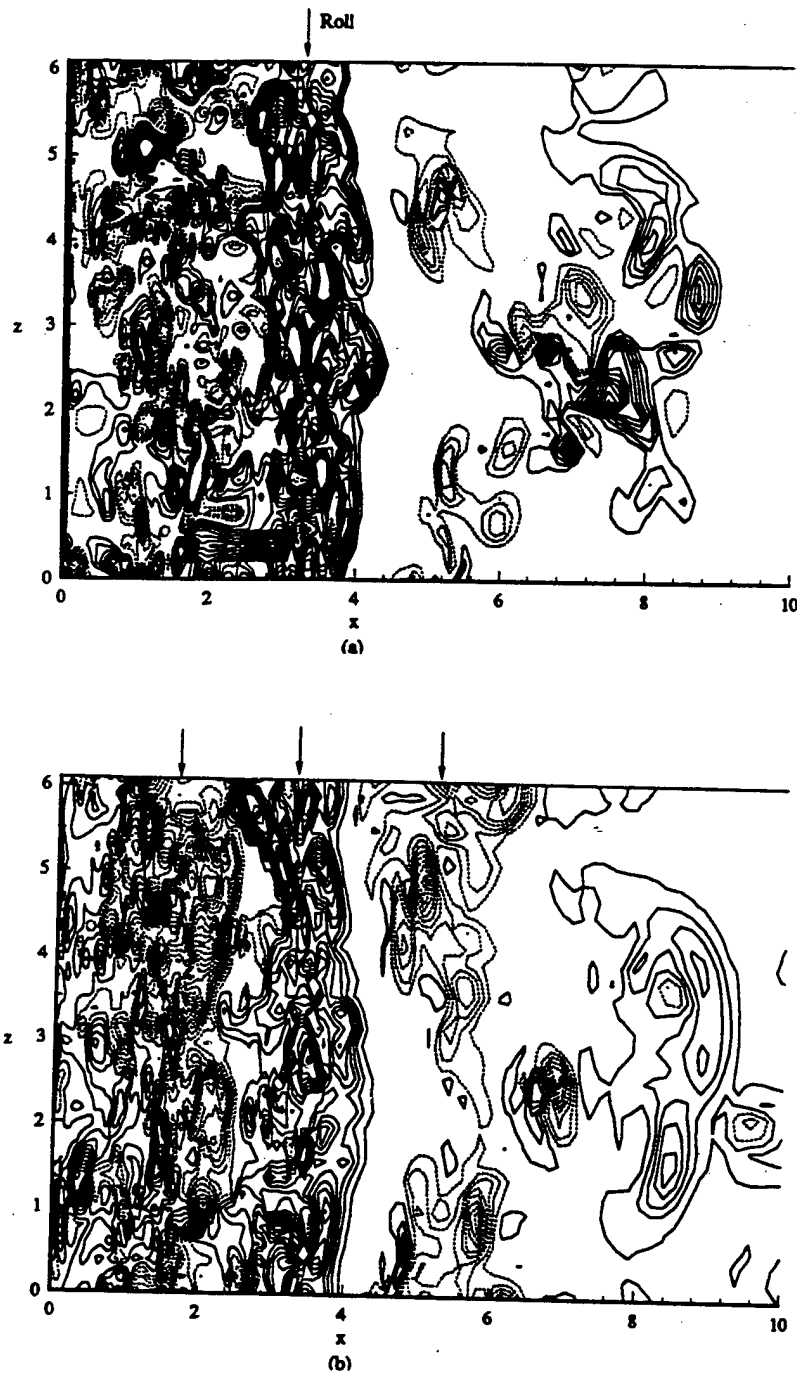


Figure 7.4.2 Contours of spanwise vorticity at $t = 45$ in x-z planes :
 (a) $y = -0.5$, (b) $y = 0$.
 Solid Lines : $(\omega_{zmin}, \omega_{zmax}, \Delta\omega_z) = (0.5, 7.5, 0.5)$
 Dashed Lines : $(\omega_{zmin}, \omega_{zmax}, \Delta\omega_z) = (-7.5, -0.5, 0.5)$.
 Arrows indicate spanwise rollers.

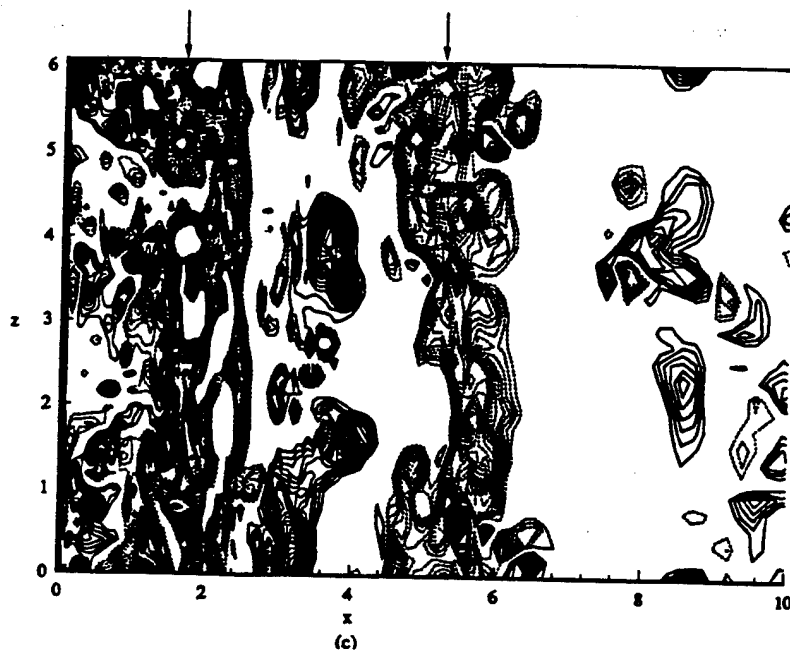


Figure 7.4.2(continued) (c) $y = +0.5$.

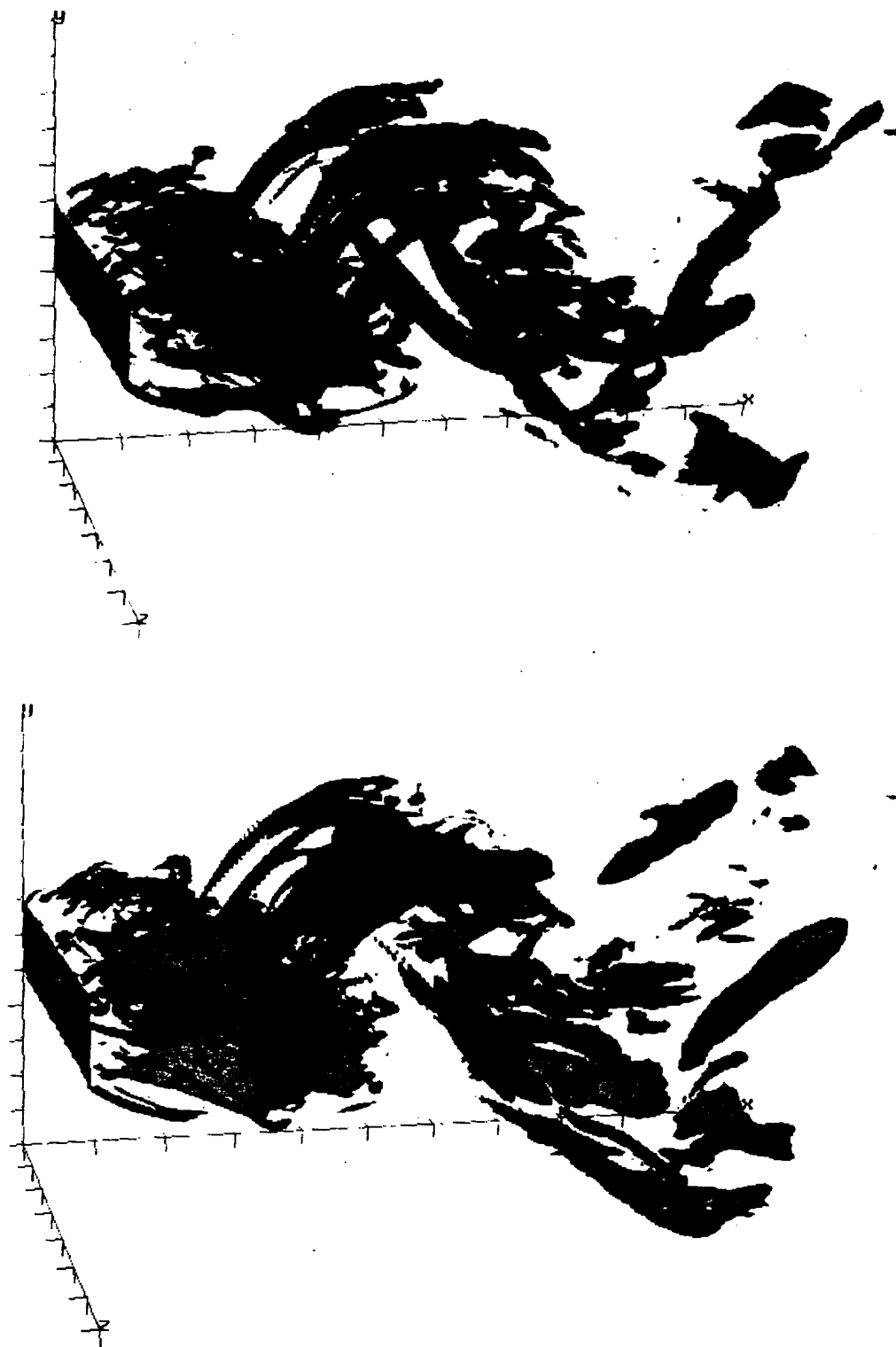


Figure 7.4.3 Surface of three-dimensional streamwise vorticity at $t = 45$.
 Surface Levels : Magenta = -2, Cyan = +2.
 Tic increments along x and z directions = 1.
 Tic increments along y -direction = 0.5.
 Origin at (0,-3,0)



Figure 7.4.4 Close-up view of the streamwise ribs.
Surface Level : Magenta = -2.
Tic increments along x and z directions = 1.
Tic increments along y -direction = 0.5.
Origin at (0,-3,0)

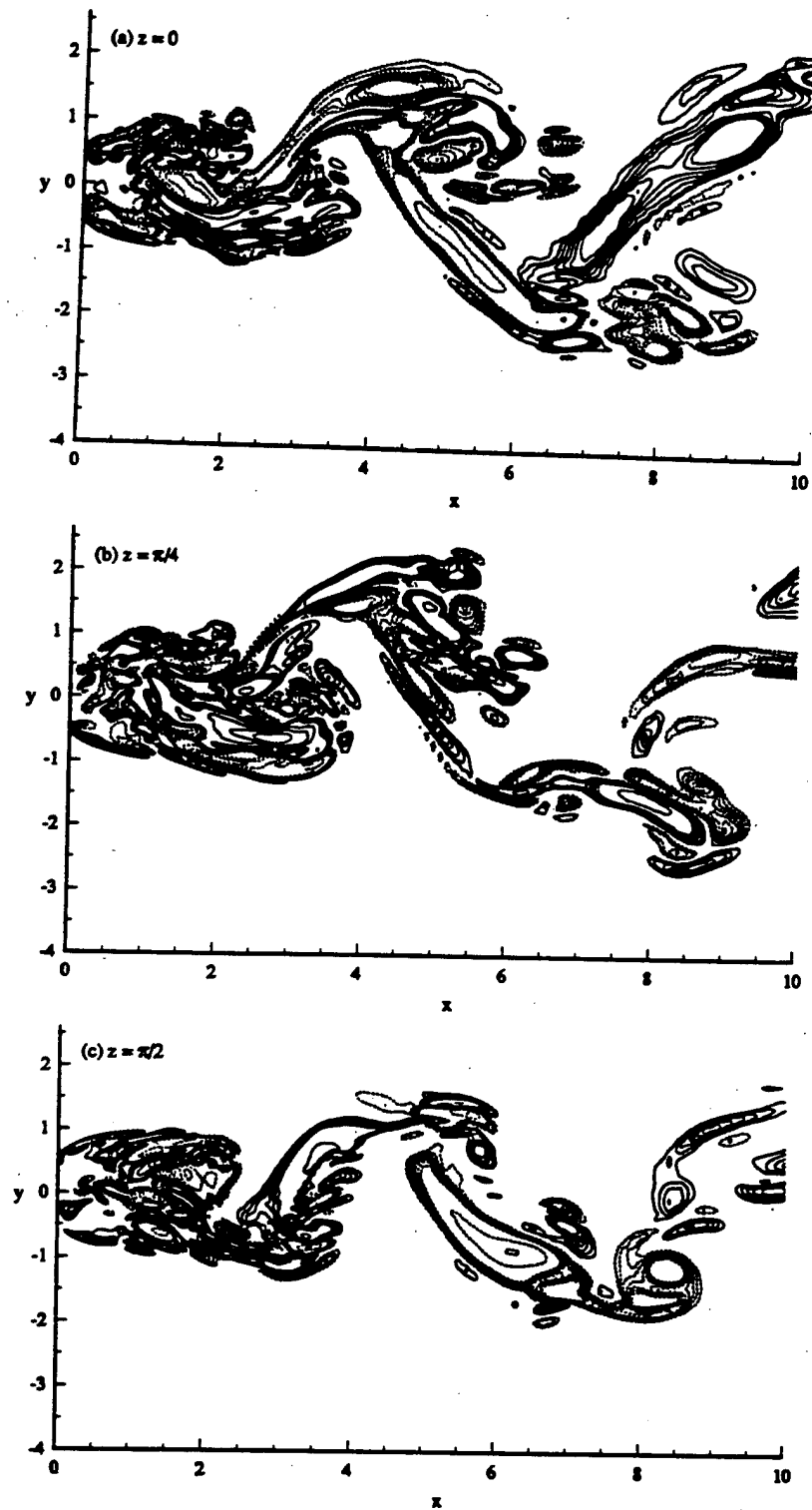


Figure 7.4.5 Spanwise variation of the streamwise vorticity for $t = 45$.

(a) $z = 0$, (b) $z = \frac{\pi}{4}$, (c) $z = \frac{\pi}{2}$.



Figure 7.4.6 Surface of three-dimensional cross-stream vorticity, ω_y , at $t = 45$.
 Surface Levels : Green = -2, Yellow = +2.
 Tic increments along x and z directions = 1.
 Tic increments along y -direction = 0.5.
 Origin at (0,-3,0)

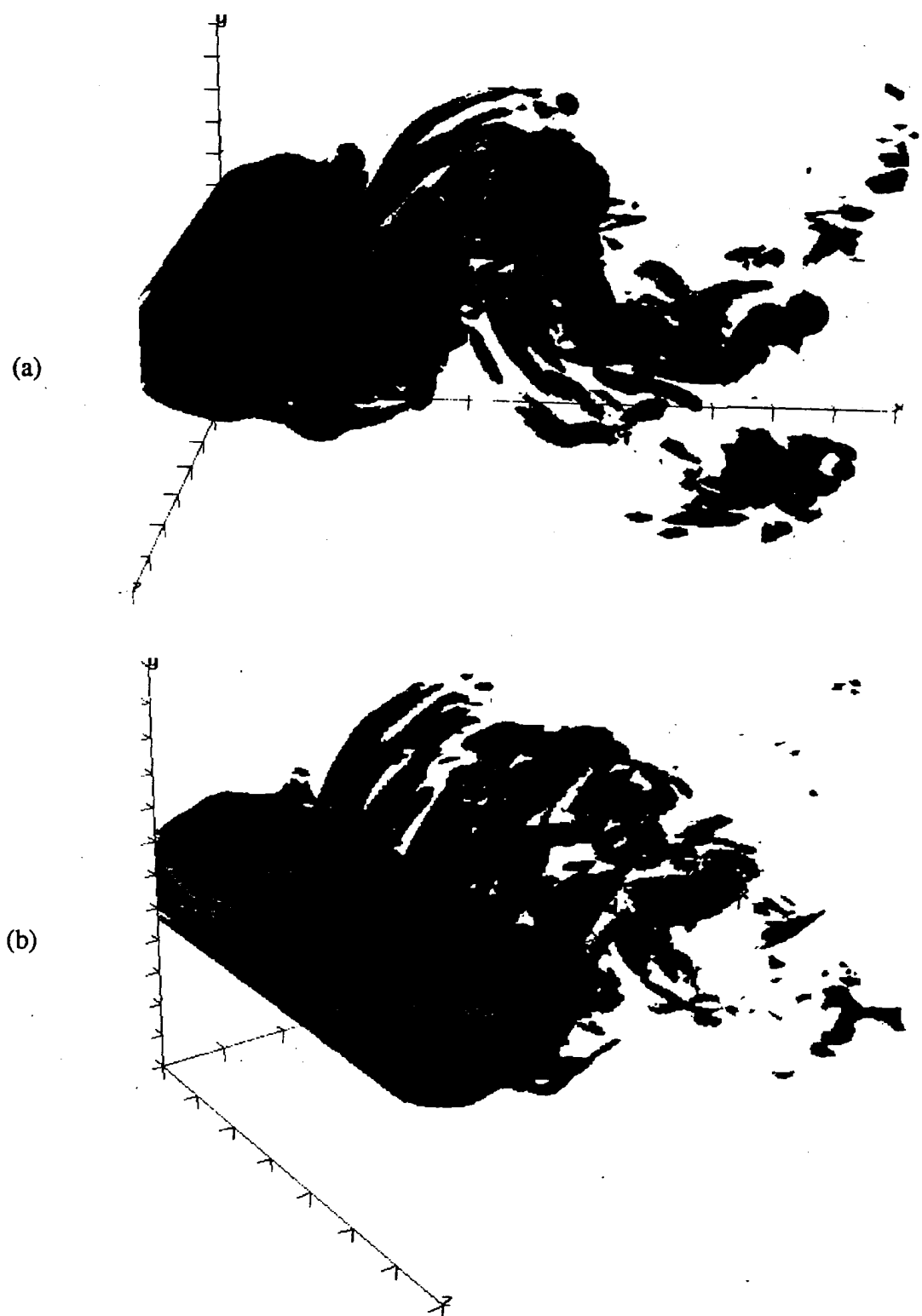


Figure 7.4.7 Surface of three-dimensional (a) strain rate magnitude, D , and (b) enstrophy, Q , at $t = 45$
Surface Levels : Red = 5, Cyan = 10.
Tic increments along x and z directions = 1.
Tic increments along y -direction = 0.5.
Origin at $(0, -3, 0)$

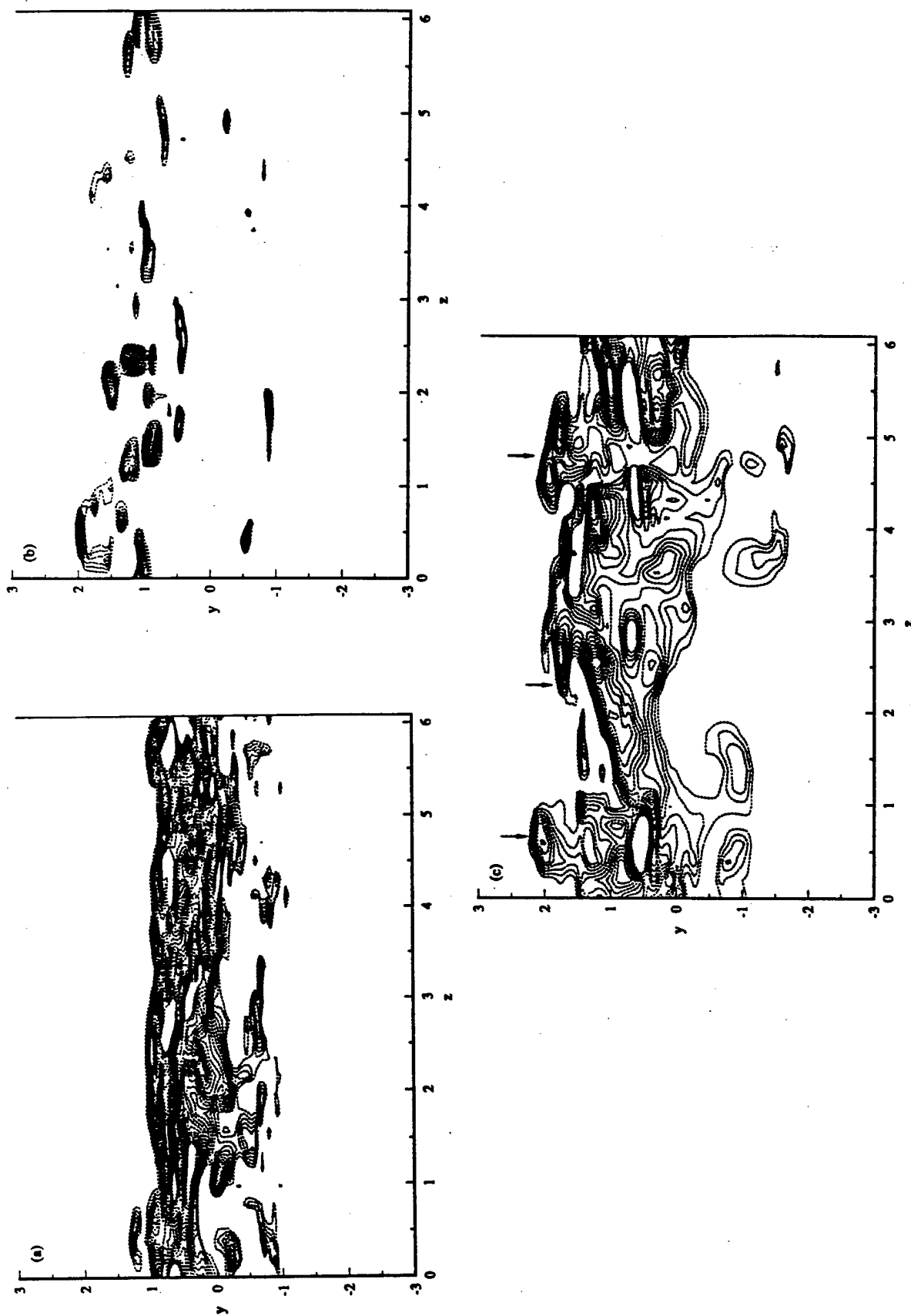


Figure 7.4.8 Contours of spanwise vorticity at $t = 45$ in :
 (a) the first core plane (CP): $x = 2$, (b) the mid-braid plane (MBP): $x = 3.6$, and
 (c) the second core plane (CP) : $x = 5.5$.
 (ω_{zmin} , ω_{zmax} , $\Delta\omega_z = (-7.5, -0.5, 0.5)$). Arrows indicate cusp regions.

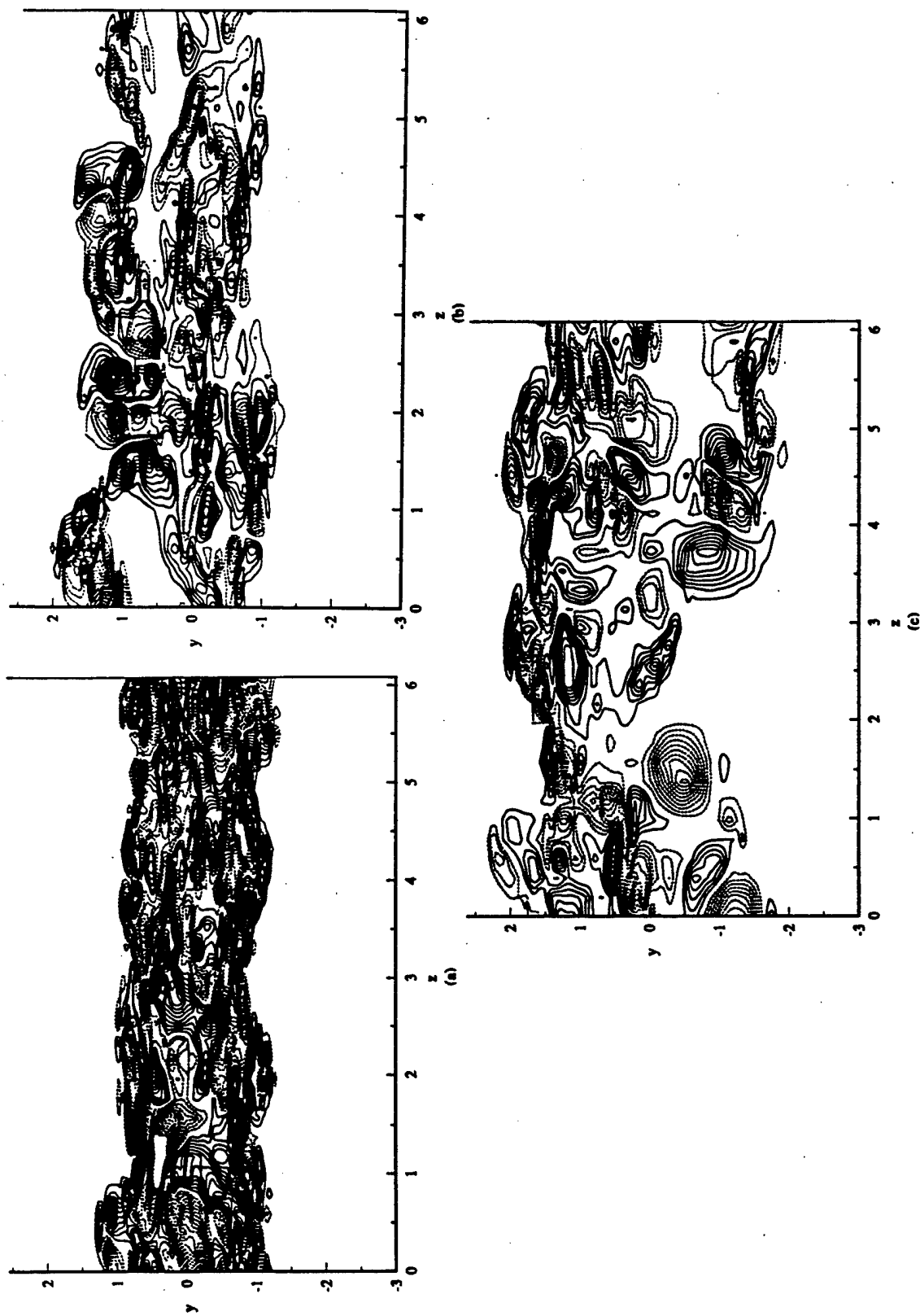


Figure 7.4.9 Contours of streamwise vorticity at $t = 45$ in :
 (a) the first core plane (CP): $x = 2$, (b) the mid-braid plane (MBP) : $x = 3.6$, and
 (c) the second core plane (CP) : $x = 5.5$.
 Solid Lines ($\omega_{x\min}$, $\omega_{x\max}$, $\Delta\omega_x = 0.5, 7.5, 0.5$).
 Dashed Lines ($\omega_{x\min}$, $\omega_{x\max}$, $\Delta\omega_x = (-7.5, -0.5, 0.5)$).

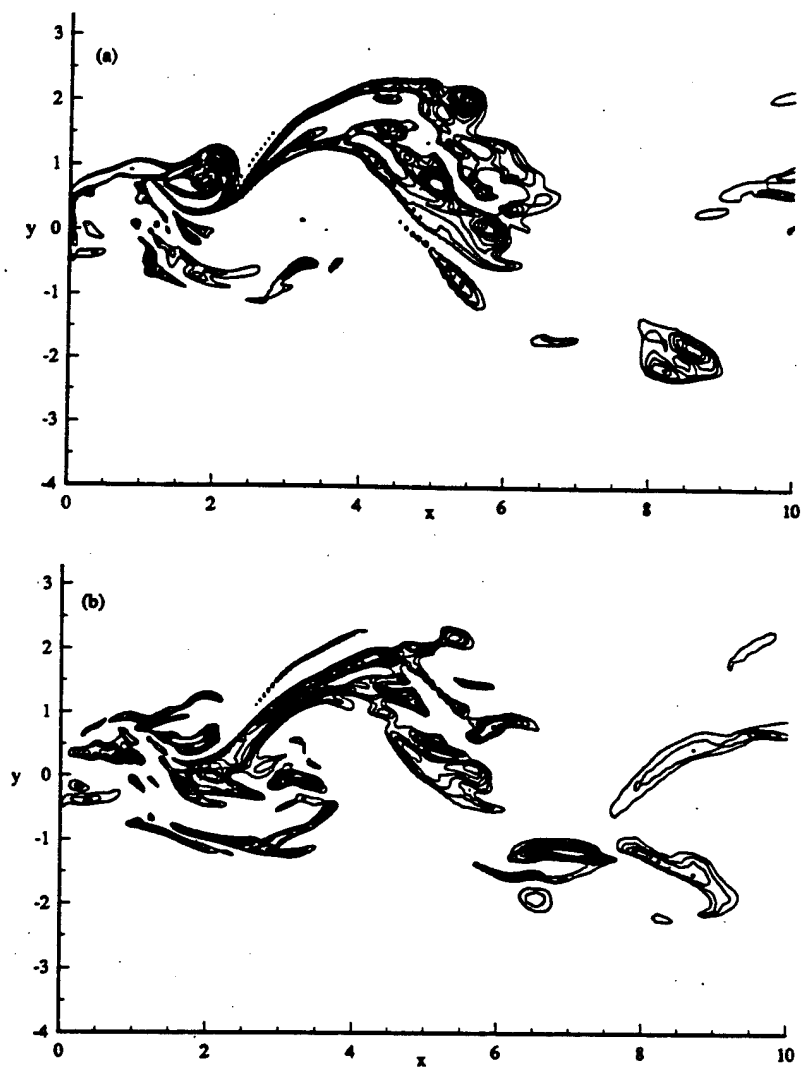


Figure 7.4.10 Contours of (a) ω_z , (b) ω_x in the rib plane (RP) at $z = \frac{3\pi}{16}$
 $(\omega_{i\min}, \omega_{i\max}, \Delta\omega_i) = (-7.5, -0.5, 0.5)$; $i = x$ or z

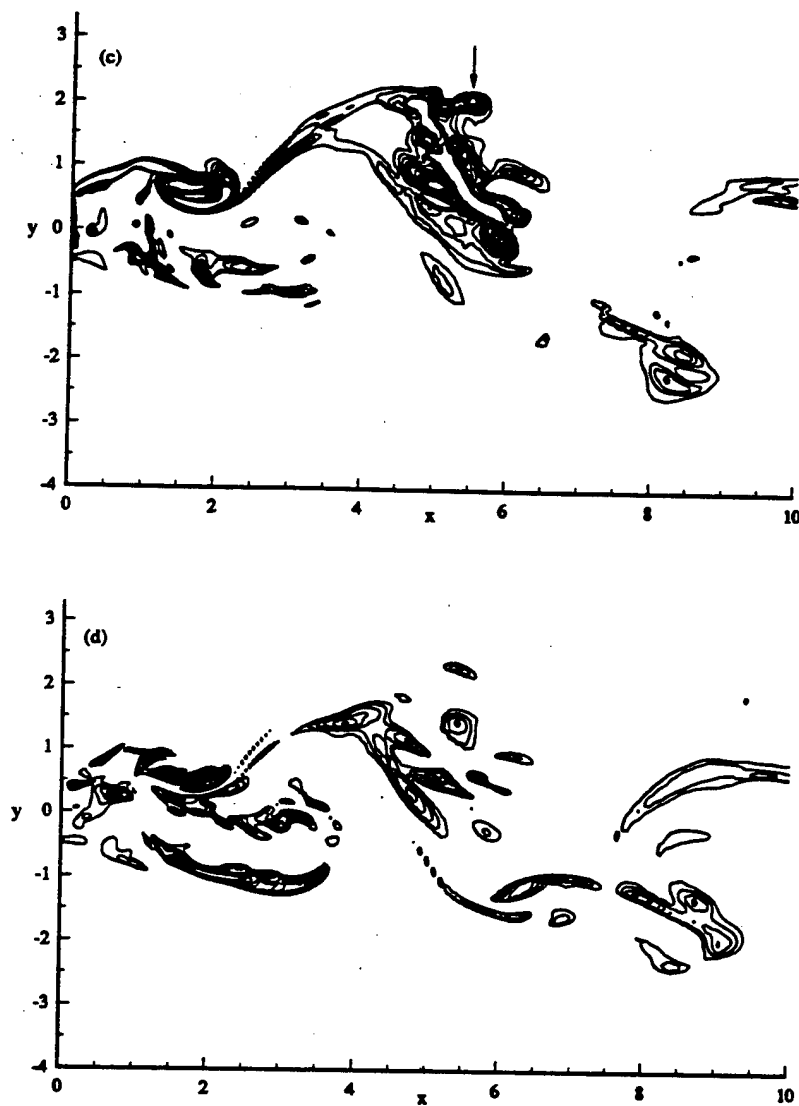


Figure 7.4.10(continued) Contours of (c) ω_z , (d) ω_x in the between-rib plane (BRP)

at $z = \frac{\pi}{4}$

$(\omega_{i\min}, \omega_{i\max}, \Delta\omega_i) = (-7.5, -0.5, 0.5); i = x \text{ or } z$
 Arrow indicates cusp region.

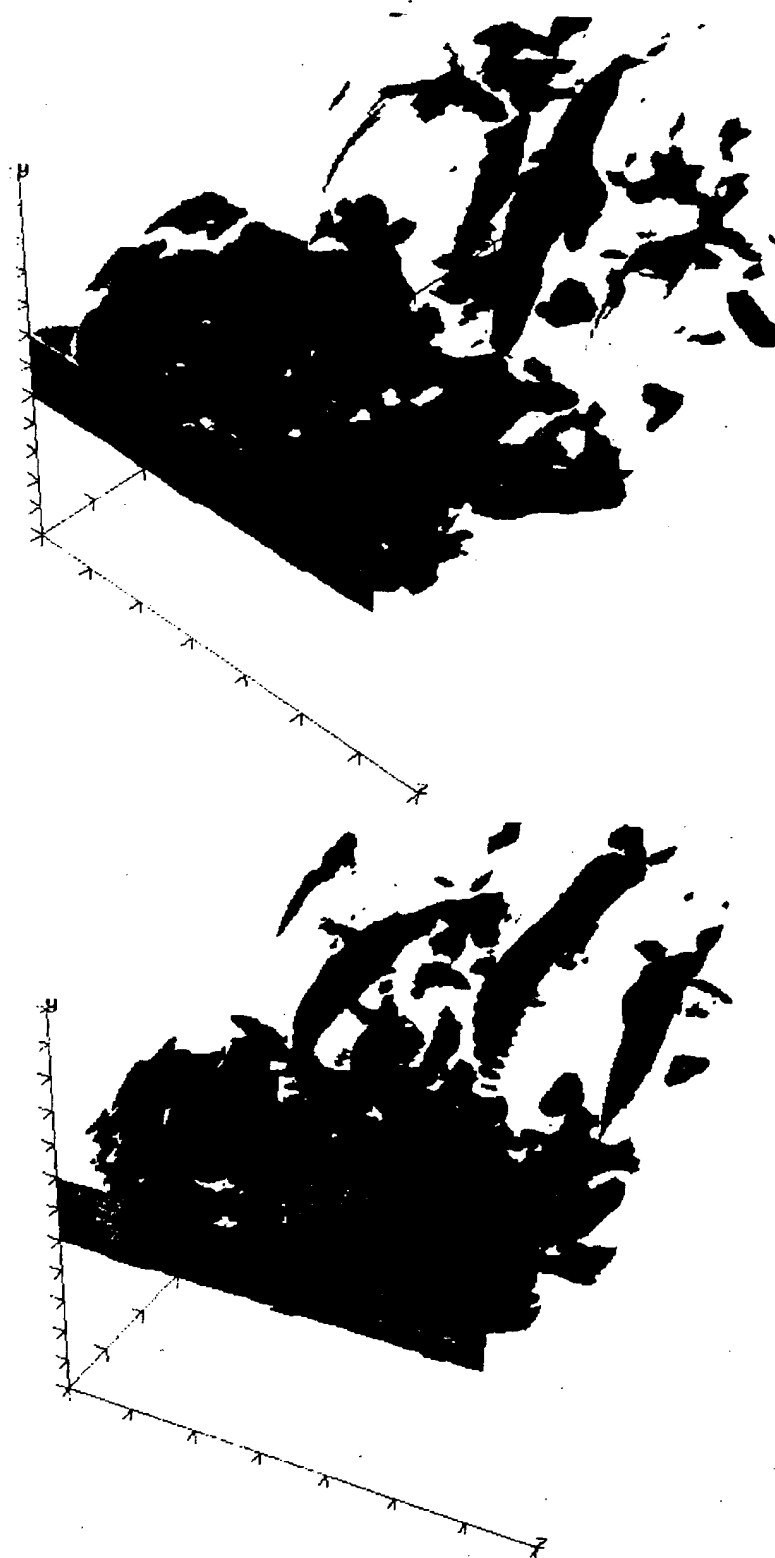


Figure 7.4.11 Contours of streamwise vorticity at $t = 55$.
Surface Level : Magenta = -2, Cyan = +2.

BIBLIOGRAPHY

- Abdallah, S., (1987a), 'Numerical Solutions for the Pressure Poisson Equation with Neumann Boundary Conditions using a Non-Staggered Grid, I', *J. Comp. Phys.*, Vol. 70, 182-192.
- Abdallah, S., (1987b), 'Numerical Solutions for the Pressure Poisson Equation with Neumann Boundary Conditions using a Non-Staggered Grid, II', *J. Comp. Phys.*, Vol. 70, 193-202.
- Abernathy, F.H., (1962), 'Flow over an Inclined Plate', *ASME J. Basic. Eng.*, Vol. 61, WA-124.
- Adams, E.W., and Johnston, J.P., (1988), 'Flow Structure in the Near-Wall Zone of a Turbulent Separated Flow', *AIAA J.*, Vol. 26, 932-939.
- Agrawal, R., (1989), 'Development of a Navier-Stokes Code on a Connection Machine', *AIAA Paper 89-1939-CP, AIAA 9th Comp. Fluid Dyn. Conf.*, 103-108.
- Anderson, D.A., Tannehill, J.C., and Pletcher, R.H., (1984), Computational Fluid Mechanics and Heat Transfer, Hemisphere Publ. Corp., New York.
- Arie, M., and Rouse, H., (1956), 'Experiments on Two-Dimensional Flow over a Normal Wall', *J. Fluid Mech.*, Vol. 1, 129-141.
- Armaly, B.F., Durst, F., Pereira, J.C.F., and Schönung, B., (1983), 'Experimental and Theoretical Investigation of Backward-Facing Step Flow', *J. Fluid Mech.*, Vol. 127, 473-496.
- Armfield, S.W., (1991), 'Finite Difference Solutions of the Navier-Stokes Equations on Staggered and Non-Staggered Grids', *Comp. Fluids*, Vol. 20, 1-17.
- Ashurst, W.T., and Meiburg, E., (1988), 'Three-Dimensional Shear Layer via Vortex Dynamics', *J. Fluid Mech.*, Vol. 189, 87-116.
- Balachandar, S., and Madabhushi, R.K., (1992), 'Spurious Modes in Spectral Collocation Methods with Two Non-Periodic Directions', ICASE Report No. 92-48, ICASE, NASA Langley Research Center, Hampton, VA, to appear in *J. Comp. Phys.*
- Bearman, P.W., and Trueman, D.M., (1972), 'An Investigation of the Flow Rectangular Cylinders', *Aero. Quart.*, Vol. 23, 229-237.
- Bell, J.H., and Mehta, R., (1992), 'Measurements of the Streamwise Vortical Structures in a Plane Mixing Layer', *J. Fluid Mech.*, Vol. 239, 213-248.
- Bernal, L.P., and Roshko, A., (1986), 'Streamwise Vortex Structures in Plane Mixing Layers', *J. Fluid Mech.*, Vol. 170, 499-525.
- Biringen, S., and Cook, C., (1988), 'On Pressure Boundary Conditions for the Incompressible Navier-Stokes Equations using Nonstaggered Grids', *Num. Heat Trans.*, Vol. 13, 241-252.

- Bradbury, L.J.S., and Moss, W.D., (1975), 'Pulsed Wire Anemometer Measurements in the Flow past a Normal Flat Plate in a Uniform Flow and in a Sheared Flow', *Proc. 4th Int. Conf. Wind Effects on Building and Structures*, London, 485-496.
- Bradbury, L.J.S., (1976), 'Measurements via a Pulsed-Wire and a Hot-Wire Anemometer in the Highly Turbulent Wake of a Normal Flat Plate', *J. Fluid Mech.*, Vol. 77, No. 3, 473-497.
- Briley, W.R., (1974), 'Numerical Method for Predicting Three-Dimensional Steady Viscous Flow in Ducts', *J. Comp. Phys.*, Vol. 14, 8-28.
- Brown, G.L., and Roshko, A., (1974), 'On Density Effects and Large Structure in Turbulent Mixing Layers', *J. Fluid Mech.*, Vol. 64, 775-816.
- Buzbee, B.L., Dorr, F.W., George, J.A., and Golub, G.H., (1971), 'The Direct Solution of the Discrete Poisson Equation on Irregular Regions', *SIAM J. Numer. Anal.*, Vol. 8, 722-736.
- Cantwell, B., and Coles, D., (1983), 'An Experimental Study of Entrainment and Transport in the Near Wake of Circular Cylinder', *J. Fluid Mech.*, Vol. 136, 321-374.
- Canuto, C., Hussaini, M.Y., Quarteroni, A., and Zang, T.A., (1988), Spectral Methods in Fluid Dynamics, Springer-Verlag, New-York.
- Castro, I.P., (1971), 'Wake Characteristics of Two-Dimensional Perforated Plates Normal to an Air-Stream', *J. Fluid Mech.*, Vol. 46, Part 3, 599-609.
- Castro, I.P., (1990), 'Turbulence in Incompressible Separated Flows', *IUTAM Symposium on Separated Flows and Jets*, Novosibirsk.
- Castro, I.P., Cliffe, K.A., and Norgett, M.J., (1982), 'Numerical Predictions of the Laminar Flow over a Normal Flat Plate', *Int. J. Num. Meth. Fluids*, Vol. 2, 61-88.
- Castro, I. P., and Haque, A., (1987), 'The Structure of a Turbulent Shear Layer Bounding a Separation Region', *J. Fluid Mech.*, Vol. 179, 439-468.
- Castro, I. P., and Haque, A., (1988), 'The Structure of a Shear Layer Bounding a Separation Region. Part 2. Effects of Free-Stream Turbulence', *J. Fluid Mech.*, Vol. 192, 577-595.
- Castro, I.P., and Jones, J.M., (1987), 'Studies in Numerical Computations of Recirculating Flows', *Int. J. Num. Meth. Fluids*, Vol. 7, 793-823.
- Chandrsuda, C., and Bradshaw, P., (1981), 'Turbulence of a Reattaching Mixing Layer', *J. Fluid Mech.*, Vol. 110, 171-194.
- Chein, R., and Chung, J.N., (1988), 'Discrete-Vortex Simulation of Flow over Inclined and Normal Plates', *Comp. Fluids*, Vol. 16, No. 4, 405-427.
- Cherry, N.J., Hillier, R., and Latour, M.P., (1983), 'The Unsteady Structure of Two-Dimensional Separated-and-Reattaching Flows', *J. Wind Engg. and Indus. Aero.*, Vol. 11, 95-105.

- Cherry, N.J., Hillier, R., and Latour, M.P., (1984), 'Unsteady Measurements in a Separated and Reattaching Flow', *J. Fluid Mech.*, Vol. 144, 13-46.
- Chorin, A.J., (1967), 'A Numerical Method for Solving Incompressible Viscous Flow Problems', *J. Comp. Phys.*, Vol. 2, 12-26.
- Chorin, A.J., (1968), 'Numerical Solutions of the Navier-Stokes Equations', *Math. Comp.*, Vol. 22, 745-762.
- Chorin, A.J., (1973), 'Numerical Study of Slightly Viscous Flow', *J. Fluid Mech.*, Vol. 57, 785-796.
- Chua, K., Lisoski, D., Leonard, A., and Roshko, A., (1990), 'A Numerical and Experimental Investigation of Separated Flow past an Oscillating Flat Plate', *ASME Non-Steady Flow Symposium*, Toronto, Canada.
- Clarksean, R., and McMurtry, P., (1990), 'Direct Numerical Simulation of a Planar Mixing Layer using the Spectral-Compact Finite Difference Technique', AIAA 90-1495, AIAA 21st Fluid Dynamics, Plasma Dynamics, and Lasers Conference, June 18-20, Seattle, Washington, U.S.A.
- Collatz, L., (1960), *The Numerical Treatment of Differential Equations*, Springer-Verlag, Berlin.
- Courchesne, J., and Laneville, A., (1979), 'A Comparison of Correction Methods used in the Evaluation of Drag Coefficient Measurements for Two-Dimensional Rectangular Cylinders', *ASME Trans.*, Vol. 101, 506-510.
- Coutanceau, M., and Defaye, J.-R., (1991), 'Circular Cylinder Wake Configurations: a Flow Visualization Survey', *Appl. Mech. Rev.*, Vol. 44, 255-305.
- Dengel P., and Hancock, P.E., (1992), Internal Report, Department of Mechanical Engineering, University of Surrey and Hermann Föttinger Inst., Berlin.
- Devenport, W.J., and Sutton, E.P., (1991), 'Near-wall Behavior of Separated and Reattaching Flows', *AIAA J.*, Vol. 29, 25-31.
- Dijlali, N., Gartshore, O.S., and Salcudean, M., (1990), 'Turbulent Flow around a Bluff Rectangular Plate Part II: Numerical Predictions', presented at the ASME Fluids Engineering Spring Conference, Paper No. 90-FE-5.
- Driver, D.M., and Seegmiller, H.L., (1985), 'Features of a Reattaching Turbulent Shear Layer in Divergent Channel Flow', *AIAA J.*, Vol. 23, 163-171.
- Dutta, P.K., (1988), 'Discrete Vortex Method for Separated and Free Shear Flows', Ph.D. Thesis, Indian Institute of Science, Bangalore, India.
- Eaton, J. K., and Johnston, J. P., (1981), 'A Review of Research on Subsonic Turbulent Flow Reattachment', *AIAA J.*, Vol. 19, 1093-1100.
- Fage, A., and Johansen, F.C., (1927), 'On the Flow of Air behind an Inclined Flat Plate of Infinite Span', *British Aero. Res. Coun. Rep. Memo.*, Vol. 1104, 81-106.

- Fail, R., Lawford, J.A., and Eyre, R.C.W., (1957), 'Low-Speed Experiments on the Wake Characteristics of Flat Plates Normal to an Air Stream', *British Aero. Res. Coun. Rep. Memo.*, Vol. 3120, 69-91.
- Fornberg, B., (1988), 'Generation of Finite Difference Formulas on Arbitrarily Spaced Grids', *Math. Comp.*, Vol. 51, No. 84, 699-706.
- Gharib, M., (1993), 'Studies of Two-Dimensional Flows via Soap-Films', Invited Lecture, American Physical Society, 46th Annual Meeting, Division of Fluid Dynamics, 21-23 November, Albuquerque, New Mexico.
- Ghia, U., and Davis, T., (1974), 'Navier-Stokes Solutions for Flow past a Class of Two-Dimensional Semi-Infinite Bodies', *AIAA J.*, Vol. 12, No. 12, 1659-1665.
- Ghia, U., Ghia, K.N., and Shin, C.T., (1982), 'High-Re Solutions for Incompressible Flow using the Navier-Stokes Equations and a Multigrid Method', *J. Comp. Phys.*, Vol. 48, 387-411.
- Goda, K., (1979), 'A Multistep Technique with Implicit Difference Schemes for Calculating Two- or Three-Dimensional Cavity Flows', *J. Comp. Phys.*, Vol. 30, 76-95.
- Govinda Ram, H. S., and Arkeri, V. H., (1990), 'Studies on Unsteady Pressure Fields in the Region of Separating and Reattaching Flows', *J. Fluid Eng.*, Vol. 112, 402-408.
- Haidvogel, D.B., and Zang, T., (1979), 'The Accurate Solution of Poisson's Equation by Expansion in Chebyshev Polynomials', *J. Comp. Phys.*, Vol. 30, 167-180.
- Hancock, P.E., and Castro, I.P., (1991), 'End Effects in Nominally Two-Dimensional Separated Flows', *Appl. Sci. Res.*, Vol. 51, 173-178.
- Harlow, F.H., and Welch, J.E., (1965), 'Numerical Calculation of Time-Dependent Viscous Incompressible Flow of Fluid with Free Surface', *Phys. Fluids*, Vol. 8, 2182-2189.
- Hayakawa, M., and Hussain, F., (1989), 'Three-Dimensionality of Organized Structures in a Plane Turbulent Wake', *J. Fluid Mech.*, Vol. 206, 375-404.
- Hillier, R., and Cherry, N. J., (1981), 'The Effects of Stream Turbulence on Separation Bubbles', *J. Wind Engg. and Indus. Aero.*, Vol. 8, 49-58.
- Hoerner, S.F., (1965), Fluid Dynamic Drag, Hoerner Fluid Dynamics.
- Hudson, J.D., and Dennis, S.C.R., (1985), 'The Flow of a Viscous Incompressible Fluid past a Normal Flat Plate at Low and Intermediate Reynolds Numbers: the Wake', *J. Fluid Mech.*, Vol. 160, 369-383.
- Hussain, A.K.M.F., (1983), Turbulence and Chaotic Phenomena in Fluids, Ed. T. Tatsumi, North-Holland, 453-460.
- Hussain, A.K.M.F., and Hayakawa, M., (1987), 'Eduction of Large-Scale Organized Structures in a Turbulent Plane Wake', *J. Fluid Mech.*, Vol. 180, 193-229.

- Igarashi, T., (1986), 'Correlation between Heat Transfer and Fluctuating Pressure in the Separated Region of a Bluff Body', *Heat Transfer 1986-Proc. Eight Int. Conf.*, San Francisco, CA, 1023-1028.
- Ingham, D.B., Tang, T., and Morton, B.R., (1990), 'Steady Two-Dimensional Flow through a Row of Normal Flat Plates', *J. Fluid Mech.*, Vol. 210, 281-302.
- Jaroch, M., (1987), 'Oil Flow Visualization Experiments in the Separated and Reattaching Flow past a Normal Flat Plate with a Long Wake Splitter Plate', *Z. Flugwiss. Weltraumforsch.*, Vol. 11, 230-236.
- Jaroch, M. P., and Fernholz, H.-H., (1989), 'The Three-Dimensional Character of a Nominally Two-Dimensional Separated Turbulent Shear Flow', *J. Fluid Mech.*, Vol. 205, 523-552.
- Jaroch, M., and Graham, J. M. R., (1988), 'An Evaluation of the Discrete Vortex Method as a Model for the Flow past a Flat Plate Normal to the Flow with a Long Wake Splitter Plate', *J. Mech. Theor. Appl.*, Vol. 7, 105-134.
- Jespersen, D.C., and Levit, C., (1989), 'A Computational Fluid Dynamics Algorithm on a Massively Parallel Computer', *Int. J. Super. Appl.*, Vol. 3, No. 4, Winter, 9-27.
- Jimenez, J., Cogollos, M., and Bernal, L.P., (1985), 'A Perspective View of the Plane Mixing Layer', *J. Fluid Mech.*, Vol. 152, 125-143.
- Joshi, D.S., (1993), 'Numerical Studies of the Wake of a Plate Normal to a Free Stream', Ph.D. Dissertation, University of Illinois at Urbana-Champaign, Urbana, Illinois.
- Joshi, D.S., Vanka, S.P., and Tafti, D.K., (1994), 'Large-Eddy Simulation of the Wake of a Normal Flat Plate', accepted in the *Symposium of Separated Flows*, ASME Summer Annual Meeting, June 19-23, Lake Tahoe, Nevada.
- Karniadakis, G.E., (1989), 'Spectral Element Simulations of Laminar and Turbulent Flows in Complex Geometries', *Appl. Num. Math.*, Vol 6, 85-105.
- Karniadakis, G.E., and Triantafyllou, G.E., (1989), 'Frequency Selection and Asymptotic States in Laminar Wakes', *J. Fluid Mech.*, Vol. 199, 441-469.
- Karniadakis, G.E., and Triantafyllou, G.E., (1992), 'Three-Dimensional Dynamics and Transition to Turbulence in the Wake of Bluff Objects', *J. Fluid Mech.*, Vol. 238, 1-30.
- Kim, J., and Moin, P., (1985), 'Application of a Fractional-Step Method to Incompressible Navier-Stokes Equations', *J. Comp. Phys.*, Vol. 59, 308-323.
- Kirchhoff, G., (1869), 'Zur Theorie freier Flüssigkeitsstrahlen', *Crelle*, v. 70.
- Kiya, M., (1989), 'Separation Bubbles', presented at the *IUTAM Conference on Separated Flows*, Grenoble.
- Kiya, M., and Arie, M., (1980), 'Discrete-Vortex Simulation of Unsteady Flow behind a Nearly Normal Plate', *Bull. JSME*, Vol. 23, No. 183, 1451-1458.
- Kiya, M., and Matsumura, M., (1988), 'Incoherent Turbulence Structure in the Near Wake of a Normal Plate', *J. Fluid Mech.*, Vol. 190, 343-356.

- Kiya, M., Sasaki, K., and Arie, M., (1982), 'Discrete-vortex Simulation of a Turbulent Separation Bubble', *J. Fluid Mech.*, Vol. 120, 219-244.
- Kiya, M., and Sasaki, K. (1983a), 'Structure of a Turbulent Separation Bubble', *J. Fluid Mech.*, Vol. 137, 83-113.
- Kiya, M., and Sasaki, K., (1983b), 'Free-stream Turbulence Effects on a Separation Bubble', *J. Wind Engg. and Indus. Aero.*, Vol. 14, 375-386.
- Kiya, M., and Sasaki, K., (1985), 'Structure of Large-Scale Vortices and Unsteady Reverse Flow in the Reattaching Zone of a Turbulent Separation Bubble', *J. Fluid Mech.*, Vol. 154, 463-491.
- Knisley, C.W., (1990), 'Strouhal Numbers of Rectangular Cylinders at Incidence: a Review and New Data', *J. Fluid Struct.*, Vol. 4, 371-393.
- Kovasznyai, L.I.G., (1948), 'Laminar Flow behind a Two-Dimensional Grid', *Proc. Cambridge Philos. Soc.*, 48.
- Ku, H.C., Hirsh, R.S., and Taylor, T.D., (1987), 'A Pseudospectral Method for Solution of the Three-Dimensional Incompressible Navier-Stokes Equations', *J. Comp. Phys.*, Vol. 70, 439-462.
- Kuwahara, K., (1973), 'Numerical Study of Flow past an Inclined Flat Plate by an Inviscid Model', *J. Phys. Soc. Japan*, Vol. 35, No. 5, 1545-1551.
- Lamb, H., (1932), *Hydrodynamics*, 6th Edition, Cambridge University Press, Cambridge.
- Lane, J.C., and Loehrke, R.I., (1980), 'Leading Edge Separation from a Blunt Plate at Low Reynolds Number', *J. Fluids Eng.*, Vol. 102, 494-496.
- Lasheras, J.C., Cho, J.S., and Maxworthy, T., (1986), 'On the Origin and Evolution of Streamwise Vortical Structures in a Plane, Free Shear Layer', Vol. 172, 231-258.
- Le, H., and Moin, P., (1991), 'An Improvement of Fractional Step Methods for the Incompressible Navier-Stokes Equations', *J. Comp. Phys.*, Vol. 92, 369-379.
- Leder, A., (1991), 'Dynamics of Fluid Mixing in Separated Flow', *Phys. Fluids*, Vol. 3, No. 7, 1741-1748.
- Lisoski, D., (1993), 'Nominally Two-Dimensional Flow about a Normal Flat Plate', Ph.D. Dissertation, California Institute of Technology, Pasadena, California.
- Leep, L.J., Dutton, J.C., and Burr, R.F., (1993), 'Three-Dimensional Simulations of Compressible Mixing Layers: Visualizations and Statistical Analysis', *AIAA J.*, Vol. 31, No. 11, 2039-2046.
- Long, L.N., Khan, M.M.S., and Sharp, H. T., (1989), 'A Massively Parallel Three-Dimensional Euler/Navier-Stokes Method', AIAA Paper No. 89-1937-CP, AIAA 9th Comp. Fluid Dyn. Conf., Buffalo, NY.

- Lowery, P., and Reynolds, W.C., (1986), 'Numerical Simulation of a Spatially-Developing Forced, Plane Mixing Layer', Dissertation, Report No. TF-26, Department of Mechanical Engineering, Stanford University, Stanford, California.
- Macaraeg, M.G., and Streett, C.L., (1986), 'Improvements in Spectral Collocation Discretization through a Multiple Domain Technique', *Appl. Num. Math.*, Vol. 2, 95-108.
- Madabhushi, R.K., (1992), Private communication.
- Madabhushi, R.K., Balachandar, S., and Vanka, S.P., (1993), 'A Divergence-Free Chebyshev Collocation Procedure for Incompressible Flows with Two Non-periodic Directions', *J. Comp. Phys.*, Vol. 105, 199-206.
- McCluskey, F., Hancock, P.E., and Castro, I.P., (1991), 'Three-Dimensional Separated Flows', *Eight Symposium of Turbulent Shear Flows*, Technical University of Munich, Sept. 9-11, Paper No. 9-5.
- Michalke, A., (1964), 'On the Inviscid Instability of the Hyperbolic-Tangent Velocity Profile', *J. Fluid Mech.*, Vol. 19, 543-556.
- Miyakoda, K., (1962), 'Contribution to the Numerical Weather Prediction-Computation with Finite Difference', *Jap. J. Geoph.*, Vol. 3, No.1, 118-119.
- Miyauchi, T., Kawano, K., and Shingou, M., (1991), 'The Coherent Structure in Turbulent Mixing Layers (Structure in the Core and Rib Regions)', *Comp. Fluids*, Vol. 19, No. 3/4, 401-412.
- Moin, P., and Kim, J., (1980), 'On the Numerical Solution of Time-Dependent Viscous Incompressible Fluid Flows Involving Solid Boundaries', *J. Comp. Physics*, Vol. 35, 381-392.
- Monkewitz, P.A., and Huerre, P., (1982), 'Influence of the Velocity Ratio on the Spatial Instability of Mixing Layers', *Phys. Fluids*, Vol. 25, 1137-1143.
- Morkovin, M.V. (1964) 'Flow around Circular Cylinders. A Kaleidoscope of Challenging Fluid Phenomena', *ASME Symposium on Fully Separated Flows*, Philadelphia, 102.
- Najjar, F.M., and Vanka, S.P., (1993), 'Numerical Study of a Separated-Reattaching Flow', *Theor. Comp. Fluid Dyn.*, Vol. 5, 291-308.
- Nakagawa, T., (1989), 'Vortex Shedding Mechanism from a Triangular Prism in Subsonic Flow', *Fluid Dyn. Res.*, Vol. 5, 69-81.
- Nakamura, Y., and Nakashima, M., (1986), 'Vortex Excitation of Prisms with Elongated, H and I — Cross-sections', *J. Fluid Mech.*, Vol. 163, 149-169.
- Oertel, J. (1990). Wakes behind blunt bodies. *Ann. Rev. Fluid Mech.*, Vol. 22, 539-564.
- Olsson, P., and Johnsson, S.L., (1990), 'A Dataparallel Implementation of an Explicit Method for the Three-Dimensional Compressible Navier-Stokes Equations', *Parallel Comp.*, Vol. 14, 1-30.

- Oran, E.S., Boris, J.P., and Brown, E.F., (1990), 'Fluid Dynamics Computations on a Connection Machine-Preliminary Timings and Complex Boundary Conditions', AIAA paper No. AIAA-90-0335, *AIAA 28th Aerospace Sciences Meeting*, Reno, Nevada.
- Oran, E.S., Boris, J.P., and DeVore, C.R., (1992), 'Reactive-Flow Computations on a Massively Parallel Computer', *Fluid Dyn. Res.*, Vol. 10, 251-271.
- Ortega, J.M., (1989), Introduction to Parallel and Vector Solution of Linear Systems, 2nd Edition, Plenum Publishing Corp., New York.
- Ota, T., and Kon, J., (1974), 'Heat Transfer in the Separated and Reattached Flow on a Blunt Flat Plate', *J. Heat Transfer*, Vol. 96, 459-462.
- Ota, T., and Itsaka, M., (1976), 'A Separated and Reattached Flow on a Blunt Flat Plate', *J. Fluids Eng.*, Vol. 98, 79-86.
- Ota, T., and Narita, M., (1978), 'Turbulence Measurements in a Separated and Reattached Flow over a Blunt Flat Plate', *Journal of Fluids Engineering*, Vol. 100, 224-228.
- Ota, T., Asano, Y., and Okawa, J., (1981), 'Reattachment Length and Transition of the Separated Flow over Blunt Flat Plates', *Bull. JSME*, Vol. 24, No. 192, 941-947.
- Ota, T., and Motegi, H., (1983), 'Measurements of Spatial Correlations and Autocorrelations in Separated and Reattached Flow over a Blunt Flat Plate', *J. Wind Engg. and Ind. Aero.*, Vol. 12, 297-312.
- Patankar, S.V., (1980), Numerical Heat Transfer and Fluid Flow, Hemisphere Publishing Corp., Washington.
- Patera, A.T., (1984), 'A Spectral Element Method for Fluid Dynamics: Laminar Flow in a Channel Expansion', *J. Comp. Phys.*, Vol. 54, 468-488.
- Pauley, L. P., Moin, P., and Reynolds, W. C., (1990), 'The Structure of Two-Dimensional Separation', *J. Fluid Mech.*, Vol. 220, 397-412.
- Perot, J.B., (1992), 'Direct Numerical Simulation of Turbulence on the Connection Machine', *Parallel CFD '92*, Rutgers University, New Brunswick, New Jersey.
- Perry, A.E., and Steiner, T.R., (1987), 'Large-Scale Vortex Structures in Turbulent Wakes behind Bluff Bodies. Part I. Vortex Formation Processes', *J. Fluid Mech.*, Vol. 174, 233-270.
- Peyret, R., and Taylor, T.D., (1983), Computational Methods for Fluid Flow, Springer Verlag, New York.
- Planche, O.H., and Reynolds, W.C., (1992), 'Direct Numerical Simulation of Compressible Reacting Mixing Layers on the IPSC860', *Parallel CFD '92*, Rutgers University, New Brunswick, New Jersey.
- Poinsot, T.J., and Lele, S.K. (1992), 'Boundary Conditions for Direct Simulations of Compressible Viscous Flows', *J. Comp. Phys.*, 101, 104-129.

- Raghavan, V.M., McCorskey, W.J., Van Dalsem, W.R., and Baeder, W.R., (1990), 'Calculations of the Flow past Bluff Bodies, including Tilt-Rotor Wing Sections at $\alpha = -90^\circ$ ', AIAA-90-0032, *AIAA 28th Aerospace Sciences Meeting*, Reno, Nevada.
- Rai, M.M., and Moin, P., (1991), 'Direct Simulations of Turbulent Flow using Finite-Difference Schemes', *J. Comp. Phys.*, Vol. 96, 15-53.
- Rayleigh, L., (1876), 'Note on Hydrodynamics', *Philosophical Magazine*, II, 441-447.
- Reynolds, W.C., and Hussain, A.K.M.F., (1972), 'The Mechanisms of an Organized Wave in Turbulent Shear Flow. Part 3. Theoretical Models and Comparisons with Experiments', *J. Fluid Mech.*, Vol. 54, 263-288.
- Roache, P.J., (1976), Computational Fluid Dynamics, Hermosa, Albuquerque, New Mexico.
- Robichaux, J., Tafti, D.K., and Vanka, S.P., (1992), 'Large-Eddy Simulations of Turbulence on the CM-2', *Num. Heat Transfer, Part B*, Vol. 21, 367-388.
- Rogers, M.M., and Moser, R.D., (1992), 'The Three-Dimensional Evolution of a Plane Mixing Layer: the Kelvin-Helmholtz Rollup', *J. Fluid Mech.*, Vol. 243, 183-226.
- Roshko, A., (1954a), 'A New Hodograph for Free-Streamline Theory', *NACA Tech. Note*, 3168.
- Roshko, A., (1954b), 'On the Drag and Shedding Frequency of Two-Dimensional Bluff Bodies', *NACA Tech. Note*, 3169.
- Roshko, A., (1954c), 'On the Development of Turbulent Wake from Vortex Streets', *NACA Tech. Rep.* 1191.
- Roshko, A., (1955), 'On the Wake and Drag of Bluff Bodies', *J. Aero. Sci.*, Vol. 22, 124-132.
- Roshko, A., and Lau, J.C. (1965), 'Some Observations on Transition and Reattachment of a Free Shear Layer in Incompressible Flow', *Proc. 1965 Heat Transfer and Fluid Mechanics Institute*.
- Ruderich, R., and Fernholz, H.-H. (1986), 'An Experimental Investigation of a Turbulent Shear Flow with Separation, Reverse Flow, and Reattachment', *J. Fluid Mech.*, Vol. 163, 283-322.
- Saati, A., Biringen, S., and C. Farhat, (1990), 'Solving Navier-Stokes Equations on a Massively Parallel Processor: Beyond the 1 GFLOP Performance', *Int. J. Super. Appl.*, Vol. 4, No. 1, Spring, 72-80.
- Sarpkaya, T., (1975), 'An Inviscid Model of Two-Dimensional Vortex Shedding for Transient and Asymptotically Steady Separated Flow over an Inclined Flat Plate', *J. Fluid Mech.*, Vol. 68, 109-128.
- Sarpkaya, T., (1992), 'Brief Reviews of Some Time-Dependent Flows', *J. Fluids Eng.*, Vol. 114, 283-298.

- Sarpkaya, T., and Kline, H.K., (1982), 'Impulsively-Started Flow about Four Types of Bluff Body', *J. Fluid Engg.*, Vol. 104, 207-213.
- Sarpkaya, T., and Ihrig, C.J., (1986), 'Impulsively Started Steady Flow about Rectangular Prisms: Experiments and Discrete Vortex Analysis', *J. Fluids Eng.*, Vol. 108, 47-54.
- Schlichting, H., (1975), Boundary-Layer Theory, Seventh Edition, Mc Graw-Hill.
- Schumann, U., (1980), 'Fast Elliptic Solvers and their Application in Fluid Dynamics', in Computational Fluid Dynamics, edited by W. Kollmann. Hemisphere Publishing Corp., New York, 402-430.
- Smits, A. J., (1982), 'Scaling Parameters for a Time-Averaged Separation Bubble', *J. Fluid Eng.*, Vol. 104, 178-184.
- Sotiropoulos, F., and Abdallah, S., (1991), 'The Discrete Continuity Equation in Primitive Variable Solutions of Incompressible Flow', *J. Comp. Phys.*, Vol. 95, 212-227.
- Stanton, T.E., (1903), 'On the Resistance of Plane Surfaces in a Uniform Current of Air', *Minutes of Proc. Inst. Civ. Eng.*, Vol. 156, 78-139.
- Steiner, T.R., and Perry, A.E., (1987), 'Large-Scale Structures in the Turbulent Wakes behind Bluff Bodies. Part II. Far-Wake Structures', *J. Fluid Mech.*, Vol. 174, 271-298.
- Strouhal, V. (1878), 'Über eine Desondere Art der Tonerregung', *Ann. Physik. Chemie. NF*, Vol. 5, 216-251.
- Strikwerda, J.C., (1984), 'Finite Difference Methods for the Stokes and Navier-Stokes Equations', *SIAM J. Sci. Stat. Comp.*, Vol. 5, 56-68.
- Tafti, D.K., and Vanka, S. P., (1991a), 'A Numerical Study of Flow Separation and Reattachment on a Blunt Plate', *Phys. Fluids A*, Vol. 3, 1749-1759.
- Tafti D.K., and Vanka, S. P. (1991b), 'A Three-Dimensional Numerical Study of Flow Separation and Reattachment on a Blunt Plate', *Phys. Fluids A*, Vol. 3, 2887-2909.
- Tamaddon-Jahromi, H.R., Townsend, P., and Webster, M.F., (1994), 'Unsteady Viscous Flow past a Flat Plate Orthogonal to the Flow', *Comp. Fluids*, Vol. 23, No. 2, 433-446.
- Taneda, S., and Honji, H., (1971), 'Unsteady Flow past a Flat Plate Normal to the Direction of Motion', *J. Phys. Soc. Japan*, Vol. 30, No. 1, 262-272.
- Taylor, G.I., (1923), *Philos. Mag.*, Vol. 46, 671.
- Temam, R., (1979), Navier-Stokes Equations. Theory and Numerical Analysis, 2nd ed., North-Holland, Amsterdam.
- Temperton, C., (1983), 'Self-Sorting Mixed-Radix Fast Fourier Transforms', *J. Comp. Phys.*, Vol. 52, 1-23.
- Thinking Machines Corporation, (1992a), *Connection Machine CM-5 Technical Summary*.
- Thinking Machines Corporation, (1992b), *CM Fortran Release Notes*.

Vanka, S.P., (1986), 'Block-Implicit Multigrid Solution of Navier-Stokes Equations in Primitive Variables', *J. Comp. Phys.*, Vol. 65, 138-158.

von Karman, Th., (1912), 'Uder den Mechanismus des Widerstandes den ein Bewegter Korper in Einer Flussigkeit Erfahrt', *Nachr. Ges. Wiss. Gottigen, Math. Phys. Klasse*, 547-556.

Wake, B.E., and T.A. Egolf, (1989), 'Implementation of a Rotary-Wing Three-Dimensional Navier-Stokes Solver on a Massively Parallel Computer', AIAA Paper No. 89-1939-CP, *AIAA 9th Comp. Fluid Dyn. Conf.*, Buffalo, NY.

Yoshida, Y., and Nomura, T., (1985), 'A Transient Solution Method for the Finite Element Incompressible Navier-Stokes Equations', *Int J. Num. Meth. Fluids*, Vol. 5, 874-890.

APPENDICES

APPENDIX A

Spatial Discretization on Rectilinear Non-Uniform Grids

The high-order accurate formulations discussed in Section 3.2 have been presented for uniform grids. For rectilinear non-uniform grids, the stencils can be modified with either Lagrange multipliers (Fornberg, 1988; Rai and Moin, 1991) or metrics formulation. In the present study, the metrics formulation is chosen since it is easier to code and can be extended to general curvilinear grids. Section A.1 outlines the modifications to the convective and diffusive derivatives in the momentum equations to accommodate for rectilinear non-uniform grids. Section A.2 presents the modification to the stencils of the pressure-Poisson equation.

A.1 Momentum Equations

In the metrics formulation, the grid in the physical space (x - y) is mapped on to the computational space (ξ - η) with constant grid spacing ($\Delta\xi=1$, $\Delta\eta=1$). The stencils of the finite-difference method are formulated in the computational space (ξ - η). The first-order derivatives of a variable ϕ (such as the velocity components) are expressed as :

$$\frac{\partial \phi}{\partial x} = \frac{\partial \xi}{\partial x} \frac{\partial \phi}{\partial \xi} \quad (\text{A.1.1})$$

$$\frac{\partial \phi}{\partial y} = \frac{\partial \eta}{\partial y} \frac{\partial \phi}{\partial \eta} \quad (\text{A.1.2})$$

where $\frac{\partial \xi}{\partial x}$ and $\frac{\partial \eta}{\partial y}$ are the first-order metrics derivatives given by :

$$\frac{\partial \xi}{\partial x} = \frac{1}{\frac{\partial x}{\partial \xi}} \quad (\text{A.1.3})$$

$$\frac{\partial \eta}{\partial y} = \frac{1}{\frac{\partial y}{\partial \eta}} \quad (\text{A.1.4})$$

The derivatives $\frac{\partial x}{\partial \xi}$ and $\frac{\partial y}{\partial \eta}$ can be computed either analytically or approximated using finite-difference stencils. Currently, a fourth-order central approach is applied to compute the metrics :

$$\left(\frac{\partial x}{\partial \xi}\right)_i = \frac{1}{12 \Delta \xi} (x_{i-2} - 8 x_{i-1} + 8 x_{i+1} - x_{i+2}) ; i = 3, Nx-2 \quad (\text{A.1.5a})$$

$$\left(\frac{\partial x}{\partial \xi}\right)_i = \frac{1}{2 \Delta \xi} (-x_{i-1} + x_{i+1}) ; i = 2 \text{ and } Nx-1 \quad (\text{A.1.5b})$$

$$\left(\frac{\partial y}{\partial \eta}\right)_j = \frac{1}{12 \Delta \eta} (y_{j-2} - 8 y_{j-1} + 8 y_{j+1} - y_{j+2}) ; j = 3, Ny-2 \quad (\text{A.1.6a})$$

$$\left(\frac{\partial y}{\partial \eta}\right)_j = \frac{1}{2 \Delta \eta} (-y_{j-1} + y_{j+1}) ; j = 2 \text{ and } Ny-1 \quad (\text{A.1.6b})$$

The first-order derivatives $\frac{\partial \phi}{\partial \xi}$ and $\frac{\partial \phi}{\partial \eta}$ are evaluated with fourth-order accurate finite-difference stencils (see Equations (3.2.1-3.2.5)). This formulation is implemented in the stencil computations of the convection and the velocity divergence terms.

The diffusion terms, $\frac{\partial^2 \phi}{\partial x^2}$ and $\frac{\partial^2 \phi}{\partial y^2}$, are formulated on non-uniform grids in the following manner :

$$\frac{\partial^2 \phi}{\partial x^2} = \frac{\partial^2 \xi}{\partial x^2} \frac{\partial \phi}{\partial \xi} + \left(\frac{\partial \xi}{\partial x}\right)^2 \frac{\partial^2 \phi}{\partial \xi^2} \quad (\text{A.1.7})$$

$$\frac{\partial^2 \phi}{\partial y^2} = \frac{\partial^2 \eta}{\partial y^2} \frac{\partial \phi}{\partial \eta} + \left(\frac{\partial \eta}{\partial y}\right)^2 \frac{\partial^2 \phi}{\partial \eta^2} \quad (\text{A.1.8})$$

The second-order derivatives, $\frac{\partial^2 \xi}{\partial x^2}$ and $\frac{\partial^2 \eta}{\partial y^2}$, are evaluated as follows :

$$\frac{\partial^2 \xi}{\partial x^2} = - \frac{\left(\frac{\partial^2 x}{\partial \xi^2}\right)}{\left(\frac{\partial x}{\partial \xi}\right)^3} \quad (\text{A.1.9a})$$

$$\frac{\partial^2 \eta}{\partial y^2} = - \frac{\left(\frac{\partial^2 y}{\partial \eta^2} \right)}{\left(\frac{\partial y}{\partial \eta} \right)^3} \quad (\text{A.1.9b})$$

where

$$\left(\frac{\partial^2 x}{\partial \xi^2} \right)_i = \frac{1}{12 \Delta \xi^2} (-x_{i-2} + 16 x_{i-1} - 30 x_i + 16 x_{i+1} - x_{i+2}) ; i = 3, Nx-2 \quad (\text{A.1.10a})$$

$$\left(\frac{\partial^2 x}{\partial \xi^2} \right)_i = \frac{1}{\Delta \xi^2} (x_{i-1} - 2 x_i + x_{i+1}) ; i = 2 \text{ and } Nx-1 \quad (\text{A.1.10b})$$

$$\left(\frac{\partial^2 y}{\partial \eta^2} \right)_j = \frac{1}{12 \Delta \eta^2} (-y_{j-2} + 16 y_{j-1} - 30 y_j + 16 y_{j+1} - y_{j+2}) ; j = 3, Ny-2 \quad (\text{A.1.11a})$$

$$\left(\frac{\partial^2 y}{\partial \eta^2} \right)_j = \frac{1}{\Delta \eta^2} (y_{j-1} - 2 y_j + y_{j+1}) ; j = 2 \text{ and } Ny-1 \quad (\text{A.1.11b})$$

The second-order derivatives $\frac{\partial^2 \phi}{\partial \xi^2}$ and $\frac{\partial^2 \phi}{\partial \eta^2}$ are evaluated with fourth and second-order accurate finite-difference stencils for the interior nodes and the nodes adjacent to the boundaries, respectively (see Equations (3.2.6-3.2.8)).

This summarizes the modifications of the finite-difference stencils for the momentum equations on non-uniform rectilinear grids. The metrics are computed at the pre-timestepping stage, stored and used subsequently during the time integration procedure.

A.2 Pressure-Poisson Equation

This section presents the modifications to CFVM (see Section 3.3.3) for non-uniform grids. The intermediate cell fluxes, \tilde{c} , are computed from the collocated velocity field, \tilde{u} , using fourth-order accurate Lagrange multipliers (Fornberg, 1988). The pressure gradients at the cell faces are formulated as :

$$\left(\frac{\partial p}{\partial x}\right)_{i+1/2} = \left(\frac{\partial x^p}{\partial \xi}\right)_{i+1/2} \left(\frac{\partial p}{\partial \xi}\right)_{i+1/2} = \frac{1}{\left(\frac{\partial x^p}{\partial \xi}\right)_{i+1/2}} \left(\frac{\partial p}{\partial \xi}\right)_{i+1/2} \quad (\text{A.2.1})$$

$$\left(\frac{\partial p}{\partial y}\right)_{j+1/2} = \left(\frac{\partial \eta^p}{\partial \eta}\right)_{j+1/2} \left(\frac{\partial p}{\partial \eta}\right)_{j+1/2} = \frac{1}{\left(\frac{\partial \eta^p}{\partial \eta}\right)_{j+1/2}} \left(\frac{\partial p}{\partial \eta}\right)_{j+1/2} \quad (\text{A.2.2})$$

The first-order metrics derivatives are evaluated with fourth-order accurate central difference schemes :

$$\left(\frac{\partial x^p}{\partial \xi}\right)_{i+1/2} = \frac{1}{24 \Delta \xi} (x_{i-2} - 27 x_{i-1} + 27 x_i - x_{i+1}) ; i = 4, Nx-3 \quad (\text{A.2.3})$$

$$\left(\frac{\partial y^p}{\partial \eta}\right)_{j+1/2} = \frac{1}{24 \Delta \eta} (y_{j-2} - 27 y_{j-1} + 27 y_j - y_{j+1}) ; j = 4, Ny-3 \quad (\text{A.2.4})$$

The near-boundary derivatives are formulated with second-order stencils :

$$\left(\frac{\partial x^p}{\partial \xi}\right)_{i+1/2} = \frac{1}{\Delta \xi} (x_i - x_{i-1}) ; i = 3 \text{ and } Nx-2 \quad (\text{A.2.5})$$

$$\left(\frac{\partial y^p}{\partial \eta}\right)_{j+1/2} = \frac{1}{\Delta \eta} (y_j - y_{j-1}) ; j = 3 \text{ and } Ny-2 \quad (\text{A.2.6})$$

The pressure gradients in the computational space, $\frac{\partial p}{\partial \xi}$ and $\frac{\partial p}{\partial \eta}$, are evaluated using the formulations discussed earlier in Section 3.3.3. The modification of the stencils in the presence of baffles and obstacles is an extension to the formulation described in Appendix D.

APPENDIX B

Formulation Of Pressure Discretization Schemes

Seven schemes considered in this study for the discretization of the pressure-Poisson equation are summarized in Table 3.7.1. This appendix describes in detail the formulations of these schemes.

B.1 Inconsistent Finite-Difference Method

The IFDM is based on a fourth-order central finite-difference scheme of the Laplacian and divergence operators for the interior nodal values and a second-order central finite-difference stencil for the near-boundary values. The discretized pressure-Poisson equation for IFDM is given by :

$$\begin{aligned} (\nabla^2 p)_{ij} &= \frac{1}{12\Delta x^2} (-p_{i-2,j} + 16p_{i-1,j} - 30p_{i,j} + 16p_{i+1,j} - p_{i+2,j}) \\ &\quad + \frac{1}{12\Delta y^2} (-p_{i,j-2} + 16p_{i,j-1} - 30p_{i,j} + 16p_{i,j+1} - p_{i,j+2}) \end{aligned} \quad (B.1.1a)$$

$$\begin{aligned} D_{ij} &= \frac{1}{12\Delta x} (\tilde{u}_{i-2,j} - 8\tilde{u}_{i-1,j} + 8\tilde{u}_{i+1,j} - \tilde{u}_{i+2,j}) \\ &\quad + \frac{1}{12\Delta y} (\tilde{v}_{i,j-2} - 8\tilde{v}_{i,j-1} + 8\tilde{v}_{i,j+1} - \tilde{v}_{i,j+2}) \end{aligned} \quad (B.1.1b)$$

for $i = 4$ to $Nx-3$ and $j = 3$ to $Ny-3$, and

$$\left(\frac{\partial^2 p}{\partial x^2} \right)_{I,j} = \frac{1}{\Delta x^2} (p_{I-1,j} - 2p_{I,j} + p_{I+1,j}) \quad (B.1.2a)$$

$$\left(\frac{\partial \tilde{u}}{\partial x} \right)_{I,j} = \frac{1}{\Delta x} (-\tilde{u}_{I-1,j} + \tilde{u}_{I+1,j}) \quad (B.1.2b)$$

$$\left(\frac{\partial^2 p}{\partial y^2} \right)_{i,J} = \frac{1}{\Delta y^2} (p_{i,J-1} - 2p_{i,J} + p_{i,J+1}) \quad (B.1.2c)$$

$$\left(\frac{\partial \tilde{v}}{\partial y} \right)_{i,J} = \frac{1}{12\Delta y} (-\tilde{v}_{i,J-1} + \tilde{v}_{i,J+1}) \quad (B.1.2d)$$

for $I = 2, 3, Nx-2, Nx-1$ and $J = 2, 3, Ny-2, Ny-1$.

Third-order one-sided finite-difference schemes are applied to compute the boundary pressure gradients (Fornberg, 1988):

$$\left(\frac{\partial p}{\partial x}\right)_{1,j} = \frac{1}{\Delta x} \left(-\frac{11}{6} p_{1,j} + 3 p_{2,j} - \frac{3}{2} p_{3,j} + \frac{1}{3} p_{4,j} \right) \quad (\text{B.1.3a})$$

$$\left(\frac{\partial p}{\partial x}\right)_{N_x,j} = \frac{1}{\Delta x} \left(\frac{11}{6} p_{N_x,j} - 3 p_{N_x-1,j} + \frac{3}{2} p_{N_x-2,j} - \frac{1}{3} p_{N_x-3,j} \right) \quad (\text{B.1.3b})$$

$$\left(\frac{\partial p}{\partial y}\right)_{i,1} = \frac{1}{\Delta y} \left(-\frac{11}{6} p_{i,1} + 3 p_{i,2} - \frac{3}{2} p_{i,3} + \frac{1}{3} p_{i,4} \right) \quad (\text{B.1.3c})$$

$$\left(\frac{\partial p}{\partial y}\right)_{i,N_y} = \frac{1}{\Delta y} \left(\frac{11}{6} p_{i,N_y} - 3 p_{i,N_y-1} + \frac{3}{2} p_{i,N_y-2} - \frac{1}{3} p_{i,N_y-3} \right) \quad (\text{B.1.3d})$$

Extracting the boundary pressures from Equations (B.1.3a-d) and substituting in Equations (B.1.2a) and (B.1.2c), the second-order derivatives for the near-boundary nodes ($i=2$ and N_x-1 , $j=2$ and N_y-1) are derived as :

$$\left(\frac{\partial^2 p}{\partial x^2}\right)_{2,j} = \frac{2}{11\Delta x^2} \left[-3 \Delta x \left(\frac{\partial p}{\partial x}\right)_{1,j} - 2 p_{2,j} + p_{3,j} + p_{4,j} \right] \quad (\text{B.1.4a})$$

$$\left(\frac{\partial^2 p}{\partial x^2}\right)_{N_x-1,j} = \frac{2}{11\Delta x^2} \left[3 \Delta x \left(\frac{\partial p}{\partial x}\right)_{N_x,j} - 2 p_{N_x-2,j} + p_{N_x-3,j} + p_{N_x-4,j} \right] \quad (\text{B.1.4b})$$

$$\left(\frac{\partial^2 p}{\partial y^2}\right)_{i,2} = \frac{2}{11\Delta y^2} \left[-3 \Delta y \left(\frac{\partial p}{\partial y}\right)_{i,1} - 2 p_{i,2} + p_{i,3} + p_{i,4} \right] \quad (\text{B.1.4c})$$

$$\left(\frac{\partial^2 p}{\partial y^2}\right)_{i,N_y-1} = \frac{2}{11\Delta y^2} \left[3 \Delta y \left(\frac{\partial p}{\partial y}\right)_{i,N_y} - 2 p_{i,N_y-2} + p_{i,N_y-3} + p_{i,N_y-4} \right] \quad (\text{B.1.4d})$$

This summarizes the stencils used for IFDM and their near-boundary modifications. To prove the inconsistency in applying the Laplacian operator instead of the divergence of the gradient operator, we consider a fourth-order discretization of the gradient operator and a second-order formulation of the divergence operator resulting in the following stencil :

$$\begin{aligned}
(\nabla \cdot (\nabla p))_{ij} &= \frac{1}{24\Delta x^2} (-p_{i-3j} + 8p_{i-2j} + p_{i-1j} - 16p_{ij} + p_{i+1j} \\
&\quad + 8p_{i+2j} - p_{i+3j}) \\
&\quad + \frac{1}{24\Delta y^2} (-p_{ij-3} + 8p_{ij-2} + p_{ij-1} - 16p_{ij} + p_{ij+1} \\
&\quad + 8p_{ij+2} - p_{ij+3})
\end{aligned} \tag{B.1.5}$$

Subtracting Equation (B.1.5) from Equation (B.1.1a) results in the following inconsistency parameter, δ_p :

$$\begin{aligned}
(\delta_p)_{ij} &= (\nabla^2 p)_{ij} - (\nabla \cdot (\nabla p))_{ij} \\
(\delta_p)_{ij} &= \frac{1}{\Delta x^2} \left(\frac{1}{24} p_{i-3j} - \frac{5}{12} p_{i-2j} + \frac{5}{8} p_{i-1j} - \frac{2}{3} p_{ij} \right. \\
&\quad \left. + \frac{5}{8} p_{i+1j} - \frac{5}{12} p_{i+2j} + \frac{1}{24} p_{i+3j} \right) \\
&\quad + \frac{1}{\Delta y^2} \left(\frac{1}{24} p_{ij-3} - \frac{5}{12} p_{ij-2} + \frac{5}{8} p_{ij-1} - \frac{2}{3} p_{ij} \right. \\
&\quad \left. + \frac{5}{8} p_{ij+1} - \frac{5}{12} p_{ij+2} + \frac{1}{24} p_{ij+3} \right)
\end{aligned} \tag{B.1.6}$$

Such inconsistency in the discretization yields to the violation to the compatibility condition as discussed in Section 3.3.4.

B.2 Consistent Finite-Difference Methods

In CFDM1, the divergence and gradients operators are discretized using a second-order central finite-difference resulting in the following pressure-Poisson equation:

$$\begin{aligned}
\frac{1}{4\Delta x^2} (p_{i+2j} - 2p_{ij} + p_{i-2j}) + \frac{1}{4\Delta y^2} (p_{ij+2} - 2p_{ij} + p_{ij-2}) = \\
\frac{1}{2\Delta x\Delta y} (\tilde{u}_{i+1j} - \tilde{u}_{i-1j}) + \frac{1}{2\Delta x\Delta y} (\tilde{v}_{ij+1} - \tilde{v}_{ij-1})
\end{aligned} \tag{B.2.1}$$

for $i = 4$ to $Nx-2$ and $j = 4$ to $Ny-2$.

The near-boundary derivatives are determined from:

$$\left(\frac{\partial}{\partial x} \left(\frac{\partial p}{\partial x} \right) \right)_{2j} = \frac{1}{4\Delta x^2} (p_{4j} - p_{2j}) \tag{B.2.2a}$$

$$\left(\frac{\tilde{u}}{\partial x}\right)_{2j} = \frac{1}{2\Delta x} (-u_1^{n+1} + \tilde{u}_{3j}) \quad (\text{B.2.2b})$$

$$\begin{aligned} \left(\frac{\partial}{\partial x} \left(\frac{\partial p}{\partial x}\right)\right)_{3j} &= \frac{1}{4\Delta x^2} (p_{5j} - 2p_{3j} + p_{1j}) \\ &= \frac{1}{4\Delta x^2} \left[\frac{18}{11} p_{2j} - \frac{31}{11} p_{3j} + \frac{2}{11} p_{4j} + p_{5j} - \frac{6}{11} \Delta x \left(\frac{\partial p}{\partial x}\right)_{1j} \right] \end{aligned} \quad (\text{B.2.2c})$$

$$\left(\frac{\tilde{u}}{\partial x}\right)_{3j} = \frac{1}{2\Delta x} (-\tilde{u}_{2j} + \tilde{u}_{4j}) \quad (\text{B.2.2d})$$

$$\begin{aligned} \left(\frac{\partial}{\partial x} \left(\frac{\partial p}{\partial x}\right)\right)_{Nx-2j} &= \frac{1}{4\Delta x^2} (p_{Nx-4j} - 2p_{Nx-2j} + p_{Nxj}) \\ &= \frac{1}{4\Delta x^2} \left[p_{Nx-4j} + \frac{2}{11} p_{Nx-3j} - \frac{31}{11} p_{Nx-2j} + \frac{6}{11} \Delta x \left(\frac{\partial p}{\partial x}\right)_{Nxj} \right] \end{aligned} \quad (\text{B.2.2e})$$

$$\left(\frac{\tilde{u}}{\partial x}\right)_{Nx-2j} = \frac{1}{2\Delta x} (-\tilde{u}_{Nx-1j} + \tilde{u}_{Nx-3j}) \quad (\text{B.2.2f})$$

$$\left(\frac{\partial}{\partial x} \left(\frac{\partial p}{\partial x}\right)\right)_{Nx-1j} = \frac{1}{4\Delta x^2} (p_{Nx-1j} - p_{Nx-3j}) \quad (\text{B.2.2g})$$

$$\left(\frac{\tilde{u}}{\partial x}\right)_{Nx-1j} = \frac{1}{2\Delta x} (-\tilde{u}_{Nx-2j} + u_{Nxj}^{n+1}) \quad (\text{B.2.2h})$$

It is to be noted that the relations given by Equations (B.1.3a) and (B.1.3b) are applied in deriving Equations (B.2.2c) and (B.2.2e). Similar expressions are determined for the near-boundary values in the y-direction.

In CFDM2, the divergence operator is discretized using a second-order central finite-difference stencil and the gradient operator is formulated with a fourth-order central finite-difference scheme resulting in the following pressure-Poisson equation :

$$\begin{aligned} &\frac{1}{24\Delta x^2} [-p_{i-3j} + 8p_{i-2j} + p_{i-1j} - 16p_{ij} + p_{i+1j} + 8p_{i+2j} - p_{i+3j}] \\ &+ \frac{1}{24\Delta y^2} [-p_{ij-3} + 8p_{ij-2} + p_{ij-1} - 16p_{ij} + p_{ij+1} + 8p_{ij+2} - p_{ij+3}] = \\ &\frac{1}{2\Delta t \Delta x} (\tilde{u}_{i+1j} - \tilde{u}_{i-1j}) + \frac{1}{2\Delta t \Delta y} (\tilde{v}_{ij+1} - \tilde{v}_{ij-1}) \end{aligned} \quad (\text{B.2.3})$$

for $i = 6$ to $Nx-5$ and $j = 6$ to $Ny-5$.

Due to the stencil size, a second-order accurate scheme for the pressure gradient is applied adjacent to the boundaries. The discretized divergences are similar to those in Equations (B.2.2); while the near-boundary pressure derivatives are determined from :

$$\left(\frac{\partial}{\partial x}\left(\frac{\partial p}{\partial x}\right)\right)_{2,j} = \frac{1}{4\Delta x^2}(-p_{2j} + p_{4j}) \quad (\text{B.2.4a})$$

$$\begin{aligned} \left(\frac{\partial}{\partial x}\left(\frac{\partial p}{\partial x}\right)\right)_{3,j} &= \frac{1}{4\Delta x^2}(p_{1j} - 2p_{3j} + p_{5j}) \\ &= \frac{1}{4\Delta x^2}\left[\frac{18}{11}p_{2j} - \frac{31}{11}p_{3j} + \frac{2}{11}p_{4j} + p_{5j} - \frac{6}{11}\Delta x\left(\frac{\partial p}{\partial x}\right)_{1j}\right] \end{aligned} \quad (\text{B.2.4b})$$

$$\left(\frac{\partial}{\partial x}\left(\frac{\partial p}{\partial x}\right)\right)_{4,j} = \frac{1}{24\Delta x^2}(6p_{2j} + p_{3j} - 14p_{4j} + 8p_{6j} - p_{7j}) \quad (\text{B.2.4c})$$

$$\left(\frac{\partial}{\partial x}\left(\frac{\partial p}{\partial x}\right)\right)_{5,j} = \frac{1}{24\Delta x^2}(6p_{3j} + p_{4j} - 14p_{5j} + 8p_{7j} - p_{8j}) \quad (\text{B.2.4d})$$

$$\begin{aligned} \left(\frac{\partial}{\partial x}\left(\frac{\partial p}{\partial x}\right)\right)_{Nx-4,j} &= \frac{1}{24\Delta x^2}(-p_{Nx-7j} + 8p_{Nx-6j} - 14p_{Nx-4j} \\ &\quad + p_{Nx-3j} + 6p_{Nx-2j}) \end{aligned} \quad (\text{B.2.4e})$$

$$\begin{aligned} \left(\frac{\partial}{\partial x}\left(\frac{\partial p}{\partial x}\right)\right)_{Nx-3,j} &= \frac{1}{24\Delta x^2}(-p_{Nx-6j} + 8p_{Nx-5j} - 14p_{Nx-3j} \\ &\quad + p_{Nx-2j} + 6p_{Nx-1j}) \end{aligned} \quad (\text{B.2.4f})$$

$$\begin{aligned} \left(\frac{\partial}{\partial x}\left(\frac{\partial p}{\partial x}\right)\right)_{Nx-2,j} &= \frac{1}{4\Delta x^2}(p_{Nx-4j} - 2p_{Nx-2j} + p_{Nxj}) \\ &= \frac{1}{4\Delta x^2}\left[p_{Nx-4j} + \frac{2}{11}p_{Nx-3j} - \frac{31}{11}p_{Nx-2j} + \frac{6}{11}\Delta x\left(\frac{\partial p}{\partial x}\right)_{Nxj}\right] \end{aligned} \quad (\text{B.2.4g})$$

$$\left(\frac{\partial}{\partial x}\left(\frac{\partial p}{\partial x}\right)\right)_{Nx-1,j} = \frac{1}{4\Delta x^2}(p_{Nx-1j} - p_{Nx-3j}) \quad (\text{B.2.4h})$$

Equations (B.2.4b) and (B.2.4g) are derived using the relations given by Equations (B.1.3a) and (B.1.3b). Similar expressions are applied for the y-component of the derivatives.

CFDM3 is assembled with a fourth-order formulation of the divergence and gradient operators yielding the following pressure-Poisson equation :

$$\begin{aligned}
& \frac{1}{144\Delta x^2} [p_{i-4,j} -16 p_{i-3,j} +64 p_{i-2,j} +16 p_{i-1,j} -130 p_{i,j} \\
& \quad +16 p_{i+1,j} +64 p_{i+2,j} -16 p_{i+3,j} + p_{i+4,j}] \\
& + \frac{1}{144\Delta y^2} [p_{i,j-4} -16 p_{i,j-3} +64 p_{i,j-2} +16 p_{i,j-1} -130 p_{i,j} \\
& \quad +16 p_{i,j+1} +64 p_{i,j+2} -16 p_{i,j+3} + p_{i,j+4}] \\
& = \frac{1}{12\Delta x} (\tilde{u}_{i-2,j} -8 \tilde{u}_{i-1,j} +8 \tilde{u}_{i+1,j} -\tilde{u}_{i+2,j}) \\
& + \frac{1}{12\Delta y} (\tilde{v}_{i,j-2} -8 \tilde{v}_{i,j-1} +8 \tilde{v}_{i,j+1} -\tilde{v}_{i,j+2})
\end{aligned} \tag{B.2.5}$$

for $i = 6$ to $Nx-5$ and $j = 6$ to $Ny-5$.

Due to the stencil size, a second-order accurate scheme is applied adjacent to the boundaries. The near-boundary derivatives are evaluated from :

$$\left(\frac{\partial}{\partial x} \left(\frac{\partial p}{\partial x} \right) \right)_{2,j} = \frac{1}{4\Delta x^2} (-p_{2,j} + p_{4,j}) \tag{B.2.6a}$$

$$\left(\frac{\partial \tilde{u}}{\partial x} \right)_{2,j} = \frac{1}{2\Delta x} (-u_1^{n+1} + \tilde{u}_{3,j}) \tag{B.2.6b}$$

$$\begin{aligned}
\left(\frac{\partial}{\partial x} \left(\frac{\partial p}{\partial x} \right) \right)_{3,j} &= \frac{1}{144\Delta x^2} (48 p_{1,j} + 8 p_{2,j} - 113 p_{3,j} + 8 p_{4,j} \\
&\quad + 64 p_{5,j} - 16 p_{6,j} + p_{7,j}) \\
&= \frac{1}{144\Delta x^2} \left[\frac{952}{11} p_{2,j} - \frac{1675}{11} p_{3,j} + \frac{184}{11} p_{4,j} \right. \\
&\quad \left. + 64 p_{5,j} - 16 p_{6,j} + p_{7,j} - \frac{288}{11} \Delta x \left(\frac{\partial p}{\partial x} \right)_{1,j} \right]
\end{aligned} \tag{B.2.6c}$$

$$\left(\frac{\partial \tilde{u}}{\partial x} \right)_{3,j} = \frac{1}{12\Delta x} (u_1^{n+1} - 8 \tilde{u}_{2,j} + 8 \tilde{u}_{4,j} - \tilde{u}_{5,j}) \tag{B.2.6d}$$

$$\begin{aligned}
\left(\frac{\partial}{\partial x} \left(\frac{\partial p}{\partial x} \right) \right)_{4,j} &= \frac{1}{144\Delta x^2} [-6 p_{1,j} + 48 p_{2,j} + 14 p_{3,j} - 113 p_{4,j} \\
&\quad + 8 p_{5,j} + 64 p_{6,j} - 16 p_{7,j} + p_{8,j}]
\end{aligned}$$

$$= \frac{1}{144\Delta x^2} \left[\frac{420}{11} p_{2j} + \frac{208}{11} p_{3j} - \frac{1255}{11} p_{4j} + 8 p_{5j} \right. \\ \left. + 64 p_{6j} - 16 p_{7j} + p_{8j} + \frac{36}{11} \Delta x \left(\frac{\partial p}{\partial x} \right)_{1j} \right] \quad (\text{B.2.6e})$$

$$\left(\frac{\partial}{\partial x} \left(\frac{\partial p}{\partial x} \right) \right)_{5j} = \frac{1}{144\Delta x^2} \left[-14 p_{2j} + 64 p_{3j} + 14 p_{4j} - 129 p_{5j} \right. \\ \left. + 16 p_{6j} + 64 p_{7j} - 16 p_{8j} + p_{9j} \right] \quad (\text{B.2.6f})$$

$$\left(\frac{\partial}{\partial x} \left(\frac{\partial p}{\partial x} \right) \right)_{Nx-4j} = \frac{1}{144\Delta x^2} \left[-14 p_{Nx-1j} + 64 p_{Nx-2j} + 14 p_{Nx-3j} - 129 p_{Nx-4j} \right. \\ \left. + 16 p_{Nx-5j} + 64 p_{Nx-6j} - 16 p_{Nx-7j} + p_{Nx-8j} \right] \quad (\text{B.2.6g})$$

$$\left(\frac{\partial}{\partial x} \left(\frac{\partial p}{\partial x} \right) \right)_{Nx-3j} = \frac{1}{144\Delta x^2} \left[\frac{420}{11} p_{Nx-1j} + \frac{208}{11} p_{Nx-2j} - \frac{1255}{11} p_{Nx-3j} \right. \\ \left. + 8 p_{Nx-4j} + 64 p_{Nx-5j} - 16 p_{Nx-6j} + p_{Nx-7j} + \frac{36}{11} \Delta x \left(\frac{\partial p}{\partial x} \right)_{Nxj} \right] \\ (\text{B.2.6h})$$

$$\left(\frac{\partial}{\partial x} \left(\frac{\partial p}{\partial x} \right) \right)_{Nx-2j} = \frac{1}{144\Delta x^2} \left[\frac{952}{11} p_{Nx-1j} - \frac{1675}{11} p_{Nx-2j} + \frac{184}{11} p_{Nx-3j} \right. \\ \left. + 64 p_{Nx-4j} - 16 p_{Nx-5j} + p_{Nx-6j} - \frac{288}{11} \Delta x \left(\frac{\partial p}{\partial x} \right)_{Nxj} \right] \quad (\text{B.2.6i})$$

$$\left(\frac{\partial \tilde{u}}{\partial x} \right)_{Nx-2j} = \frac{1}{12\Delta x} (\tilde{u}_{Nx-4j} - 8 \tilde{u}_{Nx-3j} + 8 \tilde{u}_{Nx-1j} - u_{Nxj}^{n+1}) \quad (\text{B.2.6j})$$

$$\left(\frac{\partial}{\partial x} \left(\frac{\partial p}{\partial x} \right) \right)_{Nx-1j} = \frac{1}{4\Delta x^2} (p_{Nx-1j} - p_{Nx-3j}) \quad (\text{B.2.6k})$$

$$\left(\frac{\partial \tilde{u}}{\partial x} \right)_{Nx-1j} = \frac{1}{2\Delta x} (-\tilde{u}_{Nx-2j} + u_{Nxj}^{n+1}) \quad (\text{B.2.6l})$$

Equations (B.2.6c), (B.2.4e), (B.2.4g) and (B.2.4h) are derived using the relations given by Equations (B.1.3) and (B.1.3b). Similar expressions are invoked for the y-component of the derivatives. It is observed that second-order finite-difference matrices D_{F2x} and D_{F2y} based on the CFDM2 and CFDM3 formulations have complex eigenvalues and eigenvectors which increased the work load during the computation stage of the pressure field. Further, due to the stencil formulation of these schemes, the pressure field will have high oscillations (or checker-board splitting).

B.3 Consistent Finite-Volume Methods

CFVM1 consists of a second-order finite-volume discretization of the divergence and gradients operators resulting in the following pressure-Poisson equation :

$$\begin{aligned} & \frac{1}{\Delta x_c \Delta x} (p_{i-1,j} - 2p_{i,j} + p_{i+1,j}) + \frac{1}{\Delta y_c \Delta y} (p_{i,j-1} - 2p_{i,j} + p_{i,j+1}) \\ &= \frac{1}{\Delta x \Delta x_c} ((\tilde{c}_x)_{i+1/2} - (\tilde{c}_x)_{i-1/2}) + \frac{1}{\Delta x \Delta y_c} ((\tilde{c}_y)_{j+1/2} - (\tilde{c}_y)_{j-1/2}) \end{aligned} \quad (B.3.1)$$

for $i = 3$ to N_x-2 and $j = 3$ to N_y-2 .

Adjacent to the boundaries, the following relations are imposed :

$$\left(\frac{\partial}{\partial x} \left(\frac{\partial p}{\partial x} \right) \right)_{2,j} = \frac{1}{\Delta x_c \Delta x} (p_{3,j} - p_{2,j}) \quad (B.3.2a)$$

$$\left(\frac{\partial \tilde{c}_x}{\partial x} \right)_{2,j} = \frac{1}{\Delta x_c} (-(c_x^{n+1})_{1,j} + (\tilde{c}_x)_{2+1/2,j}) \quad (B.3.2b)$$

$$\left(\frac{\partial}{\partial x} \left(\frac{\partial p}{\partial x} \right) \right)_{N_x-1,j} = \frac{1}{\Delta x_c \Delta x} (p_{N_x-2,j} - p_{N_x-1,j}) \quad (B.3.2c)$$

$$\left(\frac{\partial \tilde{c}_x}{\partial x} \right)_{N_x-1,j} = \frac{1}{\Delta x_c} (-(\tilde{c}_x)_{N_x-3/2,j} + (c_x^{n+1})_{N_x,j}) \quad (B.3.2d)$$

It is seen that no 'ad-hoc' boundary conditions are required for the pressure. Similar expressions can be written for the y-component of the operators.

In CFVM2, the divergence operator is discretized using a second-order finite-volume stencil and the gradient operator is formulated with a fourth-order central finite-volume scheme resulting in the following pressure-Poisson equation :

$$\begin{aligned} & \frac{1}{24 \Delta x_c \Delta x} [-p_{i-2,j} + 28p_{i-1,j} - 54p_{i,j} + 28p_{i+1,j} - p_{i+2,j}] \\ &+ \frac{1}{24 \Delta y_c \Delta y} [-p_{i,j-2} + 28p_{i,j-1} - 54p_{i,j} + 28p_{i,j+1} - p_{i,j+2}] \\ &= \frac{1}{\Delta x_c} ((\tilde{c}_x)_{i+1/2} - (\tilde{c}_x)_{i-1/2}) + \frac{1}{\Delta y_c} ((\tilde{c}_y)_{j+1/2} - (\tilde{c}_y)_{j-1/2}) \end{aligned} \quad (B.3.3)$$

for $i = 4$ to N_x-3 and $j = 4$ to N_y-3 .

Due to the stencil size limitation, a second-order accurate scheme is applied adjacent to the boundaries. The near-boundary derivatives are evaluated from :

$$\left(\frac{\partial}{\partial x} \left(\frac{\partial p}{\partial x} \right) \right)_{2j} = \frac{1}{\Delta x_c \Delta x} (p_{3j} - p_{2j}) \quad (\text{B.3.4a})$$

$$\left(\frac{\partial \tilde{c}_x}{\partial x} \right)_{2j} = \frac{1}{\Delta x_c} (-(c_x^{n+1})_{1j} + (\tilde{c}_x)_{2+1/2j}) \quad (\text{B.3.4b})$$

$$\left(\frac{\partial}{\partial x} \left(\frac{\partial p}{\partial x} \right) \right)_{3j} = \frac{1}{24 \Delta x_c \Delta x} (25 p_{2j} - 51 p_{3j} + 27 p_{4j} - p_{5j}) \quad (\text{B.3.4c})$$

$$\left(\frac{\partial}{\partial x} \left(\frac{\partial p}{\partial x} \right) \right)_{Nx-2j} = \frac{1}{24 \Delta x_c \Delta x} (-p_{Nx-4j} + 27 p_{Nx-3j} - 51 p_{Nx-2j} + 25 p_{Nx-1j}) \quad (\text{B.3.4d})$$

$$\left(\frac{\partial}{\partial x} \left(\frac{\partial p}{\partial x} \right) \right)_{Nx-1j} = \frac{1}{\Delta x_c \Delta x} (p_{Nx-2j} - p_{Nx-1j}) \quad (\text{B.3.4e})$$

$$\left(\frac{\partial \tilde{c}_x}{\partial x} \right)_{Nx-1j} = \frac{1}{\Delta x_c} (-(\tilde{c}_x)_{Nx-3/2j} + (c_x^{n+1})_{Nxj}) \quad (\text{B.3.4f})$$

Similarly to CFVM1, no *ad hoc* pressure boundary conditions are needed for this formulation.

CFVM3 is constructed with a fourth-order finite-volume discretization of the divergence and gradients operators giving the following pressure-Poisson equation :

$$\begin{aligned} & \frac{1}{576 \Delta x_c \Delta x} [p_{i-3j} - 54 p_{i-2j} + 783 p_{i-1j} - 1460 p_{ij} \\ & \quad + 783 p_{i+1j} - 54 p_{i+2j} + p_{i+3j}] \\ & + \frac{1}{576 \Delta y_c \Delta y} [p_{ij-3} - 54 p_{ij-2} + 783 p_{ij-1} - 1460 p_{ij} \\ & \quad + 783 p_{ij+1} - 54 p_{ij+2} + p_{ij+3}] \\ & = \frac{1}{24 \Delta x_c} [(\tilde{c}_x)_{i-3/2j} - 27 (\tilde{c}_x)_{i-1/2j} + 27 (\tilde{c}_x)_{i+1/2j} - (\tilde{c}_x)_{i+3/2j}] \\ & + \frac{1}{24 \Delta y_c} [(\tilde{c}_y)_{ij-3/2} - 27 (\tilde{c}_y)_{ij-1/2} + 27 (\tilde{c}_y)_{ij+1/2} - (\tilde{c}_y)_{ij+3/2}] \end{aligned} \quad (\text{B.3.5})$$

for $i = 5$ to $Nx-4$ and $j = 5$ to $Ny-4$.

Due to stencil size, a lower-order accurate discretization is formulated near the boundary :

$$\left(\frac{\partial}{\partial x} \left(\frac{\partial p}{\partial x} \right) \right)_{2,j} = \frac{1}{\Delta x_c \Delta x} (p_{3,j} - p_{2,j}) \quad (\text{B.3.6a})$$

$$\left(\frac{\partial \tilde{c}_x}{\partial x} \right)_{2,j} = \frac{1}{\Delta x_c} (-(c_x^{n+1})_{1,j} + (\tilde{c}_x)_{2+1/2,j}) \quad (\text{B.3.6b})$$

$$\left(\frac{\partial}{\partial x} \left(\frac{\partial p}{\partial x} \right) \right)_{3,j} = \frac{1}{24 \Delta x_c \Delta x} (25 p_{2,j} - 51 p_{3,j} + 27 p_{4,j} - p_{5,j}) \quad (\text{B.3.6c})$$

$$\left(\frac{\partial \tilde{c}_x}{\partial x} \right)_{3,j} = \frac{1}{\Delta x_c} (-(\tilde{c}_x)_{2+1/2,j} + (\tilde{c}_x)_{3+1/2,j}) \quad (\text{B.3.6d})$$

$$\begin{aligned} \left(\frac{\partial}{\partial x} \left(\frac{\partial p}{\partial x} \right) \right)_{4,j} &= \frac{1}{576 \Delta x_c \Delta x} (-51 p_{2,j} + 780 p_{3,j} - 1459 p_{4,j} \\ &\quad + 783 p_{5,j} - 54 p_{6,j} + p_{7,j}) \end{aligned} \quad (\text{B.3.6e})$$

$$\begin{aligned} \left(\frac{\partial}{\partial x} \left(\frac{\partial p}{\partial x} \right) \right)_{N_x-3,j} &= \frac{1}{576 \Delta x_c \Delta x} (p_{N_x-6,j} + 54 p_{N_x-5,j} + 783 p_{N_x-4,j} \\ &\quad - 1459 p_{N_x-3,j} + 780 p_{N_x-2,j} - 51 p_{N_x-1,j}) \end{aligned} \quad (\text{B.3.6f})$$

$$\begin{aligned} \left(\frac{\partial}{\partial x} \left(\frac{\partial p}{\partial x} \right) \right)_{N_x-2,j} &= \frac{1}{24 \Delta x_c \Delta x} (-p_{N_x-4,j} + 27 p_{N_x-3,j} \\ &\quad - 51 p_{N_x-2,j} + 25 p_{N_x-1,j}) \end{aligned} \quad (\text{B.3.6g})$$

$$\left(\frac{\partial}{\partial x} \left(\frac{\partial p}{\partial x} \right) \right)_{N_x-1,j} = \frac{1}{\Delta x_c \Delta x} (p_{N_x-2,j} - p_{N_x-1,j}) \quad (\text{B.3.6h})$$

$$\left(\frac{\partial \tilde{c}_x}{\partial x} \right)_{N_x-1,j} = \frac{1}{\Delta x_c} (-(\tilde{c}_x)_{N_x-3/2,j} + (c_x^{n+1})_{N_x,j}) \quad (\text{B.3.6i})$$

As a result of the finite-volume approach, no pressure boundary conditions are required. This summarizes the relations used to validate the various formulations.

Second-Order Finite-Difference Matrices

$$D_{F2x} = \frac{1}{\Delta x_c \Delta x} \times$$

[illegible]

(C.1)

$\frac{-1}{25}$	$\frac{1}{24}$	$\frac{27}{24}$	$\frac{-1}{24}$	0		0			
$\frac{-1}{24}$	$\frac{28}{24}$	$\frac{-54}{24}$	$\frac{28}{24}$	$\frac{-1}{24}$					
	$\frac{-1}{24}$	$\frac{28}{24}$	$\frac{-54}{24}$	$\frac{28}{24}$	$\frac{-1}{24}$				
				
					
						
0					$\frac{-1}{24}$	$\frac{28}{24}$	$\frac{-54}{24}$	$\frac{28}{24}$	$\frac{-1}{24}$
					0	$\frac{-1}{24}$	$\frac{27}{24}$	$\frac{-51}{24}$	$\frac{25}{24}$
							0	1	-1

(C.2)

APPENDIX D **Modifications of the Spatial Derivatives** **for Interior Obstacles**

To simulate interior obstacles inside the computational domain, the numerical discretization of spatial derivatives discussed in Sections 3.2 and 3.4 will require modifications in the vicinity of the obstacles. Obstacle shapes range from rectangular, square, ellipse, to circular geometries. Of these shapes, the baffle is a rectangular-shaped obstacle with an infinitesimal thickness. In the current finite-difference approach, the baffles are located midway between two grid points as shown in Figure D.1. The grid nodes upstream and downstream of the baffle are denoted by $ibaf$ and $ibaf+1$, respectively, and the grid node on the baffle is referred to as $ibaf+1/2$; the baffle extends in height from jbf to jbl . the M locations adjacent to the baffle(s). For a single baffle in the computational domain, these locations are $ibaf-1$, $ibaf$, $ibaf+1$ and $ibaf+2$ in the x -direction and extend from jbf to jbl in the y -direction (see Appendix D for definitions). M is calculated as :

$$M = 4 \times (jbl - jbf + 1) \quad (D.1)$$

The modifications to the stencils of the spatial derivatives discussed in Sections 3.2 and 3.3 are presented in this Appendix. The convective terms in the baffle vicinity are modified with fourth and fifth-order accurate discretizations depending on the size of the stencil available. The streamwise first-order derivatives on the upstream side of the baffle are written as:

$$\left(\frac{\partial \phi}{\partial x}\right)_{ibaf} = \frac{1}{\Delta x} \left(\frac{32}{35} \phi_{ibaf+1/2} - \frac{1}{6} \phi_{ibaf} - \phi_{ibaf-1} + \frac{3}{10} \phi_{ibaf-2} - \frac{1}{21} \phi_{ibaf-3} \right) \quad (D.2)$$

$$\begin{aligned} \left(\frac{\partial \phi}{\partial x}\right)_{ibaf-1} = \frac{1}{\Delta x} \left(-\frac{32}{105} \phi_{ibaf+1/2} + \phi_{ibaf} - \frac{1}{6} \phi_{ibaf-1} \right. \\ \left. - \frac{3}{5} \phi_{ibaf-2} + \frac{1}{14} \phi_{ibaf-3} \right) \end{aligned} \quad (D.3)$$

$$\left(\frac{\partial \phi}{\partial x}\right)_{ibaf-2} = \frac{1}{\Delta x} \left(\frac{128}{945} \phi_{ibaf+1/2} - \frac{5}{12} \phi_{ibaf} + \frac{10}{9} \phi_{ibaf-1} \right)$$

$$-\frac{2}{5} \phi_{ibaf-2} - \frac{10}{21} \phi_{ibaf-3} - \frac{5}{108} \phi_{ibaf-4} \Big) ; \text{ if } u_{ibaf-2} < 0 \quad (D.4)$$

$$\left(\frac{\partial \phi}{\partial x}\right)_{ibaf-2} = \frac{1}{120\Delta x} (-6 \phi_{ibaf} + 60 \phi_{ibaf-1} + 40 \phi_{ibaf-2} - 120 \phi_{ibaf-3} + 30 \phi_{ibaf-4} - 4 \phi_{ibaf-5}) ; \text{ if } u_{ibaf-2} > 0 \quad (D.5)$$

The streamwise first-order derivatives on the downstream side of the baffle are evaluated from the following relations :

$$\left(\frac{\partial \phi}{\partial x}\right)_{ibaf+1} = \frac{1}{\Delta x} \left(-\frac{32}{35} \phi_{ibaf+1/2} + \frac{1}{6} \phi_{ibaf+1} + \phi_{ibaf+2} - \frac{3}{10} \phi_{ibaf+3} + \frac{1}{21} \phi_{ibaf+4} \right) \quad (D.6)$$

$$\left(\frac{\partial \phi}{\partial x}\right)_{ibaf+2} = \frac{1}{\Delta x} \left(\frac{32}{105} \phi_{ibaf+1/2} - \phi_{ibaf+1} + \frac{1}{6} \phi_{ibaf+2} + \frac{3}{5} \phi_{ibaf+3} - \frac{1}{14} \phi_{ibaf+4} \right) \quad (D.7)$$

$$\left(\frac{\partial \phi}{\partial x}\right)_{ibaf+3} = \frac{1}{120\Delta x} (6 \phi_{ibaf+1} - 60 \phi_{ibaf+2} - 40 \phi_{ibaf+3} + 120 \phi_{ibaf+4} - 30 \phi_{ibaf+5} - 4 \phi_{ibaf+6}) ; \text{ if } u_{ibaf+3} < 0 \quad (D.8)$$

$$\left(\frac{\partial \phi}{\partial x}\right)_{ibaf+3} = \frac{1}{\Delta x} \left(-\frac{128}{945} \phi_{ibaf+1/2} + \frac{5}{12} \phi_{ibaf+1} - \frac{10}{9} \phi_{ibaf+2} + \frac{2}{5} \phi_{ibaf+3} + \frac{10}{21} \phi_{ibaf+4} + \frac{5}{108} \phi_{ibaf+5} \right) ; \text{ if } u_{ibaf+3} > 0 \quad (D.9)$$

The diffusive terms in the baffle vicinity ($i=ibaf-1, ibaf, ibaf+1, ibaf+2$) are discretized by a second-order unsymmetric stencil scheme as follows:

$$\left(\frac{\partial^2 \phi}{\partial x^2}\right)_{ibaf-1} = \frac{1}{\Delta x^2} (\phi_{ibaf-2} - \phi_{ibaf-1} + \phi_{ibaf}) \quad (D.10)$$

$$\left(\frac{\partial^2 \phi}{\partial x^2}\right)_{ibaf} = \frac{1}{5\Delta x^2} (16 \phi_{ibaf+1/2} - 25 \phi_{ibaf} + 10 \phi_{ibaf+1} - \phi_{ibaf+2}) \quad (D.11)$$

$$\left(\frac{\partial^2 \phi}{\partial x^2}\right)_{ibaf+1} = \frac{1}{5\Delta x^2} (16 \phi_{ibaf+1/2} - 25 \phi_{ibaf+1} + 10 \phi_{ibaf+2} - \phi_{ibaf+3}) \quad (D.12)$$

$$\left(\frac{\partial^2 \phi}{\partial x^2}\right)_{ibaf+2} = \frac{1}{\Delta x^2} (\phi_{ibaf+1} - 2 \phi_{ibaf+2} + \phi_{ibaf+3}) \quad (D.13)$$

In Equations (D.2-D.1.13), ϕ represents either the x -component velocity (u) or the y -component velocity (v), and $\phi_{ibaf+1/2}$ is set to zero.

For non-uniform grids, the x -components of the diffusion term, $\frac{\partial^2 \phi}{\partial x^2}$, in the near-baffle region ($i=ibaf-1, ibaf, ibaf+1, ibaf+2$) are modified with second-order accurate stencils as follows:

$$\begin{aligned} \left(\frac{\partial^2 \phi}{\partial x^2}\right)_{ibaf-1} &= \left(\frac{\partial^2 \xi}{\partial x^2}\right)_{ibaf-1} \left(\frac{\phi_{ibaf} - \phi_{ibaf-2}}{2\Delta \xi}\right) \\ &+ \left(\frac{\partial \xi}{\partial x}\right)_{ibaf-1}^2 \left(\frac{\phi_{ibaf-2} - \phi_{ibaf-1} + \phi_{ibaf}}{\Delta \xi^2}\right) \end{aligned} \quad (D.14)$$

$$\begin{aligned} \left(\frac{\partial^2 \phi}{\partial x^2}\right)_{ibaf} &= \left(\frac{\partial^2 \xi}{\partial x^2}\right)_{ibaf-1} \left(\frac{4 \phi_{ibaf+1/2} - 3 \phi_{ibaf} - \phi_{ibaf-1}}{3\Delta \xi}\right) \\ &+ \left(\frac{\partial \xi}{\partial x}\right)_{ibaf}^2 \left(\frac{16 \phi_{ibaf+1/2} - 25 \phi_{ibaf} + 10 \phi_{ibaf-1} - \phi_{ibaf-2}}{5\Delta \xi^2}\right) \end{aligned} \quad (D.15)$$

$$\begin{aligned} \left(\frac{\partial^2 \phi}{\partial x^2}\right)_{ibaf+1} &= \left(\frac{\partial^2 \xi}{\partial x^2}\right)_{ibaf+1} \left(\frac{-4 \phi_{ibaf+1/2} + 3 \phi_{ibaf+1} + \phi_{ibaf+2}}{3\Delta \xi}\right) \\ &+ \left(\frac{\partial \xi}{\partial x}\right)_{ibaf+1}^2 \left(\frac{16 \phi_{ibaf+1/2} - 25 \phi_{ibaf+1} + 10 \phi_{ibaf+2} - \phi_{ibaf+3}}{5\Delta \xi^2}\right) \end{aligned} \quad (D.16)$$

$$\begin{aligned} \left(\frac{\partial^2 \phi}{\partial x^2}\right)_{ibaf+2} &= \left(\frac{\partial^2 \xi}{\partial x^2}\right)_{ibaf+2} \left(\frac{\phi_{ibaf+3} - \phi_{ibaf+1}}{2\Delta \xi}\right) \\ &+ \left(\frac{\partial \xi}{\partial x}\right)_{ibaf+2}^2 \left(\frac{\phi_{ibaf+1} - 2 \phi_{ibaf+2} + \phi_{ibaf+3}}{\Delta \xi^2}\right) \end{aligned} \quad (D.17)$$

The streamwise pressure gradients in the baffle vicinity are modified with a second-order scheme :

$$\left(\frac{\partial p}{\partial x}\right)_{ibaf-1} = \frac{1}{2\Delta x} (-p_{ibaf-2} + p_{ibaf}) \quad (D.18)$$

$$\left(\frac{\partial p}{\partial x}\right)_{ibaf} = \frac{1}{2} \left(\frac{\partial p}{\partial x}\right)_{ibaf+1/2} + \frac{1}{2\Delta x} (p_{ibaf} - p_{ibaf-1}) \quad (D.1.14)$$

$$\left(\frac{\partial p}{\partial x}\right)_{ibaf+1} = \frac{1}{2} \left(\frac{\partial p}{\partial x}\right)_{ibaf+1/2} + \frac{1}{2\Delta x} (p_{ibaf+2} - p_{ibaf+1}) \quad (D.19)$$

$$\left(\frac{\partial p}{\partial x}\right)_{ibaf+2} = \frac{1}{2\Delta x} (-p_{ibaf+1} + p_{ibaf+3}) \quad (D.20)$$

$$\left(\frac{\partial p}{\partial x}\right)_{ibaf+1/2} = 0 \quad (D.21)$$

These modifications are incorporated in the computation of the intermediate velocity and the update procedure.

The modification to the pressure-Poisson equation in the presence of baffles will be presented for the Consistent Finite-Volume Method (see Section 3.3.3). The x -components of the cell face velocity, \tilde{c}_x , are evaluated in the near-baffle vicinity from:

$$(\tilde{c}_x)_{ibaf-1/2} = \frac{1}{2} (u_{ibaf-1} + u_{ibaf}) \quad (D.22)$$

$$(\tilde{c}_x)_{ibaf+1/2} = 0 \quad (D.23)$$

$$(\tilde{c}_x)_{ibaf+3/2} = \frac{1}{2} (u_{ibaf+1} + u_{ibaf+2}) \quad (D.24)$$

The x -component pressure gradients in the near-baffle region are formulated by :

$$\left(\frac{\partial p}{\partial x}\right)_{ibaf-1/2} = \frac{1}{\Delta x} (p_{ibaf} - p_{ibaf-1}) \quad (D.25)$$

$$\left(\frac{\partial p}{\partial x}\right)_{ibaf+1/2} = 0 \quad (D.26)$$

$$\left(\frac{\partial p}{\partial x}\right)_{ibaf+3/2} = \frac{1}{\Delta x} (p_{ibaf+2} - p_{ibaf+1}) \quad (D.27)$$

The term $\left(\frac{\partial \tilde{c}_x}{\partial x}\right)$ is evaluated with a second-order finite-volume approach near the baffle resulting:

$$\begin{aligned} \left(\frac{\partial c_x^{n+1}}{\partial x}\right)_{ibaf-1} &= \frac{(c_x^{n+1})_{ibaf-1/2} - (c_x^{n+1})_{ibaf-3/2}}{\Delta x_c} \\ &= \frac{(\tilde{c}_x)_{ibaf-1/2} - (\tilde{c}_x)_{ibaf-3/2}}{\Delta x_c} \\ &\quad - \frac{\Delta t}{24 \Delta x_c \Delta x} (-p_{ibaf-3} + 27 p_{ibaf-2} - 51 p_{ibaf-1} + 25 p_{ibaf}) \quad (D.28) \end{aligned}$$

$$\begin{aligned} \left(\frac{\partial c_x^{n+1}}{\partial x}\right)_{ibaf} &= \frac{(c_x^{n+1})_{ibaf+1/2} - (c_x^{n+1})_{ibaf-1/2}}{\Delta x_c} \\ &= \frac{-(\tilde{c}_x)_{ibaf-1/2}}{\Delta x_c} - \frac{\Delta t}{\Delta x_c \Delta x} (p_{ibaf} - p_{ibaf-1}) \quad (D.29) \end{aligned}$$

$$\begin{aligned} \left(\frac{\partial c_x^{n+1}}{\partial x}\right)_{ibaf+1} &= \frac{(c_x^{n+1})_{ibaf+3/2} - (c_x^{n+1})_{ibaf+1/2}}{\Delta x_c} \\ &= \frac{(\tilde{c}_x)_{ibaf+3/2}}{\Delta x_c} - \frac{\Delta t}{\Delta x_c \Delta x} (p_{ibaf+2} - p_{ibaf+1}) \quad (D.30) \end{aligned}$$

$$\begin{aligned} \left(\frac{\partial c_x^{n+1}}{\partial x}\right)_{ibaf+2} &= \frac{(c_x^{n+1})_{ibaf+5/2} - (c_x^{n+1})_{ibaf+3/2}}{\Delta x_c} \\ &= \frac{(\tilde{c}_x)_{ibaf+5/2} - (\tilde{c}_x)_{ibaf+3/2}}{\Delta x_c} \\ &\quad - \frac{\Delta t}{24 \Delta x_c \Delta x} (25 p_{ibaf+1} - 51 p_{ibaf+2} + 27 p_{ibaf+3} - p_{ibaf+4}) \quad (D.31) \end{aligned}$$

Since a unit perturbation is applied as a source term to determine the elements of the capacitance matrix, such source term along with all Neumann boundary conditions (or in the absence of pressure boundary conditions for CFVM) represents an ill-posed problem leading to a constant residual for the B -problem. Thus, the Neumann boundary conditions are modified on at least one of the boundaries of the computational domain with Dirichlet boundary conditions. This will alleviate the ill-posedness of the problem. For example, the y -component derivative of the cell face velocity is modified at N_y-1 as follows :

$$\begin{aligned}
\left(\frac{\partial c_y^{n+1}}{\partial y}\right)_{N_y-1} &= \frac{(c_y^{n+1})_{N_y} - (c_y^{n+1})_{N_y-3/2}}{\Delta y_c} \\
&= \frac{(c_y^{n+1})_{N_y} - (\tilde{c}_y)_{N_y-3/2}}{\Delta y_c} - \Delta x \left(\frac{\partial^2 p}{\partial y^2}\right)_{N_y-1} \\
&= \frac{(c_y^{n+1})_{N_y} - (\tilde{c}_y)_{N_y-3/2}}{\Delta y_c} - \frac{\Delta x}{\Delta y^2} (p_{N_y-2} - 2p_{N_y-1} + p_{N_y}) \quad (D.32)
\end{aligned}$$

where p_{N_y} is specified (say zero). This formulation will lead to a violation of the divergence condition for the near-boundary velocities; however, it is expected not to influence the velocity field inside the computational domain. This may be satisfied when the computational domain edges are located far from the wake region, for instance.

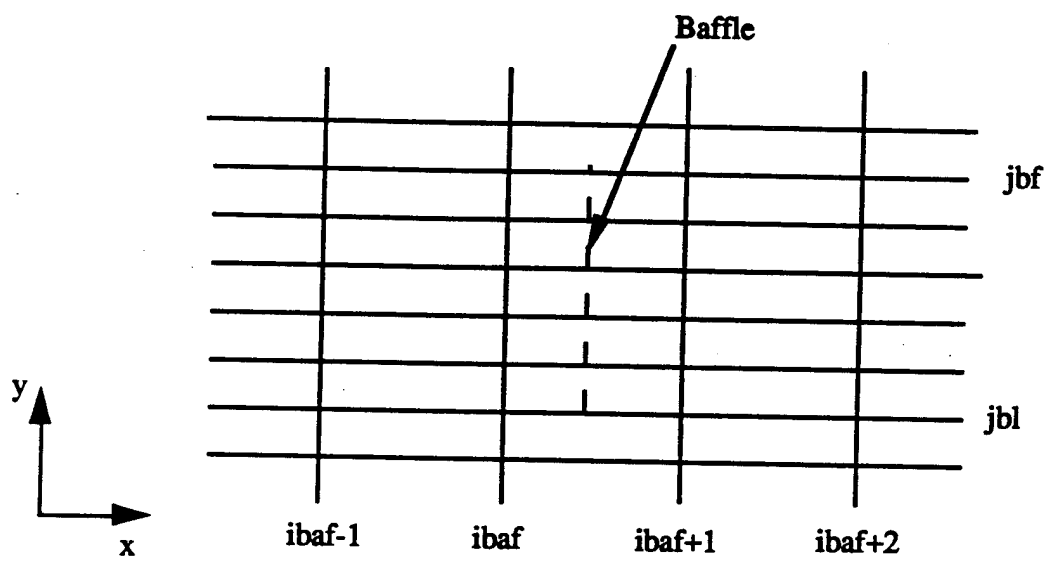


Figure D.1 Schematic of baffle position in collocated mesh

APPENDIX E

Capacitance Matrix Technique

In this appendix, we describe the Capacitance Matrix Technique algorithm following Schumann (1980). Further, we will prove that the solution P_2 to the B-problem in Equation (3.6.4d) is also the solution to the A-problem in Equation (3.6.1).

Consider a linear system $As = r$ where A is matrix of size $(N \times N)$. The matrix A has a structure such that the linear system can not be solved using direct elliptic solvers. However, a non-singular matrix B of size $(N \times N)$ can be constructed 'similar' to matrix A for which direct elliptic methods exist. B being 'similar' to A means that both matrices are equal except for a few rows ($M \ll N$). Taking M as the first rows, we can write A and B symbolically as :

$$A = \begin{array}{|c|} \hline A_1 \\ \hline A_2 \\ \hline \end{array}; B = \begin{array}{|c|} \hline B_1 \\ \hline A_2 \\ \hline \end{array} \quad \begin{array}{l} M \\ N-M \end{array} \quad (E.1)$$

where A_1 and B_1 are $(M \times N)$ matrices and A_2 is a $((N-M) \times N)$ matrix. Similarly, the source vector, r , is split as follows :

$$r = \begin{array}{|c|} \hline r_1 \\ \hline r_2 \\ \hline \end{array} \quad \begin{array}{l} M \\ N-M \end{array} \quad (E.2)$$

The capacitance matrix, C , of size $(M \times M)$ is precomputed from :

$$C = A_1 B^{-1} Q; Q = \begin{array}{|c|} \hline I \\ \hline 0 \\ \hline \end{array} \quad \begin{array}{l} M \\ N-M \end{array} \quad (E.3)$$

where I is a $(M \times M)$ unit matrix. As described in Equation (3.6.2.14), C can be determined by solving M B-problems and C^{-1} is calculated from library routines.

The following steps are applied to solve the A-problem:

- 1) first solve a B-problem :

$$B\bar{s} = r \quad (\text{E.4})$$

- 2) compute the residual vector q resulting from the first M rows of the A-problem :

$$q = A_1 \bar{s} - r_1 \quad (\text{E.5})$$

- 3) perturb the corresponding first M components of r with C^{-1} :

$$\bar{r} = r - QC^{-1}q \quad (\text{E.6})$$

- 4) solve the B-problem again with the perturbed source term :

$$Bs = \bar{r} \quad (\text{E.7})$$

The result vector s obtained by solving Equation (E.7) is also the solution to the A-problem. For proof, we first note that the lower part of Equation (E.7) certainly satisfies the lower part of the A-problem, namely, $A_2 s = r_2$ (see Equations E.1 and E.2). Therefore, it remains to show that the upper part of Equation (E.7) satisfies $A_1 s = r_1$. This proof proceeds as follows :

$$\begin{aligned} A_1 s & \stackrel{(\text{E.7})}{=} A_1 B^{-1} \bar{r} \stackrel{(\text{E.6})}{=} A_1 B^{-1} r - A_1 B^{-1} QC^{-1} q \\ & \stackrel{(\text{E.3})}{=} A_1 B^{-1} r - q \stackrel{(\text{E.5})}{=} A_1 B^{-1} r - A_1 \bar{s} + r_1 \\ & \stackrel{(\text{E.4})}{=} A_1 B^{-1} r - A_1 B^{-1} r + r_1 = r_1 \end{aligned} \quad (\text{E.8})$$

Therefore, the result obtained by solving Equation (E.7) satisfies the linear system for the A-problem.

VITA

Fady Michel Najjar was born on July 23, 1965 to Michel and Aida Najjar in Bechmizzine, a lovely town nestled in the Koura valley in Northern Lebanon. He and his sisters, Amal and Mira, grew up living in the Eastern suburb of Beirut, Horch Tabet. Although he was moving across the country during the civil war, he was able to attend College Notre-Dame de Jamhour and graduated in 1983 obtaining his Lebanese and French baccalaureates. He joined the Faculty of Engineering and Architecture at the American University of Beirut in October 1983 for his undergraduate education. He was an intern at Profabril in Lisbon, Portugal during the summer of 1986. In July 1987, he was awarded a Bachelor of Engineering degree in Mechanical Engineering with distinction. In January 1988, he joined the graduate program in the Department of Mechanical and Industrial Engineering at the University of Illinois at Urbana-Champaign. After holding a teaching assistantship during spring 1988, he began his research work with Professor Brian Thomas in fluid flow modeling for materials processing. He was awarded an outstanding research fellowship in 1989 and received his Master of Science degree in May 1990. He was the recipient of the Jerry Silver Award by the Iron and Steel Society in 1991 to recognize excellence in research at a master's level in the field of iron and steel. In June 1990, he joined the Ph.D. program under the guidance of Professor S.P. Vanka to conduct research in the area of fundamental fluid dynamics using high-performance computing. He is a member of Tau Beta Pi and Phi Kappa Phi. He is the recipient of a post-doctoral fellowship from the Division of Advanced Scientific Computing at the National Science Foundation and will join the National Center for Supercomputing Applications (NCSA) in June 1994.



OFFICE OF THE UNDER SECRETARY OF DEFENSE (ACQUISITION)
DEFENSE TECHNICAL INFORMATION CENTER
CAMERON STATION
ALEXANDRIA, VIRGINIA 22304-6145

IN REPLY
REFER TO

DTIC-OCC

SUBJECT: Distribution Statements on Technical Documents

TO: ONR/CODE 22
ATTN: AL DUMAS
ARLINGTON, VA 22217-5000

1. Reference: DoD Directive 5230.24, Distribution Statements on Technical Documents, 18 Mar 87.

2. The Defense Technical Information Center received the enclosed report (referenced below) which is not marked in accordance with the above reference.

"DIRECT NUMERICAL SIMULATIONS OF SEPARATED AND SEPARATED REATTACHING FLOWS ON MASSIVELY PARALLEL PROCESSING COMPUTERS"

N00014-92-j-1640.

3. We request the appropriate distribution statement be assigned and the report returned to DTIC within 5 working days.

4. Approved distribution statements are listed on the reverse of this letter. If you have any questions regarding these statements, call DTIC's Cataloging Branch, (703) 274-6837.

FOR THE ADMINISTRATOR:

1 Encl

for *for* *for*
GOPALAKRISHNAN NAIR
Chief, Cataloging Branch

FL-171
Jul 93

1995 1027 050
5661

DISTRIBUTION STATEMENT A:

APPROVED FOR PUBLIC RELEASE: DISTRIBUTION IS UNLIMITED

DISTRIBUTION STATEMENT B:

DISTRIBUTION AUTHORIZED TO U.S. GOVERNMENT AGENCIES ONLY;
(Indicate Reason and Date Below). OTHER REQUESTS FOR THIS DOCUMENT SHALL BE REFERRED
TO (Indicate Controlling DoD Office Below).

DISTRIBUTION STATEMENT C:

DISTRIBUTION AUTHORIZED TO U.S. GOVERNMENT AGENCIES AND THEIR CONTRACTORS;
(Indicate Reason and Date Below). OTHER REQUESTS FOR THIS DOCUMENT SHALL BE REFERRED
TO (Indicate Controlling DoD Office Below).

DISTRIBUTION STATEMENT D:

DISTRIBUTION AUTHORIZED TO DOD AND U.S. DOD CONTRACTORS ONLY; (Indicate Reason
and Date Below). OTHER REQUESTS SHALL BE REFERRED TO (Indicate Controlling DoD Office Below).

DISTRIBUTION STATEMENT E:

DISTRIBUTION AUTHORIZED TO DOD COMPONENTS ONLY; (Indicate Reason and Date Below).
OTHER REQUESTS SHALL BE REFERRED TO (Indicate Controlling DoD Office Below).

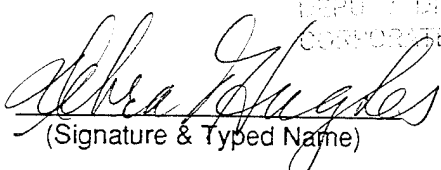
DISTRIBUTION STATEMENT F:

FURTHER DISSEMINATION ONLY AS DIRECTED BY (Indicate Controlling DoD Office and Date
Below) or HIGHER DOD AUTHORITY.

DISTRIBUTION STATEMENT X:

DISTRIBUTION AUTHORIZED TO U.S. GOVERNMENT AGENCIES AND PRIVATE INDIVIDUALS
OR ENTERPRISES ELIGIBLE TO OBTAIN EXPORT-CONTROLLED TECHNICAL DATA IN ACCORDANCE
WITH DOD DIRECTIVE 5230.25, WITHHOLDING OF UNCLASSIFIED TECHNICAL DATA FROM PUBLIC
DISCLOSURE, 6 Nov 1984 (Indicate date of determination). CONTROLLING DOD OFFICE IS (Indicate
Controlling DoD Office).

The cited documents has been reviewed by competent authority and the following distribution statement is
hereby authorized.

<u>A</u> (Statement)	OFFICE OF NAVAL RESEARCH CORPORATE PROGRAMS DIVISION ONR 553 550 NORTH QUINCY STREET ARLINGTON, VA 22217-5360	_____ (Controlling DoD Office Name)
_____ (Reason)	DEBRA T. HUGHES DEPUTY DIRECTOR CORPORATE PROGRAMS OFFICE	_____ (Controlling DoD Office Address, City, State, Zip)
 (Signature & Typed Name)	_____ (Assigning Office)	25 SEP 1995 _____ (Date Statement Assigned)